FUNDAMENTAL ATOMIC DATA AND PROTOTYPE TECHNIQUES FOR A GENERALISED COLLISIONAL-RADIATIVE MODEL OF MEDIUM-WEIGHT ELEMENTS IN FUSION AND ASTROPHYSICAL PLASMAS

by

Matthew M. Bluteau

Thesis
submitted to the Department of Physics
of the University of Strathclyde
for the Degree of Doctor of Philosophy

May 2019

Signature of Author

Date

Contents

List of Tables

List of Figures

Abstract

Quantifying the influence of heavy impurities upon plasma power balance, while seizing the opportunities they offer for passive spectroscopy, requires generalised collisional-radiative (GCR) population modelling to produce high-quality ionisation balances and cooling curves. ADAS provides a well-established framework of codes and data for the GCR modelling of light species and has been applied extensively to these scenarios. The extension of GCR modelling to medium and heavyweight elements within the ADAS framework imposes a number of updates and modifications. First, a lift of the ADAS baseline atomic structure and collision data is proposed using AUTOSTRUCTURE with the distorted-wave approximation, configuration sets selected by optimising on radiated power, and a novel, algorithmic strategy for optimising the radial scaling parameters. The truncation error of the configuration sets is bounded between an order of magnitude and 10%, while three figures of merit prove that the scaling parameter optimisation has eliminated the 20–30% structure error relative to the Cowan code. Second, fully relativistic, partially radiation-damped, Dirac R-matrix calculations of the W^{44+} ion are performed to showcase the challenges of generating fundamental data for heavy species. The calculations use a configuration interaction and close-coupling expansion that opens up the 3d-subshell, yielding previously unexplored transition arrays, [$3d^{10}4s^2$–$3d^9 4s^2 4f$] and [$3d^{10}4s^2$–$3d^9 4s4p4d$], which contribute 50% of the total radiated line power coefficient ($\mathcal{PLT}$) near the temperature of peak abundance. Third, collisional excitation by ion projectiles, not just electrons, must now be considered. A broad baseline of ion-impact excitation data is fulfilled by the restoration of a code, `a2iratbt`, that uses semi-classical, first-order perturbative equations with a limiting function, to prevent transition probability overestimates at intermediate energies, and a radial cutoff, which ensures the

infinite-energy Born limit is approached at high energies. The majority of the error in this baseline comes from the neglect of close coupling, accounting for $\approx 20\%$ in triplets and $< 5\%$ in doublets. Fourth, and most importantly, the resolution of GCR modelling must be moved to intermediate coupling. A prototype is built upon the LS-resolved analogue, predominantly by statistically splitting relevant quantities onto the intermediate-coupling manifold. Comparison to the *unresolved* fractional abundances in the literature reveal density effects of over an order of magnitude for the near neutrals, decreasing gradually towards complete agreement for the highly ionised stages. The total radiated power function and $\mathcal{PLT}$s showed better agreement, generally within 50% for the higher quality sources. Investigations into the effects of ion-impact excitation and resolution upon the GCR results are performed, showing that neither can be ignored. Also, a true set of metastable terms and levels is established. In the final analysis, the real impact of this new model can only be completely assessed by applying its results in subsequent plasma transport modelling.

Acknowledgments

Like in the film and acting business, no substantial research work is ever achieved without a great supporting cast. First and foremost, I would like to thank my primary supervisor, Dr. Martin O'Mullane. Your technical expertise with all things ADAS was essential at all points of my PhD work but in particular for the culminating project on GCR modelling. I confess at times I started to believe this piece might never reach a suitable stage of presentation, but your consistent video conversations and emails while I completed the work remotely from Canada helped me reach the finish line. My gratitude also extends to my secondary supervisor, Prof. Hugh Summers, who was the mastermind behind the overarching direction of my thesis work, and whose sage advice helped to right the ship more than a few times.

On a practical level, the work in this thesis would not have been possible without the funding provided to me by the National Science and Engineering Research Council (NSERC) of Canada and the Scottish University Physics Alliance (SUPA). I would also like to acknowledge my examination committee, Dr. Bengt Eliasson, Dr. Kevin Ronald, and Prof. Roger Hutton, all of whom contributed to an engaging and productive discussion of my thesis work.

The first eight months of my PhD were spent in Glasgow at the University of Strathclyde under the supervision of Prof. Nigel Badnell. I am grateful to you for sharing your vast technical knowledge in the area of electron-atom collisions and supporting me towards my first peer-reviewed journal article. Dr. Luis Fernández-Menchero was my office mate in the Colville building and provided a number of helpful theoretical explanations for some of my questions as a budding atomic physicist. I am also indebted to the High-Energy Laser Plasmas Group at Strathclyde who effectively adopted me because of the diminuitive size

of the ADAS group, aleviating the dreary Scottish winter with some much needed comraderie. In particular, Dr. Robbie Wilson deserves explicit mention for his friendship and assitance with the administrative task of submitting the first version of my thesis.

The remainder of my PhD was spent at the Culham Centre for Fusion Energy (CCFE), and this opened a new vista for collaborations. Dr. Stuart Henderson was an astute and patient teacher on many occasions, and the work we collaborated on, which figures prominently in this thesis, was engaging and rewarding. Dr. Alessandra Giunta made the trek from RAL Space on an number of occasions, and our side projects were enjoyable and valuable. My office mates created a relaxed yet stimulating environment in which to work, and my appreciation goes out to you all: Dr. Matthew Leyland, Dr. Jamie Beal, Dr. Alisdair Wynn, Nick Maasen, László Horváth, and Carmen Makepeace. In addition, the community of PhD students at CCFE was vibrant both academically and socially. Lunch time conversations, the weekly student meeting, and football sessions were events that undoubtedly provided me with a fuller PhD experience. There are too many peers to mention, but a few stand out: Dr. David Thomas, Dr. Sam Murphy-Sugrue (my fellow fearless leader of the CCFE Student Meetings), Dr. Jack Lovell, Tom Farley, Alistair McGann, Fred Thomas, Dr. Jonathan Shimwell, and Charlie Vincent.

Outside of the academic setting, I was fortunate to have a series of incredible roommates-cum-friends while I lived in Oxford: Anna, George, Claire, Pam, Bas, Koosje (Lindy Hop buddy!), Arnaud, Rose, Caitlin, Timo, and Claudia. Dr. Vincent Tobin deserves special mention as one of my closest friends, invaluable confidante, and morale supporter. Scott, Lynn, Mike, Brandon, and Mitch provided valuable support from across the pond, and it was always a highlight to visit them when I went home. The most welcome late addition to a PhD that I could have imagined was Katarina. You already well know my time in Oxford and life is infinitely richer for you, and the emotional support you provided helped me perservere through that final, extended home stretch. There truly ain't no mountain high enough. Thanks for the proofreading too!

To my parents, David and Heather, there is not much to say that I haven't said before, and you both already know none of this would have been possible

without you. Nontheless, I must profess my deepest and sincerest gratitude for all of the love, support, and guidance you have unreservedly provided to me over the past five years. It is hard to overstate your importance in words. My brothers, Chris and Will, played the important role of comic relief and were invaluable friends while I wrote up from home. Finally, a shout to my aunt, Suzanne, who was a clinch proofreader when I needed it most.

Previously Published Work

The content of Section 2.3.1 was previously published in Henderson S S et al. 2017 *Plasma Phys. Control. Fusion* **59(5)** 055010. The author of this thesis contributed to the discussion at group meetings, where that work was sequentially developed and guided. In particular, the author assisted in the understanding of how electron-exchange, spin-changing collision strengths affect the $\mathcal{PLT}$ at closed shells and why COWAN PWB calculations in *ic* can alleviate this deficit at higher effective ion charges. Furthermore, the author provided ion-impact excitation rate coefficients used to test the sensitivity of the configuration selection to these quantities, particularly at close shells.

The content of Sections 2.3.2 and 2.4 will soon be submitted to an appropriate journal, likely Atomic Data and Nuclear Data Tables (ADNDT), to house the radial scaling parameters that have been produced.

The content of Chapter 3 was previously published in Bluteau M et al. 2015 *J. Phys. B.* **48(195701)** 18. The author of this thesis was the primary author of that work. As such, this author executed the codes to perform the structure and collision calculations, analysed the data, created the plots, and wrote the manuscript under the guidance of the other two contributors to that paper.

To Anatole, Salvador, and Fergus, canines of days past

Chapter 1

Introduction

In recent years, the subject of heavier, high-Z_0 ions entering laboratory fusion plasmas has garnered increased attention from both plasma and atomic physics communities. This is primarily because a main obstacle that the International Thermonuclear Experimental Reactor (ITER) and future magnetic confinement fusion (MCF) devices must overcome is balancing the resilience of their plasma-facing components (PFCs) with the impact that species from the PFC materials will have upon the fusion plasma. At the moment, the high heat loads predicted for ITER favour more resilient PFC materials, which tend to be heavy metals. Tungsten ($Z_0 = 74$) is currently a top candidate, owing to its advantageous thermo-mechanical properties: a high melting point of 3 000 °C, a large heat-load capacity, a low sputtering rate [1], and a low rate of tritium co-deposition compared to carbon-based PFCs [2]. Indeed, ITER will now only use a full-tungsten divertor [3–5], a decision based on favourable trials of tungsten PFCs at the Joint European Torus (JET) [6, 7] and the Axially Symmetric Divertor Experiment Upgrade (ASDEX-U) [8, 9]. Molybdenum is another high-Z_0 species ($Z_0 = 42$) that has been used as a PFC material in tokamaks like Alcator C-Mod and NSTX-U, although it has a higher sputtering rate and so is a less likely candidate for future devices [10].

Thus, high-Z_0 elements like tungsten will invariably enter the fusion plasma by physical sputtering or evaporation [11], and the consequences can be mixed. With its large atomic number, tungsten has the potential to achieve high residual charge states—$z = Z_0 - N$ where N is the number of electrons—that can persist

into the core of tokamak plasmas. Because of the $(z+1)^4$ scaling of dipole, $\Delta n > 0$ radiative rates, tungsten ions have an increased propensity to undergo radiative transitions compared to low-Z_0 species in the same isoelectronic sequence. In other words, high-Z_0 impurity ions are efficient at radiating their energy and can greatly contribute to radiative power loss from the plasma: the coronal model yields a ${Z_0}^3$ scaling of the core power loss function [12]. The spatial region of this radiative power loss is decisive because a power imbalance in the core can readily lead to the loss of energy confinement and the quenching of all-important fusion reactions. Rough estimates [10] place the maximum tolerable concentration of tungsten in the core at $c_{\mathrm{W}}^{\mathrm{max}} = 5 \times 10^{-5}$. On the other hand, radiation power loss near the divertor is an essential process in neutralising the plasma of the divertor scrape-off layer (SOL), causing the main plasma to become effectively detached from the divertor targets and thus reducing heat loads on and impurity particle fluxes from the strike points, processes controlled by the degree of electron conduction and convection [13, 14]. The seeding of impurity species, such as argon and krypton, shows promising signs towards achieving these ends [12, 13], raising the prospect of medium-weight species being present in the plasma. A precise definition of "medium-weight" is provided in Section 1.1.

Significant modelling efforts are necessary to quantify and understand the impact of radiation losses due to these medium and heavy-weight species. Moreover, heavier species offer a rich landscape of possibilities for passive spectroscopy and plasma diagnostics. Both areas require some form of atomic population modelling, and Atomic Data Analysis Structure (ADAS) [15] is the preeminent framework used at fusion laboratories internationally. Within ADAS and more generally, the state-of-the-art approach is generalised collisional-radiative (GCR) modelling, which correctly treats the metastables of an atomic system as the dominant, time-varying populations. The total of the metastable populations for a particular atomic species approximates that atomic species' density, and these populations evolve on similar time scales to the plasma parameters. GCR modelling is applicable to finite-density, optically-thin plasmas found in both fusion and astrophysical conditions. The theoretical and practical basis for this modelling has already been laid out for lighter, low-Z_0 species [16], so this thesis instead focuses upon the modifications needed for extending GCR modelling to

medium and heavy species.

1.1 Resolution and Coupling in GCR Modelling

The most fundamental modification of GCR modelling relates to the resolution of the atomic states being modelled. For lighter species, it is known that the atomic populations are well described at LS term resolution, and this is what defines the classification of *light* elements used herein. Fine-structure splitting of the levels within a term is small, so collisions are able to establish local thermodynamic equilibrium (LTE) amongst these levels. Thus, even if J-resolved levels are required by spectroscopy, the population of the emitting level in a light species can be readily derived from its subsuming term using statistical balance. These assumptions hold for $1 < Z_0 \lessapprox 18$. However, as Z_0 increases, relativistic effects—viz. the spin-orbit interaction—cause the fine-structure splitting of the J-levels in a term to increase, making it increasingly less likely that LTE will be established amongst them. As a result, the level populations deviate from statistical balance and must be explicitly tracked in the population model. This separates *light* from *medium* elements, and as will be demonstrated in Chapter 5, this dividing line occurs at approximately argon.

A short aside on coupling schemes is needed to distinguish between *medium* and *heavy*-weight elements. From the perspective of atomic structure, J-resolved levels are not unique to a single angular momentum coupling scheme. Whether an LSJ-coupled basis set with the Breit-Pauli Hamiltonian is used or a jj-coupled basis set with the Dirac Hamiltonian, both will produce J levels. However, the resultant eigenstates will never be composed of a single basis state, and the allowance for eigenstates to be admixtures (i.e. complex linear combinations) of basis states is known as intermediate coupling (ic). Note that ic it is not a coupling scheme in the usual sense because it is not dictating how orbital momentum vector quantities should be combined. ic is the only physically accurate way to represent fine-structure levels, and so J resolution and ic are synonymous in a sense. Terms like "ic resolution" and "ic-resolved" are used as convenient misnomers throughout this thesis to indicate J resolution obtained through the ic scheme. Both medium and heavy-weight elements require ic, and although

classifications are somewhat arbitrary, *heavy* is used in this thesis to describe elements for which a fully-relativistic treatment involving jj-coupled basis states is required. An LSJ basis is composed from non-relativistic theory and, even with relativistic corrections, it will eventually become insufficient. The onset of heavy elements is around the lanthanides, so $Z_0 \gtrapprox 70$ is specified.

In the context of GCR modelling, a move to *ic* resolution involves much more than simply representing the metastable set, which includes the ground state in ADAS parlance, and the ordinary levels of the daughter ion as J levels.[1] For consistency, the parent metastables, J_ν, must share this resolution as they are the initial states for recombination and final states for ionisation. This has implications for the other resolutions used in the population model, shown in figure 1.1. Lower resolutions are used to include the contributions from more highly-excited states, but these too must be built upon the *ic*-resolved parent: $(J_\nu)nl$ for configuration average (ca) and $(J_\nu)n$ for Rydberg n-shell (ry). Consequently, the low-resolution population code in ADAS needs to be reworked because it operates with $(L_\nu S_\nu)nS$ states (bundle-nS). This task—denoted as Part 6 in figure 1.2—is not addressed in this thesis, but some more detailed comments for moving forward are presented in Section 6.1. Once the change in modelling resolution is achieved, there is the practical question of what constitutes the proper set of *ic*-resolved metastables upon which the model is built. Can this set of metastables be built from those at other resolutions—i.e. LS or ca metastable sets? Will the set of metastables be constant along an isoelectronic sequence? Some answers are provided in Chapter 5.

1.2 Modifications for Medium-Weight GCR

Many updates and modifications will be required to transition from the framework of light-weight GCR to that suitable for medium-weight elements and beyond. Figure 1.2 presents the primary conceptual blocks that are required for a *complete* implementation of medium and heavy-weight GCR modelling within ADAS, evincing the vast scale of a project that is clearly outside the remit of a

[1] Refer to Appendix C for the definitions of daughter and parent ions if this terminology is unfamiliar.

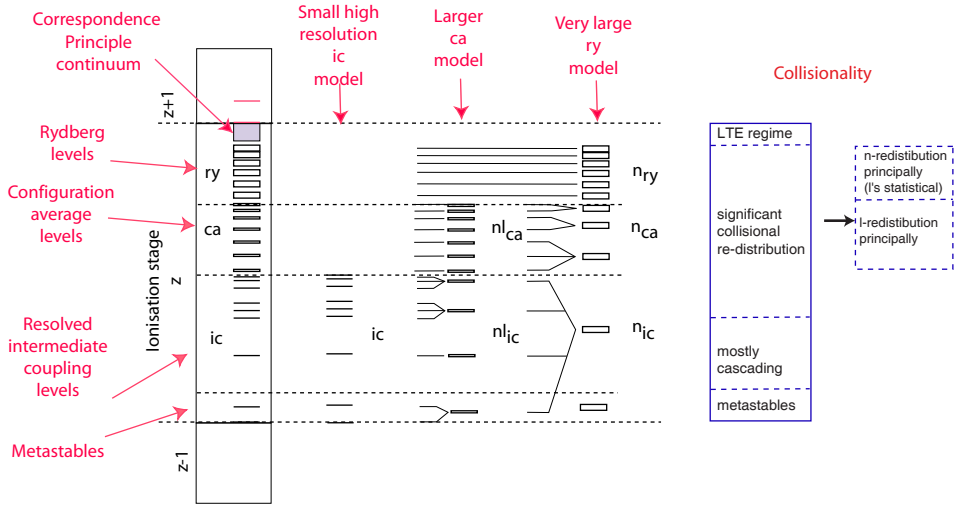

Figure 1.1: Partition of the levels of the atom into zones of collisionality and angular resolution. The diagram indicates bundled levels as narrow rectangles. Appropriate truncation of high levels at higher resolutions must be done to keep population calculations within computational bounds. With J_ν denoting the ic parent state of the $z+1$ ion, configuration average (ca) indicates states of the form $(J_\nu)nl$, and Rydberg n-shell (ry) indicates $(J_\nu)n$.

single thesis. Instead, the black typeface components will be treated in the context of a prototype to achieve some important steps towards the final objective.

Parts 1–5 in figure 1.2 express the essential need for fundamental atomic data in GCR modelling. Recombination and ionisation (Parts 4 and 5) are briefly treated in Chapter 5, but they are not the focus of this thesis. Also, Part 1 is not essential for a functioning GCR model, and it is left as a future task (see Section 6.1). Rather, atomic structure and collision data for medium and heavy-weight elements is prioritised. Part 2 handles electron-impact excitation (EIE) collision data for the low-lying, highly-resolved level set, of which there are two types. First, with the number of ionisation stages steadily increasing for each heavier element, a broad coverage of data is required, necessitating a baseline strategy that properly addresses the unique challenges associated with medium and heavy-weight species, namely relativistic effects and complex configuration interaction (CI) expansions. Chapter 2 details a lift to the present ADAS-EU baseline through novel techniques for configuration selection based on the optimisation of power coefficients and for atomic structure improvement via a radial scaling parameter (λ_{nl}) optimisation strategy based on freezing these parameters

for inner core closed shells. Both of these features are absent or incomplete in all previous baselines, but like the ADAS-EU baseline dataset, this lifted baseline uses AUTOSTRUCTURE (AUTOS) with the distorted wave (DW) approximation, a strategy that adequately handles relativistic effects to fairly high Z_0. Second, high-quality EIE collision data is to be preferred wherever possible, but as one moves to truly heavy elements, relativistic effects and CI selection become even more important and must be treated more carefully so these sophisticated and resource-intensive calculations remain tractable. Chapter 3 presents fully-relativistic, partially radiation damped, Dirac R-matrix calculations of the W^{44+} ion as an example of techniques and considerations required to treat these complex systems.

Part 3 in figure 1.2 raises another corollary of the move to *ic*-resolved population modelling: the need to include ion-impact excitation (IIE) collisions. It is well-known that IIE plays a central role in establishing the collisional LTE within LS terms but, because populations can be yielded by statistical balance assumptions, there is no need to include IIE collisions in the model. However, with the disruption of statistical balance and tracking of *ic* levels described above for medium and heavy-weight elements, these collisions must now be explicitly included. Chapter 4 commences the exploration of the parameter space where IIE is relevant from the perspective of atomic physics. In particular, it is the fine-structure, electric-quadrupole ($E2$) transitions within metastable terms that are most pertinent for population modelling. The chapter goes on to establish the theoretical and practical foundation for a baseline quality code, `a2iratbt`, for generating IIE data. It uses a semi-classical, first-order perturbative (SC-1) method with high energy and transition probability cutoffs and is shown to compare well with other methods from the literature. The parameter space for IIE is refined in Chapter 5 through population modelling, and the prospect of different ion projectiles is raised. For experimental fusion reactors, a variety of fuel ions and low-Z_0 impurities are candidates for inducing IIE. The bare nuclei of hydrogen (H), deuterium (D), tritium (T), and helium (He) are the primary fuel and ash ions present in tokamak plasmas, called protons, deuterons, tritons, and α-particles respectively. The relevant ions of impurity species will depend on the device, but beryllium, carbon, nitrogen, and neon are typically present at

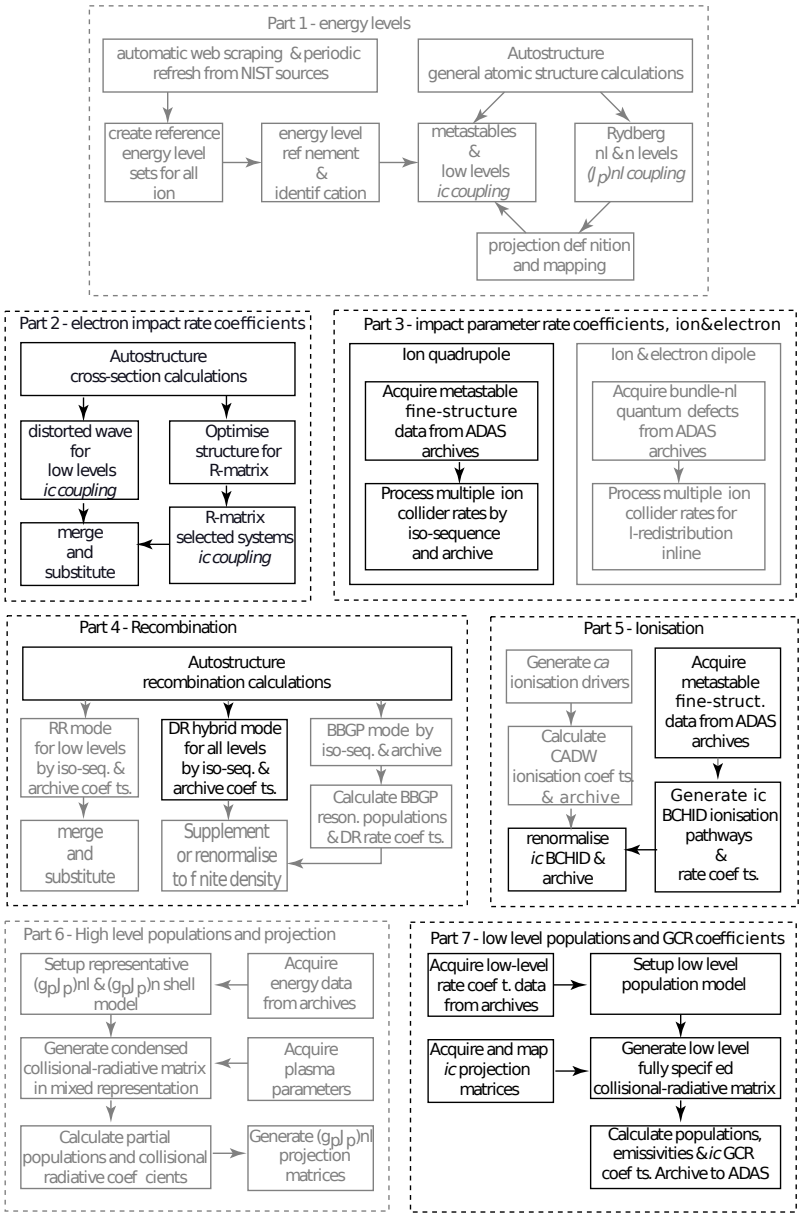

Figure 1.2: Schematic of principal code blocks for medium and heavy-weight GCR. The grey font color denotes segments that will not be treated in this thesis, and vice versa for the black font. Part 1 addresses the need for experimentally measured atomic energy levels wherever possible, something more relevant for spectroscopic purposes. Parts 2–5 address the primary atomic processes that connect the levels of the population model in finite-density, optically thin plasmas. Note that Part 3 represents the production of both IIE and EIE data using a semi-classical, impact-parameter method because EIE is also relevant to the dipole, l-redistributive transitions amongst highly-excited states. Parts 6 and 7 handle the population model at the two required coupling resolutions.

significant concentrations. In astrophysics, only proton projectiles are relevant.

Above all, the main thrust of this thesis is the elaboration of a prototype for *ic*-resolved GCR that pulls together all of the pieces from figure 1.2 in an approximate manner and allows Part 7 to be implemented. The parts of figure 1.2 that have not been directly treated in this thesis (grey font) can either be safely neglected with this prototype (Part 1, subtopics of Parts 4 and 5) or have been been incorporated in an approximate manner (Part 6). This, in turn, facilitates a quick and accurate validation of the novel components involved in modelling medium-weight elements, particularly IIE and resolution effects, while avoiding the potential pitfalls of a complete implementation. Chapter 5 details this prototyping strategy and applies it to the case study of argon, producing the first *ic*-resolved ionisation balance to date.

Chapter 2

Baseline Atomic Data for Metastable and Low-lying Levels

2.1 Introduction and Motivation

The elementary unit of GCR modelling is the low-lying, highly resolved states of an atom and any processes connecting them, for it is the radiative emission from these levels that will yield the spectroscopically observed lines and also the majority contribution to the radiated power loss. Moreover, the metastable levels[1], which possess the majority populations of each atomic species and so dominate the ionisation balance calculations, will almost always be encapsulated in this set for the plasma conditions relevant to this thesis. The data needed to represent this elementary unit of atomic states and processes are eigenenergies, Einstein A coefficients (A_{ij} or A-values), and temperature-dependent effective collision strengths (Υ_{ij}), which are internally converted to rate coefficients ($q_{i\rightarrow j}$) in ADAS. These quantities are stored by the *adf04* file format. Necessarily, these data must be provided in the appropriate resolution to suit the physical scenario being modelled, a topic elaborated upon in Chapter 5. It has already been noted that moving to medium and heavy-weight species, $Z_0 > 18$, will require *ic* resolution in the population model itself, as opposed to the current framework that only accommodates LS. From a cursory perspective, this is not in itself difficult to achieve for this particular class of levels. Indeed, it has been

[1]Recall that metastables include the ground states for ADAS purposes.

known for many years that *ic* is required for spectroscopic comparisons even for some light elements, and so a large portion of existing data and codes satisfy this requirement to a partial degree. Rather, it is the objective of complete coverage that proves troublesome: ADAS seeks to provide the capability of modelling arbitrary ions or groups of ions. This entails a vast breadth of data given the number of elements in the periodic table and all of their respective ionization stages.

Ideally, the source of all required quantities would be experimental observation, and the largest repository is the National Institute of Standards and Technology (NIST) Atomic Spectra Database.[2] Although an invaluable and quite extensive resource, NIST falls well short of universal coverage, and it does not supply collisional excitation rates. Consequently, atomic data must be sourced from theoretical calculations to fill the gaps. Great strides have been made in the field of computational atomic physics, and the accuracy of more sophisticated methods can approach that of observation. For example, the atomic structures produced by the multiconfigurational Hartree-Fock (MCHF) and multiconfigurational Dirac-Fock (MCDF) methods, to which the General-purpose Relativistic Atomic Structure Package (GRASP^0) belongs, can achieve incredible fidelity of energy levels and A-value to experiment, in many cases to less than a few percent error. Similarly for inelastic scattering, the R-matrix method and convergent close-coupling (CCC) method are the state of the art with similar levels of accuracy possible. But again, this option suffers from some ultimately fatal flaws. First, the codes that implement these methods generally require a high degree of expertise and human time investment to execute, which is demonstrated in Chapter 3. Second, the operational parameter space of the codes is not universal: convergence issues and catastrophic failure of certain approximations will inevitably crop up. Thirdly, even once the codes are running, the CPU time and physical memory required to complete the calculations can be enormous, on the order of supercomputers. On-the-fly execution is therefore out of the question, and broad data coverage is in the remit of international collaborations. Such organisations have existed, see the Iron Project [17], the Opacity Project [18, 19], and ADAS-EU [20], but even so the literature of high quality results is insufficient

[2] `https://www.nist.gov/pml/atomic-spectra-database`

for the current demands since there is no guarantee that results will exist for any particular ion.

This scattered and incomplete state of affairs demands a broad baseline of theoretical atomic data, albeit of lesser quality than the sources just described. The highest accuracy data are not always required depending upon the application. Spectroscopic comparisons and predictions will always require the highest quality data available, and the sources above should be drawn upon when possible, but radiated power studies, like [21] that aims to produce cooling factors for modelling ITER and the DEMOnstration Power Station (DEMO), are not so demanding. The accuracy of individual line wavelengths is not so influential, but the primary dipole transitions must still be within an acceptable tolerance. This is a pervasive theme in ADAS: suiting various characteristics of the data to the physical requirements of the situation, whether these characteristics be the coupling resolution or actual accuracy of energies and transition quantities. Also, if the baseline has been generated using a consistent method, then this internal consistency permits confidence in any interpolation or scaling of this data, making it more flexible and extensible than a patchwork of experimental and theoretical data.

2.1.1 Baseline Criteria

Having justified the utility of a baseline set of atomic data, the criteria for a good baseline must be specified. First, the primary criticism of other data sources up to this point has been their lack of coverage and consistency, so a baseline should provide for a broad range of ions and use a uniform method throughout. Second, the codes used to generate the baseline should be robust and user-friendly so that non-experts can produce their own data if it has not been done in advance. Third and related to the latter, the total time to run the baseline code for individual ions, which includes pre-processing and CPU time, must be on the order of a day so as to be both convenient for on-the-fly production and manageable for batch production. For modern codes, the paramount input for achieving accuracy is the selection of an appropriate set of electron configurations; however, this also tends to be the most time-consuming user task, so a strategy to automate or assist configuration selection is essential. Fourth, the baseline should be modular

in nature such that higher quality atomic data from aforementioned sources can be seamlessly substituted when it is available. This is more so a restriction upon the ADAS framework than the baseline data itself, but it affirms that the final outputs must conform to the *adf04* file format. Fifth and last, it is compulsory that the baseline exceed some threshold level of quality so that comparison with experiment is tenable, and this quality should be superior to any existing baseline. Quantifying the errors and thus the quality of atomic data is a notoriously challenging task, rife with ambiguities. ADAS contains some preliminary efforts towards categorising and standardising the consideration of errors in *adf04* data, but these have not been broadly implemented. The rudimentary convention in the atomic physics community is to compare the relative differences of energy levels, A-values, (effective) collision strengths between data sets. Therefore, the average relative differences achieved by comparing the present baseline to the more sparse high-quality data (experimental or theoretical) should be smaller than the average achieved by previous baselines, within ADAS or otherwise.

There are also specific baseline criteria due to the current goal of progressing towards *ic*-resolved GCR. Tautologically, the *adf04* files produced need to be in *ic* resolution and, as previously noted, this does not impose much of a restriction on modern structure and excitation codes. Additionally, moving to heavier species with large Z_0 means that relativistic effects must be considered in all aspects of the atomic problem. And last, because increasingly complex atoms will be encountered with increasing Z_0, the issue of configuration selection becomes even more troublesome and therefore essential to solve. A further consequence of this complexity is that the issue of metastable levels and terms will become even more prominent. The issue of IIE amongst the fine-structure levels of metastable terms is discussed at length in Chapter 4, but attention is warranted to the spin-changing transitions that typically connect metastable terms and levels. Although negligible for lower Z_0 species, these collision strengths can become substantial in relativistic systems—refer to the Collision Strength Approximations Paragraph of section 2.3.1.2 for an example of how this can influence the total radiated line power coefficient ($\mathcal{PLT}$).

2.1.2 Previous and Proposed Baselines

Previous baseline strategies already exist within ADAS. The theses of Whiteford [22] and Foster [23] describe the use of the Cowan Code, ADAS801 (COWAN) to generate baseline structure and collisional excitation data. The primary weaknesses of these baselines are that development of COWAN is effectively frozen and the plane-wave Born (PWB) method is used for calculating EIE quantities. PWB calculations are known to be inaccurate at low incident electron energies, and they do not produce spin-changing results because electron exchange is neglected. So, these baselines are of low quality, but the work of Foster introduces the important feature of configuration selection through the optimisation of promotion rules. This offers marked progress towards the complete automation of configuration selection, and an improved implementation is fully described in the coming section 2.3.1.

These baselines have been supplanted by the extensive work performed within the ADAS-EU Project [20]. In the third scientific theme report [24], a lifting of the baseline from COWAN with the PWB approximation to AUTOS with the recently added DW approximation [25] is described. The DW method for producing EIE data improves upon PWB through the use of partial wave resolution, the ability to enforce unitarity, and the provision of spin-changing transitions. Furthermore, AUTOS is still actively developed and, like COWAN, has many existing applications within ADAS, notably for state-selective dielectronic recombination data stored in the *adf09* format. However, there is a subtle shortcoming of this lift in that no optimisation of the atomic structure was performed. An example of this deficit is exposed in section 2.3.1, and a proposed solution via the optimisation of the λ_{nl} is prescribed in section 2.3.2.

So to recapitulate, a further universal lift of the ADAS *adf04* baseline is proposed along the following lines. The AUTOS code with its implementation of the DW approximation will be exploited to generate the required atomic structure and collision data. Some further information about the code along with comparison to the previous baseline code, COWAN, is provided in section 2.2.1. The main improvements effected by this baseline are described in section 2.3. Subsection 2.3.1 explains the enhanced and automated method of configuration selection based on the optimisation of promotion rules, and Subsection 2.3.2 spec-

ifies a novel strategy for a generic atomic structure optimisation through variation of the λ_{nl} in the TFDA potential (V_{TFDA}). A comprehensive evaluation of the λ_{nl} optimisation strategy is performed in section 2.4 using three newly defined figures of merit. In the end, it will be revealed that this proposed baseline fulfills all of the criteria outlined in section 2.1.1.

2.2 Baseline Codes

Although the use of AUTOS for the proposed baseline has been firmly justified and motivated, it is important to place the code in a broader context of other codes so that one can develop an awareness of the expected quality of the generated data. It was noted previously that the quantities involved in the GCR modelling of the low-lying levels derive from both atomic structure and collision calculations, each of which AUTOS can perform. However, the atomic structure calculation assumes a position of elevated significance because the collision calculation inherently depends upon it. The calculation of atomic structure underpins the entire description of radiating species within a plasma, and so it must be addressed first.

Table 2.1 provides a coarse, overarching comparison of some common structure codes but is by no means exhaustive. The codes presented can loosely be divided into two categories: those that use a nonrelativistic Hamiltonian with Breit-Pauli corrections (AUTOS and COWAN) and those that use a fully relativistic Dirac Hamiltonian—Hebrew University Lawerence Livermore Atomic Code (HULLAC), Flexible Atomic Code (FAC), and GRASP^0. This distinction becomes relevant at the extremes of the periodic table where heavy-ion cores are truly relativistic and jj-coupling is nearly perfect or, oppositely, where the Coulomb term dominates in light elements and LS-coupling is optimal. Even so, most species of interest sit inside these two endpoints, where the eigenstates have an *intermediate* behaviour matching neither a jj nor LS basis, hence intermediate coupling (ic). In this regime, it is the effects of CI that predominate, and so the configuration expansion included in the codes must be selected carefully. Accommodating multiple configurations is a minimum condition for any structure code, and AUTOS is no exception. Moreover, it is observed from table 2.1 that nearly

all codes can achieve a similar level of precision if the configuration expansion has been crafted to properly account for CI. So again, the primacy of configuration selection has been raised, further motivating the semi-automated selection procedure described in section 2.3.1.

Table 2.1: A comparative review of the popular atomic structure codes relevant to the present work, sourced from [20]. $\%E_i$ and $\%A_{j\to i}$ are the relative errors for energy eigenvalues and A-values, respectively.

Code	Method	Application	Precision ($\%E_i$, $\%A_{j\to i}$)	Comments
AUTOS	Multi-config, Breit-Pauli, Thomas-Fermi and Slater-type parametric potential	General + Auger rates + Born integrals	($\sim$ 2, $\sim$ 5), dependent on CI scope	Recently extended to multiply-occupied f-shells. Extended experience of use up to M-shell. Limited coupling scheme information. Specially tuned for dielectronic recombination and radiative recombination. Can separate term and level resolution calculations. A preferred code for ADAS.
COWAN	Multi-config, Breit-Pauli, Hartree-Fock potential	General + Auger rates + Born integrals	($\sim$ 2, $\sim$ 5), dependent on CI scope and tuning	Handles multiply-occupied f-states. Extended experience in many complex systems. Flexible coupling scheme information. Easy access to configuration average information. Executes level resolution calculation and averages to terms. A preferred code for ADAS
HULLAC	Multi-configuration, Dirac Hamiltonian; jj-coupled basis, Breit and QED	General, but extensive use with EBIT measurements	($\sim$ 2, $\sim$ 5), dependent on CI scope	Proprietary code package; structure code part matched to DW collision code and CR modelling.
FAC	Same as for HULLAC	General, but mostly astrophysics	($\sim$ 2, $\sim$ 5), dependent on CI scope and tuning	Public domain variant of HULLAC. Use and experience increasing.
GRASP^0	Multi-config, Dirac/Breit Hamiltonian; MCDF or parametric potential; various couplings and optimizations	General	($<$ 1, $<$ 3), with extensive core/valence CI	High grade code, but MCDF not always able to converge on potential. Tuned to DARC fully relativistic version of R-matrix method collision code. A preferred code for ADAS level 2 in relativistic region.

Atomic structure codes are also discriminated by how the radial factors in the basis set are determined. Forming these factors proves difficult because of the mutual electron repulsion contribution to the potential energy, $1/(|\boldsymbol{r_i}-\boldsymbol{r_j}|)$, in the radial equations and the consideration of electron exchange therein. AUTOS uses the TFDA potential ($V_{\rm TFDA}$) with optimisation of radial scaling parameters (λ_{nl}), while most other codes, including COWAN, use some variant of the Hartree-Fock (HF) method derived from the variational principle. A more detailed comparison of these methods will be given in section 2.2.1, but suffice it to say here that $V_{\rm TFDA}$ is an inferior approximation, and improving its default performance will be the objective of the λ_{nl} optimisation strategy in section 2.3.2. Nevertheless, this does not prevent AUTOS achieving precisions similar to other codes if sufficient

manual manipulation is performed. It should be noted that all structure codes will struggle to represent neutral and near-neutral species because the mutual electron repulsions are of a similar magnitude to the attractive potential that a single electron will experience. Numerically, this causes issues with many techniques.

Extensive experience has established that atomic structures produced by AUTOS can serve as a sound basis for subsequent collision calculations. Again, it is wise to situate the capabilities of AUTOS in the proper context of available collision codes, which is the purpose of table 2.2. The main distinguishing factor between the codes is whether they use a perturbative or close-coupling approach. The plane-wave Born (PWB) and distorted wave (DW) approaches are perturbative and so generally less precise but broader in scope. A deeper comparison of these perturbative methods will be given in the next section. In contrast, the CCC and time-dependent, close-coupling (TDCC) methods must solve the Schrödinger equation directly, using interaction potentials that couple intermediates states included in the close-coupling (CC) expansion. They can achieve impressive precision but are limited in their application to simple systems with few electrons. The R-matrix methods, one of which is used in Chapter 3, stand out for their ability to handle much larger atomic systems while still retaining the essential close-coupling treatment of resonances and achieving manageable computational loads. Of course, this comes at the slight cost of some precision compared to the fully close-coupled approaches, but the benefit of obtaining data for a much broader category of atomic systems far outweighs this. It is for these reasons that R-matrix data forms the majority of the high quality inputs for ADAS. However, these close-coupled variants require extensive user knowledge and attention, meaning they have not reached a level of automation appropriate for baseline mass production. It is of note that AUTOS provides the basis for a number of different collision methods, including R-matrix but itself only has the ability to perform PWB or DW type calculations.

In summation, AUTOS is a flexible and versatile code that can achieve modest accuracy in both structure and collision calculations relative to its contemporaries. It is therefore an ideal candidate to provide baseline data; however, the quality of this baseline relies upon the improvements described in section 2.3.

Table 2.2: A comparative review of the popular atomic collision codes relevant to the present work, sourced from [20]. $\%\Omega_{ij}$ is the estimated relative error of the collision strength (refer to Appendix A) produced by the given code or method. Within ADAS, "level 1" is used to refer to atomic data of baseline quality, and "level 2" for high-quality data.

Code	Method	Application	Precision ($\%\Omega_{ij}$)	Comments
AUTOS / COWAN	Born with modified threshold region	Low–moderately high z	(< 40)	Very general, stable and enabled by all structure codes with a free electron wave-function generator. No spin change. LS and ic coupling. Used for previous ADAS baselines.
CCC(-R)	convergent close-coupling (CCC); various codes	Low–moderately high z; 1–2 valence electrons	(< 5)	Highest precision, inefficient for very many energies and delimiting resonances. Limited ion scope. Currently being extended to Dirac relativistic.
DARC / DRMPS	Relativistic R-matrix method close-coupling / with pseudo-states	Low–high z	($\sim 5-10$)	Very high precision, tuned to GRASP structure and shared algebra. Resonances included. Recent pseudo-state extension adds heavy element near neutral scope and ionization capability. ic. Suitable for ADAS level 2 at low and high z.
HULLAC / FAC	Relativistic DW	Medium–high z	(~ 20)	ic. Includes spin change, but no resonances. Efficient algebra, and now used universally. Matched to HULLAC structure part.
RM / RMPS	R-matrix method close-coupling / with pseudo-states	Low–medium z	($\sim 5-10$)	LS-coupling. High precision, tuned to AUTOS and shared algebra. Resonances included. Pseudo-states allows ionization. Implemented for isoelectronic sequences with scripts. Parallelized versions. Suitable for ADAS level 1 and 2, medium-scale mass production.
RM-ICFT / RM-II	R-matrix method close-coupling with ic frame transformations / with ic inner region	Medium–moderately high z	($\sim 5-10$)	RM-ICFT as for RM, but extends to higher z ions in ic. Suitable for ADAS level 1 and 2 medium-scale mass production. RM-II gives improved higher z treatment. Suitable for ADAS level 2 and benchmarking of RM-ICFT.
RM-RD / DARC-RD	R-matrix method close-coupling with radiation damping	Medium–high z	($\sim 5-10$)	As for RM, but extends to high z ions with significant radiative or Auger branching of resonances. Suitable for ADAS level 1 and 2.
TDCC	Time-dependent, close-coupling	Low z; 1–2 valence electrons	(< 5)	Highest precision. Benchmark for low-z ionization. Used for ADAS level 2.
UCL-DW / JAJOM	LS DW with ic transformation	Medium–moderately high z	(~ 20)	Matched to AUTOS. Extension to ic via algebraic transformation. Includes spin change. No resonances. Can isolate calculation of cross sections starting with selected metastables. Falling out of use because it is inefficient in comparison with RM.

2.2.1 The Cowan Code versus AUTOSTRUCTURE

A more detailed comparison between COWAN and AUTOS is merited because these are the baseline codes of choice for ADAS. Later analysis will require a deep understanding of two. Table 2.3 outlines some important aspects of any structure calculation and provides the relevant details for each code, but for a complete reference see [25–29] for AUTOS and [30, 31] for COWAN.

The basis set is foundational to any structure or collision code since it determines the matrix elements of the Hamiltonian to be diagonalised and the coupling resolution of the final eigenstates. In the *ic* scheme relevant to AUTOS and COWAN, specifying the basis set can effectively be partitioned into two separate problems—angular and radial—since spin is trivial. The angular portion is a closed algebraic problem with exact solutions, and so differences in techniques matter little in this respect: the correct solution should be obtained regardless of how it was arrived at. So, whether it is the approach of AUTOS with Slater states and non-hierarchical vector coupling coefficient or that of COWAN with LS-coupled states and hierarchical Racah algebra, the result of the angular problem will be the same. Conversely, the radial portion requires approximate numerical solutions since the radial equations are not exactly soluble, so differences in techniques emerge here.

As noted in table 2.3 and [26], AUTOS obtains its radial factors by solving a homogeneous radial equation involving the TFDA potential (V_{TFDA}):

$$\left\{\frac{\mathrm{d}^2}{\mathrm{d}r^2} - \frac{l(l+1)}{r^2} + 2V_{\mathrm{TFDA}}(r) + \epsilon_{nl}\right\} P_{nl}(r) = 0 \tag{2.1}$$

subject to the boundary and normalization conditions,

$$P_{nl}(0) = 0 \tag{2.2}$$

$$\lim_{r\to\infty} P_{nl}(r) = 0 \tag{2.3}$$

$$\int_0^\infty P_{nl}(r)P_{n'l'} = \delta_{nn'}\delta_{ll'}. \tag{2.4}$$

V_{TFDA} is a central potential based on the assumption that the negative charge density of the electrons is distributed continuously and spherically symmetrically

within r_0, the boundary of the ion. The underlying details for the implementation used in AUTOS are given by Gombás [32]. This central potential approximately accounts for electron repulsion and exchange, and is determined from the combination of an expression for the mean potential produced by the N electrons and a factor derived from Poisson's equation and the charge density, $\varphi(x)$:

$$V_{\mathrm{TFDA}}(r) = \frac{Z_0}{r}\varphi(x) + \frac{Z_0 - N + 1}{r_0} - \frac{5\kappa_a^2}{12\kappa_k}, \tag{2.5}$$

where κ_a and κ_k are measures for the exchange and kinetic energy of the electron gas respectively, $(-N+1)/r_0$ is the potential due the other $N-1$ electrons at r_0, and $\varphi(x)$ is given by the differential equation,

$$\frac{\mathrm{d}^2\varphi(x)}{\mathrm{d}x^2} = \frac{1}{\sqrt{x}}\varphi(x)^{3/2}, \tag{2.6}$$

with $x = r/\mu$ and $\mu = 0.8853 \cdot {Z_0}^{-1/3}\,(N/(N-1))^{2/3}$. Its performance can be improved through the introduction of radial scaling parameters (λ_{nl}):

$$x = \frac{r}{\lambda_{nl}\mu}. \tag{2.7}$$

These λ_{nl} can then be varied to minimize a weighted sum of LS term energies, thus enacting a form of the variational principle. Term energies are used instead of level energies for expediency, and it is unlikely that working in this coarser resolution will invalidate the accuracy of the final levels relative to baseline requirements. AUTOS does have the capability of determining the λ_{nl} by instead minimising term or level energy differences with measured or high-quality theoretical results, but this is impractical for mass production because, as stated before, these results are sparse.

The variation of the λ_{nl} is necessary because V_{TFDA} only approximates the effects of electron correlation, and so these free parameters allow for any missing physics to be accounted. However, varying the scaling parameters for all orbitals at once frequently yields unphysical and poor results, especially for complex atoms. Section 2.3.2 presents a novel solution to this problem by algorithmically determining a set of optimised λ_{nl} for arbitrary electron configurations. The default setting for running AUTOS within ADAS is to set all of the relevant

λ_{nl} to unity. From the perspective of a single orbital, a λ_{nl} of one signifies that the assumptions underlying V_{TFDA} are exactly true: the electron in this orbital sees a potential that would be produced by a continuous and spherically symmetric distribution of the other $N-1$ electrons combined with the corrections for exchange and mutual repulsion. This physical situation is most accurate for orbitals of singly occupied valence shells or closed cores. It is well known that valence electrons tend to see a closed core as a spherically symmetric and uniform charge distribution, as guaranteed by the summation rules for the spherical harmonics that compose the angular factors in the basis set. The same applies to the electrons in the closed core themselves. Independently, as one moves to high Z_0 ($\gtrsim 36$), the effects of electron correlation become small perturbations and hence any error introduced by V_{TFDA} becomes marginal, meaning no variation of the λ_{nl} is needed. But this point is moot because the high-Z_0 limit is also where the relativistic effects dominate, and the non-relativistic or even semi-relativistic radial equation is insufficient.

In contrast, COWAN determines its radial factors from the HF equations, which are directly derived from the variational principle. Specifically, the code uses configuration average (*ca*) expressions for the energy and an iterative, self-consistent field (SCF) procedure to solve the resulting equations. The complete details are found in Chapter 7 of [31], but the important message is that the exchange interaction and mutual repulsion of electrons are inherent to this method. No approximations are made incorporating this physics. As a result, solutions of the HF equations in their various forms tend to achieve more highly accurate structures by default than the solutions of homogeneous equations. In this regard, AUTOS is slightly deficient compared to COWAN, but again, it will be shown in section 2.3.2 how this can be resolved with a new optimisation strategy for the λ_{nl} in AUTOS.

Moving to heavier atomic species, the consideration of relativistic effects in atomic structure becomes increasingly important. Both codes incorporate one-electron relativistic corrections, i.e. the mass-velocity and Darwin contributions, within the radial wave functions by including κ-averaged terms in the differential equations for the radial problem, where κ is the relativistic quantum number

defined by

$$\kappa = \begin{cases} l_i, & j = l_i - 1/2 \\ -l_i - 1, & j = l_i + 1/2. \end{cases} \tag{2.8}$$

This approximation allows the codes to retain the simpler algebra of the non-relativistic structure problem. Both codes include the one-body, spin-orbit term in their Breit-Pauli (BP) Hamiltonians, but AUTOS additionally includes the two-body terms as described in [28] and the post-diagonalization, Breit and QED energy corrections. The preceding reference also raises the subtle point that although these remaining Breit-Pauli corrections should, in theory, be evaluated using nonrelativistic wave functions, this is outweighed by the benefits of using the semi-relativistic, κ-averaged radial functions throughout the solution.

Further differences between the codes arise when considering the problem of collisional excitation, and it is here that the advantage of using AUTOS becomes most apparent. In its current state within ADAS, COWAN can only calculate collision quantities using the PWB approximation whereas AUTOS can perform calculations in both the PWB and DW approximations. Both approximations are made upon similar foundations [33–35]; the problem to be solved is stipulated by the nonrelativistic, time-independent Schrödinger equation for $N + 1$ electrons:

$$H_{N+1}\Psi = E\Psi, \tag{2.9}$$

where

$$H_{N+1} = \sum_{i=1}^{N+1} \left(-\frac{1}{2}\nabla_i^2 - \frac{Z_0}{r_i} \right) + \sum_{i>j=1}^{N+1} \frac{1}{r_{ij}} \tag{2.10}$$

and E is the total energy of the collision system.[3] This can be solved approximately with a truncated, antisymmetric expansion of the total wave function:

$$\Psi(\boldsymbol{X}_{N+1}) = \mathcal{A} \sum_{i}^{M} \Phi_i(\boldsymbol{X}_N) F_i(\boldsymbol{x}_{N+1}), \tag{2.11}$$

[3]Like with the structure problem, just because the nonrelativistic Schrödinger equation is being used does not mean a fully nonrelativistic Hamiltonian also needs to be used in the scattering problem. The BP Hamiltonian is equally well applied as an approximation for relativistic effects here. However, the additional terms do cause the subsequent mathematics to become slightly cluttered, so in the interest of clarity, it is the plain nonrelativistic Hamiltonian that has been used to demonstrate the various approximations to the scattering problem.

Table 2.3: Comparison of the atomic structure and collision attributes of AUTOS and COWAN. Recall that for magnetic transitions there is no monopole (M^0), so magnetic contributions only exist for $k \geq 2$ in the notation of this table.

Attribute	**AUTOS**	**COWAN**
basis set	non-determinantal Slater states composed of κ-averaged semi-relativistic orbitals (see text surrounding equation 2.8 about relativistic corrections)	κ-averaged semi-relativistic orbitals combined via coefficients of fractional parentage to make LS-coupled, antisymmetric basis functions
radial solution	Homogeneous radial equation incorporating V_{TFDA} with λ_{nl} optimised by minimising the weighted sum of term energies	HF equations derived from the variational principle and solved using an iterative, SCF procedure
angular solution	non-hierarchical uncoupled Slater state representation with subsequent coupling via vector-coupling coefficients defined by Eissner and Nussbaumer [26]	hierarchical Racah algebra angular momentum coupling scheme with factorisation
Hamiltonian	Breit-Pauli with one and two-body terms	Breit-Pauli with one-body spin-orbit term only
energy correction	Breit and QED	electron correlation
coupling schemes	ic and LS	ic and LS
multipoles, E^k/M^{k-1}	$k = 0, 1, \ldots, 6$	$k = 1, 2, 3$
scattering	PWB and DW	PWB; DW possible but not implemented in ADAS

where $\boldsymbol{x}_j \equiv \boldsymbol{r}_j\sigma_j$, $j = 1, \ldots, N+1$, represent the space and spin coordinates of the $N+1$ electrons; $\boldsymbol{X}_K \equiv \boldsymbol{x}_1, \ldots, \boldsymbol{x}_K$; Φ_i are the bound target eigenstates with energies E_i; F_i the eigenstate of the scattering electron with energy k_i^2/I_H; I_H is the ionisation potential of Hydrogen in whatever energy units other terms of the expression possess, a way of specifying that the final quantity is in atomic units; and $\mathcal{A}$ is the antisymmetrization operator that ensures each term in the expansion is antisymmetric with respect to the interchange of $\boldsymbol{x}_j$ for any pair of the $N+1$ electrons. As mentioned, the summation in 2.11 is over a truncated set of the bound target eigenstates, presumably obtained from a prior structure calculation, and in contrast, the exact solution would be over an infinite set of these states along with continuum target states. Plugging 2.11 into the Schrödinger equation 2.9 and forming the inner products with $\langle\Phi_i|$, one obtains a set of *coupled* second-order partial differential equations:

$$(\nabla_i^2 + k_i^2)F_i(\boldsymbol{x}_{N+1}) = \\ 2\sum_j \left[V_{ij}(\boldsymbol{x}_{N+1})F_j(\boldsymbol{x}_{N+1}) + \int K_{ij}(\boldsymbol{x}_{N+1}, \boldsymbol{x}'_{N+1})F_j(\boldsymbol{x}'_{N+1})\mathrm{d}\boldsymbol{x}'_{N+1}\right], \quad (2.12)$$

where

$$V_{ij}(\boldsymbol{x}_{N+1}) = \left\langle \Phi_i(\boldsymbol{X}_N) \left| \sum_{i=1}^{N} \frac{1}{r_{iN+1}} - \frac{Z_0}{r_{N+1}} \right| \Phi_j(\boldsymbol{X}_N) \right\rangle \quad (2.13)$$

defines the potential matrix and $K_{ij}(\boldsymbol{x}, \boldsymbol{x}')$ is the exchange kernel arising from the permutation component of $\mathcal{A}$ and accounts for the phenomenon of electron exchange in the collision. The task now is to solve 2.12, and it is at this point that the various approximations are made.

The Born approximation invokes the assumption that the scattering electron and target do not interact significantly, which is only valid at high collision energies or for lower-charged targets. As a result, the scattering electron can be represented throughout the collision by an incoming plane wave, hence the PWB as an abbreviation, and the target will be in its ground state. The equation for the total wave function 2.11 becomes

$$\Psi(\boldsymbol{X}_{N+1}) = \Phi_n(\boldsymbol{X}_N)e^{i\boldsymbol{k}_n\cdot\boldsymbol{r}_{N+1}}, \quad (2.14)$$

having utilised $F_n = e^{i\boldsymbol{k}_n \cdot \boldsymbol{r}_{N+1}}$ and $F_i = 0, i \neq n$. Significantly, there is no longer a sum of bound target eigenstates nor an antisymmetrization operation, so electron exchange and resonance contributions are not included. The exchange kernel term in equation 2.12 is therefore dropped, and upon substitution of 2.14, an expression for the differential cross section can be obtained:

$$\frac{\mathrm{d}\sigma_{ij}}{\mathrm{d}\Omega} = \frac{M^2 |\boldsymbol{k}_j|}{|\boldsymbol{k}_i|} \left| \int V_{ij}(\boldsymbol{x}_{N+1}) e^{i\boldsymbol{K}\cdot\boldsymbol{r}_{N+1}} \mathrm{d}\boldsymbol{x}_{N+1} \right|^2 , \tag{2.15}$$

where $\boldsymbol{k}_i$ and $\boldsymbol{k}_j$ are the vectorized wavenumbers of the incoming and outgoing electron, respectively, $\boldsymbol{K} = \boldsymbol{k}_i - \boldsymbol{k}_j$ is the momentum transfer, and Ω represents the solid angle instead of the collision strength like elsewhere in this thesis. The primary advantage of the PWB method is that the quantities it requires can easily be obtained from atomic structure calculations, making the determination of cross sections and collision strengths very efficient. But this comes at the cost of limited scope of accuracy and applicability: for arbitrary z, PWB calculations only have guaranteed validity at high collision energies, where resonances and electron exchange are unimportant. In fact, the PWB approximation becomes exact in the limit of infinite projectile energy, an important trait that will be used in the scattering calculations of Chapters 3 and 4. The valid range of scattering energies is somewhat extended approaching neutral targets because the assumption of no interaction between target and projectile is largely true. However, the improved performance of the collision calculation is moderated by the difficulties encountered in the structure calculation for neutral and near-neutral species. Since these structure issues tend to be more severe than the breakdown of the Born approximation for higher z, PWB calculations are generally of higher quality for species with a larger residual charge. Moreover, the PWB approximation cannot produce results for transitions that only proceed through electron exchange, such as spin-changing transitions under pure LSJ coupling: $\Delta S > 0$ is forbidden by selection rules. As will be discussed in section 2.3.1.2, the use of *ic* partially mitigates this limitation, but not generally.

In contrast, the DW approximation is obtained by replacing the electrostatic interaction terms of 2.10 with a mean central-field potential, which for AUTOS is V_{TFDA} from the structure calculation (equation 2.5). Following this modifica-

tion through, the V_{ij} term of equation 2.12 will become V_{TFDA}, thus losing its dependence on the radial coordinates of any atomic electrons. Consequently, the system of scattering equations specified by 2.12 become decoupled, allowing a set of independent radial equations for the free-electron wave functions to be isolated:

$$\left\{ \frac{\mathrm{d}^2}{\mathrm{d}r_{N+1}^2} - \frac{l(l+1)}{r_{N+1}^2} + 2V_{\mathrm{TFDA}}(r_{N+1}) + k_i^2 \right\} F_i(r_{N+1}) = 0. \tag{2.16}$$

This is nearly identical to equation 2.1 of the structure problem; however, $k_i^2 > 0$ is enforced whereas ϵ_{nl} can be positive (continuum state) or negative (bound state). Note that V_{TFDA} in the structure problem of equation 2.1 applies to $N-1$ atomic electrons while in equation 2.16 it applies to all N atomic target electrons and so will have a slightly different form. Ostensibly, the scattering problem is now solved since the scattering matrices should be determined by the asymptotic form of these free-electron wave functions; however, this only yields results for *elastic* scattering. Rather, one must use the Kohn variation principle [36, 37]:

$$K_{ii'}^{\mathrm{K}} = -\left\langle \Psi_i \left| H_{N+1} - E \right| \Psi_{i'} \right\rangle^t, \tag{2.17}$$

where t refers to trial functions, $\Psi_i = \mathcal{A}\Phi_i(\boldsymbol{X}_N)F_i(\boldsymbol{x}_{N+1})$ is one of the terms from the full expansion in 2.11, and the index i is said to denote the scattering channel, $i \equiv (\Gamma SL\pi)^{\mathscr{T}} kl = (SL\pi)^{\mathrm{T}}$. $\mathscr{T}$ indicates the target and T the total of the target coupled with the scattering electron, kl. As noted in footnote 3 above, the $N+1$ electron Hamiltonian can take various forms, and AUTOS uses a version of the BP Hamiltonian to include relativistic effects in this fundamentally nonrelativistic framework.

Because only *elastic* scattering effects are considered directly in the wave functions, the salient feature of DW approximation is that the *inelastic*, off-diagonal terms of the reactance K-matrix must be comparatively small—typically $1/2$ is an acceptable threshold above which the DW approximation should no longer be trusted or used. This is generally true for ions over a few times ionized. Making this assumption, the transmission matrix can be determined by neglecting terms quadratic in K,

$$T_{ii'} = \frac{-2iK_{ii'}^{\mathrm{K}}}{1 - iK_{ii'}^{\mathrm{K}}} \approx -2iK_{ii'}^{\mathrm{K}}, \tag{2.18}$$

and subsequently the collision strength determined:

$$\Omega_{ii'} = (2S+1)(2L+1)\left|T_{ii'}\right|^2 = (2S+1)(2L+1)4\left|K^{\mathrm{K}}_{ii'}\right|^2. \tag{2.19}$$

The main advantage of DW over PWB calculations is that electron exchange is included via antisymmetrization of the trial wave functions, and so transitions that are normally "forbidden" by selection rules become calculable—e.g. the spin-changing transitions mentioned above. This can prove decisive in the context of excited metastable states that cannot undergo radiative decay to the ground or have comparatively small A-values; introducing a collisional connection between such metastables and the ground can have a measurable impact upon the population distribution and GCR coefficients such as the $\mathcal{PLT}$, cf. section 2.3.1.

Like the PWB approximation, DW calculations neglect any coupling between scattering channels, so there are no resonance contributions to the collision strengths or cross sections. Resonances tend to influence rates only in the low-temperature domain, which can loosely be defined as lying well below the ionization potential of the particular ion under consideration. For fusion plasmas and any plasma in ionization equilibrium, the temperatures at which a given ion exists tend to peak above one half of the ionisation potential ($\chi^{(z)}$), usually outside the low-temperature regime in which resonances are important. Thus, DW results are expected to be suitably accurate for baseline purposes. Moreover, the DW approximation should track the background collision strength of any fully close-coupled method, and then resonances can be superposed, post hoc, by other techniques similar to a dielectronic recombination (DR) calculation. This is yet another advantage over PWB, which will not match the true background until the high energy regime.

As noted above, the DW approximation is only valid when the inelastic, off-diagonal elements of the K matrix are small compared to the elastic, diagonal ones. This is most problematic for neutral targets where the elastic collision strength is zero, and so the underlying assumption of the approximation necessarily collapses. Interestingly, this is the exact opposite scenario to that of the PWB approximation, in which the collision portion of the calculation actually performs better for neutral targets. However, the previous qualifying statements about the problem of structure calculations for near neutrals still stand, and this

is independent of any approximations made in the collision calculation. Therefore, any improvements garnered by using PWB over DW for neutral or near-neutral targets is likely marginal. Overall, it can be concluded that the DW approximation implemented in AUTOS marks a definite improvement over the PWB implementation of COWAN or AUTOS's own PWB.

2.3 Baseline Improvements

Up to this point, no improvements upon the previous baseline implemented by the third scientific theme of the ADAS-EU project [24] have been suggested (henceforth, ADAS-EU baseline). It too used AUTOS with its DW approximation to mass produce atomic structure and collisional excitation data in the *adf04* format. As detailed in the previous section 2.2.1, this offers a definite improvement over the baselines of Whiteford [22] and Foster [23] because these both use the PWB approximation to solve the inelastic scattering problem. However, the ADAS-EU baseline is deficient for two reasons.

First, although it does incorporate the configuration sets determined from the automated promotion-rule method of Foster, this method is itself incomplete and in some cases inaccurate. Crucially, the version of ADAS808 used by these previous baselines does not properly consider metastable configurations, and in some cases important metastables can be omitted because their inclusion can decrease the functional being maximised[4] even though they have an obvious influence upon the population balance. Therefore, the promotion-rule and $\mathcal{PLT}$ optimisation technique of Foster must be applied to all metastable configurations, and strategies must be developed to handle the merging of the configuration sets determined from the independent operation of the code upon these metastable bases. The details of this implementation are provided in section 2.3.1.

Second, no optimisation of the atomic structure within AUTOS is performed: the λ_{nl} defined in section 2.2.1 are all set to unity. In some cases, this can lead to unsatisfactory atomic structures, and the errors are propagated to other quantities. A concrete example is presented in the configuration selection section 2.3.1 where the atomic structure errors of AUTOS give rise to inaccurate $\mathcal{PLT}$ coeffi-

[4]The details of the optimisation procedure are provided in the following section 2.3.1.

cients; in fact, it is this consistent effect upon the $\mathcal{PLT}$ that spawned the drive to improve the atomic structure in an AUTOS baseline. Of course, AUTOS can internally vary all of the λ_{nl} and iteratively approach a solution by minimising the weighted sum of term energies; however, such a technique is not reliable and dilutes the correlations between important configurations. Therefore, a method to determine better default λ_{nl} is described in section 2.3.2.

2.3.1 Configuration Selection

It has been noted previously in sections 2.1.1 and 2.2 that the selection of the target electron configuration set is not only one of the most difficult inputs but also the primary determinant of accuracy in the *ic* regime. The difficulty of selecting an appropriate set of configurations inevitably derives from the fact that an atomic target is fully represented by an infinite number of excited configurations, both bound and continuum. Consequently, any finite set used in a computer code will necessarily introduce a truncation error. This can be partially alleviated by the introduction of pseudostate expansions to account for the continuum states, but the neglect of important bound configurations tends to be the largest error. The source of this error is twofold: first, configuration mixing is a pivotal factor in the atomic structure problem, but the major contributions usually come from small groupings of bound configurations, partitioned according to parity in this *ca* picture. Selecting the *correct* configurations can therefore capture the majority of the physics. Secondly, it is usually only a small set of bound configurations that dominate the contribution to the radiated power: these are configurations that possess strong radiative decay pathways to the ground and corresponding collisional excitation pathways populating them from the ground. Usually these two factors go hand in hand, but it is not obvious *ab initio* what this essential set of configurations involved in configuration mixing and large power emission will be. Thus, the imperative cannot be overstated for an automated algorithm to determine configuration sets that encapsulate the essential physics of the structure and collision problem.

The discussion above suggests a way forward for selecting the most impor-

tant bound configurations of an atomic target. It is the radiated power from an atomic species that provides an holistic grounding in observation because this measures not only the radiation from all possible transitions in the atom but also the population distribution of the excited states. Moreover, the quantification of radiative power loss from impurities has become a topic of concern for the development of ITER baseline scenarios and conceptual DEMO tokamak designs [38]. For example, the steady-state heat loads predicted for current baseline designs of ITER are well above tolerable limits for metallic divertors [39, 40], and the seeding of noble gases and nitrogen to produce radiative cooling is being explored for both DEMO and ITER [13, 14]. However, the negative effect of introducing these impurities is that the plasma core power balance is also affected, which in turn affects the fusion power yield. As a result, accurate theoretical cooling factors are needed; these are a combination of the ionisation balance, $f^{(z)}$, and the total radiated line power coefficient ($\mathcal{PLT}$). Although both invariably depend upon the resolved low-level set of the ionic species under consideration, it is the $\mathcal{PLT}$ that measures the power contribution due to collisional excitation and is directly dependent upon the energy level differences and A-values. Furthermore, the $\mathcal{PLT}$ is a quantity for which seeking an extremum makes sense and so can be optimised. Each configuration in the infinite set that represents an atom will make some positive contribution to the radiated power, however infinitesimally small that might be: the $\mathcal{PLT}$ will asymptotically approach a finite limit as more highly excited configurations are added because each of these will have less and less population. Therefore, determining the finite configuration set that maximises the $\mathcal{PLT}$ will achieve a representation that is closest to reality according to this metric. The same cannot be said about the ionization balance. The other coefficients needed to construct $f^{(z)}$ in the generalised, metastable-resolved picture are known collectively as GCR coefficients within ADAS, and they include ionisation and recombination components. The details of these quantities will be discussed further in the context of extending GCR modelling to *ic* resolution in Chapter 5. A consistent set of ionisation, recombination, and $\mathcal{PLT}$ coefficients for elements up to W have been generated by Pütterich using the techniques described in previous studies [41, 42], and it will provide the main comparison in the following sections. The $\mathcal{PLT}$s are generated using atomic data from COWAN,

and the configuration sets for each isoelectronic sequence are the same as those for the W isonuclear work. It is this assumption about the configuration sets that can be improved: in general, the important configurations for one ion of an isoelectronic sequence will not be the same as those for another ion.

One could conceivably also select configuration sets based upon observed spectral lines, and indeed this is the approach most detailed theoretical studies adopt. Although this may be necessary to achieve the accuracy required for the lines of interest, it can also bias the atomic structure to such a degree that it is no longer useful in more generic studies. Furthermore, such a technique is not easily automated and more prone to the omission of configurations that might not be observable but have a large impact via configuration mixing: refer to the work on W^{44+} in Chapter 3 and [43].

2.3.1.1 Selection Methodology

The selection of configurations is automated by varying a set of rules that define excited configurations to be built on an initial ground or metastable configuration. For example, the rules dictate the allowed change in the n and l quantum numbers when promoting electrons from valence and closed shells. A full specification of each rule is given in table 2.4 and discussed in detail by Foster [23]. The optimal set of rules for an initial metastable configuration, σ, is the one that maximises the value of the normalised $\mathcal{PLT}$ coefficient associated with this base configuration:

$$\mathcal{P}^{(z)}_{\mathrm{LT},\sigma} = \frac{N_\sigma}{N_{\mathrm{tot}}} \sum_{j>i} \Delta E_{ij} A_{j\to i} \mathscr{F}^{(\mathrm{exc})}_{j\sigma} [\mathrm{Wm}^3], \tag{2.20}$$

where i and j represent the lower and upper levels spanning the atomic energy levels defined in the electron configuration sets, ΔE_{ij} is the $j \to i$ transition energy, $A_{j\to i}$ is the spontaneous emission coefficient, $\mathscr{F}^{exc}_{j\sigma}$ is the component of the population of the jth level associated with excitation from level σ divided by the electron density, and N_σ and N_{total} represent the metastable/base and total population of the ion, respectively.

The code, called ADAS808 in ADAS, works as follows. First, as input, the code requires a reference electron temperature T_e and density N_e, the element and ionisation stage, and the driving configuration. T_e and N_e are set equal to the

Table 2.4: Promotion rules used to define configuration sets.

Rule	Description	Rule	Description
#1	Number of valence shells	#14	Promote closed shells (y/n)
#2	Max Δn (1st valence shell)	#15	Max Δn promotion (closed shell)
#3	Min Δn (1st valence shell)	#16	Min Δn promotion (closed shell)
#4	Max Δl (1st valence shell)	#17	Max Δl promotion (closed shell)
#5	Min Δl (1st valence shell)	#18	Min Δl promotion (closed shell)
#6	Max Δn (2nd valence shell)	#19	Add configs. of same complex (y/n)
#7	Min Δn (2nd valence shell)	#20	Shift valence electron to
#8	Max Δl (2nd valence shell)		unfilled 4f as extra ground
#9	Min Δl (2nd valence shell)	#21	Add all nl configurations of
#10	Max n (closed shell)		outer valence shell (y/n)
#11	Min n (closed shell)	#22	If #21 add opposite or both
#12	Max l (closed shell)		parities to valence shell
#13	Min l (closed shell)	#23	Cowan specific rules

ionisation potential $\chi^{(z)}$ of the ion and a density of 10^{13} cm^{-3} (typical of fusion plasmas), respectively. Here, $\chi^{(z)}$ is used as a substitute for the temperature of peak ion abundance, $T^{(\mathrm{pk.})}$. It is desirable to specify a temperature near $T^{(\mathrm{pk.})}$ for reasons explained in section 5.3.1.1: under ionisation equilibrium conditions, ions will only exist in substantial fractions near $T^{(\mathrm{pk.})}$, so this temperature is taken as the input to the population model. It is not possible to restrict the density in a similar manner, hence why a representative tokamak value must be selected. This deficiency is mitigated because N_e tends to be more spatially uniform, except near the divertor. Although the temperature of peak ion abundance is lower than $\chi^{(z)}$, optimising at $T_\mathrm{e} = \chi^{(z)}$ ensures that the $\mathcal{PLT}$ coefficient is in the temperature domain where it plateaus rather than where it has a large gradient.

Next, each rule is initialised to zero except for rule #1 and rules #10 to #13. The former is set to unity, while the code loops around different values for the latter, gradually opening each inner shell. Within each of these loops, the code progresses iteratively by sequentially performing a set of rule changes (defined in table 2.5). If the rule change produces a new valid set of configurations[5], then the $\mathcal{PLT}$ coefficient from equation 2.20 is determined. The atomic energy levels, spontaneous emission coefficients and collision strengths are calculated using COWAN in *ca* mode. After all rule changes have been attempted, the change producing the largest $\mathcal{PLT}$ coefficient is chosen as the reference case if it remains within a set of pre-defined level count, configuration count, and power threshold

[5]If COWAN fails to converge, then the given set of electron configurations are deemed invalid.

limits, so the calculation must also be performed in *ic* resolution at this point. For this analysis, a small configuration set (*cs*) is defined with a level count limit of 1000, configuration count limit of 30, and a power threshold of 0.001%. Large configuration sets (*cl*), which only adhere to the power threshold limit, are used to estimate the top-up corrections discussed in section 2.3.1.2. The optimisation process then continues using the new rule set as the initial conditions for the next set of changes.

Table 2.5: Rule change sequence during each iteration of the optimisation code ADAS808. # numbers correspond to the defined rules given in table 2.4.

Iteration 1						Iteration >1			
1:	#4=-1	6:	#6=1	10:	#17=-1	1:	#2=#2+1		#22=1
	#5=-1		#7=1		#18=-1	2:	#3=#3-1	15:	#21=1
2:	#2=1		#8=-1	11:	#17=1	3:	#4=#4+1		#22=0
	#3=1		#9=-1		#18=1	4:	#5=#5-1	16:	#20=1
	#4=-1	7:	#8=1	12:	#15=1	5:	#6=#6+1	17:	#2=#2+1
	#5=-1		#9=1		#16=1	6:	#7=#7-1		#4=#4+1
3:	#4=1	8:	#6=1		#17=1	7:	#8=#8+1	18:	#6=#6+1
	#5=1		#7=1		#18=1	8:	#9=#9-1		#8=#8+1
4:	#2=1		#8=1	13:	#21=1	9:	#15=#15+1	19:	#15=#15+1
	#3=1		#9=1		#22=1	10:	#16=#16-1		#17=#17+1
	#4=1	9:	#17=-1	14:	#21=1	11:	#17=#17+1		
	#5=1		#18=-1		#22=0	12:	#18=#18-1		
5:	#8=-1	10:	#15=1			13:	#19=1		
	#9=-1		#16=1			14:	#21=1		

The optimisation of the C-like Ar^{12+} and Ca-like Kr^{16+} configuration sets is shown in figure 2.1. The level and configuration count limits were relaxed allowing the code to run until either the change in the power was below 0.001% or until the rule changes produced no further valid configuration sets. A convergence in the $\mathcal{PLT}$ coefficient according to the 0.001% threshold is found for both ions despite the linear increase in levels at the end of each iteration. For less complex structure calculations, such as the C-like ground configuration, this convergence occurs within a total level count set by computational restraints. More complex ions with an open 3d-, 4d-, or 4f- shell, such as the Ca-like case, typically require a far higher number of levels before convergence in the $\mathcal{PLT}$ coefficient is achieved. Moreover, this convergent behaviour substantiates earlier claims that the majority of the atomic physics is encompassed by a set of lower-lying configurations/levels.

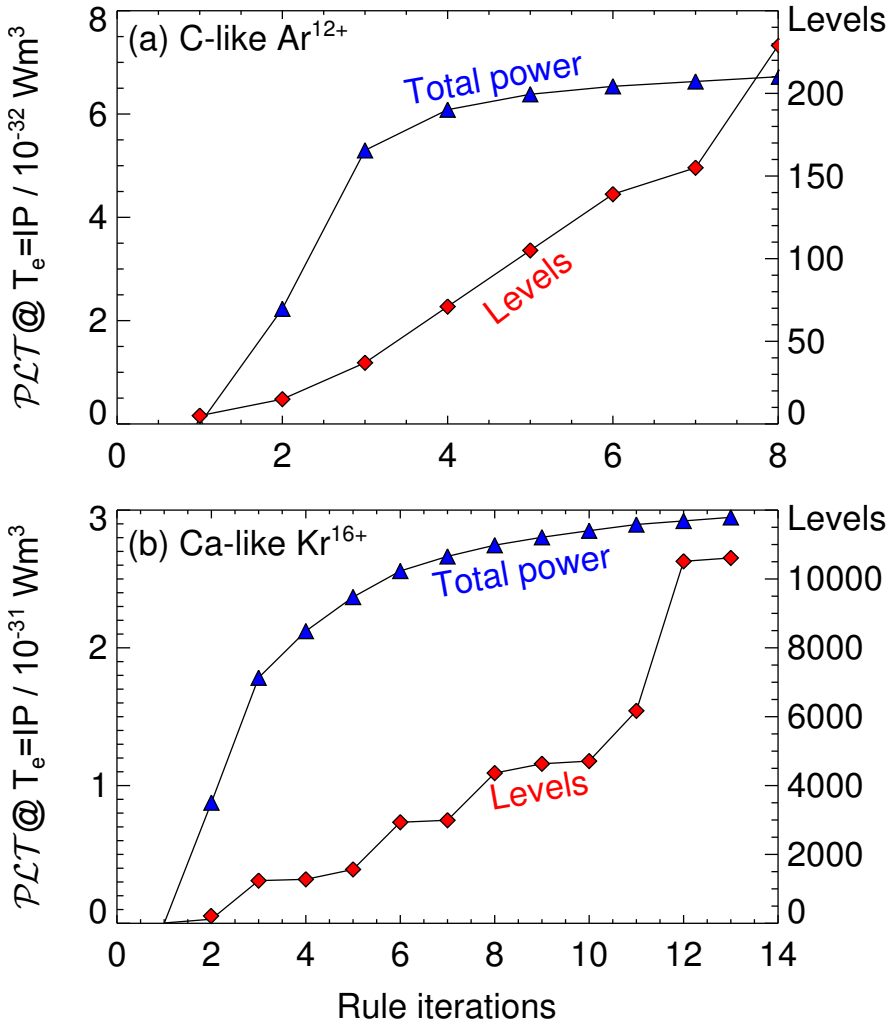

Figure 2.1: Convergence of optimisation of the (a) C-like Ar^{12+} $2s^2$ $2p^2$ ground configuration and the (b) Ca-like Kr^{16+} $3s^2$ $3p^6$ $3d^2$ ground configuration. The (blue) triangles show the radiated line power selected at the end of each iteration, and the (red) diamonds indicate the associated number of levels. The radiated power is calculated using $T_e = \chi^{(z)}$ and $N_e = 10^{13}$ cm^{-3}.

Metastable Optimisation A highly populated metastable configuration can (but not always) act to decrease the ground configuration $\mathcal{PLT}$ coefficient due to the factor N_1/N_{total} in equation 2.20, causing this configuration and its associated promotional rule to be omitted from the final set. However, metastable configurations can offer new pathways for electron promotion and will invariably have a large impact upon the population model. As a result, the optimisation procedure detailed in the previous subsection is automatically carried out for each metastable driving configuration, ensuring all such configurations are included in

the final set. The set of metastables for each ion in each isoelectronic sequence has been manually curated and most have been tested with small-scale population calculations; the full list can be found in the isonuclear *adf54* files. A similar strategy of using population models to define metastables is planned as a means of standardising the metastable sets used across ADAS at all relevant angular-momentum resolutions. It is supported by the finding that metastable configurations vary along an isoelectronic sequence—see figure 2.2—and the analogous finding of the multi-resolution GCR model in sections 5.2.2 and 5.3.2. Trends in metastability are useful here: the ratio of the metastable and ground configuration populations versus ion charge are shown in figure 2.2 for ions with a Be-like, Mg-like, and V-like ground configuration. Typically, the ratios drop below $\approx 10^{-3}$ when the ion charge $z > 5$. A similar behaviour is seen for *ic* levels: the maximum metastable level decreases with increasing z, but the relationship is not linear like for *ca*, cf. section 5.3.1.1.

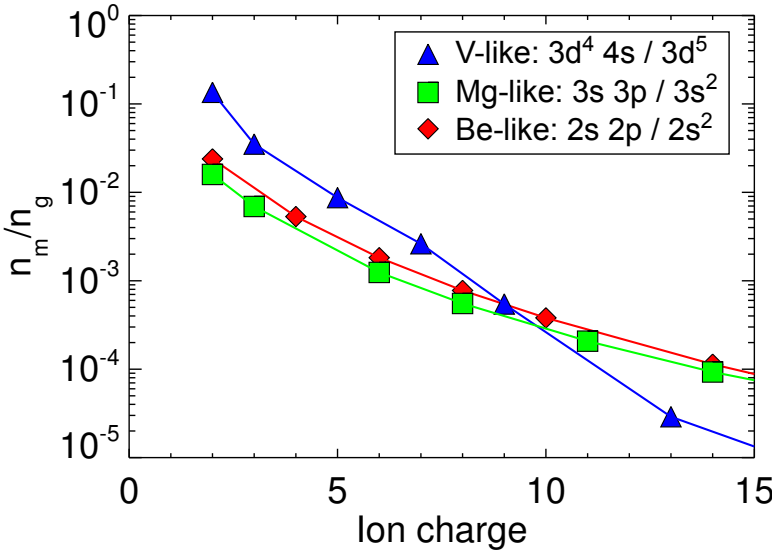

Figure 2.2: The ratio of the metastable and ground configuration populations for ions in the Be-like (red curve, diamond markers), Mg-like (green curve, square markers), and V-like (blue curve, triangle markers) iso-electronic sequences calculated using the ADAS collisional-radiative model.

This logically raises the question of how metastability relates to resolution. In particular, the configuration-selection procedure is performed in *ca* resolution with metastables defined accordingly, but the ultimate goal is a baseline in *ic*: is there a possibility that by working in the coarser *ca* approximation some config-

urations that contain metastable *levels* might be inadvertently omitted? From the extensive empirical evidence amassed by running the codes, the answer is that when an *ic* level is metastable, it is almost always true that the parent configuration is also metastable. The inverse requires some qualifiers: a metastable configuration will almost certainly contain at least one metastable *ic* level, but not all of the constituent levels need be metastable.[6] However, there are exceptions. For some closed shells and subshells, particularly where first valence promotion is to a d or f-shell, metastability will arise in some levels but not the source configuration. An archetype is Pd-like W^{28+}, which has the ground configuration [Kr]$4d^{10}$, resulting in the single ground level, $^1S_0$. The first excited configuration is [Kr]$4d^9$4f, which spawns a multitude of levels with $J > 1$ that are effectively isolated from the ground level and so become metastable. However, from the *ca* perspective the [Kr]$4d^9$4f $\rightarrow$ [Kr]$4d^{10}$ transition is a dipole one, so this configuration does not exhibit metastability. This issue is alleviated by the very fact that this is a dipole transition, meaning this excited configuration is included in the initial optimisation with the ground; the other closed shell anomalies tend to share this saving feature as well. Section 5.3.2 will extend these comments when comparing metastability between *ca* and *LS* or between *LS* and *ic*.

Having determined the appropriate metastables, the act of adding together all of the configurations derived from the promotion rules associated with each metastable will usually raise the number of levels above the original level limit (even after removing any duplicate configurations). In extreme cases, COWAN will fail to converge with the large number of configurations included in the calculation. Therefore, two additional steps are required to reduce the number of configurations. When COWAN fails to converge, the optimisation code removes all configurations with quantum number $n > n_{grd} + 2$, where n_{grd} is the maximum quantum number of the ground configuration. If this condition is not met, then the highest quantum number n, even parity configurations promoted from the metastables are removed. The parity condition is removed if a convergence is still not reached.

With a valid configuration set, a further reduction is performed to keep the

[6] A metastable configuration with no metastable levels has not been observed in the course of this work.

calculation within the (cs) limits. First, the ground and metastables are included along with the first excited configuration (of opposite parity) to ensure that the metastable is tied to at least one other configuration. Next, a collisional-radiative population calculation is carried out to determine $\mathscr{F}_{j1}^{(\mathrm{exc})}$, and then the configuration transition pairs are arranged in descending order in terms of their individual contribution to the total power, $\Delta E_{ij} A_{j\to i} \mathscr{F}_{j1}^{(\mathrm{exc})}$. The configuration pair is included if the calculation remains within the calculation limits. After the addition of a configuration pair, the dominant (de-)populating configurations associated with the upper configuration are included. Without these additional configurations, all of the radiative decay will falsely be channelled back down the same path as the collisional excitation. This can lead to an artificially high radiation estimate.

The inclusion of metastables can have a varied effect on the ground $\mathcal{PLT}$ coefficient that is recalculated following the merging of all configuration sets from metastable bases as described above. On the one hand, the addition of a metastable configuration will cause a reduction in the $\mathcal{PLT}$ coefficient because of the normalisation factor, N_σ/N_{total}, in equation 2.20. The magnitude of this effect will depend upon how large the population of this metastable is relative to the ground population. On the other hand, including a metastable may increase the ground $\mathcal{PLT}$ because it opens up additional excitation pathways, which can then lead to radiative decay to the ground. The magnitude of this effect is more difficult to predict from underlying variables and will inherently depend upon the distribution of the atomic levels and what excitation and decay pathways are possible. Generally speaking, any collisional excitations to levels that have direct dipole transitions to the ground will dominate the contributions to this extra power. Overall then, the net impact of adding metastables will be a balance of these two effects, which are themselves related and not decoupled, meaning an increase or decrease of the ground $\mathcal{PLT}$ is possible but hard to predict.

Take as an example the isoelectronic sequences between Ca-like and Ni-like: these have the ground configuration $3d^i$ and the two metastable configurations $3d^{i-1}\ 4s$ and $3d^{\bar{i}-2}\ 4s^2$ with $1 \le i \le 10$ and $2 \le \bar{i} \le 10$. We wish to determine the effect that adding these metastables have upon the final ground $\mathcal{PLT}$. Starting from the near-neutral species of these sequences, it is observed that a strong

excitation-decay pathway is available from the $3d^{i-1}$ 4s metastable to the ground, proceeding through the $3d^{i-1}$ 4p excited configuration:

$$3d^{i-1}\ 4s \xrightarrow{\text{EIE}} 3d^{i-1}\ 4p \xrightarrow{\text{rad. decay}} 3d^{i} \tag{2.21}$$

Therefore, this $3d^{i-1}$ 4s metastable is typically included in the initial ground optimisation step because of this significant contribution to the $\mathcal{PLT}$. The addition of $3d^{\bar{i}-2}$ $4s^2$ in the secondary metastable optimisation step only causes a slight decrease to the $\mathcal{PLT}$ from re-normalisation, so the overall effect of the metastables is to increase the ground $\mathcal{PLT}$ in this case. Moving to slightly higher ion charges, the balance shifts: the extra excitation pathway introduced by the $3d^{i-1}$ 4s metastable no longer outweighs the normalisation, and the net effect of adding the metastable configurations is to decrease the $\mathcal{PLT}$ by as much as $20 - 30\%$. Finally, entering the highly charged regime, the balance shifts again. The metastables hardly exhibit metastability anymore, supported by figure 2.2, and so the re-normalisation is inconsequential. However, because the metastable populations are comparatively small, the additional contributions to the power through new pathways is also small, and so the net result is $\leq 5\%$ increase of the $\mathcal{PLT}$s.

2.3.1.2 Accuracy and Errors

It now remains to prove that the automated method described above achieves the desired result of minimizing errors associated with the selection of configurations. Accuracy hinges upon the essential bound configurations that contribute most to configuration mixing and radiated power being identified and included.

Top-up Estimate For the present purposes, the entire problem of configuration selection reduces to what truncated set of configurations, bounded by computational resources, best describes the infinite set of the actual atomic system. Therefore, it is essential to estimate this truncation error, or equivalently, the amount needed to "top-up" derived quantities like the $\mathcal{PLT}$ so as to cover their omissions. Using the projection matrices of GCR theory [16] is the ideal estimate of the excluded line power, but the required data is only available for isonuclear

sequences up to neon and only in LS-term resolution. Consequently, a simpler estimate of the top-up is adopted:

$$\mathcal{PLT}^{tot} = \mathcal{PLT}^{ic(cs)} \frac{\mathcal{PLT}^{ca(cl)}}{\mathcal{PLT}^{ca(cs)}}, \tag{2.22}$$

where (cs) denotes the small configuration set size, and (cl) the large. The resulting corrected coefficients are presented in figure 2.3 along with the temperatures of peak abundance at which they are calculated. The truncation error itself is estimated by the fractional quantity in 2.22, but it is more convenient to analyse a Δ factor,

$$\Delta(y_1, y_2) = \frac{\max(\{y_1, y_2\})}{\min(\{y_1, y_2\})} - 1, \tag{2.23}$$

where y_1 and y_2 denote the two quantities that are under examination.

Of course, the comparison of $\mathcal{PLT}^{ca(cl)}$ and $\mathcal{PLT}^{ca(cs)}$ coefficients will only accurately estimate the truncation error if other forms of error are constant between the two cases. For *ca* calculations, the other primary source of error is that introduced by the coarseness of level bundling, i.e. resolution error. Recall, it is necessary to calculate the top-up estimate in *ca* resolution because the (cl) calculation will either fail or take too long in *ic*. As the name suggests, *ca* averages over all of the levels belonging to a particular configuration, neglecting the finer details of level resolution and the influence this can have upon the population calculation. The errors introduced by working in *ca* resolution are addressed in section 3.2 of [21]: a full discussion is outside of the current scope because the goal is strictly an *ic*-resolved baseline. To summarise, significant resolution error is observed around most closed shell ions (e.g. Pd-like, Kr-like, and Ar-like) due to the existence of *ic* metastables that are not part of a metastable configuration. This effect is clearly observed for the tungsten $\mathcal{PLT}$ results in figure 2.4 where the $\mathcal{PLT}^{tot}$ values are on average reduced by 30% relative to the $\mathcal{PLT}^{ca(cl)}$ ones at a few of the shell boundaries. However, $\lessapprox 10\%$ error occurs for the remaining sequences, suggesting that the resolution error should not greatly affect the selection of configurations. In addition, this resolution error is almost exclusively restricted to low-lying levels where fine-structure energy splitting is more pronounced; for configurations with high-n valence electrons, j and l sublevels are nearly energy degenerate, and so grouping levels into configurations is a good

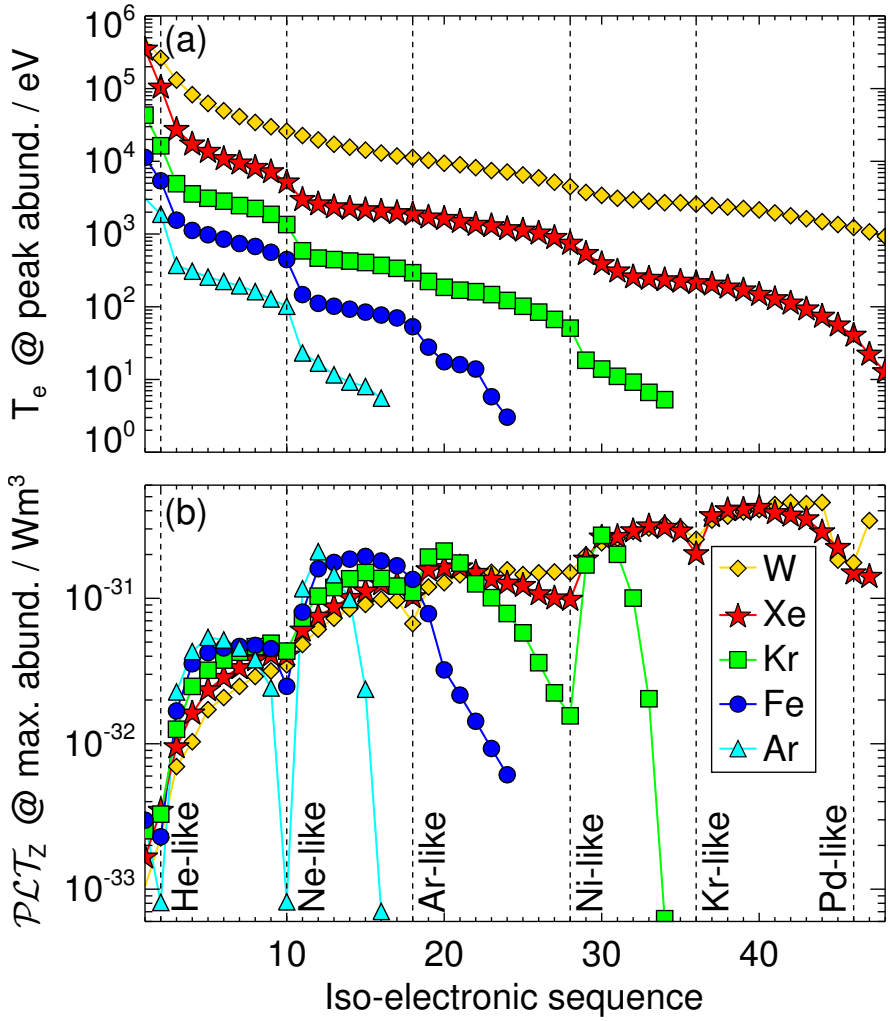

Figure 2.3: (a) The temperatures of peak abundance for each ion found using the ionisation and recombination coefficients defined by Pütterich [44] and (b) the corresponding $\mathcal{PLT}^{tot}$ coefficients (see text, equation 2.22) at each temperature given in (a) determined using COWAN.

approximation. As a result, the magnitude of resolution error across the $ca(cs)$ and $ca(cl)$ configuration sets is about equal, and hence comparing $\mathcal{PLT}^{ca(cl)}$ and $\mathcal{PLT}^{ca(cs)}$ should offer a good estimate of the truncation error.

Figure 2.5 plots the Δ values using the $\mathcal{PLT}^{ca(cl)}$ and $\mathcal{PLT}^{ca(cs)}$ coefficients for W, Kr, and Fe as input. There arise some difficulties in deducing the truncation error directly from the Δ values of this plot. Large Δ values are observed for the highly-charged, heavy species with an open p-shell of more then two free holes or with an open d-shell of more than two electrons and more than two free holes. For the open p-shell case, a significant proportion of line power comes from

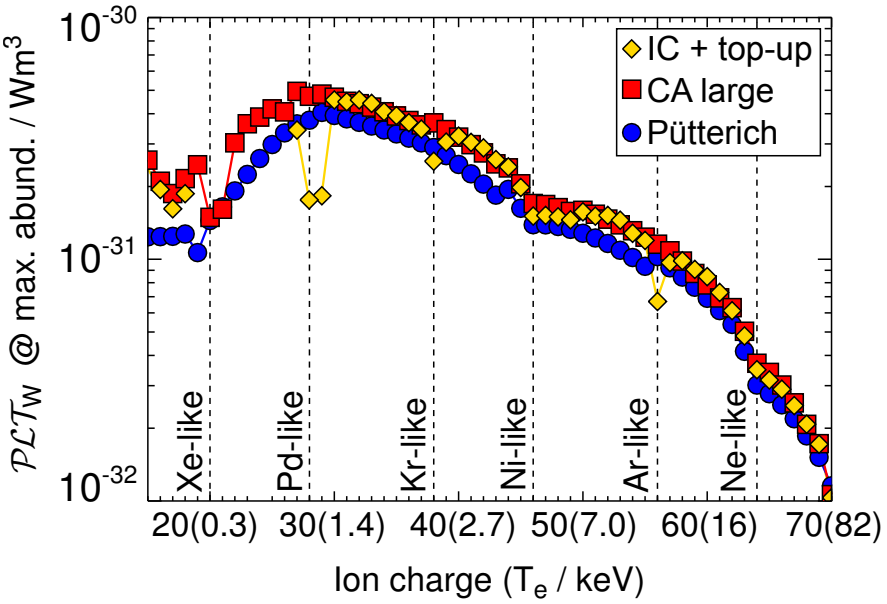

Figure 2.4: $\mathcal{PLT}$ results for tungsten. Yellow diamonds and red squares show the $\mathcal{PLT}^{tot}$ (see text, equation 2.22) and $\mathcal{PLT}^{ca(cl)}$ coefficients at the temperature of peak abundance, respectively. Equivalent $\mathcal{PLT}^{ca(cl)}$ coefficients from Pütterich [44] are shown by blue circles.

transitions involving the opening of closed inner n-shells. The small configuration sets have omitted including configurations of these types because they produce unexpected and strange behaviour in the results of the ic calculation: e.g. incorrect dipole limit behaviour and poor energy levels. Until further investigation is possible and because the calculations are sensible for ca, it was decided to keep these configurations in the $ca(cl)$ set. This explains the majority of the discrepancy found for these highly charged ions of W and Kr, and thus these should not be seen as representative of the truncation error. Further investigation into the source of this phenomenon, ideally with other codes, is needed. Conversely for lower charged species in this domain, less power is generated through these troublesome inner shell transitions because these excited configurations lie well above $\chi^{(z)}$ and the lower temperatures at which these lower-z species exist is not sufficient to populate them. Much of the difference between the (cl) and (cs) sets is eliminated, and the remaining difference can be identified with the truncation error. In the other case of high-z species with open d-shells, the majority of power emanates from the 4f $\rightarrow$ 3d transition, and this transition is excluded from the (cs) configuration sets because of the large number of levels spawned by the 4f shell. Again, this largely accounts for the increased Δ values, but here this can be

associated with the truncation error. However, as the charge of isoelectronic ions decreases, the metastability will increase like in figure 2.2, which will shift power from the 4f $\rightarrow$ 3d transitions to those driven by excitation from the metastables. These metastable configurations tend to involve fewer levels and are therefore more likely to be included in the (cs) sets.

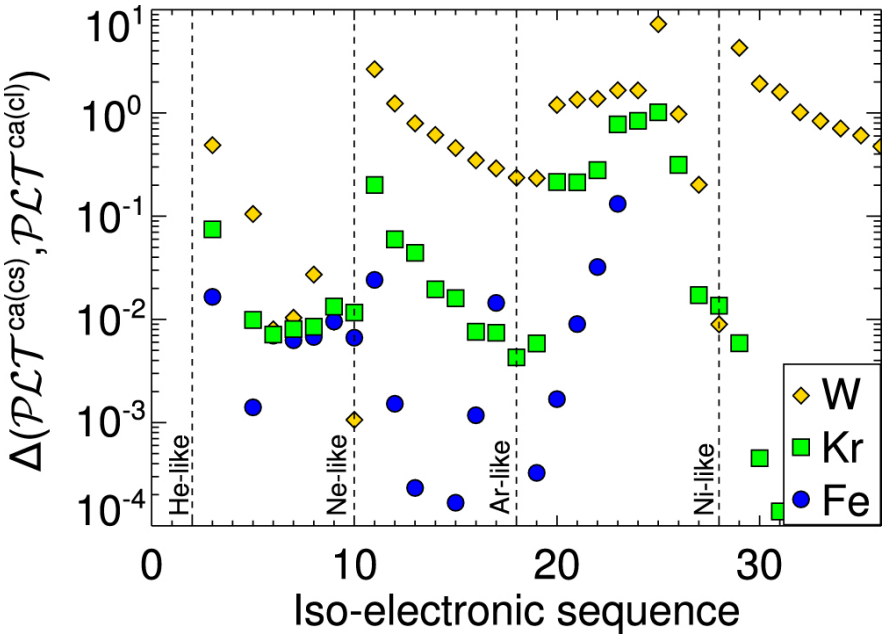

Figure 2.5: Comparison of $\mathcal{PLT}^{ca(cl)}$ and $\mathcal{PLT}^{ca(cs)}$ coefficients using Δ across the W, Kr, and Fe isonuclear sequences. These representative values were obtained using the temperature of peak abundance for each ion found using the ionisation and recombination coefficients defined by Pütterich et al. [41].

Overall, the truncation error is best described as being bounded by the Fe and W cases in figure 2.5 with the caveat of W being unrepresentative for open p-shells. Furthermore, the comparison between the $\mathcal{PLT}^{ca(cl)}$ result for tungsten with that from Pütterich in figure 2.4 gives an estimate of the truncation error for previous baseline data. Increases of more than 50% relative to the previous baseline are observed for lowly ionised stages on the left end of the plot. More modest increases of between 20% and 10% are seen for the remaining ionisation stages. Nonetheless, these results suggest a definite presence of truncation error in previous baselines that has now been accounted for with this new baseline technique. Therefore, it is safest to always include a top-up correction with the ADAS808 (cs) configuration sets, and the strength of this method is that the error has now been quantified and corrected.

Collision Strength Approximations Another potential source of error for the configuration selection method is that the PWB approximation is being used to generate the collision data. The deficiencies of PWB calculations relative to DW ones have already been detailed in section 2.2.1, so the question is raised about why AUTOS with DW has not been used as the code to generate atomic data in the context of this work. COWAN with PWB has been selected primarily to limit computation time, but a second equally important reason pertaining to atomic structure error is revealed in the next section.

In practice, the shortcomings of the PWB approximation are mitigated to some degree. It is electric dipole transitions that influence the $\mathcal{PLT}$ most, and this is especially true for situations where the total population of a configuration is similar for both *ic* and *ca* resolutions. As shown in figure 2.4 and explained in section 2.3.1.2, *ic* and *ca* populations agree for the majority of cases. Because of the large magnitude of strong dipole collision strengths, the PWB approximation will usually introduce a smaller relative error. Even so, PWB collision strengths can still be in error of $\approx 40\%$ at low energies relative to those from DW. But this problem is alleviated for heavier elements with higher z since the ionization balance pushes these ions to higher temperatures relative to the lighter ions of the same isoelectronic sequence: at higher temperatures, the higher energy portions of the collision strengths are selected by the convolution with the Maxwellian distribution, and this is where the PWB approximation converges. Correspondingly, for low ionization stages, the threshold region matters more, but even DW collision strengths are in error here because resonances are neglected. A close-coupled technique—section 2.2—should be employed, so it is less worthwhile to discuss the advantage of using DW in these cases.

In contrast, when the configuration population differs significantly between *ic* and *ca* calculations, the inclusion and quality of non-dipole and forbidden transition data matter. Again referring to the Metastable Optimisation paragraph of section 2.3.1.1, the most influential differences between *ic* and *ca* will occur for metastable levels and configurations, and the discrepant cases arise at shell and subshell boundaries. The deficit of PWB collision strengths in such cases is that electron exchange between bound and free electrons is not included, meaning no values are present for forbidden transitions that are known to be important

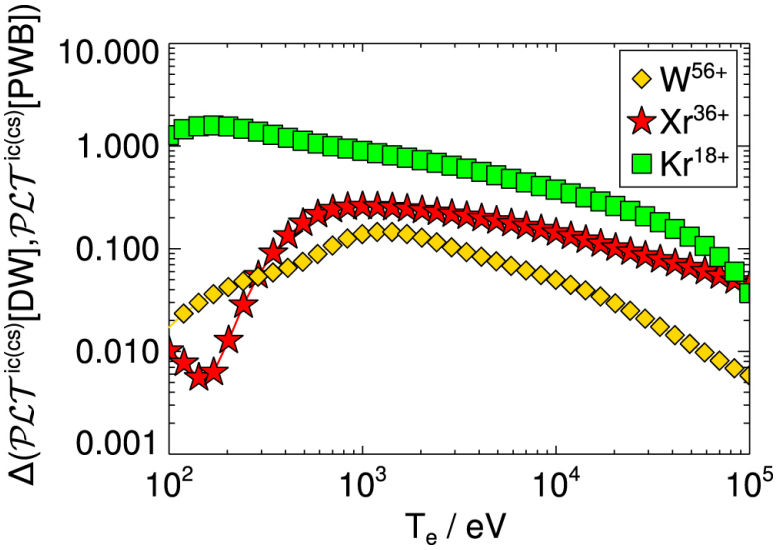

Figure 2.6: Comparison of the Ar-like $\mathcal{PLT}^{ic(cs)}$ coefficients at $N_e = 10^{19}$ m^{-3} generated with and without spin-changing transitions. The spin-changing collision strengths are generated from AUTOS in DW mode and supplement the COWAN *adf04*.

for these scenarios. The impact of neglecting these transitions upon the $\mathcal{PLT}$ is shown in figure 2.6. Two trends are apparent: first, the impact of adding the spin-changing transitions appears to be larger for smaller ion charges, z, since the Δ values increase going from W^{56+} to Xe^{36+} to Kr^{18+} across most of the temperature range. The reason for this is that relativistic corrections in the target Hamiltonian, which scale as $(\alpha Z_0)^2$, cause spin-system breakdown: final eigenstates can have components from basis states of different spin but equal parity and total angular momentum. Therefore, connections between spin systems are already present for high-Z_0 species, and so the addition of spin-changing transitions has a smaller effect. Secondly, the effect of adding spin-changing transitions diminishes with increasing temperature for all of the isoelectronic ions. This is a direct consequence of the $1/\varepsilon^2$ decrease at high energies for the collision strengths of forbidden, exchange transitions. In the end, the Kr^{18+} case proves that the inclusion of spin-changing transitions can be essential, further justifying the move towards a complete DW baseline.

Another form of transition that has been neglected in this work is IIE. Of particular concern are the transitions between fine-structure metastable levels in the $ic(cs)$ calculation, especially when these level populations begin to deviate from statistical balance around shell boundaries. This specific category of IIE

transition will serve to redistribute the metastable level populations, altering the normalisation factor, $N_\sigma/N_{\rm tot}$, but nothing else in equation 2.20. However, results in section 5.4 appear to suggest that IIE has a negligible effect upon the power coefficients. Further investigation is required since IIE does have a noticeable impact upon the fractional abundances, which should be propagated to $\mathcal{P}_{\rm tot}$.

Atomic Structure Error It was observed in the preceding section that it would be most efficient to conduct the configuration selection work with AUTOS in DW mode since electron exchange transitions are automatically included; however, there is a decisive shortcoming of AUTOS. If AUTOS is run with the default strategy of setting all λ_{nl} for the target to 1, then unsuitable and altogether inaccurate atomic structures can result. This has direct implications for the $\mathcal{PLT}$ as shown in figure 2.7(b), where the $\mathcal{PLT}^{ic(cs)}$ coefficients from both AUTOS and COWAN are compared for Ar-like Fe^{8+}. Substantial differences are apparent, and at the temperature of peak ion abundance, there is a difference of $\approx 20-30\%$ that is directly attributable to variation in the atomic structure. This can be concluded because both the AUTOS and COWAN results in figure 2.7 use the PWB approximation for the collision calculation, leaving only the atomic structure data as a point of difference. Moreover, the Δ factor in pane (b) is not constant with temperature, which means this is not simply the shift of the energy levels being directly propagated to the $\mathcal{PLT}$ but also some influence of the collisional and radiative rate coefficients in the population model. Figure 2.7(a) proves that it is the AUTOS calculation that is in error relative to COWAN because the COWAN energies are in far better agreement with those from NIST. This should be no surprise given the extensive comparison of AUTOS and COWAN given in section 2.2.1. COWAN tends to achieve better atomic structures because the HF equations are derived from the variational principle but also because there are a set of tuning parameters originally set by Cowan [31] that assist with the final structure.

2.3.2 Scaling Parameter Optimisation

It is intended that the following work will soon be published in ADNDT.

Section 2.3.1.2 clearly demonstrates the inadequacy of the default structure produced by AUTOS in certain circumstances: discrepancies of 20–30% in the

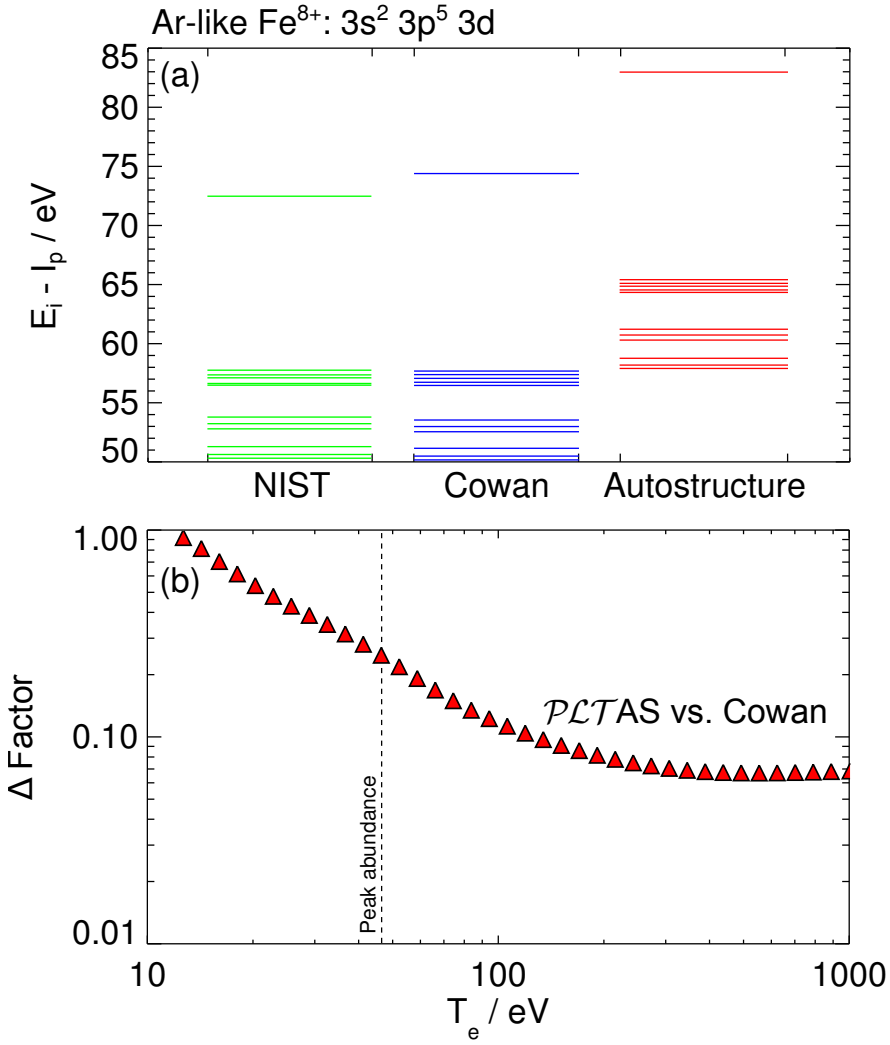

Figure 2.7: (a) Comparison of level energies from NIST (green), COWAN (blue), and AUTOS (red) for the metastable configuration $3s^2 3p^5 3d$. I_p is the ionisation potential of Ar-like Fe^{8+} which is -233.586 eV. (b) Comparison of the $\mathcal{PLT}^{ic(cs)}$ coefficients calculated using COWAN and AUTOS for Ar-like Fe^{8+}. The number of the transitions in the AUTOS calculation has been reduced to match that of COWAN for a true comparison. Both use the PWB approximation.

$\mathcal{PLT}$ just above were attributed directly to the atomic structure. This situation must be rectified if AUTOS is to fulfill the requirements for the present baseline outlined in section 2.1.1 and if the advantages of using DW collision strengths are to be fully realised. The λ_{nl} were introduced in section 2.2.1 as adjustable parameters for each nl orbital that can be used to improve the potential term, V_{TFDA}, in the radial equation 2.1 of AUTOS. Moreover, these λ_{nl} can be varied through an internal optimisation procedure that minimises the weighted sum of all the LS term energies (by default), with the intention of producing better atomic structures. However, optimising every λ_{nl} over every term included in the calculation can dilute the correlations between subsets of terms and λ_{nl}, leading to anomalous and even unphysical λ_{nl} values. The remedial strategy adopted here involves fixing the inner core λ_{nl} to pre-determined, optimised values whilst optimising the λ_{nl} of the valence orbitals [45]. Then, isoelectronic trends can be used to smooth out any anomalous values that persist. These isoelectronic trends are compelling and present for the vast majority of calculated ions across all isoelectronic sequences; moreover, V_{TFDA} varies smoothly with Z_0, so it stands to reason that the modifications to this potential, i.e. λ_{nl}, should also vary smoothly. The isolated and rare nature of these anomalous values combined with this information leads to the strong suspicion that these anomalous values are produced by the minimisation procedure finding local minima rather than the global minimum.

For each isoelectronic sequence, the configuration basis set is determined using the same algorithmic power-based technique from the preceding section 2.3.1. The rules were adjusted for this study to limit the electron promotions from the metastable configurations to $\Delta n \leq 2$ and to include the ground complex configurations. These configuration sets were sufficient to account for configuration interaction, whilst not significantly diluting the minimisation. In this analysis, the same configuration basis set is used for all ions in a sequence with tungsten as the optimising element. This simplification did not significantly change the isoelectronic scaling parameter trends shown later in figure 2.8. Again, the configuration sets as determined by ADAS808 for all ions are available as supplementary data in *adf27* files, and these configurations sets are unique to each ion of an isoelectronic sequence.

To determine the optimised values of the inner core λ_{nl} of a particular ion, it

Table 2.6: Prescription to determine the first iteration λ_{nl} for the novel AUTOS structure optimisation. $N \equiv$ the number of target electrons. For each isoelectronic sequence N, the λ_{nl} sets are determined for a range of nuclear charges up to $_{74}$W: $N \leq Z_0 \leq 74$. Thus, the notation, $\{nl\}_{N=X}$, designates the λ_{nl} value for the species in the isoelectronic sequence X with an atomic number Z_0. All λ_{nl} for orbitals up to $nl = 4\text{f}$ are set for each case, and some $n = 5$ parameters are introduced above Mg-like ($N = 12$).

Sequence	**Fixed λ_{nl}**	**Variable λ_{nl}**	**Tied λ_{nl}**	**Fixed $\lambda_{nl} = 1$**
$0 < N < 4$	none	1s, 2s, 2p	3s=2s, 3p=2p	3d–4f
$4 \leq N < 13$	none	1s, 2s, 2p, 3d	4s=3s=2s, 4p=3p=2p, 4d=3d	4f
$13 \leq N < 37$	$\{1s, 2s, 2p\}_{N=12}$	3s, 3p, 3d, 4f	4s=3s, 4p=3p, 4d=3d	5s
$37 \leq N < 47$	$\{1s, 2s, 2p\}_{N=12}$, $\{3s, 3p, 3d\}_{N=36}$	4s, 4p, 4d, 4f	5s=4s, 5p=4p, 5d=4d, 5f=4f	5g

is necessary to first assess the isoelectronic sequences with an open 1s shell, then those with an open 2s shell, and so on up to the ground orbital of the ion. The assumption in this systematic approach is that closed-shell λ_{nl} values do not vary from one isoelectronic sequence to another. Note that the λ_{nl} are still varied for at least two sequences after becoming core orbitals to demonstrate this assumption. In addition to fixing the inner core λ_{nl} in the minimisation, it is also possible to tie together scaling parameters of equal l and thus set $\lambda_{nl} \equiv \lambda_l$; this matches the original description in [26]. In this work, nl-dependent λ_{nl} values are used for the fixed inner core orbitals, and then tied for equal l for the remaining ground and valence orbitals. An overview of the optimisation setup for all isoelectronic sequences is given in table 2.6.

Sequences from Li-like to Mg-like are first investigated. The results of the optimisation for the λ_{1s}, λ_{2s}, and λ_{2p} are shown in figure 2.8a–c. Along an isoelectronic sequence with increasing Z_0, a decay towards unity is found for λ_{1s} in (a). In contrast, the 2s and 2p cases are largely independent of Z_0. There is a slight decrease of λ_{2s} with increasing Z_0 in (b) along the isoelectronic sequences plotted. The λ_{2p} values exhibit the opposite, slightly increasing with Z_0 except for the B-like sequence which rises dramatically. Currently, the cause of the latter trend is unclear; however, it could be explained in terms of the sensitivity of the Thomas-Fermi-Dirac-Amaldi (TFDA) potential to λ_{nl}. As Z_0 increases, the Coulomb potential dominates and therefore bigger changes to λ_{nl} are required to have an effect. This assumption is discussed in the following section.

Most significantly, as the isoelectronic sequence increases (i.e. more electrons

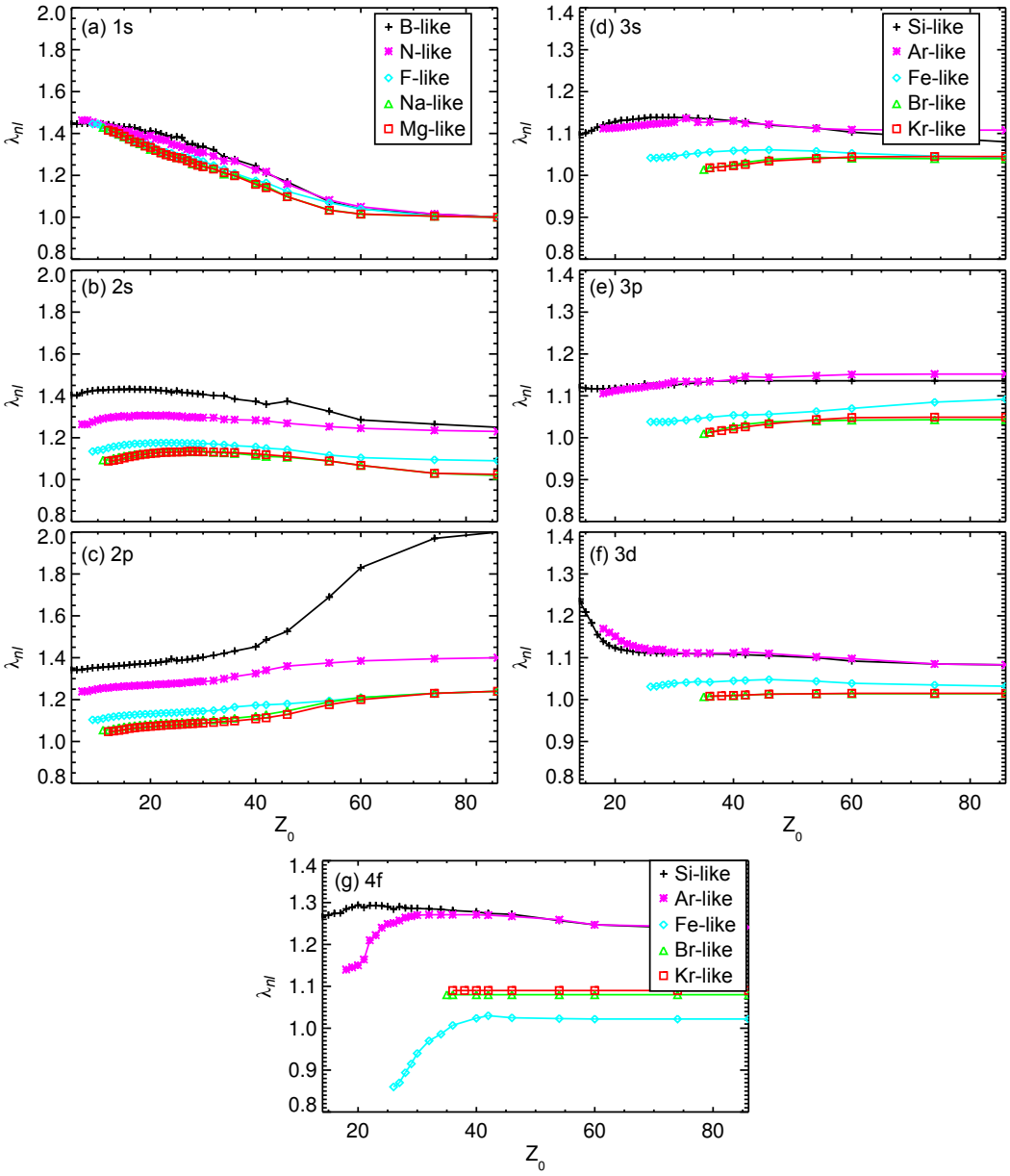

Figure 2.8: Optimised radial scaling parameters as a function of element charge for different isoelectronic sequences. In (a−c), the 1s, 2s, and 2p orbital scaling parameters are shown for sequences: B, N, F, Na, and Mg -like. The $n = 3$ and 4f orbital scaling parameters are shown in (d−f) and (g), respectively for sequences: Si, Ar, Fe, Br, and Kr -like. The inner orbital scaling parameters in d−g are set to those values shown for the Mg-like sequence in a−c, as prescribed in table 2.6.

are added) the λ_{nl} values begin to converge. In other words, the isoelectronic lines overlap. For the λ_{1s}, $\lambda_{2s}$and λ_{2p} values, this occurs at Na-like and Mg-like as shown by the red and green curves in figure 2.8a–c, and the phenomenon continues for higher sequences. These λ_{nl} values are therefore fixed to their Mg-like values for all subsequent isoelectronic sequences, as indicated in rows three and four of table 2.6.

Optimised λ_{nl} values for a selection of the lower isoelectronic sequences (Be, B, F, Ne, and Mg)-like have been previously documented [46–50]. Reasonable agreement between the previous literature and the study presented here is found at low nuclear charge; however deviations are found at higher nuclear charge. This deviation occurs because the previous studies focus on R-matrix collision calculations and therefore only include relativistic Breit-Pauli correction terms perturbatively, whereas this study uses the κ-averaged semi-relativistic radial equation. For heavy species, relativistic effects can no longer be treated as a perturbation.

The next set of isoelectronic sequences from Al-like to Kr-like are used to investigate the λ_{3l} parameters with a fixed inner core determined from the previous set of sequences. The optimised λ_{3l} values are shown in figure 2.8d–f, and the λ_{4f} in figure 2.8g. These λ_{nl} display even less Z_0 dependence than that found for λ_{2l}. The overlap of the λ_{3l} values occurs for Br-like and Kr-like and therefore these values are fixed as the inner core, in addition to those from Mg-like, for the sequences from Rb-like onwards. The overlap of the Si-like and Ar-like curves is coincidental and not exploitable. For Rb-like to Xe-like, the optimised λ_{4l} values all have approximately the same values as those shown in 2.8g for Br-like and Kr-like; Fe-like is an anomalous case that requires further investigation.

The strategy outlined above is first carried out with $\lambda_{nl} = 1$ as the starting conditions in the minimisation. Once a full set of optimised parameters have been determined for every ion, a second iteration of the optimisation is then performed. This time, the starting λ_{nl} values are set to those obtained from the first iteration, and the prescription outlined in table 2.6 is again carried out. Finally, a spline fit of the scaling parameters along an isoelectronic sequence is used to identify and correct any anomalous parameters obtained from the initial minimisation. The λ_{nl} for all explicitly calculated ions will be stored in an *adf54* file in ADAS, and

reading routines that handle interpolation will be provided so that the λ_{nl} values for an arbitrary ion can be queried.

There is a physical basis for this strategy that is worth elaborating upon. The stability and spherical symmetry of closed quantum shells and subshells causes a clear distinction between electrons that occupy the orbitals in these closed shells and those that do not—viz. valence electrons. It proves useful in atomic physics to think about the core electrons being effectively independent of the valence electrons: they are a negligible perturbation from the perspective of one of the core electrons since it will interact much more strongly with the other core electrons. However, the converse is certainly not true. For instance, Palmeri et al. [51] show that for complex species the effects of core polarisation and penetration upon the valence electrons cannot be neglected. Thus, it is to be expected that a set of consistent core orbital λ_{nl} can be found moving between isoelectronic sequences that share the same core. On the other hand, the valence electrons will be quite sensitive to the particular isoelectronic sequence, and so they must always be free for optimisation so a unique set of λ_{nl} can be determined for the specific ion. Moreover, tying λ_{nl} of the same l has a physical basis. Spatial probability densities of electrons in orbitals of the same l but different n will share the same shape but be scaled in radial size. As a result, these electrons will tend to "see" or "experience" a similar potential, $V_{\mathrm{TFDA}}(nl) \sim V_{\mathrm{TFDA}}(n'l)$, and it is on this basis that the higher n valence orbitals are coupled by l to lower n valence orbitals.

2.4 Evaluation of Scaling Parameter Optimisation

Whether the new strategy for λ_{nl} optimisation yields measurable improvements overall must now be determined. Because of the complexity of atomic structure and the need for concurrent improvement of both structure and power measures, there is no single figure of merit to assess the efficacy of the λ_{nl} optimisation. The typical comparators for atomic structure in the literature are energy level eigenvalues, radiative data (e.g. transition probabilities, oscillator strengths, etc.), and

variation between the radiative data calculated using different gauges.[7] Studies in atomic structure tend to amass data of this sort from various theoretical and often sparse experimental sources with which to compare the calculations being presented. Methods of comparison are fairly ad hoc, and there is little consensus on how to measure the degree of agreement between structures from different sources. Consequently, studies of atomic structure are time consuming and difficult to automate: for the detail required by spectroscopic analysis, this will undoubtedly remain the state of play for some time. Moreover, the effects on power emission measures are almost never investigated. A new approach is needed for the present purposes.

Fortunately, the standard of comparison required for evaluating the new baseline is less demanding than for the spectroscopic analysis of ions. Only generic indicators of structure and power improvement are needed, not cogent arguments for why one theoretical calculation is superior to another. Therefore, the following three-pronged approach has been adopted for assessing the merit of the new λ_{nl} optimisation strategy (shorthand *opt*) versus the default strategy of setting all λ_{nl} to 1 (shorthand *def*). The isonuclear ions, K-like Fe^{7+} and C-like Fe^{20+}, will be used as examples throughout to showcase instances where our new optimisation strategy does and does not offer improvements according to the figures of merit. Structure calculations with AUTOS (*def* and *opt*) and COWAN were done with the following configuration sets:

$$\begin{aligned}
Fe^{7+}: \quad & [Ne] + \{3s^23p^63d, \quad 3s^23p^64s, \quad 3s^23p^64p, \quad 3s^23p^64d, \\
& 3s^23p^64f, \; 3s3p^63d^2, \; 3s^23p^53d^2\} \\
Fe^{20+}: \quad & [He] + \{2s^22p^2, \; 2s^22p3s, \; 2s^22p3p, \; 2s^22p6p, \; 2s^22p6d, \\
& 2s^22p7p, \; 2s^22p7d, \; 2s2p^3, \; 2s2p^23s, \; 2s2p^23p, \\
& 2s2p^23d, \; 2s2p^24s, \; 2s2p^24p, \; 2s2p^24d, \; 2s2p^25p, \\
& 2s2p^25d, \; 2s2p^26p\},
\end{aligned}$$

and the λ_{nl} for the *opt* case:

[7] In this context, a gauge refers to the specific operator that is used to calculate the electric matrix elements. Refer to equations 2.24–2.26

Ion	1s	2s	2p	3s	3p	3d	4s	4p	4d	4f
Fe^{7+}	1.362	1.118	1.066	1.123	1.111	1.116	1.123	1.111	1.116	1.116
Fe^{20+}	1.362	1.399	1.396	1.399	1.396	1.000	1.399	1.396	1.000	1.000

These λ_{nl} values may be slightly different from those in the final *adf54* that eventually enters central ADAS because the analysis that follows was performed before some final tweaks of the λ_{nl} optimisation work. These recent modifications do alter the atomic structures slightly, but they do not change the gross conclusions of the ions that are investigated here as case studies.

2.4.1 δ_k Figure of Merit

It was briefly mentioned that the variation in radiative data caused by using different gauges can be an effective figure of merit for atomic structure. Considering only dipole radiative transitions in the nonrelativistic limit for the moment, there are three gauges that the electric dipole matrix elements are commonly calculated in:

$$\left\langle \gamma JM \left| \sum_i \boldsymbol{r}_i \right| \gamma' J' M' \right\rangle, \tag{2.24}$$

$$2(E'-E)^{-1} \left\langle \gamma JM \left| \sum_i \boldsymbol{\nabla}_i \right| \gamma' J' M' \right\rangle, \tag{2.25}$$

$$2(E'-E)^{-2} \left\langle \gamma JM \left| \sum_i \boldsymbol{\nabla}_i V \right| \gamma' J' M' \right\rangle, \tag{2.26}$$

defining the length, velocity, and acceleration gauges, respectively. In these equations, E and E' are the energies (Ryd) of the states γJM and $\gamma' J' M'$, V is the central-field potential energy (Ryd), and i indexes the electrons in the atom. In theory, the results of each gauge should be identical to each other; that is to say, the dipole matrix element is gauge invariant. However, when approximate wave functions are used, which is always the case for multi-electron atoms, differences will arise between the gauge results: the derivatives involved in the velocity 2.25 and acceleration 2.26 gauges cause the most worry. But this is not simply an issue of the numeric precision of the wave function representation, and one can appreciate this by considering the construction of the electric dipole transition operator, $\mathscr{M}^{\mathrm{e}}_{LM}$, which is used in forming the dipole matrix elements. The complete details

of forming this operator from the electromagnetic potentials whilst incorporating the generality of gauge transformations are mathematically involved and outside the scope of this thesis (see Grant [52, 53]), but the broad-brush argument can be distilled as follows. Making a quick transition to relativistic mechanics, the transition operator, $\mathscr{M}^{\mathrm{e}}_{LM}$, corresponding to transverse oscillations of the electromagnetic field has the same selection rules as the longitudinal transition operator, $\mathscr{M}^{\mathrm{l}}_{LM}$, so the most general form must be a coherent linear combination:

$$\mathscr{M}^{\mathrm{e}}_{LM}(G_L) = \mathscr{M}^{\mathrm{e}}_{LM} + G_L \mathscr{M}^{\mathrm{l}}_{LM}. \tag{2.27}$$

The arbitrary coefficient, G_L, effectively selects the gauge: $G_L = 0$ for $L = 1$ corresponds to the Coulomb gauge, which yields the velocity operator in the nonrelativistic limit, and $G_L = \sqrt{(L+1)/L}$ corresponds to the Babushkin gauge, which yields the length operator in the nonrelativistic limit. For the gauge invariance of this expression to hold, $\mathscr{M}^{\mathrm{l}}_{LM}$ must vanish, and it can be shown that

$$\mathscr{M}^{\mathrm{l}}_{LM} \propto \Phi_{LM} \left(\frac{\partial \rho}{\partial t} + \boldsymbol{\nabla} \cdot \boldsymbol{j} \right), \tag{2.28}$$

where Φ_{LM} is the scalar multipole potential, and ρ and $\boldsymbol{j}$ are the electron charge density and current. The expression in brackets on the right side of 2.28 is identified as one side of the continuity equation, $\partial\rho/\partial t + \boldsymbol{\nabla} \cdot \boldsymbol{j} \equiv 0$. It is the adherence of the continuity equation that is not guaranteed for approximate, multi-electron wave functions derived from variational or perturbation methods: although charge conservation is built into the wave equation, the non-local nature of commonly used potentials means that charge conservation becomes something much more complicated.

Given this context, there has been ample discussion in the literature about the correct gauge to use in the calculation of the electric dipole matrix elements: contributions from Starace and Grant dominate [52, 54–56], but it is Kobe [57] who provides the final solution. Hata and Grant [58] produce a condensed explanation: whatever gauge is selected for calculation of the dipole matrix elements, it must match the gauge used in producing the wave function basis and interaction potentials. This seems to fly in the face of gauge invariance, but arises because one is typically not at liberty to select the phase factors of the wave function basis

and because approximate wave functions are in use. Yet, this misses the aim of the present investigation: the main concern is to obtain some measure of atomic structure quality with which a comparison of the *opt* and *def* λ_{nl} optimisation strategies can be implemented. Rewinding slightly, it will be recalled that the reason for a lack of gauge invariance in equation 2.27 was the violation of the continuity equation ($\partial\rho/\partial t + \boldsymbol{\nabla} \cdot \boldsymbol{j} \neq 0$), which is only avoided by exact wave functions. Therefore, approximate wave functions that more closely obey the continuity equation will exhibit a reduced dependence upon $\mathscr{M}^1_{LM}$ in equation 2.27 and so approach the gauge invariance of the exact wave functions. It is in this sense that an equalisation of the various gauge results indicates a convergence of the wave functions upon the exact forms that they approximate, and it is from this that a figure of merit can be derived.

Nevertheless, approximate gauge invariance is not a perfect measure, as Grant [53] states: "It is now generally accepted that a weak dependence of radiation matrix elements on G_L [in equation 2.27] is one indicator of wave function quality in many-electron systems, although it is insufficient on its own to guarantee the physical correctness of numerical radiative transition rates." In other words, an agreement between the radiative emission measures calculated in different gauges does not guarantee that these values will be close to actual observations. This is similar in many respects to the concepts of accuracy versus precision, which is synonymous with "wave function quality" here, yet it would be incorrect to claim that approximate gauge invariance offers no indication of atomic structure accuracy. Rather, it is most correct to state that the approximate gauge equalisation described above is a necessary, but not sufficient, condition for the convergence of approximate wave functions upon their exact, physically accurate forms. Therefore, any figure of merit derived from the concept of gauge invariance should be used in conjunction with other independent benchmarks if one is seeking to gain an absolute measure of atomic structure quality: this is the motivation for the additional atomic structure figure of merit defined in section 2.4.2. Otherwise, when used on its own, a gauge invariance figure of merit is best suited for relative comparisons: e.g. providing evidence for whether one calculation is better than another. It is this interpretation upon which the figure of merit in this section is to be based.

There still remains the question of which gauges should be considered, since theoretically there are an infinite number from which to choose. In practice, only the length, velocity, and acceleration gauges introduced in equations 2.24–2.26 are used. The acceleration gauge is widely acknowledged to be of dubious accuracy because it weights the integrand towards small-r, the region where the wave function is least well known due to approximations for many-electron interactions. As a result, this gauge is rarely ever considered in the literature let alone computed as an output from computer codes, so it will be ignored for the remainder of this section. This leaves the length and velocity gauges as the ingredients for measuring gauge invariance.

The deviation between the length and velocity gauges has been quantified with the following function:

$$\delta_k = \frac{|gf_{ij}^{(\mathrm{len})} - gf_{ij}^{(\mathrm{vel})}|}{\max(gf_{ij}^{(\mathrm{len})}, gf_{ij}^{(\mathrm{vel})})}, \tag{2.29}$$

where gf_{ij} is the weighted oscillator strength for transition $i \rightarrow j$, (len) and (vel) denote the length and velocity gauges respectively, and k is an index for the transitions with one-to-one mapping, $k \mapsto ij$. The (len) and (vel) forms of gf_{ij} are both available outputs from AUTOS for electric dipole transitions. A significant flaw of this measure is that it treats all transitions equally, whereas in atomic population modelling the behaviour of a particular system is almost always determined by a small group of the strongest dipole transitions: certainly this is the case for radiated power. The most obvious solution is to attach weight factors, w_k, to each δ_k, and a suitable definition for the present purposes is

$$w_k = \frac{A_{ij}^{(\mathrm{opt})} + A_{ij}^{(\mathrm{def})}}{2}, \tag{2.30}$$

where A_{ij} is the spontaneous transition probability (s^{-1}). An average of the A_{ij} from the *def* and *opt* cases ensures that a symmetric weight factor is applied to the respective δ_k from each case: namely, the w_k applied to $\delta_k^{(\mathrm{def})}$ will be identical to the w_k for $\delta_k^{(\mathrm{opt})}$. This simplifies the statistical analysis to follow.

Weighted population statistics of the δ_k can now be calculated; these are direct

Table 2.7: Weighted statistics of δ_k for the $E1$ transitions of K-like Fe^{7+}. The descriptor "all" denotes that all possible $E1$ transitions have been considered, while "ground" denotes that only the $E1$ transitions terminating at the ground level have been included. N represents the number of transitions. The p-value is the critical p-value from the statistical equivalence test; see text for more details.

Description	$\bar{\boldsymbol{\delta}}_{\rm w}$	$\boldsymbol{\sigma}^{\mathbf{2}}_{\rm w}$	$\boldsymbol{\sigma}_{\rm w}$
def, all	0.459 662	0.016 634	0.128 973
opt, all	0.408 749	0.009 810	0.099 045
def, ground	0.482 142	0.016 819	0.129 687
opt, ground	0.420 755	0.009 018	0.094 964
$N_{\rm all}$ =	586		
$N_{\rm ground}$ =	32		
p(crit.) =	0.611 880		

Table 2.8: Weighted statistics of δ_k for the $E1$ transitions of C-like Fe^{20+}. The descriptor "all" denotes that all possible $E1$ transitions have been considered, while "ground" denotes that only the $E1$ transitions terminating at the ground level have been included. N represents the number of transitions. The p-value is the critical p-value from the statistical equivalence test; see text for more details.

Description	$\bar{\boldsymbol{\delta}}_{\rm w}$	$\boldsymbol{\sigma}^{\mathbf{2}}_{\rm w}$	$\boldsymbol{\sigma}_{\rm w}$
def, all	0.066 396	0.007 920	0.088 997
opt, all	0.097 825	0.011 901	0.109 091
def, ground	0.084 806	0.013 743	0.117 230
opt, ground	0.062 200	0.008 568	0.092 561
$N_{\rm all}$ =	38 135		
$N_{\rm ground}$ =	77		
p(crit.) =	9.5×10^{-211}		

analogues of the usual statistics:

$$\bar{\delta}_{\rm w} = \frac{\sum_k w_k \delta_k}{\sum_k w_k} = \sum_k w'_k \delta_k, \tag{2.31}$$

$$\sigma^2_{\rm w} = \frac{\sum_k w_k (\delta_k - \bar{\delta}_{\rm w})^2}{\sum_k w_k} = \sum_k w'_k (\delta_k - \bar{\delta}_{\rm w})^2, \tag{2.32}$$

where $w'_k = w_k / \sum_m w_m$ are the normalised weight factors. The δ_k for the electric dipole ($E1$) transitions of Fe^{7+} and Fe^{20+} have been calculated, and the weighted statistics are presented in tables 2.7 and 2.8.

For Fe^{7+}, table 2.7 shows a definite differentiation between the *def* and *opt* cases. The weighted mean, $\bar{\delta}_{\rm w}$, is lower for the *opt* case than for the *def* case.

Referring to equations 2.29 and 2.31, a small $\bar{\delta}_{\mathrm{w}}$ is a direct indication that the difference between the length and velocity gauge values of gf_{ij} is on average small, and because this is a weighted mean, this difference must be small for the strongest transitions also. Again, this is a proxy for wave function and overall structure quality, hinting that some improvement has been made by our novel λ_{nl} optimisation strategy.

But the statistical significance of this result would ostensibly be invalidated by the sizes of the weighted standard deviations, σ_{w}.[8] Both means are within 1σ deviation of each other; however, this simplistic approach neglects critical information relating the two cases and is overly conservative even if each δ_k distribution was treated independently. The *def* and *opt* data sets are correlated perfectly by transition, $k \mapsto ij$, so this is an instance of paired data. To determine if the means of each sample differ by a statistically significant amount, the difference between each paired value, $D_k = \delta_k^{(\mathrm{def})} - \delta_k^{(\mathrm{opt})}$, is assessed, reducing this to a problem of a single randomly distributed variable. In keeping with prioritising the important transitions, it is the weighted mean of the D_k sample distribution, $\bar{D}_{\mathrm{w}}$, that will be tested, with a confirmed hypothesis of $\bar{D}_{\mathrm{w}} = 0$ indicating that the $\delta_k^{(\mathrm{opt})}$ and $\delta_k^{(\mathrm{def})}$ distributions do not differ substantially. Oppositely, a confirmed hypothesis of $\bar{D}_{\mathrm{w}} \neq 0$ would indicate that the two δ_k distributions are statistically different, and it is the main objective of this section to determine if the new λ_{nl} optimisation strategy (*opt*) has garnered improvements compared to the default (*def*) case.

There are two approaches for constructing a statistical hypothesis test for such a scenario. First, one can assume that the weighted mean of the paired differences population, μ_D, is zero ($\mathrm{H}_0 : \mu_D = 0$) and test for the significance of the this quantity being different from zero ($\mathrm{H}_{\mathrm{a}} : \mu_D \neq 0$). In practice, this involves the familiar two-sided Student's t-test. Second, one starts by instead assuming that μ_D is substantially different from zero ($\mathrm{H}_0 : \mu_D \neq 0$) and then test for the significance of it being equivalent to zero ($\mathrm{H}_{\mathrm{a}} : \mu_D = 0$)—this is what is known as equivalence testing. Although this approach is simply the logical negation of the first, its implementation is notably different and more suited to the current

[8] The weighted standard deviation does not have a unique definition, and so its interpretation as the definitive measure of deviation about the weighted mean is somewhat uncertain. A full discussion of alternatives is outside the current scope.

scenario. One can only appreciate why equivalence testing is more appropriate by describing the implementation itself. There is no single distribution that applies to $\mu_D \neq 0$, so to construct a test statistic for the null hypothesis, H_0, one must quantify what is meant by *substantially different*. Setting a tolerance, Δ, within which one would expect μ_D to lie is the most straightforward, and the hypotheses become

$$\mathrm{H}_0 : |\mu_D| > \Delta, \quad \mathrm{H}_\mathrm{a} : |\mu_D| < \Delta. \tag{2.33}$$

The test of H_a is then a compound of two, one-sided Student's t-tests:

$$\left[F_{t,n-1}\left(t_1 = \frac{\bar{D}_\mathrm{w} - \Delta}{\sigma_{D,\mathrm{w}}/\sqrt{n}}\right) < \alpha\right] \wedge \left[1 - F_{t,n-1}\left(t_2 = \frac{\bar{D}_\mathrm{w} + \Delta}{\sigma_{D,\mathrm{w}}/\sqrt{n}}\right) < \alpha\right], \tag{2.34}$$

where $F_{t,n-1}(x) = \int_{-\infty}^{x} f_{t,n-1}(u)\mathrm{d}u$ is the cumulative t-distribution function with $n-1$ degrees of freedom, and α is the significance level, set to 0.05 for the present testing. Thus, the two location-scaled t-distributions are centred respectively at the boundaries, Δ and $-\Delta$, and the "sidedness" of the tests is inwards towards zero: i.e. the upper tail of the t-distribution centred at $-\Delta$ and the lower tail of the t-distribution centred at Δ. The critical p-value for the overall equivalence test is defined as follows. If both of the constituent conditions in equation 2.34 are false, then the critical p-value is the lesser of the two p-values from the one-sided t-tests, otherwise it is the greater of the two p-values. In other words, whichever component p-value is closest to causing the overall equivalence test to either fail or succeed.

Why is the second approach of equivalence testing superior to the single two-sided t-test? For many of the ions to be presented, the sample sizes, n, are large, causing the standard error ($\sigma_{D,\mathrm{w}}/\sqrt{n}$) to be very small. Consequently, the location-scaled t-distributions are narrowly peaked, and setting a significance level, α, as a determinant of proximity is no longer meaningful. Introducing the Δ tolerance in equivalence testing affords a higher degree of flexibility in determining what "close enough" means while still maintaining the rigour of a statistical hypothesis test. The magnitude of Δ depends upon the variable being tested, and for the present purposes, it is set to 0.05: since δ_k is effectively a relative error, see equation 2.29, and $\bar{D}_\mathrm{w}$ is the weighted mean of the arithmetic difference between the two cases, $\Delta = 0.05$ roughly corresponds to an allowance

of a 5% error in either direction *on average*.

Returning to Fe^{7+} and the results of table 2.7, the large p(crit.)-value, which exceeds the selected significance level, $\alpha = 0.05$, indicates that the null hypothesis of the equivalence test must be accepted: the assumption that the weighted means, $\bar{\delta}_{\mathrm{w}}^{(\mathrm{def})}$ and $\bar{\delta}_{\mathrm{w}}^{(\mathrm{opt})}$, are *significantly* different is correct, and it is very unlikely the means are equivalent. Furthermore, this provides strong evidence for the initial suspicion that the *opt* case is better than the *def* case from the perspective of atomic structure; it can be concluded that $\bar{\delta}_{\mathrm{w}}^{(\mathrm{opt})}$ is smaller than $\bar{\delta}_{\mathrm{w}}^{(\mathrm{def})}$.

On the other hand, the results for Fe^{20+} in table 2.8 display the opposite. The weighted means appear to be quite close, which is confirmed by the diminutive p(crit.)-value that is well below 0.05: the null hypothesis of differing $\bar{\delta}_{\mathrm{w}}$ must be rejected, and the alternative hypothesis of equivalent $\bar{\delta}_{\mathrm{w}}$ accepted. Statistically speaking, then, there is no difference between the *def* and *opt* case for Fe^{20+}. Another notable observation is that in addition to the weighted means being equivalent, they are both smaller in magnitude than in the Fe^{7+} case. Therefore, it can be suggested that not only has the structure difference between the *def* and *opt* cases been eliminated but also much of the absolute structure error. However, as mentioned above, one cannot definitively comment on physical correctness solely from the evidential basis of gauge invariance of radiative matrix elements. Physical arguments supporting the increased accuracy of highly ionized cases, like Fe^{20+}, are made towards the end of this section while referencing figure 2.13, but inevitably, a final conclusion must be delayed until supplementary analysis in section 2.4.2.

Another lens by which to assess the gauge variation across optimisation cases is by observing the cumulative distribution of the δ_k. Again, it is critical to account for the relative importance of transitions, and this can be done by partitioning the cumulative distributions into bands based on the weighting factors from equation 2.30. The selection of the banding is somewhat arbitrary, but the following three categories tend to produce coherent pictures: $w_k > w_{\max}/10^2$ for the strongest transitions, $w_{\max}/10^3 < w_k < w_{\max}/10^2$ for intermediate strength transitions, and $w_k < w_{\max}/10^3$ for the weakest transitions. The cumulative distributions for Fe^{7+} are displayed in figures 2.9 and 2.10, and for Fe^{20+} in figures 2.11 and 2.12. When interpreting these plots, there is one critical feature

that must be determined: where is the nonstationary inflexion point of the cumulative distribution curve located? The reason being that the derivative of the cumulative distribution curve yields the actual δ_k distribution, and so a nonstationary inflexion point will yield the maximum derivative and hence peak of the δ_k distribution. For normally distributed δ_k distributions, an assumption which underpins most of this analysis and generally does hold, the peak of the distribution also corresponds to the arithmetic mean. The cumulative distribution has been used instead of the more direct distribution itself because it improves the ability to distinguish between multiple cases on a single plot: overlapping normal distributions are harder to differentiate between than their corresponding "S" shaped cumulative distributions.

The conclusions from these plots are similar to those obtained from the weighted statistics, as should be expected. Figures 2.9 and 2.10 for Fe^{7+} show a clear distinction between the *opt* and *def* cases in the top two panes, which correspond to the top two weighting bands and so encompass $w_k > w_{\max}/10^3$. There is little notable difference between the ground $E1$ and all $E1$ transition categories. The inflexion point of the $\delta_k^{(\mathrm{opt})}$ cumulative distribution is located at a lower δ_k value than that of $\delta_k^{(\mathrm{def})}$. This is direct visual confirmation of the weighted statistics analysis that the important dipole transitions tend to have lower δ_k values on average for the *opt* case than for the *def* case. Moreover, these inflexion points are located around $\delta_k = 0.4$, in accord with the values of table 2.7. However, the bottom pane of these figures does not match this behaviour: the *opt* and *def* cumulative distributions lie nearly on top of each other and there is no difference of the inflexion point. This is not a problem because this pane corresponds to the weakest transitions, $w_k < w_{\max}/10^3$, so these transitions affect a minimal if not negligible impact upon the weighted statistics. Regardless, it is still worthwhile showing this weighting band to monitor how the weakest transitions are behaving.

Once again, Fe^{20+} provides an example where the optimisation strategy has not improved the structure noticeably, although this is not so apparent from figures 2.11 and 2.12. The symmetric "S" shape is absent from the cumulative distributions in both figures, indicating the underlying distributions are no longer truly normal but skewed. Thus, the the mode of the underlying distribution (i.e.

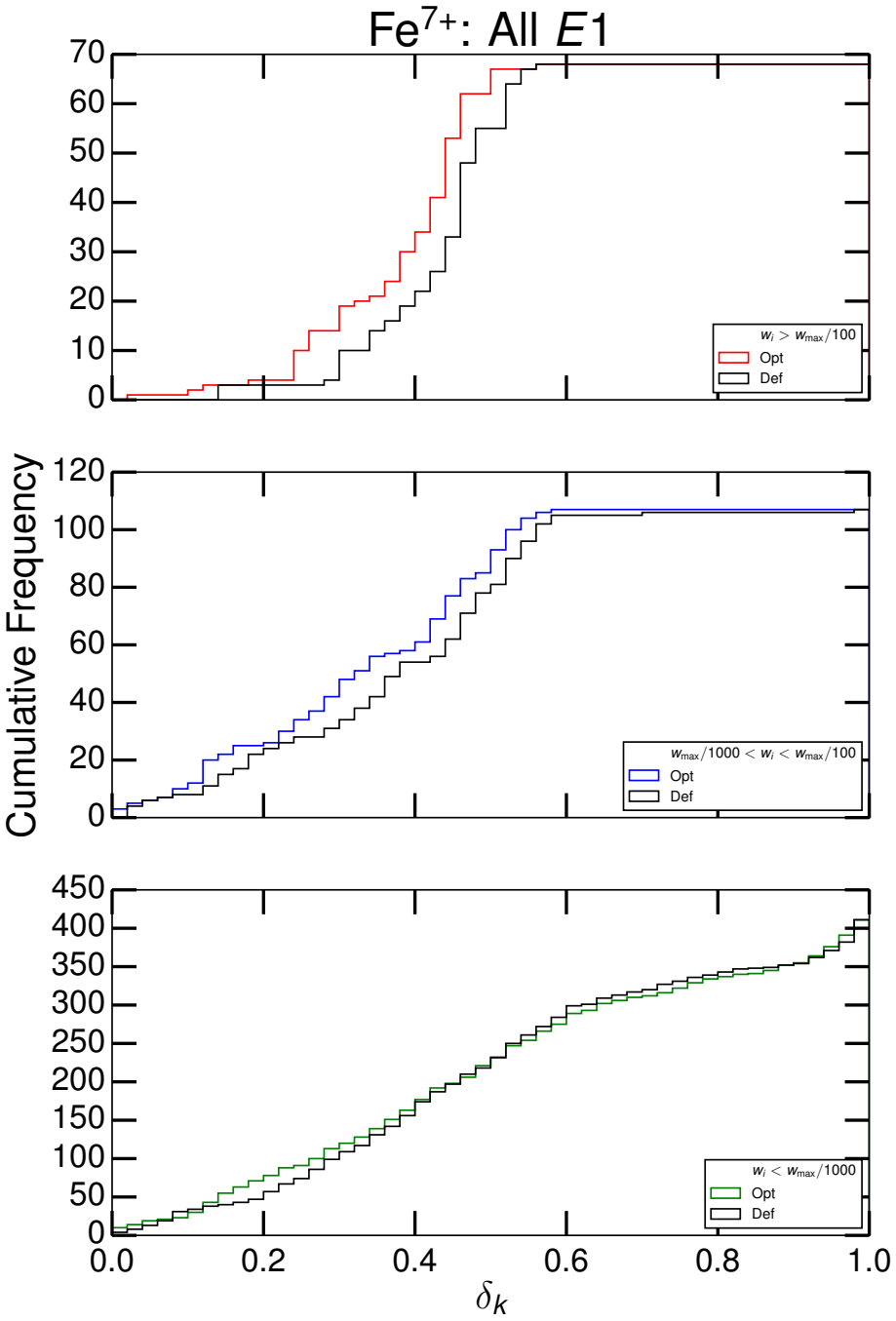

Figure 2.9: Cumulative distribution of δ_k for all dipole transitions of K-like Fe^{7+}. The histograms of the cumulative distributions have been partitioned by weighting factor values, w_k defined in equation 2.30, and the title of each legend defines the range of weighting factor values applicable to the associated δ_k values for that histogram. For example, the top pane shows the cumulative distribution composed of all δ_k values that have $w_k > w_{\max}/100$, where $w_{\max}$ is the largest weighting factor of all transitions considered. The weighting factors are indexed with $i \equiv k$. A cumulative distribution is shown for each λ_{nl} case: colour lines for *opt* and black lines for *def*.

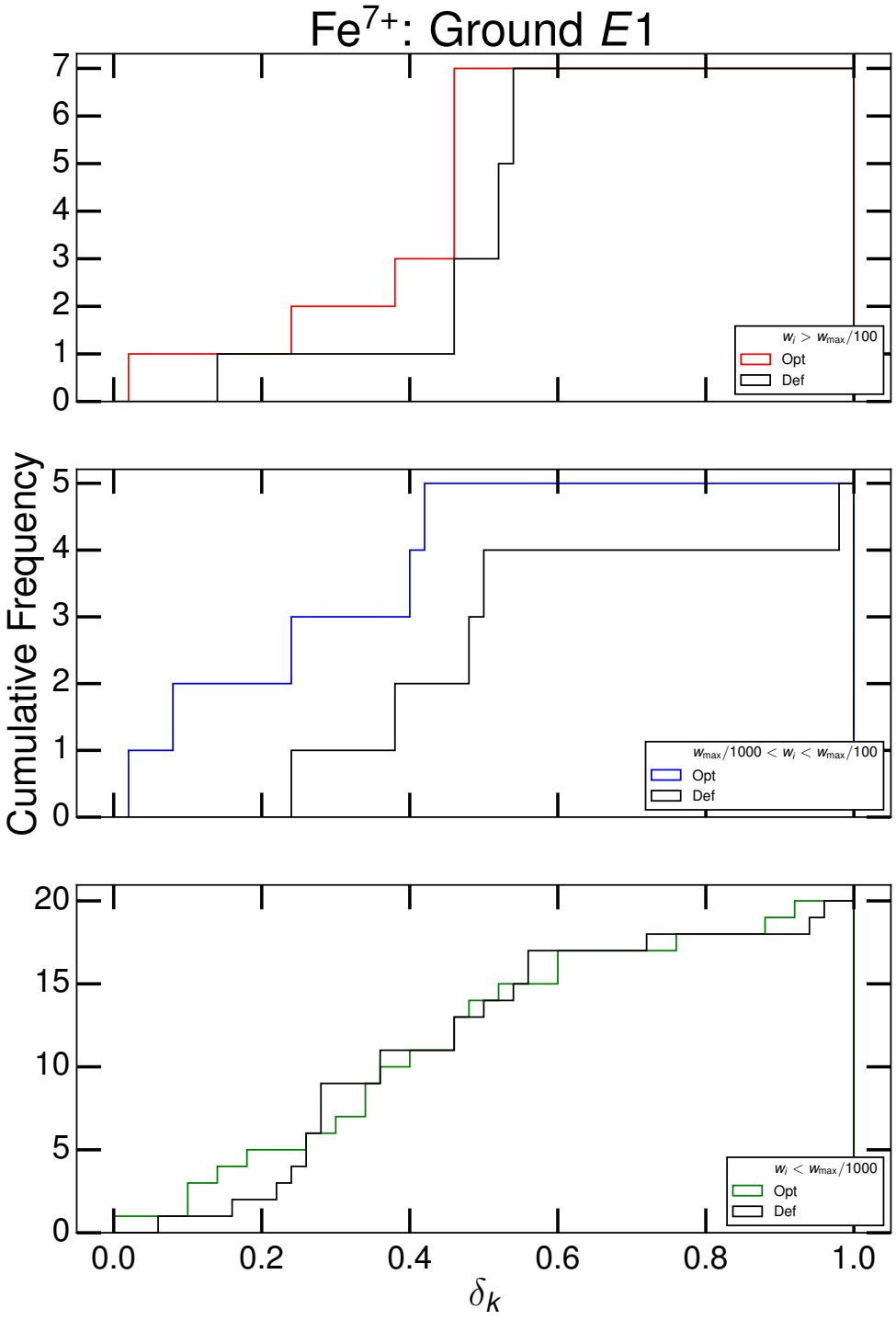

Figure 2.10: Cumulative distribution of δ_k for dipole transitions to the ground state of K-like Fe^{7+}. See caption of figure 2.9 for description of plots.

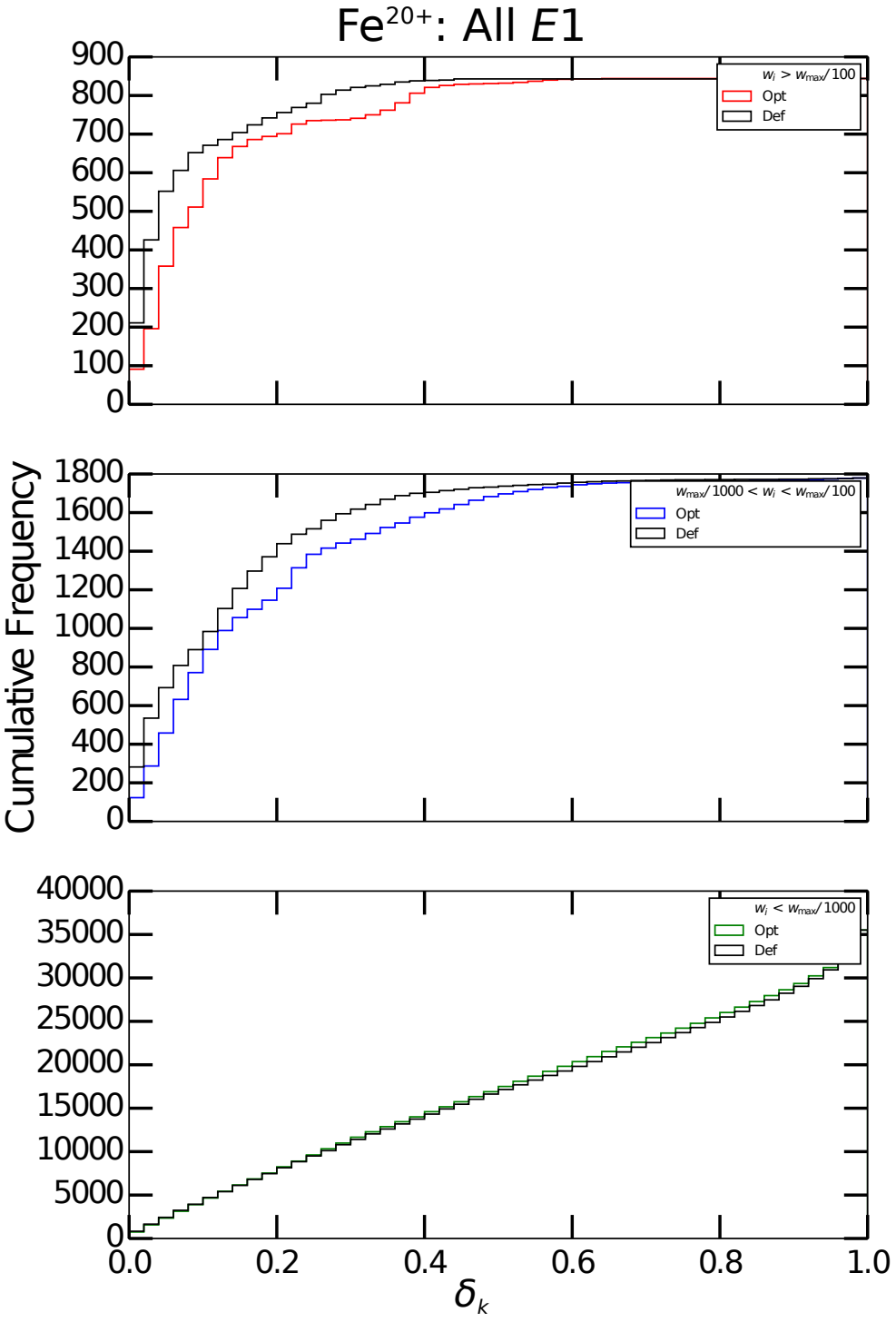

Figure 2.11: Cumulative distribution of δ_k for all dipole transitions of C-like Fe^{20+}. See caption of figure 2.9 for description of plots.

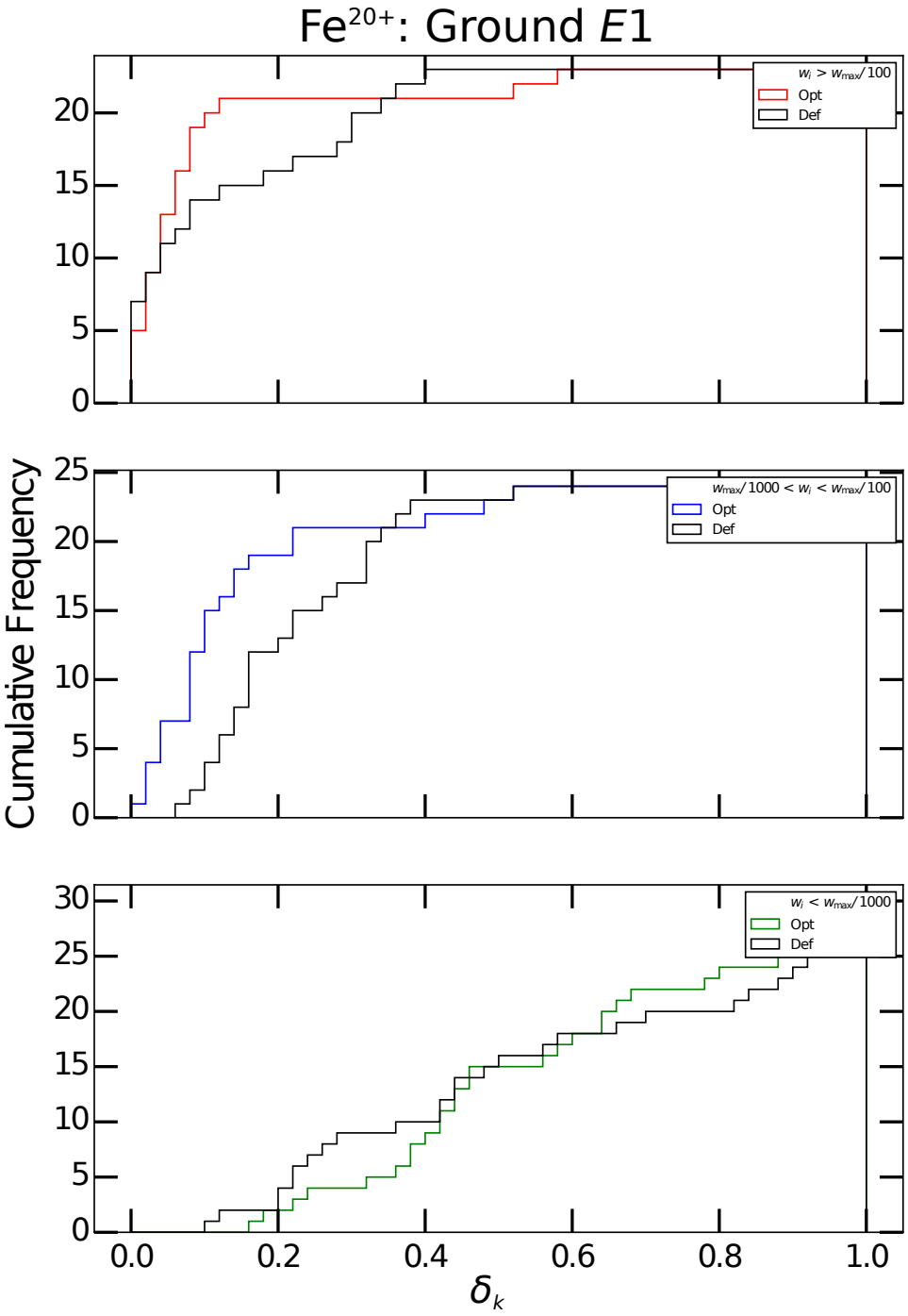

Figure 2.12: Cumulative distribution of δ_k for dipole transitions to the ground state of C-like Fe^{20+}. See caption of figure 2.9 for description of plots.

the steepest slope) may no longer be synonymous with the mean. Even so, it is still useful to observe how the modes of these distributions compare. The top pane of figure 2.11, corresponding to $w_k > w_{\max}/10^2$, show essentially overlapping steepest slope points very near to $\delta_k = 0$, and the cumulative distributions are only slightly discrepant at higher δ_k. This is in line with the findings from the weighted statistical analysis: both $\bar{\delta}_{\rm w}$ are close to zero and statistically equivalent.

The preceding two case studies of Fe^{7+} and Fe^{20+} have proved useful for detailing the mechanics of the δ_k figure of merit analysis and also provide archetypes for the two possible outcomes when comparing the *opt* and *def* cases. But as with most work in this study and ADAS, generality is sought, so isonuclear and isoelectronic studies must be performed. Weighted statistics and cumulative distribution plots have been generated for a number of ions in the iron isonuclear sequence to complete the picture that was initiated with the preceding two ions. Drawing from these examples, the primary outputs from the statistical analysis are the weighted means, $\bar{\delta}_{\rm w}^{(\rm opt)}$ and $\bar{\delta}_{\rm w}^{(\rm def)}$, and the corresponding equivalence test, all conducive to graphical representation; the cumulative distribution histograms, however useful, provide congruent information and are not space efficient, so they have been omitted. Results have also been generated for the argon isonuclear sequence, an element of particular interest for Chapter 5.

Figure 2.13 assembles the results of the weighted statistical analysis for the iron isonuclear sequence. A clear trend is observable. Iron ions below approximately 13-times ionised have statistically significant lower $\bar{\delta}_{\rm w}^{(\rm opt)}$ than $\bar{\delta}_{\rm w}^{(\rm def)}$, signifying the new λ_{nl} optimisation strategy, *opt*, has improved the atomic structure of all ions in this regime. Conversely, above 13-times ionised the $\bar{\delta}_{\rm w}$'s are equivalent according to the equivalence test: the *opt* case does not offer an improvement over *def*. Moreover, there is an overall trend of decreasing $\bar{\delta}_{\rm w}$ with increasing ionisation stage for both cases. All of these trends can be explained by the same physical reason. The λ_{nl} are part of the TFDA potential used in the calculation of the Hamiltonian in AUTOS, equations 2.5–2.7. The purpose of the TFDA potential is to allow for a initial approximation of Ψ to be obtained that still accounts for the mutual repulsion of electrons, and the λ_{nl} enable flexibility in bending the nl-orbitals into more optimum shapes that account for this repulsion. As the ion charge increases and the number of electrons decrease, the effects

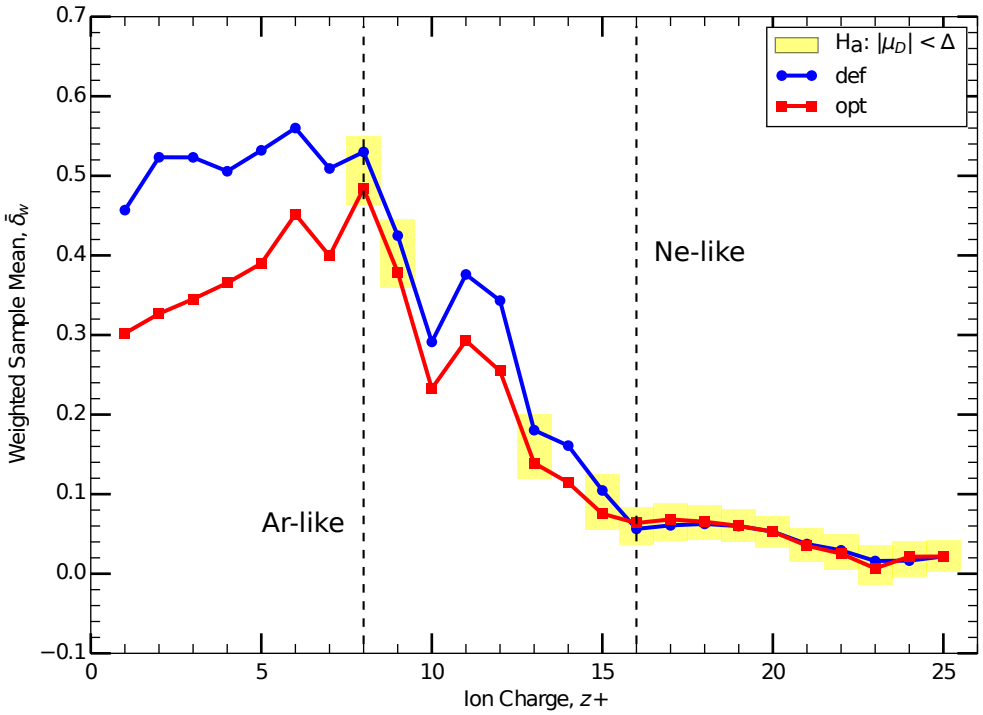

Figure 2.13: $\bar{\delta}_{\mathrm{w}}^{(\mathrm{opt})}$, $\bar{\delta}_{\mathrm{w}}^{(\mathrm{def})}$, and corresponding equivalence test along the Fe isonuclear sequence. The filled yellow boxes around paired $\bar{\delta}_{\mathrm{w}}$ points indicate that the alternative hypothesis ($\mathrm{H_a}$: $|\mu_D| < \Delta$) is accepted at a significance of $\alpha = 0.05$, and so $\bar{\delta}_{\mathrm{w}}^{(\mathrm{def})}$ and $\bar{\delta}_{\mathrm{w}}^{(\mathrm{opt})}$ are equivalent for the ion under question.

of electron repulsion and exchange decrease, becoming small perturbations, and therefore the orbitals that compose Ψ more closely resemble hydrogenic ones. Consequently, the need to "bend" the orbital basis functions and indeed the need of the TFDA potential itself is diminished; however, this does not mean that the λ_{nl} determined through the optimisation strategy will approach unity for high-z cases. Indeed, a number of the λ_{nl} for iron and argon below are relatively far from unity in instances where the *opt* and *def* cases are statistically equivalent—see figure 2.8. Rather, high-z cases can be classified as insensitive to the exact values of λ_{nl}, meaning that the variance of these scaling parameters does not influence the atomic structure much. Here, "high-z" is quantified using the ratio, Z_0/N, and the cutoff varies depending on the weight classification of the species under consideration; more details will be provided in the future publication of this work. Overall, this supports the hypothesis that smaller $\bar{\delta}_{\mathrm{w}}^{(\mathrm{def})}$ and $\bar{\delta}_{\mathrm{w}}^{(\mathrm{opt})}$ values for higher-z species indicates more accurate structures have been obtained, but

corroborating evidence from proceeding sections is required before definitively concluding on the matter.

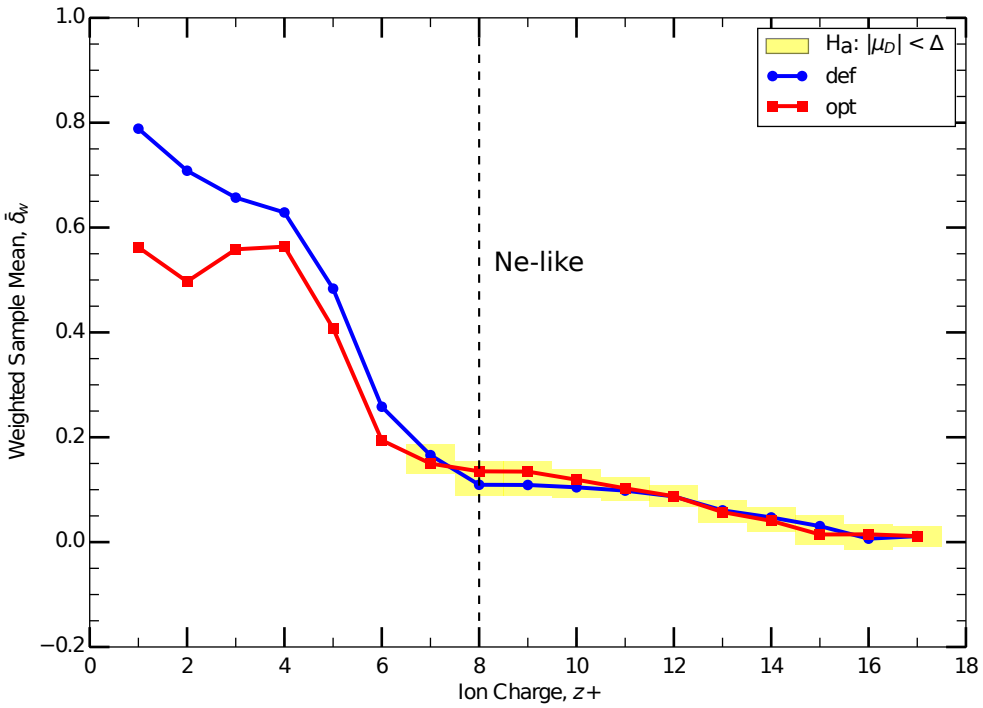

Figure 2.14: $\bar{\delta}_{\mathrm{w}}^{(\mathrm{opt})}$, $\bar{\delta}_{\mathrm{w}}^{(\mathrm{def})}$, and corresponding equivalence test along the argon (Ar) isonuclear sequence. The filled yellow boxes around paired $\bar{\delta}_{\mathrm{w}}$ points indicate that the alternative hypothesis ($\mathrm{H_a} : |\mu_D| < \Delta$) is accepted at a significance of $\alpha = 0.05$, and so $\bar{\delta}_{\mathrm{w}}^{(\mathrm{def})}$ and $\bar{\delta}_{\mathrm{w}}^{(\mathrm{opt})}$ are equivalent for the ion under question.

Similar characteristics are observed for the two $\bar{\delta}_{\mathrm{w}}$ results along the argon isonuclear sequence presented in figure 2.14. For $z \geq 7$, the $\bar{\delta}_{\mathrm{w}}$'s of the two cases are statistically equivalent, and vice versa for $z < 7$. This provides strong evidence that the new baseline *adf04* files for argon used in Chapter 5 are an improvement upon the previous AUTOS baseline. Further analyses of isonuclear sequences will be made in a future publication and are omitted here for brevity: the primary purpose of this subsection was to establish a viable figure of merit to judge the new λ_{nl} optimisation strategy, not investigate a broad range of specific examples.

2.4.2 $\Delta_r E$ Figure of Merit

It was mentioned in the previous section that the δ_k figure of merit, which is based upon the principle of gauge invariance, should be supported by additional performance metrics when assessing atomic structure accuracy. To recapitulate, a minimal dependence of the radiative matrix elements upon the gauge of calculation is an indicator of wave function quality, but this alone does not ensure the physical accuracy of the radiative transition rates or atomic structure. A figure of merit that more directly relates to the observables of the atomic structure is therefore warranted. Moreover, the δ_k figure of merit cannot directly assess effects upon radiated power from the atomic system under examination, and so a benchmark that transparently relates to the power measures is also desirable.

There are two atomic structure observables that match these criteria: energy eigenvalues of the atomic states, E_i, and radiative transition rates between these states, e.g. $A_{i\rightarrow j}$, gf_{ij}, and S_{ij}. A figure of merit based on the E_i is preferable for the present circumstances because it more directly influences the radiated power. This can be appreciated by considering the low density limit of the ground state $\mathcal{PLT}$,

$$\lim_{N_\mathrm{e}\rightarrow 0} \mathcal{P}_{LT,1} = \sum_i \left(\Delta E_{1i}\right) q^{(\mathrm{e})}_{1\rightarrow i} \tag{2.35}$$

Of course, the EIE rate coefficient, $q^{(\mathrm{e})}_{1\rightarrow i}$, does have an indirect dependence upon the radiative transition rate, viz. Gaunt factor representations, and the radiative transition rates will influence the finite density atomic population model, but all of this adds an unnecessary layer of complexity. Moreover, transition energies, and hence E_i, are much simpler and less ambiguous to measure experimentally than radiative transition rates. Consequently, measured values of E_i are much more abundant and possess lesser uncertainties. This is a valuable trait for further validation, even though these experimental values will not be used as the reference in the systematic analysis to follow; the reasons for this are given directly below.

Contrary to the δ_k analysis, the theory behind an eigenenergy figure of merit is relatively simple: the eigenenergies of the calculation under consideration should be as close as possible to whatever reference eigenenergies have been selected. For the present purposes of generating an improved baseline, evidence of broad agreement amongst all calculated eigenenergies is sought since it is a general com-

parison of the *def* and *opt* cases that is of interest. Unlike studies focussing on spectroscopic applications, the aim is not to determine whether a small subset of transition energies achieve the best possible accuracy. It then remains to quantify what "close" means for eigenenergies and to specify which values are to be used as a reference. It has been stated that the standard reference for atomic data within ADAS is the NIST Atomic Spectra Database [59] and that although it is expansive, there is no guarantee of coverage for a given ion. Moreover, even the data present for an arbitrary ion can be sparse in terms of energy levels reported, and this can complicate the task of energy level or term matching. The most convenient solution is to use the eigenenergies produced from another computer code as a reference because then the configuration expansion can be matched to the present AUTOS calculations, guaranteeing completeness and greatly simplifying the task of term and level mapping.

COWAN is the obvious option for reference: it is robust, it has an large experience base within ADAS, and it constitutes the previous ADAS baseline, facilitating a vital comparison. Admittedly, there is a glaring potential issue: how can the physical correctness of COWAN be guaranteed so that it merits use as a reference source? In other words, might differences observed between COWAN and AUTOS indicate that COWAN is in error rather than the inverse? The honest answer is that such a guarantee cannot be made, but it is possible to suggest that COWAN may offer improved physical accuracy of eigenenergies over AUTOS. Although the V_{TFDA} potential with λ_{nl} optimisation offers a reliable approach to atomic structure calculations, it tends to be outperformed by the variational HF method available in COWAN, and this proposition is further substantiated in section 2.2.1. Furthermore, first-hand experience in the ADAS community has been that COWAN comes closer to reproducing NIST eigenenergies than does AUTOS. These comments justify the use of COWAN as a reference source; however, it will be important to periodically benchmark results with those available from NIST to ensure improved accuracy is actually being achieved.

To measure the accuracy of eigenenergies, a relative difference formula is adopted,

$$\Delta_r E_{i,(\mathrm{case})} = \frac{E_{i,(\mathrm{case})} - E_{i,\mathrm{Cowan}}}{E_{i,\mathrm{Cowan}}}, \tag{2.36}$$

where (case) is either (opt) or (def) and i indexes the atomic eigenstates to which

the eigenenergies belong. The resolution of the eigenstates for which these differences are calculated is open to selection. For the following analysis, *LS*-coupling is used primarily to reduce the number of eigenenergies that must be considered and because analysing the fine structure is excessive for the present goals. In addition, *LS* terms simplify the task of mapping the eigenstates between the AUTOS and COWAN calculations, and although this seems like a somewhat technical note, the step of mapping eigenstates is absolutely essential for meaningful relative differences to be calculated. A development version of the offline ADAS code, ADAS7#5, was used to perform the term matching, but further developments are required before robust performance and reliability can be guaranteed for general consumption. Moreover, this is one of the components that will need to be included in a complete implementation of medium-weight GCR so that matching to experimental NIST values can be performed—refer to figure 1.2.

Like in the previous section 2.4.1, a complete statistical analysis of the $\Delta_r E_i$ distribution could be performed to determine whether the *opt* and *def* cases differ substantially according to this quantity. Since the relative differences can be negative, an ordinary mean of $|\Delta_r E_i|$ would be appropriate or perhaps a mean weighted by the radiative transition rate of the corresponding eigenstate to the ground state. However, at the time of writing, this is envisioned as a future implementation task that is not central to the present conclusions; a quick confirmation of the δ_k figure of merit results is sufficient.

The $\Delta_r E_i$ values for both *opt* and *def* cases can be readily presented in the form of a bar chart on a per ion basis, and this has been done for the example ions from section 2.4.1, Fe^{7+} and Fe^{20+}, in figures 2.15 and 2.16, respectively. Both figures appear to support the conclusions of the δ_k analysis. For Fe^{7+}, figure 2.15 plainly shows an improvement of the term eigenenergies of the *opt* case over the *def* case, and this is true relative to both COWAN and NIST reference values. The *opt* term energies are all within 2% of their COWAN counterparts (unfilled blue bars), while the *def* term energies have relative errors (light green bars) starting at approximately 8% for $i = 2$ and decreasing linearly to about 2% by $i = 31$. The sparse $\Delta_r E_i$ values relative to NIST are all below 6% for *opt* whereas the opposite is true in the *def* case. These observations corroborate the conclusion that the new optimisation strategy of λ_{nl} has resulted in a measurable improvement of the

atomic structure of Fe^{7+}. Of particular note is that all of the *def* $\Delta_r E_i$ values are positive while the *opt* values are more equally distributed between the positive and negative ranges. This indicates a systematic error is present in the *def* case, and the absence of this error in the *opt* case is revealing of the physical reasons for why this new strategy is successful. Determining the source of the systematic error requires recalling the comparison made between the atomic structure calculations of AUTOS and COWAN in section 2.2.1. Table 2.3 summarises this comparison and dictates three possible sources of difference between the codes. CI effects do not factor into this discussion because the same configuration expansion is used by all codes and cases.

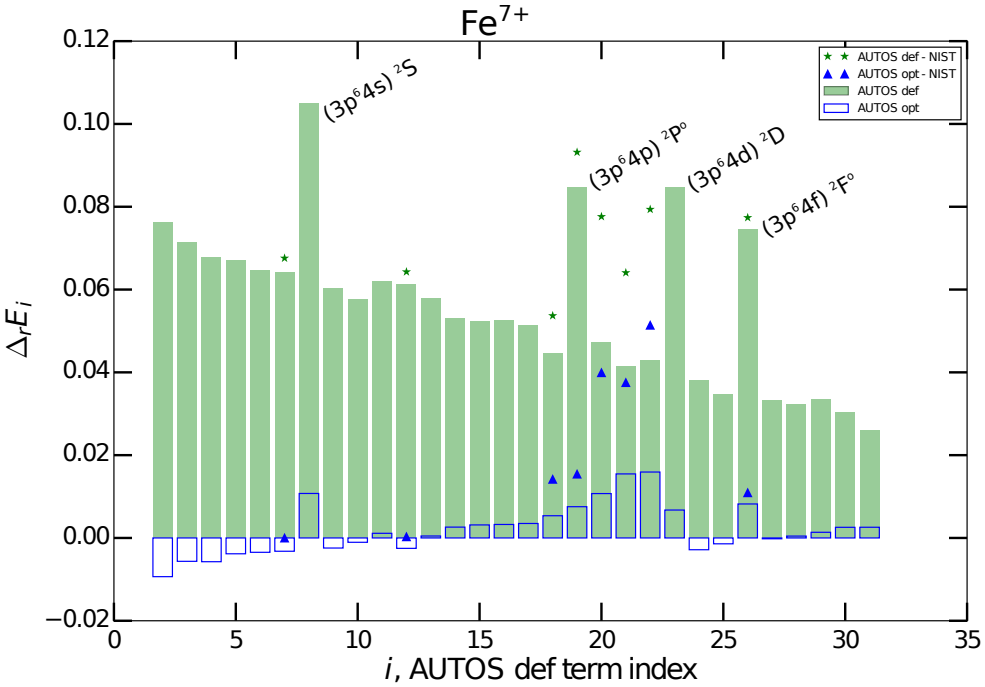

Figure 2.15: Bar chart of relative energy difference values, $\Delta_r E_i$, versus *def*, energy-ordered *LS* term index, i, for Fe^{7+}.

First, for the baseline processing relevant to this thesis, the Hamiltonian operator used in AUTOS includes two-body relativistic terms and further relativistic considerations are made: consideration of the small component of the wave function, inclusion of the Breit interaction, and QED corrections. COWAN also uses the Breit-Pauli Hamiltonian but does not include these additional relativistic corrections. AUTOS was run in *def* mode but without its additional relativistic settings so as to match the relativistic approach of COWAN in order to determine

whether this might be a source of systematic error. The resulting relative errors were on the order of 10^{-4}, which supports the position that additional relativistic corrections are not influential in this instance.

Second, COWAN includes an electron correlation correction to the configuration average energies while AUTOS does not. The correlation correction has a weak dependence on the specific configuration to which it is applied, so in principle it can affect the relative term and level energies calculated for an atom. However, this effect is truly minor, producing approximately a half of a percent correction to the relative energies for Fe^{7+}. So again, this cannot account for the systematic difference observed in figure 2.15. The true role of the correlation correction is obtaining better agreement of the absolute eigenenergies, and it can primarily be viewed as a shift applied to all of the eigenenergies from a calculation.

Thirdly, the two codes differ in their approach for solving the radial portion of the Shrödinger equation. With the previous two options eliminated, this then must be the source of the systematic error present in the *def* case, an unsurprising fact given that the *opt* case does not exhibit such systematic errors and the only variation between the two is the optimisation of the λ_{nl}—i.e. a variation in the solution of the radial problem. The task of answering why a systematic error is present for the *def* $\Delta_r E_i$ and what this indicates about our λ_{nl} optimisation strategy effectively reduces to a comparison of the potential energy terms in the radial equations and the solution procedures as per table 2.3 and the subsuming section 2.2.1. Briefly, the HF equations used in COWAN minimise the configuration average energies out of necessity because the equations are derived from the variational principle, and electron repulsion and exchange are accounted for in a central-field, spherically averaged model of the atom. In contrast, AUTOS minimises a weighted sum of term energies by varying the λ_{nl}, and the energies are derived from a set of homogeneous radial equations (equation 2.1) that contain V_{TFDA}. As noted in section 2.2.1, the TFDA atomic potential is a cruder approximation of mutual electron repulsion and exchange than the inherent terms that arise in the HF equations, and one must vary the λ_{nl} to arrive at better solutions.

It is in this context that the systematic error of the *def* $\Delta_r E_i$ can be understood. Setting all of the λ_{nl} to a fixed value, unity or otherwise, eschews the determination of an optimised solution, so in all likelihood a complete consid-

eration of electron repulsion and exchange is neglected. There is of course the possibility that the optimised solution will also correspond to all $\lambda_{nl} = 1$, and this can be valid under circumstances to be explored shortly, but for the present example of Fe^{7+}, this is emphatically not the case. Rather, one is led to the conclusion that the systematic error present in the *def* case relative to COWAN is due to an improper treatment of electron repulsion and exchange, which is a direct result of $\lambda_{nl} = 1$ yielding a poor description from V_{TFDA} in this instance. And further, because the *def* AUTOS eigenenergies are systematically larger than the COWAN ones, indicated by the positive *def* $\Delta_r E_i$ values in figure 2.15, it must be deduced that V_{TFDA} with $\lambda_{nl} = 1$ overestimates the electron repulsion and exchange effects. The exchange interaction of fermions manifests as an effective repulsion between the electrons, and hence contributes positively to the potential energy of the atomic states, just like the electrostatic Coulomb repulsion does. A corollary of the above is that the λ_{nl} from the *opt* case must produce a V_{TFDA} that better accounts for electron exchange and mutual repulsion; this is the fundamental physical reason behind the initial observation that the new λ_{nl} optimisation strategy has improved the atomic eigenenergies of Fe^{7+}.

Another interesting observation of figure 2.15 is that the *def* case has a few anomalous upward spikes deviating from the linear downward trend, and the terms to which these relative error spikes belong have been labelled. The common feature to each of these spikes is that the configurations involve a closed 3p-shell with a $4l$ orbital on top. All of the other terms belong to the configuration $3p^5 4s^2$. Why then does the *def* case perform comparatively poorly for a closed versus open 3p-subshell and the *opt* case not? Following the reasoning from the systematic error investigation above, the cause of the present phenomenon must too be attributed to some aspect of the λ_{nl} optimisation: no other differences between the codes are significant in this instance and the only variation between the *opt* and *def* cases is the λ_{nl} values. The pivotal observation is that the electric potential experienced by an electron in a closed subshell is notably different than when the subshell is open, and so the orbital that describes this electron, here the 3p, must also be different between the closed and open subshell configurations. The HF procedure naturally accounts for this because there is a separate set of equations for each configuration, and so a separate set of radial

orbital components, $P_{nl}(r)$, specific to each configuration. On the other hand, AUTOS produces a single set of $P_{nl}(r)$ and corresponding λ_{nl}, and both open and closed subshell configurations are composed from these. The variation of the λ_{nl} assists in reconciling the disparity that orbitals from different configurations would exhibit, producing a single set of orbitals that are effectively an optimal balance of the behaviours across all configurations. Moreover, the new λ_{nl} optimisation strategy inherently considers the critical behaviour of closed (sub)shells, and this is further substantiated by the lack of any disparity between the closed and open 3p-subshell configurations for the *opt* case in figure 2.15. In the absence of such optimisation, like in the *def* case, it is highly unlikely that a balance is achieved, meaning pronounced differences between closed and open subshells should be expected, explaining the spikes in figure 2.15.

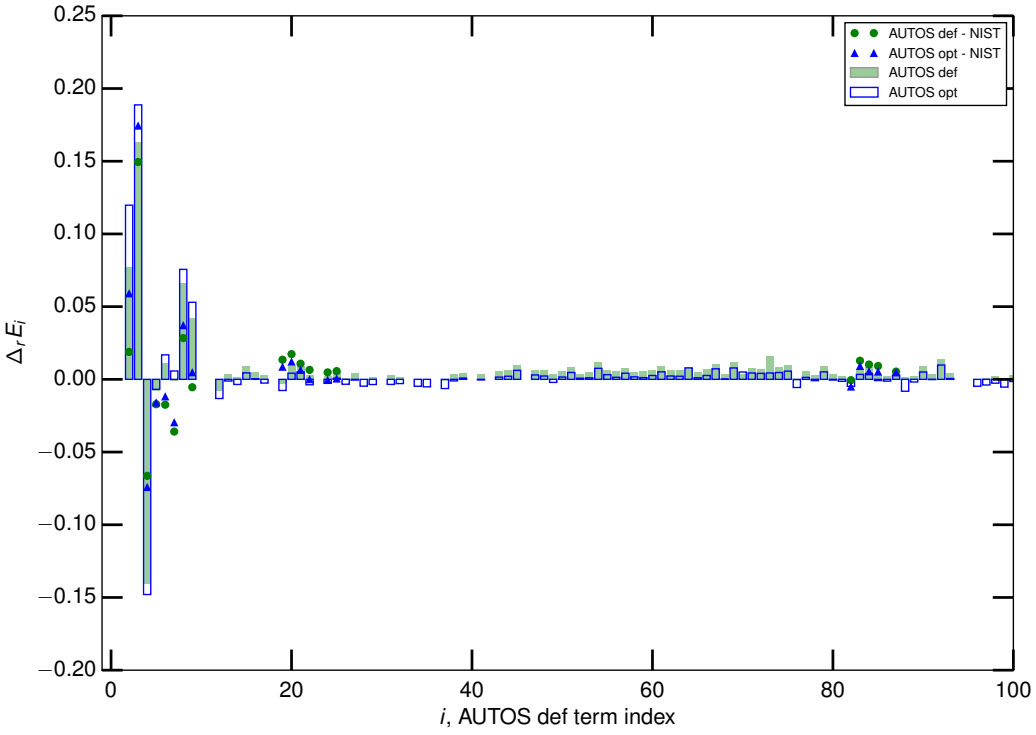

Figure 2.16: Bar chart of relative energy difference values, $\Delta_r E_i$, versus *def*, energy-ordered *LS* term index, i, for Fe^{20+}.

Dissimilarly, figure 2.16 displays a high level of agreement amongst all the sources of term energies for Fe^{20+}. The $\Delta_r E_i$ relative to COWAN (bars in figure) are mostly under 2% except for the terms in the ground configuration ($i < 10$) which reach as high as 20% relative error. It is a similar story for the $\Delta_r E_i$ val-

ues relative to NIST, although marginally better agreement is observed for the ground configuration terms. Furthermore, both the *def* and *opt* cases achieve similar $\Delta_r E_i$ values for each term energy relative to either reference source. These observations suggests that both the *opt* and *def* cases provide suitable and physically correct atomic structures and that the two cases have converged upon each other. Such conclusions are a direct corroboration of the conclusions from the δ_k figure of merit analysis in section 2.4.1: the close $\bar{\delta}_{\mathrm{w}}$ values and the rejection of the statistical equivalence test null hypothesis also recommended that the *opt* and *def* cases yielded equivalent structures for Fe^{20+}. Moreover, the suspicion and delayed conclusion from the δ_k analysis of Fe^{20+} can also be resolved. It was suspected that the small absolute values of the $\bar{\delta}_{\mathrm{w}}$ might also indicate an improved physical correctness and accuracy of the atomic structure, and the results of figure 2.16 certainly support this.

The physical reason behind the concord of figure 2.16 is invariably the same as for the results from the δ_k analysis in the preceding subsection. Quoting from that section, "[a]s the ion charge increases and the number of electrons decrease, the effects of electron repulsion and exchange decrease, becoming small perturbations, and therefore the orbitals that compose Ψ more closely resemble hydrogenic ones. Consequently, the need to 'bend' the orbital basis functions and indeed the need of the TFDA potential itself is diminished". As a result, there is little discernable need for the variation of the λ_{nl}, meaning not only that the *opt* and *def* cases should converge but also that they will converge upon the physically accurate result.

2.4.3 $\mathcal{PLT}$ Figure of Merit

The results of the previous two sections provide convincing evidence that our new λ_{nl} optimisation strategy has yielded measurable improvements to certain facets of the atomic structures of interest. However, it was asserted at the beginning of the subsuming section 2.4 that the $\mathcal{PLT}$ must also be monitored to ensure amelioration of the impurity radiated power. This, after all, was the original motivation to search for a λ_{nl} optimisation strategy first mentioned in section 2.3.2 and [21]; errors in the AUTOS $\mathcal{PLT}$ results were directly attributed to the relatively poor atomic structure, and so the minimization of the atomic structure error should

improve the radiated power description as well. But this is not a guarantee. Although the δ_k and $\Delta_r E_i$ figures of merit measure facets of the atomic structure that will influence the $\mathcal{PLT}$, viz. energy levels and wave function quality, the relationships connecting them are complex. Thus, it must be explicitly checked that an improvement in the atomic structure has also produced improvements in the $\mathcal{PLT}$ and radiated power.

The zero density limit of the $\mathcal{PLT}$, equation 2.35, was used in section 2.4.2 to motivate the use of the energy level differences as a figure of merit, but the finite density expression is used here in practice:

$$\mathcal{PLT} = \mathcal{P}^{(z)}_{\mathrm{LT},\sigma} = \sum_{j>k} \Delta E_{kj} A_{j\to k} \mathscr{F}^{(\mathrm{exc})}_{j\sigma}, \tag{2.37}$$

where $\mathscr{F}^{(\mathrm{exc})}_{j\sigma}$ is the effective contributions to the excited populations, j, due to collisional excitation from the metastables, σ,

$$\mathscr{F}^{(\mathrm{exc})}_{j\sigma} = -\frac{1}{N_\mathrm{e}} \sum_{i=1}^{O} \mathscr{C}^{-1}_{ji} \mathscr{C}_{i\sigma}. \tag{2.38}$$

A complete derivation and description of these quantities is presented in [15] and [60], and a résumé is provided in Appendix C. Evidently, a population calculation is required to determine the $\mathcal{PLT}$, and therefore, data for collisional processes is needed in addition to the structure calculations analysed above. From a technical standpoint, little additional information is needed to drive the collision calculations, but there is a significant increase in computation time. The population calculation that yields the $\mathcal{PLT}$s is performed by the ADAS208 code, and this is done in a simplified form. Only the single ionization stage is considered with no processes connecting to adjacent stages included; therefore, it is solely direct collisional and radiative processes amongst the low-lying, highly resolved ordinary and excited states that are considered. The influence of higher, more coarsely bundled levels are not condensed and then projected onto this picture, nor is ionization or recombination considered. This simplified approach is acceptable for the present analysis because the detailed atomic calculations being compared affect only these same low-lying, highly resolved states of the atom. The other neglected processes involved in a more complex population calculation

can be seen as a constant external variable that will not alter the findings of the present relative comparison.

Like in the previous section, the question of identifying a reference source of data must be resolved before a meaningful comparison of the *opt* and *def* case $\mathcal{PLT}$s can be performed. Once again, COWAN recommends itself as the most suitable candidate primarily because it is was the source of the fundamental data used in the context of the ADAS808 code, which automates the preparation of the driver datasets required for large-scale, off-line production of ADAS baseline atomic data for complex atoms [15]. Moreover, as stated before, the goal is to prove that the replacement of COWAN by AUTOS as the source of baseline fundamental atomic data is warranted. To do this, it must be shown that AUTOS can reproduce the previous baseline $\mathcal{PLT}$ results to a satisfactory degree. Once this is achieved, one can be more confident that the advantage of spin-changing transitions introduced by using AUTOS with DW scattering calculations is not compromised by any atomic structure errors.

The above implies a need to compare like with like. Since COWAN uses the PWB approximation for calculating collision quantities, so too should AUTOS when juxtaposing results from the two. Furthermore, the actual set of levels and the collisional-radiative processes amongst these levels should also match as much as possible so that the population models can be unambiguously compared. The *adf04* files, which contain the specific ion atomic data presently under discussion, must then nearly match in terms of the atomic states and transitions present, although the numeric values will differ. While this may seem to be a trivial requirement, the implications can be quite significant, as will be seen in the following example.

Throughout the antecedent discussion about the figures of merit, the iron isonuclear sequence has been the test bed for assessing the performance of our new λ_{nl} optimisation strategy, *opt*. This narrative will now be culminated and concluded. Fe^{7+} has provided a consistent example of an atomic system where the *opt* case has produced a measurable improvement in the figures of merit, and figure 2.17 likewise suggests that this is also true for the $\mathcal{PLT}$, although this is not immediately apparent. Inspecting the default "full" cases where all levels and transitions have been retained, it would appear that the *def* result (solid blue

line) agrees better with COWAN (solid black line) than does the *opt* result (solid red line). However, AUTOS computes up to the $k = 6$ order of 2^k-pole electric and magnetic transitions, whereas COWAN only includes $E1$ and $E2/M1$, and as a result, there are many more transitions present in the AUTOS *adf04* files than in the COWAN one. Typically, these higher order multipoles above $E2/M1$ are of little consequence because both the radiative and collisional components of the transition are relatively weak, but exceptions are possible, especially when moderate magnitudes of the transition quantities are achieved and previously unavailable pathways involving metastables states are opened. Indeed, this is the case here because the reduction of the AUTOS transition set to match that of COWAN (labelled "reduced" in legend of figure) noticeably alters the AUTOS $\mathcal{PLT}$s. In the *opt* case of figure 2.17, this action brings the $\mathcal{PLT}$ into better agreement with the COWAN result, moving the solid red to the thick-dashed red line, whereas in the *def* case it eliminates the agreement, moving the solid blue to the thick-dashed blue line. Therefore, the agreement initially observed between the *def* case using the "full" transition set and COWAN is completely fortuitous. It would appear, then, that this is another confirmation of the new λ_{nl} optimisation strategy, which compounds the conclusions derived from the other figures of merit. The agreement between the "reduced" *opt* case $\mathcal{PLT}$ and that of COWAN proves that the previous baseline can be reproduced, and concomitantly, any errors due to atomic structure error have been minimized.

On a physics note, the reason why the presence of additional higher multipole transitions *lowers* the $\mathcal{PLT}$ in both the *opt* and *def* cases can be understood through examination of the fine-hash, red curve from figure 2.17, labelled "AS op, reduced + $E3$". This curve corresponds to the case where the AUTOS *opt* transitions have first been restricted to match those of COWAN, and then some of the most important $E3$ transitions from those initially excluded have been added back to the *adf04* file. Upon closer scrutiny, it is observed that all but one of these added transitions involve the metastable level 2, [Ar]3d $^2\mathrm{D}_{2.5}$, and crucially, these transitions open up a direct path from the set of excited levels, $\{23, 25, 28, 29\}$, to this metastable that was previously unavailable. In fact, these excited states had no direct connections to either of the ^{2}D ground term metastable levels 1 and 2 prior to the inclusion of $E3$ transitions, and consequently, they were

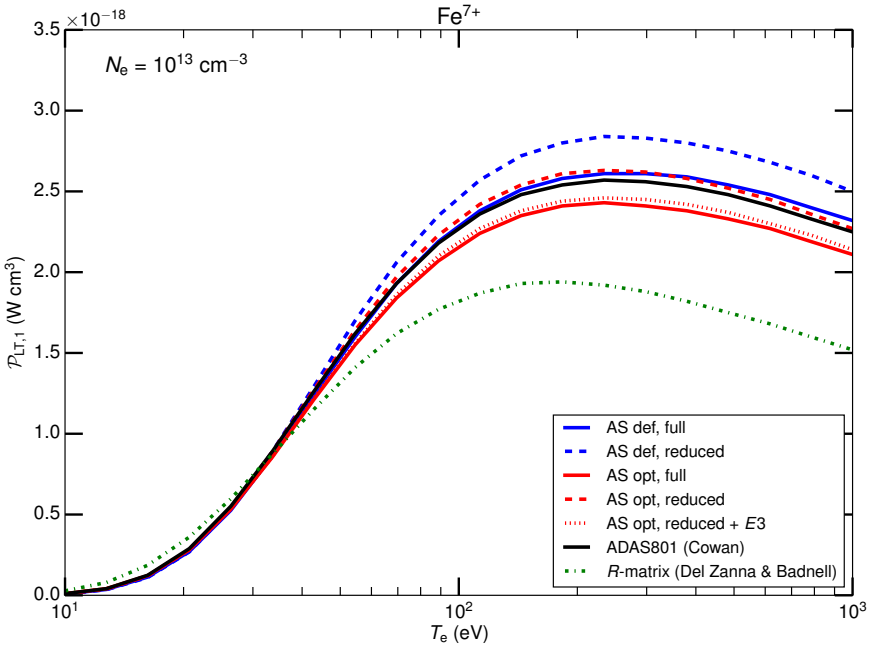

Figure 2.17: $\mathcal{PLT}$ of the ground state, 1, versus electron temperature, T_e, for K-like Fe^{7+} at $N_e = 10^{13}$ cm^{-3}. An expanded description of the curve labels are as follows. The solid black, "ADAS801 (Cowan)" line is for the COWAN result, which only includes $E1/M2$ transitions, and is described further in the text. The solid, blue, "AS def, full" line denotes the *def* case AUTOS result, i.e. all $\lambda_{nl} = 1$, with all transitions included, while the dashed, blue, "AS def, reduced" line is for the same case but with the transitions reduced to match those of COWAN. There are three separate curves for the *opt* case: the solid, red, "AS opt, full" line denotes the case where all transitions output by AUTOS are included; the dashed, red, "AS opt, reduced" line is for the case where the transition set has been restricted to match that of the "ADAS801 (Cowan)" result; and the fine-hash, red, "AS opt, reduced + $E3$" line is same as the former "AS opt, reduced" case, but a few influential $E3$ transitions from high J and L states have been added (see text for further explanation). Finally, the dot-dashed, green, "R-matrix (Del Zanna & Badnell)" result represents the R-matrix method calculation of Del Zanna and Badnell [61], truncated to match the levels of the other calculations.

able to accumulate a fairly substantial population fraction on the order of 10^{-1} because the cascade from higher states is effectively trapped there. With the addition of the $E3$ transitions predominantly to level 2, some of the population is diverted from the cascade to the ground, thus reducing the $\mathcal{PLT}$ associated with the ground level. At the temperatures and densities under consideration, it is collisional de-excitation from these excited states that dominates.

In addition, a high-quality R-matrix result (Del Zanna & Badnell) exists for K-like Fe^{7+}. Across most of the temperature domain, this $\mathcal{PLT}$ is is lower than all of the others, and the "AS opt, full" curve achieves the closes agreement with it. This further supports the conclusion that the novel λ_{nl} optimisation strat-

egy in combination with the DW approximation has produced a superior *adf04* dataset compared to previous baselines. An important caveat is that the levels in the R-matrix *adf04* were truncated to match those in the other calculations of figure 2.17. Without this step, the comparison would not be meaningful because there is a substantial contribution to the $\mathcal{PLT}$ from these truncated, high-lying levels that the other files neglect. The reason that this R-matrix result is lower than the other DW and PWB results is likely because of additional transitions made possible by CC. Just as with the $E3$ transitions discussed immediately above, these additional transitions can divert some of the cascade that would otherwise terminate at the ground state. However, further investigation is required to confirm this hypothesis.

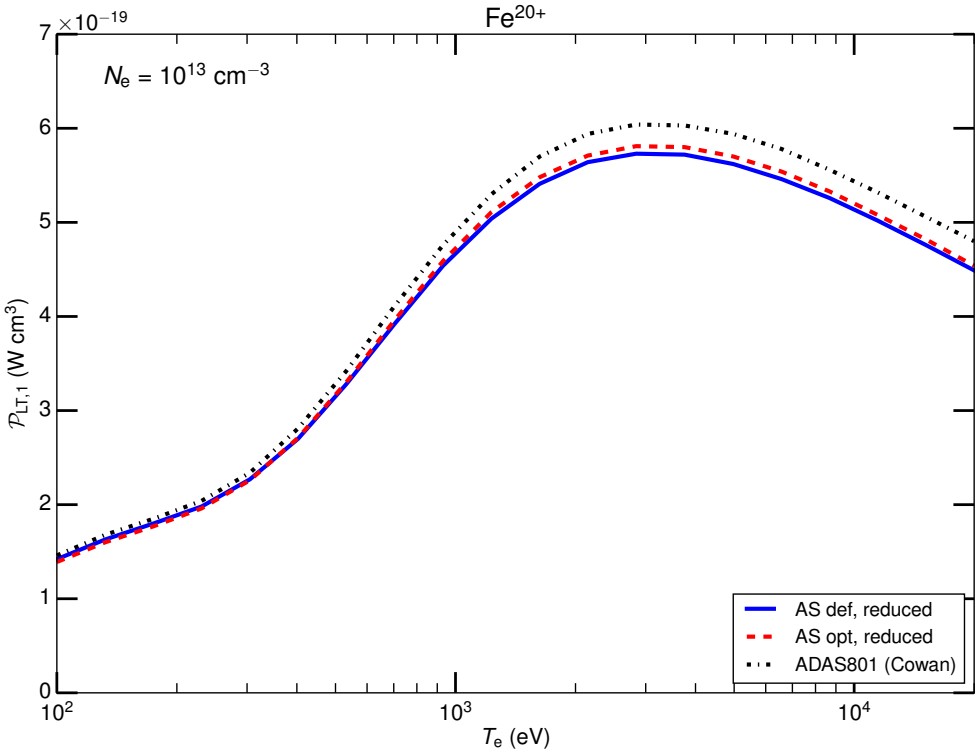

Figure 2.18: $\mathcal{PLT}$ of the ground state, 1, versus electron temperature, T_e, for C-like Fe^{20+} at $N_e = 10^{13}$ cm^{-3}. An expanded description of the curve labels are as follows. The dash-dot, black, "ADAS801(Cowan)" line is for the COWAN PWB result, which only includes $E1/M2$ transitions and is described further in the text. The solid, blue, "AS def, reduced" line denotes the *def* case AUTOS PWB result, i.e. all $\lambda_{nl} = 1$, with the transitions reduced to match those of COWAN. The dashed, red, "AS opt, reduced" line denotes the *opt* case AUTOS PWB result with the transitions reduced to match those of COWAN.

On the other hand, figure 2.18 displays a conformity between the Fe^{20+} $\mathcal{PLT}$s

of all cases upon matching of the transition sets. Once again, this affirms the findings from the previous figures of merit: at this higher ionization stage, not only have the *opt* and *def* cases come into accord with each other but also with COWAN. More $\mathcal{PLT}$ comparisons along the Fe isonuclear sequence should be performed, but the process of matching transition sets to COWAN is not yet fully automated and so somewhat time consuming. It is reasonable from this vantage to predict that the $\mathcal{PLT}$ behaviour will be split between the Fe^{7+} and Fe^{20+}, just as for the other two figures of merit. Overall, the success of the new λ_{nl} optimisation strategy has been well substantiated by all three figures of merit.

Chapter 3

High-quality, Electron-impact Excitation Calculations

3.1 Introduction

Although the importance of an *adf04* baseline dataset was well motivated and justified in Chapter 2, there still remains an open admission from within that chapter: higher-quality fundamental atomic data, when available, should almost always be preferred. Therefore, attention must be devoted to the attainment of these high-quality data for heavier species if effective GCR modelling is to be done. Predictably, the production of such data becomes increasingly difficult the higher one goes in atomic number for two reasons.

First, as the nuclear charge Z_0 increases, the relativistic effects in the structure calculation become non-negligible. Even as low as $Z_0 \sim 10$, relativistic corrections to energy levels are noticeable but can be introduced using perturbative approaches like the Breit-Pauli Hamiltonian in AUTOS, thus maintaining the simplicity of nonrelativistic or semi-relativistic basis functions and algebra. However, for $Z_0 \gtrsim 30$, relativistic effects on the wave functions themselves become significant, signalling that perturbative methods are less and less accurate and that the fully-relativistic Dirac equations should instead be solved. From the perspective of the radial wave functions, there are four times as many equations

to solve under the Dirac-Hartree-Fock technique as there are under the nonrelativistic Hartree-Fock. Moreover, a single nonrelativistic electron configuration, in general, corresponds to several relativistic ones as a direct consequence of jj-coupling, and this means more energies must be determined.

Secondly, it is generally true that the more electrons in a configuration the more complex will be the atomic structure and collision problem. For instance, configurations containing partially filled d or f shells can easily spawn in excess of 50 LS terms and perhaps thrice that in J levels. Isoelectronic sequences where these class of configurations form the ground complex will quickly reach computer memory limits when one attempts to include a suitable number of excited configurations in the CI and CC expansions: the Hamiltonian matrix scales as N_B^2 where N_B is the number of basis functions in the respective coupling scheme. It is the purpose of this chapter to provide a limited view of the techniques applied to tackle these unwieldy problems.

Before proceeding, one should recall that the quantities sought are those contained in the *adf04* ADAS file format: eigenenergies, A-values, and temperature-dependent collisional excitation data (Ω_{ij} or Υ_{ij}). It is these quantities that define the low-lying, highly resolved states of an atom and dominate the population distribution therein. Furthermore, the collisional excitation rates are those due to EIE because this process dominates in nearly all spatial and temporal domains of fusion plasmas, barring cases where charge exchange (CX) or ion-impact excitation (IIE) are active. A detailed explanation is provided in Chapter 4 for why this is true and where it does not hold in relation to IIE. In the interest of completeness, the other fundamental data needed for GCR can be found in a recent work on the ionization balance of the W isonuclear sequence by Pütterich et al. [62], and some general comments are made in Chapter 5.

The exact methodology selected to generate data for medium to heavy species will depend on a variety of factors such as computing resources, time available, accessibility to codes, and the preferences and familiarity of the producer therewith. Consequently, there is a great deal of variability, and it proves most fruitful to consider a specific example from which generalizations can be observed. The importance of tungsten (W) as a PFC material has been motivated at the beginning of Chapter 1, and W^{44+} is an ion of particular interest for spectral diagnostics

on JET, being located in the core of the tokamak plasma. Spectral lines in the soft x-ray region have been observed by the bent crystal spectrometer, KX1 [63]. For W^{44+}, lines in this region are produced by transitions to the 3d-subshell. In particular, the transitions in the [$3d^{10}4s^2$–$3d^9 4s^2 4f$] and [$3d^{10}4s^2$–$3d^9 4s4p4d$] transition arrays[1] are dominant because the upper levels are populated directly by excitation from the ground, as summarized in [64]. Lines for these transitions have been observed experimentally using EBITs [64–67], and theoretical atomic structure calculations by Fournier [68] and Spencer et al. [69] confirm large oscillator strengths. However, based on present literature searches, no collision calculation or spectral modelling gives a complete consideration to both of these obviously important, 3d-subshell transition arrays, so the present objective is to rectify this shortcoming. Two wavelengths in particular appear to be relevant, corresponding to particular levels within the transition array configurations: 5.76 Å and 5.94 Å.

The criteria for a new calculation of W^{44+} data are clear. To improve upon the PWB and DW baseline calculations mentioned in section 2.1.2 and match the literature, a full CC approach must be used, and due to the high residual charge of W^{44+}, $z = 44$, the radiation damping of resonances should also be considered [70]. Moreover with $Z_0 = 74$, tungsten exceeds the lower bounds for relativistic effects established above, meaning some level of relativistic considerations is necessary. Above all, the 3d-subshell transitions previously identified must be included. Prior to the collision calculations presented here, no data in the literature satisfied all of these conditions. The present work seeks to fill this gap in the W^{44+} EIE collision data by executing fully-relativistic, partially-damped, Dirac R-matrix calculations with Dirac Atomic R-matrix Codes (DARC), a code suite further described in section 3.2.2. These calculations include configurations with a 3d-hole so that the [$3d^{10}4s^2$–$3d^9 4s^2 4f$] and [$3d^{10}4s^2$–$3d^9 4s4p4d$] transition arrays are accommodated. AUTOS was also employed in various capacities to support these calculations, including its DW approach for generating EIE data.

There are previous EIE calculations for W^{44+} with which to benchmark and thus assess the strengths and weaknesses of the new calculations. Relativistic

[1] A transition array consists of all possible radiative transitions between all sublevels of the two specified configurations.

R-matrix calculations have been performed by Ballance and Griffin [71] with effectively the same codes used here, so a comparison with their results is essential. However, their calculations do not include any configurations involving excitation from the 3d-subshell, which constitutes a serious shortcoming from the present perspective and is the primary motivation for this study.[2] Conversely, the Ballance and Griffin calculations do include a full treatment of all types of radiation damping, whereas the current study only contains a partial treatment. The reasons for including only the core radiation of Rydberg resonances (type-I damping) are detailed in section 3.2.2. Additionally, Das et al. have conducted fully relativistic DW calculations for W^{44+} and other W ions in [72]. Their study does not satisfy the criterion of using a CC method, and more importantly, it omits a crucial configuration, $3d^9 4s4p4d$, the effect of which is further investigated in section 3.2.1. Consequently, comparison with their results has been omitted.

It was already noted in section 2.4 that the task of comparing atomic structures and collision calculations is complex and lacks a formal framework in the literature. A bespoke and detailed analysis of eigenenergies, radiative emission rates, collision strengths, and effective collision strengths from all pertinent sources is unavoidable for validating high-quality data and will be performed here. Such an in-depth analysis largely obviates any benefit from using the coarser figures of merit from section 2.4. However, there is still value in using the $\mathcal{PLT}$ and related coefficients like the photon emissivity coefficient ($\mathcal{PEC}$) as a means of comparing fundamental atomic data because they are connected to population modelling. And ultimately, it is a proper population model of the W^{44+} spectrum that is the goal for high-quality data like this. It is only in this way that a truly accurate sense of the importance of the 3d-subshell transition arrays can be obtained. The modelling behind the $\mathcal{PLT}$ and $\mathcal{PEC}$ results presented here is done through ADAS routines but falls short of the *ic*-resolved GCR that is the primary aim of this thesis; this work was carried out before that goal was achieved.

The remainder of the chapter is structured as follows. Section 3.2 describes the calculation methodology, and it is divided into four subsections. First, section 3.2.1 lists and explains the specification of the CI expansion, which is critical

[2] It should be noted that the importance of opening-up the 3d-subshell for diagnostic purposes was not appreciated until a preliminary survey of what might constitute the main emission lines was conducted.

for an accurate investigation of the 3d-subshell transitions and differentiates the present results from previous works. Second, section 3.2.2 provides the necessary technical and physics details for the use of the DARC and AUTOS codes. Third, section 3.2.3 discusses some important issues regarding infinite energy collision strength limits. Lastly, section 3.2.4 roughly outlines the theoretical foundation of the atomic population modelling performed as part of the subsequent analysis. Section 3.3 presents the results of the present calculations along with the relevant analysis in three sections: atomic structure, collision data, and atomic population modelling.

3.2 Methodology

3.2.1 CI and Structure Determination

Consideration of the 3d-subshell transition arrays, [$3d^{10}4s^2$–$3d^9 4s^2 4f$] and [$3d^{10}4s^2$–$3d^9 4s4p4d$], requires the inclusion of configurations with a 3d-hole. Apart from the $3d^9 4s^2 4f$ and $3d^9 4s4p4d$ configurations, there are several other configurations to consider due to the possibility of mixing, and it was not immediately obvious which ones should have been included in the CI of the target structure calculation. One must be prudent in selecting the CI due to computer memory limits at the collision calculation stage: a compromise between the number of J-resolved levels and the overall accuracy of results must be reached. Two structure codes were employed at this juncture: AUTOS, which was introduced in section 2.2.1, and GRASP^0 [73–76], which uses the many-electron Dirac Hamiltonian with the Breit interaction included and a basis set of Dirac-Fock spinors. The further theoretical and practical details that underpin the implementation of GRASP^0 are quite involved, and the broader field of relativistic quantum theory has been expertly presented in a monograph by Grant [53] to which the reader is directed. In short, GRASP^0 approaches the problem from a fully-relativistic foundation and thus satisfies the stipulations made about relativistic effects in section 3.1. The comparison between the GRASP^0/DARC results versus those of AUTOS will partly serve to show how important the relativistic effects are in this problem.

The final CI included 13 configurations and resulted in 313 $LSJ\pi$ levels, all

below the ionization limit:

$$3d^{10}4s^2,\ 3d^{10}4s4p,\ 3d^{10}4s4d,\ 3d^{10}4s4f,\ 3d^{10}4p^2,\ 3d^{10}4p4d,$$
$$3d^{10}4p4f,\ 3d^{10}4d^2,\ 3d^{10}4d4f,\ 3d^{9}4s^24p,\ 3d^{9}4s^24d,\ 3d^{9}4s^24f,$$
$$3d^{9}4s4p4d.$$

Emphasis must be placed upon the $3d^9 4s4p4d$ configuration, which has not been considered in either structure or collision calculations until now. In fact, it is because of this omitted configuration that a proper modelling of the important 3d-subshell transition arrays for W^{44+} has not been possible. The $3d^9 4s4p4d$ configuration mixes heavily with $3d^9 4s^2 4f$, and the subsequent effect upon the radiative data of the dominant 3d-subshell transitions is presented in table 3.1. Observing the changes between row 1 and 2 clearly shows this effect, and notably, the $^3P_1^\circ$ to ground transition increases by three orders of magnitude. Thus, comparison of the dominant 3d-subshell transitions between calculations is only sensible if they both include the $3d^9 4s^2 4f$ and $3d^9 4s4p4d$ configurations. No further mention will be made of the Das et al. calculations for exactly this reason, and preliminary comparison of this work's collision data with theirs immediately revealed large discrepancies. It should be noted that the effect of strong mixing between adjacent configurations related by a promotion and demotion of l quantum numbers has been well documented in previous cases, such as Sn^{10+} and Pr^{21+} [77, 78]. Table 3.1 also shows some other candidate configurations that were omitted due to their lack of influence on the radiative data: $3d^{10}4f^2$, $3d^9 4p^3$, and $3d^9 4s4p^2$.

The primary comparison is with a calculation by Ballance and Griffin [71], so it is important to rationalize the differences in the CI basis sets. Row 4 contains the results for the union of the CI basis sets used in this work's calculations, and it can be observed that the addition of the $3d^{10}4l5l'$ configurations do have a moderate effect on the 3d-subshell transitions relative to row 2. Ideally, all of these configurations should be included in the CI and CC expansions, but the 397 levels generated by these configurations is computationally inhibitive to the subsequent collision calculation given available resources. Because the soft x-ray, 3d-subshell transitions are the focus of this study, the $3d^{10}4l5l'$ configurations

had to be omitted from the CI. However, further influence of these configurations will be assessed in section 3.3.3 by merging Ballance and Griffin's data for the $n = 5$ levels into this work's dataset and observing the effect upon the modelled results.

This work's GRASP^0 results closely mimic the AUTOS results in table 3.1. An extended average level (EAL) calculation, which optimizes a weighted trace of the Hamiltonian matrix, was used for the GRASP^0 calculation. The target orbitals produced were used in the subsequent DARC collision calculation, which is described in section 3.2.2. In addition, comparisons are made in section 3.3.3 to modelled results derived from PWB calculations using COWAN (refer to section 2.2.1). The CI expansion for these calculations is slightly different, combining configurations from this work and Ballance and Griffin's:

$$3d^{10}4s^2,\ 3d^{10}4s4p,\ 3d^{10}4s4d,\ 3d^{10}4s4f,\ 3d^{10}4s5s,\ 3d^{10}4s5p,$$
$$3d^{10}4s5d,\ 3d^{10}4s6s,\ 3d^{10}4s6p,\ 3d^{10}4s6d,\ 3d^{9}4s^{2}4d,\ 3d^{9}4s^{2}4f,$$
$$3p^{5}3d^{10}4s^{2}4p,\ 3p^{5}3d^{10}4s^{2}4d.$$

The aim of this CI basis set was to achieve more breadth of excited-state coverage.

3.2.2 DARC and AUTOSTRUCTURE Execution

The Dirac R-matrix, partially damped EIE results presented in this study were generated using the DARC suite, developed by Norrington [76] and modified to incorporate parts of the parallel R-matrix codes [79–81]. The present calculation procedure is almost identical to that described in [82]; however, the present work does not perform a fully damped calculation, as mentioned earlier, so the outer region portion is slightly different.

If all possible types of radiation damping are to be accounted for, the bound $(N+1)$-electron eigenvalues, eigenvectors, and dipole matrix elements need to be handled, which is a computationally expensive task. Moreover, because configurations with an open 3d-subshell are included in the CI and CC expansion, the number of levels in the calculation is nearly doubled compared to Ballance and Griffin: 168 levels in their calculation versus 313 in the present one. As a consequence, the computational demand of the present problem is greater initially,

Table 3.1: Summary of AUTOS radiative data produced for W^{44+} while varying the CI basis set. A_{ki} is the Einstein A-coefficient (transition probability); S_{ik} is the line strength; and $g_i f_{ik}$ is the weighted oscillator strength. The base 13 configurations are those listed in section 3.2.1 but with $3d^9 4s4p4d$ replaced by $3d^{10}4f^2$. All subsequent entries are for the configurations that have been added or removed from this basis. BG07 refers to the configurations used in Ballance and Griffin's W^{44+} calculations [71].

CI	k	i	A_{ki} (s^{-1})	S_{ik}(au)	$g_i f_{ik}$	$(-1)^\pi(2S_k+1)$	L_k	J_k	k conf.	Lvs
base 13	126	1	1.31E+14	0.040392	2.07237	-3	2	1	$3d^9 4s^2 4f$	134
	134	1	4.25E+14	0.118734	6.28700	-1	1	1	$3d^9 4s^2 4f$	
	116	1	1.16E+11	0.000038	0.00189	-3	1	1	$3d^9 4s^2 4f$	
$+3d^9 4s4p4d$	288	1	1.11E+14	0.030694	1.63157	-3	2	1	$3d^9 4s4p4d$	326
	304	1	1.42E+14	0.038086	2.04257	-1	1	1	$3d^9 4s^2 4f$	
	308	1	1.13E+14	0.030244	1.62454	-3	1	1	$3d^9 4s4p4d$	
$+3d^9 4s4p4d$	275	1	1.09E+14	0.030123	1.60008	-3	2	1	$3d^9 4s4p4d$	313
$-3d^{10}4f^2$	291	1	1.38E+14	0.037198	1.99348	-1	1	1	$3d^9 4s^2 4f$	
	295	1	1.18E+14	0.031645	1.69855	-3	1	1	$3d^9 4s4p4d$	
$+3d^9 4s4p4d$	359	1	1.05E+14	0.030072	1.58174	-3	2	1	$3d^9 4s4p4d$	397
+BG07 ($4l5l'$)	374	1	1.11E+14	0.030929	1.64053	-1	1	1	$3d^9 4s^2 4f$	
	388	1	1.15E+13	0.003136	0.16751	-3	1	1	$3d^9 4s4p4d$	
$+3d^9 4s4p^2$	182	1	1.31E+14	0.040416	2.06936	-3	2	1	$3d^9 4s^2 4f$	190
	190	1	4.21E+14	0.117906	6.24096	-1	1	1	$3d^9 4s^2 4f$	
	172	1	1.16E+11	0.000037	0.00189	-3	1	1	$3d^9 4s^2 4f$	
$+3d^9 4p^3$	151	1	1.31E+14	0.040400	2.06867	-3	2	1	$3d^9 4s^2 4f$	172
	168	1	4.22E+14	0.117990	6.24569	-1	1	1	$3d^9 4s^2 4f$	
	136	1	1.16E+11	0.000037	0.00189	-3	1	1	$3d^9 4s^2 4f$	

and it is not practical to further expand the calculations by including all forms of radiation damping at this point in time. However, the outer region code independently has the capability to include type-I damping via Multichannel Quantum Defect Theory (MQDT) [83] at minimal computational cost. Type I damping constitutes the radiative transition of a core, non-Rydberg electron starting from an intermediate, $(N+1)$-electron resonance; type-I damping tends to dominate because of the $1/n^3$ scaling of autoionization and Rydberg radiation rates. This is supported by the results in section 3.3.2, and so the limited damping approach seems to be a suitable approximation. The outer region calculations were run both with and without type-I damping to facilitate subsequent comparison.

The relevant physics parameters for the problem are as follows. The CI and CC expansions both incorporate all configurations determined in section 3.2.1 resulting in 313 $LSJ\pi$ levels. Moreover, although the calculations are already split into exchange and nonexchange components at the spatial R-matrix box boundary, they can be further partitioned in angular momentum space, since exchange effects reduce at high angular momentum values. Thus, a large J value for the symmetries is selected above which electron exchange effects can be neglected

even in the inner region; in the present case, full close-coupling equations were solved for $0.5 \leq J \leq 16.5$ and the nonexchange versions for $17.5 \leq J \leq 35.5$. The actual R-matrix boundary is selected automatically such that all the bound orbitals have probability densities below an arbitrary threshold of 10^{-3}; these settings resulted in an R-matrix radial boundary of 1.33 a_0. When specifying the generation of continuum-electron orbitals, one should ensure that the energy range of these orbitals for each angular momentum exceeds the intended range of scattering electron energies by approximately a factor of 1.8 in practice. A maximum scattering energy of 1100 Ryd was used for these calculations to match Ballance and Griffin, and so the maximum energy eigenvalue of the continuum-electron basis orbitals for a given angular momentum value should exceed ≈ 1800 Ryd. For the exchange case, this required 34 basis orbitals per angular momentum value, and for the non-exchange case this required 30 basis orbitals per angular momentum.

The features of EIE collision strengths are dominated by intermediate resonances in the energy range defined by transitions between target levels. These resonances manifest as sharp and narrow peaks, meaning the collision strengths need to be evaluated on a fine energy mesh in this region. The mesh parameters used for the outer region code are summarized in table 3.2. One will also note from table 3.2 that a further division has been introduced within the exchange case. Only for $J\Pi$ symmetries with $J \leq 8.5$ was the full fine mesh employed in the resonance region. MXE = 48000 was chosen for this fine mesh in order to closely mimic the number of points used in the previous DARC calculations by Ballance and Griffin [71]. From visual inspection, this number of mesh points appears to correctly resolve the sharply spiked resonances. Furthermore, the *effective* collision strengths are nearly invariant compared to those calculated from collision strengths on a mesh with half as many points, indicating a convergence of the mesh.

In the interest of having more collision data for comparison, AUTOS runs were also conducted using the same CI as for DARC/GRASP^0. The isolated target structure calculation used an *ic* scheme with semi-relativistic, κ-averaged orbitals. Multi-electron interactions are included through the Thomas-Fermi-Dirac-Amaldi model potential with scaling orbital parameters, λ_{nl}, determined through a vari-

Table 3.2: Summary of mesh cases and parameters for PSTGF. MXE is the number of points for the outer region energy mesh, and EINCR in the step size of the mesh in Ryd/z^2. The resonance region is enclosed by the range, $[E_2 - E_{\text{incr}}, E_{313} + E_{\text{incr}}]$ and the high energy region by $(E_{313} + E_{\text{incr}}, 1100 \text{ Ryd}]$. E_i is the energy eigenvalue of the ith excited level relative to the ground in Rydbergs: $E_2 = 6.34789294$ Ryd and $E_{313} = 1.61979116 \times 10^2$ Ryd

Case		**Resonance Region**	**High Energy Region**
Exchange	$0 \leq J \leq 8.5$	MXE=48000 EINCR=6.701E-06	MXE=720 EINCR=0.0002562
	$9.5 \leq J \leq 16.5$	MXE=360 EINCR=0.0002252	
Nonexchange	$17.5 \leq J \leq 35.5$	MXE=1008 EINCR=0.0002636	

ational method of all possible orbitals: 1s, 2s, 2p, 3s, 3p, 3d, 4s, 4p, 4d, 4f. The scattering problem is solved using a Breit-Pauli distorted wave (BPDW) approach as described in section 2.2.1. These AUTOS calculations were performed prior to and thus independently of the new AUTOS baseline described and evaluated in Chapter 2.

3.2.3 Born Limits

It is important to give attention to the infinite energy limits of collision strengths[3] since their values correlate strongly with those of the background collision strengths over a wide range of energies. This will become even more apparent in the context of the IIE calculation in Chapter 4. A limitation of the DARC/GRASP^0 suite is that these infinite energy limits are only calculated for the electric dipole-allowed transitions: $\Delta J = \pm 1$ and parity change.

To rectify this absence of data, the numerical values of the non-dipole collision strengths are extrapolated during convolution with the Maxwellian to produce the respective Υ_{ij}. Because transitions with Born limits and those truly forbidden by selection rules cannot be differentiated, it is assumed the highest energy calculated collision strength, $\Omega(E_f)$, has nearly reached the infinite energy limit, and so $\Omega(E_f)$ is extrapolated as a constant. Although this is usually a good approximation, it relies on calculating the collision strengths to an arbitrarily high energy. Alternatively, the Born limits may be obtained from a different program and spliced into the collision strengths file; a linear interpolation involving this

[3]The infinite energy limit refers to the asymptotic behaviour of the collision strength as the scattering electron energy approaches infinity.

point can then be used. However, because two different structure calculations are being effectively combined, one must question how close the structure calculations are and whether it even makes sense to combine the results from different theories.

In the present case, the possibility of using the Born limits from the AUTOS calculation was explored since Ballance and Griffin used Born limits from AUTOS for their calculations [71]. The only potential metric for determining the suitability of the AUTOS Born limits is a comparison of the (electric) dipole-allowed transition limits from GRASP^0 and AUTOS. In practice, this is simply a comparison of the line strengths—see Burgess & Tully [84]. A linear comparison of the line strengths from the two codes reveals that only 24% of the transitions lie within 20% of each other, with a mean percent difference of 6185% and a weighted mean percent difference of 11%. The weighting factors, w_{ik}, are defined as

$$w_{ik} = \frac{r_{ik}}{\sum_{j,l} r_{jl}} \; ; \quad r_{jl} = \log(S_{jl}/S_{\max}) \; . \tag{3.1}$$

Based on this weighting scheme, the large discrepancy between the weighted and unweighted means suggests that the differences between line strength values tends to be relatively larger at lower magnitude line strengths. Indeed, this supposition is supported by the observation of a linear scatter plot of the line strengths (GRASP^0 S_{ij} versus AUTOS S_{ij}), and it is a trend one might expect to see. Thus, the amount of agreement between the DARC and AUTOS dipole limits depends on how much importance one places upon the low and high magnitude values separately.

There is no reason to doubt that this behaviour would not also extend to the Born limits; however, the effect would likely be exacerbated since the average magnitudes of the infinite energy limits decreases by approximately an order of magnitude for each subsequent multipole order. In the absence of any Born limits from GRASP^0 with which to compare, this less than conclusive evidence from the dipole limits comparison does not resolve the issue of whether any accuracy might be gained from splicing the AUTOS Born limits. Given this uncertainty, it is not believed the effort of manually tampering with the collision strength files is worthwhile, and so the default behaviour of extrapolating the high energy collision strengths as constants for transitions without $E1$ dipole limits is retained.

3.2.4 Atomic Population Modelling

The total emissivity in a spectrum line, $i \rightarrow k$, is given by

$$\varepsilon_{i \rightarrow k} = N_i A_{i \rightarrow k}, \tag{3.2}$$

where N_i is the population density of the upper state, i, in ionization stage z and $A_{i \rightarrow k}$ is the radiative transition rate from i to the lower state, k. The $A_{i \rightarrow k}$ values are straightforward to obtain from the structure calculation for an ion; however, the N_i's require some form of atomic population modelling. Since the fundamental atomic data forms the input to whatever model is constructed, it is through the population structure of the N_i's that the collision data will influence any observable quantities. In other words, the atomic population model is what connects the collision data to observable quantities, emphasising the model's pivotal role as a tool to compare different fundamental datasets. Just as for the EIE cross-section data, full atomic population modelling that incorporates the 3d-subshell transitions is limited in the literature for W^{44+}. Clementson et al. [66] present the calculated spectrum for W^{44+} in an electron-beam ion trap (EBIT) plasma environment using a collisional-radiative (CR) model based on fundamental data from FAC. However, these results are not applicable for laboratory fusion plasmas because a mono-energetic electron beam is assumed and the densities are slightly too low at around 5×10^{11} cm^{-3}. This deficit in the W^{44+} modelled spectrum will be addressed by using the new fundamental atomic data that incorporates the dominant 3d-subshell transitions along with an atomic population model produced at suitable plasma conditions.

The modelling of the N_i's employed here is a restricted form of the GCR theory that is described in Appendix C: the assumption is made that the lifetime of solely the ground state is far greater than any of the excited states' lifetimes, including any potential metastable states. This was determined based on preliminary modelling that revealed collisional excitation from the metastable levels of W^{44+} does not have a significant effect on excited state populations until an electron density of $N_e \approx 10^{16}$ cm^{-3}, far outside the parameter space of current MCF devices and the proposed ITER limits [11]. It is the large energy separation amongst the metastables and ground, caused by the large residual charge, $z = 44$,

that is responsible for the absence of density effects in the current context. As a result, *all* atomic levels of W^{44+} will be in *quasi-static equilibrium* relative to the ground state, which dominates the description of the ion's population.

The population density of the ground is denoted by N_1, and the rate of population density change of an excited state, j, is

$$\frac{\mathrm{d}N_j}{\mathrm{d}t} = C_{j1}N_1 + \sum_i C_{ji}N_i \ . \tag{3.3}$$

The C_{ji} are elements of the collisional-radiative matrix and are defined by

$$C_{ji} = A_{i\to j} + N_\mathrm{e} q^\mathrm{e}_{i\to j}, \tag{3.4}$$

where $q^\mathrm{e}_{i\to j}$ is the electron-impact excitation or de-excitation rate coefficient depending on the energy ordering of i and j, and $A_{i\to j} = 0$ if $j > i$. Enforcing the quasi-equilibrium condition on the excited states ($\mathrm{d}N_j/\mathrm{d}t = 0$) and isolating for N_i in (3.3), one obtains

$$N_i = -\sum_j (C_{ij})^{-1} C_{j1} N_1 \ . \tag{3.5}$$

This suggests the definition of the effective population contribution coefficient for excitation:

$$\mathscr{F}^{(\mathrm{exc})}_{i1} = \frac{\sum_j (C_{ij})^{-1} C_{j1}}{N_\mathrm{e}} \ . \tag{3.6}$$

Hence, the line emissivity can be expressed as

$$\varepsilon_{i\to k} = N_\mathrm{e}\, N_1\, \mathcal{PEC}^{(\mathrm{exc})}_{1,i\to k} \ , \tag{3.7}$$

where the definition for the excitation $\mathcal{PEC}$ has been used:

$$\mathcal{PEC}^{(\mathrm{exc})}_{1,i\to k} \equiv \ \mathscr{F}^{(\mathrm{exc})}_{i1} A_{i\to k} \ . \tag{3.8}$$

The $\mathcal{PEC}$ is a useful derived data type, and one can obtain a more intuitive sense of it by considering the low density limit where collisional (de-)excitation between excited levels is neglected. Thus, recalling (3.4), the collisional coupling coefficients between excited levels become $C_{ij} = A_{j\to i}$, and from the ground

$C_{i1} = N_{\rm e} q^{\rm e}_{1\to i}$. Accordingly, the low density limit for the excitation $\mathcal{PEC}$ is

$$\mathcal{PEC}^{(\rm exc)}_{1,i\to k} = \frac{q^{\rm e}_{1\to i} A_{i\to k}}{\sum_{j<i} A_{i\to j}} \ . \tag{3.9}$$

So in the low density limit, the excitation $\mathcal{PEC}$ is given by the product of the EIE rate coefficient from the ground and the branching ratio of the radiative decay. This reaffirms the assumptions that have been made: the excited state levels are populated solely by collisional excitation from the ground and subsequently de-populated by spontaneous emission to any possible lower level. Therefore, the $\mathcal{PEC}$ is an effective quantity for estimating the diagnostic importance of a transition because it accounts for the population distribution of levels, a conclusion that equally applies in the more complex, finite density scenario.

It is the finite-density version of the excitation $\mathcal{PEC}$ in equation 3.8 that will be used by routines in ADAS for this analysis. These routines use effective collision strengths produced in the manner described above and stored in the *adf04* file format. Additionally, relativistic effects can cause classically weak, higher order electric and magnetic radiative transitions to approach similar magnitudes as the typically dominant dipole ($E1$) transitions; therefore, accurate atomic population modelling requires inclusion of at least some non-dipole transition probabilities, $A_{j\to i}$, for high z ions. PSTGF only produces $E1$ data derived from the dipole long-range coupling coefficients, so $E1$, $E2/M1$, and $E3/M2$ radiative data from GRASP^0 was substituted into the final *adf04* file: there is no problem of consistency between codes here, in contrast to the infinite energy Born limits. Comparison with the A-values in the *adf04* file of Ballance and Griffin revealed that they only include radiative transitions up to the quadrupole ($E2/M2$). The extra $E3$ data is included because of the overlapping selection rules and comparable magnitudes with $M2$. Further comparison of the radiative data is conducted in section 3.3.1.

3.3 Results and Discussion

3.3.1 Structure Data

A portion of the energy level results are summarised in table 3.3 along with comparison to other experimental and theoretical values. Errors relative to the NIST compiled experimental values are given in brackets for all theoretical calculations. The theoretical results are from the following calculations: the GRASP^0 and AUTOS results from this study, Ballance and Griffin's GRASP^0 [71], and Safronova and Safronova's relativistic many-body perturbation theory (RMBPT) [85]. It is noted that a recent calculation by Spencer et al. [69] has been omitted from the detailed comparison to follow. Although their calculation includes the important $3d^9$ core configurations, it uses non-relativistic radial orbitals. The authors themselves note that their largest error is likely due to unaccounted relativistic effects, and so detailed comparisons are restricted to methods that use fully or kappa-averaged relativistic radial orbitals. It is briefly observed that this work's structure results have a similar degree of agreement with Spencer et al. as the other fully relativistic results in their study.

From a qualitative observation of the errors in table 3.3, it is evident that the Safronova and Safronova (S&S) theoretical results are closest to the experimental NIST results. Moreover, the present GRASP^0 and Ballance and Griffin's GRASP^0 results appear to be of similar accuracy, while the AUTOS results perform comparatively the worst but objectively still quite well. This ordering can be predicted somewhat since one would not expect the AUTOS calculations that use the κ-averaged Dirac equation to outperform the fully κ-dependent Dirac equation used in the other calculations. For the lower levels being considered, the GRASP^0 values should be quite similar since they are from the same code and CI effects from the different, higher lying configurations will not extend down this far. The S&S values derive from a paper that focussed exclusively on the atomic structure problem and thus did not need to balance time and computational resources with a corresponding collision calculation.

Table 3.3: Lowest 50 energy level eigenvalues of W^{44+}. All values are in cm^{-1}. The bracketed values to the right of some theoretical values denote the absolute and percent difference with the experimental NIST values, respectively. The jj-term assignment is strictly for the present GRASP^0 calculations; equivalence of levels between different results is determined on a symmetry ($J\pi$) and energy (E) mapping. The subscripts have the following meanings. NIST denotes the NIST experimental values compiled from various sources [65]; GR denotes the present GRASP^0 results; AS denotes the present AUTOS results; BG07 denotes the Ballance and Griffin results [71]; and SS10 denotes the Safronova and Safronova results [85].

i	jj-term	J	E_{NIST}	E_{GR}	E_{AS}	E_{BG07}	E_{SS10}
1	$4s^2$ (1/2,1/2)	0	0	0	0	0	0
2	4s4p (1/2,1/2)°	0	695000	696599(-1599\0.23%)	680476(14524\2.09%)	697338(-2338\0.34%)	696870(-1870\0.27%)
3	4s4p (1/2,1/2)°	1	752560	754900(-2340\0.31%)	738077(14483\1.92%)	756118(-3558\0.47%)	752290(270\0.04%)
4	4s4p (1/2,3/2)°	2	1494400	1510410(-16010\1.07%)	1500353(-5953\0.40%)	1511424(-17024\1.14%)	1505330(-10930\0.73%)
5	$4p^2$ (1/2,1/2)	0	1588000	1610234(-22234\1.40%)	1598341(-10341\0.65%)	1603286(-15286\0.96%)	1589470(-1470\0.09%)
6	4s4p (1/2,3/2)°	1	1641230	1654698(-13468\0.82%)	1645076(-3846\0.23%)	1657295(-16065\0.98%)	1641860(-630\0.04%)
7	$4p^2$ (1/2,3/2)	1	2345700	2370326(-24626\1.05%)	2367366(-21666\0.92%)	2364982(-19282\0.82%)	2347790(-2090\0.09%)
8	$4p^2$ (1/2,3/2)	2	2362700	2380945(-18245\0.77%)	2380127(-17427\0.74%)	2375598(-12898\0.55%)	2359810(2890\0.12%)
9	4s4d (1/2,3/2)	1	2782700	2807138(-24438\0.88%)	2826740(-44040\1.58%)	2801178(-18478\0.66%)	2781700(1000\0.04%)
10	4s4d (1/2,3/2)	2	2809500	2835916(-26416\0.94%)	2854715(-45215\1.61%)	2829810(-20310\0.72%)	2809010(490\0.02%)
11	4s4d (1/2,5/2)	3	2943800	2980289(-36489\1.24%)	3007602(-63802\2.17%)	2974581(-30781\1.05%)	2952430(-8630\0.29%)
12	4s4d (1/2,5/2)	2	2988500	3025731(-37231\1.25%)	3047061(-58561\1.96%)	3019918(-31418\1.05%)	2997790(-9290\0.31%)
13	$4p^2$ (3/2,3/2)	2	3210900	3244954(-34054\1.06%)	3254573(-43673\1.36%)	3239406(-28506\0.89%)	3211110(-210\0.01%)
14	$4p^2$ (3/2,3/2)	0	3249000	3283304(-34304\1.06%)	3288983(-39983\1.23%)	3277012(-28012\0.86%)	3251480(-2480\0.08%)
15	4p4d (1/2,3/2)°	2		3542869	3548176	3536793	3516410
16	4p4d (1/2,3/2)°	1		3686507	3685971	3679726	3649830
17	4p4d (1/2,5/2)°	3		3793159	3802977	3786985	3759910
18	4p4d (1/2,5/2)°	2		3795417	3804873	3789273	3760590
19	4s4f (1/2,5/2)°	3		4296920	4306386	4292056	4268490
20	4s4f (1/2,7/2)°	2		4324408	4333915	4319207	4293610
21	4s4f (1/2,5/2)°	4		4354514	4375712	4349717	4324560
22	4s4f (1/2,5/2)°	3		4381359	4401322	4376049	4347880
23	4p4d (3/2,3/2)°	2	4383000	4422045(-39045\0.89%)	4431516(-48516\1.11%)	4416368(-33368\0.76%)	4385180(-2180\0.05%)
24	4p4d (3/2,3/2)°	0		4443019	4451669	4437256	4406260
25	4p4d (3/2,3/2)°	1		4453869	4463503	4448129	4415630
26	4p4d (3/2,3/2)°	3	4458000	4501932(-43932\0.99%)	4512851(-54851\1.23%)	4495374(-37374\0.84%)	4460510(-2510\0.06%)
27	4p4d (3/2,5/2)°	4	4505300	4547619(-42319\0.94%)	4564787(-59487\1.32%)	4541971(-36671\0.81%)	4511020(-5720\0.13%)
28	4p4d (3/2,5/2)°	2		4587583	4604286	4582203	4549230
29	4p4d (3/2,5/2)°	1		4711801	4729592	4705746	4667050
30	4p4d (3/2,5/2)°	3	4667000	4720344(-53344\1.14%)	4738811(-71811\1.54%)	4712765(-45765\0.98%)	4669890(-2890\0.06%)

Table 3.3: (continued)

i	jj-term	J	E_{NIST}	E_{GR}	E_{AS}	E_{BG07}	E_{SS10}
31	4p4f (1/2,5/2)	3		5106504	5099115	5101065	5069120
32	4p4f (1/2,5/2)	2		5149812	5139452	5144560	5110970
33	4p4f (1/2,7/2)	3		5174655	5178086	5169893	5135570
34	4p4f (1/2,7/2)	4		5175709	5179078	5169835	5136020
35	$4d^2$ (3/2,3/2)	2		5671068	5684603	5662259	5621680
36	$4d^2$ (3/2,3/2)	0		5746101	5759234	5732092	5690100
37	$4d^2$ (3/2,5/2)	3		5808133	5826269	5801275	5762150
38	$4d^2$ (3/2,5/2)	4		5816599	5831429	5810323	5772640
39	$4d^2$ (3/2,5/2)	2		5843017	5861428	5834560	5794100
40	$4d^2$ (3/2,5/2)	1		5877633	5898701	5866642	5823700
41	4p4f (3/2,7/2)	4		5917488	5934565	5912767	5876050
42	4p4f (3/2,5/2)	3		5927978	5932078	5922956	5884140
43	4p4f (3/2,5/2)	2		5957126	5961349	5951431	5910810
44	4p4f (3/2,7/2)	5		5970835	5983185	5965829	5926610
45	4p4f (3/2,5/2)	1		5971049	5970842	5966743	5927040
46	4p4f (3/2,7/2)	3		5986398	5999033	5981863	5941010
47	4p4f (3/2,5/2)	4		5991059	6004943	5983469	5938830
48	$4d^2$ (3/2,3/2)	2		6007925	6028552	6000992	5958400
49	4p4f (3/2,7/2)	2		6114914	6137006	6105042	6055560
50	$4d^2$ (5/2,5/2)	4		6137752	6158685	6126041	6072960

Because of extensive comparison with the Ballance and Griffin (B&G) results, it is important to obtain an overall concept of how the energy levels compare between the two calculations, something difficult to grasp from raw data tables. Accordingly, figure 3.1 provides an illustrative graphic of the energy ranges of the configurations included in the two calculations. Below approximately 8×10^6 cm^{-1}, the configuration energy ranges visually match to a small degree of error. This is quantitatively substantiated by the proximity of the energy levels in table 3.3 and a mean percent difference of 0.13% for all intersecting levels. However, above this threshold, the energy ranges are completely discrepant owing to the differences in the CI expansions. In the present calculations (left), there is an energy gap between the first open 3d-subshell configuration ($3d^9 4s^2 4p$) and the highest closed 3d-subshell configuration (4d4f). On the other hand, the $3d^{10} 4l 5l'$ configurations, which B&G include, coincidently and neatly fill this energy gap. The implications of this gross difference in energy level distribution will be investigated throughout the remainder of the paper, especially in relation to the CC expansion and effect upon the collision data.

Additionally, a sample of the radiative data from this work's GRASP^0 structure is presented in table 3.4. Apart from wavelengths, negligible experimental radiative data is available, and so only theoretical results are supplied for comparison. The theoretical results are from the same calculations as in the energy level table 3.3, excepting the addition of Fournier's *ab initio* calculations [68] and the omission of the present AUTOS results for brevity. The Fournier gf values for the 212–1 and 290–1 transitions are discrepant because the $3d^9 4s 4p 4d$ configuration was not included in that calculation, and as demonstrated in section 3.2.1, the $3d^9 4s 4p 4d$ configuration mixes heavily and greatly changes the radiative data of these 3d-subshell transitions. Consequently, comparison of these transitions with calculations that do not include this configuration are not meaningful. Otherwise, the Fournier gf values tend to agree well with the corresponding GRASP^0 results, except for the rather weak transitions 129–6 and 73–10 that differ by about a factor of three.

The B&G GRASP^0 results also appear to be in close agreement with this work's GRASP^0 results in this particular sample, except in instances where the magnitude of the gf value is small or the velocity to length ratios are not close to unity. In

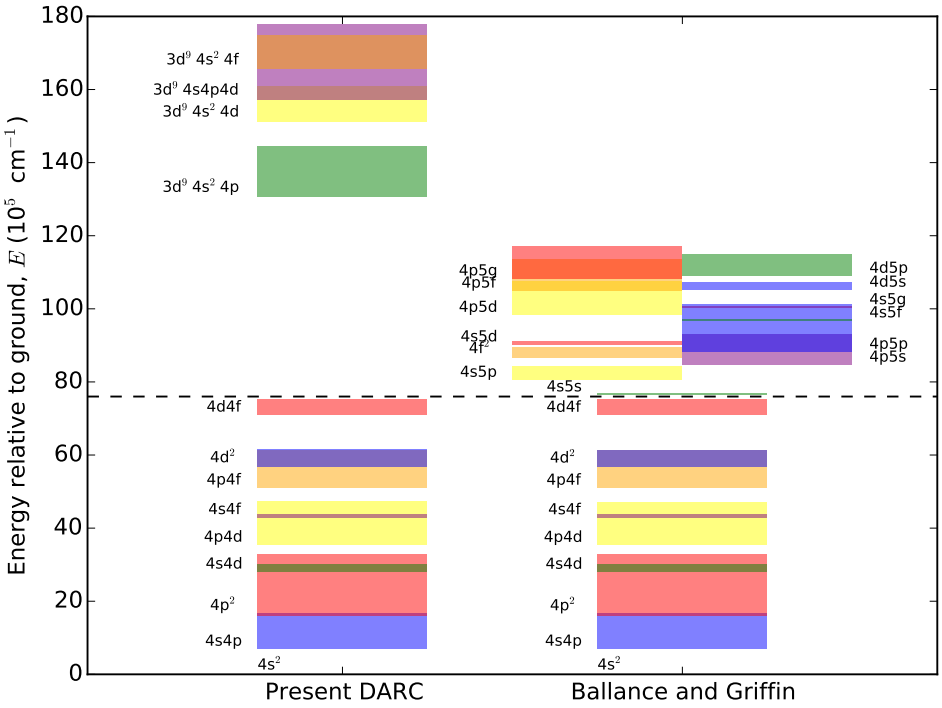

Figure 3.1: Energy ranges of the configurations included in the present DARC calculations and the Ballance and Griffin calculations. Non-relativistic configuration specifications are used for brevity with the understanding they encompass multiple relativistic sub-configurations. The energy ranges are determined by assigning each jj-coupled level to the corresponding configuration which contributes the dominant component the level's state vector. This method can be ambiguous in cases where strong configuration mixing is present.

both cases, this is to be expected when comparing calculations with different CI expansions. A full scope but necessarily more coarse comparison with this work's results was conducted using scatter plots analogous to those in figure 3.3. Neither the dipole line strengths, S_{ik}, nor the radiative transition probabilities up to quadrupole order revealed any systematic differences between the calculations, and 73% of the values agree within 20% relative error of each other, meaning there is reasonable accord overall. The dipole line strengths are directly proportional to the infinite energy limits of the corresponding EIE collision strength, and so this information will be relevant for the analysis of the collision data in section 3.3.2.

On the other hand, the S&S radiative data exhibit a binary behaviour: they either agree well with the present results or disagree by a few orders of magnitude.

Based on the energy level values quoted by S&S, it is concluded with a high degree of certainty that this disagreement is not due to a level mismatching by the present work; however, significant differences in the wavelength values for these conflicting transitions was observed. Upon further investigation, the wavelengths given by S&S do not agree with their own energy level values. Thus, it is suggested that there has been a labelling error in their work. To confirm this hypothesis, further investigation with AUTOS was performed to provide a corroborative third party result. The relevant results from using the CI expansion in section 3.2.1 already existed, and an additional run was conducted using the CI from the S&S work. In both cases, the AUTOS results agreed well with the present GRASP^0 results, supporting the validity of the present work and pointing to a labelling error in the S&S results.

Table 3.4: Radiative data: weighted oscillator strength (gf) and wavelength (λ) values for W^{44+}. GR denotes the present results generated using GRASP[0]; F98 denotes the results from Fournier [68]; BG07 denotes the results from Ballance and Griffin [71]; and SS10 denotes the results from Safronova and Safronova [85]. The AUTOS results are not presented for the sake of brevity. The level specifications are for the present results, and mapping of levels between the different calculations was determined by matching symmetry ($J\pi$) and energy (E), as in the case of the energy level table. Conversion from A_{ki} values to gf values for the BG07 data was necessary for comparison, and their calculated energies are used to do so. For compactness, $\star = (3d^9(^2D_{5/2})4s_{1/2})^\circ_2 4p_{3/2}$. All results are in the length gauge, and v/l denotes the ratio of the velocity gauge to the length gauge. Values presented in the format X.XXX ± YY represent scientific notation in base 10: X.XXX $\times 10^{\pm YY}$.

i	k	jj-coupled CSF of k	J_i	J_k	gf_{GR}	v/l_{GR}	gf_{BG07}	v/l_{BG07}	gf_{F98}	gf_{SS10}	λ_{GR} (Å)
1	295	$(\star)^\circ_{7/2}4d_{5/2}$ (7/2,5/2)°	0	1	9.028−01	0.89	–	–	–	–	5.7330
1	290	$3d^9(^2D_{3/2})4s^24f$ (3/2,5/2)°	0	1	1.610+00	0.90	–	–	5.844+00	–	5.7438
1	275	$(\star)^\circ_{1/2}4d_{3/2}$ (1/2,3/2)°	0	1	1.894+00	0.91	–	–	–	–	5.7917
1	212	$(\star)^\circ_{3/2}4d_{5/2}$ (3/2,5/2)°	0	1	3.820−01	0.89	–	–	1.954+00	–	5.9485
1	208	$(\star)^\circ_{5/2}4d_{3/2}$ (5/2,3/2)°	0	1	4.201−01	0.91	–	–	–	–	5.9616
1	207	$(\star)^\circ_{3/2}4d_{5/2}$ (3/2,5/2)°	0	1	4.923−01	0.92	–	–	–	–	5.9655
1	81	$3d^9(^2D_{3/2})4s^24p$ (3/2,3/2)°	0	1	2.912−02	0.91	–	–	2.800−02	–	6.9483
6	129	$3d^9(^2D_{3/2})4s^24d$ (3/2,3/2)	1	0	5.017−04	0.00	–	–	1.292−03	–	6.9367
1	78	$3d^9(^2D_{5/2})4s^24p$ (5/2,3/2)°	0	1	2.562−01	0.91	–	–	2.379−01	–	7.2056
1	75	$3d^9(^2D_{3/2})4s^24p$ (3/2,1/2)°	0	1	1.519−01	0.91	–	–	1.412−01	–	7.3524
4	83	$3d^9(^2D_{3/2})4s^24p$ (3/2,3/2)°	2	2	1.580−04	0.90	–	–	1.488−04	–	7.7453
4	82	$3d^9(^2D_{3/2})4s^24p$ (3/2,3/2)°	2	3	1.303−04	0.01	–	–	1.237−04	–	7.7580
2	74	$3d^9(^2D_{3/2})4s^24p$ (3/2,1/2)°	0	2	9.193−05	2.20	–	–	8.710−05	–	7.7670
3	74	$3d^9(^2D_{3/2})4s^24p$ (3/2,1/2)°	1	2	1.301−04	8.70	–	–	1.294−04	–	7.8015
6	82	$3d^9(^2D_{3/2})4s^24p$ (3/2,3/2)°	1	3	1.875−04	0.08	–	–	1.738−04	–	7.8462
4	79	$3d^9(^2D_{5/2})4s^24p$ (5/2,3/2)°	2	3	1.999−04	0.01	–	–	1.839−04	–	8.0730
4	77	$3d^9(^2D_{5/2})4s^24p$ (5/2,3/2)°	2	2	7.144−05	0.91	–	–	6.886−05	–	8.0880
4	76	$3d^9(^2D_{5/2})4s^24p$ (5/2,3/2)°	2	4	4.136−04	0.01	–	–	3.961−04	–	8.0991
2	72	$3d^9(^2D_{5/2})4s^24p$ (5/2,1/2)°	0	2	1.379−04	0.88	–	–	1.313−04	–	8.0998
3	73	$3d^9(^2D_{5/2})4s^24p$ (5/2,1/2)°	1	3	3.229−04	0.01	–	–	2.998−04	–	8.1327
3	72	$3d^9(^2D_{5/2})4s^24p$ (5/2,1/2)°	1	2	8.764−05	3.00	–	–	8.684−05	–	8.1380
6	77	$3d^9(^2D_{5/2})4s^24p$ (5/2,3/2)°	1	2	1.469−04	0.04	–	–	1.494−04	–	8.1840
11	76	$3d^9(^2D_{5/2})4s^24p$ (5/2,3/2)°	3	4	1.940−04	2.00	–	–	3.014−04	–	9.1878
10	73	$3d^9(^2D_{5/2})4s^24p$ (5/2,1/2)°	2	3	3.580−05	2.90	–	–	1.389−04	–	9.7800
3	12	4s4d (1/2,5/2)	1	2	8.387−02	1.00	7.694−02	–	8.768−02	7.500−02	44.2929
3	10	4s4d (1/2,3/2)	1	2	1.775+00	1.00	1.795+00	–	1.776+00	1.689+00	48.2882
1	6	4s4p (1/2,3/2)°	0	1	1.095+00	0.83	1.139+00	0.99	1.099+00	1.060+00	60.6907
3	8	$4p^2$ (1/2,3/2)	1	2	7.290−01	0.99	7.460−01	–	7.256−01	–	61.6827

Table 3.4: (continued)

i	k	jj-coupled CSF of k	J_i	J_k	$gf_{\rm GR}$	$v/l_{\rm GR}$	$gf_{\rm BG07}$	$v/l_{\rm BG07}$	$gf_{\rm F98}$	$gf_{\rm SS10}$	$\lambda_{\rm GR}$ (Å)
6	13	$4p^2$ (3/2,3/2)	1	2	2.351+00	1.00	2.393+00	–	2.404+00	2.244+00	63.0756
4	12	4s4d (1/2,5/2)	2	2	6.591−01	1.00	6.753−01	–	6.882−01	6.350−01	66.2383
6	12	4s4d (1/2,5/2)	1	2	4.271−01	1.00	4.199−01	–	3.878−01	–	73.2493
1	3	4s4p (1/2,1/2)°	0	1	1.364−01	0.59	1.415−01	1.00	1.376−01	1.320−01	132.4223
3	4	4s4p (1/2,3/2)°	1	2	5.643−05	1.00	5.873−05	–	5.637−05	–	133.6916
1	16	4p4d (1/2,3/2)°	0	1	2.185−04	1.50	1.484−04	0.99	–	–	27.1909
1	29	4p4d (3/2,5/2)°	0	1	1.598−04	0.95	3.392−04	1.10	–	–	21.3138
1	59	4d4f (3/2,5/2)°	0	1	3.357−05	0.01	4.694−05	0.91	–	–	13.8487
1	71	4d4f (5/2,7/2)°	0	1	1.885−04	0.08	2.402−04	1.00	–	–	13.3697
2	7	$4p^2$ (1/2,3/2)	0	1	5.135−01	1.00	5.191−01	0.99	–	–	59.9089
2	9	4s4d (1/2,3/2)	0	1	6.148−01	1.00	6.249−01	1.00	–	–	47.6077
2	40	$4d^2$ (3/2,5/2)	0	1	3.898−05	0.81	5.350−05	0.79	–	–	19.3960
2	45	4p4f (3/2,5/2)	0	1	6.580−05	1.10	9.251−05	1.20	–	–	19.0480
8	19	4s4f (1/2,5/2)°	2	3	6.398−01	1.00	6.714−01	–	–	–	52.5430
4	11	4s4d (1/2,5/2)	2	3	1.860+00	1.00	1.887+00	–	–	–	68.3293
75	129	$3d^9(^2D_{3/2})4s^24d$ (3/2,3/2)	1	0	2.243−01	0.87	–	–	–	–	40.5992
20	45	$4d^2$ (3/2,5/2)	2	1	7.047−01	0.87	–	–	–	9.000−01	60.9793
7	25	4p4d (3/2,3/2)°	1	1	7.485−01	1.00	–	–	–	7.140−01	48.2905
8	28	4p4d (3/2,5/2)°	2	2	5.357−03	1.00	–	–	–	8.350−01	45.6454
8	26	4p4d (3/2,3/2)°	2	3	1.071+00	1.00	–	–	–	6.550−01	47.4473
10	17	4s4f (1/2,5/2)°	2	3	3.092−02	0.97	–	–	–	2.490+00	104.8515
17	38	4p4f (3/2,5/2)	3	4	1.973+00	1.00	–	–	–	4.389+00	49.7191
29	39	4p4f (3/2,7/2)	1	2	4.511−02	0.94	–	–	–	1.614+00	88.8178

3.3.2 Collision Data

Moving now to the collision problem, a sample of the data from this work's DARC and AUTOS DW calculations is provided in figures 3.2 and 3.4, and figure 3.2 also contains data from the Ballance and Griffin (B&G) calculations [71] for comparison.[4] This data is provided in the form of collision strengths and effective collision strengths. The dimensionless collision strength, Ω_{ij}, for the transition between atomic states i and j, is related to the cross-section, $\sigma(i \to j)$, by

$$\sigma(i \to j) = \frac{\pi a_0^2 I_{\mathrm{H}}}{g_i k_i^2} \Omega(i,j)\,, \tag{3.10}$$

where g_i is the statistical weight of the initial state, k_i the wavenumber of the incident electron, a_0 denotes the Bohr radius and I_{H} is the ionization potential of the hydrogen atom in the units used for k_i^2.

The effective collision strength, Υ_{ij}, is the thermal average of the collision strength, typically a Maxwellian average such as that used in the present work:

$$\Upsilon_{ij} = \int_0^\infty \Omega(i,j) e^{(-\epsilon_j/kT_{\mathrm{e}})} \mathrm{d}(\epsilon_j/kT_{\mathrm{e}}) \tag{3.11}$$

where ϵ_j is the final energy of the scattering electron, T_{e} the electron temperature, and k denotes Boltzmann's constant. The Maxwell-Boltzmann distribution is non-relativistic, and relativistic effects become significant for $T_{\mathrm{e}} \gtrsim 20$ keV $\approx 2.3 \times 10^8$ K, relevant to the electron temperatures expected at ITER. In keeping with ADAS convention, no relativistic corrections are applied to the electron distribution functions used to produce the Υ_{ij} values in this work. The relativistic Maxwell-Jüttner distribution only requires the application of a simple multiplicative factor to the Maxwell-Boltzmann Υ_{ij} values.

Damping effects are apparent in both the collision strengths and effective collision strengths in figure 3.2, and the present AUTOS DW results are always less than the DARC results. This should be expected since DW calculation does not include resonance contributions to the effective collision strengths, which are certainly present for these transitions. However, the high energy behaviour of

[4] The energy levels, radiative rates, and effective collision strengths from the present work are available in the adf04 file format on the OPEN-ADAS website: `http://open.adas.ac.uk/detail/adf04/znlike/znlike_mmb15][w44ic.dat`

the DW results does approach that of the DARC results as would be expected. Figures 3.2(b) and 3.2(f) display transitions that would be forbidden under *LS* selection rules, and as such they have infinite energy limits of zero. All calculations shown tend towards this limit and become close in an absolute sense. Conversely, the transition in subfigure 3.2(d) would be a strongly allowed dipole under *LS* selection rules, and so it exhibits the divergent behaviour at high energies typical of that category.

There are obvious differences in the damped effective collision strengths between the present results and the B&G results for transitions 1–2 and 1–24, figures 3.2(b) and 3.2(f) respectively. Both of these transitions are non-dipole ($J = 0 \rightarrow 0$) and comparatively small in magnitude; therefore, damping effects and any differences in the CC expansion tend to be more pronounced. The lack of a full damping treatment in the present work could explain the discrepancies; however, one must first compare the undamped data to resolve the true origin of any differences. Unfortunately, the undamped B&G results are only presented in graphical form in their paper and the original data files are not available [86]. Furthermore, only data for the damped *effective* collision strengths are available, not the damped collision strengths. A visual comparison with the plots in the Ballance and Griffin paper is still useful. Comparing the undamped Υ_{ij} with those of B&G, one still observes large differences: this work's results are larger by about the same factor as in the damped case. Any differences in the undamped Υ_{ij} must be due to differences in the resonant structure of the undamped Ω_{ij}. Indeed, comparing the collision strengths in figures 3.2(a) and 3.2(e) with the B&G collision strengths plotted in their paper, there are intensity peaks present in *this work's* results that are not present in the B&G results, a direct indication that there are additional intermediate resonances in the present CC expansion. For example, transition 1–2 will have the resonance $3d^9 4s^2 4p nl$ available in this work's calculations but not in B&G's. Combining this and the observation that the relative amount of damping in the present results is comparable to the B&G results—inferred again from visual inspection—it is reasonable to conclude that the differences observed here are most likely due to the differences in the CI and CC expansions and not differences in the treatment of radiation damping. Moreover, discrepancies due to varying resonant enhancement between calculations

should be less pronounced in strong dipole allowed transitions, and this is exactly what is observed for the dipole 1–3 transition in figures 3.2(c) and 3.2(d).

Since these are only two cases, it is not possible to apply this conclusion in general, and it would be impractical to analyze every transition in this manner: there are 2843 intersecting transitions for the two calculations. However, a slightly larger subset of about 15 transitions was analyzed in similar detail, and the same conclusion was reached: the present damped Υ_{ij} tend to agree quite well with those of B&G for strong transitions, but weaker transitions display variable levels of agreement. Still, this is not enough evidence to extrapolate the conclusion, so a broader scope technique must be used. The approach was to select temperatures of interest and then compare the damped Υ_{ij} values from the two calculations for all intersecting transitions. Graphically, this results in the comparison scatter plots presented in figures 3.3(a) and 3.3(c), one at a temperature near that of peak abundance for W^{44+} ($\approx 3 \times 10^7$ K) and the other at a lower temperature. The intersecting levels involved in these transitions have an index cutoff of $i = 71$, corresponding to the last $3d^{10}4d4f$ level. Figure 3.1 displays that above this configuration, the energy level distributions do not intersect, and therefore there are no overlapping transitions involving levels above this cutoff.

The limited damping treatment of this work compared to B&G means the present collision data should be systematically *larger*, and this would manifest as a statistically significant number of points lying below the $y = x$ line. However, figures 3.3(a) and 3.3(c) display the exact opposite: what appears to be a significant number of points above the $y = x$ lines and so a systematic trend towards this work's Υ values having comparatively *smaller* magnitudes. Because the density of points in the vicinity of the $y = x$ line is not readily estimated, it cannot be immediately concluded that this is a statistically significant trend. Calculating the fraction of points within an uncertainty region of 20% around the $y = x$ line can elucidate the situation, and the results of this calculation are presented in the caption of figure 3.3. The values of 63% and 44% for the all transitions cases indicate that although there is reasonable agreement between most points at these temperatures, a significant portion do lie outside the uncertainty region. Additionally, plotting the ratio of the effective collision strengths, $R = \Upsilon_{\mathrm{BG}}/\Upsilon_{\mathrm{present}}$, versus a relevant independent variable as in figures 3.3(b)

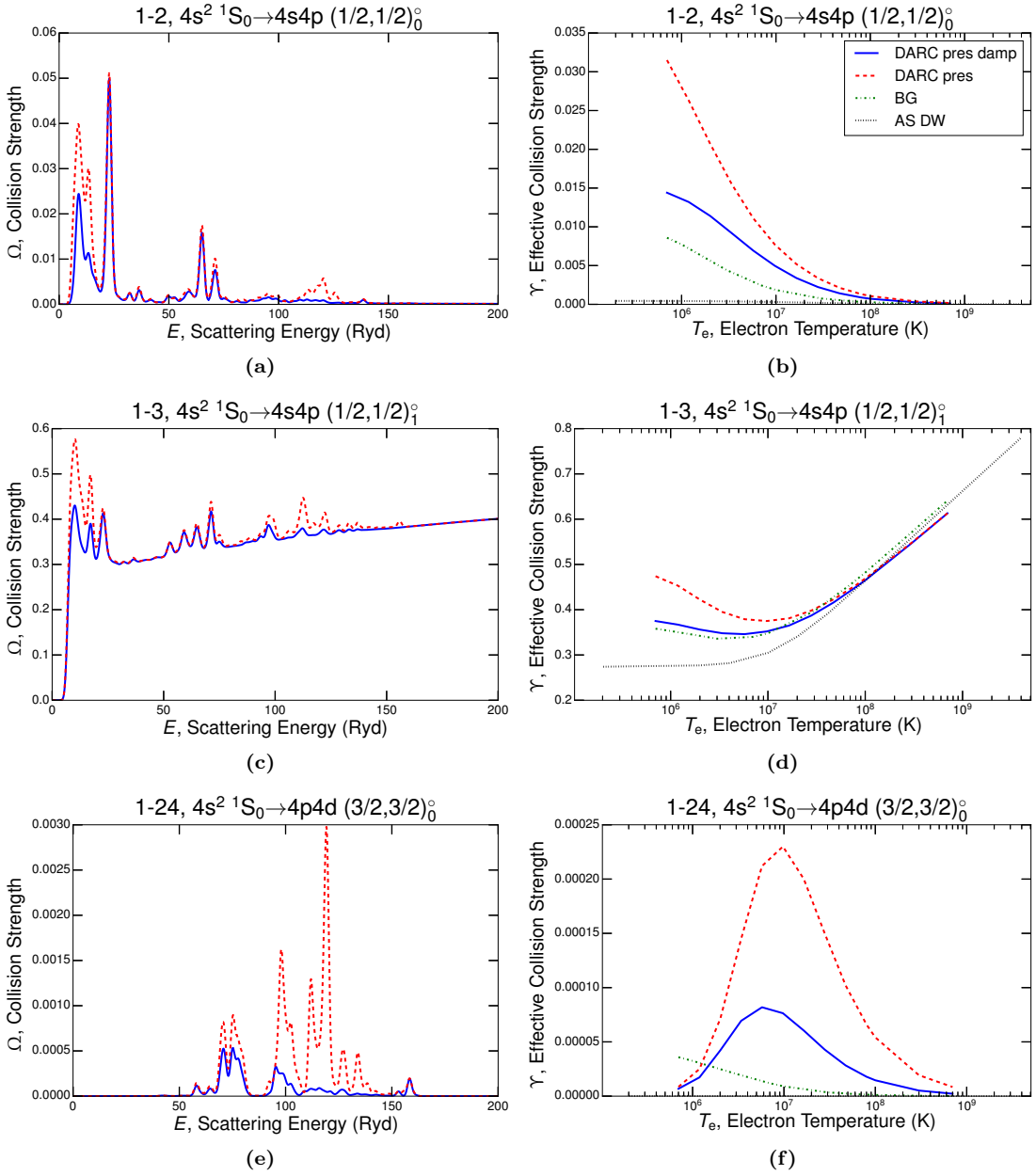

Figure 3.2: Collision strength, Ω, and effective collision strength, ϒ, results for the three transitions presented by B&G in [71]. Figures (a), (c), and (e) display the convolution of the present Ω data with a 2.205 Ryd (30 eV) Gaussian function; this 'smoothes' the dense resonance peaks while still retaining the information about where the peaks are strongest, making interpretation and viewing easier. The dashed (red) line is for the undamped data, and the solid (blue) line for the damped data. Figures (b), (d), and (f) show the present ϒ data (DARC pres and DARC pres damp) along with the present AUTOS DW (AS DW) results and the corresponding Ballance and Griffin (BG) results [71]. Refer to the legend in (b) for the line styles corresponding to each data set.

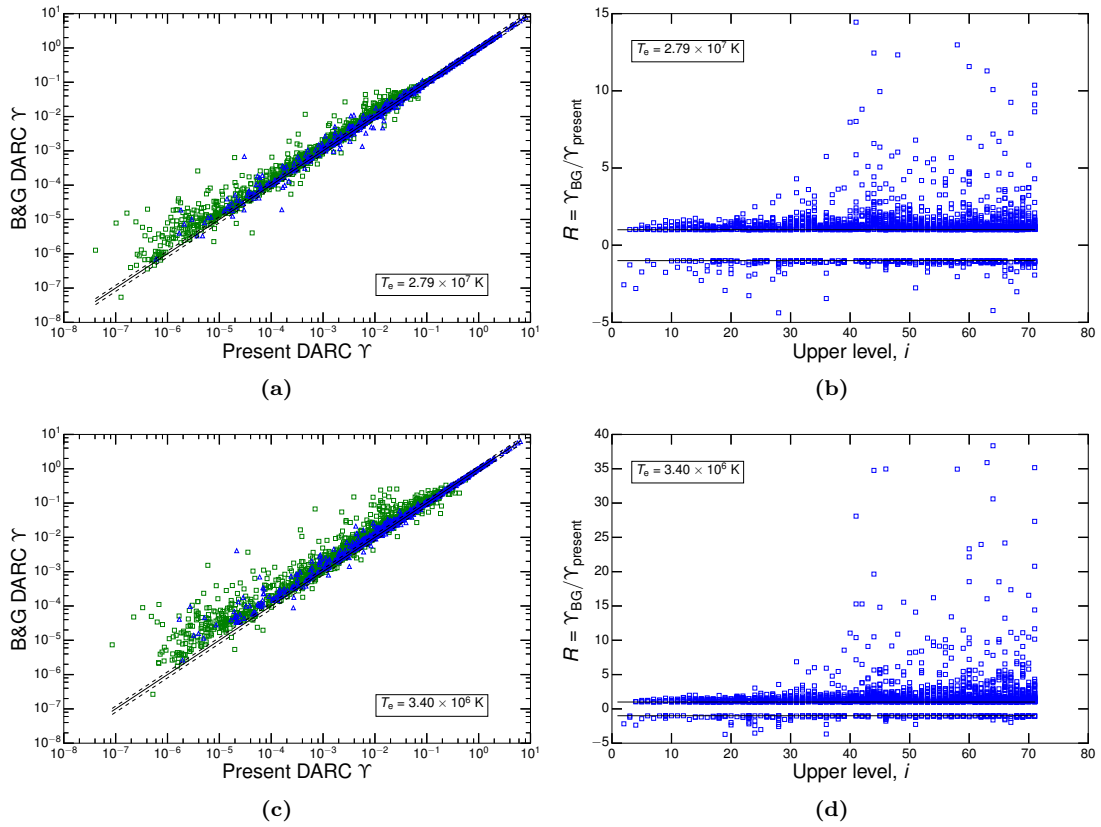

Figure 3.3: Comparison — (a) and (c) — and ratio — (b) and (d) — scatter plots of effective collision strength values, Υ, from the two primary calculations: Ballance and Griffin's (B&G) fully damped DARC versus the present, partially damped DARC. The temperature at which the Υ values are being sampled is indicated by the boxed value on each plot. For the comparison plots, (a) and (c), the (blue) triangles denote dipole transitions, and the (green) squares denote non-dipole transitions. The dotted lines demarcate the 20% error region around the $y = x$ line, and the percentage of points within the error regions are as follows: (a) all = 63%, dipole = 82%, non-dipole = 56%; (c) all = 44%, dipole = 68%, non-dipole = 35%. For the ratio plots, (b) and (d), the binary positive or negative behaviour of the ratio is defined by $R = \Upsilon_{\rm BG}/\Upsilon_{\rm present}$ if $\Upsilon_{\rm BG} > \Upsilon_{\rm present}$ or $R = -\Upsilon_{\rm present}/\Upsilon_{\rm BG}$ if $\Upsilon_{\rm BG} < \Upsilon_{\rm present}$. The ratio is plotted versus the upper level, i, of the transition in each case.

and 3.3(d) can reveal important systematic trends. Both of these plots show a clear asymmetry of higher Υ_{ij} values from the B&G calculations. Hence, the significance of the systematic trend is supported.

Since the systematic trend is the opposite to what was expected, there must be another, more significant systematic effect involved other than the limited radiation damping treatment. From the observation of no systematic deviation of the dipole line strengths in section 3.3.1 and the proximity of energy levels in table 3.3, it is deduced that the systematic difference cannot be caused directly by differences in the atomic structure. Several indicators suggest that this other systematic effect must be additional resonant enhancement for low to intermediate scattering energies in the B&G calculations. Firstly, the comparison plots in figures 3.3(a) and 3.3(c) both show that the trend towards larger Υ_{BG} values is relatively greater for weaker transitions. The non-dipole transitions, because they tend to be weaker, display a greater susceptibility to the trend, supported by the lower error region percentages and a visibly larger spread of values. Juxtaposing figures 3.3(a) and 3.3(c), which only differ by the sampling temperature, reveals that the trend of larger Υ_{BG} values is enhanced at lower electron temperature, an observation that is also true for figures 3.3(b) and 3.3(d). The preceding observations support the claim of additional resonant enhancement because resonances tend to affect weaker, non-dipole transitions to a larger degree and even more so at lower T_{e}.

Secondly, it is seen from the ratio plots in figures 3.3(b) and 3.3(d) that the Υ_{BG} values are increasingly large compared to this work as the index of the upper level, i, increases. The upper level is relevant for resonant enhancement considerations because it restricts the possible levels that can be involved in the intermediate $(N+1)$ resonant states. As the upper level of a transition approaches the level intersection cutoff of $i = 71$ ($E \approx 8 \times 10^6$ cm^{-1} in figure 3.1), the transition will increasingly only have access to resonances involving levels that are discrepant between the calculations. Consequently, the tendency for Υ values to disagree more at higher i that is observed in figures 3.3(b) and 3.3(d) is consistent with the proposition of discordant resonant enhancement.

However, this now begs the question why it is that the B&G results have systematic, additional resonant enhancement, especially when the present calcu-

lations include a larger number of levels. The answer must derive from the differing structure of the CC expansions and thus the differing atomic energy level distribution that is summarized in figure 3.1. The non-intersecting, $n = 5$ energy levels in the B&G calculation are immediately above the dashed-line threshold; hence, these levels will be more accessible for resonance formation if the electron distribution functions peaks close to the excitation energy of the transition under consideration. In contrast, the 3d-hole configurations lie ~ 60 Ryd higher, as do resonances with the same n-value. Furthermore, 3 of these 4 configurations have a strong dipole $4p, 4f \rightarrow 3d$ type-I radiation damping transition. Finally, some common initial configurations—$4p^2$, 4p4f, $4d^2$, and 4d4f—have no single electron promotions to 3d-hole resonances, unlike B&G where resonances can be formed by promotion to $n = 5$.

One point should be clear from the preceding discussion: it is the composition of the CI and CC expansion that most influences the behaviour of the collision data being compared. Indeed, it is still possible that the present calculations neglect a large amount of damping, which would be hidden by the cancellation of the two systematic effects; however, this is unlikely given the analysis of figure 3.2. The objective of including consideration of the soft x-ray, 3d-subshell transitions has necessarily shaped the CI/CC expansion used in the present calculations, and so differences with other calculations should be expected. In the end, a true assessment of the merits of these two primary calculations can only be obtained through the application of the data in the atomic population modelling to follow.

Figure 3.4 shows the collision data for the strongest three 3d-subshell transitions. Because of the strength of these $E1$ transitions, resonances appear to be unimportant and the behaviour due to direct Coulomb excitation dominates. Such observations are supported by a sharp jump in the collision strengths at the energy threshold of each transition. The limited number of resonance peaks is due to the fact that the upper levels in these transitions are close to the highest energy level included in the present calculation, meaning there are comparatively few intermediate resonant states available. Furthermore, good agreement is observed between the AUTOS DW results and the DARC effective collision strengths. Again, this can be accounted for by the relative sparsity and small magnitude of resonances for these transitions. One might be tempted to conclude that it would

be simpler and less time consuming to have only used the DW results; however, it is difficult to predict whether the results will still be similar following atomic population modelling. So it is prudent to carry all available results—present DARC, AUTOS DW, COWAN PWB, and B&G DARC —forward and assess any differences following the final analysis.

3.3.3 Atomic Population Modelling

As noted in section 3.1, determination of the total radiated power loss from W^{44+} is one of the desirable outputs from atomic population modelling, which can double as a comparative measure of the fundamental data. The excitation line power coefficient for a transition, $j \to k$, is defined by

$$P_{L,1,j\to k} = \Delta E_{jk} \mathcal{PEC}^{(\mathrm{exc})}_{1,j\to k} = \Delta E_{jk} A_{j\to k} \mathscr{F}^{(\mathrm{exc})}_{j1} \ , \tag{3.12}$$

which has units of (W cm^3) and is simply the relevant $\mathcal{PEC}$ multiplied by the energy difference between the levels involved, ΔE_{jk}. The total excitation line power coefficient, $\mathcal{P}^{(z)}_{\mathrm{LT},\sigma} \equiv \mathcal{PLT}$, is the sum of the $P_{L,1,j\to k}$ over all possible transitions, as defined in (2.37), and is directly proportional to the total radiated power loss of the ionization stage. Although the $\mathcal{PEC}$s and power coefficients give much of the same information, $\mathcal{PEC}$s are preferred in spectroscopic applications while power coefficients are needed for estimates of radiated power loss. Both are employed in the subsequent analysis and are largely interchangeable in cases where general conclusions about a transition are being sought.

The total excitation line power coefficients from the various calculations are plotted versus electron temperature in figure 3.5(a), along with a selection of relevant, contributing $\mathcal{P}_{L,1,j\to k}$ from the present DARC work. Observing the individual $\mathcal{P}_{L,1,j\to k}$ values, the dominant transition across most of the T_e range is unsurprisingly the dipole allowed 6–1 (60.93 Å) transition; however, towards lower T_e the VUV 3–1 (132.88 Å) transition is stronger due to its lower energy difference. Most importantly for this work, the strongest line from the open 3d-subshell transition arrays is the highlighted 275–1 (5.77 Å) transition. It is the value of the power coefficient at peak abundance temperatures that is of most concern (see section 5.3.1.1), and a critical observation is that the 275–1 3d-subshell line

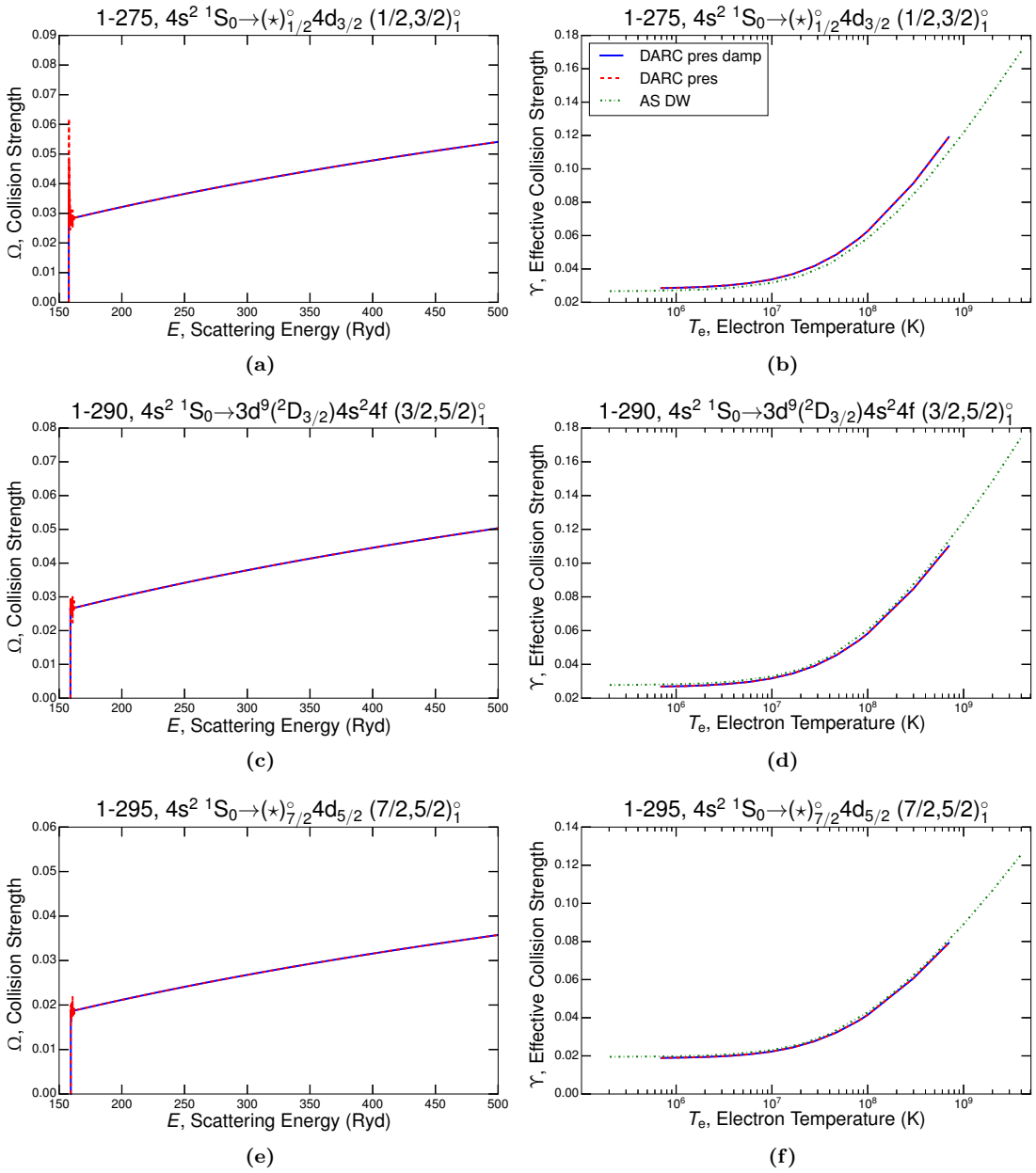

Figure 3.4: Present results for the dominant 3d-subshell transitions in the transition arrays, $[3d^{10}4s^2–3d^9 4s^2 4f]$ and $[3d^{10}4s^2–3d^9 4s4p4d]$. In contrast to figure 3.2, (a), (c), and (e) are the 'raw' Ω data sets that have not been convoluted; no convolution is required for these transitions because of the limited resonance structure. Again, the dashed (red) line is for the undamped data, and the solid (blue) line for the damped data. Figures (b), (d), and (f) display the Υ data for both the DARC and AUTOS DW calculations. Refer to the legend in (b) for the corresponding line styles. In the level specifications, the substitution, $\star \equiv (3d^9(^2D_{5/2})4s_{1/2})^\circ_2 4p_{3/2}$, is used.

contributes an equal amount to the total radiated power as does the VUV 3–1 line in this region.

The salient feature of the $\mathcal{PLT}$ lines in figure 3.5(a) is the departure of the B&G result from the other calculations at high T_e, commencing just before the demarcated region of peak abundance. What causes this behaviour is evident from the individual $\mathcal{P}_{L,1,j\to k}$ lines, just discussed: the 275–1 (5.77 Å) line, which is not included in the Ballance and Griffin calculations, rises to a 50:50 power contribution with the strong VUV 3–1 (132.88 Å) transition in the peak abundance region. Omission of this line along with others of comparable magnitude in the [$3d^{10}4s^2$–$3d^9 4s^2 4f$] and [$3d^{10}4s^2$–$3d^9 4s4p4d$] transition arrays leads to the relative reduction in the $\mathcal{PLT}$ seen in the B&G results. Otherwise, the $\mathcal{PLT}$ values from the other calculations, both of which include at least some of the important 3d-hole configurations, agree well across the given T_e domain with no relative errors over 50% and convergence at high T_e, notably in the shaded region of peak abundance. This reiterates a common theme: the primacy of the configurations included in the collision calculation and subsequent modelling. Without appropriate consideration of the 3d-subshell transitions, a large contribution to the radiated power from W^{44+} will be missed, reaffirming the decision to focus attention on these transitions.

Figure 3.5(b) provides a more detailed point of comparison between the calculations by showcasing the $\mathcal{PEC}$s for the same transitions as the individual $\mathcal{P}_{L,1,j\to k}$ lines in figure 3.5(a). Although the $\mathcal{PEC}$s and $\mathcal{P}_{L,1,j\to k}$ only differ by an energy factor, it is interesting to note the effect that this has upon the importance of the 275–1 (5.77 Å) line; the $\mathcal{P}_{L,1,j\to k}$ values are comparatively higher because of the large energy difference between level 275 and 1. Agreement between the theories in figure 3.5(b) is quite good for the strong dipole allowed transitions (3–1, 6–1, 275–1), and the moderate discrepancy between the DARC and DW results for the 3–1 line can be explained through application of the zero density limit expression in (3.9). This provides a good approximation in the present circumstance because density effects on level populations are largely absent until $N_e \approx 10^{16}$ cm^{-3}. The dominant A-value in the sum of (3.9) is $A_{3\to 1}$ by many orders of magnitude, and so the $A_{3\to 1}$ in the numerator will be effectively cancelled. Thus, it must be variation in the excitation rate coefficient, $q^e_{1\to 3}$, that causes differences in the

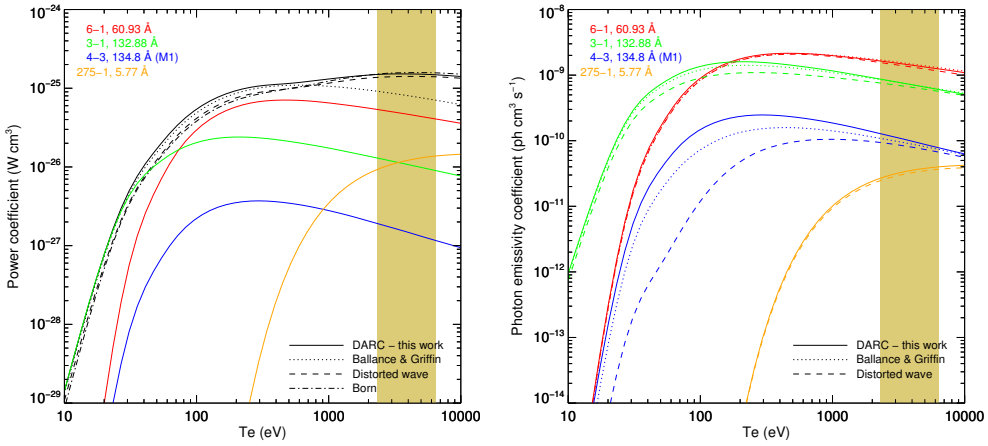

Figure 3.5: $\mathcal{PLT}$, $\mathcal{P}_{L,1,j\to k}$, and $\mathcal{PEC}$ values derived from the relevant fundamental datasets for W^{44+} versus electron temperature, T_e. The shaded vertical bar represents the T_e range where the fractional abundance of W^{44+} in the coronal equilibrium approximation is greater than 0.1. (a) shows the total excitation line power coefficients, $\mathcal{PLT}$, as the enveloping (black) lines, and these have been calculated for the four Υ_{ij} datasets with line styles indicated in the figure: the Ballance and Griffin DARC and the present DARC, AUTOS DW, and COWAN PWB. A sample of the strongest and most relevant contributing individual lines from the present DARC work have been emphasized (coloured) and labelled. (b) displays the $\mathcal{PEC}$ lines for the corresponding $\mathcal{P}_{L,1,j\to k}$ lines in (a). The line styles denote different datasets as labelled in the figure: Ballance and Griffin's DARC and the present DARC and AUTOS DW. *Note*: there are no Ballance and Griffin results for the 275–1 (5.77Å) $\mathcal{PEC}$ line. The indices from this work's GRASP^0 calculation are used—refer to tables 3.3 and 3.4.

$\mathcal{PEC}$ values—recall, excitation from the ground dominates in the zero density limit. Indeed, the AUTOS DW $\Upsilon_{1\to 3}$ values are systematically lower than the corresponding DARC values because of the absence of resonant enhancement; this explains why the DW $\mathcal{PEC}$ is also lower across the temperature range.

On the other hand, the spin-changing, $M1$, 4–3 transition displays notable differences between all of the calculations, but the $\mathcal{PEC}$ values do eventually converge at high T_e. Again, these differences can be understood through the use of the zero density limit for the $\mathcal{PEC}$, and just as above, the contributions from the radiative transition probabilities cancel due to the dominance of the $A_{4\to 3}$ value. The $\Upsilon_{1\to 4}$ values for the various calculations reproduce the ordering of the 4–3 $\mathcal{PEC}$ lines in figure 3.5(b): the AUTOS DW $\Upsilon_{1\to 4}$ are less than both of the DARC results because of the absence of resonances, and this work's DARC $\Upsilon_{1\to 4}$ are larger than B&G's for less obvious reasons. The trend of relatively larger B&G Υ values observed in section 3.3.2 in no way means that this work's Υ

values for a particular transition cannot be larger as is the case here; however, the cause of this is indeterminable without the ability to look at the B&G Ω_{ij} data.

There are several conclusions relevant to radiated power loss from the observations of figure 3.5. First, the importance of the soft x-ray 3d-subshell transitions: the $\mathcal{PLT}$ lines from figure 3.5(a) clearly show that neglecting the [$3d^{10}4s^2$–$3d^9 4s^2 4f$] and [$3d^{10}4s^2$–$3d^9 4s4p4d$] transition arrays will greatly reduce predictions of radiated power loss from W^{44+}. Thus, these transition arrays must be included in the collision calculations upon which any effort to model radiated power loss is built. Second, there is evidence that the omission of transitions involving the $3d^{10}4l5l'$ configurations (henceforth, $n = 5$ transitions) has little effect upon the $\mathcal{PLT}$ values. B&G collision data for the $n = 5$ transitions was merged into the present DARC data, and a negligible effect upon the modelled quantities in figure 3.5 was observed. The $\mathcal{PEC}$s still agreed to within a few percent except for the 4–3, $M1$ transition which agreed within 10%. Even though this merging is not a replacement for a full calculation with all of the relevant configurations, it strongly indicates that the $n = 5$ transitions are not essential for radiated power loss considerations in general and therefore also for the 3d-subshell transitions. As discussed in section 3.3.2, the $n = 5$ configurations do provide additional resonant enhancement for lower level transitions, and the effect of this in the context of population modelling will require further investigation outside the current scope of the present study.

Thirdly, the overall proximity between the present DARC, COWAN PWB, and AUTOS DW results in figure 3.5(a) propounds the suitability of the non-close coupling theories as baseline descriptions of the radiated power from W^{44+}. However, this statement in no way recommends that the more intensive DARC calculations are unnecessary. From a detailed spectroscopic perspective, one must assess the suitability of a particular dataset on a transition-by-transition basis, and the small number of transitions presented in figure 3.5 do not allow any generalizations to be made. Another technique is required.

Because W^{44+} is a heavy and relatively complex species, there are so many transitions that describing it with individual line emissivities is overwhelming and lacks an overarching perspective: one cannot see the forest for the trees. In

response, envelope lines are produced and defined by a vector of feature photon emissivity coefficients ($\mathcal{F}$-$\mathcal{PEC}$s), that are composite features of many $\mathcal{PEC}$ lines over a wavelength region. Suppose the spectral interval of interest, $[\lambda_0, \lambda_1]$, is partitioned by N_p elements of the set, $\{\lambda_i \equiv \lambda_0 + i(\lambda_1 - \lambda_0)/N_p : i = 0, \ldots, N_p - 1\}$, then the envelope feature photon emissivity coefficient vector is defined as

$$\mathcal{F}\text{-}\mathcal{PEC}^{(\mathrm{exc})}_{1,i} = \sum_{j,k;\lambda_{j\to k}\in[\lambda_0,\lambda_1]} \mathcal{PEC}^{(\mathrm{exc})}_{1,j\to k} \int_{\lambda_i}^{\lambda_{i+1}} \varphi_{j\to k}(\lambda)\mathrm{d}\lambda \tag{3.13}$$

where $\varphi_{j\to k}(\lambda)$ is the normalized emission profile of the spectrum line $j \to k$ that defines the line broadening.

The spectral features resulting from the $\mathcal{F}$-$\mathcal{PEC}$ vectors of the various W^{44+} datasets are plotted in figure 3.6; portions of soft x-ray and VUV regions are represented. As might be expected, the intensities of the features which envelop strong transition lines agree well—the peaks labelled by 6–1 & 8–3 ($\sim$ 61 Å) and 3–1 & 4–3 ($\sim$ 132 Å). However, the 6–1 feature does display some wavelength discrepancy. The COWAN PWB result overestimates slightly compared to the two DARC results. For features of less intense lines, the disagreements are larger: the COWAN PWB result differs from the two DARC results by nearly an order of magnitude for both the 12–4 & 11–4 ($\sim$ 66 Å) and 12–6 ($\sim$ 73 Å) features. Additionally, the 10–3 & 9–2 ($\sim$ 48 Å) peak exhibits both intensity and wavelength discrepancies between all the calculations. Overall, figure 3.6 also clarifies the wavlength coverage of these three datasets. Of most relevance for this work is that there is no B&G result for the 275–1 & 290–1 ($\sim$ 7 Å) feature, which is the third most intense. Again, this corresponds to the dominant soft x-ray, 3d-subshell transitions that have been of concern throughout, and the present DARC result is in close agreement with the COWAN PWB. In addition, this DARC work has no data between 10 Å and 20 Å corresponding to where the $n = 5$–4 lines lie.

The underlying message from the observations of figure 3.6 is that there are enough differences between the CC and non-CC calculations such that applications in detailed spectroscopy could produce disparate results—for example, when calculating the line emissivity, $\varepsilon_{i\to k}$, from (3.2). However, the two DARC results do agree very well for overlapping spectral intervals. This further supports

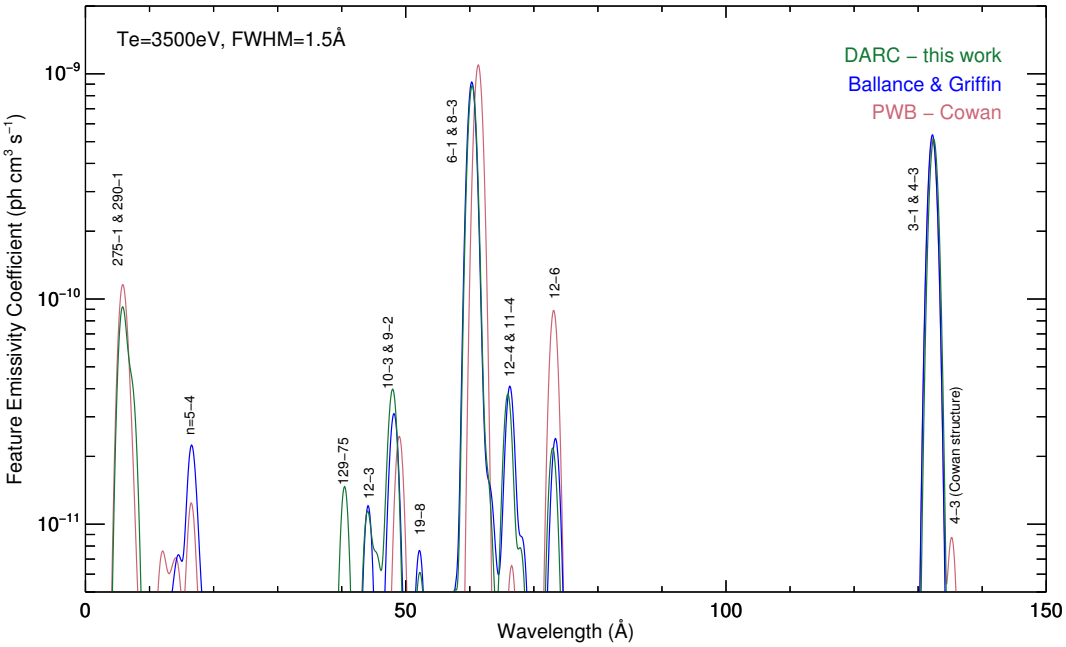

Figure 3.6: The envelope feature photon emissivity coefficient ($\mathcal{F}$-$\mathcal{PEC}$) vectors for various W^{44+} calculations plotted versus wavelength at $T_e = T_i = 3.5$keV, where T_i is the ion temperature. The calculations shown are those indicated in the top right, colour-coded legend: Ballance and Griffin's DARC, and the present DARC and PWB based on Cowan's code(COWAN). The Doppler broadening by the velocity distribution of the radiating ions has been applied using the default Maxwellian distribution with $T_i = T_e$. In addition, the results were convolved with an ideal spectrometer instrument function with a FWHM of 1.5 Å. The vertical labelling of the peaks denotes the transition(s) for the dominant excitation $\mathcal{PEC}$(s) within the feature; the indices from this work's GRASP^0 calculation are used—refer to tables 3.3 and 3.4.

the conclusion above that the neglect of the $n = 5$ transitions has not significantly affected the modelled results. A possible criticism of this conclusion is that only strong emission lines are being considered in figure 3.6 and that differences between the datasets might become more apparent for weaker lines. But this point is self-defeating: the fact that these lines are weak and not part of this spectrum means they unlikely to be observed and so are less important from an experimental standpoint. Therefore, for both spectroscopic and radiated power applications, it is recommended that this work's DARC *adf04* file with the merged $n = 5$ transition data from B&G be used.

Chapter 4

Baseline-quality Ion-impact Excitation Calculations

4.1 Introduction

An implicit assumption has been made in both Chapters 2 and 3 that electron projectiles dominate the collisional excitation of impurity species in relevant plasma environments. In fact, this is a common assumption in the fields of atomic and plasma physics, and the literature abounds with work pertaining to fundamental EIE collision data and its application to CR models, exclusive of any other collision mechanisms. However, there is a whole other class of charged particles in a plasma that can function as collision projectiles: the positive ion species, whether fuel ions, fusion products, or impurity species. Compared to EIE, there are far fewer literature sources for ion-impact excitation (IIE), and they tend to be less sophisticated. This can be explained almost entirely by classical mechanics, even though collisional excitation is fundamentally quantum, because of Ehrenfest's Theorem and the Correspondence Principle.

For EIE, the classical analogue is two spheres of equal mass colliding elastically, representing the free electron projectile and one of the bound target electrons with which it interacts. Classical mechanics specifies that these types of collisions result in large relative energy transfers. In the extreme case of a head-on collision, the projectile will transfer all of its energy to the target. Large changes in energy translate to changes in the principal quantum number, n, of

the bound electron. It is these n-changing transitions that are central to population modelling and line emission power. On the other hand, for IIE the classical analogue is two spheres of vastly different mass colliding elastically, representing the ion projectile (m_i) interacting with one of the bound atomic electrons (m_e) and $m_\mathrm{i} \gg m_\mathrm{e}$. In this case, classical mechanics dictates that there are small energy transfers from the projectile to the target, but changes in direction of the target are more pronounced. This causes changes in the angular momentum, which translates to variation of the l and j quantum numbers of the atomic electron. Therefore, IIE transitions tend to be restricted within ry configurations and LS terms of the highly-resolved, lower-energy states. Because the energy differences are small, these collisions are particularly efficient for light species, resulting in the well-known effect that ry states and LS terms have an internal statistical balance of their respective sub-states. However, precisely because a statistical balance can be assumed, there is no need to explicitly include IIE transitions in the model, thus explaining the neglect of this process compared to EIE.

Although this classical differentiation between IIE and EIE is useful for a preliminary sense of the problem, more precision is required for a serious study. To this end, the cross section schematics for an arbitrary transition have been created in figure 4.1 using more detailed information about the respective collision processes. By way of juxtaposition, they compactly summarise the effects of the different projectiles and how these differences propagate to the final rates used in the population model. The cross sections are plotted versus the initial, relative projectile speed, $u_p = u$, as opposed to the relative energy since this provides a more intuitive, physical representation; after all, the rate coefficient is formed by the product of the cross section and relative projectile speed, $q_{i\to j} = \langle u_p \sigma_{i\to j}(u_p) \rangle$. The following facts were used to compose these schematics. First, the cross sections for both EIE and IIE tend to peak at the same velocity for a given transition, $u_p \sim \sqrt{2\Delta E_{ij}}$. The underlying reason is that once the projectile has sufficient energy to excite the transition, it is the nature of the perturbing potential that determines the excitation cross section. This potential is dependent upon the magnitude of the projectile charge—not the sign—and the collision time, which is directly related to the relative projectile speed. Technically, the integrals involved in the cross section or collision strength are dependent on a dimensionless

parameter, ξ, which is the ratio between the atomic frequency, $\Delta E_{ij}/\hbar$, and the collision time. More discussion about this informative parameter is provided in section 4.4.1.1. More generally, the parameters used throughout this chapter are defined in table 4.2, and most are also defined in the glossary.

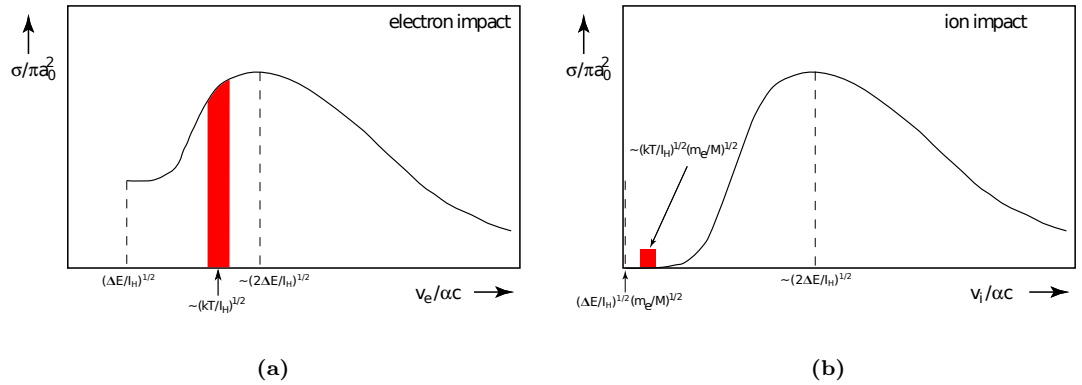

Figure 4.1: Schematic graphs of EIE, (a), and IIE, (b), cross sections versus relative projectile speed, v_p, for an arbitrary transition, $i \to j$. The red or shaded bars represent the speed domains where the Maxwell-Boltzmann distribution would peak at a temperature, $T \equiv T_\mathrm{e} \equiv T_\mathrm{p}$. Divisions by I_H indicate the use of Rydberg energy units, while division by αc or πa_0^2 indicate the use of atomic units.

Secondly, the excitation thresholds—left dotted lines in figure 4.1 (a) and (b)—are determined by the transition energy, so in energy space $\varepsilon_i^{(\mathrm{thr.})} = \Delta E_{ij}$. Converting to speeds,[1] the EIE threshold is $u_p^{(\mathrm{thr.})} = \sqrt{\Delta E_{ij}}$ whereas the IIE threshold is $u_p^{(\mathrm{thr.})} = \sqrt{\Delta E_{ij}/M}$. Of course, the speed threshold for EIE is also scaled by $1/\sqrt{M}$, but since $m_\mathrm{e} = 1$ in atomic units, $M = \frac{m_t}{m_t+1} \approx 1$ for $m_t >> 1$. Thus, the mass scaling has the effect of greatly reducing the IIE speed threshold relative to that of EIE: compare sub-figure 4.1(a) to (b).

Thirdly, at threshold, the IIE cross section is suppressed towards zero due to the repulsive and adiabatic nature of the interaction. The descriptor, *adiabatic*, is used in the quantum and not the thermodynamic sense here, and a complete definition is given in section 4.4.1.1. Briefly, a perturbation is adiabatic if it is slowly varying and so smoothly transports the atomic wave function between a well-defined initial and final state of the same quantum numbers. Hence, no transition occurs. In contrast, the EIE cross section is finite at threshold as

[1] When using Rydbergs for the transition energy but retaining atomic units for the speed, the kinetic energy equality becomes $Mu_p^2/2 = \Delta E_{ij}/2$, so $Mu_p^2 = \Delta E_{ij}$.

a result of the attractive interaction and the quantum phenomenon of electron exchange: the incoming electron is readily drawn into the target and a transition is possible right at the threshold.

Finally, consider the other component of how the rate is formed: the Maxwellian speed distribution. Assuming the equipartition theorem holds, the average kinetic energies of electrons and any ion species in a plasma will be equal, meaning their energy distributions will be the same. Consequently, the peak region of the *ion* speed distribution at a given temperature will be scaled by a mass factor of $M^{-1/2}$ relative to the *electron* speed. This results in the simple, well-known phenomenon that positive ions in a plasma travel at lesser speeds than the electrons when both species are in mutual thermodynamic equilibrium. Although slow relative ion speed is often quoted as the sole reason why IIE rates will be negligible, this is not the whole story. Figure 4.2 clearly shows that the peak domain of the Maxwell-Boltzmann distribution also becomes narrower as the relevant mass increases, which can have serious implications for the formation of rates.

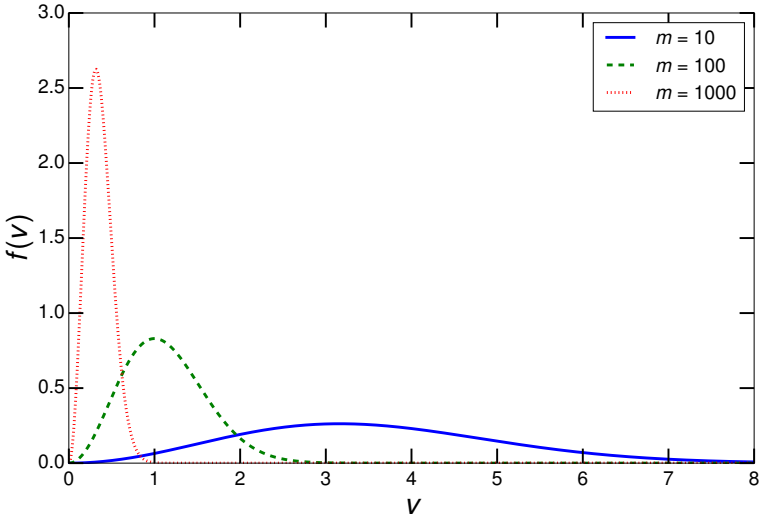

Figure 4.2: The Maxwell-Boltzmann probability density function, $f(v)$, versus speed, v, for different particle mass values, m. A common temperature of $kT = 25$ Ryd has been set.

A more precise qualitative explanation for why EIE has dominated the subject of collisional excitation in plasmas can now be offered. Recalling that the excitation rate is formed by the thermal average of the cross section and speed product, one can estimate the magnitude of a rate by determining the relative domains where the Maxwellian speed distribution—the vertical, red bars in figure 4.1—

and excitation cross section have their respective peaks. If these peak domains overlap, then one can expect a larger rate than if these domains overlap to a lesser degree or do not intersect at all. Furthermore, because of the Maxwellian narrowing effect displayed in figure 4.2, this relative location of peaks is more influential when determining IIE rates than EIE ones: an ion speed distribution will be more *selective* of the speeds relevant to the formation of the rate than the electron distribution.

Again, it is useful to refer to both schematics in figure 4.1 since they provide a visual summary of the situation. Starting with the electron-impact case of figure 4.1(a), it is assumed that the plasma temperature, T, is such that the electron speed distribution peaks near the peak of the excitation cross section, $\sigma_{i\to j}$, for this arbitrary transition, and so a substantial excitation rate should result. That this is a good assumption *in general* remains to be shown, but the present aim is simply to demonstrate that for a transition with a significant EIE rate at a given temperature, the corresponding IIE rate will likely be inconsequential. Moving to ion-impact in figure 4.1(b), it is known from the previous observations that the excitation threshold and speed distribution peak will be scaled by $M^{-1/2}$ relative to the electron-impact analogues, but the cross section peak will remain at largely the same u_p. Combining these effects with that of the suppression of the IIE cross section at threshold explains what figure 4.1(b) visually represents: the Maxwellian peak tends to lie on a portion of the IIE cross section that is closer to the threshold than to the peak, and so it lies on a portion that is nearly zero in magnitude. As a result, it is reasonable to estimate that the IIE rate will be small and even negligible compared to that of EIE. It is notable that if the peak of the IIE cross section was also scaled by $M^{-1/2}$, then this contrast would not be so dramatic, although the suppression at threshold would still likely ensure the comparatively small magnitudes of IIE rates.

4.1.1 IIE Rules of Thumb

Recall that the parameters used in this section are defined in table 4.2. All of the preceding observations comparing EIE to IIE produce what might be called an *archetype* that is broadly applied to dismiss the need for IIE in population models. However, this need not always be case, and the first step towards com-

prehending alternate excitation scenarios is determining the conditions needed for more pronounced IIE rates. Referring again to figure 4.1(b), the aim of having the cross section peak as close to the red bar as possible can be achieved through two mutually compatible mechanisms. First, a small transition energy, ΔE_{ij}, will result in a cross section peak at lower projectile speeds; and second, the Maxwellian peak itself can be shifted to higher speeds by increasing the plasma temperature: $u_p^{(\mathrm{pk})} = (2kT_p/M)^{1/2}$.

For an individual transition, it is straightforward to make an order of magnitude estimate of whether the IIE rate will be significant relative to the EIE rate. The discussion so far has clarified that only two parameters in this rough approximation are responsible for determining the magnitude of a rate: the projectile temperature, T_p, and the transition energy, ΔE_{ij}. Thus, it simply remains to find a relation between these variables that defines the condition for when the peaks of the Maxwellian distribution and the cross section are approximately aligned. Following the reasoning of [87], one can estimate that the peak of the EIE cross section will occur at a reduced projectile energy somewhere in the range of 1 to 10 times the transition energy,

$$\Delta E_{ij} \lesssim \varepsilon_i^{(\mathrm{e})} \lesssim 10\Delta E_{ij}. \tag{4.1}$$

Converting to velocity using the expression for kinetic energy of a reduced particle measured in Rydbergs, $\varepsilon_p = M u_p^2$, with $M \approx m_\mathrm{e} = 1$, the range becomes

$$\sqrt{\Delta E_{ij}} \lesssim u_\mathrm{e} \lesssim \sqrt{10\Delta E_{ij}}. \tag{4.2}$$

Now, as stated above, the EIE and IIE cross sections peak at approximately the same relative projectile velocity, $u_\mathrm{e}^{(\mathrm{pk})} \approx u_\mathrm{i}^{(\mathrm{pk})}$, so using 4.2 and the kinetic energy of a reduced particle in the centre-of-mass (COM) frame, one can obtain the estimated *reduced* energy range for the peak of the IIE cross section:

$$M\Delta E_{ij} \lesssim \varepsilon_i^{(\mathrm{i})} \lesssim 10M\Delta E_{ij}. \tag{4.3}$$

As an example, if the projectile is a proton (i.e. ^{1}H nucleus) then $M \approx m_\mathrm{p} \approx 2\ 000$, and so one would expect the cross section for an arbitrary transition to peak at

an incident energy of somewhere between 2 000 and 20 000 times ΔE_{ij}, or more simply $\varepsilon_i^{(\mathrm{i})} \gg \Delta E_{ij}$.

Now, in order to maximize the resulting rate coefficient for the transition of interest, the peak of the Maxwellian distribution function should overlap that of the cross section: $kT_\mathrm{i} \approx \varepsilon_i^{(\mathrm{pk})}$. Thus, a range of the most relevant temperatures for IIE can be established:

$$M\Delta E_{ij} \lesssim kT_\mathrm{i} \lesssim 10M\Delta E_{ij}. \tag{4.4}$$

Since M is typically quite large for IIE cases, it is more succinct to say $\Delta E_{ij} \ll kT_\mathrm{i}$. Furthermore, when an equilibrium ionization balance of a particular element is established—which is often the case—the temperature at which each ion species of the isonuclear sequence will peak in abundance can be fairly well approximated by the ionisation potential of that species: $kT_\mathrm{i}^{(\mathrm{pk})} \approx \chi^{(z)}$. Putting this all together, one gets the most practically useful equation for estimating whether a transition will have a significant IIE rate:

$$\Delta E_{ij} \approx kT^{(\mathrm{pk.})}/M \approx \chi^{(z)}/M\,. \tag{4.5}$$

So, it is transitions with a small ΔE_{ij} relative to the plasma temperature or the ionisation potential for which IIE can produce large rates. Indeed it has already been mentioned that for low-Z_0 species, it is large IIE rates and not EIE rates that are responsible for establishing statistical balance amongst the nearly degenerate, fine-structure levels. In such circumstances, it is not necessary to explicitly include IIE rates in any CR modelling. However, as higher-Z_0 species are considered, the degeneracy and hence statistical balance of fine-structure levels breaks down, but the IIE rates can be substantial with $\Delta E_{ij} \ll \chi^{(z)} \approx kT^{(\mathrm{pk.})}$ still holding true. Under these circumstances, IIE rates should be included, but it is only through CR modelling that one can judge the impact and necessity of including IIE or not. The exploration of the plasma parameter space where IIE must be explicitly included in CR models will be done in section 5.3.1.

4.2 Literature Review

Given that IIE collision will be needed in certain plasma scenarios, the broad categories of calculation approaches are introduced in this section. As with EIE in Chapter 3, the trade-off between accuracy and computational resources must ultimately be balanced when selecting a technique. Moreover, the limitations and inherent assumptions of a technique need to be considered in the context of the input parameters for the scattering problem to be solved. For instance, the Born approximation becomes exact in the limit of infinite projectile energy, but it grossly overestimates the IIE collision strength at low energies because it does not account for the repulsive nature of the interaction, only the magnitude of the charge. Therefore, this is an ideal technique for extremely high temperature plasmas because the Born approximation is computationally inexpensive, but it is inaccurate under other conditions regardless of the computational resources used.[2]

Both EIE and IIE are fundamentally quantum processes, so an approach to IIE based on quantum mechanics is required. Yet the applicability of classical mechanics to the scattering problem should not be ignored, especially if it reduces the computational load. Classical mechanics has been evoked frequently, for good reason, in describing certain collision phenomena since even the atomic target itself can be accurately described semi-classically in some circumstances—viz. Gaunt factors close to unity. The degree to which classical approximations can be introduced will depend on the physical conditions and is quite a subtle point that forms a recurring theme in this review. To start with, the quantum nature of the scattering event is determined by the possible interaction between the projectile and target wave functions. This can be quantified by considering the de Broglie wavelength of the projectile, $\lambda\!\!\!^{-} = 1/p = 1/(Mu_p)$, in relation to some dimension of the scattering event relative to the target. Alder and Winther [88] choose half the distance of closest approach for a head-on collision, $a = z_p z_t/(Mu_p^2)$, and they define the dimensionless ratio of a to $\lambda\!\!\!^{-}$ as a parameter that measures the degree

[2]The importance of the Born approximation in the context of the semi-classical method used in this work is explored in sections 4.2.1 and 4.3.1

of interaction between wave functions:

$$\eta = \frac{a}{\lambda\!\!\!^{-}} = \frac{z_p z_t}{u_p}. \tag{4.6}$$

If $\eta \gg 1$, then $\lambda\!\!\!^{-} \ll a$, and the projectile wave function will have little opportunity to overlap the target wave function because its physical extent is small compared to how close it approaches the target. Therefore, the projectile motion can be accurately approximated by a compact wave packet travelling along a *classical* trajectory. There are two potential differences between IIE and EIE by the measure in equation 4.6. First, larger z_p ion projectiles will result in larger η values and thus a more "classical" scattering compared to EIE where $z_p = 1$. Second, ion projectiles tend to have slower relative speeds, u_p, than electron projectiles because of the mass factor in the distribution function, and this is another factor that produces preferentially larger η values for IIE over EIE.

Yet, there is another manner in which IIE is more conducive to a semi-classical treatment. From the perspective of a fully quantum calculation, highly oscillatory, continuum wave functions of ion projectiles are computationally expensive to represent, and the number of partial waves, l, needed in the collision strength sum, $\Omega = \sum_l \Omega_l$, scales as $\sqrt{M}$. So, ions are less tractable in a quantal treatment than electrons are, which is a mathematical corollary of the physical fact that the relatively large mass of ion projectiles ($m_{\mathrm{i}} \gg m_{\mathrm{e}}$) leads to small de Broglie wavelengths and therefore a less wave-like character. This is not to say that classical approximations for EIE are not appropriate; for instance, Seaton [89] describes an effective method to calculate optically allowed, EIE cross sections using the impact parameter method. However, it must be acknowledged that EIE reactions are fundamentally more "quantum", which explains why so much effort has been devoted to topics like close-coupling and electron exchange for this type of scattering.

Combining the classical approximation of hyperbolic projectile trajectories with a quantum method for the excitation of the target results in a *semi-classical* approach to the scattering problem—one that has been historically popular for IIE calculations. Such an approach is advantageous because the neglect of any projectile-target wave function interaction greatly reduces the computational ex-

pense of the scattering calculation. There is an implicit assumption here that the projectile is without any internal quantum states and so cannot be itself excited—i.e. it is a structureless classical object. Another advantage is that accurate results are guaranteed when $\eta \gg 1$, which is true over a large parameter space for ion projectiles. There are two subclasses of semi-classical approaches. If first-order perturbation theory is applied to quantify the excitation of the atom under the influence of the perturbing projectile potential, then one has the semi-classical, first-order perturbative (SC-1) method, which is described further in section 4.2.1. On the other hand, if the time-dependent Schrödinger equation is solved directly under the influence of the classically determined perturbing potential, then one has the semi-classical, close-coupled (SC-CC) method, which is discussed in section 4.2.2. The SC-1 method has been selected for the production of IIE data in this thesis and for the ADAS baseline. The purpose of the following literature review will be to place the SC-1 method in its proper context.

Returning to equation 4.6, if $\eta \ll 1$ then $\lambda\!\!\!^{-} \gg a$, and the Born approximation applies. The extent of the projectile wave function is so large compared to the classical distance of approach that the target will "see" an incident planar wave. In between this limit and $\eta \gg 1$, neither semi-classical methods nor the Born approximation are completely accurate, and more sophisticated quantum methods must be used. A short résumé of the quantal methods applicable to IIE is provided in section 4.2.3 to complete the literature review, and a central question will be assessing how these compare to the semi-classical treatments. Indeed, the semi-classical approaches can be extended and improved with various modifications involving cutoffs and limits to achieve greater agreement with the quantal treatments. The infinite-energy Born limit, $\Omega_{ij}{}^{(\mathrm{inf})}$, can be directly related to one of these cutoffs, providing a link between the extreme η limits and thus ensuring the validity of the *modified* semi-classical approach across the entire parameter space. Much of the subsequent discussion will centre on these modifications since the applicability of the semi-classical approach depends on them.

Another pivotal aspect of any approach to the scattering problem is the interaction term used. It will take a fundamentally different form in quantum and semi-classical approaches and thus is intertwined with the themes raised above. Recalling the conclusions from section 4.1.1, the fine-structure transitions within

terms are most susceptible to IIE, so the electric quadrupole ($E2$) component of the interaction is the dominant term of the interaction.[3] Furthermore, it is common for semi-classical approaches to adopt a long-range approximation of the quadrupole interaction potential to simplify the calculation, and this is also done for the present work. The validity of these assumptions in the context of more advanced techniques will be investigated further in the following review sections.

In summary, there are three primary questions that this literature review must answer in relation to the modified SC-1 technique that will eventually be implemented:

1. Is a fully quantal treatment required for calculating IIE collision data?
2. What forms and approximations of the interaction potential are appropriate for baseline data?
3. Is a close-coupled method required for IIE collision data, or will first-order perturbation theory suffice?

As hinted at the beginning of this section, the answers to these questions will depend upon one's objectives and constraints. For the present purposes, an expeditious achievement of *ic*-resolved GCR is the foremost goal, and this requires a broad coverage of IIE collision data generated rapidly. Therefore, baseline-quality data is the objective like in Chapter 2, and it must achieve an accuracy within acceptable error bounds of high-quality data. Section 4.2.4 will conclude on this matter.

4.2.1 SC-1 Methods

In the limited field of IIE studies, the SC-1 approach is undoubtedly the most popular because of its simplicity yet remarkable accuracy. The lineage of the various implementations is traced in figure 4.3, and they all derive from Seaton [90], henceforth S64. Given its foundational role, this source warrants a thorough summary of its methodology. S64 itself derives from the semi-classical approach

[3]The magnetic dipole term is also allowed by selection rules, but its contribution is far smaller because the magnetic field of the bombarding particle is only of order u_p/c as compared with the electric field.

applied to nuclear excitation by Alder et al. [91], and this is the true seminal work on the subject. Applying the *nuclear* excitation equations to *atomic* excitation is ostensibly quite straightforward, but a number of complications arise. First, since the physical extent of a nucleus is vastly smaller than an atom, the possibility of the projectile penetrating the target is not covered in [91], but this proves to be an important phenomenon for atomic excitation. Second, the condition of $\eta \gg 1$ holds far better for nuclear excitation, so perturbation theory tends not to break down, but the same cannot be guaranteed for atomic excitation.

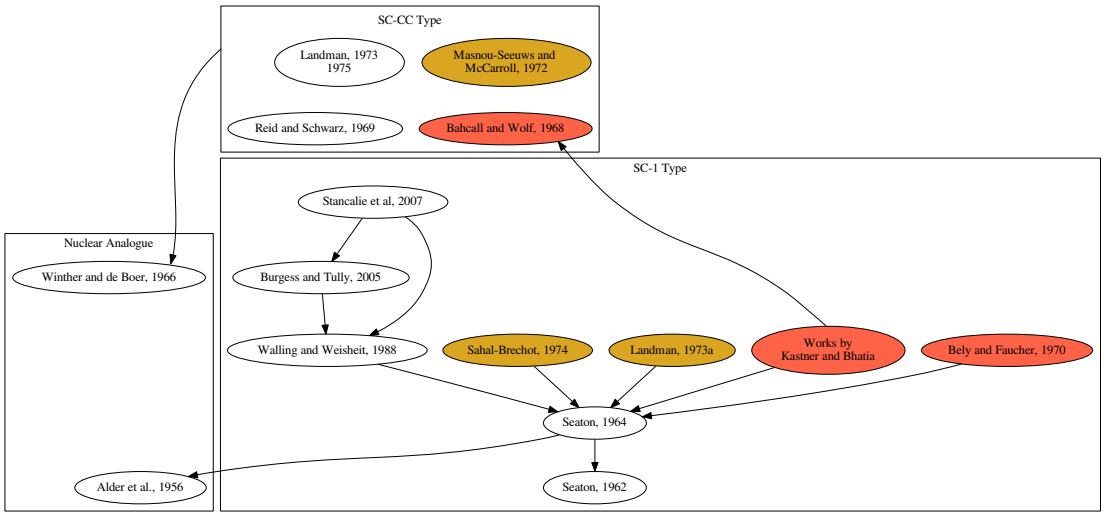

Figure 4.3: Lineage of popular SC-1 and SC-CC IIE implementations within the literature. Red bubbles indicate erroneous implementations, while yellow indicates a suspicion of flaws but insufficient evidence in the paper to confirm this. The arrows point towards the source or basis of a given calculation. Each arrow originates from a more recent calculation and points to a previous calculation, upon which the recent calculation is based or derives from.

S64 addresses these problems by partitioning the projectile energy space into three physically motivated regimes:

(a) **Low Energies**—Referring back to equation 4.6, $\eta \gg 1$ will be ensured for low values of u_p, so there is negligible interaction of the projectile and target wave functions. In other words, the Coulomb repulsion keeps the ion projectile far away from the target atom. The transition probabilities from first-order perturbation theory, $P_{ij}^{(1)}$, are small and accurate in this weak interaction regime, and the cross section is given by

$$\sigma_{i\to j} = \int_0^\infty P_{ij}^{(1)}(b) 2\pi b \, \mathrm{d}b, \tag{4.7}$$

where b is the impact parameter. The interaction potential used in determining $P_{ij}^{(1)}$ is given by the quadrupole ($\lambda = 2$) term from an expansion of $|\boldsymbol{r_p} - \boldsymbol{r}|^{-1}$:

$$\frac{1}{|\boldsymbol{r_p} - \boldsymbol{r}|} \approx P_2(\hat{\boldsymbol{r}}_{\boldsymbol{p}} \cdot \hat{\boldsymbol{r}}) \frac{r^2}{r_p^3}, \tag{4.8}$$

where $\boldsymbol{r_p}$ is the projectile coordinate, $\boldsymbol{r}$ is the atomic electron coordinate, P_2 is the Legendre polynomials of order two, and this expression is strictly valid for $r_p > r$—hence the concern about penetrating trajectories. In the present regime, the distance of closest approach, $\rho(b)$, is greater than the average radius of the target atom, r_0, for any b, so $r_p > r$ is always guaranteed.

(b) **Intermediate Energies**—The condition $\eta \gg 1$ no longer applies, and interaction between the projectile and target wave functions is possible. Consequently, $P_{ij}^{(1)}$ begins to overestimate the transition probability for some b, so a *cutoff*, b_1, is introduced such that $P_{ij}^{(1)}(b_1) = 1/2$, and it is assumed $P_{ij}^{(1)}(b) = 1/2$ for $b < b_1$. Thus, the cross section becomes

$$\sigma_{i\to j} = \frac{1}{2}\pi b_1^2 + \int_{b_1}^{\infty} P_{ij}^{(1)}(b) 2\pi b \, \mathrm{d}b. \tag{4.9}$$

This is accurate as long as $\rho_1 > r_0$ such that the approximation for the interaction potential does not break down. ρ_1 is the distance of closest approach for the cutoff impact parameter, b_1.

(c) **High Energies**—At this point, the projectile has sufficient energy to penetrate the target for a number of its trajectories, and the approximation in equation 4.8 breaks down. More precisely, the distance of closest approach for the first cutoff at intermediate energies, ρ_1, will now be less than r_0, so a new cutoff, b_0, is introduced such that $\rho(b_0) = \rho_0 = r_0$, and the cross section is now

$$\sigma_{i\to j} = \pi b_0^2 P_{ij}^{(1)}(b_0) + \int_{b_0}^{\infty} P_{ij}^{(1)}(b) 2\pi b \, \mathrm{d}b. \tag{4.10}$$

These modifications to the calculation of IIE cross sections entirely capture the physical nature of the scattering problem, and this is evinced by the remark-

able agreement achieved by S64 [90] with more sophisticated techniques—see figure 4.5. But there are two shortcomings. First, S64 deliberates on the somewhat arbitrary nature of selecting $P_{ij}^{(1)}(b_1) = 1/2$ for the cutoff at intermediate energies. This choice corresponds to a strong coupling collision in which the final state is equally likely to be the upper or lower atomic level, yet it is probably more physically accurate that the result of a strong coupling transition should be determined by the statistical weights of the upper and lower levels. Second, the use of the mean atomic radius, r_0, as the cutoff for high energies does not guarantee the exact high energy scaling of the cross section.[4] Put another way from the perspective of collision strengths, this cutoff cannot ensure that the correct infinite energy Born limit, ${\Omega_{ij}}^{(\mathrm{inf})}$, will be reached. Both of these problems will be addressed by reference [92], henceforth BT05, at the end of this section.

Proceeding chronologically, Bely and Faucher [93] implement a similar version of the SC-1 approach but, instead of partitioning the energy space, they use a different functional form for the transition probability that automatically guards against the overestimates of $P_{ij}^{(1)}$ as described above:

$$P_{i\to j}^{(\mathrm{II})} = \frac{P_{ij}^{(1)}}{\left(1 + P_{ij}^{(1)}/4\right)^2}. \tag{4.11}$$

This is exactly the result one would obtain from considering the transition matrix of a two-state system and is borrowed from the quantal, Coulomb-Bethe theory of [94]. Indeed, this eliminates the need to distinguish between the low (a) and intermediate (b) energy regimes because $P_{i\to j}^{(\mathrm{II})} \approx P_{ij}^{(1)}$ for $P_{ij}^{(1)} \to 0$, but it does not safeguard against the effects of penetrating collisions at high energies (c) where the long-range form of the quadrupole interaction in equation 4.8 breaks down. BT05 [92] provides the details of why this is the case in their section 6: the limiting function 4.11 mitigates the divergence of the collision strength at high energies, but it does not completely eliminate it. As a result, the high energy behaviour of rate coefficients from [93] will be incorrect, even though they confusingly state the correct scaling of $q_{i\to j} \propto T^{-1/2}$.

Landman [95] also emulates S64 [90] with some minor modifications to the

[4]This cutoff does ensure that $\sigma_{i\to j} \propto u_p^{-2}$ as would be expected for a quadrupole order transition, but the full solution would also give the constant of proportionality in this expression.

transition probability. The intermediate energy (b) cutoff is determined by considering the transition probabilities at a particular impact parameter, b_1, for all transitions in a configuration, not just an individual transition: $\sum_j P_{ij}^{(1)}(b_1) = 1/2$. Then, $P_{ij}^{(1)}$ of the individual transition under consideration is given by,

$$P_{ij}^{(2)} = \begin{cases} P_{ij}^{(1)}(b) & \text{if } b \geq b_1, \\ 2\frac{b}{b_1}\left(1/2 - g_i\right) - \left(1/2 - 2g_i\right) & \text{if } \frac{1}{2}b_1 \leq b \leq b_1, \\ g_i & \text{if } b < \frac{1}{2}b_1, \end{cases} \tag{4.12}$$

where g_i is the ratio of the statistical weight for level i to that of the entire configuration it is a part of:

$$g_i = \frac{\omega_i}{\sum_k \omega_k}. \tag{4.13}$$

So, instead of setting $P_{ij}^{(1)}(b) = 1/2$ for $b < b_1$, it linearly varies $P_{ij}^{(1)}$ from $1/2$ at b_1 to g_i at $b_1/2$, below which it stays at g_i. This method has the apparent advantage that transitions, which are forbidden by $E2$ selection rules (and so have no transition probability at first order) but proceed through close-coupling channels, can be calculated. But this is crude, and fairly large disagreement by about a factor of three is presented in the paper for the $3s^2 3p^2\ {}^3P_{0\to1}$ transition when compared to a SC-CC calculation [96]. Moreover, implementing this type of functionality adds considerably to the complexity of the code implementation, negating some of the advantage that a SC-1 approach has through simplicity. Thus, if these types of transitions are required—an open question still—it is likely more worthwhile to go through the effort of implementing a proper SC-CC code. Apart from this assessment, there are a number of real problems with the implementation. The author notes that instead of calculating the weight and cutoff over the whole configuration, doing so over an LS term would likely be more accurate. Reciprocity will be violated here since $P_{ij}^{(1)}$ should be proportional to $1/\omega_i$ not ω_i. Above all, the author commits the same mistake as in the previous reference [93]: the high energy regime (c) is not explicitly handled, so the possibility remains that $b_1 < r_0$ will arise, yielding inaccurate results.

The work by Sahal-Bréchot [97] proceeds in a similar manner to Landman [95] but avoids some of the pitfalls. First, for the intermediate energy (b) cutoff, it

uses b_1 such that

$$P_{ij}^{(1)}(b_1) = \frac{\omega_j}{\sum_k \omega_k}, \tag{4.14}$$

where k varies over the levels of the encompassing LS term. This expression does not violate reciprocity like the preceding case, but the b_1 determined is no longer common to the set of transitions in the term. As such, it uses an average of the b_1's from the "allowed" transitions within a term and applies this to determine any transitions that only proceed through collisional coupling: ${}^3\mathrm{P}_{0\to1}$ is the recurring example. This purely close-coupled component is given by

$$\sigma_{i\to j} = \left(\frac{\omega_j}{\sum_k \omega_k}\right) \pi \bar{b}_1^2. \tag{4.15}$$

As before, the author admits this is a fairly crude estimate of these close-coupling transitions, and the overhead to implement this functionality does not appear to be worthwhile. And again, this source falls foul and neglects the high energy (c) regime, although it at least openly admits to doing so and justifies that the energies relevant to their study do not result in $\rho_1 < r_0$. Any cross sections produced in this manner will not be appropriate, in general, for producing rate coefficients because of the necessary sampling at high energies when convolving with the Maxwellian distribution. The work does go on to calculate rate coefficients, and these data should be used with caution at higher temperatures.

A series of papers by Kastner, Bhatia, and various collaborators [98–101] attempt to present an even more simplified version of the SC-1 approach than in S64; however, they make several pivotal mistakes as pointed out in a review article [102]:

> For high energies, their cross section is based on an expression given by Bahcall and Wolf (1968) which erroneously has an $E^{-1/2}$ behaviour. Since they do not consider any approximation for intermediate energies, their cross sections have an unrealistic cusp where their high and low energy approximations meet.

Although the high energy behaviour is corrected in one of the subsequent papers [99], the neglect of the intermediate energy (b) regime is a persistent feature, inevitably leading to overestimates. Therefore, this body of work does not merit

further mention.

A significant résumé and improvement of the SC-1 technique is made by Walling and Weisheit [103], henceforth WW88. Their methodology closely follows that of S64 [90], but they extend the method to $E1$ and $E3$ multipole orders, so the scope of this work is comparatively broad. They use the same $P_{ij}^{(1)}(b_1) = 1/2$ cutoff at intermediate energies but, for some reason, opt to not use symmetrised kinematic variables in the cross section expression—i.e. they do not account for the inelastic nature of the collision. This is not a fatal flaw, but it certainly impairs their methodology to some degree. On the other hand, they take the important step of fitting the high energy cutoff of bullet (c), b_0, such that the cross section obtained from equation 4.10 will asymptotically approach the infinite energy limit of a quantal calculation. In WW88, the Bethe approximation is used to obtain an EIE cross section that is then scaled by ${z_p}^2$ to obtain an estimate of the IIE cross section,[5] and it is this cross section that is applied to determine r_0 and hence b_0. Although setting r_0 to the mean atomic radius seems to have a sound physical basis, it was already noted that this prescription does not guarantee the exact high energy behaviour of the cross section, whereas this new *fitting* technique does. Of course, there is an underlying assumption being made that the infinite energy limit used in fitting is also accurate. The Bethe approximation is not exact at high energy and itself requires a cutoff: WW88 handle this by assuming the radial integrals are hydrogenic, thus obviating the troubles with the Bessel functions. So, there is undoubtedly a large degree of uncertainty for these results, likely 30% or greater. In contrast, the current implementation takes results from the Born approximation, which is exact in the infinite energy limit, and uses those in its determination of r_0, elmininating much of this uncertainty. More on this topic will follow. Independent of these deficiencies, WW88 makes an astute general observation about the importance of IIE collisions for atomic population modelling; it is concluded that a verdict on the influence of IIE upon an atom's population model must be done on a case-by-case basis. This largely echoes the pending discussion and conclusions in section 5.3.1.

Culminating the SC-1 method is the work by Burgess and Tully [92], already

[5] This scaling by ${z_p}^2$ applies directly to the cross section size, while the mass scaling discussed in section 4.1 will apply to the energy or velocity axis.

abbreviated to BT05. By all accounts, this work identifies and rectifies all of the mistakes and limitations of the previous SC-1 attempts detailed above, and so it is judged to be the most complete and accurate version of the method. As such, BT05 is used as the basis for the present implementation in this thesis. The creation of the new code, `a2iratbt`, was necessary because the one described by BT05 appears to have been lost.[6] The details of implementation will be presented in section 4.3.1, but it is helpful to summarise the primary differences with the other literature sources. Again, the reasoning and partitioning of the problem is quite similar to S64:

(a) **Low Energies**—No changes are required because $P_{ij}^{(1)}$ stays small and first-order perturbation theory holds.

(b) **Intermediate Energies**—As before, $P_{ij}^{(1)} > 1$ must be guarded against in this regime for any trajectory so that charge conservation is maintained. BT05 uses a more flexible and arguably more accurate manner of limiting $P_{ij}^{(1)}$ than S64, similar in spirit to reference [93]. Instead of the simplistic $P_{ij}^{(1)}(b_1) = 1/2$, a *modified* transition probability is given by

$$P_{ij}^{(2)} = P_{\mathrm{ub}}\phi\left(P_{ij}^{(1)}/P_{\mathrm{ub}}\right), \tag{4.16}$$

where ϕ is some function such that $\phi(x) \approx x$ as $x \to 0$, and $\phi(x) \leq 1 \,\forall\, x \geq 0$, ensuring $P_{ij}^{(2)}$ never exceeds a specified upper bound, P_{ub}. Here, x is a dummy variable. Some options for ϕ and P_{ub} are given in BT05 section 5, all of which maintain symmetry reciprocity of the transition probability and collision strength, unlike [90, 95]. One option results in $P_{ij}^{(2)} \to \omega_j/(\omega_i + \omega_j)$ when $P_{ij}^{(1)}$ becomes large, which is what one would expect for a strong coupling collision for the strict two-state problem, absent from collisional coupling to any other states. This is better than S64, but it does not go as far as reference [97] which uses the weights for the entire encompassing LS term, thus allowing it to calculate quantities for transitions that only proceed through close coupling. However, as already argued above, the inaccuracy of the resulting cross sections along with the extra effort required

[6] The paper claims the code is accessible through the relevant IOP website, but there are no attached files. Moreover, the authors themselves are no longer capable of retrieving these resources.

for implementation leads to the conclusion that an SC-CC method should be implemented if these transitions are required. Consequently, it is proposed that the present implementation is the best compromise for the SC-1 method.

(c) **High Energies**—BT05 determines the cutoff to prevent penetrating trajectories in a manner similar to WW88: the cutoff r_0 is determined such that the collision strength matches the Born approximation asymptotically at infinite energy, ${\Omega_{ij}}^{(\mathrm{inf})}$. The details are provided around equations (16) and (17) of BT05 [92], followed by explanations of why other implementations in the literature fail. Thus, the correct high energy behaviour of the IIE collision strength and cross section is guaranteed to a greater degree for BT05 and the present implementation than in WW88, assuming ${\Omega_{ij}}^{(\mathrm{inf})}$ from the Born approximation is of a better quality than from the Bethe approximation, which should always be the case. Moreover, implementations like S64 and a number of the SC-CC ones in what follows, although they get the functional form of the high energy behaviour correct, do not ensure that the collision strength will approach ${\Omega_{ij}}^{(\mathrm{inf})}$—or equivalently, that the cross section falls off with the correct constant of proportionality, $\sigma_{i\to j} = Cu_p^{-2}$. Overall, this technique provides a reliable anchor rooted in quantum mechanics in the $\eta \ll 1$ limit where the semi-classical assumption is no longer valid, quite apart from the failings of the long-range quadrupole interaction term for penetrating collisions. Thus, this *fitting* to ${\Omega_{ij}}^{(\mathrm{inf})}$ should be seen as more of a necessity rather than some improvement of the methodology.

4.2.2 SC-CC Methods

The SC-CC method, like its SC-1 sibling, makes the same assumption of classical hyperbolic trajectories for the projectile: it assumes there is no interaction between the projectile wave function and that of the atomic system, meaning the projectile can be treated as a structureless charged object. Correspondingly, it has the same domain of applicability defined by $\eta >> 1$ from equation 4.6. However, instead of invoking first-order perturbation theory to calculate transition probabilities, this method solves the time-dependent Schrödinger equation

directly through appropriate manipulation and taking the inner product with the final state $\langle J'M'|$. This results in a coupled set of differential equations:

$$\dot{a}_{J'M'}(t) = i \sum_{J,M} a_{JM}(t) \langle J'M' | H_{E2}(t) | JM \rangle e^{-i(E_J - E_{J'})t}, \tag{4.17}$$

where $H_{E2}(t)$ is the electric quadrupole interaction. The form of this interaction depends upon the approximations made, if any, and so it is specific to the particular implementation; however, the most common approach in the literature is to use the long-range quadrupole interaction term as specified by equation 4.8 in the context of the SC-1 method. Substituting this assumption, the matrix element in equation 4.17 will abide by the proportionality,

$$\langle J'M' | H_{E2}(t) | JM \rangle \propto -\frac{\langle r^2 \rangle}{r_p^3}, \tag{4.18}$$

which again is only valid for $r_p > r$, meaning some form of cutoff must be enforced. The choice of interaction term and any cutoffs in relation to it is one of the open questions of this literature review, and it will be discussed in relation to each source given below. A useful summary of the interaction terms in the literature are given in table 4.1. Solving equation 4.17 yields the transition probabilities, $P_{JM \to J'M'} = |a_{J'M'}(t = \infty)|^2$, which can be substituted into the impact parameter expression for the cross section, equation 4.7, as with the SC-1 method. The primary advantages of this method over SC-1 are twofold. At intermediate energies, the transition probabilities calculated here will not suffer from the breakdown of first-order perturbation theory. Also, transition probabilities for collisions that proceed exclusively through close coupling can be calculated depending on the CC expansion used, whereas by default these are not handled by SC-1 methods—although there are rudimentary techniques for estimating their magnitude in section 4.2.1. The effect of these advantages over the SC-1 method will be assessed in section 4.2.4.

Like the SC-1 method, the original application of an SC-CC approach was for nuclear excitation [104], henceforth WD66, as seen in figure 4.3. A number of works dealing with atomic excitation draw directly or indirectly from the corresponding code. It uses the long-range form of the $E2$ interaction term (equa-

tion 4.18), but because penetrating trajectories are unimportant in the parameter space of nuclear excitation, they do not consider how to appropriately guard against the collapse of this term. Also, the kinematic variables and equations are symmetrised, but this involves a more complex technique because a trajectory no longer corresponds to a single quantum transition. The loss of energy associated with the inelastic excitation process has the greatest effect upon the cross section at low energies, exactly where this quantity is highly suppressed by the adiabaticity—see section 4.4.1.1. As a result, this symmetrisation step is quite often neglected in the SC-CC literature, although for the best accuracy it should be included.

The earliest application of the SC-CC method to atomic excitation was made by Bahcall and Wolf [105]. The implementation is the same as WD66 [104], but symmetrisation is neglected. Moreover, the issue of penetrating collisions at high energies is deferred because the authors say such energies are not relevant to their study. Although this may be the case, it is unsafe to calculate rate coefficients from cross sections or collision strengths that are limited in this manner. Furthermore, the authors attempt to mitigate this shortcoming by applying a *fitting* formula to a few data points generated from the explicit solution of equation 4.17, thus allowing them to extend their cross sections to higher energy. Unfortunately, they derive the incorrect asymptotic for the cross section in their *fitting* formula: the cross section should go as ε_i^{-1} at high energy but their formula yields $\varepsilon_i^{-1/2}$. This source will be neglected in subsequent comparisons for these reasons.

Another early and much cited implementation is Masnou-Seeuws and McCarroll [106]. The authors make the important observation that the problem is most accurately handled using a molecular basis to calculate the matrix elements, but then they revert to the long-range, atomic form of the $E2$ interaction (equation 4.18) for their actual calculations. This molecular representation is adopted by some of the quantal, close-coupled (Q-CC) sources in the following section 4.2.3. Similar to Bahcall and Wolf [105], the authors claim that the problem they address does not go to sufficiently high energies for penetration to be an issue and, therefore, no cutoff is imposed to mitigate the breakdown of the long-range interaction term. Although the avoidance of penetrating trajectories does not invalidate these results, this practice is unsound for the purposes of

this thesis where a broad temperature and energy range for the collision data is sought. However, comparisons with this work are still useful. There is a sign error in the formation of the matrix elements for the $p^2\ ^3P$ transitions, which was caught by reference [107]. Therefore, only the sp ^2P results are appropriate for comparison.

A foundational SC-CC source is Reid and Schwarz [108], henceforth RS69, from which a myriad of other implementations derive. Its implementation largely follows that of WB66 [104], but it is the first SC-CC source to implement a cutoff at high energies. This is achieved by setting the interaction term (equation 4.18) to a constant for $r_p \lesssim \langle r^2 \rangle^{1/2}$. Although this is slightly different than the high energy cutoffs for the SC-1 methods, it achieves largely the same effect. In addition, this source opts against symmetrising the differential equations and variables, which should be a minor error but a deficiency nonetheless.

The following works derive directly from the RS69 implementation [108] but add minor modifications that are now listed. References [109–112] alter the interaction matrix element by replacing the RHS of equation 4.18 with $\left\langle \min\left(r, r_p\right)^2 / \max\left(r, r_p\right)^3 \right\rangle$. The functions "min" and "max" return the minimum and maximum of their arguments, respectively. This expectation value is calculated in an analytic but approximate manner by using scaled hydrogenic orbitals in the effective charge of the ion. Moreover, this form of the matrix element should ensure a physically meaningful form of the interaction even for trajectories that penetrate the ion—i.e. $r_p < r$. However, one must keep in mind that this is an approximation, so the correct high energy limit is not guaranteed, unlike our SC-1 implementation. These sources claim to achieve 10% accuracy in the worst-case scenario based on the findings from references [113, 114], which will be explained fully in section 4.2.4. Briefly, there should be a negligible difference between using a SC-CC versus Q-CC approach, and the neglect of additional contributions to the interaction term like polarisation should cause at most 10% variation below the high energy regime. Reference [115] makes this SC-CC implementation symmetrised, but this is a more difficult task than in WB66 [104] because of the new form of the interaction term just described. It is found that the effect of symmetrisation is at most 9% at the lowest energy calculated in this study, and it diminishes quickly as the energy increases. Then, references [116–120] pur-

port to further enhance this SC-CC implementation by mimicking the inclusion of a polarisation potential from the molecular Q-CC approaches. This has the effect of introducing virtual dipole-coupling to accessible states in the CC expansion, and the authors present results that show a consequent 60% decrease of the cross sections in the peak region compared to previous iterations in this RS69 heritage. However, this is in direct contradiction to the conclusions above about an estimated 10% error for these previous iterations. As will become clear through the remainder of this literature review, it is strongly suspected an error in implementation has been made while introducing this polarisation potential.

Landman and his collaborators provide the final significant SC-CC method that merits discussion in this review: [107, 121–124]. This implementation is effectively a copy of WB66 [104], but unlike a number of its contemporaries, it does modify this approach to handle the issue of penetrating collisions at high energies. In the same fashion as S64 [90], it sets the transition probability to a constant for impact parameters below a certain cutoff defined by a dimension of the atom. More technically, $P_{ij}^{(1)}(b) = P_{ij}^{(1)}(b_1)$ for $b \leq b_1$, and b_1 is defined by $\rho(b_1) = r_0$. For these sources, r_0 is set to the expectation value of the atomic radial coordinate, $\langle r \rangle$, obtained from wave functions in the literature. Once again, one should recall that this strategy does not guarantee the correct high energy limit of the collision strength, but it does guard against incorrect limiting behaviour. A distinguishing feature of this work is that intermediate-coupled eigenstates are used in forming the CC expansion, whereas all of the previous SC-CC sources use LSJ-coupled eigenstates. This lifts the restriction of strict LS selection rules for a number of transitions, and so spin-changing, *inter*-multiplet transitions can be calculated. However, these transitions will generally be low in magnitude, and it is already known that these types of transitions—between terms—are not favoured by IIE. Rather, it is the effect of this additional close-coupling upon the *intra*-multiplet transitions that is more significant, and variation of between 15–20% is claimed [107, 124].

4.2.3 Fully Quantal Treatments

Moving to the quantal, close-coupled (Q-CC) class of methods, the assumption of classical trajectories is no longer made as with the semi-classical treatments, so

the complete wave function of the target atom and projectile must be handled in the time-dependent Schrödinger equation. This results in a more complex set of coupled, second-order differential equations that are numerically difficult to solve because of the highly oscillatory nature of the radial equations: small step sizes to resolve these oscillations translate to more points for evaluation. That there are few Q-CC calculations for IIE in the literature is less so because of the computational expense and more so that this extra expense does not yield significant gains in accuracy over the semi-classical counterparts. This point will be fully justified in the next section. Q-CC methods have the distinct advantage that one no longer needs to worry about whether η from equation 4.6 is of an appropriate value for the problem; however, this does not obviate all of the concerns for the high energy regime because part of this is contingent on the interaction term used. It so happens that the Q-CC implementations in the literature have used relatively sophisticated forms for the interaction potential, and so short-range effects that become important at high energies are handled accurately. But this is a product of decisions made by authors in the literature rather than an inherent feature of the Q-CC method. The presentation of Q-CC approaches is necessary because they offer the most accurate theoretical results and so are essential for benchmarking more approximate methods. Two classes of Q-CC methods in the literature are now briefly described.

The first application of a Q-CC method was by Faucher in [125], henceforth F75, for Fe^{12+}. It relies on an atomic basis set that explicitly considers the Coulomb nature of the relative radial motion of the projectile and target ions, keeping the problem fairly similar to the SC-CC formulation. However, F75 draws attention to the substantial computational difference between the two methods. It selects an interaction term given by the expectation value of $\min(r, r_p)^2 / \max(r, r_p)^3$ as in reference [109, 110] but, in this case, no approximate hydrogenic forms are used to simplify the expression and the expectation value is calculated exactly. As mentioned above, this form of the interaction potential will ensure there are no singularities for small values of r_p.

Second, Heil et al. [114, 126] present a version of Q-CC that uses a self-consistent field, quasi-molecular basis set, meaning the projectile and atomic target are treated as a single molecular entity—e.g. the proton impact of O^{3+} is

represented by the OH^{2+} molecule. The interaction energy is quantified by two adiabatic potentials for the molecular states, $^2\Pi$ and $^2\Sigma$, which is the most complete and accurate representation to date. Not only is the short-range interaction handled correctly, but the long-range asymptotic expansion of the interaction produces a polarisation term that follows the usual quadrupole term:

$$V_\Sigma - V_\Pi \sim -\frac{3\langle r^2\rangle}{5r_p^3} + \frac{\alpha_\Pi - \alpha_\Sigma}{2r_p^4} + \ldots, \tag{4.19}$$

where α_Π and α_Σ are the perpendicular and parallel polarisabilities of the ion. The finding by Heil et al. most relevant to other calculations, quantal or otherwise, is that this polarisation term can have a significant effect on the final IIE cross sections, estimated at about 10% variation below the high energy regime. This will be true for the F75 [125] work, which only includes the electric quadrupole term of the Coulomb interaction.

4.2.4 Comparative Analysis

Having briefly described the major contributions to the SC-1, SC-CC, and Q-CC literature, it is now possible to answer the questions posed at the beginning of this review. First, is a fully quantal (Q-CC) treatment required for calculating IIE collision data? In fact, this question is directly addressed in reference [113], which compares the Q-CC approach of F75 [125] with the SC-CC approach of Landman [107, 121]. Therein, it is concluded that there is no difference between the quantal and semi-classical treatment of IIE for Fe^{12+}, as long as the same interaction term is used in both treatments. This was determined by using the same long-range, electric quadrupole interaction in the Q-CC calculation as in the SC-CC calculation, resulting in nearly identical transition probabilities—and hence cross sections—for the two. The applicability of this conclusion can safely be extended to ions of similar and higher charge because η of equation 4.6 will have similar values, but as with so many phenomenon in atomic physics, it cannot be guaranteed for near-neutral systems. Also, the Q-CC results of Heil et al. [114, 126] support this conclusion. The Q-CC cross sections for Al-like Fe^{13+} (figures 4.5 and 4.6) and B-like O^{3+} (figure 4.7) show good agreement with the SC-1 and SC-CC contemporaries. Only the *foster1997* [118] calculation of

O^{3+}, a RS69 descendent, uses the same interaction potential as the Q-CC calculations, explaining the near perfect agreement in figure 4.7. Hence, the variation between the Q-CC *heil1983* result for Fe^{13+} and the semi-classical ones is due to differences in the interaction potential and not any discrepancy between a semi-classical and quantal treatments. Reference [102] verifies this by recalculating the SC-CC *masnou-seeuws1972* [106] result using the same atomic data as for the *heil1983* [114] calculation. Following this critical step, the Q-CC *heil1983* calculation, made using the long-range quadrupole coupling, displays excellent agreement ($< 5\%$) with the SC-CC result.

Therefore, it can be confidently resolved that the hypothesis and supporting theoretical reasoning from the beginning of section 4.2 have been vindicated: it is demonstrably true that ion projectiles are well described by a classical hyperbolic orbit, and this assumption can be applied to the scattering problem with negligible loss of accuracy to the result. Furthermore, it should be noted that the scarcity of Q-CC results in the literature, along with the significant computational expense of this type of calculation, makes it a wholly inadequate method for the baseline objective currently sought. A semi-classical approach will more than suffice.

In the above conclusions, it was a necessary presupposition that the same interaction potential be used when comparing calculations, leading logically to the second question: what form of the interaction potential is appropriate for baseline data? Since the long-range, electric quadrupole term of the Coulomb interaction is most common in the literature—and used in the present implementation—this question reduces to answering whether this approximate form of the interaction potential is sufficient for a baseline calculation. The crux of this question is identified by the review in reference [102], which points to an apparent contradiction between the conclusions of Heil et al. [114] and Faucher and Landman [113] in relation to the effects of different interaction potentials. However, [102] does not resolve the ostensible conflict, and providing the correct explanation has the added benefit of answering the question at hand. Table 4.1 outlines the distinguishing features of the interaction potentials used by the calculations under discussion, and the indexing established in the first column is used for shorthand in the text to follow. The primary conclusions from the two papers under examination are

now summarised.

Faucher and Landman [113]:

1. There is no difference between a quantal and semi-classical, close-coupled approach for the case of Fe^{12+} when both approaches use the same interaction term.

2. The cause of the difference between calculations B and C (table 4.1) thus resides in the interaction term. The long-range quadrupole term used in B becomes inaccurate at small impact parameters when compared to the complete electrostatic quadrupole term used in C, and this manifests at "high" energies ($\gtrapprox$ 50 Ryd $\approx$ 680 eV), as would be expected. However, the magnitude of the relative differences are quite minor, as can be observed in figure 4.4 (figure 1 of original reference [113]).

Heil et al. [114]:

1. The neglect of short-range components of the interaction term has little impact except at 'high energies'—i.e. the long-range form is quite accurate over most of the energy range, but 'high energies' is never explicitly defined.

2. Rather, the polarisation component of the interaction term constitutes the larger correction over the more important *intermediate* part of the energy range (for this ion, Fe^{13+}), yielding $\sim 10\%$ variation.

Table 4.1: Feature comparison of relevant close-coupled, IIE calculations.

Index	Description	Quantal (Q) or Semiclassical (SC)	Interaction Term	Penetrating Collisions
A	Masnou-Seeuws and McCarroll [106]	SC	Derived from molecular potential but with only the long-range quadrupole component: $V_\Sigma = -\frac{2}{5}\frac{\langle r_i^2\rangle}{R^3}$ and $V_\Pi = \frac{1}{5}\frac{\langle r_i^2\rangle}{R^3}$, where R is the projectile radial coordinate and r_i is the target electron radial coordinate	Penetrating collisions in the high energy regime will not be handled correctly due to the approximation of the long-range interaction term
B	Landman [121]	SC	Long-range, quadrupole: $V_2(r, r_i) = \frac{4\pi}{5}\sum_{m=-2}^{2}\frac{r_i^2}{r^3}Y_{2m}(\hat{r})Y_{2m}(\hat{r}_i)$	A cutoff in the high energy regime ensures the correct functional form of the cross-section and ensures no violations by the interaction term
C	Faucher [125]	Q	Coupling potential given as: $V_{\gamma_i\gamma_j}(r) = Y_0(r)\delta_{ij} + \nu_{ij}\mathscr{Y}_2(r)$, r is the projectile radial coordinate, but unfortunately the exact forms of Y_0 and $\mathscr{Y}_2$ are in Faucher (1974), a thesis difficult to retrieve. Reid [102] claims that this potential reduces to: $\langle r_<^2/r_>^3\rangle$	Regardless of the accuracy of Reid's claims, it appears as though this interaction term should be valid for small r corresponding to penetration of the electron cloud; however, the term appears to only be the quadrupole component.
D	Faucher [125]	Q	Long-range, quadrupole: $V_2(r, r_i) = \frac{4\pi}{5}\sum_{m=-2}^{2}\frac{r_i^2}{r^3}Y_{2m}(\hat{r})Y_{2m}(\hat{r}_i)$	Unclear whether a cutoff in the high energy regime was used, but it can be assumed given good agreement with B.
E	Heil *et al.*, fig. 1, curve I [114]	Q	'Full interaction' in a molecular basis representation with the Lippman-Schwinger equation (mathematical representation outside current scope)	Although never shown explicitly, this interaction is claimed to give appropriate treatment of penetrating collisions. These should be the most accurate calculations of all those considered.
F	Heil *et al.*, mentioned in text [114]	Q	Long-range (asymptotic) form with quadrupole and polarisation components (molecular basis still): $\epsilon_\Sigma(R) = \frac{13}{R} - \frac{q}{R^3} - \frac{\alpha_\Sigma}{2R^4}$ and $\epsilon_\Pi(R) = \frac{13}{R} + \frac{q}{2R^3} - \frac{\alpha_\Pi}{2R^4}$	As these are long-range (asymptotic) forms, penetrating collisions will not be treated correctly; no indication is given whether a cutoff is attempted (assumed not).
G	Heil *et al.*, fig. 1, curve II [114]	Q	Long-range (asymptotic) form with quadrupole components only (molecular basis still): $\epsilon_\Sigma(R) = \frac{13}{R} - \frac{q}{R^3}$ and $\epsilon_\Pi(R) = \frac{13}{R} + \frac{q}{2R^3}$	As these are long-range (asymptotic) forms, penetrating collisions will not be treated correctly; no indication is given whether a cutoff is attempted (assumed not).

The potential contradiction that Reid [102] identifies is between the second items above. Although Faucher and Landman [113] admit that the deviations only become important at *high* energies, Reid seems to think that the graphs show differences at *intermediate* energies: "Faucher and Landman (1977)... inferred that the cross sections are altered even at intermediate energies when the long-range quadrupole interaction is modified by use of the expectation value of $r_<^2 r_>^{-3}$" and "[i]n the cross sections, these differences have a *significant* effect for energies in and above the region where the cross sections are maximum" (emphasis added). If these assertions are true, then indeed they would be in contradiction to the conclusion of Heil et al. [114] that it is the inclusion of the polarisation term and not the complete consideration of the Coulomb interaction at short-range that leads to the most variation at intermediate energies. However, the confusion is caused by the lack of a clear definition of the energy domains to which *intermediate* and *high* refer.

Consulting figure 4.4, it is true that the larger discrepancy for transition $J : 0 \rightarrow 2$ does occur around the peak of the cross-section. It has been noted multiple times in the literature that the peaks of cross-sections tend to lie in the intermediate energy range defined by S64 [90] in section 4.2.1, explaining why Reid claims that the results in figure 4.4 support the conclusion that penetrating collisions can influence cross-sections even in the intermediate energy range. Yet, where the intermediate energy range is actually located requires further scrutiny. Recall that the definition of the high energy regime in S64 is simply where $\rho(b_1) < r_0$ occurs, but the b_1 parameter only applies to SC-1 calculations, and it is a SC-CC calculation (B) that is being considered here. Fundamentally, the onset of the high energy regime for an SC-CC calculation is different than that for an SC-1 one: a degree of agreement and consistency between the two can be expected, but Reid's blanket application of S64's definition is technically incorrect. Rather, a universal definition of the high energy regime is where the cross section obtained using a long-range quadrupole potential begins to deviate from the result obtained with the complete quadrupole potential, indicating that short-range contributions within the physical extent of the atom are no longer negligible. So, the deviation of the cross sections in figure 4.4 that starts at approximately 50 Ryd is itself the definition of the onset of the high energy regime, since the only material difference

between the two curve styles is the use of the long-range versus the complete form of the quadrupole interaction term (B versus C).

The transition probabilities in figure 3 of Faucher and Landman [113] provide further support. Inspecting curve (3) in figure 3b [113], corresponding to $E = 50$ Ryd and thus nearly the peak of the $J : 0 \rightarrow 2$ transition, one can see that the transition probabilities due to calculations B and C begin to deviate substantially at an impact parameter of approximately $0.75a_0$, which yields a distance of closest approach $\rho \approx 1.03a_0$, corresponding in turn to a penetration of about 5% of the ions charge density distribution. For its high energy cutoff, the SC-CC calculation B uses $r_0 = \langle r_{3\mathrm{p}} \rangle = 0.706a_0$, but Faucher and Landman [113] comment that this is likely an underestimate exactly because the transition probabilities begin to differ at ρ values larger than this. Once again, therefore, the issue of the best high energy cutoff has been raised. Here, the authors are suggesting that the use of an average radial coordinate is problematic. It seems to underestimate the radial cutoff, and as a solution, these authors propose a cutoff related to the charge density distribution. For instance, the cutoff could be set to the atomic radius at which 90% of the atomic charge distribution is within the associated sphere defined by that radius. Radii that capture a high percentage of the charge distribution tend to be larger than the average atomic radius. Larger cutoffs mean that trajectories will penetrate the atom at lower energies, consistent with the high energy regime for this study occurring at a lower energy than expected. Of course, the strategy of matching the asymptotic limit of the collision strength to the Born approximation avoids all of this uncertainty.

There are some further holes in Reid's assessment that are worthy of comment. First, no mention is made of the fact that different ionic systems are being compared, and that the energy regimes for Fe^{12+} will differ from those of Fe^{13+}, the ion addressed by Heil et al. [114]. Some sense of this can be gained by noting the difference between the onset of the high energy regime under the S64 prescription: ~ 7.5 keV for Fe^{13+} and ~ 2.0 keV for Fe^{12+}. Although these are certainly overestimates in light of the comments above, it should still hold that the "true" high energy regime of Fe^{12+} lies well below that of Fe^{13+}. This largely explains why the peaks of the cross sections for Fe^{13+} in figure 1 of Heil et al. [114] are far removed from the onset of the high energy regime while those of Fe^{12+} in fig-

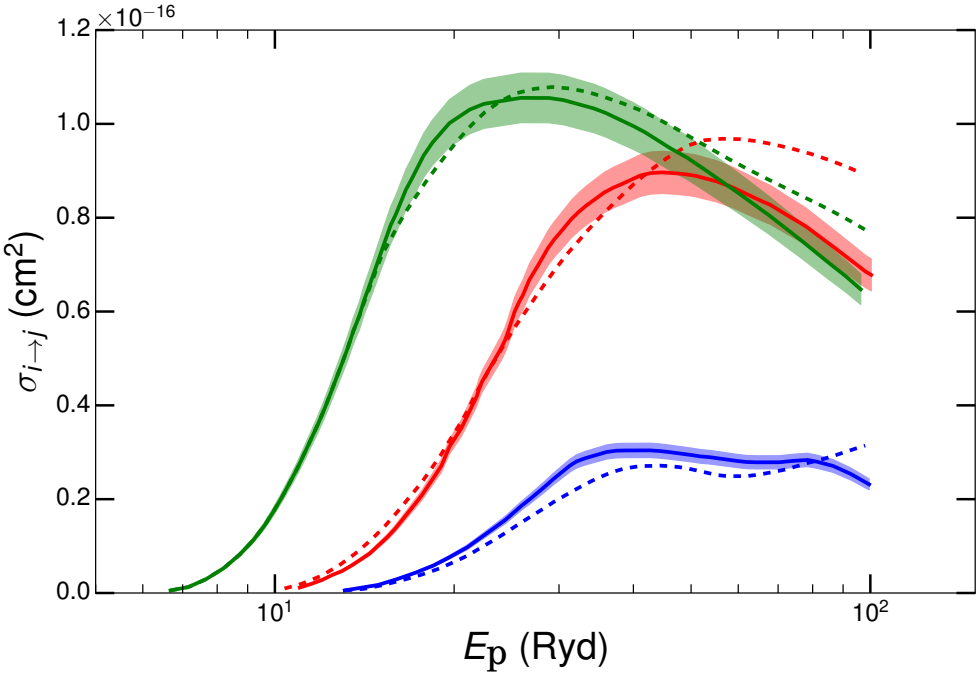

Figure 4.4: Proton-impact excitation of Si-like Fe^{12+}. The dashed lines are the SC-CC result from Landman [121], B in table 4.1. The solid lines are the Q-CC result from Faucher [125], C in table 4.1, and the semi-transparent regions surrounding these lines represent a 5% error. All transitions are within the ^{3}P term. In $J \to J'$ notation, green is $1 \to 2$; red is $0 \to 2$; and blue is $0 \to 1$, which is forbidden under $E2$ selection rules.

ure 4.4 of this thesis are not. Second, Reid makes no mention of the fact that Heil et al. [114] employs the conclusions of Faucher and Landman [113] to reinforce their own analysis. Both papers agree on the conclusion that the asymptotic (i.e. long-range) form of the interaction potential does not significantly compromise the scattering problem until *high* energies—with all of the antecedent caveats that descriptor entails. Heil et al. [114] can then freely make the assertion that polarisation is the largest correction at *intermediate* energies without any possibility of contradiction.

Thus, Reid's confusion about the validity of the long-range potential at intermediate energies has been resolved, and along the way an important point was made clear; the inaccuracies of the long-range interaction potential will only become significant at high energies, but this high energy regime can occur near the peaks of excitation cross sections. This conclusion bears weight because many authors in the literature have dismissed the need to account for penetrating orbitals based on average atomic radii that likely underestimate the proper cutoff.

As such, the problem of correctly dealing with the high energy cutoff is shifted to lower energy regimes than might be expected, making it pivotal for getting the cross section right at its most influential values. This bolsters our strategy of matching to the exact Born approximation in the infinite energy limit, avoiding any of the deficiencies of the long-range potential in this regime while still permitting its general application to reap the associated computational savings.

On the other hand, the effect of the polarisation interaction potential will occur across the intermediate energy range, and it should account for less than 10% variation based on the cases observed in the work of Heil et al., although this will depend on the specific application. For the objective of baseline IIE data, such a level of error is acceptable, especially since implementing a polarisation correction in the current framework is nontrivial. However, the most recent descendants of the RS69 SC-CC method [116–120] claim that the inclusion of a polarisation term can cause up to a 60% reduction of the cross section near its peak compared to previous versions of their SC-CC method. This claim must be addressed because it jeopardises the simplifying assumption that the polarisation term can be neglected. Only the results of Heil et al. [114, 126] also include the effects of polarisation via their molecular potential, so these two sources offer the sole points of comparison and validation. Luckily, Al-like Fe^{13+} is one of the most studied ions in the IIE literature, so there are many calculations with which to juxtapose. Figure 4.5 displays the cross section for Heil et al. [114] (*heil1983*) alongside a selection of others from the literature. None of the other calculations include the polarisation term, and they represent a mix of SC-1 and SC-CC methods, which confounds the analysis. Although some of the SC-1 calculations differ by around 50% (some of our own `a2iratbt` calculations along with *bely1970* and *sahal-brechot1974*), most of this variation is due to differences in the atomic data—more details to follow. Also, there is the as yet unquantified factor of CC effects; therefore, it is really comparison with the SC-CC calculations in this graph that should be considered—*masnou-seeuws1972* and *landman1973*. Both of these results exhibit only about 20% difference with the *heil1983* cross section, and some of the variation is attributable to differences in atomic data. However, the point is that nowhere near a 60% variation is observed like that claimed by the RS69 descendants. The results for B-like O^{3+} in figure 4.7 tell a

similar story. A 25% reduction of the SC-1 `a2iratbt` result is seen relative to the other two calculations that include polarisation effects. Again, some of this derives from differences in the atomic data, and interestingly, the SC-1 result from WW88 [103] achieves incredible agreement ($< 5\%$) with the more sophisticated calculations because it uses, purportedly, the same atomic structure data. The principal takeaway is that nothing close to a 60% reduction is observed. Consequently, this suggests there is an error in the RS69 descendants, so it is bizarre that the *foster1997* cross section in figure 4.7 agrees well with the *heil1982* one. If a calculation erroneously claims that 60% variation is observed because of the inclusion of the polarisation term, then it would not be expected that this same calculation then achieves good agreement with another similar calculation that also includes the polarisation term but does not make claims of 60% variation. In the absence of further cases for testing, this must be left as an open problem, but there is undoubtedly great uncertainty surrounding the claim of 60% reduction caused by polarisation. Hence, the neglect of polarisation in the present implementation is confidently retained. In summary, it is completely appropriate to use the long-range electric quadrupole interaction in IIE baseline calculations.

It remains to pose the third question of this review: is a CC method required for IIE baseline data, or will first-order perturbation theory suffice? In this case, the answer is less straightforward because the degree of collisional coupling is highly dependent upon the target system and its atomic structure. Broadly speaking, the effect of close coupling is to reduce the cross section of any transitions allowed at first-order and increase any that are forbidden by selection rules, assuming the lower level is collisionally coupled to at least some other states in the CC expansion. This coupling is much less important in a two-state doublet term, like the ^{2}P inspected above, which is usually quite isolated from other states, whereas it will be more noticeable in a three-state triplet like ^{3}P where the $J : 0 \rightarrow 1$ transition proceeds exclusively through close coupling. So, the two-state assumption of first-order perturbation theory unsurprisingly applies better to two-state doublets versus three-state triplets. However, it is not possible to say anything quantitative without recourse to specific examples. References presenting SC-CC methods are quick to dismiss the validity of the SC-1 method, saying it is wholly inadequate at intermediate energies where first-order pertur-

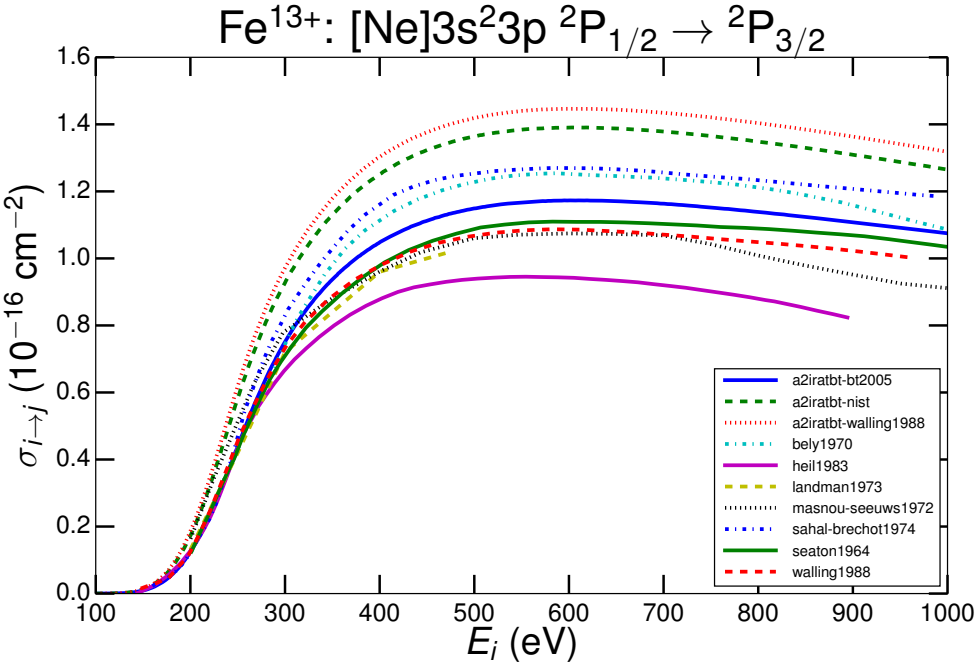

Figure 4.5: Proton-impact excitation of the $3s^2 3p\ ^2P_{1/2} \rightarrow\ ^2P_{1/2}$ transition in Al-like Fe^{13+}. The legend gives the line styles for the following sources. Those prefixed with *a2iratbt* belong to the present ADAS baseline implementation of the SC-1 `a2iratbt` code but with different atomic data: suffix *bt2005* indicates use of the atomic data from BT05 [92], *nist* from NIST [127], and *walling1988* from WW88 [103]. The other curves are from the literature and are described in the text: *bely1970* [93], *heil1983* [114], landman1973 [95], *masnou-seeuws1972* [106], *sahal-brechot1974* [97], *seaton1964* = S64 [90], *walling1988* = WW88 [103].

bation breaks down, but as will be seen, they often go on to show comparisons with SC-1 calculations that agree quite well. Of course, they are stating nothing that is not already known to the producers of the SC-1 calculations: *unmodified* first-order perturbation theory is wholly inadequate, but the point missed is that *modified* versions of SC-1 approaches fare remarkably well if the modifications are grounded in physical justification. By inspecting a variety of comparisons in the literature, it is possible to make a more informed conclusion based on inference.

Again, the example of Al-like Fe^{13+} in figure 4.5 is instructive because so many calculations from different methods exist. It is now analysed from the perspective of contrasting SC-CC and SC-1 methods. Before proceeding, it is necessary to account for the variation of the input atomic structure data. In particular, the discrepancy between the *walling1988* and *a2iratbt-walling1998* curves is unsettling because of the similarity of the underlying methods. WW88 uses $S_{ij}{}^{(2)} = 0.243$ and cites [128] for the wave functions that produce this value,

but BT05 also claims to use the wave functions of [128] and instead arrives at ${S_{ij}}^{(2)} = 0.1619$. S64 uses a similar value of ${S_{ij}}^{(2)} = 0.162$ derived from slightly different wave functions. It is believed that WW88 has incorrectly reported its ${S_{ij}}^{(2)}$ value because upon using ${S_{ij}}^{(2)} = 0.1619$ with the `a2iratbt` code and settings to match the WW88 cutoffs (*a2iratbt-walling1988-3*), the result perfectly agrees with the WW88 (*walling1988*) cross section in figure 4.6. However, there is a deeper issue that the `a2iratbt` calculation with the NIST line strength, ${S_{ij}}^{(2)} = 0.21995$, results in the curve that is farthest from the Q-CC result of Heil et al. (*heil1983*). Similar to the discrepancy with WW88, the majority of this gap can be attributed to differences in the atomic data because *heil1983* uses the wave functions of [128] that produce ${S_{ij}}^{(2)} = 0.1619$. Upon using this value, the `a2iratbt` calculation falls to the *a2iratbt-bt2005* curve in figure 4.5, agreeing much better with the *heil1983* result. Now the question becomes which ${S_{ij}}^{(2)}$ value is correct? Ultimately, the reason for this discrepancy must be resolved by atomic structure physicists, but the NIST value [129] has been independently verified by an experimental measurement [130] and a separate GRASP^0 calculation [131]. Therefore, ${S_{ij}}^{(2)} = 0.21995$ should be accepted as the definitive value for this transition in Fe^{13+}.

With the atomic data input now a controlled variable, it is possible to assess the differences between the SC-CC and SC-1 attempts in figure 4.5. The SC-1 results, *seaton1964* and *walling1988*, achieve remarkable agreement ($< 5\%$) with the two SC-CC results, *landman1973* and *masnou-seeuws1972*, across most of the energy range, but the *masnou-seeuws1972* curve dips at higher energies with an incorrect-looking falloff. It is suspected this is because of the use of a long-range potential without a proper cutoff. The SC-1 result from the new `a2iratbt` code with similar atomic data to the other results (*a2iratbt-bt2005*) achieves slightly less good agreement ($< 10\%$) arising from the difference in how $P_{ij}^{(1)}$ is limited: *seaton1964* and *walling1988* use the cutoff described for S64 in section 4.2.1 while *a2iratbt-bt2005* uses that from BT05 with $\phi(x) = \tan(2x)/2$. Further discussion on how these limiting strategies affect the collision data is contained in section 4.4.1.4. Overall, because such good agreement is observed between these SC-1 and SC-CC results, it must be concluded that the effect of close coupling is fairly minor in this case.

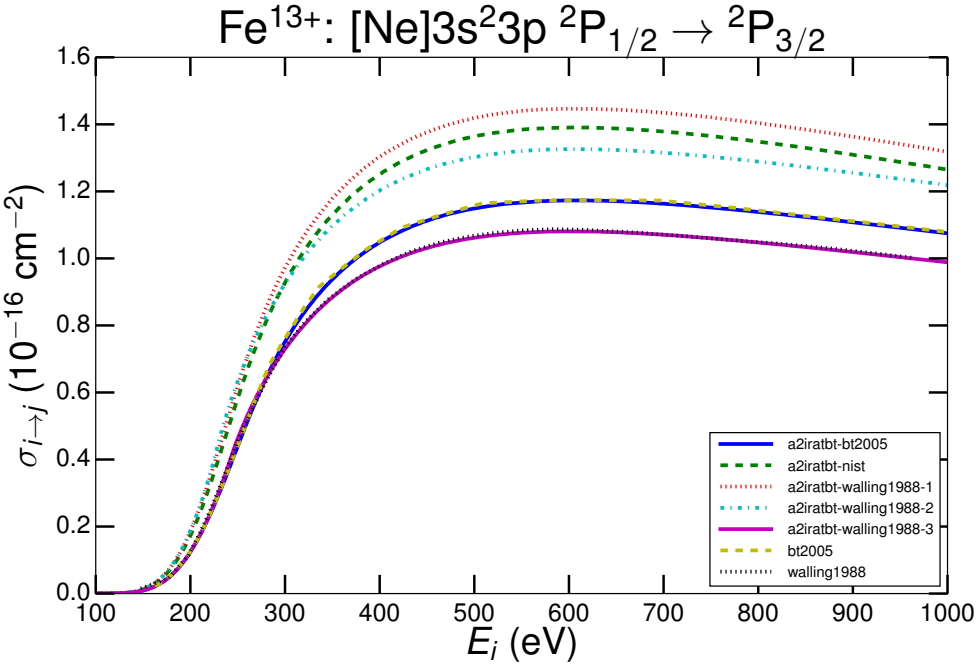

Figure 4.6: Proton-impact excitation of Al-like Fe^{13+} as in figure 4.5 but with aligned atomic data. Legend entries prefixed with *a2iratbt* belong to the present ADAS baseline implementation of the SC-1 `a2iratbt` code but with different atomic data: suffix *walling1988-1* indicates use of the atomic data from WW88 [103], *walling1988-2* also from WW88 but with the cutoff and limiting function to match WW88, *walling1988-3* from BT05 [92] and with the cutoff and limiting function to match WW88. The literature sources *bt2005* and *walling1988* are the same as in figure 4.5.

Next, consider the example of B-like O^{3+} in figure 4.7, which was already mentioned in the investigation of the polarisation interaction. It was concluded therein that most of the variation between the CC results, *heil1982* and *foster1997*, and the `a2iratbt` SC-1 result comes from atomic data differences because the WW88 result achieves close agreement ($< 5\%$) by purportedly using the same inputs. A similar third period analogue ion, Al-like S^{3+}, was first studied by RS69 using the SC-CC method without polarisation corrections. The SC-1 approach of BT05 [92] achieves a fairly constant variation of approximately 13% with this result, and WW88 does even better with $< 5\%$. Therefore, it is concluded that close coupling is a fairly minor effect for these transitions occurring between the two levels of a ^{2}P term.

The previous three examples have all been for transitions between the two levels of a doublet term, where it is was acknowledged earlier that the degree of close coupling will be smaller. A triplet term is more susceptible to CC effects, and

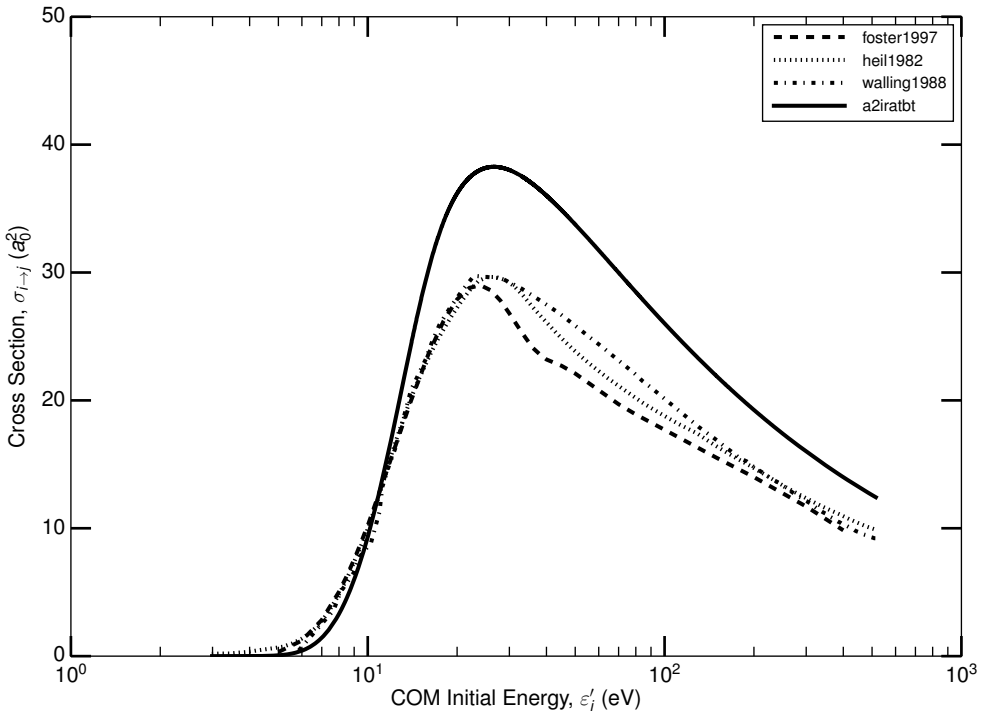

Figure 4.7: Proton-impact excitation of the $2s^2 2p\ ^2P_{1/2} \rightarrow\ ^2P_{1/2}$ transition in B-like O^{3+}. The legend sources are [118], a descendant of the SC-CC RS69, for *foster1997*; [126], a Q-CC result, for *heil1982*; [103], a SC-1 result, for *walling1988* = WW88; and the new SC-1 ADAS code, `a2iratbt`.

transitions within the ground ^3P term of Si-like Fe^{12+} offer a well studied example. WW88 [103] compares its SC-1 result to the Q-CC result of F75 [125] using the same input atomic data. It achieves quite good agreement for the $J : 1 \rightarrow 2$ transition of at worst 10% around the maximum of the cross section. Recall that there should be little difference between a semi-classical and quantal treatment. The disagreement at higher energies is due to the different interaction terms used—asymptotic versus complete—because WW88 can achieve better agreement by using a r_0 cutoff that matches the Born calculation of F75. The agreement for the $J : 0 \rightarrow 2$ transition is not as good, peaking at about 25%. Although the different interaction terms will account for some of this, the dominant effect is the loss of flux through close coupling to the first-order forbidden $^3P_{0\rightarrow 1}$ transition. In addition, the SC-1 [95] and SC-CC [121] results of Landman display a fair level of consistency for this ion. Like before, the $J : 0 \rightarrow 2$ transition displays a larger CC suppression than the $J : 1 \rightarrow 2$, only about 10% in this case, but an SC-1 estimate is also produced for the forbidden $J : 0 \rightarrow 1$ transition, and this

exhibits a larger discrepancy of approximately 25%. As previously concluded in section 4.2.1, the extension of the SC-1 technique to treat forbidden transitions is likely too crude for the additional effort involved. It must also be kept in mind that these forbidden transitions tend to be of smaller magnitude and so less influential in the context of a population model.

A comparison of rate coefficients in a triplet term is performed by WW88 for 2s2p ^{3}P of Be-like Ne^{6+} against the SC-CC calculation of [109], a descendent of RS69. The level of agreement is quite high in this case, approximately 5% for the two allowed transitions, with the SC-1 slightly overestimating relative to the SC-CC because of the neglect of close coupling to the forbidden transition, $J : 0 \rightarrow 1$. Later when comparing IIE data relevant to modelling argon in section 4.4.2, the Be-like isoelectronic analogue is compared for the present SC-1 `a2iratbt` result against another SC-CC RS69 descendent [110] in figures 4.22 and 4.25. Correcting for the atomic data input, disagreement of less than 20% is observed for both allowed transitions. The third result (*ryans1998*) is ignored because of the uncertainty surrounding the implementation of the polarisation correction.

In conclusion, the results from correctly implemented SC-1 methods tend to attain high fidelity with those from SC-CC methods after correcting for any atomic data or interaction term variation. The best cases ($< 5\%$) are transitions within doublet terms that closely emulate a true two-state system, whereas less agreement ($\approx 25\%$) is witnessed for higher order multiplets because of the stronger CC effects through intermediate states within the term. For the purposes of an expeditious baseline, these CC effects on allowed transitions can safely be neglected at the moment. However, the impact of neglecting forbidden transitions remains an open question, although it is suspected to be small. Overall, it is concluded from this literature review that the SC-1 method implemented in `a2iratbt` should be more than adequate for the present baseline purposes. The use of the long-range quadrupole potential with fitting to the Born approximation asymptote will avoid any deficienies from neglecting short-range effects, and the polarisation correction should be negligible. A semi-classical approach introduces no significant error compared to a quantal one, and the effects of close coupling can be safely deferred to a later update of the baseline.

Table 4.2: Parameter definitions for IIE scattering calculations in this chapter. Unless otherwise stated, all energy quantities are in Rydberg units (Ryd) throughout this chapter, while all other quantities are in atomic units (au).

z_t	target charge number	${S_{ij}}^{(2)}$	quadrupole atomic line strength (au)
z_p	projectile charge number	ω_i	statistical weight of target level, i
m_t	target mass (au)	ω_j	statistical weight of target level, j
m_p	projectile mass (au)	ε_i	initial kinetic energy of reduced projectile in COM frame (Ryd)
M	reduced mass (au) $= \frac{m_p m_t}{m_p+m_t}$	ε_j	final kinetic energy of reduced projectile in COM frame (Ryd)
ΔE_{ij}	atomic transition energy (Ryd)	ε	geometric mean kinetic energy in COM frame (Ryd) $= (\varepsilon_i \varepsilon_j)^{1/2}$

4.3 Methodology

It was explained in section 4.2.1 that the work of BT05 [92] represents the most complete and correct formulation of the SC-1 method in the literature and should form the basis of any subsequent implementation. However, it was also noted that the accompanying computer code has been lost to the abyss. Consequently, the replacement of this code was a priority, and it is achieved with the new ADAS code, `a2iratbt`. This code will be used to provide baseline quality IIE data within ADAS for the foreseeable future. The basic details of the methodology and implementation are provided in section 4.3.1, but a detailed account of the code is provided in a reference manual that will soon be placed in central ADAS. Subsequently, a new ADAS data format, *adf06*, is introduced in section 4.3.2 to hold the IIE collision data produced by `a2iratbt`.

4.3.1 A New ADAS Code: a2iratbt

Proceeding along the lines established by BT05 [92], S64 [90], and Alder et al. [91], the ion projectile is treated as a classical particle with position vector, $\boldsymbol{r_p}$, travelling along a hyperbolic trajectory determined by the electrostatic Coulomb potential of the target ion, z_t/r_p. The differential excitation cross section is then simply the product of the Rutherford differential cross section and the transition probability:

$$\mathrm{d}\sigma_{i\to j} = P_{ij}^{(1)}(\theta) \cdot \frac{1}{4\pi} \left(\frac{z_t z_p}{\varepsilon}\right)^2 \csc^4(\theta/2)\mathrm{d}\Omega. \tag{4.20}$$

In turn, the transition probability is obtained through first-order perturbation theory, which states

$$P_{ij}^{(1)} = \frac{1}{\omega_i} \sum_{M_i M_j} \left| b_{ij}(t=\infty) \right|^2 , \tag{4.21}$$

where

$$b_{ij} = -i \int_{-\infty}^{+\infty} \langle j \left| H(t) \right| i \rangle \, e^{i\omega t} \mathrm{d}t. \tag{4.22}$$

The interaction Hamiltonian, $H(t)$, is given by the Coulomb interaction energy,

$$H(t) = \int \gamma(\boldsymbol{r}) \varphi(\boldsymbol{r}, t) \mathrm{d}\tau, \tag{4.23}$$

where $\gamma(\boldsymbol{r})$ is the atomic charge density, $\boldsymbol{r}$ is the position vector of the atomic electron, $\mathrm{d}\tau$ is the spatial volume element, and

$$\varphi(\boldsymbol{r}, t) = \frac{z_p}{|\boldsymbol{r} - \boldsymbol{r_p}|} - \frac{z_p}{r_p} \tag{4.24}$$

is the interaction potential. Notice the second term that is subtracted represents the interaction between the centres of mass, which determines the scattering trajectory but does not influence the excitation. As already explained in section 4.2.1, the first term of the interaction potential is expanded in multipole components:

$$\frac{1}{|\boldsymbol{r_p} - \boldsymbol{r}|} = \sum_{\lambda}^{\infty} P_\lambda(\hat{\boldsymbol{r}}_{\boldsymbol{p}} \cdot \hat{\boldsymbol{r}}) \frac{r^\lambda}{r_p^{\lambda+1}}. \tag{4.25}$$

For the fine-structure transitions germane to IIE in this thesis, the quadrupole ($\lambda = 2$) term is the first non-zero and also dominant one in this expansion, and it is assumed that only this term should be retained, recovering equation 4.8. After a great deal of algebra and manipulation, one arrives at an expression for the *unmodified* transition probability,

$$P_{ij}^{(1)}(\varepsilon, \theta) = \frac{4MB_{E2}\varepsilon^3}{{z_p}^2 {z_t}^4} \sin^4(\theta/2) \frac{\mathrm{d}f_{E2}}{\mathrm{d}\Omega}(\theta, \xi), \tag{4.26}$$

where $B_{E2} = (15/(8\pi))S_{ij}{}^{(2)}/\omega_i$ is the reduced radiative transition probability, and ξ is the dimensionless adiabaticity parameter defined by

$$\xi = \frac{z_p z_t \sqrt{M}\,|\Delta E_{ij}|}{\varepsilon(\sqrt{\varepsilon_i} + \sqrt{\varepsilon_j})}. \tag{4.27}$$

This yields expressions for the cross section in atomic units, $[a_0^2]$,

$$\begin{aligned}\sigma_{i\to j} &= \frac{\pi {z_p}^2 {z_t}^2}{2\varepsilon_i \varepsilon} \int_0^\pi P_{ij}^{(1)}(\varepsilon,\theta)\csc^4(\theta/2)\sin\theta \mathrm{d}\theta \\ &= \frac{2\pi M B_{E2}\varepsilon_j}{{z_t}^2} \int_0^\pi \frac{\mathrm{d}f_{E2}}{\mathrm{d}\Omega}(\theta,\xi)\sin\theta\mathrm{d}\theta \\ &= \frac{M B_{E2}\varepsilon_j}{{z_t}^2} f_{E2}(\xi),\end{aligned} \tag{4.28}$$

and the collision strength, [dimensionless],

$$\begin{aligned}\Omega_{ij} &= M\varepsilon_i\omega_i\sigma_{i\to j} \\ &= \frac{\pi M\omega_i {z_p}^2 {z_t}^2}{2\varepsilon} \int_0^\pi P_{ij}^{(1)}(\varepsilon,\theta)\csc^4(\theta/2)\sin\theta\mathrm{d}\theta \\ &= \frac{2\pi M^2 B_{E2}\omega_i\varepsilon^2}{{z_t}^2} \int_0^\pi \frac{\mathrm{d}f_{E2}}{\mathrm{d}\Omega}(\theta,\xi)\sin\theta\mathrm{d}\theta \\ &= \frac{M^2 B_{E2}\omega_i\varepsilon^2}{{z_t}^2} f_{E2}(\xi).\end{aligned} \tag{4.29}$$

The differential excitation cross section function, $\mathrm{d}f_{E2}/\mathrm{d}\Omega$, is an important quantity defined, for the $E2$ case, by

$$\frac{\mathrm{d}f_{E2}}{\mathrm{d}\Omega}(\theta,\xi) = \frac{3\pi}{200}\left[I_{2,-2}^2 + \frac{2}{3}I_{2,0}^2 + I_{2,2}^2\right]\csc^4(\theta/2), \tag{4.30}$$

where $I_{2,\mu}$ are classical orbit integrals involving hypergeometric functions. The symmetrised adiabaticity parameter, ξ, is addressed at length in section 4.4.1.1. Evaluating these integrals can be an arduous task, so BT05 [92] developed a convenient strategy involving straight line orbit approximations, $(\mathrm{d}f_{E2}/\mathrm{d}\Omega)_{\mathrm{st}}$, that quickly and accurately yields values of $\mathrm{d}f_{E2}/\mathrm{d}\Omega$. A two-dimensional data array of the ratio, $\Lambda(\theta,\xi) = (\mathrm{d}f_{E2}/\mathrm{d}\Omega)/(\mathrm{d}f_{E2}/\mathrm{d}\Omega)_{\mathrm{st}}$, is generated on a fairly fine mesh in advance and stored. This ratio is advantageous for interpolation because Λ is slowly varying and $\Lambda(0,\xi) = \Lambda(\theta,0) = 1$. Values of $\mathrm{d}f_{E2}/\mathrm{d}\Omega$ are retrieved by

interpolating Λ and then multiplying by $(\mathrm{d}f_{E2}/\mathrm{d}\Omega)_{\mathrm{st}}$. Details of the straight line orbit approximations and this ratio are provided in the Appendix of BT05 [92]. Extensive reference to Appendix II E.4 of Alder et al. [91] is made therein.

Equations 4.26, 4.28, and 4.29 constitute the *unmodified* expressions for the SC-1 approach to the inelastic scattering problem, but it has been pointed out many times already that these are wholly inadequate for producing accurate collision data in any regime except at low energies. Therefore, a number of modifications must be made to these expressions before they can be properly exploited. Proceeding according to the energy regimes identified by S64 [90], it is noted:

(a) **Low Energies**—No changes are required because $P_{ij}^{(1)}$ stays small and first-order perturbation theory holds.

(b) **Intermediate Energies**—To ensure that $P_{ij}^{(1)} \leq 1$ for all trajectories, the *modified* transition probability is given by

$$P_{ij}^{(2)} = P_{\mathrm{ub}}\phi\left(P_{ij}^{(1)}/P_{\mathrm{ub}}\right), \tag{4.31}$$

where ϕ is some function such that $\phi(x) \sim x$ as $x \to 0$, and $\phi(x) \leq 1, \forall x \geq 0$, ensuring $P_{ij}^{(2)}$ never exceeds a specified upper bound, P_{ub}. Here, x is a dummy variable. The choice of ϕ and P_{ub} are to some extent arbitrary, but symmetry reciprocity of the final transition probability should be maintained. Some options for ϕ are listed by equation 4.50, but outside of the parameter variation studies in section 4.4.1.4, the default used in `a2iratbt` is $\phi(x) = \tanh(2x)/2$, effectively a smooth version of the $P_{ij}^{(1)}(b_1) = 1/2$ cutoff used in S64.

Selecting P_{ub} is less ambiguous. Since $P_{ij}^{(1)} \propto 1/\omega_i$, $P_{ij}^{(2)}$ must be as well if reciprocity is to be maintained. Consulting equation 4.31, the simplest option is to make $P_{\mathrm{ub}} \propto 1/\omega_i$ and ensure $\phi\left(P_{ij}^{(1)}/P_{\mathrm{ub}}\right)$ is symmetric. An advantageous option is the definition,

$$P_{\mathrm{ub}} = \frac{H(\omega_i, \omega_j)}{\omega_i} = \frac{2}{{\omega_i}^{-1} + {\omega_j}^{-1}}\frac{1}{\omega_i} = \frac{2\omega_j}{\omega_i + \omega_j}, \tag{4.32}$$

where $H(x_1, x_2, \ldots, x_n)$ is the harmonic mean. Not only does this sym-

metrise the ratio, $P_{ij}^{(1)}/P_{\rm ub}$ and guarantee $P_{ij}^{(2)} \propto 1/\omega_i$, but if $\phi \to 1/2$ when $P_{ij}^{(1)}$ becomes large, then $P_{ij}^{(2)} \to \omega_j/(\omega_i + \omega_j)$. In other words, strong coupling transitions ($P_{ij}^{(1)}$ large) will have a transition probability determined by the statistical weights of the levels involved in the transition.

(c) **High Energies**—A radial cutoff, r_0, centred on the atomic target is set just as in S64. For trajectories with $\rho(\theta) < r_0$, the transition probability is set to its value when $\rho(\theta_0) = \rho_0 = r_0$. More succinctly, $P_{ij}^{(2)}(\theta) = P_{ij}^{(2)}(\theta_0)$ for $\rho(\theta) < r_0$. After adjusting the collision strength expression, it can be shown—see the beginning of section 6 in BT05—that the infinite energy limit, ${\Omega_{ij}}^{(\rm inf)}$, has the form

$$\lim_{\varepsilon_j \to \infty} \Omega_{ij} = \frac{4}{5}\left(\frac{M z_p}{r_0}\right)^2 S_{ij}. \tag{4.33}$$

Then, ${\Omega_{ij}}^{(\rm inf)}$ is obtained from the Born approximation of AUTOS, allowing r_0 to be solved for in equation 4.33. With r_0 set in this manner, Ω_{ij} is guaranteed to approach ${\Omega_{ij}}^{(\rm inf)}$ given by the Born approximation, which is exact in this limit.

Incorporating these modifications, equations 4.28 and 4.29 become

$$\begin{aligned}\sigma_{i\to j} = \frac{{z_p}^2 {z_t}^2}{2\varepsilon_i \varepsilon}\Bigg[&\int_0^{\theta_0} P_{i\to j}^{(2)}(\varepsilon,\theta)\sin^{-4}(\theta/2)\sin\theta \mathrm{d}\theta \\ &+ P_{i\to j}^{(2)}(\varepsilon,\theta_0)\int_{\theta_0}^{\pi}\sin^{-4}(\theta/2)\sin\theta\mathrm{d}\theta\Bigg]\end{aligned} \tag{4.34}$$

$$\begin{aligned}\Omega_{ij} = \frac{M\omega_i {z_p}^2 {z_t}^2}{2\varepsilon}\Bigg[&\int_0^{\theta_0} P_{i\to j}^{(2)}(\varepsilon,\theta)\sin^{-4}(\theta/2)\sin\theta \mathrm{d}\theta \\ &+ P_{i\to j}^{(2)}(\varepsilon,\theta_0)\int_{\theta_0}^{\pi}\sin^{-4}(\theta/2)\sin\theta\mathrm{d}\theta\Bigg]\end{aligned} \tag{4.35}$$

with $\theta_0 = 2\arcsin\left(z_p z_t/\varepsilon r_0 - z_p z_t\right)$, the COM scattering angle at which $\rho(\theta_0) = r_0$. The important effects that these changes have upon the collision data is investigated in section 4.4.1.4. Practically, it is convenient to use a change of variable:

$$u = \frac{\varepsilon}{z_p z_t}\sin(\theta/2). \tag{4.36}$$

BT05 explains why this is beneficial, and equations (10)–(13) from [92] are the final ones used in the `a2iratbt` calculations.

Typically, it is the rate coefficient ($q_{i\to j}$) or effective collision strength (Υ_{ij}) that is required for processing in ADAS, and these are obtained through the usual relations:

$$\Upsilon_{ij} = \int_0^\infty \Omega_{ij} e^{-s} \mathrm{d}s \tag{4.37}$$

with $s = \varepsilon_j/(kT)$, and

$$q_{i\to j} = \frac{2\sqrt{\pi} a_0^2 \alpha c}{\omega_i M^{3/2}} \left(\frac{I_H}{kT_e}\right)^{1/2} \exp(-\Delta E_{ij}/kT_\mathrm{e}) \Upsilon_{ij}. \tag{4.38}$$

For the integration in equation 4.37, it is convenient to partition the energy space into two intervals, each with a different integration technique. The partitioning energy, ε_b, is determined by an iterative scheme that ensures it is beyond the peak of the integrand. In the interval $[0, \varepsilon_b]$, the 1-D adaptive Gaussian integrator technique, `dqags`, from the `SLATEC` numeric library[7] is used, while for $[\varepsilon_b, +\infty]$ Gauss-Laguerre integration is used. The `dqags` routine is also applied to the integrals in equation 4.35.

The input to `a2iratbt` is simple, but some of the atomic data required can be difficult to source. The transition energy (ΔE_{ij}), quadrupole line strength ($S_{ij}{}^{(2)}$), and Born limit ($\Omega_{ij}{}^{(\mathrm{inf})}$) for the transition of interest are all taken from a precursor AUTOS run in the proposed ADAS framework for mass production, which is orchestrated through Perl scripts in the offline ADAS subcategory, `adas1#2`. The IIE calculations for Chapter 5 use the enhanced baseline features of Chapter 2 in this precursor AUTOS run, and it is envisioned this will be the default behaviour for mass production. However, there is flexibility, and the producer is able to specify arbitrary input for AUTOS in this framework.

4.3.2 A New ADAS File Format: adf06

Storing the IIE collision data produced by `a2iratbt` raises a practical problem within ADAS. Since EIE only ever involves an electron projectile, there is no field to store projectile parameters in the existing file format for specific ion excitation

[7] `http://www.netlib.org/slatec/index.html`

data, *adf04*. The objective within ADAS is the capability to exploit IIE data involving an arbitrary structureless projectile—it is not simply proton-impact that is of concern. Therefore, the *adf04* file format is inadequate, and a new file format, *adf06*, has been developed. As shown in figure 4.8, the *adf06* format is almost identical to the *adf04* format except that the collision data is broken into blocks specific to each projectile. The header lines of these blocks give the necessary information about the projectile for use in other ADAS routines. In accordance with ADAS requirements, reading routines in both Fortran and IDL have been concurrently developed to facilitate the exploitation of this data.

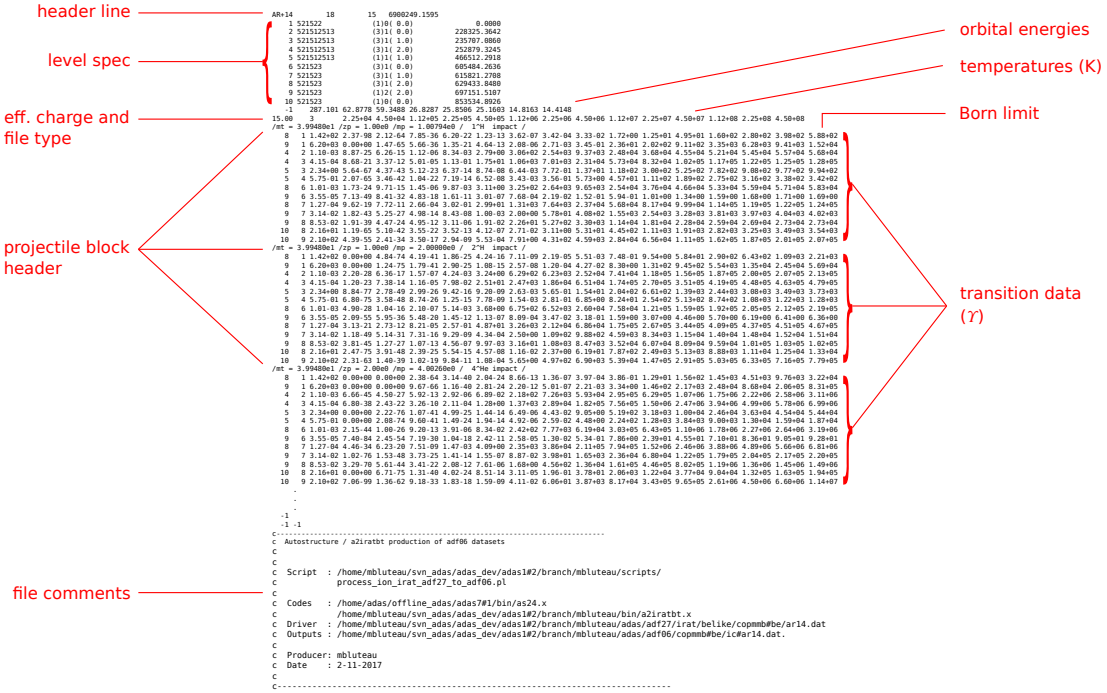

Figure 4.8: An example of the new *adf06* file format for Be-like Ar^{14+}. This format holds IIE collision data in blocks specific to each ion projectile. It is identical to the *adf04* format except for these blocks. The block headers give the information, `/mt = [target mass in amu] /zp = [projectile charge] /mp = [projectile mass in amu] / [human-readable projectile tag]`. Effective collision strengths (Υ_{ij}'s) have been shown here in accordance with the type specifier 3.

4.4 Results and Discussion

4.4.1 Parameter Variation Studies of IIE

Although the theory behind IIE scattering has been detailed in section 4.3.1, a critical practice in many fields of physics is determining how physical quantities depend on their parameters, both explicitly and implicitly. Insight about the parametric dependence of a quantity yields manifold benefits. First, it can assist in establishing scaling laws that can extend the results into parameter spaces where direct calculation may not be possible or feasible. Second, it can provide an independent means of validating certain aspects of the calculations: either unexpected or missing parameter dependence can indicate deficiencies in the understanding of the applied theory or errors therein. Third, understanding how a quantity varies with its parameters grants one a deeper physical intuition and understanding about the quantity itself. The purpose of the parametric studies in this thesis will be to reap the latter two benefits, which will prove particularly helpful when analysing the effects of projectile variation upon the GCR model of argon in section 5.3.1.2.

All parametric studies must begin with a firm grounding in the equations used to calculate the quantities of interest. Of course, this has already been done in section 4.3.1, but it is useful to restate the concluding equations and make a clear distinction between the equations for the *unmodified* and *modified*, SC-1 theories. The unmodified form displays the influence of the physical parameters, whereas the modified form emphasises the impact of technical parameters. In this context, physical parameters are defined as those parameters that depend directly upon the fundamental physical characteristics of the system: mass, charge, radiative line strength of the atomic transition, etc. On the other hand, technical parameters are defined as those parameters that relate to the particular method being used, e.g. any cutoff used in integration or limiting behaviour enforced upon the transition probability. The differentiation of *physical* and *technical* parameters is in no way meant to suggest that the technical parameters have no physical basis, but rather this classification is made to emphasise the distinction between parameters that are universal to any applied method (physical) and those that arise solely because of the particular method being used (technical). Indeed, it is

frequently the case that technical parameters are introduced to make the method more physically accurate, as the results of section 4.4.1.4 should prove.

The *unmodified*, first-order equations for the transition probability, cross section, and collision strength from section 4.3.1 are restated here:

$$P^{(1)}_{i\to j}(\varepsilon,\theta) = \frac{4MB_{E2}\varepsilon^2\varepsilon_j}{{z_p}^2{z_t}^4}\sin^4(\theta/2)\mathrm{d}f_{E2}/\mathrm{d}\Omega \tag{4.39}$$

$$\sigma_{i\to j} = \frac{2\pi MB_{E2}\varepsilon_j}{{z_t}^2}\int_0^\pi \mathrm{d}f_{E2}/\mathrm{d}\Omega\sin\theta\mathrm{d}\theta = \frac{2\pi MB_{E2}\varepsilon_j}{{z_t}^2}f_{E2}(\xi), \tag{4.40}$$

$$\Omega_{ij} = \frac{2\pi M^2B_{E2}\varepsilon_i\varepsilon_j\omega_i}{{z_t}^2}\int_0^\pi \mathrm{d}f_{E2}/\mathrm{d}\Omega\sin\theta\mathrm{d}\theta \quad = \frac{2\pi M^2B_{E2}\varepsilon_i\varepsilon_j\omega_i}{{z_t}^2}f_{E2}(\xi). \tag{4.41}$$

These equations have been simplified as much as possible in an attempt to clearly display the explicit physical parameter scaling; however, it is not possible to give the explicit scaling of $\mathrm{d}f_{E2}/\mathrm{d}\Omega$ due to the complexity of its analytic integral representation. Notwithstanding this, simpler expressions for $\mathrm{d}f_{E2}/\mathrm{d}\Omega$ and its integral, $f_{E2}(\xi)$, can be obtained in both the high and low energy limits—corresponding to low and high ξ limits, respectively. These limiting behaviours and the parameter dependence of $f_{E2}(\xi)$ are investigated in section 4.4.1.1 where the adiabaticity parameter, ξ defined by equation 4.27, is used as a proxy for the other physical parameters. Once the ξ dependence of $f_{E2}(\xi)$ is known, the approximate scaling of the collisional quantities relative to the physical parameters can be determined from equations 4.39–4.41. Investigating the physical parameter dependence of IIE collision quantities introduces an extra dimension compared to the equivalent exercise for EIE because the projectile can now assume a range of mass and charge values, $\{m_p \in \mathbb{R}, z_p \in \mathbb{N}\}$, as opposed to $z_p = 1$ and $m_p = m_\mathrm{e} = 1$ for an electron. Therefore, the physical parameters have been subdivided into projectile and target categories, investigated in sections 4.4.1.2 and 4.4.1.3, respectively. The physical parameters are listed in table 4.3.

Since the parameter dependence of a variety of collision quantities will be investigated, figure 4.9 provides a visual summary of how these quantities are related and which parameters enter at each step. As a reminder, the rate coefficient, $q_{i\to j}$, is related to the effective collision strength, Υ_{ij}, by equation 4.38.

The parameter dependence ascertained from equations 4.39–4.41 will not cor-

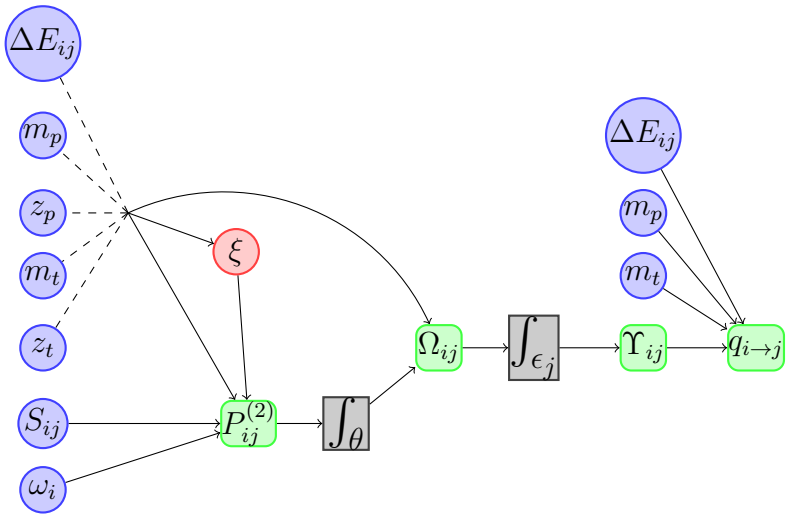

Figure 4.9: Parameter dependence and interrelation of collision quantities. The green, rounded-corner boxes contain the collision quantities of interest; the blue circles contain the parameters; and the grey boxes contain integration steps. The collision quantities are built from left to right as indicated by the flow of arrows.

respond exactly to the results of the current IIE calculations since a *modified* form of the SC-1 method is used. In most cases, the unmodified and modified forms will agree with each other, especially if one is only seeking to determine parameter scaling where a lesser degree of accuracy and precision is required. Even so, at higher energies the unmodified SC-1 method suffers serious errors and should not be used for any purpose. As a result, the effects of the modifications need to be elucidated along with their dependence upon the technical parameters.

The *modified*, SC-1 equations for the transition probability, cross section, and collision strength are:

$$P_{i\to j}^{(2)}(\varepsilon,\theta) = P_{\text{ub}}\phi\left(P_{i\to j}^{(1)}/P_{\text{ub}}\right) \tag{4.42}$$

$$\begin{aligned}\sigma_{i\to j} = \frac{{z_p}^2{z_t}^2}{2\varepsilon_i\varepsilon}\Bigg[&\int_0^{\theta_1} P_{i\to j}^{(2)}(\varepsilon,\theta)\sin^{-4}(\theta/2)\sin\theta\mathrm{d}\theta \\ &+P_{i\to j}^{(2)}(\varepsilon,\theta_1)\int_{\theta_1}^{\pi}\sin^{-4}(\theta/2)\sin\theta\mathrm{d}\theta\Bigg]\end{aligned} \tag{4.43}$$

Table 4.3: Parameters involved in IIE, SC-1 calculations.

Category		Parameters
Physical	Projectile	m_p, z_p
	Target	m_t, z_t, ΔE_{ij}, S_{ij}, ω_i
Technical		r_0, $\phi(x)$, P_{ub}

$$\Omega_{ij} = \frac{M\omega_i {z_p}^2 {z_t}^2}{2\varepsilon}\left[\int_0^{\theta_1} P^{(2)}_{i\to j}(\varepsilon,\theta)\sin^{-4}(\theta/2)\sin\theta \mathrm{d}\theta + P^{(2)}_{i\to j}(\varepsilon,\theta_1)\int_{\theta_1}^{\pi}\sin^{-4}(\theta/2)\sin\theta\mathrm{d}\theta\right] \tag{4.44}$$

with $\theta_1 = 2\arcsin\left(z_p z_t/\varepsilon r_0 - z_p z_t\right)$. Therefore, the technical parameters of interest for the modified SC-1 method are the effective target radius, r_0, and the transition probability limiting function, $\phi(x)$. The neglect and variation of these parameters will be investigated in section 4.4.1.4.

The complete set of parameters considered in this section are listed in table 4.3 according to their relevant subcategories.

4.4.1.1 The Adiabaticity Parameter, ξ

Self-evidently, the adiabaticity parameter, ξ, measures the adiabaticity of a collision: large ξ corresponds to a highly adiabatic collision, and small ξ to a diabatic collision. However, the meaning of the term *adiabatic* for quantum processes is different than perhaps the more familiar thermodynamic definition. The quantum meaning of adiabatic derives from the **adiabatic theorem**, which was stated originally by Born and Fock as follows:

Definition 4.1. A physical system remains in its instantaneous eigenstate if a given perturbation is acting on it slowly enough and if there is a gap between the eigenvalue and the rest of the Hamiltonian's spectrum [132].

In more modern times, it has been shown that the requirement of a discrete eigenvalue spectrum is actually unnecessary. The utility of the theorem is apparent in slightly more technical language:

Definition 4.2. Suppose the Hamiltonian of a system changes gradually from

some initial form H^i to some final form H^f; thus, the time of action, $\tau = t_f - t_i$, is large ($\tau \to \infty$) and $\partial H/\partial t$ is small ($\partial H/\partial t \to 0$). Then, the adiabatic theorem states that if the particle was initially in the $|n\rangle$ eigenstate of H^i, it will be carried under the Schrödinger equation into the $|n\rangle$ eigenstate of H^f [133].

So, an adiabatic, quantum process is one where a perturbation, large or small, acts slowly enough ($\tau \gg 1$) that the eigenstate index, n, is unaltered. To be more precise, the variation time of the Hamiltonian, τ, is "slow enough" if it is much greater than the characteristic time for change of the state's wave function, τ_a. The ratio, τ/τ_a, is then a discriminator between adiabatic ($\tau/\tau_a \gg 1$) and diabatic ($\tau/\tau_a \to 0$) processes. Although the functional form of the eigenstate may change ($\psi_n(x,t_i) \neq \psi_n(x,t_f)$), this change is well defined in terms of a sequence of singular eigenstates of the time-varying Hamiltonian for each instant in time. Conversely, a diabatic, quantum process is defined by a large, instantaneous change in the system's Hamiltonian: $\partial H/\partial t \to \infty$ and $\tau \to 0$. As a result, the spatial probability density does not have time to adapt, $|\psi(x,t_i)|^2 = |\psi(x,t_f)|^2$, but there is typically no eigenstate of the final Hamiltonian that matches the functional form of the initial eigenstate. Therefore, the final state must be a linear combination of the final Hamiltonian eigenstates, and so no unique quantum number can be assigned.

Such terminology is readily applied to quantum scattering: the modification to the Hamiltonian is caused by the incoming projectile, and the rapidity of the modification is determined by the transit time of the projectile relative to the time scale of the atomic state. Linking with the characteristic quantities defined above, τ will be associated with the projectile transit time, which can be estimated for classical orbits by

$$\tau \equiv t_{\text{transit}} = \frac{a}{v\sin(\theta/2)} = \frac{z_p z_t \epsilon}{M v_i^2 \cdot v_i} = \frac{z_p z_t \sqrt{M}\epsilon}{\varepsilon_i^{3/2}}, \tag{4.45}$$

where $a = z_p z_t/(M v_i^2)$, v_i is the initial projectile velocity, and $\epsilon = 1/\sin(\theta/2)$ is the eccentricity of the orbit. When considering an individual transition excited by a collision, τ_a will be defined by the atomic period of the transition, $T_a = 2\pi/\omega_a = 2\pi\hbar/\Delta E_{ij}$ [SI] $= \Delta E_{ij}{}^{-1}$ [au]. Therefore the adiabatic discriminator, τ/τ_a,

is the ratio between the collision time and the atomic period:

$$\frac{\tau}{\tau_a} = \frac{t_{\text{transit}}}{T_a} = \frac{z_p z_t \sqrt{M\epsilon}}{\varepsilon_i^{3/2}} \cdot \Delta E_{ij} = \xi\epsilon. \tag{4.46}$$

This ratio is in fact the origin of the adiabaticity parameter's definition. An adiabatic collision will be classified by $\xi\epsilon \gg 1$, and a diabatic by $\xi\epsilon \approx 0$, but since the collision quantities of interest integrate over θ, one frequently omits ϵ from these expressions and imposes these conditions upon ξ to stipulate the degree of adiabaticity. The adiabaticity parameter is not a parameter in the strict mathematical sense because it depends on a variable input, the projectile collision energy, in its various forms: ε, ε_i, ε_j. Moreover, it depends on more fundamental physical parameters, z_p, z_t, M, and ΔE_{ij}—see equation 4.27. Hence, there are many ways a collision can be made more or less adiabatic. The collision energy enters into the denominator of ξ, so small energies will correspond to a more adiabatic collision (ξ large) and large energies a more diabatic collision (ξ small). Physically, a small collision energy means a long collision time (t_{transit} large in equation 4.45), so the changes in the Hamiltonian caused by the projectile can be much slower than the characteristic time of the atomic state: $\tau/\tau_a \gg 1$. The inverse is of course true for large collision energies.

All of the physical parameters are contained in the numerator of the expression for ξ, equation 4.27, so any increase in z_p, z_t, M, or ΔE_{ij} will result in a more adiabatic collision. The physical basis for these parameter dependencies is evident from equations 4.45 and 4.46. The particle charges, z_p and z_t, determine the magnitude of the electrostatic potential that the projectile travels through and hence the distance of closest approach, $2a$, which enters into equation 4.45. Larger charges mean a greater electrostatic force, a larger distance of approach, and a longer path length overall. This leads to a greater collision time, t_{transit}, and hence greater adiabaticity. The transition energy, ΔE_{ij}, is inversely proportional to the period of atomic oscillation, T_a, analogous to how the difference in frequencies of acoustic waves determines the envelope 'beat' frequency of the resulting sound wave. Therefore, a larger ΔE_{ij} leads to a smaller characteristic time of change for the atomic system, τ_a, and consequently a more adiabatic collision. At a given fixed energy, an increase in M will cause a decrease in velocity, and hence an

increase of the transit time of the reduced particle.

What is the consequence of a collision being adiabatic or diabatic upon the collision quantities? Consider an adiabatic collision first and apply the adiabatic theorem. If modification to the atomic Hamiltonian caused by the projectile is gradual, then the theorem states that system will remain in the eigenstate $|n\rangle$ of the slowly varying Hamiltonian throughout the collision. The extreme states of a collision are specified with the projectile at an infinite distance from the target, so the initial and final Hamiltonians must be equal, $H^i = H^f$, meaning the initial and final eigenstates will not only have the same quantum number but the same functional form as well: $|nt_i\rangle = |nt_f\rangle$. So for a perfectly adiabatic collision, an atom that starts in eigenstate $|n\rangle$ of the isolated-atom Hamiltonian will end up in this exact same eigenstate after the collision: no atomic transition can occur and the transition probability is zero. The cross section and collision strength must also be zero at collision energies satisfying adiabatic conditions. The adiabatic perspective goes part of the way to explaining why IIE cross sections and collision strengths tend towards zero as collision energies approach the transition energy threshold. Similarly, the rate coefficient and effective collision strength will tend to zero for temperatures that have distribution functions peaking at adiabatic energies.

Now consider a diabatic collision: the modification to the initial Hamiltonian, H^i, occurs rapidly so that at any intermediate time during the collision, t_m, the target state must be some linear combination of the eigenstates of H^m, $|n(t_m)\rangle = \sum_i^\infty c_i \, |n_i(t_m)\rangle$. Even though $H^f = H^i$ for collisions and ostensibly the initial and final target states should be the same, the intermediate situation means that there is some probability of a transition. Obtaining an approximation of what this probability might be is outside the scope of this thesis, and one is referred to discussions of the *sudden approximation* in the literature.

All of the preceding comments have been derived solely from the adiabatic theorem; therefore, these predictions can be used as an independent verification of the SC-1 calculations once the ξ scaling of the SC-1 equations has been determined. The adiabaticity parameter only enters into the collision equations through $\mathrm{d}f_{E2}/\mathrm{d}\Omega$ and its integral $f_{E2}(\xi)$, so ascertaining their scaling will also set the ξ scaling of the collision quantities overall.

Simplified forms of the Coulomb trajectory functions, $\mathrm{d}f_{E2}/\mathrm{d}\Omega$ and $f_{E2}(\xi)$, which directly display the scaling dependence, can be obtained in the extrema domains of ξ. The primary results are presented here, and further details are contained in Appendix A of [103] and section II E.6 of [91]. In the limit of $\xi \gtrapprox 1$, one can express the Coulomb trajectory functions in terms of the power series of Whittaker functions. From this, the main variation of $\mathrm{d}f_{E2}/\mathrm{d}\Omega$ goes as $\sim e^{-\xi(2\epsilon+\pi)}$, and when integrated over θ, this leads to a main variation of $\sim e^{-2\pi\xi}$ for $f_{E2}(\xi)$. The exponential decrease of both quantities with increasing ξ is plainly observable in figures 4.10–4.12. $\mathrm{d}f_{E2}/\mathrm{d}\Omega$ decreases by about 5 decades as ξ increases from $0 \to 2$ in figure 4.10, and this is corroborated by figure 4.11 where $A(\xi = 0) = 1.8$ and $A(\xi = 2) = 1.5 \times 10^5$. Similarly, $f_{E2}(\xi)$ declines sharply in figure 4.12, starting around $\xi = 0.5$. As a result, all of the collision quantities in equations 4.39–4.41 will exhibit this exponential decrease towards zero in the regime of large ξ. This agrees perfectly with the general predictions of the adiabatic theorem. The probability of transition will tend to zero the more adiabatic a collision is (i.e. the greater ξ is), and the results from `a2iratbt` in figure 4.13 also reflect this scaling.

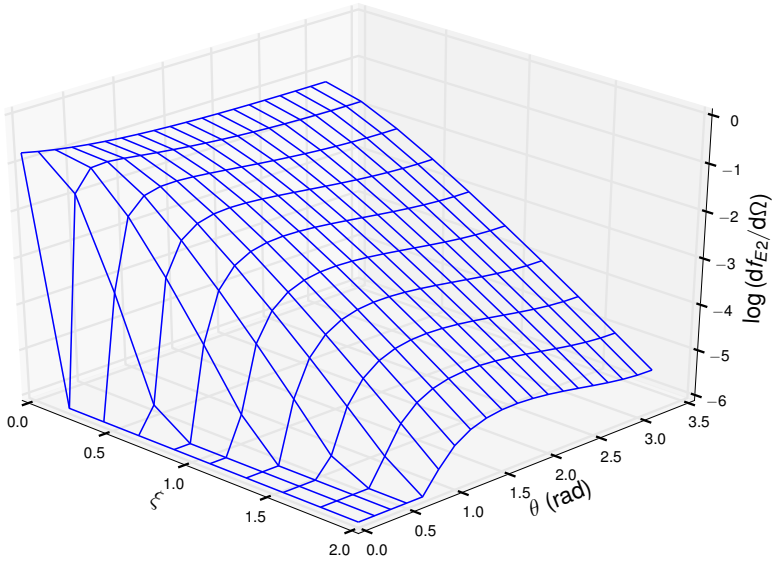

Figure 4.10: Three dimensional wire plot of $\mathrm{d}f_{E2}/\mathrm{d}\Omega$ for observation of ξ dependence. This is the classical approximation of this function. Function values were obtained through numeric integration of the orbit integrals.

In the opposite extreme of $\xi = 0$, the exponential terms containing ξ are

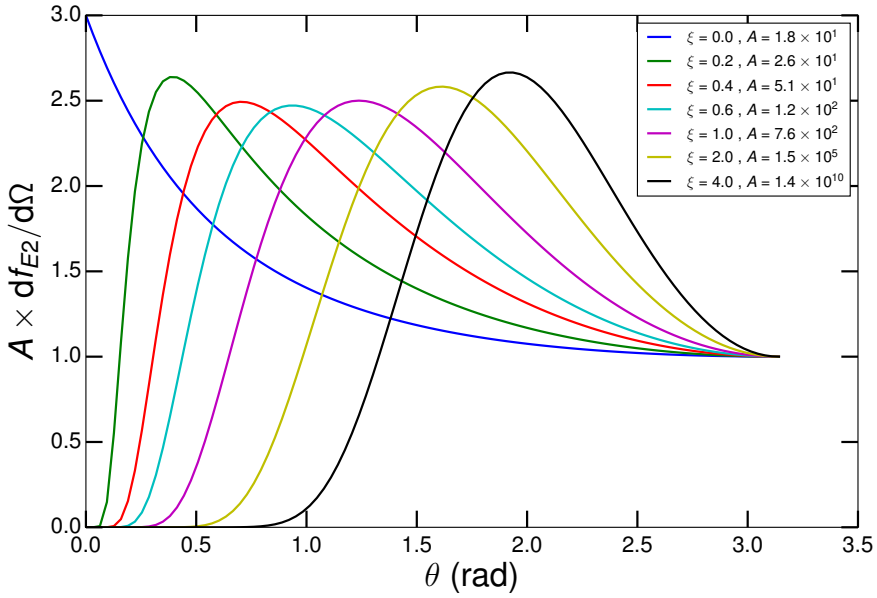

Figure 4.11: Angular distribution of the classical $\mathrm{d}f_{E2}/\mathrm{d}\Omega$ at specified ξ values. The function value has been normalised to unity at $\theta = \pi$, resulting in the normalisation coefficients, A, which multiply the entire curves so that similar magnitudes are achieved for ease of plotting.

eliminated from the orbit integrals that compose $\mathrm{d}f_{E2}/\mathrm{d}\Omega$, so these integrals can be performed explicitly with analytic, elementary functions:

$$\frac{\mathrm{d}f_{E2}}{\mathrm{d}\Omega}(\theta,0) = \frac{\pi}{75}\left\{1+3\left[1-\left(\frac{\pi-|\theta|}{2}\right)\tan\left(|\theta|/2\right)\right]^2\sec^4(\theta/2)\right\}, \tag{4.47}$$

$$f_{E2}(0) = \frac{8\pi^2}{25}\left(\frac{\pi^2}{16}-\frac{1}{3}\right) \approx 0.8954. \tag{4.48}$$

Because there is no longer any ξ dependence in these expressions, the Coulomb trajectory functions of order $E2$ will tend to a constant as $\xi \to 0$. This is most clearly demonstrated in figure 4.12 where the $f_{E2}(\xi)$ curve levels off to a constant value at the low ξ end of the plot. The underlying reason for this is that the $\mathrm{d}f_{E2}/\mathrm{d}\Omega$ curve along θ quickly approaches the shape and magnitude of $\frac{\mathrm{d}f_{E2}}{\mathrm{d}\Omega}(\theta,0)$, which is demonstrated by the sequential curves $\xi \in \{0.4, 0.2, 0\}$ of figure 4.11. With this, the collision quantities of equations 4.39–4.41 must also tend to constant values for $\xi \to 0$. Is this congruent with the predictions of the adiabatic theorem? For highly diabatic collisions (ξ small), the theorem as stated here simply predicts that a transition is possible, so a constant transition probability or collision strength

certainly satisfies this loose condition. It is worthwhile noting that the Coulomb trajectory functions only approach constant values for $\xi \to 0$ when $\lambda > 1$, because in the dipole case, $f_{E2}(\xi)$ diverges as $\ln(1/\xi)$.

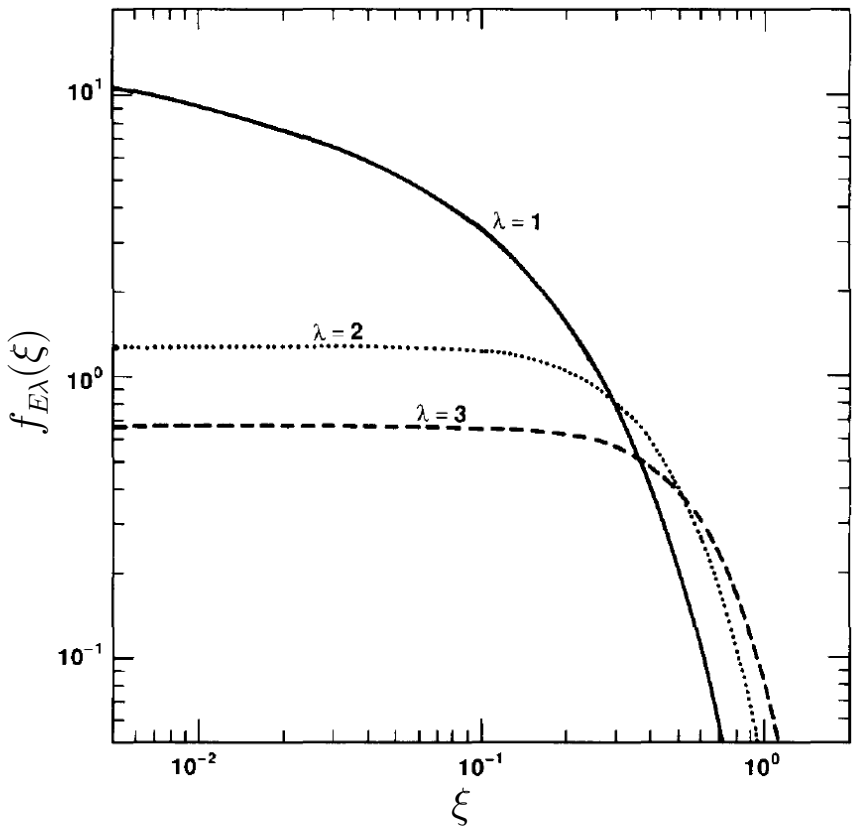

Figure 4.12: The integral Coulomb trajectory functions, $f_{E\lambda}(\xi)$, plotted versus ξ. No inner cutoff has been applied during integration, so the use of these quantities in equations 4.40 and 4.41 yield the *unmodified* SC-1 collision quantities. Reprinted figure 3 from *Physics Reports*, **162**, R. S. Walling and J. C. Weisheit, "Bound-state Excitation in Ion-ion Collisions", 1–43, ©(1988), with permission from Elsevier.

The last requisite piece to fully investigate the parameter scaling of the IIE collision quantities is now in place. These conclusions about the ξ scaling of the collision quantities, in conjunction with equations 4.39–4.41, will be applied in the subsequent sections to both validate and explain the changes caused by independently varying the physical parameters from table 4.3. In addition, equation 4.33 for the infinite energy limit is needed. Some notes on the method used: validating the scaling behaviour with an individual parameter requires first a qualitative prediction using the tools just mentioned and then a check against the actual results from the `a2iratbt` code. It was found that the easiest manner for checking

the expected behaviour was to generate plots of each collision quantity (Ω_{ij}, $\sigma_{i\to j}$, Υ_{ij}, $q_{i\to j}$) versus ε_j or T_p as appropriate, and each plot would contain multiple curves corresponding to the variation of the relevant input parameter. Practically, the results are generated by taking the set of inputs from a base case and varying the parameter of interest independently of the others. The base case used in the results below is the proton impact of B-like Ar^{13+}, yielding the following initial parameter values:

$$
\begin{aligned}
z_t &= 13 & z_p &= 1 \\
m_t &= 72820.75 \text{ au} & m_p &= 1836.15 \text{ au} \\
\Delta E_{ij} &= 0.190869 \text{ Ryd} & A_{j\to i} &= 1.30 \times 10^{-3} \text{ s}^{-1} \\
\omega_i &= 2 & \omega_j &= 4 \\
\Omega_{ij}^{(\text{inf})} &= 1.195 \times 10^5 \text{ au.}
\end{aligned}
$$

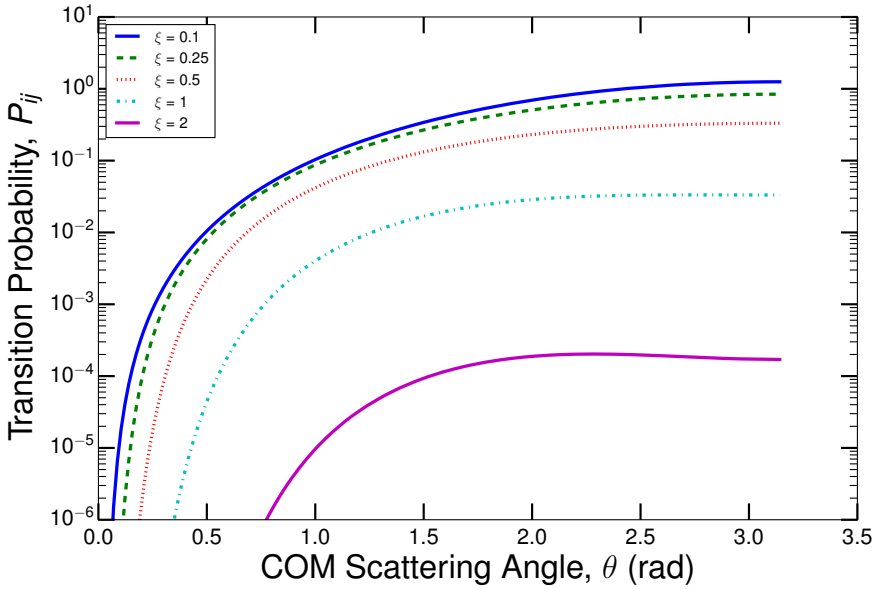

Figure 4.13: The transition probability for an arbitrary $E2$ transition at various ξ values, produced by the `a2iratbt` code.

4.4.1.2 Projectile Parameters

As noted above, the scaling with the projectile parameters offers two additional dimensions compared to the EIE problem, but even within the literature of IIE

calculations, the subject is not well studied. Anticipating the application of these rates in the CR modelling of laboratory devices containing various fuel and impurity ions, an understanding of the influence that different projectiles have upon the underlying collision quantities will be essential. The work of WW88 [103], detailed in the literature review section 4.2.1, also presents some limited physical parameter variation studies in its section 4, so these findings will provide a useful and independent verification of the conclusions to be made.

Consider first the projectile mass, m_p. Although this is truly an independent variable, the quantity that is actually used in the scattering equations and codes is the reduced mass, M, so it is best to assess the chain of influence in a step-by-step manner. Typically $m_p \ll m_t$, and so

$$M = \frac{m_p m_t}{m_p + m_t} \approx m_p. \tag{4.49}$$

Therefore, the value of M is more sensitive to the projectile mass than the target mass for most purposes, at least until the two masses become of similar magnitude. A comparison of figures 4.14 and 4.16 proves that this assertion is also reflected in the results from the code. Increasing m_t from one to one hundred times the mass of argon in figure 4.16 causes little effect upon any of the collision quantities because a larger m_t only reinforces the approximation of equation 4.49. Thus, M is effectively constant in this regime, meaning none of the parameters in the scattering equations are changing and the results must be the same. It is only when m_t is *reduced* by two orders of magnitude (and thus approaches m_p) that any significant change in the collision quantities is observed. This explains why the effect of target isotopes is not a concern. In contrast, figure 4.14 displays all of the collision quantities varying noticeably with comparatively small increases of m_p. Again, it is critical to emphasise how this differs from EIE where $M \approx m_\mathrm{e}$ always holds, so the variation of collision quantities with either projectile or target mass never occurs.

With the understanding that $M \approx m_p$ for most cases, it is possible to predict the effects of varying m_p upon the collision quantities more precisely. At low energies and temperatures meaning $\xi > 1$, it is the exponential decrease of $\mathrm{d}f_{E2}/\mathrm{d}\Omega$ and $f_{E2}(\xi)$ with ξ in equations 4.39–4.41 that dominates the behaviour

of the collision quantities: even though there is also an explicit factor of M in these equations, it will not overcome the exponential influence of ξ at low energies. Since a factor of $M^{\frac{1}{2}}$ is in the numerator of ξ (equation 4.27), increasing m_p will cause ξ to also increase, enhancing the suppressive adiabatic nature of the collision. Consequently, the collision quantities should all decrease with increasing m_p at low energies and temperatures, which is observed in figure 4.14. At the opposite limit of high energies and thus $\xi \to 0$, $f_{E2}(\xi)$ tends to a constant indicating an insensitivity to ξ, and it is rather the asymptotic infinite energy limit of 4.33 that will determine the scalings. The factor of M^2 in this expression dictates that an increase of m_p should induce an increase in the collision quantities as well. All of the collision quantities produced by `a2iratbt` in figures 4.14 reflect this behaviour at high energies and temperatures. Overall then, the scaling with m_p (and thus M) is mixed: m_p is positively correlated with Ω_{ij} and $\sigma_{i\to j}$ (Υ_{ij} and $q_{i\to j}$) at high energies (temperatures) but negatively correlated at low energies (temperatures), and so logically at some intermediate energy there is an inflection point where these opposing effects nearly cancel out.

Next, consider the projectile charge, z_p. A factor of z_p in the numerator of ξ implies that a higher projectile charge produces a more adiabatic collision at a given ε_j. Again, it is at low energies that the exponential suppression, $f_{E2}(\xi) \sim e^{-2\pi\xi}$, takes over and for which changes in ξ will be most influential. Thus, the increase in ξ caused by an increase in z_p should lead to a decrease of the collision quantities at low energies or temperatures. Observing figure 4.15, this behaviour is replicated by the `a2iratbt` results on the left side of the plots where a stark suppression of the collision quantities manifests with increasing z_p. For high energies, equation 4.33 shows that there is an explicit factor of ${z_p}^2$ in the infinite energy Ω_{ij} limit, so the collision quantities should positively correlate with z_p in this regime. Such is the observation for the curves at high energies and temperatures in figure 4.15, confirming that the `a2iratbt` results behave as predicted. As with m_p, the scaling behaviour of the collision quantities with z_p is non-uniform.

These findings for the scaling with m_p and z_p completely agree with observations in WW88 around their figure 13. The same inflection point effect is observed for their cross sections, with a negative correlation at low energies, switching to

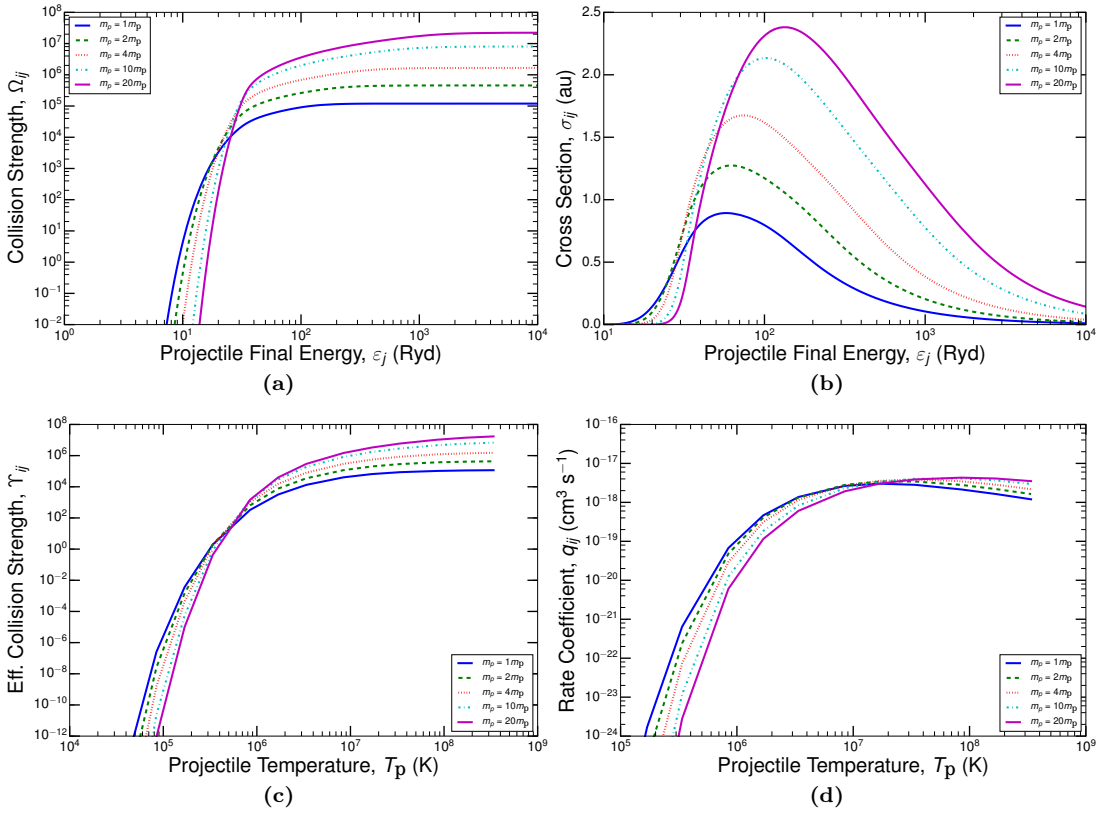

Figure 4.14: Variation of collision quantities with the projectile mass, m_p

positive correlation at high energies. Moreover, the sensitivity to m_p and z_p of the IIE collision quantities opens up the possibility for projectile isotope effects to be observed in laboratory plasmas, and this is explored further via *ic*-resolved GCR modelling in section 5.3.1.2, Chapter 5.

4.4.1.3 Target Parameters

Parameters associated with the target in the inelastic scattering problem have enjoyed more attention because they equally apply to EIE; nonetheless, they require analysis here to validate the present results. Briefly recall the target mass, m_t. Its influence was already partially discussed in conjunction with that of m_p because both parameters are symmetric inputs to the reduced mass, M. There it was noted that the collision quantities are fairly insensitive to m_t because of the simple fact that $m_t \gg m_p$ leads to $M \approx m_p$—figure 4.16 portrays this clearly relative to the higher sensitivity in figure 4.14. In rare circumstances, the ion

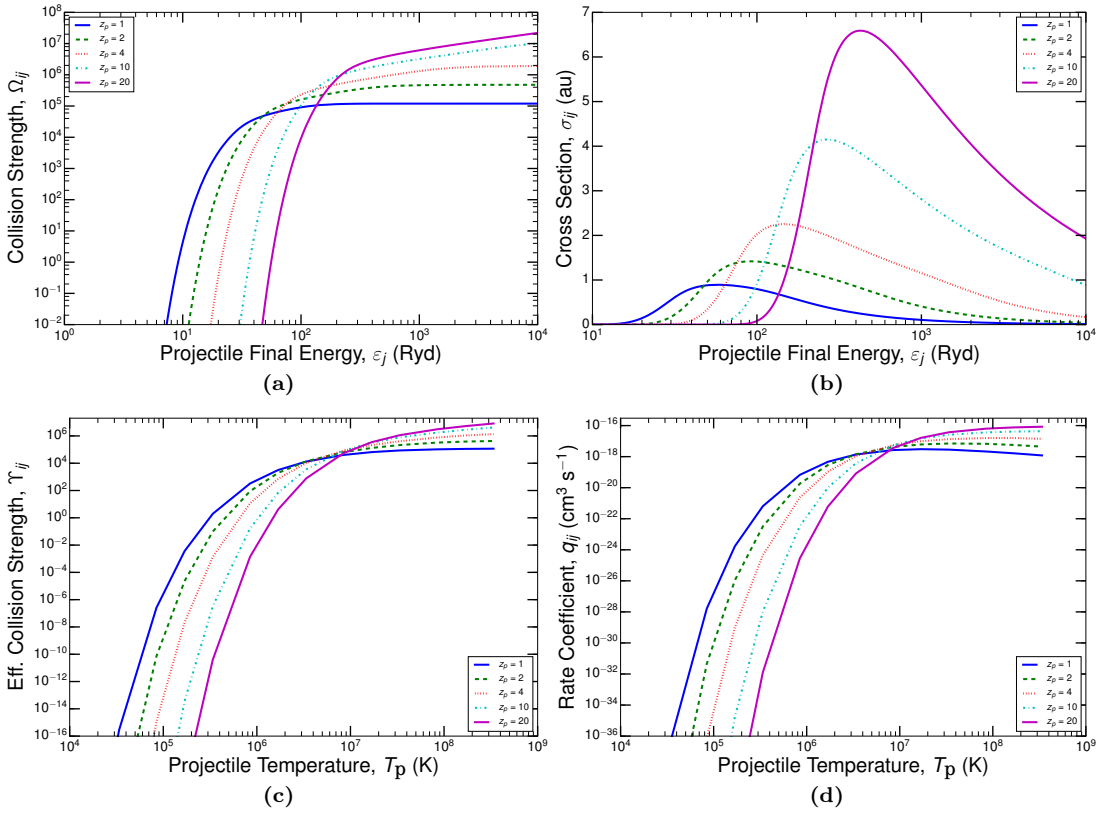

Figure 4.15: Variation of collision quantities with the projectile charge, z_p

projectile mass may approach or even exceed the target mass, allowing for a greater sensitivity to m_t; an example would be impurity species that are excited by ions in the same isonuclear sequence, but concentrations tend to be so low that this is a negligible process. Regardless, the scaling of the collision quantities with m_t should mimic that of m_p, and this is reflected in figure 4.16.

Next, consider the target charge, z_t. Like the projectile charge, it has a linear factor in the expression for ξ, 4.27, meaning increased adiabatic suppression for increased z_t, but in this case there is an additional ${z_t}^{-2}$ factor in equations 4.40 and 4.41. Note that this ${z_t}^{-2}$ factor agrees with the scaling typically quoted for EIE Ω_{ij}. Thus, the suppression of the collision quantities at low energies and temperatures should be quite prominent with increasing z_t, and this is indeed reflected in figure 4.17. Unlike all previous parameters, the infinite energy limit, equation 4.33, does not contain an explicit dependence on z_t; however, the line strength, S_{ij}, inherently depends upon z_t, and it is present in equation 4.33. Because S_{ij} is another input parameter that is explored in the following and, for

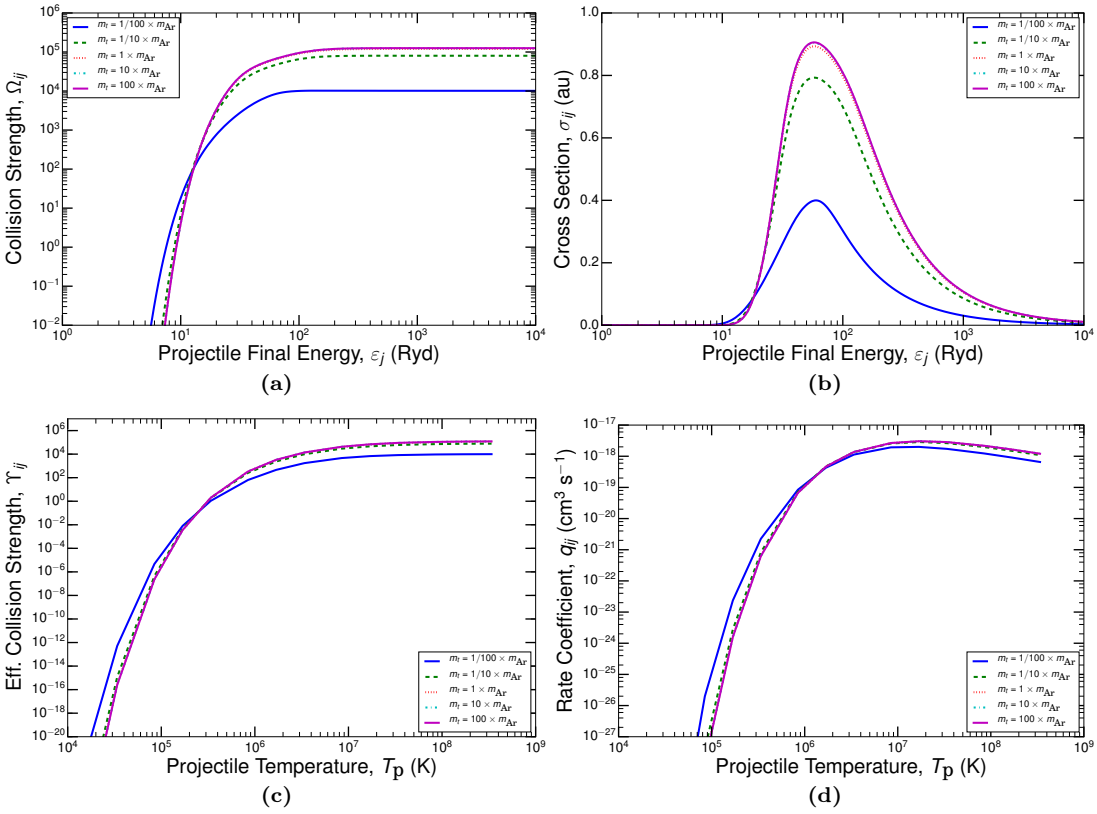

Figure 4.16: Variation of collision quantities with the target mass, m_t

the sake of simplicity, the indirect variation of $\Omega_{ij}{}^{(\mathrm{inf})}$ with z_t is not considered here. In other words, the covariance of any input parameters is neglected in preference of a purely independent, but artificial, variation of each parameter. Consequently, there will be no variation of the collision quantities with z_t at high energies, and this forced behaviour is visible in each plot of figure 4.17, with all curves converging at high energy or temperature.

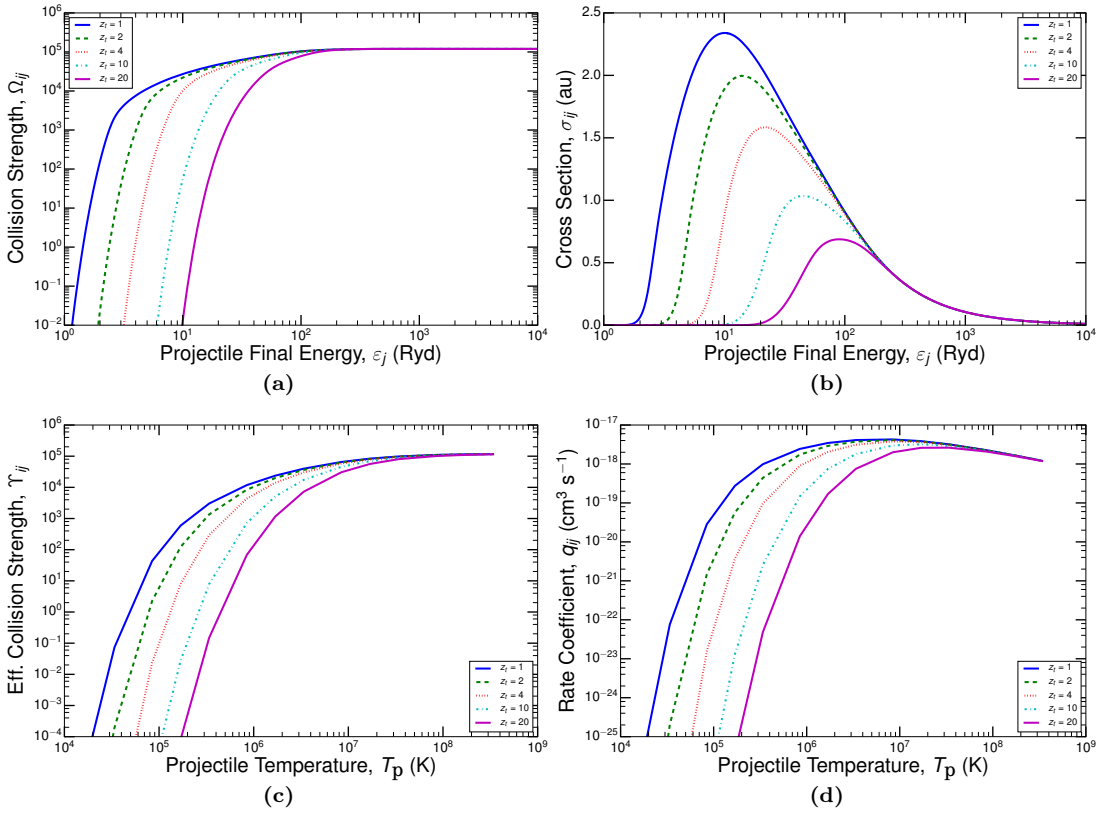

Figure 4.17: Variation of collision quantities with the target charge, z_t

The scaling with transition energy, ΔE_{ij}, is superficially similar to that with z_t. Both have a linear factor in the expression for ξ, leading to the enhanced suppression at low ε_j or T_p, and both have no explicit influence on $\Omega_{ij}{}^{(\mathrm{inf})}$, although once again S_{ij} will indirectly depend on ΔE_{ij}. The similarity of figure 4.18 to figure 4.17 confirms that the `a2irabt` result also abides by these statements. However, one must appreciate that these similarities are mathematically superficial and fortuitous since the physical basis of their influence on the collision quantities is quite different. Take the adiabaticity of the collision: ΔE_{ij} directly determines the atomic frequency and thus the time period of the atomic system,

while z_t influences the transit time of the projectile. Of course, the two are not independent of each other, but that complexity is neglected here. Again, these observations agree with those of WW88 [103] in the vicinity of their figure 12. They explain the relative insensitivity of the cross section peak for the smaller ΔE_{ij}: for $\xi < 0.1$ (i.e.very diabatic transitions achieved with small ΔE_{ij}) $f_{E2}(\xi)$ becomes insensitive to ξ, and thus the transition probabilities tend to converge, leading to similar peaks of the cross sections.

It is worthwhile to note that as $\Delta E_{ij} \to 0$ for $z_t = 0$ (i.e. the excitation of nearly degenerate levels in a neutral atom), the results from `a2iratbt` should approach those from impact-parameter methods and codes that assume straight projectile trajectories and energy-degenerate, l-changing collisions like in references [134–136]. However, comparison is not currently possible because the straight-trajectory codes used in those references address only dipole transitions while `a2iratbt` is restricted to quadrupole.

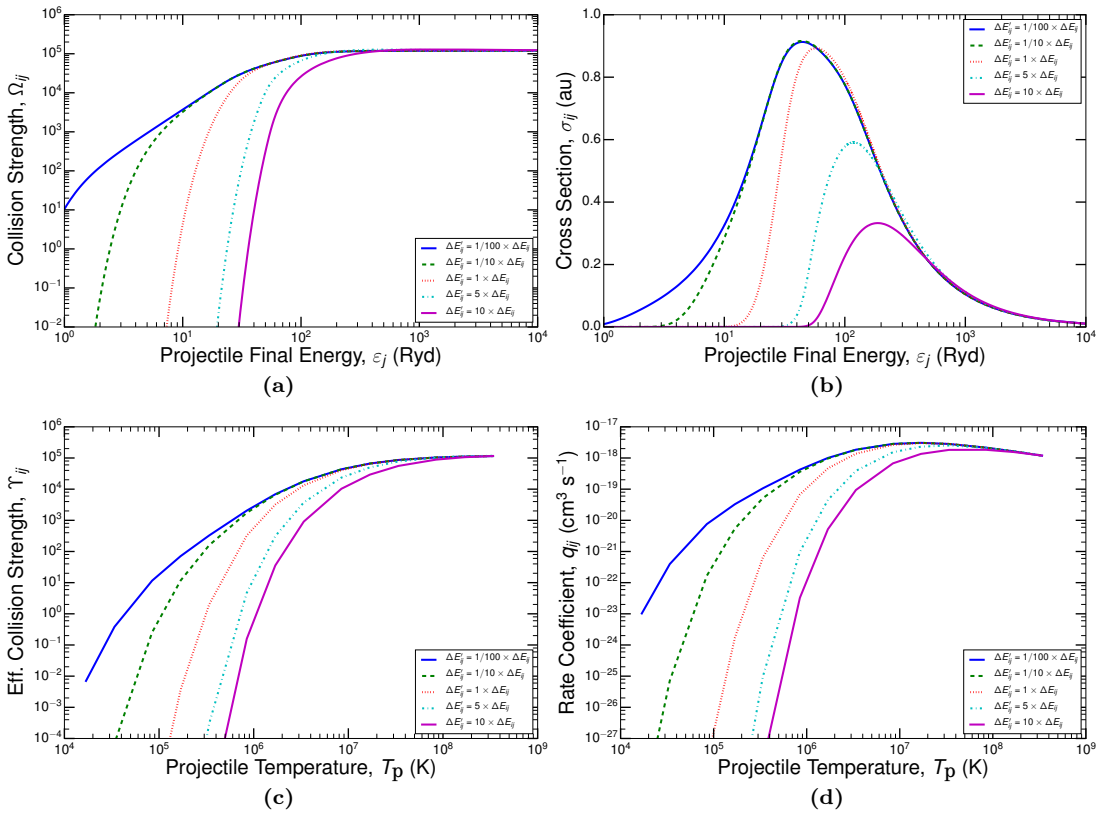

Figure 4.18: Variation of collision quantities with the transition energy, ΔE_{ij}

Finally, there is the atomic transitions probability, $A_{j \to i}$, that is internally

converted to the line strength, S_{ij}. The two are directly proportional to each other if all other parameters are constant, so they can be treated interchangeably here. Equations 4.39–4.41 and that for ${\Omega_{ij}}^{(\mathrm{inf})}$ (4.33) contain a simple linear factor of S_{ij}, and there is no dependence of ξ upon this purely atomic parameter. Therefore, the collision quantities should vary in a positive linear fashion with $A_{j\to i}$ or S_{ij}, uniformly across energy and temperature. Figure 4.19 shows that the `a2iratbt` results reproduce this exact behaviour. An increase of the A-value produces an increase of all the collision quantities, and vice versa for a decrease. The constant of proportionality is not quite unity across the plotted domains, but it does become so at high energies and temperatures.

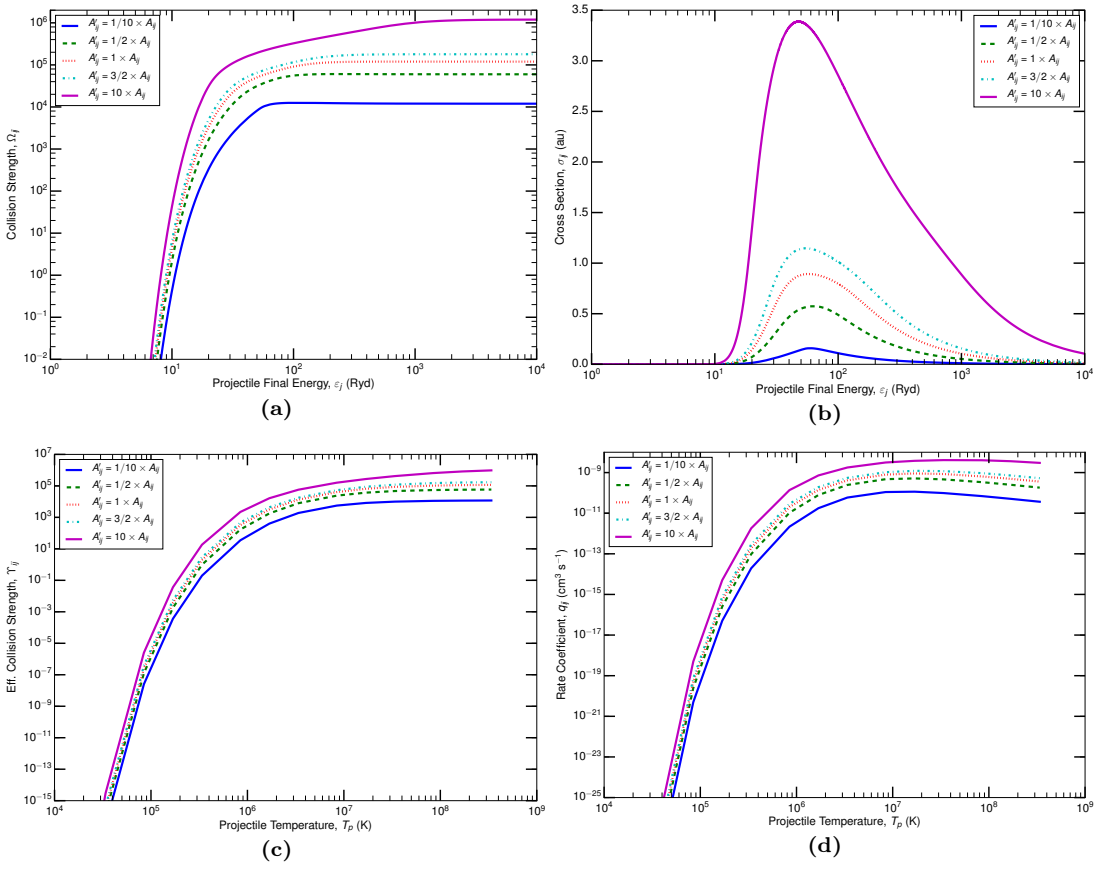

Figure 4.19: Variation of collision quantities with the transition probability, $A_{j\to i}$

4.4.1.4 Technical Parameters

A brief investigation of the technical parameters is merited because they have been introduced to purportedly improve the physical accuracy of the results: this must be proven. It is recalled that two modifications to the pure SC-1 methodology have been introduced according to [92], the details of which are in sections 4.2.1 and 4.3.1. First, in equation 4.42 the first-order perturbative transition probability, $P_{ij}^{(1)}$, is limited by the combination of an upper bound parameter, P_{ub}, and a function, $\phi(x)$. The selection of these parameters is somewhat arbitrary, so there is room for exploration, but any selection should abide by reciprocity conditions (i.e. the time reversed transition probability should be numerically the same). This effectively fixes P_{ub} to the definition adopted in equation 4.32 because of an additional advantage that $P_{ij}^{(2)}$ becomes the mean of the statistical weights for strongly coupled transitions, as would be physically expected (see neighbouring comments of that equation). Therefore, $\phi(x)$ will be considered as the changeable parameter, and a number of possible cases are explored here:

$$\phi(x) = \begin{cases} \tanh(2x)/2 & \text{if Case 1,} \\ \min(x, 1/2) & \text{if Case 2,} \\ \frac{x}{(1+x/4)^2} & \text{if Case 3,} \\ \sin^2(\sqrt{x}) & \text{if Case 4,} \\ x & \text{if Case 5.} \end{cases} \tag{4.50}$$

These all have physical justifications. Case 2 is the form selected in the pioneering work of Seaton on the impact-parameter method [89, 90]; the reasoning is that $P_{ij}^{(1)}$ becomes increasingly unreliable as it approaches unity, and 1/2 is a fairly conservative point at which to cut off and stop trusting values any higher. Although this sounds fairly crude, it produces remarkable agreement with most fully-quantal results as was seen in section 4.2.4. Case 1 is basically a smoothed out version of Case 2, and it is the default selection for the `a2iratbt` code. Cases 3 and 4 are obtained by generalizing from a simple two-state, close-coupled transition matrix, the details of which can be found in section 5 of [92]. Case 3 was originally used by Bely and Faucher [93], and both cases yield similar re-

sults. Lastly, Case 5 sets $P_{ij}^{(2)} = P_{ij}^{(1)}$, lifting any restrictions on the transition probability used.

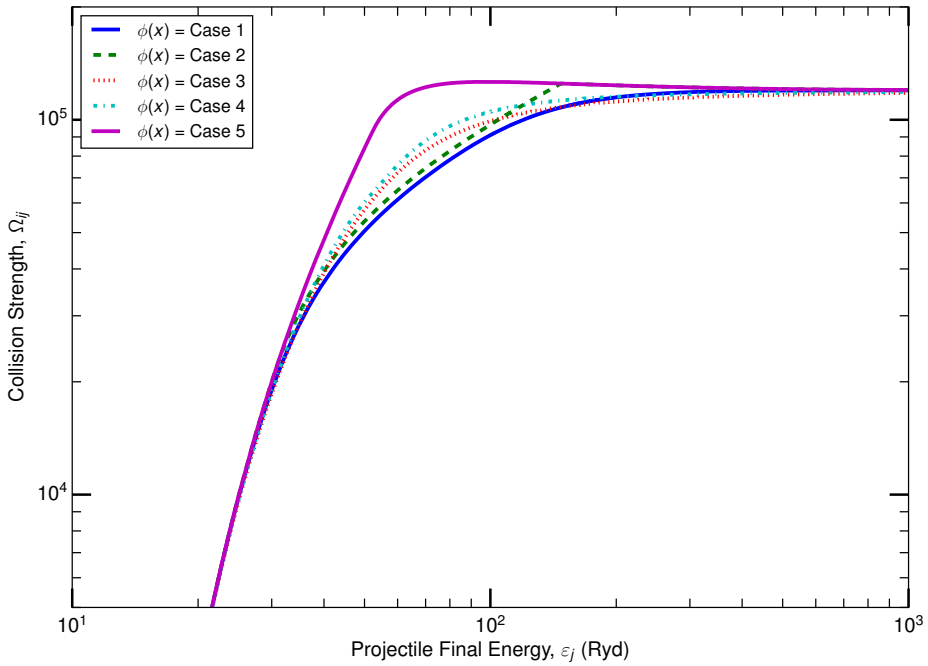

Figure 4.20: Variation of Ω_{ij} with the selection of different $\phi(x)$ limiting functions.

All of these cases have been plotted for the base example of B-like Ar^{13+} in figure 4.20. The greatest deviation between the cases is observed at intermediate energies where it is to be expected. At these intermediate energies, perturbation theory begins to break down for most atomic systems, but the energies are not so high that projectile trajectories impinge upon the atom itself, meaning the effective target radius safeguard is not yet involved. Indeed, this energy regime was the motivation for a curtailment of $P_{ij}^{(1)}$ in the first place, and so it is no surprise that a change of how this restriction is applied via $\phi(x)$ will cause the most variation here. Convergence at high ε_j is guaranteed by the consideration of the effective target radius, r_0, that is still used here via equation 4.44, and convergence at low energies is ensured by the fact that the weak coupling assumption holds, leading to $\phi(P_{ij}^{(1)}/P_{\text{ub}}) \sim P_{ij}^{(1)}/P_{\text{ub}}$ as $P_{ij}^{(1)} \to 0$. Cases 1–4 are more tightly grouped together, although Case 2 exhibits a strange kinked behaviour at higher ε_j and aligns with Case 5 right before all of the Ω_{ij} converge. This is likely a result of the kinked nature of the $\phi(x)$ function itself for Case 2, but further investigation is warranted. However, the salient observation from figure 4.20 is

that Case 5 overestimates Ω_{ij} at intermediate energies because $P_{ij}^{(2)} = P_{ij}^{(1)}$ and $P_{ij}^{(1)}$ is an overestimate.

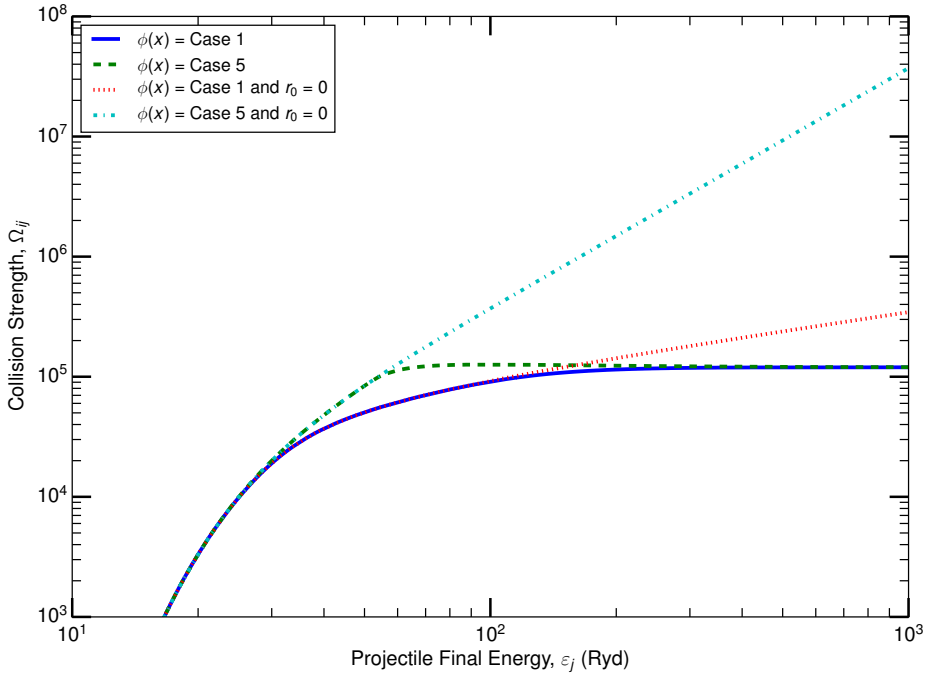

Figure 4.21: Variation of Ω_{ij} with the neglect of the effective target radius, r_0.

Secondly, an effective target radius, r_0, was introduced to avoid the blow up of the long-range potential involved in calculating $P_{ij}^{(1)}$, equation 4.35. This becomes relevant at high ε_j where a substantial number of trajectories are able to penetrate the boundary of the atom. Section 6(i) and (ii) in reference [92] show that if no cutoff is introduced in the integral equation that determines Ω_{ij} (cf. equation 4.44), then the collision strength will diverge as ε_j^2 if $P_{ij}^{(1)}$ is used directly or $\varepsilon_j^{1/2}$ if $P_{ij}^{(2)}$ is used. These divergences at varying powers of ε_j are observed in figure 4.21 for Cases 1 and 5 of $\phi(x)$. Recall that Case 5 corresponds to using $P_{ij}^{(1)}$ directly, and hence why this case displays the quicker ε_j^2 divergence compared to Case 1 where $P_{ij}^{(2)}$ somewhat mitigates the breakdown. The effect of neglecting any cutoff is replicated by setting $r_0 = 0$ within the code.[8]

[8]The setting of $r_0 = 0$ must be done internally because it is not an input parameter. r_0 is instead determined from equation 4.33, so ${\Omega_{ij}}^{(\mathrm{inf})}$, along with the other input parameters, will determine the effective target radius.

4.4.2 IIE Data for Argon

The correct operation of the `a2iratbt` code has now been well justified through comparisons with the literature in section 4.2 and the parameter variation studies immediately above. Its first application will be to provide the IIE rate coefficients needed for the *ic*-resolved GCR modelling of argon in Chapter 5. Although there is IIE collision data for a fair number of argon ions in the literature, the coverage is not complete, which once again highlights the need for the present `a2iratbt` baseline. To further validate the baseline data, some comparisons with literature sources of the IIE of argon ions are provided below. Unless otherwise stated, the `a2iratbt` calculation uses atomic data produced by AUTOS, and the relevant quantities can be found in *adf06* files in the ADAS database.

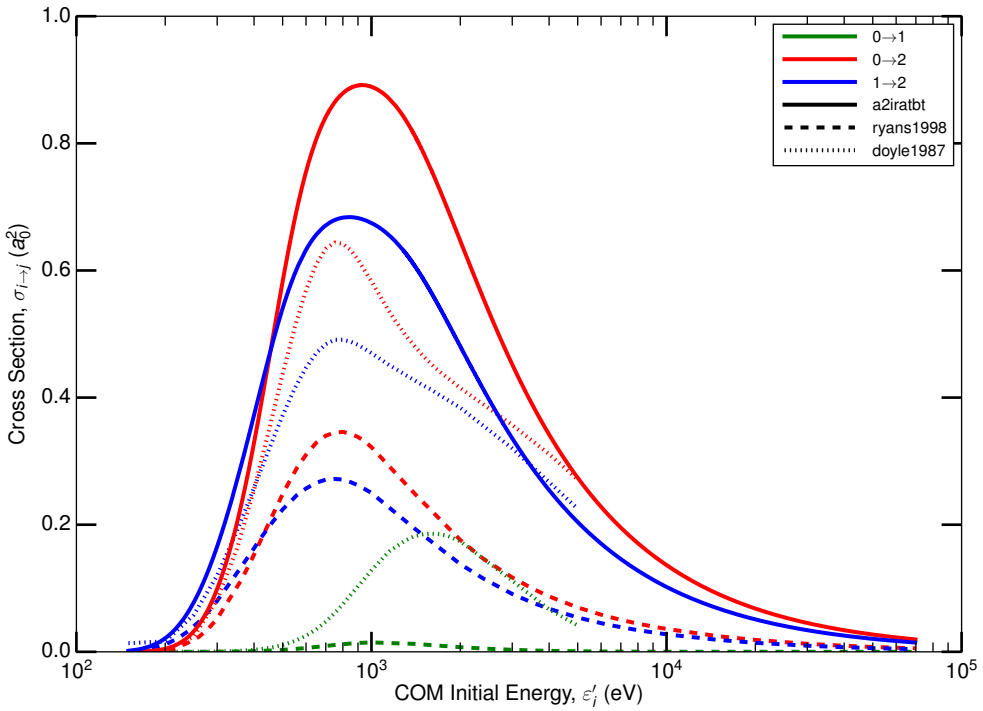

Figure 4.22: Proton-impact excitation cross sections for transitions within the 2s2p ^{3}P term of Be-like Ar^{14+}. The line colours specify the relevant fine-structure transition according to the legend, where the notation $J \to J'$ corresponds to the transition $^3P_J \to {}^3P_{J'}$. Recall that `a2iratbt` cannot calculate results for the $0 \to 1$ transition because it proceeds entirely through CC channels and is therefore forbidden under first-order perturbation theory. The line styles give the source of the calculation, again according to the legend. *a2iratbt* denotes the present ADAS baseline implementation of the `a2iratbt` code, a SC-1 method; *ryans1998* is the SC-CC calculation from reference [119]; and *doyle1987* is the SC-CC calculation from reference [110].

Be-like Ar^{14+} provides an interesting but also archetypal case of IIE collision

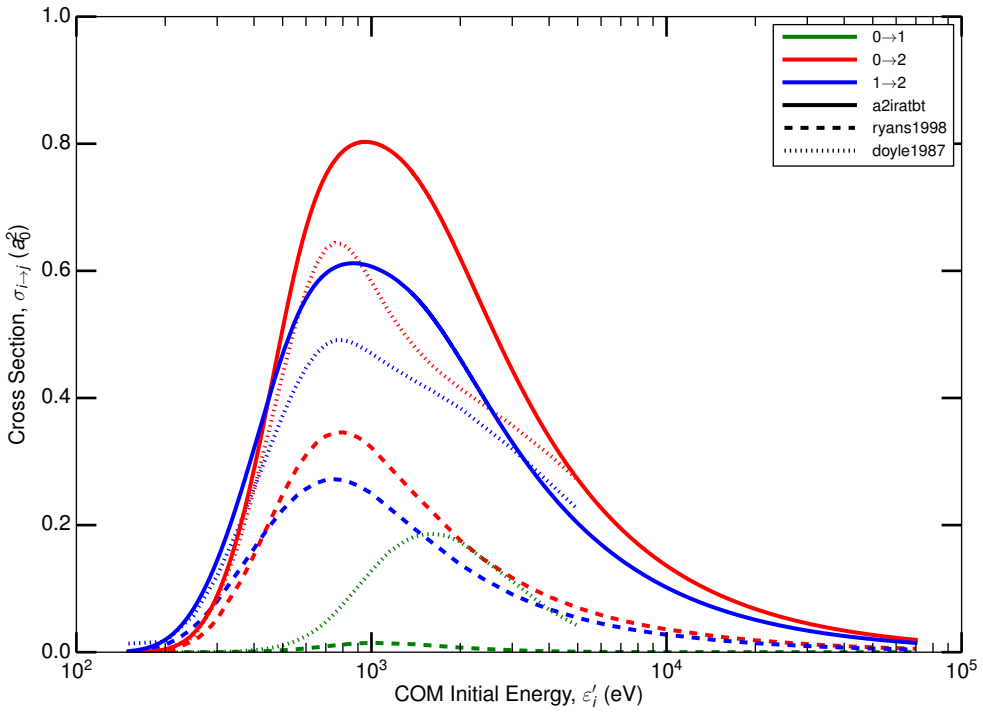

Figure 4.23: Proton-impact excitation cross sections for transitions within the 2s2p ^{3}P term of Be-like Ar^{14+}. The line colours specify the relevant fine-structure transition according to the legend, where the notation $J \to J'$ corresponds to the transition $^3P_J \to {}^3P_{J'}$. Recall that `a2iratbt` cannot calculate results for the $0 \to 1$ transition because it proceeds entirely through CC channels and is therefore forbidden under first-order perturbation theory. The line styles give the source of the calculation, again according to the legend. *a2iratbt* denotes the present ADAS baseline implementation of the `a2iratbt` code, a SC-1 method; the atomic data used as input has been matched to the other literature calculations in this plot in contrast to figure 4.22. *ryans1998* is the SC-CC calculation from reference [119], and *doyle1987* is the SC-CC calculation from reference [110].

data. Cross sections for proton and α-particle impact are presented in figures 4.22 and 4.24, respectively. At face value, the disagreement is quite large between all three calculations presented. The SC-1 `a2iratbt` results exceed the SC-CC *ryans1998* results by a factor of two or more and are greater than the SC-CC *doyle1987* results by about 40% relative to the latter. However, the two SC-CC results disagree with each other by about 50% relative to *ryans1998*, and even more so for the $J : 0 \to 1$ transition. This discrepancy was discussed in section 4.2.4 in the context of the polarisation correction, since it is the only significant difference between the two SC-CC calculations. There is sufficient doubt surrounding the *ryans1998* result that its disagreement with the other two results can be safely couched for the moment. Diving further into the disagreement between

the `a2iratbt` and *doyle1997* results, the first port of call is always the atomic data input to the codes. The `a2iratbt` calculation uses ${S_{ij}}^{(2)} = 5.495 \times 10^{-3}$ for the $0 \rightarrow 2$ transition, which agrees quite well with a NIST MCDF calculation[9], while the *doyle1987* calculation uses a $\langle r^2 \rangle_{2\mathrm{p}}$ value in forming the matrix elements that would result in ${S_{ij}}^{(2)} = 4.641 \times 10^{-3}$. A $\sim 20\%$ reduction of the line strength causes the `a2iratbt` cross sections to be reduced by the same proportion, which can be observed in figure 4.23, and brings this result into much closer agreement with *doyle1987*. The remaining 20% disagreement is attributable to the neglect of close coupling in the SC-1 `a2iratbt` result and is acceptable for baseline purposes. It is a similar story for the $1 \rightarrow 2$ transition along with the rate coefficients in figure 4.25. On a tangential note, the α-impact cross sections for `a2iratbt` increase by a factor of three compared to proton-impact (figure 4.24 versus 4.22), while the *ryans1998* result does not even achieve a factor of two increase. Given the extensive parameter variation study of section 4.4.1, it is contended that the scaling of the `a2iratbt` result is more substantiated and thus trustworthy, further fuelling doubt in the *ryans1998* result and other recent descendants of the RS69 [108] code that include a polarisation correction.

Next, consider the adjacent ion, B-like Ar^{13+}, and the associated IIE cross sections in figure 4.26. Perhaps surprisingly, the disagreement between the SC-1 `a2iratbt` calculation and the SC-CC *foster1997* calculation, which does include a polarisation correction, is not nearly as bad as seen for Be-like Ar^{14+}. The error of the proton-impact cross sections is 50% relative to the *foster1997* result, increasing to 55% for the α-impact cross sections. This marginally better agreement is caused by less CC flux losses in this doublet transition and the atomic data input for each calculation agreeing to a larger degree—only 10% variation in the line strength is seen. However, the still fairly substantial size of the disagreement is somewhat dubious given the previous discussion about suspected errors in the polarisation correction; moreover, the α-impact cross section for *foster1997* has a somewhat strange shape that does not bolster confidence in their technique.

Switching now to some comparisons with an SC-CC method of slightly different heritage, the SC-1 proton-impact cross sections from `a2iratbt` are compared against those from the SC-CC method of Landman (*landman1979*) for Mg-like

[9] `https://nlte.nist.gov/MCHF/Elements/Ar/Be_18.40.MCDHF-ai-lin.dat.mp`

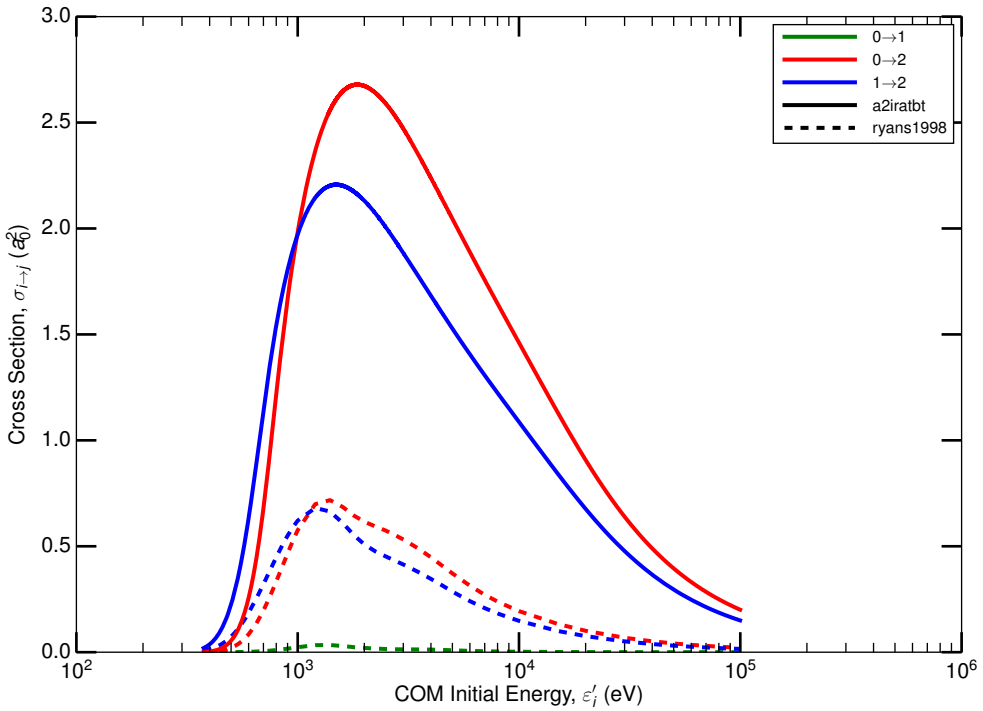

Figure 4.24: α-impact excitation cross sections for transitions within the 2s2p ^{3}P term of Be-like Ar^{14+}. The line colours specify the relevant fine-structure transition according to the legend, where the notation $J \to J'$ corresponds to the transition $^3P_J \to {}^3P_{J'}$. Recall that `a2iratbt` cannot calculate results for the $0 \to 1$ transition because it proceeds entirely through CC channels and is therefore forbidden under first-order perturbation theory. The line styles give the source of the calculation, again according to the legend. *a2iratbt* denotes the present ADAS baseline implementation of the `a2iratbt` code, a SC-1 method; *ryans1998* is the SC-CC calculation from reference [119].

Ar^{6+} in figure 4.27. The agreement is not particularly good: 50% and 40% reductions relative to the `a2iratbt` result are observed for the $0 \to 2$ and $1 \to 2$ transitions, respectively. Yet again, ensuring consistent atomic data input is essential: the wave functions used by *landman1979* come from reference [128], as with a few other literature sources above, and they produce a line strength that is about 20% lower than that used for the `a2iratbt` calculation. Correspondingly, the `a2iratbt` calculation will be reduced by approximately 20% if the lower line strength value is used, and this places both results within a more reasonable degree of error for the baseline. Because this is a triplet system, it is expected the remaining discrepancy is caused by CC effects.

Finally, take S-like Ar^{2+} in figure 4.28, for which the literature source is again an SC-CC calculation in the Landman heritage. Disagreement between the two

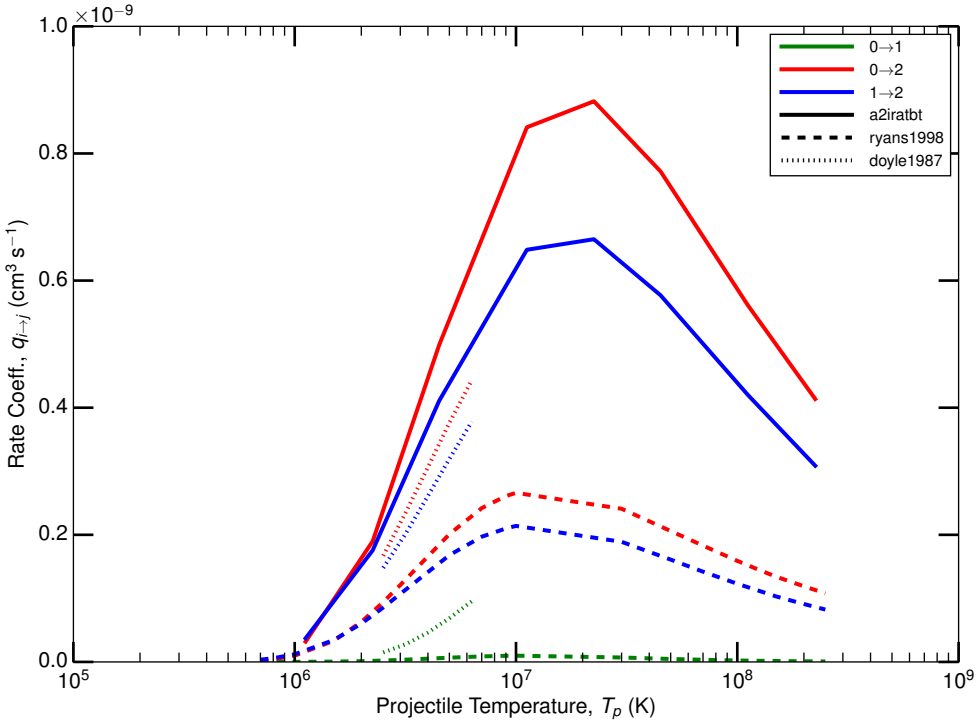

Figure 4.25: Proton-impact excitation rate coefficients for transitions within the 2s2p ^{3}P term of Be-like Ar^{14+}. The line colours specify the relevant fine-structure transition according to the legend, where the notation $J \to J'$ corresponds to the transition $^3P_J \to {}^3P_{J'}$. Recall that `a2iratbt` cannot calculate results for the $0 \to 1$ transition because it proceeds entirely through CC channels and is therefore forbidden under first-order perturbation theory. The line styles give the source of the calculation, again according to the legend. *a2iratbt* denotes the present ADAS baseline `a2iratbt` code, a SC-1 method; *ryans1998* is the SC-CC calculation from reference [119]; and *doyle1987* is the SC-CC calculation from reference [110]. The temperature range for *doyle1987* is quite limited because the calculation focussed on an astrophysical regime of interest.

calculations is similar to that for Mg-like and unsurprising since both deal with transitions in ^{3}P terms. Note that the ordering of the J levels in this triplet is inverted relative to the others in this section. A 30% reduction relative to the SC-1 `a2iratbt` result is observed for the $2 \to 1$ transition, and 50% for the $2 \to 0$ transition, in keeping with the increased close coupling this transition will have to the $1 \to 0$ transition. Again, the alignment of the atomic data input does much to reconcile these disparities. Although *landman1980* [124] does not quote the line strength or $\langle r^2 \rangle$ value used, it is indicated that the wave functions from reference [128] have again been used. In every other instance, these wave functions produced line strengths that underestimated by approximately 20% those produced by AUTOS for the `a2iratbt` calculation. Therefore, a 20% reduction of

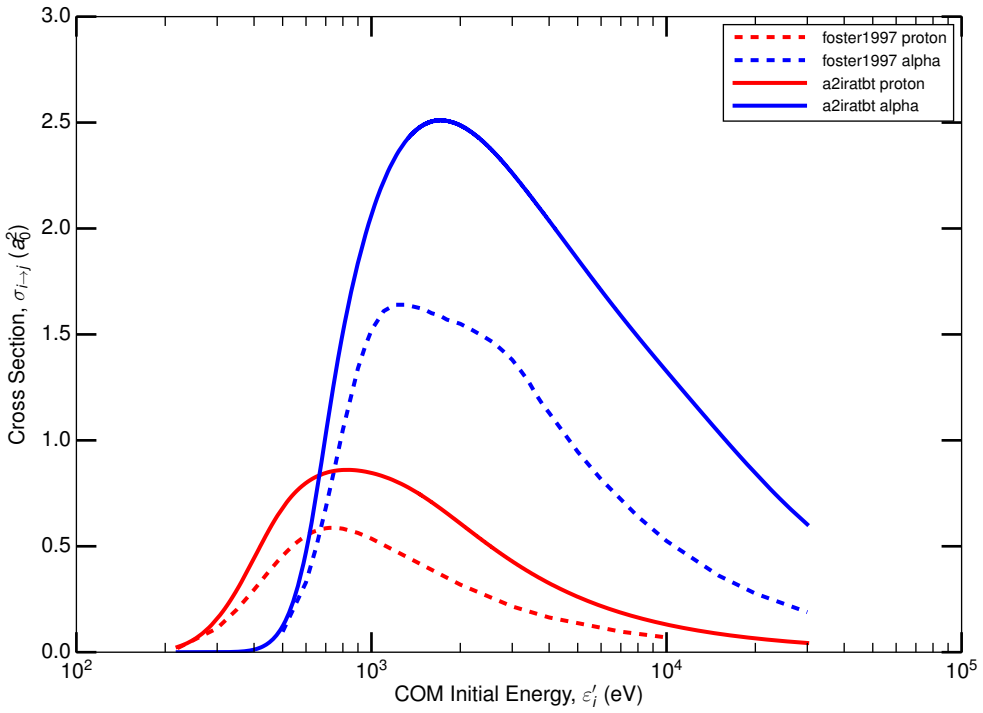

Figure 4.26: Proton and α-impact excitation cross sections for the $2s^2 2p\ ^2P_{1/2} \rightarrow\ ^2P_{3/2}$ transition of B-like Ar^{13+}. The line colours specify the ion projectile: red for protons and blue for α particle. The line styles give the source of the calculation according to the legend. *a2iratbt* denotes the present ADAS baseline `a2iratbt` code, a SC-1 method. *foster1997* is the SC-CC calculation from reference [118].

the `a2iratbt` cross sections should result from using the same line strength as the *landman1980* calculation, bringing the SC-1 results into an acceptable error margin with the SC-CC results.

Overall, the SC-1 `a2iratbt` results tend to overestimate the cross section and rate coefficient of $E2$-allowed transitions compared to SC-CC results in the literature. This is to be expected given the two-state assumption and neglect of CC implicit to the SC-1 method, as explained at length in section 4.2.4. However, some of this overestimate is attributable to a systematic difference between atomic line strengths produced by AUTOS and those used in the SC-CC calculations. All of the AUTOS line strengths assessed here were larger than the values used in the SC-CC calculations, and in two cases—Be-like Ar^{14+} and Al-like Fe^{13+}—comparison with higher-quality NIST results showed that the AUTOS result was closer. Because many of the SC-CC calculations source atomic data from similar sources, it is likely these collision results are actually underestimates because the

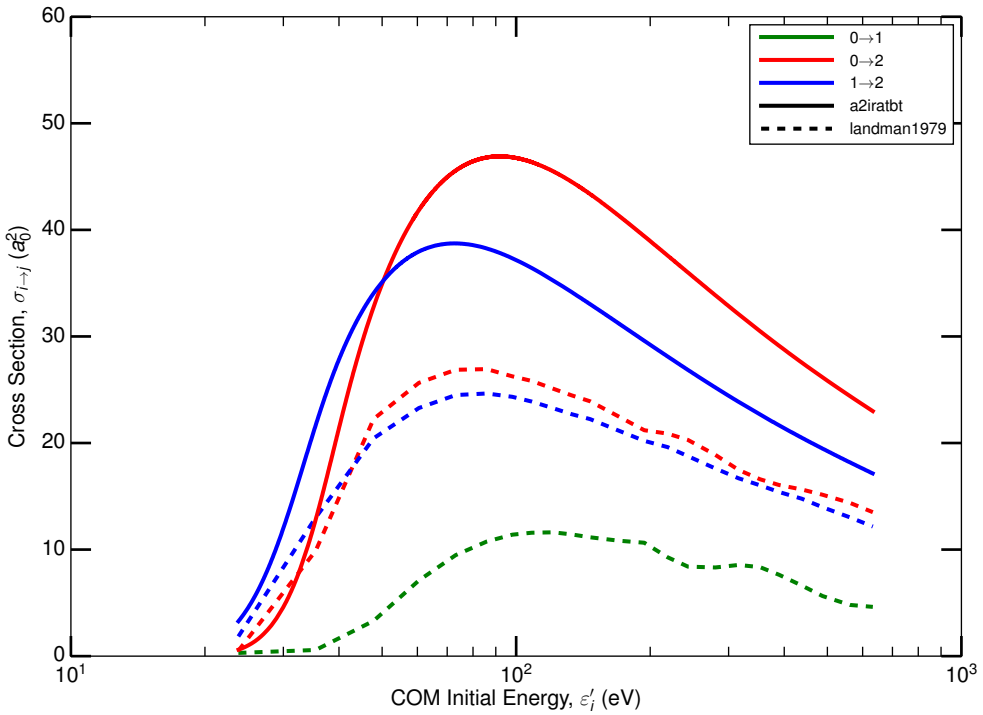

Figure 4.27: Proton-impact excitation cross sections for the transitions within the 3s3p ^{3}P term of Mg-like Ar^{6+}. The line colours specify the relevant fine-structure transition according to the legend, where the notation $J \to J'$ corresponds to the transition $^3P_J \to {}^3P_{J'}$. Recall that `a2iratbt` cannot calculate results for the $0 \to 1$ transition because it proceeds entirely through CC channels and is therefore forbidden under first-order perturbation theory. The line styles give the source of the calculation, again according to the legend. *a2iratbt* denotes the present ADAS baseline `a2iratbt` code, a SC-1 method. *landman1979* is the SC-CC calculation from reference [123].

atomic data seems to be underestimated. But further investigation is required to establish whether the underestimated line strengths constitute a systemic trend throughout the SC-CC results. This also misses the salient point: one must always correct for the atomic data when comparing collision calculations, and once this was done with the ions analysed here, the SC-1 data produced errors relative to the SC-CC data well within the limits for a baseline. What can be said is that the "true" collision data will lie somewhere between the SC-1 `a2iratbt` baseline data and the SC-CC literature results. Where these literature results exist, an easily quantifiable error region can be established and appropriately handled by ADAS routines and data structures; however, the details are outside the present scope. In the end, it can firmly be concluded that the `a2iratbt` baseline is suitable for widespread use in ADAS and also for the specific task of

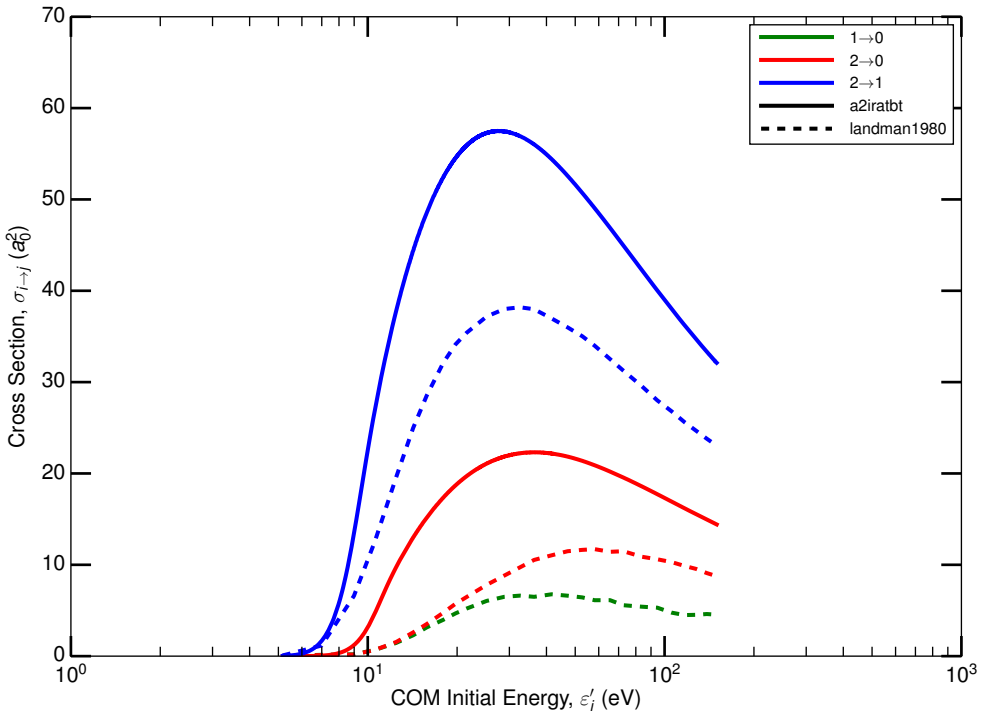

Figure 4.28: Proton-impact excitation cross sections for the transitions within the $3s^2 3p^4\ ^3P$ term of S-like Ar^{2+}. The line colours specify the relevant fine-structure transition according to the legend, where the notation $J \to J'$ corresponds to the transition $^3P_J \to\ ^3P_{J'}$. Notice that the level ordering is inverted compared to the other ^3P terms investigated, with $^3P_2$ now the ground level. Recall that `a2iratbt` cannot calculate results for the $1 \to 0$ transition because it proceeds entirely through CC channels and is therefore forbidden under first-order perturbation theory.The line styles give the source of the calculation, again according to the legend. *a2iratbt* denotes the present ADAS baseline `a2iratbt` code, a SC-1 method. *landman1980* is the SC-CC calculation from reference [124].

ic-resolved GCR modelling of argon ahead.

Chapter 5

Prototyping *ic*-Resolved GCR Modelling with Argon

5.1 Introduction

The need for *ic*-resolved GCR modelling was motivated in Chapter 1, and the requisite machinery to practically demonstrate the effects of this finer resolution is described here. Preceding chapters have laid the foundation. Chapter 3 showcased one of the prominent techniques for producing high-quality EIE collision data for heavy species and the specialist considerations required therein. Chapter 4 introduced the SC-1 method for calculating IIE collision data, which will be needed to accurately model fine-structure levels that deviate from statistical balance. And Chapter 2 established an enhanced fundamental atomic data baseline that will be integral in modelling heavy species, for which high-quality data is invariably patchy in coverage. Now these pieces must be assembled.

Prototype machinery for the *ic*-resolved GCR model is constructed as a fully functional first cut at the problem, but also serves to uncover any issues for a future, more complete implementation. The following section 5.1.1 substantiates why argon is a fitting case study and test bed, and section 5.1.2 introduces the time-saving approximations made when implementing GCR modelling in *ic* resolution.

5.1.1 Argon Case Study

First and foremost, argon (Ar) is a ripe testing ground for GCR modelling because it is suspected to be the lowest Z_0 element ($Z_0 = 18$) that can no longer be considered a light species. The qualifier "light" is being used here as defined in section 1.1: to classify low-Z_0 species for which LS coupling yields accurate atomic populations in GCR modelling. Argon lies close to the boundary between light and medium species, so deviations from statistical balance of fine structure levels within LS terms should be apparent. This hypothesis can be formed because of the fairly substantial residual charges that are possible with a Z_0 of 18; for example, Be-like Ar^{14+} in figure 5.15 exhibits a clear CR regime, and the separation of its fine-structure levels in the ^{3}P metastable term should lead to violations of statistical balance. Ultimately, the truly appropriate resolution for argon can only be determined by comparing the GCR modelling results at different resolutions.

Second, argon is an element that is relevant to both laboratory and astrophysical plasmas. For instance, in future fusion burning devices like ITER and DEMO, the seeding of impurity species will be necessary to produce sufficient radiative cooling so that divertor heat loads are within acceptable regimes [13], while at the same time not compromising the power balance of the core. Argon is a candidate for such a purpose that has been and is being used on current devices like JET and ASDEX-U [137–139], so there is immediate demand for fundamental and derived atomic data required to model the radiative cooling by argon. It will be the objective of this chapter and case study to provide an improved estimate of the argon cooling curve through the novel approach of *ic*-GCR.

In solar astrophysics, several argon lines will be observed by the SPICE spectrometer on the future Solar Orbiter mission [140, 141]. These lines will be used to derive the composition and First Ionisation Potential (FIP) maps in the solar upper atmospheres that will be connected to the particle composition at the spacecraft, derived from in situ measurements. Linking these two types of measurements across spatial domains is important for tracking coronal mass ejections and the solar wind as they travel towards Earth. Moreover, argon lamps are used for the ground calibration of SPICE and other solar spectrometers, with lines from near-neutral stages recorded. Both of these tasks will benefit from an *ic*-resolved

version of the GCR model.

Third, argon does not lie much above silicon, which is the heaviest element to have been given the full GCR treatment prior to the current work [60]. Since fundamental atomic data is typically generated along isoelectronic sequences, the sources for DR and electron-impact ionisation data used in silicon GCR can almost wholly be used for argon up to Si-like. It then remains to cover the four ionisation stages from P-like Ar^{3+} to neutral argon. Introductory remarks on fundamental data are presented in 5.1.3, and some further details for each isonuclear ion are provided in Appendix B.

One criterion for which argon slightly misses the mark is relativistic effects; a Z_0 of 18 is simply not large enough for the atomic structure to show large discrepancies [31]. Thus, a test of the influence of relativistic corrections or even a fully relativistic approach in GCR modelling will not be possible. But the other conclusions from Chapter 3 are still pertinent: high-quality R-matrix EIE data with carefully selected configuration interactions are needed for all GCR efforts. Comparisons with the baseline data from Chapter 2 can substantiate this claim while simultaneously giving an estimate of the baseline error. A limited investigation on this point is done in section 5.4.3.

5.1.2 GCR Theory and Approximations

The extension to LSJ/ic-resolved GCR is built directly upon the metastable LS-term resolved GCR methodology detailed by Summers et al. [16] and Giunta [60], and the reader is referred to these sources for the fundamentals of GCR modelling framework. More generally, the reader is referred to the ADAS manual [15] for details about any ADAS routines or file formats mentioned henceforth. A brief synopsis of terminology and relevant equations is provided in Appendix C. The purpose of this section is to briefly identify the main theoretical and practical *modifications* needed to extend LS-resolved GCR modelling (henceforth LS-GCR) to LSJ/ic-resolved GCR (henceforth ic-GCR). In keeping with a prototype, the modifications described in this section involve a number of approximations. In particular, the primary prototyping approximation is to split LS-resolved quantities onto the respective ic-resolved manifold using the statistical weights of the relevant terms and levels; of course, this is only necessary when J-resolved data

is unavailable or a particular code would require a substantial overhaul to achieve J resolution.

The modifications and approximations for each component of this *ic*-GCR prototype are as follows.

5.1.2.1 Low-lying Ordinary and Metastable Levels

The lowly-excited ordinary and metastable levels of an atom constitute the elementary unit of population modelling in plasmas, and so a set of isonuclear *adf04* data files are required when modelling the ionisation balance or cooling curve of a particular element. Evidently, the coupling resolution of these files must match the resolution of the intended GCR modelling, and there is no modification needed in this instance because the *adf04* format already handles LSJ/ic atomic data. Availability of this data, then, is ostensibly the only issue, and the state of affairs for argon, *ic*-resolved *adf04* data is discussed in section 5.1.3.1.

However, there is an additional, subtle problem relating to the handling and identification of metastables in these *adf04* files. Whereas the energy order of LS metastables for isoelectronic sequences ranging over the light elements is fairly uniform and fixed, this cannot be said about medium and heavy element classes. Firstly, the fanning of fine-structure levels leads to the possibility that levels from one term can become interspersed with levels from another, and this will vary depending on Z_0 and N, the number of electrons. Secondly, even though the energies of fine-structure levels within a term tend to be positively correlated with J, this is not always guaranteed and negative correlations can arise. Consequently, the identification and matching of metastables in *adf04* and other relevant file types must be more flexible and robust under *ic* conditions. The heavy-lifting in this case is done by ADAS807.

Additionally, there is an implicit assumption being made in the above that all fine-structure levels of a metastable term will themselves be metastable and that all metastable levels belong to a corresponding metastable term: this is likely not true. The question was already explored for the different case of *ca* versus *ic* resolution in the Metastable Optimisation discussion of section 2.3.1.1. There it was concluded that a metastable configuration must contain at least one metastable level, but certainly not all levels in a metastable configuration are

guaranteed to be metastables themselves nor will all metastable levels necessarily derive from a metastable configuration. So, there are definite discrepancies in the parameter space, and there is no reason this would not also apply to the metastables when comparing *ca* versus *LS* or *LS* versus *ic*. It is unlikely that metastable levels unrelated to a metastable term or configuration will arise for argon, because it was noted earlier that this tends to happen for high-J levels resulting from d and f shell promotions of a closed shell or subshell configuration. In the end, the only way to make definitive conclusions about metastability in both *ic* and *LS* resolution is to actually carry out the population modelling and look at the behaviour of the various state populations. This is done for *LS* in section 5.2.2 and for *ic* in section 5.3.2.

5.1.2.2 Ionisation

In general, the dominant ionising process between adjacent isonuclear ions is the direct, electron-impact ionisation from the daughter metastables, X_{σ}^{z+}, to the parent metastables, $X_{\nu}^{(z+1)+}$: $S_{\sigma\rightarrow\nu}^{(\mathrm{direct})}$. Therefore, *ic* metastable-resolved ionisation data is required, but unlike the case of *adf04* data, very few such theoretical calculations exist owing to the increased complexity of the problem. Such data is not widely available at *LS*-term resolution, so this is a problem common to both forms of GCR modelling. One approximate solution in *LS* resolution was proposed by Summers and Hooper [142] and is based on creating fractionation formulae using the semi-empirical equation of Burgess and Chidichimo [143]. The formulae can then be normalised to higher-quality *ca* ionisation rates, and the procedure has been automated in ADAS as described by [60]. In other words, a less sophisticated technique is used to determine the splitting ratios (i.e. fractionation) that produce resolved ionisation rates from unresolved ones. Then, these splitting ratios are applied to the unresolved ionisation rates obtained from a more sophisticated technique. A detailed discussion of the merits of this particular approximation are outside of the current scope, and this topic is handled at length in reference [60].

Although this method could in principle be extended to *ic* resolution, the gain in accuracy is questionable. The fractionation approach is already a crude approximation at *LS* resolution, and so the error on rates will be larger than any

marginal improvement in accuracy by extending to *ic*.

As a result, it is advantageous to statistically split the *LS*-resolved ionisation rates onto the *ic* manifold for the present case study:

$$S^{(\mathrm{direct})}_{L_\sigma S_\sigma J_\sigma \to L_\nu S_\nu J_\nu} = \frac{2J_\nu + 1}{(2L_\nu + 1)(2S_\nu + 1)} S^{(\mathrm{direct})}_{L_\sigma S_\sigma \to L_\nu S_\nu}. \tag{5.1}$$

Here, $(2L_\nu+1)(2S_\nu+1) = \sum_{J_\nu \in L_\nu \oplus S_\nu}(2J_\nu+1)$ is the total statistical weight of the final term. This formula equally applies to other asymmetric collision quantities, like the cross-section; however, symmetric quantities like Ω_{ij} and Υ_{ij} require an additional, analogous fraction for the initial level and term on the right-hand side of 5.1. A new IDL procedure within ADAS, `stat_split_adf07.pro`, has been written to perform this splitting of *LS*-resolved rates stored in the *adf07* format.

Although the metastable-to-metastable ionisation described above is essential for calculating a metastable-resolved ionisation balance, it is also necessary to consider ionisation from the ordinary daughter levels, X_i^{z+}, to the parent metastables, $X_\nu^{(z+1)+}$: $S^{(\mathrm{direct})}_{i\to\nu}$. These rates are needed for determining the *quasi-static equilibrium* of the excited states through loss terms, and they contribute stepwise components to the direct ionisation from the metastables. Presently for *LS*-GCR, these rates adopt the Exchange Classical Impact Parameter (ECIP) procedure from [144], which is most appropriate for Rydberg states. As above, this is an approximation for *LS*-resolved rates, so again is most prudent and expeditious to statistically split these rates according to equation 5.1. The implementation is quite different in this case and enacted through modifications within ADAS807.

5.1.2.3 Recombination

As with ionisation of the lowly-excited states, *ic* resolution of recombination rates is required, going from the recombining parent, J_p levels to both the ordinary and metastable levels of the recombined daughter. Unlike ionisation though, there are two physical processes that contribute to the overall phenomenon of recombination: DR and radiative recombination (RR). Whereas RR only really contributes to transitions terminating in the lowly-excited states, DR is involved in both these transitions and the populating of highly-excited and collisional

redistributed levels that are encompassed by the bundle-n calculation. Therefore, DR is also mentioned in the context of section 5.1.2.4.

DR data is stored in the *adf09* format, and like the *adf04* format, it already accommodates *ic*-resolved parents and daughters. The standard *adf09* file contains final, recombined daughter states in both resolved (LS or ic) and Rydberg (n) forms. The former is evidently needed for the inclusion of DR rates in the low level set population model, while the latter constitutes an important supplement to the bundle-n population model. Fortunately, this standard data is already available up to the Al-like recombining sequence, but above this the calculation becomes unwieldy, and another approach must be adopted. For this argon case study, bespoke DR data has been generated for the Si-like to Cl-like recombining sequences, the details of which are provided in section 5.1.3.3. The sources of the standard file data up to Al-like is also given in that section.

Although RR data is available in *ic*-resolved *adf48* files up to Al-like as a byproduct of the DR project [145], the inclusion of these files in the GCR workflow has not been streamlined. So, RR data is generated using ADAS211, which only operates in LS. The RR rates in ADAS211 are calculated using bound-free Gaunt factors, and in principle, these expressions can be extended to any resolution including *ic*. However, as the ADAS manual notes [15], resolution to LSJ is likely over precise. Thus, the practice of statistically splitting the LS-resolved RR rates is applied here as well. This is similar to the splitting of the ionisation rates, but now the splitting fraction involves the daughter (recombined) level and term weights (index i) as opposed to the parent (recombining) weights (index ν), because recombination is in the reverse direction, and it is the final state that determines these splitting factors. So, equation 5.1 becomes

$$\alpha^{\mathrm{rr}}_{\mathrm{zd},L_\nu S_\nu J_\nu \to L_\sigma S_\sigma J_\sigma} = \frac{2J_\sigma + 1}{(2L_\sigma + 1)(2S_\sigma + 1)} \alpha^{\mathrm{rr}}_{\mathrm{zd},L_\nu S_\nu \to L_\sigma S_\sigma}, \tag{5.2}$$

where strictly speaking the index, σ, only applies to daughter metastables but here extends to any lowly-excited daughter state. In practice, this splitting operation is implemented in a less direct manner through ADAS807 and its automated creation of template *adf08* files that drive the ADAS211 calculation.

5.1.2.4 Bundle-n Population Calculation

The preceding sections have addressed the population model of the highly-resolved, low level set and the implications of moving to *ic* resolution, and now it remains to extend this to the population model of the highly-excited but low-resolution states and their influence via condensation and projection. Because the parent states are now in *ic* resolution, these highly-excited states should now take the form, $(\gamma_p J_p)n$, i.e. a Rydberg electron built upon a J-resolved core, where γ_p is a unique index for levels of the same J within or between terms. This is the true bundle-n model, and in many ways it is simpler than the bundle-nS model selected for LS-GCR. However, there is a practical problem: the code that handles this high level population model, ADAS204, can only perform the bundle-nS style calculation. The move to a bundle-n calculation is an undertaking that is outside the scope of this case study and thesis, but it will be a central feature of any future upgrade to *ic*-GCR—cf. section 6.1.

Once again, the solution involves the statistical splitting of LS-resolved quantities. ADAS204 will still be used to produce a projection matrix in bundle-nS form, which can then be used in the low-level population model. Under LS-GCR, the mapping of this projection data onto the LS manifold is done with n-shell normalised weights and fractional parentage coefficients, and it is fairly trivial to further split these statistically. The n-shell normalised weight for a particular daughter term, i, which is part of the spin system, S, built upon the parent, $\nu \equiv L_p S_p$, is given by

$$\omega_{L_i,\nu,nS} = \frac{2L_i + 1}{\sum_{j\in\{\nu\cap nS\}} 2L_j + 1}, \tag{5.3}$$

where $\{\nu \cap nS\}$ denotes the set of all terms belonging to the nS bundle built upon the parent ν. The *ic* analogue is obtained by simply substituting L_i with J_i:

$$\omega_{J_i,\nu,nS} = \frac{2J_i + 1}{\sum_{j\in\{\nu\cap nS\}} 2J_j + 1}. \tag{5.4}$$

The second component of splitting the projection matrices is the fractional parentage coefficients, which measure what fraction of a spin system is allocated

to a particular metastable parent, ν. In LS, these coefficients are given by

$$F_{L_pS_p,S} = \frac{2S_p + 1}{\sum_{\rho\in\{S\cap\nu'\}} 2S_\rho + 1}, \tag{5.5}$$

where $\{S\cap\nu'\}$ denotes the set of all parent terms that connect to the recombined spin system, S. And the *ic* coefficients easily follow:

$$F_{L_pS_pJ_p,S} = \frac{2J_p + 1}{(2L_p + 1)(2S_p + 1)} F_{L_pS_p,S}. \tag{5.6}$$

All of these quantities are stored in the cross-referencing file subclass *adf18/-a17_p208*, and little modification is necessary to store the *ic* versions. The automated creation of these files by ADAS807 is where the equations above are implemented, and so this is a modification that was made to this portion of the GCR workflow.

5.1.2.5 IIE

Finally, the most novel aspect of the new ADAS machinery needed for *ic*-GCR is that related to the proper consideration of ion-impact excitation (IIE). As noted already in sections 4.1.1, ion projectiles are most likely to influence transitions with relatively small energy differences ($\Delta E_{ij} \ll \chi^{(z)}$), such as quadrupole transitions amongst fine-structure levels of metastables terms or the dipole transitions that assist in l redistribution of the highly-excited $(\gamma_p J_p)n$ states. Chapter 4 provided the requisite details behind the production of IIE rates for electric quadrupole transitions and an extensive analysis of their underlying behaviour along with comparison to the literature. Only the quadrupole transitions have been addressed because these are most likely to impact the population model.

Practically, there are two ways that IIE rates could be added to the GCR workflow. First and most obviously, since IIE Υ_{ij}'s are the same collision quantity as the EIE Υ_{ij}'s that are stored in *adf04* files, it seems natural to also include this IIE data in these files. In fact, such functionality already exists for proton-impact excitation through P-lines. These are identical to the lines holding EIE Υ_{ij}'s except prepended by a 'P': the differentiation is necessary because the driving population of proton-impact excitation is obviously protons (N_p) rather than

electrons (N_e), and so the pre-multiplier will be different for each case. However, the inclusion of P-lines has not been extended to the code that actually conducts the advanced population model in GCR, ADAS208, and the functionality is limited to only proton projectiles—each ion projectile requires a separate density specification.

Rather, there is an alternate and more economical route to the inclusion of IIE rates. A careful analysis of the system of linear population equations reveals that the only GCR coefficient where transitions amongst metastable levels arise is the effective metastable cross-coupling coefficient (Q^{cd}):

$$Q^{cd}_{\sigma\to\rho} = \left(C_{\rho\sigma} - C_{\rho j}C^{-1}_{ji}C_{i\sigma}\right)/N_e, \tag{5.7}$$

where $C_{\rho\sigma} = A_{\sigma\to\rho} + N_e q^{(e)}_{\sigma\to\rho} + N_i q^{(i)}_{\sigma\to\rho}$ for $\rho \neq \sigma$ and $A_{\sigma\to\rho} = 0$ for $\rho > \sigma$—refer to Appendix C for the derivation of the Q^{cd}. None of the other CR matrix elements in equation 5.7 contain the intra-metastable, IIE rate coefficient, $q^{(i)}_{\sigma\to\rho}$, so this contribution can easily be separated from the rest of the expression for which the collisional processes are only EIE:

$$Q^{cd}_{\sigma\to\rho} = Q^{cd}_{\sigma\to\rho}{}^{(e)} + \sum_i \frac{N_i}{N_e} q^{(i)}_{\sigma\to\rho}, \tag{5.8}$$

where an explicit sum has now been included over the possible ion colliders. Put simply, the contribution of intra-metastable IIE transitions can be incorporated as a simple supplement to the Q^{cd}, after the primary population calculation is executed. A new ADAS IDL procedure, `supp_qcd_iie.pro`, has been created to implement this post-processing step, pulling in the IIE rates from the appropriate *adf06* files and using a user specified mix of ion projectiles.

5.1.3 Fundamental Data for GCR

The accuracy of GCR modelling, like any form of modelling, depends strongly on the quality of the data input. Discussion at the beginning of Chapter 2 addressed the important point that the quality of the data should be tailored to the accuracy required by the application. The purpose of GCR modelling is to produce the most complete and accurate description of an atomic element under

dynamic plasma conditions, such that applications to spectroscopy are possible and the highest quality ionisation balance is produced. Consequently, the best quality atomic data must be sought from all possible sources, experimental or theoretical. There is an additional criterion for the present goal of achieving *ic*-GCR: fundamental data is required in both *LS* and *ic* resolution, and there must be a consistency between the two (e.g. the same configuration sets should be used in producing the datasets). This will allow for the effects of resolution upon the population model to be unambiguously isolated and identified when making comparisons—all other variables are fixed.

It is no small task to collect the complete set of fundamental data needed for GCR modelling, but the use of centralised databases is of great assistance. Indeed, a central purposes of ADAS is to assemble the highest quality atomic data from a range of sources for precisely this type of modelling. Most of the data for argon used herein was already present in the ADAS database and so in an immediately (or nearly) useable format for the analysis computer programs. However, there are invariably gaps along an isonuclear sequence perhaps because there is a delay incorporating new sources into the database or more likely the data simply does not exist. Argon is no different. A complete literature search for all ions of an element is essential, but if there is still a deficient data class for an ion, then the missing data must be generated following a baseline calculation methodology, like that for *adf04* data in Chapter 2.

Four classes of fundamental atomic data are required for *ic*-GCR and three for *LS*-GCR, each associated with an ADAS data format:

1. Energy levels, radiative transition probabilities (A-values), and effective collision strengths (Υ_{ij}) associated with the low-lying, highly-resolved (*LS* or *ic*) level set—*adf04* data

2. Metastable-resolved, zero-density ionisation rate coefficients—*adf07* data

3. Parent-metastable and final-state resolved, zero-density DR rate coefficients—*adf09* data

4. Fine-structure resolved, IIE rate coefficients for *ic*-GCR—*adf06* data

Each data class is separately addressed in the subsections that follow. Also, the

primary source of a particular datum is cited, where practical, in preference to the database in which it is found.

5.1.3.1 Energy Levels, A-values, and Effective Collision Strengths—*adf04*

The collection and pre-processing of the quantities that constitute the *adf04* data is the most painstaking stage of atomic population modelling because even though all of the data may be present in the database, the highest quality version of each component is rarely in one file. Energy levels in theoretical collision calculations are not shifted to experimental values as a rule, so mapping and merging to the NIST *adf04* stubs must be done; orbital energies needed for the bundle-n calculation are rarely provided, so a complementary COWAN run must be performed to provide these; filtering and stricter formatting must also be enforced; etc. Moreover, self-consistent files in both LS and ic resolution need to be obtained, but from the perspective of collision calculations, such results are almost never presented. To cope with this limitation, the strategy adopted herein is to acquire an *adf04* file from a high-quality, ic-resolved collision calculation where possible, supplement it as above, and then use ADAS routines to bundle this file to LS resolution, ensuring the desired consistency between the different resolution files. More detailed steps of this pre-processing are given in Appendix B, and the original sources that have been spliced are listed in table 5.1. Some broad observations about each sub-class are possible from this table.

Energy Levels The gold standard for energy levels values come from experimental studies, and shifting to these values is essential for line identification in spectroscopy. The largest resource of experimental and high-quality theoretical energy levels is the NIST Atomic Spectra Database (ASD), for which *adf04* stubs[1] already exist. Table 5.1 shows that the database has taken nearly all of the energy levels for argon ions from a single primary source, Saloman [146]. This source is itself a compilation of many experimental and some theoretical results, as indicated in column four of table 5.1, and the reader is referred to it for any further details on an individual ion basis. Naturally, these compiled values still do not

[1]These stubs contain level information only; no transition data is included.

Table 5.1: The sources of *adf04* data used for the GCR modelling of argon in this case study. Unless otherwise stated, the resolution of the files is LSJ/ic, which is then bundled to LS as explained in the text. The fractions in the "Coverage" column give the number of NIST levels that have been matched to the theoretical levels of the collision calculation in the numerator and the total number of levels in the final *adf04* in the denominator. Some levels in the original *adf04* from the collision calculation had to be removed because of being over the ionisation potential or because of the restriction of $n < 6$ for the population calculation; these cases are indicated by †.

		***adf04* sources**				
Seq.	**Ion**	**Energy Levels**	**Type**	**Coverage**	**Υ Values**	**Type**
H	17+	Saloman [146]	theor.	complete	Ludlow et al. [147]	BP R-matrix
He	16+	"	theor.	27/31 (4f)	Whiteford et al. [148]	ICFT R-matrix
Li	15+	"	exp.	18/24 (4f, 5f, 5g)	Liang and Badnell [149]	ICFT R-matrix
Be	14+	"	exp.	16/166 †	Fernández-Menchero et al. [49]	ICFT R-matrix
B	13+	"	exp.	27/204	Liang et al. [48]	ICFT R-matrix
C	12+	"	exp.	34/198	Ludlow et al. [147]	BP R-matrix
N	11+	"	exp.	41/186	Ludlow et al. [147]	BP R-matrix
O	10+	"	exp.	38/228	Ludlow et al. [147]	BP R-matrix
F	9+	"	exp.	68/195	Witthoeft et al. [46]	ICFT R-matrix
Ne	8+	"	exp.	89/131 †	Liang and Badnell [47]	ICFT R-matrix
Na	7+	"	exp.	complete †	Liang et al. [150]	ICFT R-matrix
Mg	6+	"	exp.	68/206 †	Fernández-Menchero et al. [50]	ICFT R-matrix
Al	5+	"	exp.	41/155	Ludlow et al. [147]	BP R-matrix
Si	4+	"	exp.	45/203 †	Ludlow et al. [147]	BP R-matrix
P	3+	"	exp.	57/181	Ludlow et al. [147]	BP R-matrix
S	2+	"	exp.	124/174 †	Munoz Burgos et al. [151]	ICFT R-matrix
Cl	1+	"	exp.	95/143 †	Griffin et al.(2007) [152] *new*	LS RMPS ic, λ_{nl} opt DW
Ar	0+	NIST sources [127]	mix	complete	Arnold et al. [153]	BP RMPS

provide complete coverage of all the levels present in the corresponding collision calculations, which can be observed from the fractions given in column five. But, by the very fact these levels are not present in experimental studies, they are likely unimportant from a spectroscopic perspective, so any loss of accuracy is presumed negligible.

***A*-values** Similar to energy levels, experimental results for the A-values are desirable, and the NIST ASD is once again a valuable resource. However, the data for transition probabilities tend to be much more scarce and possess far greater uncertainties. From H-like Ar^{17+} to Na-like Ar^{7+}, A-value data is nearly non-existent in the database, and even until singly-ionised argon, the coverage is quite patchy. The preponderance of these experimental values carry a C and D quality rating, loosely representing a 25% and 50% uncertainty, respectively. Consequently, the preference within ADAS is for a consistent set of data from a reliable structure code—this principle loosely applies to all sparse data types that ADAS collects. A spot-check of theoretical values from the collision calculations of table 5.1 showed that these values all agreed within measurement uncertainty

of the C and D quality NIST A-values. Furthermore, no ADAS routine currently exists to automatically merge these external A-values nor is there an ADAS data format to hold them. A possible route forward would be to add the A-values to the already existing NIST *adf04* stubs and concurrently extend the *adf04* merging program in offline ADAS, ADAS7#5, so that it can merge the A-values from the stub into the transition lines of the collision calculation *adf04* with which the stub is presumably being merged. It was deemed that the benefit of merging these A-values into the collision data for the argon ions up to S-like Ar^{2+} was marginal and far outweighed by the additional effort to do so. The default A-values from the theoretical collision calculations are used for all of these ions in this study.

On the other hand, ArI and ArII must be treated as special cases because the spectra of these species have been extensively studied and, consequently, more reliable experimental data exists. In particular, NIST hosts a subset of its database in what is called the "Handbook of Basic Atomic Spectroscopic Data", which provides the most persistent and spectroscopically important lines of neutral and singly-ionised elements [154]. Comparing these A-values to those from the collision calculations cited in column 5 of table 5.1, it was found that the two sources differed by an average relative error of $\approx 42\%$. This was deemed significant enough to warrant manually merging the NIST database values into the *adf04* files of ArI and ArII.

Effective Collision Strengths GCR modelling requires excitation rate coefficients over a wide range of temperatures[2], so correspondingly the cross sections or collision strengths are needed over a large range of energies to facilitate the Maxwellian convolution. Furthermore, excitation rates are needed for as many transitions amongst levels in the low-lying set (i.e. those in the *adf04*) as selection rules will allow. These requirements prove infeasible for experiments to fulfill: measurements of cross sections can typically only be made over a limited energy range and for a few transitions within an ionic system [155–157]. Therefore, experimental results are most valuable for validating theoretical results that

[2]A wide temperature range is not necessarily needed so that the model itself is applicable over a more sweeping parameter space (although indeed this helps), but more precisely because it assists with extrapolation and interpolation of the coefficients for smooth operation of the various codes.

supply the Υ_{ij}'s used in the GCR models.

The theoretical collision data for all argon ions are cited in column six of table 5.1. These are almost uniformly R-matrix method calculations in *ic* resolution, considered high quality (level 1 or 2) data within ADAS based on the classifications of table 2.2 in section 2.2. There are two classes of R-matrix calculations for argon: Breit-Pauli (BP) and intermediate coupling frame transformation (ICFT). The BP type uses a level-resolved basis set with corresponding Breit-Pauli Hamiltonian, and carries this resolution through the entire machinery of the R-matrix method. This is the most complete form of semi-relativistic R-matrix calculation possible, but as a result it can become intractable because of large Hamiltonian matrices that must be diagonalised.[3] In response to this limitation, the intermediate coupling frame transformation (ICFT) approach to R-matrix calculations was developed [158]. It works by forming the unphysical scattering K-matrix in LS coupling, which is less expensive computationally, and then transforms these matrices into intermediate coupling (*ic*). Despite being an approximation relative to the BP type, ICFT R-matrix calculations achieve remarkable fidelity, especially when compared to other transformation methods that proceed directly through the *physical* K and S matrices. Depending on the assiduity of the producer, ICFT results can achieve somewhere above baseline quality and just below the highest quality.

5.1.3.2 Ionisation Rate Coefficients—*adf07*

It was already noted in section 5.1.2.2 that the most important contribution to ionisation is the direct rates between metastables of adjacent stages but that such data is effectively non-existent in the literature. This naturally led to the strategy outlined therein to split unresolved ionisation data to the required resolution. Unresolved rates themselves are available from a variety of theoretical and experimental sources or a mix thereof through semi-empirical formulae. For argon, unresolved rate coefficients are taken from [159]: this work is both a comprehensive review of available unresolved ionisation data and a presentation of new theoretical calculations to fill in any gaps. Its primary methodology is to

[3]However, with advances in High Performance Computing, this restriction is nowadays less of a issue.

compare the available measured cross sections along an isoelectronic sequence with the corresponding theoretical results from FAC [160] to assess their accuracy and appropriateness. These comparisons are facilitated by a novel scaling law, similar in many respects to Burgess and Tully's for excitation [84], that conveniently compresses the energy and cross section axes, causing the cross section to tend towards a limiting function at high z along an isoelectronic sequence; this in turn enables parameterized fits of the cross sections. The FAC calculation uses the Coulomb-Born-exchange approximation of a relativistic DW approach for the direct ionisation and includes excitation-autoionisation contributions by explicitly calculating excitation and autoionisation rates also in the relativistic DW approach. The spline fits are then made in two manners:

1. For neutral and singly-ionised species, the FAC calculation tends to be less accurate, while measurements are naturally smoothed out; therefore, spline fits are made to the scaled, experimentally measured cross sections.

2. For the remainder of ions, the calculated cross sections—FAC or otherwise—are more accurate, while measurements tend to be more erratic; therefore, spline fits are made to the scaled, theoretical cross sections, which are validated against the measured ones.

Finally, rate coefficients are obtained through the usual Maxwellian convolution and then formatted to the *adf07* standard.

5.1.3.3 DR Rate Coefficients—*adf09*

The changes to the production of DR rates for both LS and ic-resolved GCR have already been outlined in section 5.1.2.3 and [161]. These modifications required a collaborative effort over many years and published articles, of which [161] is the introduction to the series and its methodology. AUTOS is the computer code underpinning the DR project, and it implements the independent processes and isolated resonance using distorted waves (IPIRDW) method. The raw autoionisation and radiative rates are mostly produced by AUTOS, but a post-processing step by ADASDR (ADAS702 in ADAS) to supplement radiative transitions between highly-excited Rydberg states and create the partial rates is needed. In addition, experimentally measured energies are added at the post-processing stage

to ensure accurate positioning of the resonances, a requisite condition for the correct low-temperature behaviour of the recombination rates.

The output from the codes is stored in a version of the *adf09* file format tailored specifically to the new requirements of finite density population modelling: partial rates to level (or term) and bundle-n resolved final states, the summed total rates, and the important recombining parent are stored. Separate files are produced for different "core excitations" of the recombining parent. For example, consider a possible dielectronic capture to the Li-like ground state:

$$1s^2 2s[^2S_{1/2}] + e^- \rightarrow 1s^2 3l[^2L_J]nl'. \tag{5.9}$$

This would be classified as a $n = 2 \rightarrow n' = 3$ core excitation because the 2s electron of the parent target was excited to a $3l$ in the intermediate resonance on the right, which would then radiatively stabilise to complete the DR process. The individual source of the *adf09* DR data for each argon ionisation stage up to P-like Ar^{3+} is given in table 5.2 along with the available core excitations that are considered.

Below the Al-like recombining sequence towards neutral, no DR project datasets are available because of the increasing size of the data produced as more atomic electrons are added. Although recent calculations of *ic* and *LS* parent-resolved DR rate coefficients have been published for these particular argon ions [177], these are *totals* and so not resolved by final states, as required for GCR modelling.

In the absence of appropriate DR data for these ionisation stages, a strategy was devised that involves partitioning the problem into two parts, resulting in two separate *adf09* files. First, the Tungsten DR project has created an accelerated and compacted "hybrid" variant of AUTOS for DR, which retains ic/LS resolution of initial parent and final *core* states but *ca* and *ry* resolution for the outer electron. The resulting *adf09* data are reduced in size but retain the representative n-shell rates, so they are compatible as the supplement to the ADAS204 bundle-nS population calculation. They are denoted as "hybrid" in table 5.2. The configuration sets and *adf27* driver file templates for the production of this new data are also taken from the Tungsten DR Project [162]. Both hybrid and standard files were produced by that work, but only the ground state was considered

Table 5.2: The sources of argon *adf09* data used for the GCR modelling in this case study. Unless otherwise indicated, the DR data are available in both *LS* and *ic* resolution. The core excitations are given in the format n–n', where n is the principal quantum number of one of the parent core electrons and n' is that electrons principal quantum number in the intermediate resonance (more details in the text). The core excitations marked with ⋆ are cases where the *adf09* data had to be regenerated so that the representative n-shell grids matched between files; the same driver *adf27* files are used but for this minor tweak. The new MOM17 calculations are described in the text: configuration sets and *adf27* driver files of [162] are used.

		***adf09* Information**		
Recombining	**Recombined**	**Type**	**Source**	**Core excitations**
H-like Ar^{17+}	He-like Ar^{16+}	standard	Badnell (2006) [163]	1–2
He-like Ar^{16+}	Li-like Ar^{15+}	"	Bautista and Badnell (2007) [164]	1–2, 2–2, 2–3
Li-like Ar^{15+}	Be-like Ar^{14+}	"	Colgan et al. (2004) [165]	2–2, 2–3
Be-like Ar^{14+}	B-like Ar^{13+}	"	Colgan et al. (2003) [166]	2–2, 2–3
B-like Ar^{13+}	C-like Ar^{12+}	"	Altun et al. (2004) [167]	2–2, 2–3 ⋆
C-like Ar^{12+}	N-like Ar^{11+}	"	Zatsarinny et al. (2004) [168]	2–2, 2–3 ⋆
N-like Ar^{11+}	O-like Ar^{10+}	"	Mitnik and Badnell (2004) [169]	2–2, 2–3 ⋆
O-like Ar^{10+}	F-like Ar^{9+}	"	Zatsarinny et al. (2003) [170]	2–2, 2–3 ⋆
F-like Ar^{9+}	Ne-like Ar^{8+}	"	Zatsarinny et al. (2006) [171]	2–2, 2–3 ⋆
Ne-like Ar^{8+}	Na-like Ar^{7+}	"	Zatsarinny et al. (2004) [172]	2–3
Na-like Ar^{7+}	Mg-like Ar^{6+}	"	Altun et al. (2006) [173]	2–3 ⋆, 3–3, 3–4
Mg-like Ar^{6+}	Al-like Ar^{5+}	"	Altun et al. (2007) [174]	2–3, 3–3, 3–4
Al-like Ar^{5+}	Si-like Ar^{4+}	"	Abdel-Naby et al. (2012) [175]	3–3, 3–4 ⋆
		hybrid	Kaur et al. (2017) [176]	3–3, 3–4
Si-like Ar^{4+}	P-like Ar^{3+}	standard (truncated)	MOM17	3–3, 3–4
		hybrid	MOM17	2–3, 3–3, 3–4, 3–5
P-like Ar^{3+}	S-like Ar^{2+}	standard (truncated)	MOM17	2–3, 3–3, 3–4, 3–5
		hybrid	MOM17	2–3, 3–3, 3–4
S-like Ar^{2+}	Cl-like Ar^{1+}	standard (truncated)	MOM17	2–3, 3–3, 3–4
		hybrid	MOM17	3–3
Cl-like Ar^{1+}	Ar-like Ar^{0+}	standard (truncated)	MOM17	3–3

as a recombining parent. Therefore, the driver files and production scripts have to be modified to cope with multiple metastable parents. There already exists a DR project hybrid file for the Si-like recombining sequence, but otherwise this data must be generated anew.

The second part of generating this low-stage DR data involves the standard variant of AUTOS for DR, described immediately above as part of the DR project. It is executed without looping over the *ca* and *ry* states of the outer, recombining electron that result when a core electron radiates from the intermediate capture state. Thus, only partial rates to the lowly-excited final states are generated, saving computation time; these truncated standard *adf09* files are compatible with the supplementation of recombination rates into the low-lying level set of an *adf04* file (i.e. "R-line" creation), and they are denoted by "standard (truncated)" in table 5.2. Because this technique neglects a whole class of final states, the *total* DR rate coefficients are inaccurate and unsuitable for further use. All novel DR data generated as part of this work is indicated by "MOM17" in the source column of the table.

Since these DR data are novel, some form of validation is needed. A comparison of the *total* DR rate coefficients with those from the literature is presented in figure 5.1. The most sophisticated calculations are ostensibly those from reference [177] mentioned above (ATLAB15 in plot), and results from the *ic* parent-resolved hybrid files of the novel strategy (MOM17 *ic*) compare quite favourably for all ions. Agreement is best at higher temperatures with larger discrepancies apparent at low temperatures, especially for Ar^{3+} and Ar^{4+}. This is to be expected since the effect of resonances is most prominent at low temperature, and the lower resolution of the hybrid files will be deficient in this respect. However, the fractional abundances in figures 5.4 and 5.5 suggest that the most relevant temperatures for these stages will lie outside of these low temperature domains where the DR rate coefficients disagree most. Moreover, it is obvious that the MOM17 *ic* and *LS* results are more accurate than the widely-used data from reference [178] (MMCV98).

5.1.3.4 IIE Rate Coefficients—*adf06*

All relevant details for the production of IIE, $E2$-order rates have already been specified in section 4.3. To summarise, the primary input for an individual ion is contained in an *adf27* driver file for AUTOS, and then the relevant atomic parameters to drive the `a2iratbt` calculation are taken from the output `olg` file. A sample *adf27* used in this study for the IIE rates of an N-like Ar^{11+} target is shown in figure 5.2. The configuration sets and λ_{nl} parameters (last line of figure) for all of the argon ions are the same as those used in the optimisation work of section 2.3.2. Because only transitions between metastable levels are needed, the *adf06* output is truncated compared to the full *adf04* output that results from the configuration sets above. For this work, the truncation was performed based on where the last level belonging to an *LS* metastable term is located, with the metastable *LS* terms being taken from the current standard ADAS list—see table 5.4. The limitations of this list and further discussion about *ic* metastables is contained in sections 5.2.2 and 5.3.2. The unique λ_{nl} values for the argon isonuclear sequence are provided in table 5.3.

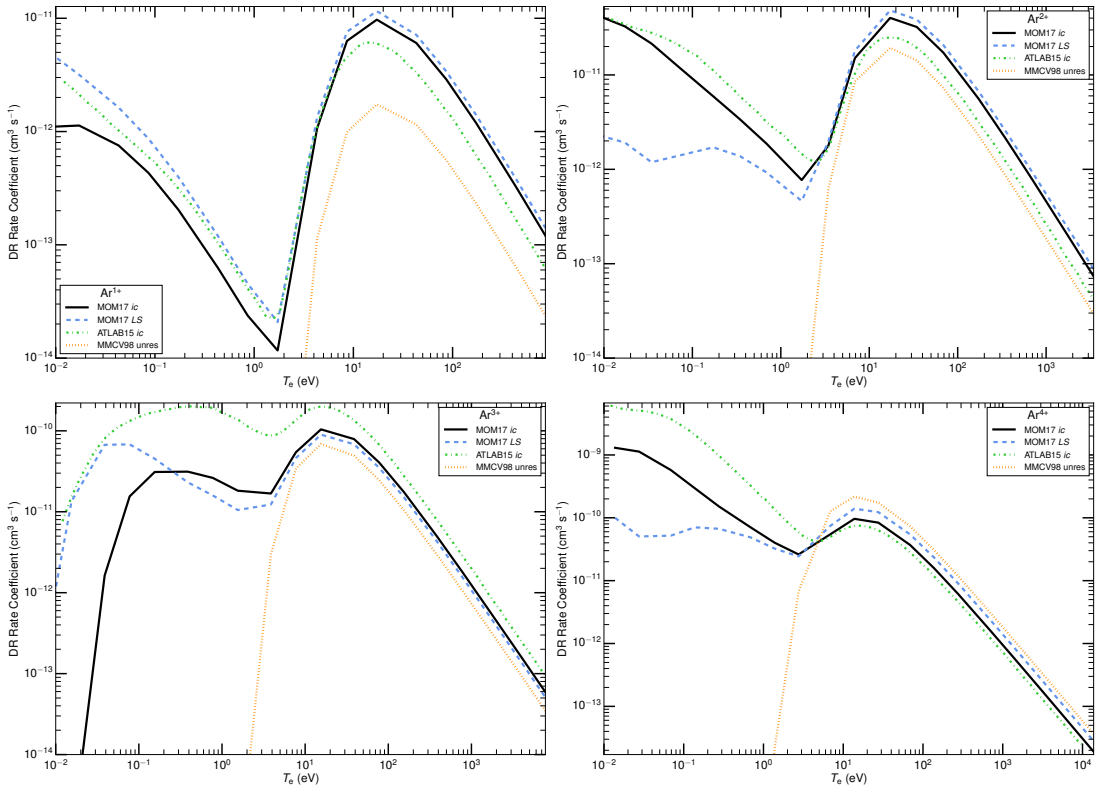

Figure 5.1: Comparison of total DR rate coefficients for Ar^{1+} to Ar^{4+}. The totals for the novel strategy of the present work (MOM17) are from the hybrid-type *adf09* files, and two resolutions for the recombining metastable parent are shown, *LS* and *ic*. ATLAB15 denotes the *ic* parent total from reference [177], while MMCV98 designates the unresolved total from reference [178].

5.2 *LS*-resolved GCR Model

Although the ultimate objective of this chapter is investigating the *ic*-resolved GCR model of argon, the *LS*-resolved results are novel because argon is the heaviest element to have been treated thus far, so they too need validation. Results from the *LS*-GCR model are presented in section 5.2.2, and comparisons with the literature are made in section 5.2.3. Another consequence of shifting to heavier species is that some of the existing procedures for performing the GCR model become cumbersome and impractical, so an update to the implementation is discussed in section 5.2.1.

```
A.S. n-like structure - energies + radiative rates + a2irat adf06
&SALGEB  CUP='ICR' RAD='E2' BORN='INF' KCOR1=1 KCOR2=1 MXCONF=14 MXVORB=9
         NMETAJ=15 KUTSS=-9 KUTSO=0 KUTOO=1 &END
 2 0  2 1  3 0  3 1  3 2  4 0  4 1  4 2  4 3
  2    3    0    0    0    0    0    0    0
  2    2    1    0    0    0    0    0    0
  2    2    0    1    0    0    0    0    0
  2    2    0    0    1    0    0    0    0
  2    2    0    0    0    0    0    1    0
  2    2    0    0    0    0    0    0    1
  1    4    0    0    0    0    0    0    0
  1    3    1    0    0    0    0    0    0
  1    3    0    1    0    0    0    0    0
  1    3    0    0    1    0    0    0    0
  1    3    0    0    0    1    0    0    0
  1    3    0    0    0    0    1    0    0
  1    3    0    0    0    0    0    1    0
  0    5    0    0    0    0    0    0    0
&SMINIM  NZION=18 NLAM=10 IREL=2 IBREIT=1 QED=1 ORTHOG='NO' MSTEP=12 &END
1.392  1.306  1.267  1.306  1.267  1.240  1.306  1.267  1.240  1.000
```

Figure 5.2: Example of an *adf27* driver file to produce IIE collision data for N-like Ar^{11+}. This file drives the AUTOS run, and the output is used by `a2iratbt` to calculate the $E2$ excitation rates.

5.2.1 Implementation Update

Prior to this work, the GCR coefficients, produced as *adf10* fragments by ADAS208, were aggregated into isoelectronic *adf10* files on a unified z-scaled (reduced) temperature and density grid by ADAS403. Subsequently, isonuclear *adf11* files were generated by ADAS404 through interpolating the isoelectronic *adf10* files onto a single *unscaled* temperature and density grid for practical exploitation. A drawback of this implementation is that the metastable-resolved coefficients require a separate *adf10* file for each possible metastable-to-metastable connection. Moving to heavier species and especially *ic* resolution, the number of files quickly increases and handling becomes problematic.

As a result, a new implementation has been devised that skips the intermediate step of isoelectronic *adf10* files. An unscaled temperature and density grid is provided as input, and the new IDL procedures drive the ADAS208 calculation for each isonuclear ion on this same grid. Consequently, the task of merging the *adf10* fragments into final *adf11* files is, in principle, more straightforward. However, there is a technical problem worth noting. In its current form, ADAS204 only operates safely in the reduced temperature domain $T_e > 5 \times 10^3$ K$/z^2$, restricting the temperatures at which the projection matrix can be generated.

N	Z_0/N	1s	2s	2p	3s	3p	3d	4s	4p	4d	4f
1	18.00	1.000	1.000	1.000	1.000	1.000	1.000	1.000	1.000	1.000	1.000
2	9.00	1.459	1.223	0.935	1.223	0.935	1.000	1.000	1.000	1.000	1.000
3	6.00	1.459	1.422	1.542	1.422	1.542	1.000	1.000	1.000	1.000	1.000
4	4.50	1.448	1.472	1.250	1.472	1.250	1.401	1.472	1.250	1.000	1.000
5	3.60	1.417	1.431	1.370	1.431	1.370	1.413	1.431	1.370	1.413	1.000
6	3.00	1.407	1.371	1.334	1.371	1.334	1.309	1.371	1.334	1.309	1.000
7	2.57	1.392	1.306	1.267	1.306	1.267	1.240	1.306	1.267	1.240	1.000
8	2.25	1.376	1.236	1.195	1.236	1.195	1.143	1.236	1.195	1.143	1.000
9	2.00	1.361	1.172	1.130	1.172	1.130	1.088	1.172	1.130	1.088	1.000
10	1.80	1.340	1.112	1.069	1.112	1.069	1.007	1.112	1.069	1.007	1.000
11	1.64	1.351	1.125	1.079	1.125	1.079	1.100	1.125	1.079	1.100	1.000
12	1.50	1.355	1.118	1.068	1.160	1.054	1.087	1.160	1.054	1.087	1.395
13	1.38	1.355	1.118	1.068	1.101	1.087	1.099	1.101	1.087	1.099	1.283
14	1.29	1.355	1.118	1.068	1.120	1.117	1.139	1.120	1.117	1.139	1.285
15	1.20	1.355	1.118	1.068	1.126	1.130	1.149	1.126	1.130	1.149	1.288
16	1.12	1.355	1.118	1.068	1.119	1.123	1.185	1.119	1.123	1.185	1.240
17	1.06	1.355	1.118	1.068	1.106	1.117	1.202	1.106	1.117	1.202	1.171
18	1.00	1.351	1.308	1.268	1.085	1.055	1.030	1.008	1.050	1.030	1.000

Table 5.3: Radial scaling parameters (λ_{nl}) used in AUTOS runs for the argon isonuclear ions. These are found below the SMINIM namelist in the *adf27* driver files, and they apply to both the production of IIE data with `a2iratbt` and DW EIE data as part of the improved baseline described in Chapter 2. Values given here may differ slightly from those that enter central ADAS because of minor tweaks in the methodology that occurred too late for inclusion in the present work. It is not anticipated that this will result is materially significant effects upon the final structure or collision data.

One attempted solution was to generate the projection matrix in the restricted temperature domain and then extrapolate it onto the universal unscaled temperatures at which the ADAS208 calculation was performed under the new IDL procedures, but this proved unstable and unworkable. In the end, it was found that the most robust strategy was to restrict the reduced temperature grids of both the ADAS204 and ADAS208 calculations and then extrapolate the *adf10* fragments onto the final temperatures requested within the new IDL procedures. The approach of extrapolation is justified and not as risky as usual because the GCR coefficients have fairly well defined limiting behaviour at extreme temperatures. In fact, this type of extrapolation is already treated extensively within ADAS404, and the implementation here is a simplified version of the one within that routine.

The high temperature behaviour is straightforward for all cases and at all densities, but the low temperature behaviour can be problematic since it may depend on the density. This is particularly true for the α^{cd}'s where three-body recombination only becomes relevant at high densities and low temperatures. In these cases, the reduced temperature limit defined above can cause trouble

because the α^{cd} coefficient

The implementation (GCR17) has been benchmarked against the previous Si GCR work [60] that is present in central ADAS under the tag, GCR96. Figure 5.3 shows that there is nearly perfect agreement between the two implementation styles in terms of the effective recombination coefficients (α^{cd}) and effective ionisation coefficients (S^{cd}) presented; however, there are some deviations at lower temperatures due to extrapolation differences, and also some discrepancies at higher densities. This work has also uncovered flaws in the Si GCR data for a few ions not presented in figure 5.3, but corrections bring those results to a similar level of agreement.

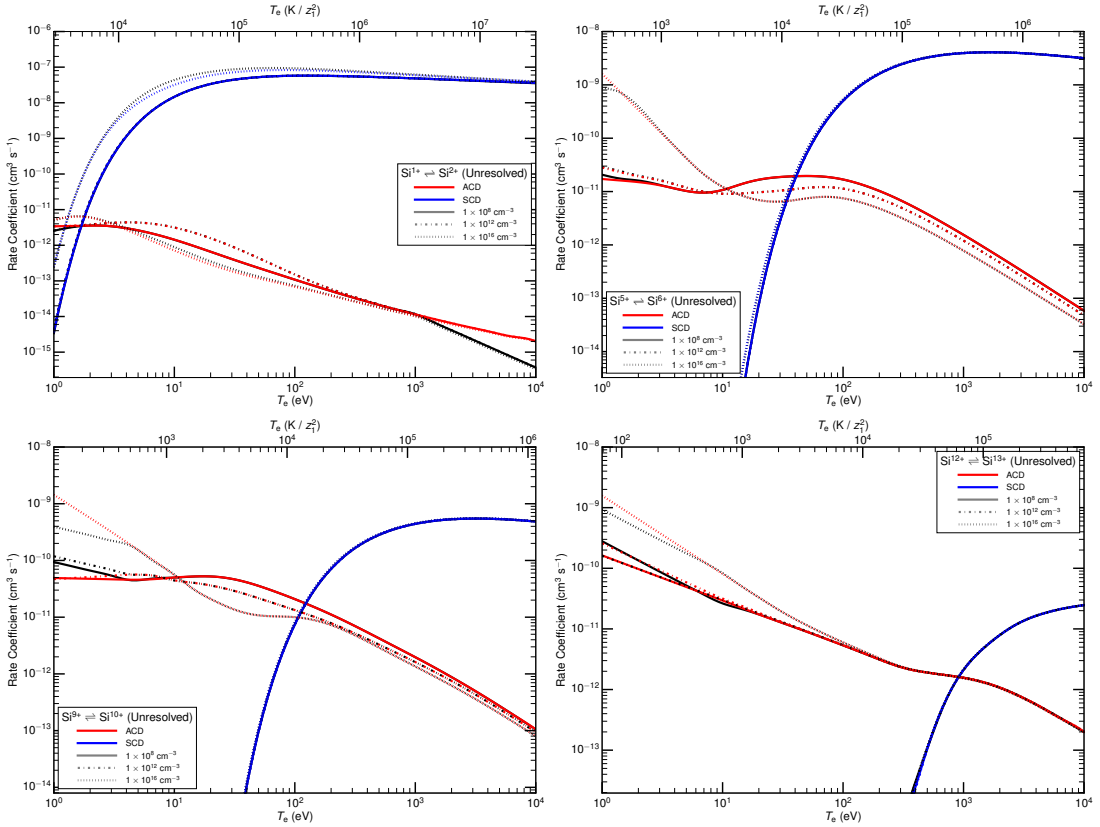

Figure 5.3: Benchmarking of effective recombination (ACD, red) and ionisation (SCD, blue) coefficients for silicon. The colored lines denote the results from the new IDL procedures (GCR17), and the black lines represent the results in central ADAS (GCR96) from [60]. The different line styles indicate the relevant electron density, N_{e}, as specified by the legend.

This new implementation will be included in a future ADAS release. The restrictions imposed by ADAS204 can be mitigated by the suggestions for future development in section 6.1.

5.2.2 Results

The two primary results of interest from any atomic population model are the ionisation balance—stage or metastable resolved—and cooling curve. These are presented for argon using the GCR implementation update applied to the *LS*-resolved model: figures 5.4, 5.5, and 5.6. Extensive comparison of the unresolved fractional abundances and radiated power with the literature is made in the following section 5.2.3, so comment of those results is reserved until then. The metastable, *LS*-resolved fractional abundances in figure 5.5 appear, superficially, quite similar to the unresolved fractional abundances of figure 5.4. Indeed, the $T^{(\mathrm{pk.})}$ points in the bottom pane show that the metastable peak abundances tend to clump around the peak abundance for their subsuming stage. The most notable exception is Ar^{2+} which has significant metastable populations with peak abundances that are separated in temperature. But this comparison lacks rigour, and the only true way to directly quantify the impact of modelling atomic populations at different resolutions is through subsequent plasma-transport modelling at these varying degrees of resolution. However, some hints of resolution effects are covered in section 5.2.3.1 and the *ic* results of section 5.3.

Another relevant observation about figure 5.5 is that many of the metastable fractional abundances are quite small across the temperature range, and some do not even make it above the 10^{-4} cutoff in the top pane. This raises the question of whether all of the selected metastables actually merit their name and whether some might be better classified as ordinary states. Distinguishing between metastable and ordinary states is not straightforward, in part because of how metastability is defined. Ultimately, it is the *lifetime* of a state relative to the plasma timescales that determines whether this state is metastable or not. However, determining these lifetimes requires dynamic population modelling under transient ionisation-recombination conditions, something that is outside of the current scope and overkill for considering the plasma globally. Rather, equilibrium solutions for the ionisation balance are most commonly used and with great success. Under equilibrium conditions, all potential metastables are in a steady-state, so they do not have lifetimes—the lifetimes are infinite in fact. Instead, it is the steady-state population density that will determine the influence of a particular state and thus whether it can be considered metastable. ADAS405

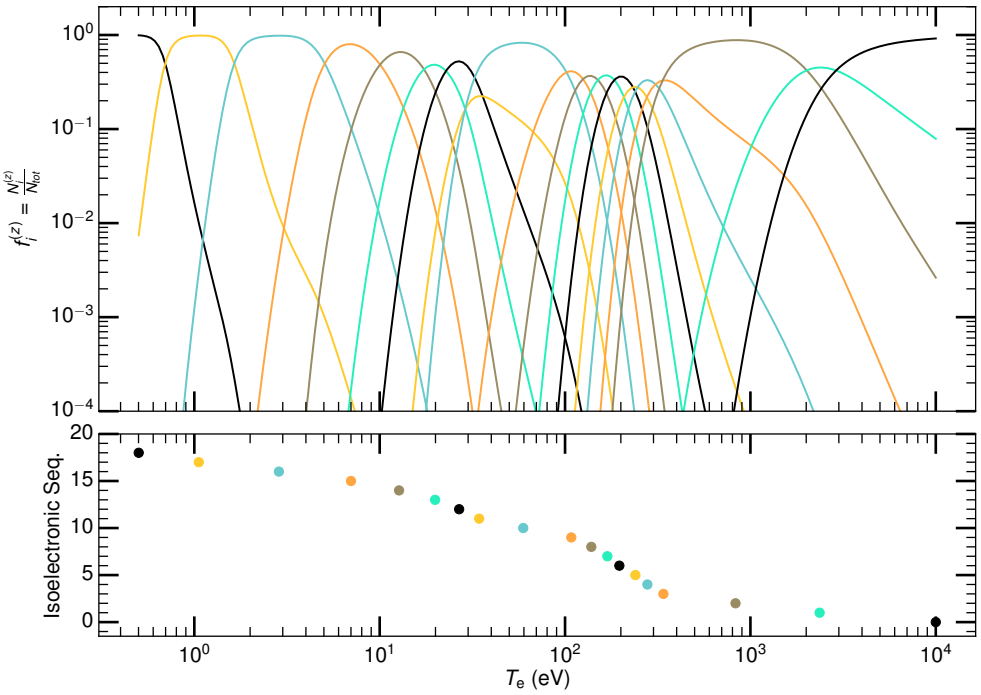

Figure 5.4: Unresolved fractional abundances for argon derived from the *LS*-resolved model at $N_e = 10^{12}$ cm^{-3}. The top pane displays the fractional abundance curves, and the bottom pane gives the temperature of peak abundance, $T^{(pk.)}$, for each ionisation stage. Ionisation stages are demarcated according to color.

is used in this work to produce equilibrium fractional abundances, which are directly proportional to the population densities. For the present purposes, it is therefore sufficient to define a cutoff (i.e. threshold) condition directly upon the fractional abundances of the relevant states to separate between metastable and ordinary ones.

There are two meaningful approaches that can be adopted for implementing the fractional abundance cutoff, and the simplest is to enact a global cutoff across the relevant temperature range for the element, selecting only those states that attain fractional abundances above this level to be designated as true metastables. The other strategy is to take $T^{(pk.)}$ of the dominant state for each ionisation stage, and then add up the metastable fractional abundances in decreasing order at this temperature until one reaches 98% of the stage fractional abundance. Only states that contribute to the sum are retained as metastables. Although slightly more sophisticated than the former, this strategy yields nearly the same result, except it does not report the ^{1}S term of Ar^{2+} as being metastable. Since this is a minute

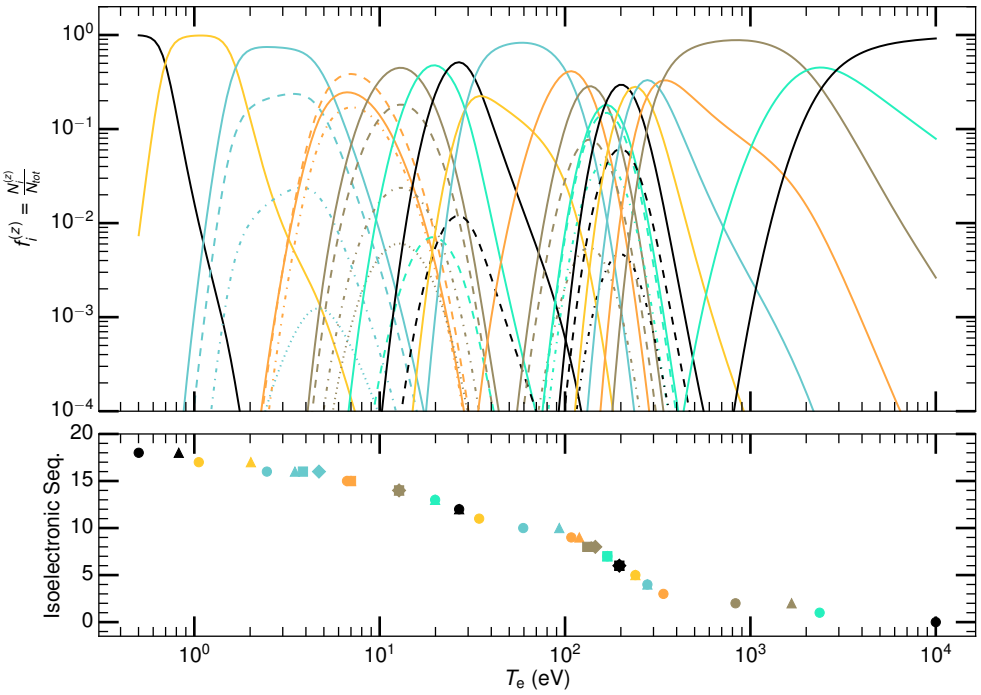

Figure 5.5: *LS*-resolved metastable fractional abundances for argon at $N_e = 10^{12}$ cm^{-3}. The top pane displays the metastable-resolved fractional abundance curves, and the bottom pane gives the temperature of peak abundance, $T^{(\mathrm{pk.})}$, for each metastable. Ionisation stages are demarcated according to color, while the *LS* metastables within each stage are differentiated by line style (top pane) or marker style (bottom pane).

difference that does not affect the subsequent interpretation or likely the final modelled results, these two approaches are considered equivalent in what follows, and the global cutoff has been used in the subsequent analysis. Although other implementations might be possible, these are the most physically meaningful that were devised for this study.

The results from the global cutoff method with 10^{-2} as the threshold are shown in the fifth column of table 5.4 (Global Cut), having used $N_e = 10^{12}$ cm^{-3} as input to the ADAS405 calculation. For all argon ions, the metastables reported by this technique are fewer or equal to those from the ADAS standard list (column four). There are three reasons for this discrepancy. First, the standard ADAS list of *LS*-term metastables has been deduced from a mix of selection rules, intuition, and experience. It serves as a guideline for what the term metastables will likely be for an arbitrary ion under pure *LS*-coupling conditions. On the other hand, the *LS* data used in the current model and global cutoff result has been bundled

Table 5.4: *LS*-term metastables for argon from two different sources. The column titled "ADAS" contains the standard list of *LS*-term metastables used as a rough guide within ADAS. The column titled "Global Cut" contains the metastables according to the threshold procedure applied to the GCR model fractional abundance results, as described in the text. This was performed at $N_e = 10^{12}$ cm^{-3}. A simplified, non-superscript notation for the *LS* terms has been employed for succinctness: $[2S+1][L] \equiv {}^{(2S+1)}L$.

Seq.	Ion	Config.	ADAS	Global Cut
Ar	0	$3s^2 3p^6$ $3s^2 3p^5 4s$	1S 3P	1S
Cl	+1	$3s^2 3p^5$ $3s^2 3p^4 3d$	2P 4D	2P
S	+2	$3s^2 3p^4$ $3s^2 3p^3 3d$	3P 1D 1S 5D	3P 1D 1S
P	+3	$3s^2 3p^3$	4S 2D 2P	4S 2D 2P
Si	+4	$3s^2 3p^2$ $3s 3p^3$	3P 1D 1S 5S	3P 1D 1S
Al	+5	$3s^2 3p$ $3s 3p^2$	2P 4P	2P
Mg	+6	$3s^2$ 3s3p	1S 3P	1S 3P
Na	+7	3s	2S	2S
Ne	+8	$2s^2 2p^6$ $2s^2 2p^5 3s$	1S 3P	1S
F	+9	$2s^2 2p^5$ $2s^2 2p^4 3s$	2P 4P	2P
O	+10	$2s^2 2p^4$ $2s^2 2p^3 3s$	3P 1D 1S 5S	3P 1D
N	+11	$2s^2 2p^3$	4S 2D 2P	4S 2D 2P
C	+12	$2s^2 2p^2$ $2s 2p^3$	3P 1D 1S 5S	3P 1D
B	+13	$2s^2 2p$ 2s2p	2P 4P	2P
Be	+14	$2s^2$ 2s2p	1S 3P	1S
Li	+15	2s	2S	2S
He	+16	$1s^2$ 1s2s	1S 3S	1S
H	+17	1s	2S	2S

from *ic*-resolved *adf04* files, so pure *LS* coupling is not replicated. Ar-like is an instructive example and archetype. Under *LS* coupling, there is no spontaneous emission from the $3p^5 4s\ ^3P$ term to the $3p^6\ ^1S$ ground term because it would be spin-changing, and this accounts for why the ^3P term is predicted to be metastable by the ADAS list. However under *ic*, the $^3P_1 \rightarrow {}^1S_0$ radiative transition has a moderately strong *A*-value, producing a strong *A*-value in the corresponding *LS adf04* file of $4.4 \times 10^7\ s^{-1}$. This is sufficiently large that the ^3P term will not be metastable, accounting for the discrepancy with the ADAS list. Further discussion of discrepancies between *pure LS* coupling and the quasi-*LS* conditions achieved with the bundled *adf04* files of the current *LS*-model is also raised in section 5.3.1.1. An important point is that pure *LS* conditions are rare and not necessarily a desirable target.

The second reason that the ADAS list and global cutoff results differ is because the ADAS list implicitly assumes the metastable states will be constant along an isoelectronic sequence. In reality, the z scaling of term energies and *A*-values will cause the metastables to vary, and an assessment of metastable trends along isoelectronic sequences will be necessary to produce a global list of metastable states for all elements. Third, metastability is inherently dependent on the electron density, adding another layer of complexity to this question. For example, performing the global cutoff method at $N_e = 10^4\ cm^{-3}$ yields only the ground (lowest energy) term for each argon ion, in accordance with the coronal model. So, although the list of metastables in table 5.4 should now be considered the recommended one for subsequent transport modelling, this recommendation only applies in the vicinity of $N_e = 10^{12}\ cm^{-3}$. A more robust solution for determining the true metastables would be to perform an ADAS406 calculation to yield the fractional abundances under transient ionisation-recombination conditions and thus definitively reveal the *time scale* over which each proposed metastable evolves; however, this is outside of the current scope. Overall, these observations suggest that the current *LS*-GCR model produces a more accurate list of term metastables, and looking ahead to section 5.3.2, the analysis of *ic*-level metastables confirms this conclusion. Ultimately, *ic* is the truer representation of reality, and its verdict matters most.

In addition, it is interesting to assess metastability from the perspective of *ca*

versus *LS* resolution, just as *ca* versus *ic* was compared in section 2.3.1.1. The *adf54* files from the configuration selection work show that only the ground configuration is considered a metastable state across the argon isonuclear sequence—the top configuration in each ion row of table 5.4. Juxtaposing with the global cut-off results, nearly all of the terms selected as metastable fall within the ground term, indicating a high level of consistency between these resolutions. There is one anomalous case where the ^{3}P term from the 3s3p first-excited configuration of Mg-like is found to be metastable. This happens because the A-value for the $^3\mathrm{P} \rightarrow {}^1\mathrm{S}$ transition is small enough ($2.38 \times 10^5\,\mathrm{s}^{-1}$) that the upper term achieves metastability, in contrast to the structurally similar Ar-like case discussed immediately above. Thus, the conclusions from comparing *ca* and *ic* metastability extend to this scenario also: if a configuration is metastable, then it must contain a metastable term, but not all terms of a metastable configuration need be metastable, e.g. O-like and C-like in the table. Moreover, there are rare circumstances around shell boundaries where metastable terms can arise but the associated configuration is not metastable: the case of Mg-like above. However, the same cannot be said for the *LS* metastables from the standard ADAS list. Far from being a rare occurrence, metastable terms that don't belong to a metastable configuration appear across the isonuclear sequence, not just at shell boundaries. It follows that the pure *LS* account of metastability is not consistent with that of *ca*.

Lastly, the radiated power coefficients in figure 5.6 possess a few notable features. Except at low and high temperatures, the total radiated power function ($\mathcal{P}_{\mathrm{tot}}$) from the unresolved and *LS*-resolved models are nearly identical. The difference at low temperatures is likely due to extrapolation differences. Contributions from the $\mathcal{P}_{\mathrm{RB}}$ are only significant near the extrema of the temperature domain, and there are only marginal differences between the unresolved and *LS* form of the $\mathcal{P}_{\mathrm{RB}}$. So, it is the $\mathcal{PLT}$ that will dominate in most instances, and more comparisons are made in section 5.4.

5.2.3 Models of Argon in the Literature

For the present case study, two aspects can be tested with a literature review. First, the more practical modifications of the GCR implementation outlined above

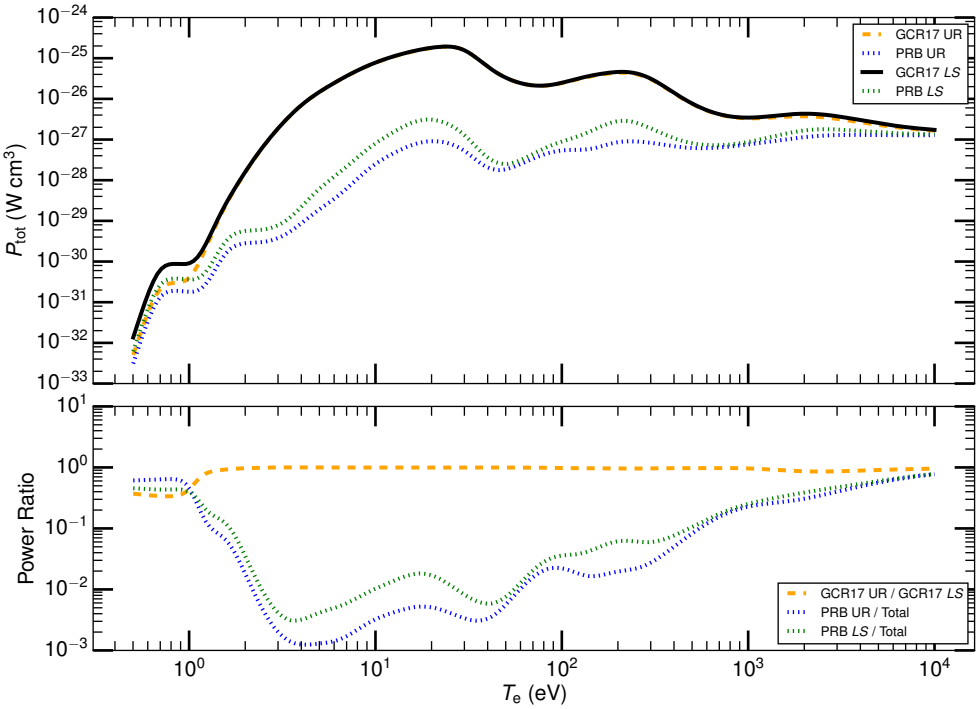

Figure 5.6: Cooling curves (total radiated power function) from the *LS*-resolved model for argon at $N_e = 10^{12}$ cm^{-3}. The top pane shows $\mathcal{P}_{tot}$ from the unresolved (GCR17 UR) and *LS*-resolved (GCR17 *LS*) forms of the model, along with the respective recombination-bremsstrahlung-cascade radiated power coefficient ($\mathcal{P}_{RB}$) contributions to the totals. The bottom pane displays the relevant ratios from the top pane.

are checked for applicability outside of previously studied ions. The simple act of increasing Z_0 and the associated shifts in temperature and density scales can cause even the most robust techniques to eventually fail. Second, the *LS*-GCR model for argon, upon which the extension to *ic*-GCR is based, needs to be validated. Of course, this will be limited to some extent because the *LS*-GCR model itself supersedes all previous attempts in terms of sophistication: two steps forward are being made, and both require assessment.

The radiated power loss from an impurity species can be split into two parts, and there are a number of literature sources that only address one or the other. The first part is to determine the fractional abundances of metastable-resolved or stage (unresolved) populations for an element, and the literatures sources for these data are detailed in the following section 5.2.3.1. In the literature, the unresolved fractional abundances of the ionisation stages are collectively referred to as the ionisation balance or charge state distribution (CSD). Second, the radiative

processes associated with each stage or metastable that actually lead to power loss must be described, and this topic is handled near the end of this chapter in section 5.4.1. It is important to note that this is somewhat of a false division and these parts are not truly independent. The degree to which they can be considered independently ultimately depends upon the model selected. Evidently, in a GCR model all of the underlying coefficients are intertwined and determined by the same set of input data.

5.2.3.1 Fractional Abundances

Depending on the plasma conditions, an equilibrium or transient solution of the fractional abundances might be required, but the equilibrium solution is most often quoted because of its simplicity and fairly broad applicability. In both cases, it is the ionisation and recombination processes between states that are the determining factors, and differences between approaches enter by how the rates of these processes are determined and the resolution of the states that are considered. The approaches for argon that are considered in this review loosely fall into three categories: coronal ionisation equilibrium (CIE) models, ADAS models, and Average Ion Models (AIMs), all of which are resolved by ionisation stage (i.e. stage-to-stage). In contrast, the present work will be the first metastable-resolved (*LS* or *ic*) ionisation balance to our knowledge. The metastable-resolved and stage-unresolved fractional abundances are defined by the ratios $N_\sigma^{(z)}/N_{\rm tot}$ and $N^{(z)}/N_{\rm tot}$, respectively, where

$$N_{\rm tot}(N_{\rm e}, T_{\rm e}) = \sum_{z=0}^{Z_0} \sum_{\sigma=1}^{M_z} N_\sigma^{(z)} \tag{5.10}$$

is the number density of all ions belonging to element X, $N_\sigma^{(z)}$ is the population density of metastable σ within ionisation stage z, and $N^{(z)} = \sum_\sigma N_\sigma^{(z)}$ is the number density of the ionisation stage z.

CIE Models Overwhelmingly, the most prevalent model for producing fractional abundances is the CIE model, especially in astrophysics where the concept of coronal plasma conditions originated. In the context of fractional abundances, the implications of the CIE model are that only the ground states of each ion

need to be tracked and that the ionisation and recombination coefficients are uninfluenced by the excited populations (i.e. density effects), meaning zero-density coefficients can be used. Thus, the problem of establishing the unresolved fractional abundances is reduced to finding appropriate zero-density ionisation and recombination coefficients between all relevant stages. To wit, in the CIE limit, the ratio of adjacent stage populations is given by

$$\frac{N^{(z+1)}}{N^z} = \frac{S_{z\to z+1}}{\alpha_{z+1\to z}}. \tag{5.11}$$

The ionisation and recombination coefficients referenced here are the same quantities needed for the input to the GCR model, except metastable resolution is required for the latter as was discussed in sections 5.1.3.2 and 5.1.3.3. Comparisons are made below for each source in the CIE model category.

Although somewhat dated, Arnaud and Rothenflug [179], henceforth AR85, is still one of the most popular references for obtaining unresolved fractional abundances in the CIE limit. It provides a collection of the requisite zero-density ionisation and recombination coefficients for a wide range of elements including argon, along with the resulting coronal limit CSDs. In terms of methodology, it mirrors a similar effort in [180], and the recombination coefficients, both RR and DR, are primarily taken from there. These, in turn, can be traced back through a series of papers by Jacobs et al. [181] that extend the Burgess General Formula (GF) [182] to include contributions of autoionisation to excited recombining states. These DR coefficients are of an inferior quality to those from the DR project [161] used in the present study (see table 5.2). The main focus of the work is improving the calculation of collisional ionisation, for which it uses a parameterized expression from [183] for the exchange Coulomb-Born method, and the parameters are adjusted to fit experimental data where available. This yields the direct ionisation (DI) contribution, and the excitation autoionisation (EA) contribution is taken from a variety of literature sources too numerous to give here. This approach likely yields an improvement over the much used (and abused) semi-empirical Lotz formula [184]. Again, both are of lesser quality compared to the data from [159] used in the current study: that source directly calculates the exchange Coulomb-Born and EA contributions in FAC and com-

pares to vastly extensive measurements that have been made in the time elapsed since the work in [183].

There are a series of works that, in effect, update AR85 but are still worth mentioning. Sutherland and Dopita [185] extend the ionisation rates from [183] into non-equilibrium regimes and also improve the consideration of DR for H-like ions by reviving more complicated expressions from the works of Seaton. Mazzotta et al. [178] collect a large number of updates to DR rate calculations across a range of isoelectronic sequences up to the year 1998; this has an appreciable effect upon the ionisation balance, and correspondingly this is a frequently referenced source. Two papers from groups at Auburn University [177, 186] make their own improvements to the argon DR data, yielding marked changes in the fractional abundances. Reference [177] was used to validate the new DR data from this study in section 5.1.3.3.

Fournier et al. [187], hereafter FCMG98, is another work that largely shares the same heritage, but it focusses exclusively on argon and therefore merits further detailing. The DR data is taken from Mazzotta et al. [178], while the RR data is generated through the assumption of detailed balance applied to photoionisation cross sections from a Hartree-Slater computer code; this approach is materially the same as [180], which is used in all sources above. The DI contribution to ionisation employs the Lotz formula [184], making it somewhat less advanced than AR85 and progeny. However, it couples this with a contemporaneously novel approach to EA that the same group of authors present in a separate paper [188]. It differs most significantly from the EA approaches in previous sources because it does not assume a unitary branching ratio for autoionisation from continuum levels and so must calculate both autoionisation and radiative rates. It is unclear whether the combination of this approach to EA and the DI formula of Lotz marks an improvement over previous approaches to ionisation estimates.

Finally, the most advanced effort in the category of argon CIE models is Bryans et al. [189], hereafter BLS09. It draws upon a number of substantial advances in the area of ionisation and recombination rate calculations compared to the previous sources. In fact, it uses largely the same zero-density coefficients that are employed in the current GCR model. Ionisation rates are taken from Dere [159], which is described in section 5.1.3.2. DR rates come from the DR

Project [145], described at length in section 5.1.3.3, and any missing rates are filled in using Mazzotta et al. [178], namely for Ar^0 through Ar^{3+} recombined ions. As a reminder, this gap is addressed in the present work by generating new DR data (see section 5.1.3.3); accordingly, it is assessed to be of a higher quality than the DR data used in BLS09 [178]. RR rates are also taken from [178], which are in turn generated from the detailed balance of photoionisation cross sections in [180]; large differences with the current study are not expected for RR. Because of the similarities in fundamental *zero-density* data, BLS09 will be an important work with which to compare, since it functions as an independent zero-density limit for the present GCR model.

Average Ion Models Much of the content in this thesis should prove that modelling atoms at term or fine-structure resolution is a complex task, requiring significant computing resources and databases only available quite recently. Prior to these modern developments, approximations in the modelling techniques were necessary, and one popular option was the Average Ion Model (AIM). As the name suggests, the finer complexities of the ionic systems are averaged over in some way. At one extreme of simplicity, all the ions of an element can be lumped together and considered as a single averaged ion. This is the approach taken by the popular works of Post et al. [190, 191], hereafter P77. The average ion itself is modelled with Rydberg n-shell (ry) states, $\bar{P}_n$:

$$\bar{P}_n = \sum_{i=0}^{Z_0} f(i) P_n(i) \tag{5.12}$$

where $P_n(i)$ are the ry populations of each ionisation stage, i, and $f(i)$ are the fractional abundances, neither of which are actually tracked in this model. The $\bar{P}_n$ are solved from a set of rate equations with the loss and growth rates being determined by hydrogenic expressions for recombination, ionisation, and excitation. These rates and the representative energy levels are themselves determined by the $\bar{P}_n$, so these equations must be solved iteratively, with the initial condition provided by the Saha-Boltzmann equation. However, because the $f(i)$ are not tracked, the AIM is only really useful for providing radiative power loss or mean charge state estimates for an element. It is discussed further in the following sec-

tion 5.4.1, but it should be apparent from the extensive discussion on resolution and coupling that this version of AIM is quite a coarse approximation

One step up in complexity is achieved by considering the ionisation stages individually but retaining the *ry* resolution of each stage. FLYCHK is one code suite that adopts this method [192], and the AIM it employs is discussed here. All ions of an element are treated hydrogenically with appropriate screening effects. The set of $P_n(i)$ are solved with rate equations and rates similar to those immediately above, but now with a far greater number of dimensions and no necessity for an iterative approach, because the energy levels and rates for each ion are in principle immediately known from analytic, hydrogenic expressions. An equilibrium solution of fractional abundances can be obtained in this version by imposing a global steady state condition on all populations of all ions, although FLYCHK offers many different modes corresponding to different plasma conditions. In some respects, this AIM is more sophisticated than the CIE model because it does not assume that only the ground state is dominant, meaning CR density effects can manifest. Of course, this is tempered by the fact that the rates underpinning the model are of a fairly low quality. Compared to a GCR model with projection, the AIM will neglects some high n effects. Any AIM will encounter truncation effects because some cutoff in n must invariably be enforced to keep the problem tractable: FLYCHK uses $n \leq 10$ for each ion. This shortcoming is mitigated by the fact that FLYCHK targets high-density plasmas where the collisional limit is lowered, so DR from high n is suppressed. Above all, the dominant flaw is the low resolution of this AIM: DR through $\Delta n = 0$ inner electron excitations is neglected and the statistical balance that makes bundling by n possible will break down even more severely and sooner than the much discussed breakdown in *LS*. Although not relevant to the discussion of fractional abundances and power coefficients in this section, it should also be noted that such low resolution is also not appropriate for spectroscopy.

ADAS Models Finally, there are two preexisting results for argon fractional abundances within ADAS. Both are stage-to-stage resolved. The first is denoted by the year 85 within the ADAS nomenclature, and it takes the zero-density coefficients and CIE model of AR85 [179] and scales that to a bundle-n calculation,

thus approximately accounting for density effects. It lies somewhere in between the CIE and AIM approaches above. Secondly, the JET baseline denoted by the year 89 is also available. This is effectively a *ry* atomic model for each ionisation stage with rates similar to those in AIMs, but a coronal assumption is also made so that only the ground state is tracked for the fractional abundances. This should be considered the lowest quality data available.

Comparisons The most relevant comparison for the *LS*-GCR model is with the CIE model of BLS09 [189] because the result from that model should serve as the zero-density limit of the *LS*-GCR result. In other words, for low densities, any GCR model should asymptotically approach the CIE model, so if the same underlying zero-density recombination and ionisation rate coefficients have been used, the outputs of the two models should, in theory, be identical. A comparison of the *unresolved* fractional abundances at a finite density for the GCR model ($N_\mathrm{e} = 10^{12}$ cm^{-3}) is presented in figure 5.7(a), which exhibits large differences between the two models, as might be expected. These differences are especially prominent for the near-neutral stages but persist through the middle ionisation stages until agreement is observed at high temperatures for the highly-ionised stages. However, it must be justified whether the entirety of this variation can be attributed to the density effects that are included in the GCR model. To this end, the comparison has been reproduced at a very low density of $N_\mathrm{e} = 10^4$ cm^{-3} in figure 5.7(b), and under this condition, all density effects will be absent.

First, consider the near neutrals. These are brought into much closer agreement in figure 5.7(b), suggesting that the majority of the difference observed in figure 5.7(a) is indeed attributable to the influence of ordinary and highly-excited states through collisional excitation at finite density—i.e. density effects. Is this reasonable? A closer inspection of the α^cd's and S^cd's for these stages reveals that most have a fairly modest density dependence, but Ar^0 has an S^cd that is greatly enhanced with increasing density. This accounts for the substantially lower fractional abundance of Ar^0 in figure 5.9 compared to BLS09, and this deficit propagates to the abundance fraction of subsequent stages. The enhancement of the Ar^0 S^cd comes almost entirely from the projected influence of the bundle-nS calculation; a pure bundle-nS (ADAS204) calculation confirms the sensitivity

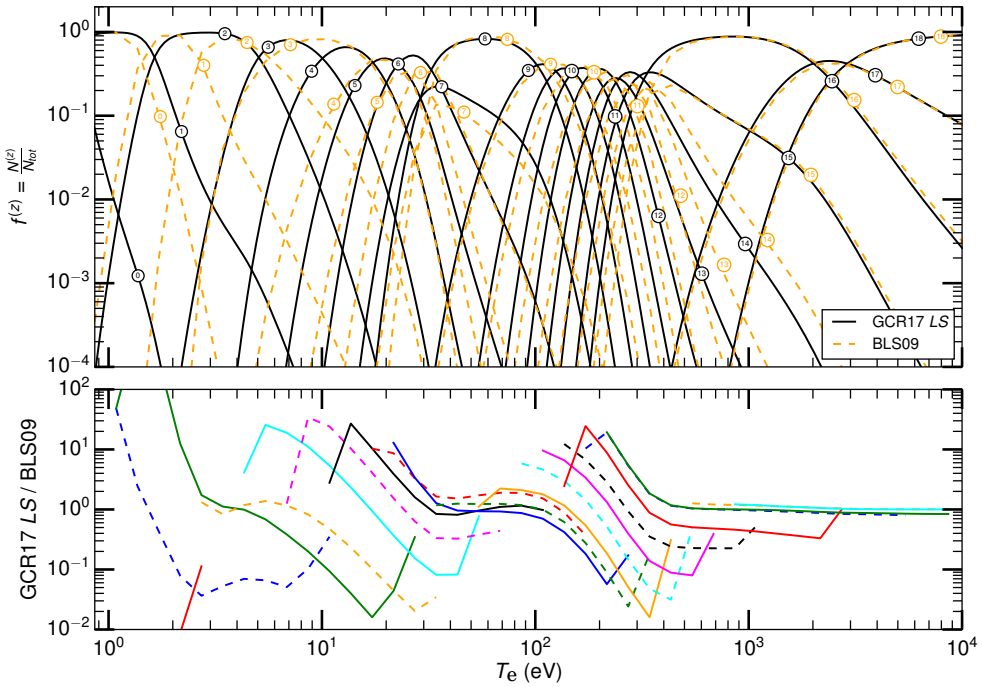

(a)

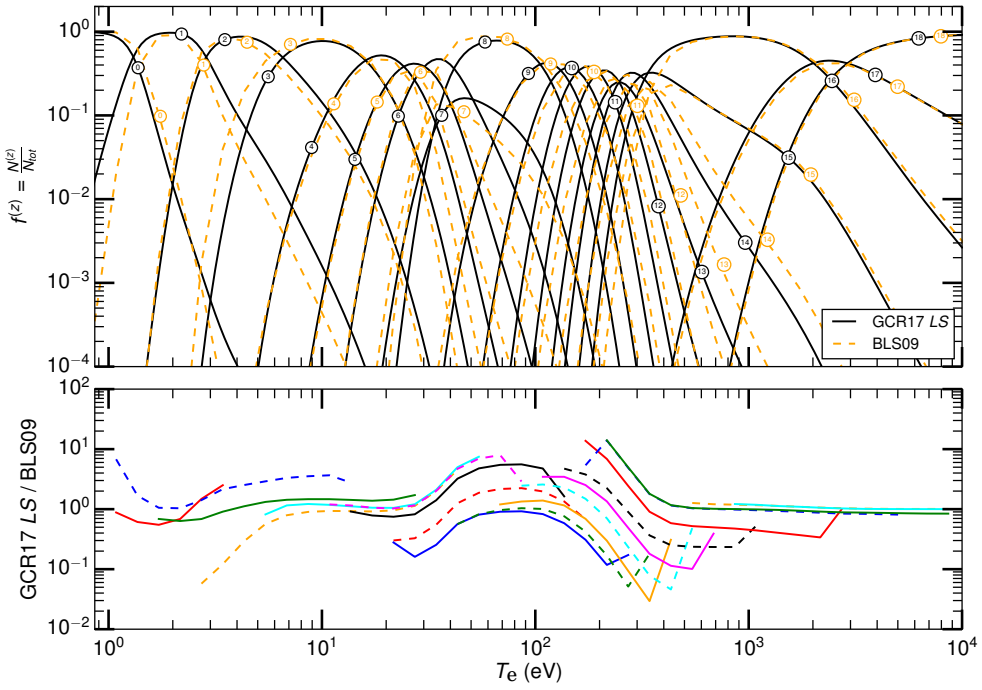

(b)

Figure 5.7: Comparison of unresolved fractional abundances for argon: present work using *unresolved* coefficients derived from *LS*-resolved run (GCR17 *LS*) versus Bryans et al. [189] (BLS09) at (a) $N_e = 10^{12}$ cm^{-3} and (b) $N_e = 10^4$ cm^{-3}. The small numbers in circles that lie on the fractional abundance curves (top panes in a and b) denote the ionisation stage z.

of the S^{cd} to density, suggesting that this is a real phenomenon. Once a new bundle-n code is created, this result should be verified. However, even though these near-neutral stages are in better agreement at low density, the differences are not completely eliminated. This is partly because the DR rate coefficients used in BLS09 are *ic* parent-resolved, whereas for the *LS*-GCR model they are in *LS* resolution. There are subtle differences between these two resolutions of DR rate coefficients, as seen in figure 5.1, but more significant are the differences between the MMCV98 data used by BLS09 and the MOM17 data used for the present result.

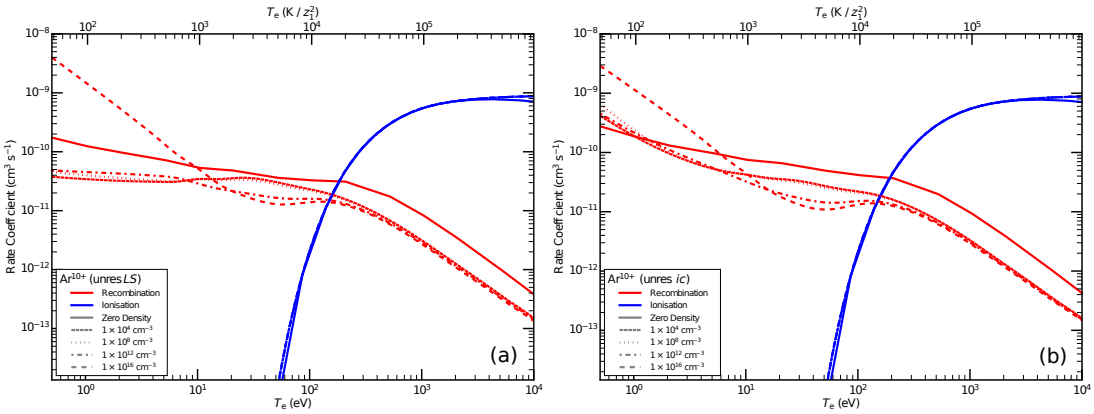

Figure 5.8: Unresolved, effective ionisation and recombination rate coefficients for Ar^{10+} from (a) *LS* and (b) *ic*-resolved models. Ar^{10+} is the ionizing and recombined system for the S^{cd} and α^{cd}, respectively. The zero-density ionisation and recombination rate coefficients are shown with solid lines, and the GCR coefficients are shown at varying densities, denoted by the line styles in the legends. The use of grey lines in the legend indicate that these line styles apply to both the α^{cd} (red) and S^{cd} (blue) coefficients.

Discrepancies are also observed at low density for some of the middle ionisation stages—Ar^{8+} through Ar^{14+}—in figure 5.7(b). The source of this discrepancy is that the low-density α^{cd}'s do not approach the zero-density total rate coefficients as shown in figure 5.8, which applies to both the *LS* and *ic*-resolved models. It was confirmed that this behaviour manifests in previous GCR models for silicon and neon. The difference between *LS* and *ic* parent-resolved DR rate coefficients is marginal at the relevant temperatures, and the BLS09 fractional abundances use the same DR project data excepting this negligible difference in resolution. The ionisation data is the same, and any differences between RR data is also negligible. Moreover, a check of the *LS*-resolved fractional abundances at $N_{\mathrm{e}} = 10^4$ cm^{-3} shows that no significant metastable populations, other than the ground, were

present. Thus, the only remaining explanation is that the definition of the α^{cd} does not guarantee it will align with the total, zero-density recombination rate coefficient in the low density limit—though in many cases this does occur. BLS09 uses the total, zero-density recombination rate coefficient from the ground *parent* level (ν), which is defined as

$$\alpha_{\nu}^{(z+1)+} = \sum_{i} \left(\alpha_{\nu \to i}^{\mathrm{dr}} + \alpha_{\nu \to i}^{\mathrm{rr}} \right), \tag{5.13}$$

where the index, i, encompasses all bound final states of any resolution. Similarly, the definition of α^{cd} in equation C.10 shows a summation over the final-state-resolved recombination rates, $r_{i\nu} \equiv \alpha_{\nu \to i}^{\mathrm{dr}} + \alpha_{\nu \to i}^{\mathrm{rr}}$, but now with CR matrix elements involved. It is not obvious that this expression will reduce to a simple sum of the $r_{i\nu}$, suggesting the discrepancy in definitions arises because of the fundamental CR assumption that the target states will have a population, however small. Further investigation on this point is required.

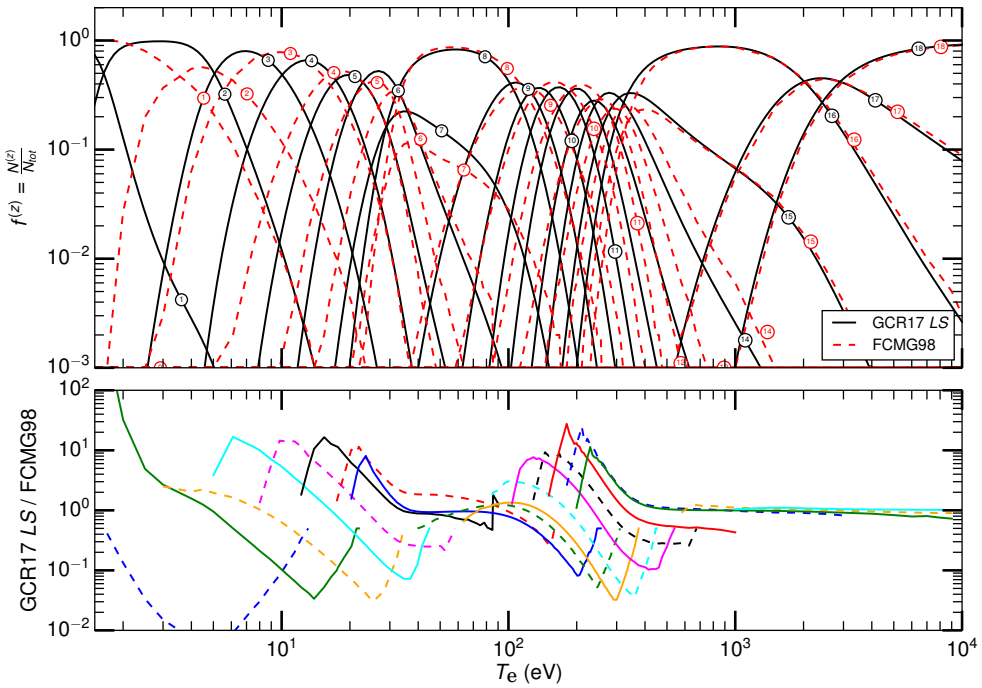

Figure 5.9: Comparison of unresolved fractional abundances for argon: present work using *unresolved* coefficients derived from *LS*-resolved run (GCR17 *LS*) versus Fournier et al. 1998 (FCMG98) [187]. The GCR17 *LS* model was calculated at an electron density of $N_{\mathrm{e}} = 10^{12}$ cm^{-3}. The small numbers in circles that lie on the fractional abundance curves (top pane) denote the ionisation stage z.

Comparison with another important CIE model literature source, FCMG98 [187], yields a similar result as with BLS09: see figure 5.9. This is unsurprising given the similar heritage of the ionisation and recombination rate coefficients used in FCMG98, BLS09, and their ancestor, AR85 [179]. Disagreement of the fractional abundances is worst for the near neutrals at this finite density, improving marginally with increasing ionisation stage until convergence is reached for He-like and beyond. Once again, reproducing this comparison at a low density of $N_\mathrm{e} = 10^4$ cm^{-3} improves the agreement, but similar discrepancies remain for Ne-like Ar^{8+} to B-like Ar^{14+}. The reason is the same as when comparing with BLS09: the α^{cd}'s do not approach the zero-density, total recombination rate coefficients. Lingering differences of the near neutral fractional abundances can also be attributed to fundamental discrepancies in the DR rate coefficients used. The other literature sources under the AR85 lineage—Sutherland and Dopita [185] and Mazzotta et al. [178]—all share these comparative features because they are quite similar. They have therefore been omitted from explicit comparison.

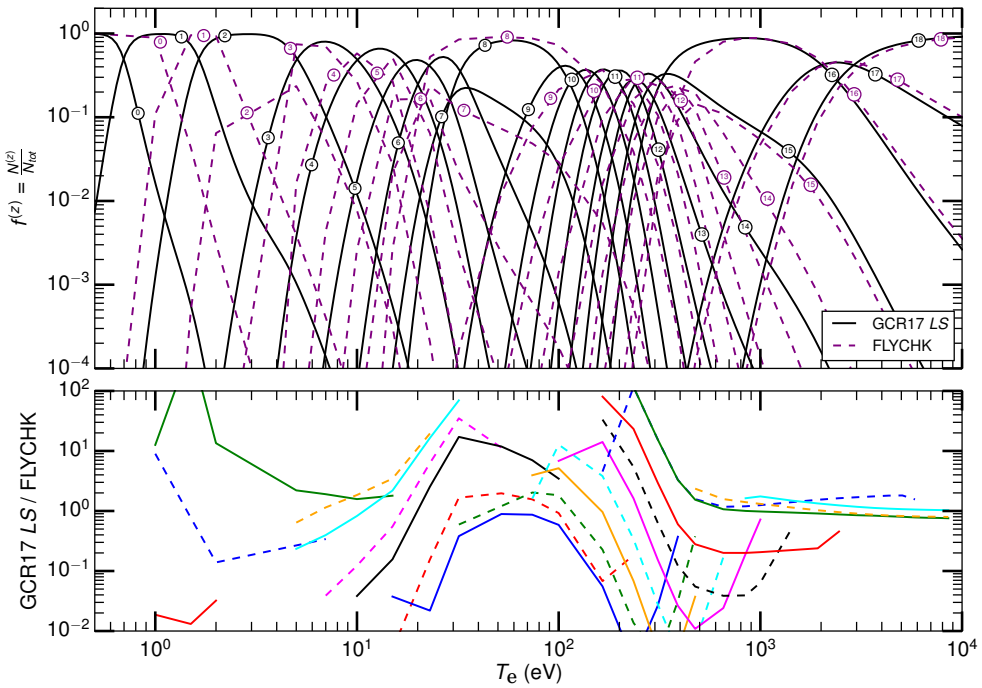

Figure 5.10: Comparison of unresolved fractional abundances for argon: present work using *unresolved* coefficients derived from *LS*-resolved model (GCR17 *LS*) versus FLYCHK [192]. Both models were calculated at an electron density of $N_\mathrm{e} = 10^{12}$ cm^{-3}. The small numbers in circles that lie on the fractional abundance curves (top pane) denote the ionisation stage z.

Next, consider the comparison with the AIM-type model of FLYCHK in figure 5.10. Similar trends to the above are apparent in the ratios of the bottom pane. Differences between the fractional abundances is worst for near neutral stages at low temperature but slowly improves until convergence is achieved at high temperatures for the highly-ionised stages. However, the average relative differences in this case are larger than for any of the CIE models. This is to be expected since the FLYCHK AIM is fundamentally a high-density model that relies on the corresponding statistical balance within n-shells in these domains. Results at $N_e = 10^{12}$ cm^{-3} lie at the lower bound of this model's applicability. Furthermore, the FLYCHK results on the web[4] do not allow for the temperature grid to be set, resulting in a poor logarithmic spacing of points at low temperatures, but the trend is clear.

Finally, consider the two lower-quality ADAS models, ADAS85 and ADAS89, in figures 5.11(a) and 5.11(b), respectively. Again, the ratios in the bottom panes reveal similar trends to the previous comparisons, but now the agreement for the middle ionisation stages, Ne-like Ar^{8+} to B-like Ar^{14+}, is much better. This suggests that there is an internal consistency within ADAS for the definition of the α^{cd}, and the disagreement with literature sources likely comes down to differences in this definition. Moreover, these baseline data perform quite well in the context of the other literature sources, with no gross errors evident.

[4]For unregistered users `https://www-amdis.iaea.org/FLYCHK/ZBAR/csd018.php`

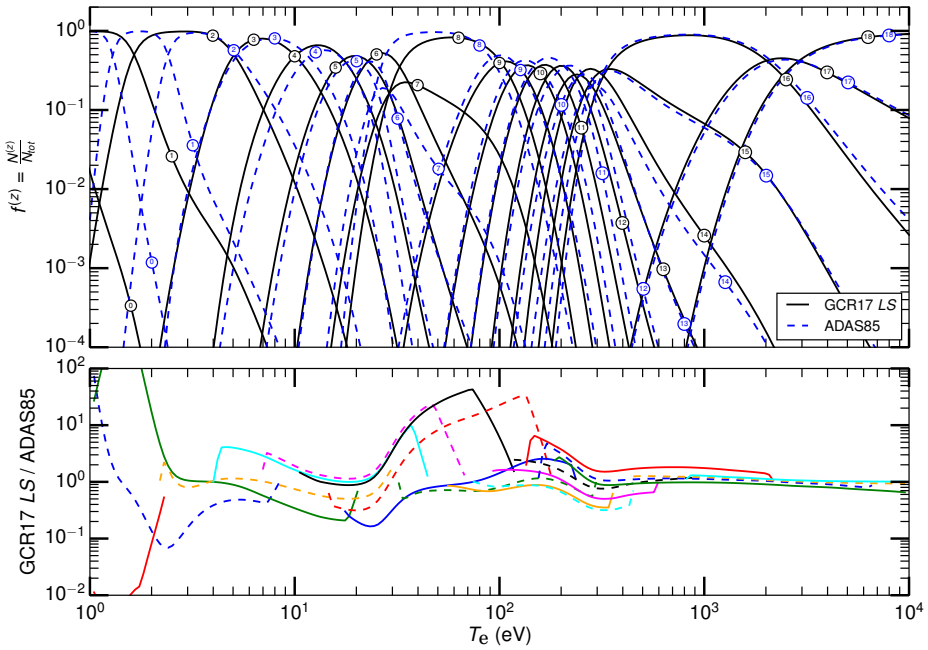

(a)

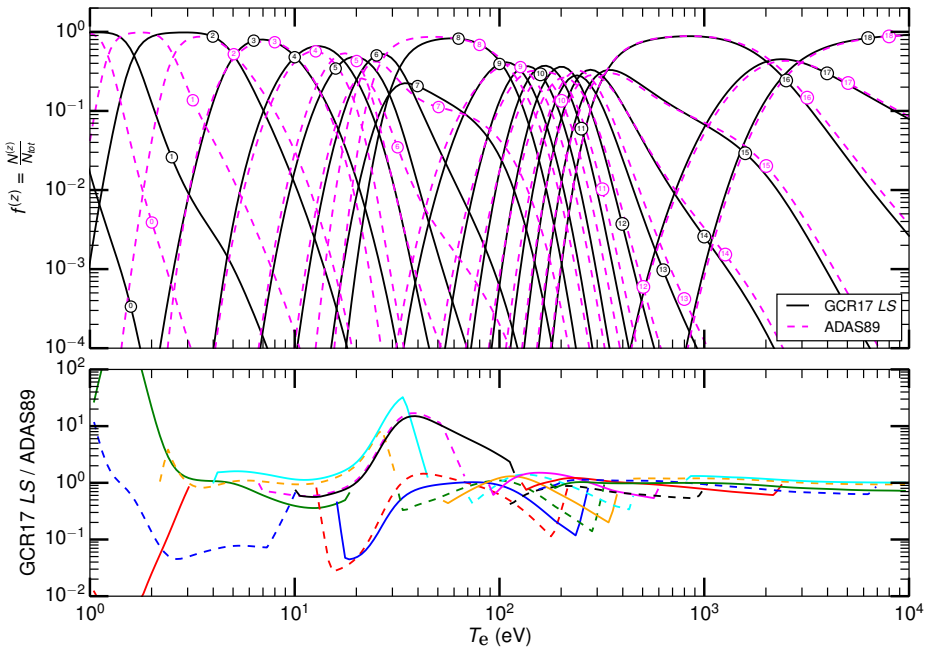

(b)

Figure 5.11: Comparisons of unresolved fractional abundances for argon: present work using *unresolved* coefficients derived from the *LS*-resolved model (GCR17 *LS*) versus (a) the year 85 GCR coefficients in ADAS (ADAS85) and (b) the year 89 GCR coefficients in ADAS (ADAS89). All models were calculated at an electron density of $N_e = 10^{12}$ cm^{-3}. The small numbers in circles that lie on the fractional abundance curves (top panes in a and b) denote the ionisation stage z.

5.3 First *ic*-resolved Ionisation Balance

The culmination of this chapter and thesis is an intermediate-coupled ionisation balance. This section presents the *ic*-resolved metastable fractional abundances for argon, a first for any element within ADAS and, it is believed, the literature. Figure 5.12 displays the result at $N_e = 10^{12}$ cm^{-3}, and the cluttered nature of the metastable fractional abundances shows that handling these data in modelling codes will bring challenges. The energy-ordered ground level is always represented by a solid line within an ionisation stage, so an intriguing observation from this figure is that the dominant metastable level is not always the ground level. Some spread in $T^{(\mathrm{pk.})}$ for the metastables in a stage are possible, as seen in the bottom pane, but by and large, they cluster around $T^{(\mathrm{pk.})}$ of the ionisation stage, just like the *LS* case in figure 5.5.

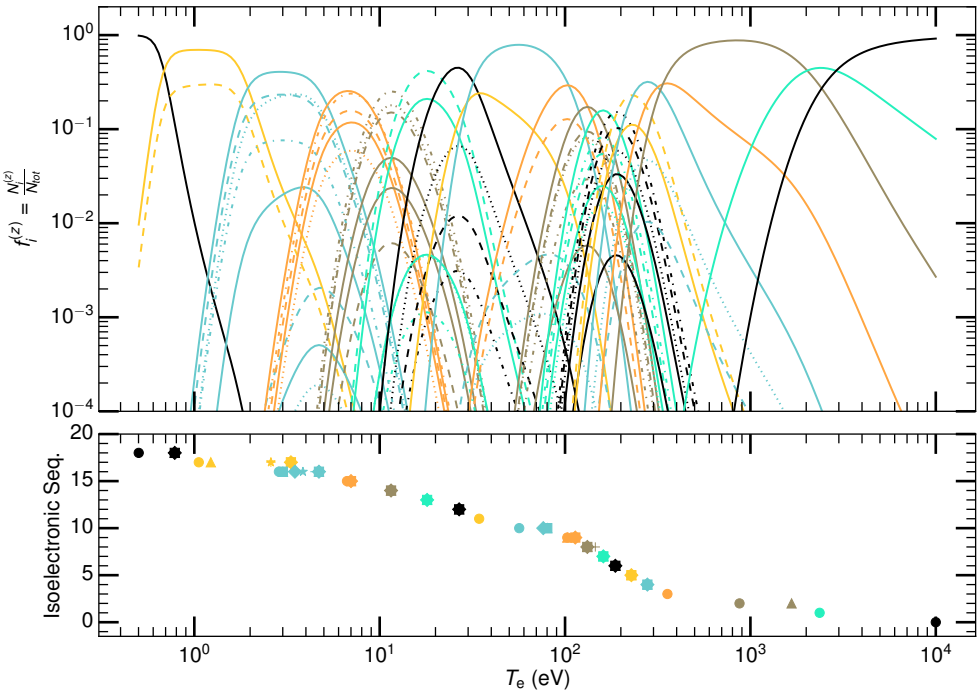

Figure 5.12: *Ic*-resolved metastable fractional abundances for Ar from the novel GCR model at $N_e = 10^{12}$ cm^{-3}. The top pane displays the metastable-resolved fractional abundance curves, and the bottom pane gives the temperature of peak abundance, $T^{(\mathrm{pk.})}$, for each metastable. Ionisation stages are demarcated according to color, while the *ic* metastables within each stage are differentiated by line style (top pane) or marker style (bottom pane). No IIE rates have been included.

Because this is the first result of its kind, no direct comparisons are possible,

but there are other avenues to validation. The effects upon the power coefficients and cooling curves are explored in section 5.4. A means of qualifying the differences between fractional abundances in different resolutions is explored in section 5.3.3. Also, the *ic*-resolved GCR model needs to explicitly include ion-impact excitation (IIE) between the fine-structure metastables, and section 5.3.1 assesses this novel topic. Another important question is whether all of the fine-structure levels within a metastable term will themselves also be metastable. Section 5.3.2 distinguishes between genuine and superfluous *ic* metastables using the newly generated fractional abundances and compares these to the analogous results that were generated from the *LS*-GCR model in section 5.2.2. However, the ultimate test of the atomic population model resolution will be through subsequent application in transport and plasma modelling.

5.3.1 Influence of IIE

An important question to answer is where the inclusion of IIE rates in population modelling is necessary. Section 4.1 outlined some "rules of thumb" for predicting where IIE rates would be significant in the parameter space of an atomic system. The culmination was equation 4.5 from which it was concluded that only transitions with extremely small energy differences relative to the ionisation potential or ion temperature are affected by IIE. Then, the observation was made that this readily applies to fine-structure levels and is of particular importance for levels belonging to metastable terms since these will dominate the atomic population model. From this line of reasoning, it was concluded that IIE rates between fine-structure metastables must be explicitly included in any *ic*-resolved GCR model. These rules have been constructed purely from an atomic physics basis, but the behaviour of an atom in a plasma is described by an atomic population model that connects the atomic physics of the constituent with the plasma physics of the macroscopic whole. The true influence of IIE will only be apparent through the lens of GCR modelling.

The bulk of studies in the literature have neglected a consideration of collisions with positive ions in their models, often for justifiable reasons: light elements are modelled well with *LS*-term populations, which implicitly assume the collisional mixing of IIE produces a statistical balance amongst the sub-levels. But there

are some noteworthy exceptions that address IIE explicitly when analysing emission line ratios. Here, an emission line that is sensitive to either the electron temperature or density is compared to a line that is relatively insensitive to the independent variable. Density or temperature dependent emissions lines tend to be correlated with forbidden transitions because the collisional rates (excitation and de-excitation) associated with the upper level actually have a chance to be of a similar magnitude as the smaller A-values in the CR regime of densities. However, forbidden lines are necessarily quite weak in intensity, so the only observable ones tend to be those associated directly with or fed by metastable levels of a substantial population. So, these forbidden lines are often the same fine-structure metastable transitions that have been focussed on throughout this thesis.

In solar spectroscopy, it has long been known that collisional excitation by *protons* must be incorporated in population models for a variety of line intensity ratios. One of the earlier examples is the coronal green line [90] of Fe^{13+}, $3s^2 3p\ ^2P_{3/2} \rightarrow 3s^2 3p\ ^2P_{1/2}$, along with the Fe^{12+} spectrum [193] and the spectra from number of Be-like ions [87, 194]. Forbidden lines are also relevant for laboratory, and particularly tokamak plasmas, because their long wavelengths emit in the visible region where the light can be relayed via fibre optics and the calibration of spectrometers is simple [101, 195–199]. Also, Doppler broadening is more visible at these long wavelengths. However, these line ratio studies treat the ratio of two lines within a single ionisation stage, which removes the need to determine the abundance of that ionisation stage, and so a single-stage atomic population model is completely sufficient for most cases.[5] These models are mostly of a simplified nature, considering only collisional (de)excitation and spontaneous emission rates in LSJ or ic resolution. Furthermore, these studies only consider *protons* as the projectile species rather than other fuel ions. Therefore, this class of work is effectively orthogonal to the present objectives of determining radiated power loss and the associated precursor of fractional abundances.

Notwithstanding these comments, special mention of [196] is merited because

[5]Of course, there will be a loose dependence of the excited state populations upon the adjacent ionisation stages, meaning the relative abundance of these stages would in theory need to be determined. However, the variation this causes amongst the highly-resolved, low-level set from which these emission lines originate will almost always be negligible; indeed, this is what justifies the *quasi-static equilibrium* assumption and allows for the influence of the excited populations to be condensed and projected upon the metastables.

this work presents the metastable populations of the second period sequences B-like through F-like (ground configuration $2s^2 2p^k$, $k = 1 \ldots 5$) both with and without proton-impact excitation for Cr, Fe, and Ni. Although the CR model is quite simple, the results unambiguously show that the inclusion of proton-impact excitation is significant: depending on the sequence, variations of 10% to 20% can be expected, with differences as high as a factor of 2 observed in some cases. Another notable study is [199] that looks at the intensity ratio of the EUV emission lines, 114.412 Å [$1s^2 2s 2p^2\ ^2P_{3/2} \rightarrow 1s^2 2s^2 2p\ ^2P_{3/2}$] / 117.144 Å [$1s^2 2s 2p^2\ ^2P_{1/2} \rightarrow 1s^2 2s^2 2p\ ^2P_{1/2}$], produced by the Fe^{21+} ion in both EBIT and stellarator plasmas. Contrary to the rest of the literature, it applies a fairly sophisticated *ic*-resolved CR model that accounts for ionisation and recombination processes in addition to collisional (de-)excitation and radiative decay; however, the source of its ionisation and recombination data is not disclosed, and given the extensive attention that was required for a proper consideration of these processes in the context of the present GCR model, it is suspected that these processes are handled in an *unresolved* manner. Moreover, nothing is said of the influence of highly-excited states. Even so, this result is undeniably more advanced than its contemporaries, and it still makes largely the same finding: proton-impact excitation must be included in the CR model if a correct physical interpretation of the measured intensity ratios is to be formed. Interestingly, it was found that the variation of the proton to electron density ratio by injection of an iron pellet also caused the intensity ratio to vary measurably. The injection of an iron pellet can affect the plasma temperature and energy confinement in addition to the density ratio, so it must be finely tuned to avoid disrupting the plasma.

Reference [200] is a study that does not fall into the same category as the above. It has the same objective as the present work: to estimate the radiated power loss from tokamak plasmas caused by impurity species. It is unique because it includes contributions from proton-impact excitation within the power loss estimate. A coronal model is used but with a second temperature parameter included to simulate deviations from equilibrium, and no mention is made of ionisation and recombination data. Also, it seems like only the total excitation line power loss is considered, since no mention is made of the recombination-cascade-bremsstrahlung contribution. New calculations for proton-impact excitation cross

sections are presented, but with a simple technique to incorporate the physics. Their findings show that even at coronal equilibrium, protons are responsible for about 30% of the total radiative loss involving iron ions at $T_e = 2$–3 keV. The accuracy of this claim is open to interpretation given the numerous approximations used and the fact that the total radiated power function is found to not vary with IIE in section 5.4.2 of this work. Regardless, this source can be cited as an example for the potential influence of IIE in atomic population modelling.

In total, these previous works address a number of specific or isolated cases where IIE must be included in the population model if a valid result or correct intepretation is to be produced. However, they do not attempt a general conclusion, which is the aim of the present work. Moreover, the majority of these works have assumed an equality between electron and ion densities based on quasi-neutrality: $N_e = \sum_i N_i$. Although this is broadly true, it can be violated under non-equilibrium conditions. Furthermore, most studies only consider proton projectiles, meaning $N_e \approx N_p$ is assumed, which can breakdown if there are significant concentrations of other positive ions. As noted above, reference [199] finds that the variation of the $N_p : N_e$ ratio is possible by introducing heavy impurities, and this variation noticeably influences the line ratios. The new *ic*-resolved GCR implementation allows the ion projectile densities to be set explicitly and without restriction—see section 5.1.2.5. Similarly, $T_e = T_i$ is usually assumed, but because of the slow thermalisation time scales for ion projectiles, there are many non-equilibrium plasma scenarios where the ion temperature can be greater than the electron temperature, sometimes by as much as a factor of two. At the moment, the consideration of separate ion temperatures is not handled by the *ic*-resolved GCR model, but a straightforward modification of the IDL routine mentioned in section 5.1.2.5 is all that should be necessary to achieve this.

5.3.1.1 Metastable Scans

Prior to the *ic*-GCR results, a general parameter-space scan was performed to find plasma conditions influenced by IIE effects. In equilibrium balance, each ionisation stage will only be present in a substantial quantity over a fairly limited temperature range. Under such conditions, the temperature at peak abundance of an ion, $T^{(\mathrm{pk.})}$, is taken as representative of the temperature input for rates

when modelling the ion. Knowing $T^{(\mathrm{pk.})}$ requires the ionisation balance to have already been determined, but baseline data such as the 89 series ADAS data or the ionisation potential ($\chi^{(z)}$) are sufficient to estimate $T^{(\mathrm{pk.})}$. Ions are not bound to any particular density range, and the plasma density will be determined by the operational constraints of the experimental device or astrophysical environment, which can vary widely. Thus, it is possible to limit the temperature domain but not the density domain for a particular ion. The only remaining independent variable from this simplified standpoint is the impurity element and the array of ions it spawns.

This investigation tracks the dominant metastable level populations along a selection of isoelectronic sequences to see how these populations vary with and without IIE. For each ion, the population model is simple: they are for a single stage, only include collisional and spontaneous emission rates for the low-lying states, and do not consider the *projected* influence from highly-excited states—the topic of projection is briefly explained at the end of Appendix C. This corresponds to running ADAS205 or ADAS208 with the minimum *adf04* input. Ultimate accuracy is not the objective here, so the neglect of these facets is justified: a rough sense of where IIE is influential will still be possible. The requisite *adf04* files are taken from the previous AUTOS DW baseline created under ADAS-EU [24]. The IIE Υ_{ij}'s in the *adf06* files were added directly to the corresponding transitions in the *adf04* files. This procedure produces the same result as adding the IIE rate coefficients to the Q^{cd} coefficients that was described in section 5.1.2.5. An electron density of 10^{13} cm^{-3} was selected as a typical value for JET plasmas, and two temperature cases were used in line with the above: $T_{\mathrm{e}} = T_{\mathrm{i}} = T^{(\mathrm{pk.})}$ obtained from the stage-to-stage ionisation equilibrium calculation of ADAS405 with 89 series input data, and $T_{\mathrm{e}} = T_{\mathrm{i}} = \chi^{(z)}/k$, with the ionisation potentials sourced from NIST.

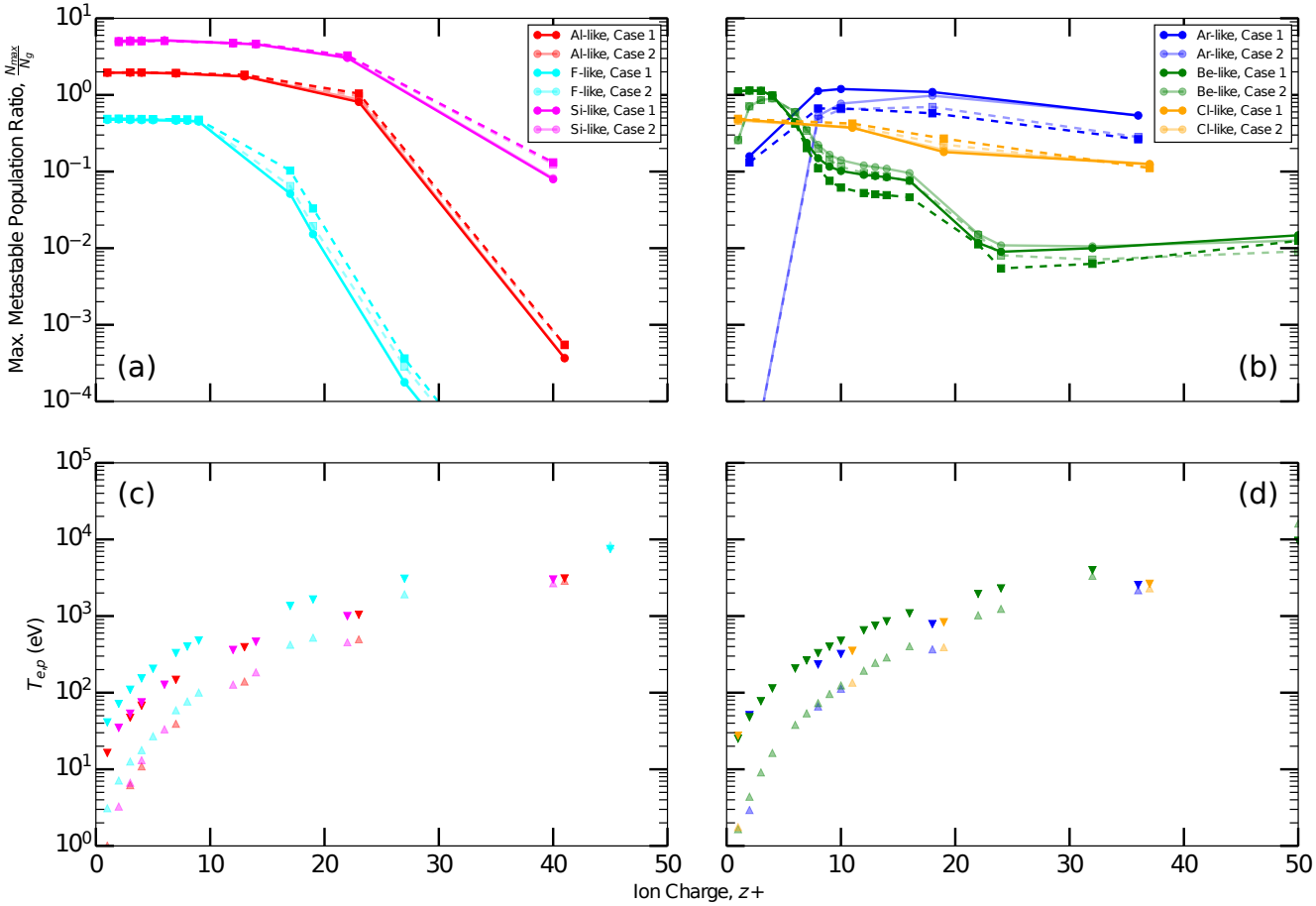

Figure 5.13: The maximum metastable population population ratio, N_{max}/N_g, with and without IIE along the Al, Ar, Be, Cl, F, and Si-like isoelectronic sequences. Only protons were considered as ion projectiles. Temperature case 1 (completely opaque) uses $T_\mathrm{e} = T_\mathrm{p} = \chi^{(z)}/k$, and case 2 (semi-transparent) uses $T_\mathrm{e} = T_\mathrm{p} = T^{(\mathrm{pk.})}$ obtained from ADAS405 with the 89 series baseline data. Subfigures (a) and (b) plot N_{max}/N_g versus ion charge excluding IIE (solid lines, circle markers) and including IIE (dashed lines, square markers) at these two temperatures. All markers (circle, square, triangle) denote the ions where an ADAS208 population calculation was performed. Subfigures (c) and (d) give the two temperatures used in the population models of the ions in the respective subfigure directly above. Case 1 is denoted by the opaque, downward pointing triangles, and case 2 by the semi-transparent, upward facing triangles. $N_\mathrm{e} = N_\mathrm{p} = 10^{13}$ cm^{-3} was used for all calculations.

Figure 5.13 depicts the results of this investigation. In subplots (a) and (b), the ratio of the maximum metastable population to the ground state, N_{max}/N_g, is used as a proxy for all of the metastable populations of the particular ion. Therefore, it is the variation of this quantity with the inclusion or exclusion of IIE that is of primary interest and will indicate how influential IIE is upon the population calculation. Figure 5.14 presents the relative difference,

$$\Delta N = \frac{\left| N_{max}^{(\text{iie})} - N_{max}^{(\text{no iie})} \right|}{N_{max}^{(\text{no iie})}} = \frac{\left| (N_{max}/N_g)^{(\text{iie})} - (N_{max}/N_g)^{(\text{no iie})} \right|}{(N_{max}/N_g)^{(\text{no iie})}}, \tag{5.14}$$

caused by this binary consideration of IIE. The behaviour of N_{max}/N_g along an isoelectronic sequence can broadly be split into two categories represented separately by figures 5.13 (a) and (b). First, subplot (a) shows this ratio decreasing as z increases, meaning the metastability in these systems decreases at higher z. Further, the inclusion of IIE (dashed lines) causes the ratio to increase above approximately $z = 10$, and figure 5.14 displays fairly large relative changes associated with the Al, F, and Si-like isoelectronic sequences. Of course, because the absolute value of N_{max}/N_g is decreasing along these sequences, the importance of the relative changes also diminishes, but nonetheless the results are meaningful. This type of behaviour is associated with isoelectronic sequences that have a ground term with multiple levels. Both Al-like and F-like have a doublet ^{2}P ground term that splits into two levels ($J = 1/2, 3/2$), and Si-like has a triplet ^{3}P ground term that splits into three levels ($J = 0, 1, 2$). The IIE transitions that are included in these cases will connect the ground level ($J = 1/2$ or 0) to the other excited levels in the term, enhancing the populations of these metastables, and thus accounting for the increase of N_{max}/N_g. The insensitivity to IIE at low z can be explained by the fact that LS-coupling holds well in this regime and the density selected means these states are already in LTE without the help of IIE rates. What role IIE plays in the context of LS resolution is explored more below. Another observation is that all of the relevant quantities in this category of behaviour are insensitive to the two temperatures chosen. For ions that lie in the CR regime, the two temperatures fall where the collisional rates have largely plateaued; however, at high z this may no longer be true because the two temperature cases converge anyway, as seen in figure 5.13(c).

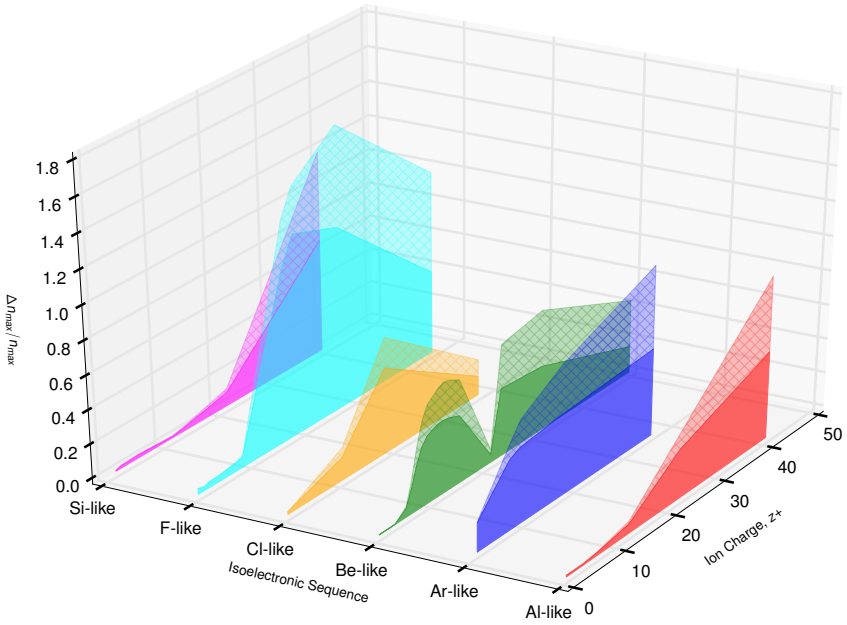

Figure 5.14: The relative difference of the maximum metastable population, ΔN, caused by the inclusion of IIE along the Al, Ar, Be, Cl, F, and Si-like isoelectronic sequences. This relative difference is calculated according to equation 5.14 and the input values are derived from figures 5.13 (a) and (b). Note that because a modulus operation is used in equation 5.14, information about whether the inclusion of IIE causes an increase or decrease to the maximum metastable population is lost here in comparison to figure 5.13. Temperature case 1 is represented by the lower, more opaque, completely filled polygons, while case 2 is represented by the more transparent, cross-hatched polygons "on top" of those from case 1 (i.e. the case 2 ΔN values are stacked on those from case 1). Again, $N_\mathrm{e} = N_\mathrm{p} = 10^{13}$ cm^{-3} was used.

A second type of behaviour is observed in figure 5.13 (b). Here, N_{max}/N_g is comparatively constant along the isoelectronic sequences, and the inclusion of IIE causes the ratio to drop, in contrast to the previous category of behaviour. Figure 5.14 confirms that these are significant relative changes. The Cl-like sequence is anomalous because although the ratio plateaus along z, it does see an increase rather than a decrease upon adding IIE, unlike the two other cases in this category. For the two characteristic cases of Ar-like and Be-like, the atomic structure features a ^{1}S ground term and level ($J = 0$) and a ^{3}P metastable term with the usual three levels. In this scenario, the IIE transitions that are supplemented are only between the levels of the ^{3}P metastable term since transitions from the ground would not be of order $E2$: recall, IIE rates should be most substantial for *intra*-metastable term transitions not *inter*-metastable term transitions. So, IIE

transitions will redistribute the populations of the ^{3}P levels internally rather than enhance these populations from the ground level. In *ic*, the $^3P_1$ level will have an A-value to the ground level, and so the redistributive effect of IIE amongst the ^{3}P levels will actually provide the $J = 0, 2$ levels with additional pathways to the ground, thus suppressing them and explaining the corresponding drop in N_{max}/N_g. Similar to the previous behaviour category, the effects of IIE are negligible at low z for all of the sequences; however, there is more sensitivity to the two temperature cases. In relation to only N_{max}/N_g, this is most evident for the near neutral states of Ar-like and Be-like in figure 5.13, but differences can be discerned across the z range. This sensitivity to temperature also extends to the differences introduced by IIE; figure 5.14 shows notable differences between the ΔN values at moderate ion charges for the two temperature cases. In this z range, $T^{(\mathrm{pk.})}$ and $\chi^{(z)}$ still differ significantly (plots (c) and (d) of figure 5.13), and moderately large z values are amenable to creating the conditions for CR regimes.

Coupling resolution and density effects are inextricably bound. In regimes where *LS* coupling is appropriate, the inclusion of IIE transitions are essential for establishing LTE and the associated statistical balance amongst levels of the *LS* terms. An implicit assumption is being made here: if one is working at J resolution in a regime also appropriate to *LS*, while using the typical approach that only considers EIE and spontaneous emission, then the only missing physics will be IIE. This assumption holds under *LSJ* coupling where the inclusion of IIE will recover the *LS* term populaitons, but it is inaccurate for *ic*. Namely, strict *LS* selection rules do not apply in *ic*, since state eigenvectors are no longer pure basis set vectors. As a result, there will be radiative transitions with significant A-values between some sublevels of two distinct terms but no spontaneous emission between the terms themselves. This can alter the atomic population greatly, and some examples are provided below. In general, one should not expect to recover the results of an *LS*-resolved model by adding IIE rates to an *ic*-resolved one if the fine-structure effects are significant for the atom in question. Indeed, this is the main reason why a switch to *ic* is desirable, and further discussion in the context of different modelling regimes is made surrounding figures 5.15 and 5.16. On the other hand, where fine-structure effects can be neglected, like

with light species, then *ic* will approach *LSJ* coupling, and the inclusion of IIE *should* bring an *ic*-resolved model into closer agreement with an *LS*-resolved one; that is, IIE should hasten the onset of LTE conditions for the term levels. But this is not observed for either of the two Be-like ions presented. Rather for the lighter C^{2+} case in figure 5.18, one observes the onset of LTE at a lower density but this is independent of IIE being considered.

There are practical implications related to these coupling considerations because the *LS*-resolved *adf04* files for the present Argon Case Study (section 5.1.3.1) have been produced by bundling *ic*-resolved *adf04* files. Because of the forbidden transitions that are present in the *ic* files, the resulting *LS* files will be fundamentally different than those produced from pure *LS* calculations, with observable consequences for the resulting term populations: compare the *LS* populations for Be-like Ar^{14+} in figure 5.15 against figure 5.16. The same occurs for C^{2+} below, and discrepancies were also found in section 5.2.2 when analysing the metastable terms predicted by the standard ADAS list which used pure *LS* selection rules versus those predicted by the *LS*-GCR model that uses bundled *adf04* files. Although the results in this section suggest that the pure *LS* data achieves closer agreement with the *ic* data, a look ahead to section 5.3.2 shows that metastables of Be-like are an anomalous case, and in general, the bundled *LS* data achieves better agreement with *ic*. Pure *LS* conditions are rare in reality, and the ADAS database contains few pure *LS* calculations. Rather, the past success in modelling light elements with term populations has been predicated on *LS*-resolved data with mixed state vectors bundled in.

The density domain was investigated for individual ions because of the complexity involved in interpretation. The population models that follow are constructed as described at the beginning of this section for figures 5.13 and 5.14, now with a wide range of densities using the ADAS208 program A corresponding *LS*-resolved calculation is also performed. The Be-like sequence was judged as a suitable test case because of the rich behaviour observed in figure 5.13(b). Then, Ar^{14+} was selected as an example of a moderate z ion in this sequence that should have measurable fine-structure effects and is definitely influenced by IIE at least at the density of 10^{13} cm^{-3} and $T^{(\mathrm{pk.})} \approx 300$ eV used in the previous step. Figure 5.15 shows the density-scaled population ratio, $N_i/(N_\mathrm{e}N_1)$, at different

resolutions for the ^{3}P term with the level populations including IIE compared to LS term populations with no IIE. In the coronal regime, the population to ground ratio, scaled by N_e, is flat because $N_i/N_1 \propto N_e q_{1\to i}$, while at LTE, it will decrease linearly because $N_i/N_1 \propto \omega_1/\omega_i$, a constant.

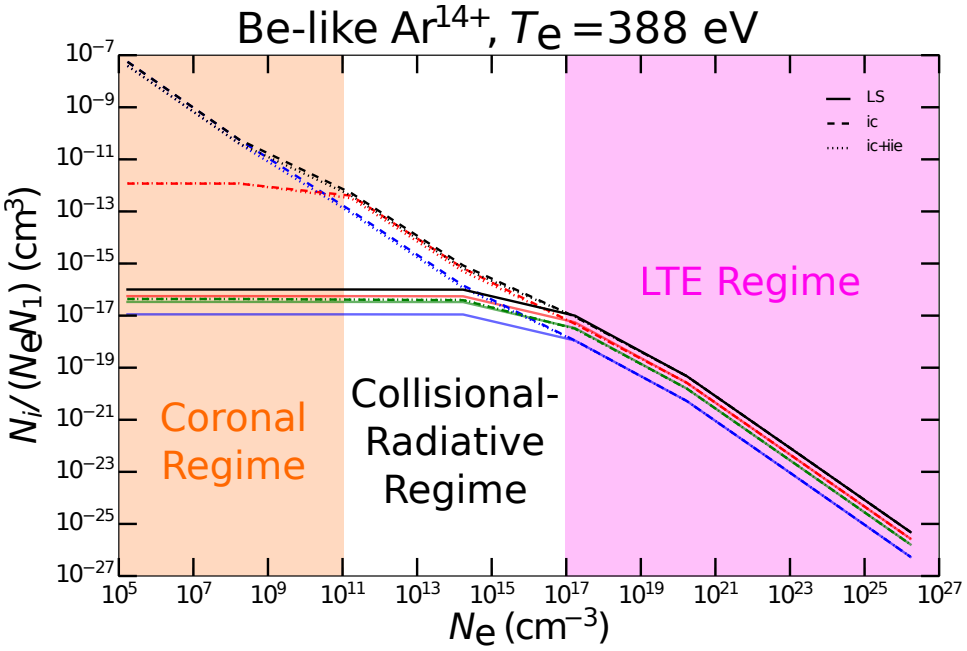

Figure 5.15: Scaled metastable population ratios, $N_i/(N_eN_1)$, for Be-like Ar^{14+} across all density domains, indicated by vertical bands with labels. The term considered is ^{3}P, the first excited above the ^{1}S ground, and the sub-levels are distinguished by colour as specificed in figures 5.16 and 5.17. Only proton-impact exciation is included for the "iie" case.

For Ar^{14+} at $T_e = 388$ eV, which is near its $T^{(pk.)}$, the low density coronal regime extends to approximately $N_e = 10^{11}$ cm^{-3}. Justification is provided by table 5.5 where in the $N_e = 10^8$ cm^{-3} block, all of the A-value to collision rate ratios are large numbers, except from transition $2 \to 4$. Consequently, spontaneous emission dominates the population distribution both within the ^{3}P metastable term (columns 6 and 7) and from the ground (column 8). Also, this explains why IIE has no effect upon the population distribution in the coronal regime: collisions, whether by electrons or ions, are dominated by the radiative decay of these levels. It is here too that differences between LS-coupling and ic are most prominent. In figure 5.15, the LS data has been produced by bundling the ic data, so there is an A-value present for $^3\text{P} \to {}^1\text{S}$, meaning this term effectively loses its metastablility and behaves like an ordinary term: this manifests as the

Table 5.5: Collisional and radiative quantities for Be-like Ar^{14+} at $T_e = 388$ eV. The indices in the transition column are for the levels, $1 : {}^1S_0$, $2 : {}^3P_0$, $3 : {}^3P_1$, $4 : {}^3P_2$.

Transition	$A_{j\to i}$	$q^{(e)}_{i\to j}$	$q^{(p)}_{i\to j}$	$q^{(p)}/q^{(e)}$	$\frac{A_{j\to i}}{(N_e q^{(e)})}$	$\frac{A_{j\to i}}{(N_e q^{(e+p)})}$	$\frac{A_{3\to 1}}{(N_e q^{(e+p)})}$
					$N_e = 10^8$		
$1 \to 3$	2.610+06	3.217−11	—	—	8.113+08	—	—
$2 \to 3$	6.830+00	9.540−11	—	—	7.160+02	—	2.736+08
$2 \to 4$	9.190−04	8.319−11	5.307−10	6.379+00	1.105−01	1.497−02	4.252+07
$3 \to 4$	5.640+01	1.016−10	4.381−10	4.312+00	5.551+03	1.045+03	4.836+07
					$N_e = 10^{13}$		
$1 \to 3$					8.113+03	—	—
$2 \to 3$					7.160−03	—	2.736+03
$2 \to 4$					1.105−06	1.497−07	4.252+02
$3 \to 4$					5.551−02	1.045−02	4.836+02
					$N_e = 10^{22}$		
$1 \to 3$					8.113−06	—	—
$2 \to 3$					7.160−12	—	2.736−06
$2 \to 4$					1.105−15	1.497−16	4.252−07
$3 \to 4$					5.551−11	1.045−11	4.836−07

horizontal, solid, black line on the left hand side of the figure in the coronal and collisional-radiative regimes. Contrarily, the *LS* data in figure 5.16 comes from a true *LS*-coupled structure and collision calculation, so there is no *A*-value for ${}^3P \to {}^1S$, and therefore the ${}^3P$ term maintains is metastability—the scaled ratio decreases approximately linearly with density. This "true" *LS* case comes closer to reproducing the *ic* results in the coronal regime, but there are still sizeable differences if one compares the individual level populations. The reason is because only level 2 (${}^3P_0$) is truly metastable in the *ic*-resolved model, while the other two levels behave as ordinary levels, depleting the summed population of the term. As a result, the real behaviour of the term and its sublevels, as predicted by the *ic* model, is actually in between the pure and imitated *LS* models.

At the opposite end of the density domain is the LTE regime, which occurs for $N_e \gtrsim 10^{17}\,\mathrm{cm}^{-3}$ for Ar^{14+}. Observing the $N_e = 10^{22}\ \mathrm{cm}^{-3}$ block of table 5.5, this regime is typified by universally small ratios, $A_{j\to i}/q_{i\to j}$, confirming that collisions dominate the rate equations for these metastable levels. Once again, IIE rates have no impact upon the populations even though they are the larger collision rate for two of the transitions considered here. Under LTE conditions,

the dominance of collisional excitation and de-excitation leads to a statistical balance of these processes and the corresponding establishment of Boltzmann distributions, $N_j/N_i = \omega_i/\omega_j \exp\left(-(E_i - E_j)/kT_\mathrm{e}\right)$, for the relative populations of all levels, which are independent of the collision rates themselves. This is the physical reasoning behind the mathematical occurrence of N_e becoming the dominant term in the rate equations, not $q_{i\to j}$, leaving only the statistical weights. This explains why the *LS*-resolved model exactly agrees with the *ic*-resolved one in this regime: the weights of the levels, ω_i, are used to split the *LS* term population, which is what Boltzmann statistics prescribes. Both figure 5.15 and 5.16 display the behaviour at high N_e, so the LTE regime is independent of how the *LS* data is prepared.

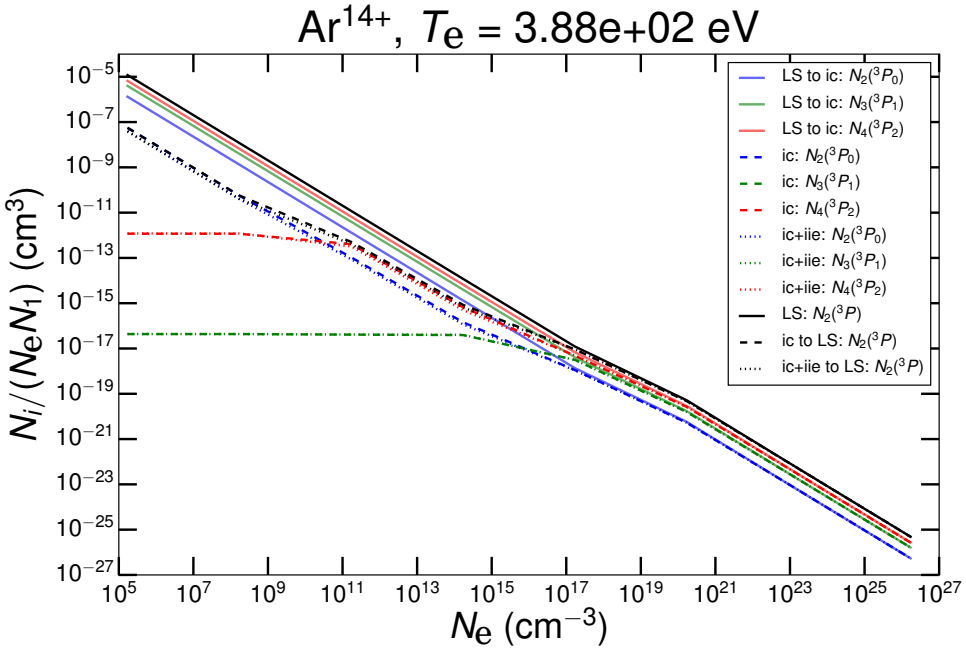

Figure 5.16: Scaled metastable population ratios, $N_i/(N_\mathrm{e}N_1)$, for Be-like Ar^{14+}. The term considered is ^{3}P, the first excited above the ^{1}S ground, and the sub-levels are distinguished by colour as indicated in the legend. The *LS*-term population has been calculated using pure *LS* data in this instance. Only proton-impact excitation has been included.

The final modelling regime for Ar^{14+} is the intermediate density CR regime. From figure 5.15, it is seen to exist in the density range, 10^{11} cm^{-3} $\lesssim N_\mathrm{e} \lesssim$ 10^{17} cm^{-3} for this particular ion. As its name suggests, it is characterised by comparable collisional and radiative rates, and the $N_\mathrm{e} = 10^{13}$ cm^{-3} block of table 5.5 shows a balance of ratios: the ratios for transitions within the ^{3}P term

(columns 6 and 7 excluding the $1 \rightarrow 3$ row) tend to be about 10^{-2}, indicating the prominence but not total dominance of collisions, whereas the $1 \rightarrow 3$ transition and comparisons to its radiative rate (column 8) are around 10^{3} in magnitude, demonstrating that this radiative decay is also still important. Because of this intermediate nature, the behaviour of the population model is necessarily more complex and cannot be described with simple mathematical expressions like in the previous two regimes. However, these are precisely the conditions where the population model is most sensitive to the values of the collisional rates, explaining why it is in this regime that the level populations are influenced by the inclusion of IIE. Figure 5.17 depicts a zoomed view of the scaled population ratio in this CR density regime, with 15–20% variation of the $J = 0, 2$ level populations apparent because of IIE. For the case of an excited ^{3}P term above a ^{1}S ground, the enhanced redistribution amongst the ^{3}P levels caused by the IIE transitions will lead to a suppression of the metastable levels because of the $^3\mathrm{P}_1 \rightarrow {}^1\mathrm{S}_0$ spontaneous emission that provides additional pathways to the ground.

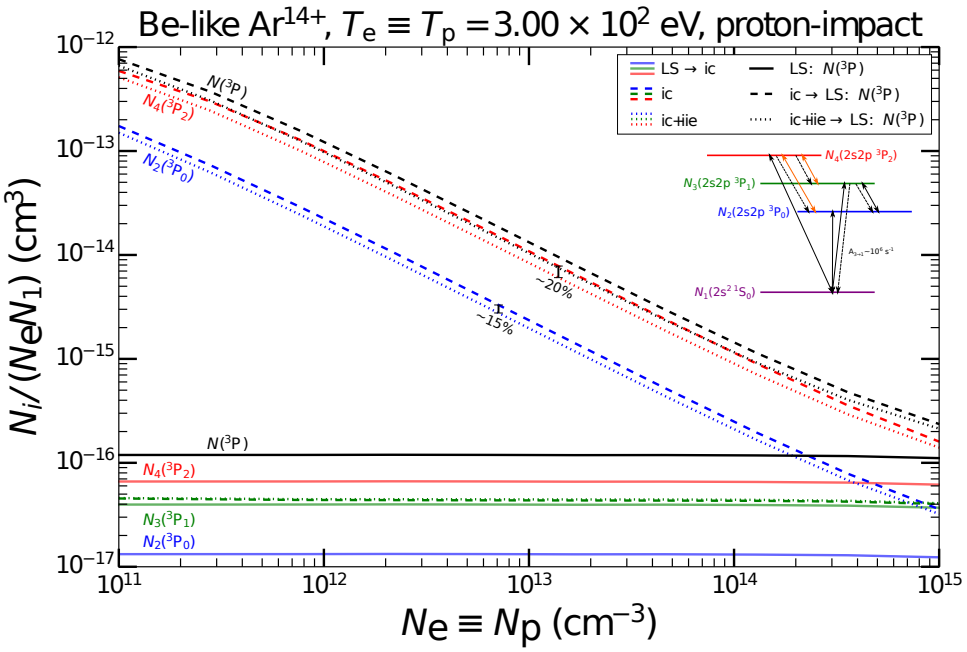

Figure 5.17: Scaled metastable population ratios, $N_i/(N_\mathrm{e}N_1)$, for Be-like Ar^{14+} in the CR density regime. The term considered is ^{3}P, the first excited above the ^{1}S ground, and the sub-levels are distinguished by colour, as indicated in the legend. Only proton-impact excitation has been included.

Now consider the example of a low-z ion in the Be-like sequence: the analogous

scaled population ratio results for C^{2+} are presented in figure 5.18. There are important differences. First, there is no apparent variation caused by the inclusion of IIE in any of the density domains. This seems to occur because of the equally important observation that there is no CR regime present for these levels. This is not to say that there will be no CR regime for other levels or at term resolution. Consulting table 5.6, it is noted that collisional rates dominate the transitions within the ^{3}P term across all of the density blocks, in contrast to Ar^{14+}, where the coronal regime experienced a near complete control by spontaneous emission. So, LTE is established by collisions amongst the levels of the ^{3}P term across all densities. But below $10^{12}\,\mathrm{cm}^{-3}$, the "forbidden" $1 \rightarrow 3$ spontaneous emission depletes the population of level 3 far faster than the collisions can, making it behave as an ordinary level, and thus accounting for the difference with the *LS* results at these lower densities. Moreover, there is no "sweet spot" where a balance between this relatively large radiative decay (it is small in absolute terms) and the collisions within the term is achieved. Therefore, at no point is the population model particularly sensitive to the collisional rate coefficients, explaining the independence from IIE effects; this problem is compounded by the fairly low $T^{(\mathrm{pk.})}$ which suppresses the IIE rate coefficient more so than the EIE one, supported by the fairly low ratio of these quantities in table 5.6. Overall, most of this behaviour can be explained by the small energy differences between these levels which allows for collisions to be so much more significant than spontaneous emission.

In summary, there are a number of factors that must align to produce a noticeable influence of the IIE rates upon the dominant metastable populations and thus the population model in general. First and foremost, the impurity ion must be one for which a CR regime specific to the metastable levels exists. This criterion is typically satisfied by moderately charged ions ($z \gtrapprox 10$) because they produce an appropriate degree of fine-structure splitting that allows radiative and collisional rates to be comparable but still small enough for IIE to be significant. These effects can persist to more highly charged ions but tend diminish with increasing z. Second, T_e must lie outside of the steeply suppressed region of the IIE collisional rates for the metastable level transitions of interest. Lastly and self evidently, T_e and N_e must lie within the region delineated by this CR regime.

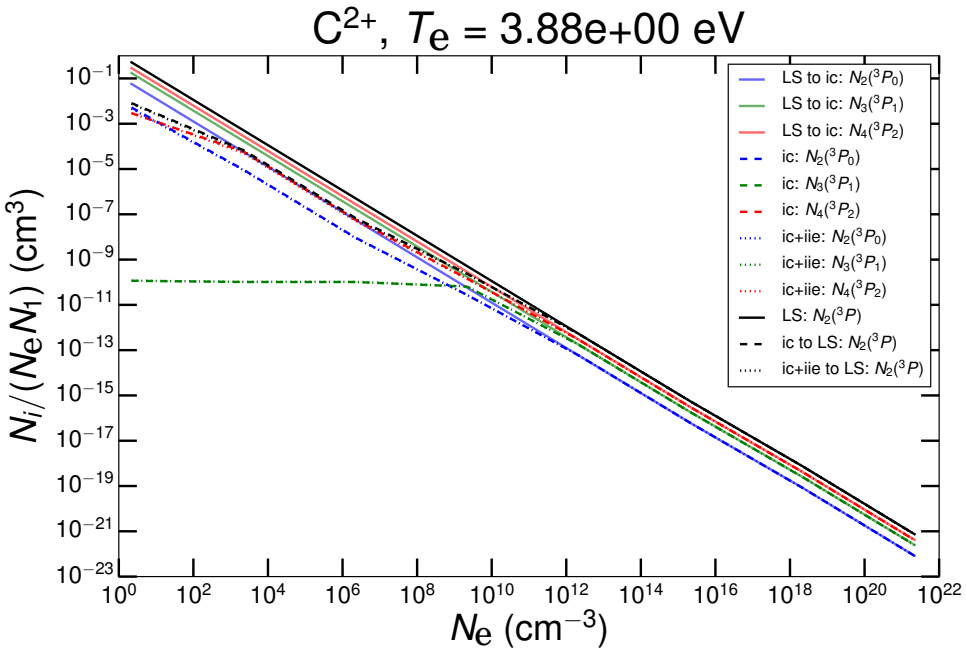

Figure 5.18: Scaled metastable population ratios, $N_i/(N_\mathrm{e}N_1)$, for Be-like C^{2+} across a broad density range. The term considered is ^{3}P, the first excited above the ^{1}S ground, and the sub-levels are distinguished by colour, as indicated in the legend. Only proton-impact excitation has been included.

Whether this is satisfied will be determined by the operational constraints of the plasma.

5.3.1.2 Influence of IIE on Argon Fractional Abundances

The analysis of Be-like Ar^{14+} in the preceding section suggests that at least one of the isonuclear argon ions will have metastable populations that are sensitive to IIE. So, the effect of IIE upon the *ic* metastable fractional abundances is now examined, using the technique from section 5.1.2.5 of directly supplementing the Q^{cd}'s.

The top pane of figure 5.19 presents the ratios of *ic*-resolved fractional abundances that include proton-impact excitation to those that do not for all argon ions. Nearly a third of ionisation stages possess metastables with fractional abundances that are affected positively or negatively by $\approx 10\%$ in the vicinity of their respective $T^{(\mathrm{pk.})}$: S-like Ar^{2+}, Mg-like Ar^{6+}, O-like Ar^{10+}, N-like Ar^{11+}, C-like Ar^{12+}, and Be-like Ar^{14+}. Above the $T^{(\mathrm{pk.})}$, these variations caused by proton

Table 5.6: Collisional and radiative quantities for Be-like C^{2+} at $T_e = 3.88$ eV. The indices in the transition column are for the levels, $1 : {}^1S_0$, $2 : {}^3P_0$, $3 : {}^3P_1$, $4 : {}^3P_2$.

Transition	$A_{j\to i}$	$q^{(e)}_{i\to j}$	$q^{(p)}_{i\to j}$	$q^{(p)}/q^{(e)}$	$\frac{A_{j\to i}}{(N_e q^{(e)})}$	$\frac{A_{j\to i}}{(N_e q^{(e+p)})}$	$\frac{A_{3\to 1}}{(N_e q^{(e+p)})}$
					$N_e = 10^2$		
$1 \to 3$	6.140+01	2.444−09	—	—	2.512+08	—	—
$2 \to 3$	2.310−07	3.932−08	—	—	5.875−02	—	1.562+07
$2 \to 4$	8.030−14	2.493−08	1.181−08	4.739−01	3.221−08	2.186−08	1.671+07
$3 \to 4$	1.390−06	3.453−08	9.074−09	2.627−01	4.025−01	3.188−01	1.408+07
					$N_e = 10^6$		
$1 \to 3$					2.512+04	—	—
$2 \to 3$					5.875−06	—	1.562+03
$2 \to 4$					3.221−12	2.186−12	1.671+03
$3 \to 4$					4.025−05	3.188−05	1.408+03
					$N_e = 10^{13}$		
$1 \to 3$					2.512−03	—	—
$2 \to 3$					5.875−13	—	1.562−04
$2 \to 4$					3.221−19	2.186−19	1.671−04
$3 \to 4$					4.025−12	3.188−12	1.408−04

impact tend to increase, and one of the metastables of Ar^{14+} achieves the largest deviation of $\approx 30\%$ at about three times its temperature of peak abundance. Below $T^{(pk.)}$, all of the variations decrease quickly, returning the ratios to one. This is consistent with the behaviour of IIE described in Chapter 4 and in particular the discussion of the adiabaticity parameter (ξ) in section 4.4.1. All IIE collision quantities are suppressed at low temperature or energy because the transition becomes more adiabatic, explaining why the variations of the fractional abundances with IIE also approach zero below their $T^{(pk.)}$. On the other hand, IIE collisions tend to benefit from increased temperatures and energies because of the mass factor that enters into the high energy limit of Ω_{ij}—see equation 4.33. This explains why the fractional abundance variations increase above $T^{(pk.)}$.

Figure 5.19 also shows that the inclusion of IIE does not alter $T^{(pk.)}$, but the magnitude and distribution of the metastables within an ionisation stage are changed. This is a direct consequence of the fact that only the Q^{cd}'s are being supplemented with IIE rates: the Q^{cd}'s tend to affect the distribution of metastable populations within an ionisation stage because they are the effective rates between these metastables. Unless one of those metastables has an increased

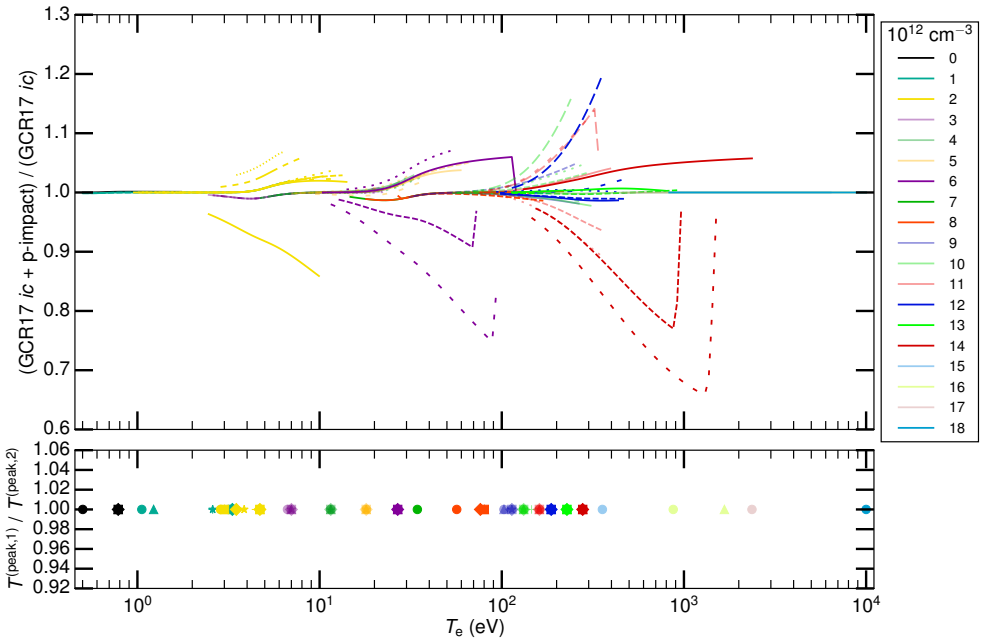

Figure 5.19: Ratios of *ic*-resolved fractional abundances that include proton-impact excitation (GCR17 *ic* + p-impact) to those that do not (GCR17 *ic*) for argon. The legend provides the ionisation stage that corresponds to each line colour, and the different line styles denote the separate metastable levels within each stage. The bottom pane provides the analogous ratio of the temperature at peak abundance, $T^{(\mathrm{pk.})}$, for each *ic* metastable.

propensity to ionise or recombine to adjacent stages, this redistribution is kept *within* the stage under consideration.

Figures 5.20 and 5.21 present the Q^{cd}'s for a sample of argon ions. A subset of Q^{cd}'s for S-like Ar^{2+} are shown in figures 5.20(a) and (b), and these display some contrasting behaviour that summarises the situation for this ion. In figure 5.20(b), the Q^{cd}'s shown are exclusively for the transitions amongst the levels of the ^{5}D metastable term. These levels are quite tightly packed between 144885–144911 cm^{-1}, corresponding to a maximum energy difference that is 0.1% of $kT^{(\mathrm{pk.})}$ for the entire ionisation stage. Therefore, IIE inclusion has a substantial magnitude for these transitions according to the rules of thumb constructed in section 4.1. A number of transitions in this figure have Q^{cd}'s that are noticeably enhanced *at or near* $T^{(\mathrm{pk.})}$, and the fractional abundances associated with the metastable levels of the ^{5}D term show the greatest variations due to adding proton-impact collisions. Some metastable fractional abundances in this term are enhanced while others are suppressed, indicating that the change in the Q^{cd}'s caused by

IIE redistributes populations predominantly *within* the term itself. However, it was determined in section 5.2.2 that the ^{5}D term is not actually metastable according to the results of the *LS*-GCR model; therefore, a discussion about the importance of these variations is somewhat irrelevant. In contrast, the Q^{cd}'s of the ^{3}P term in figure 5.20(a) do not show a notable enhancement by IIE near $T^{(\mathrm{pk.})}$, although there is some minor variation at higher temperatures for transitions $1 \rightarrow 2$ and $1 \rightarrow 3$ between levels of the ^{3}P ground term. For these cases, the energy separation is just slightly too large: about an order of magnitude more than the separations between the ^{5}D levels. This is also the case for all of the other transitions in this system involving the $^1D_2$ and $^1S_0$ levels. Consequently, all true metastable levels of Ar^{2+} exhibit very little variation of their fractional abundances with the addition of IIE in figure 5.19. The curves referred to here are the yellow ones (consult legend for shade), excluding the three outliers that deviate most from one. Again, these outer curves correspond to levels of the ^{5}D term that was determined to not be a true metastable.

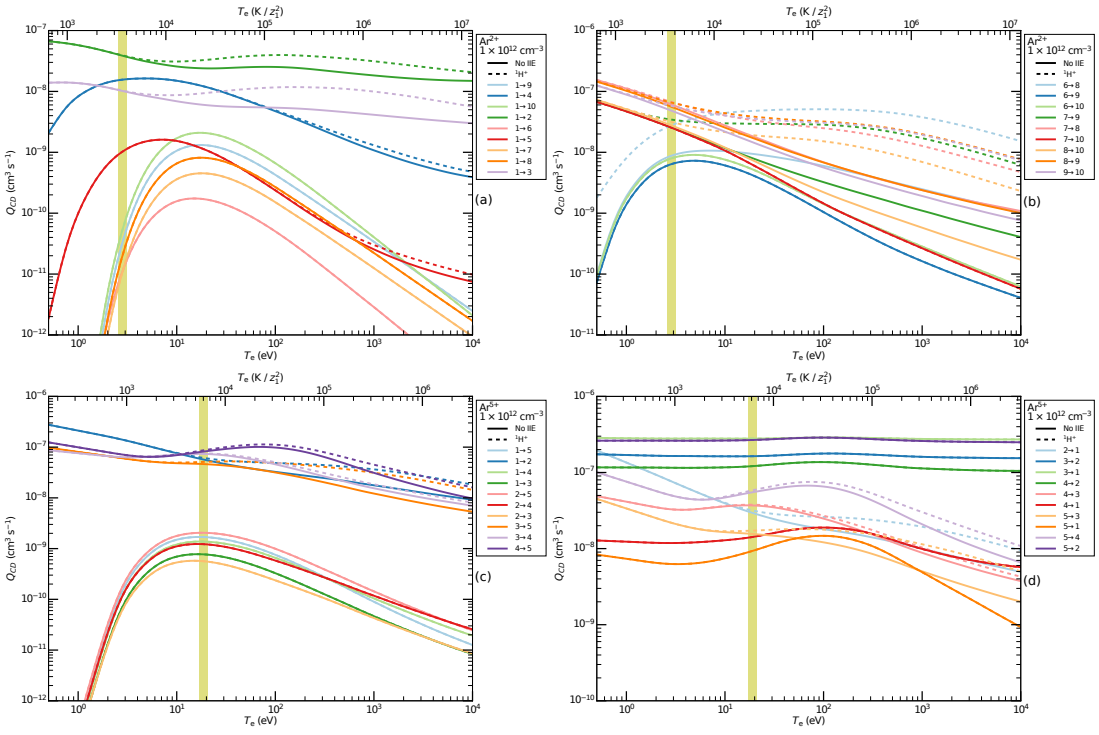

Figure 5.20: Q^{cd} coefficients for Ar^{2+}, (a) and (b), and Ar^{5+}, (c) and (d), with proton-impact excitation supplemented (dashed lines) and without (solid lines). The left column contains the Q^{cd}'s corresponding to excitation, while the right column contains those for de-excitation. $T^{(\mathrm{pk.})} \pm 5\%$ for the ionisation stage is indicated by the yellow vertical bar.

Al-like Ar^{5+} is an example where IIE does not influence the metastable-resolved fractional abundances. Figure 5.20(c) presents the Q^{cd}'s associated with excitation for this ion. The group of larger magnitude Q^{cd} values at the top half of the plot correspond to *intra*-term transitions, i.e. within the ^{2}P and ^{4}P metastable terms, while the lower grouping of Q^{cd}'s correspond to *inter*-term transitions, i.e. between the ^{2}P and ^{4}P terms. The *intra*-term transitions involve levels of the same parity and $|\Delta J| < 3$, so $E2$ selection rules are satisfied, and the energies are relatively small ($\approx 1\%$) compared to $kT^{(pk.)}$, which accounts for the minor enhancement by proton impact at higher temperatures; however, conditions simply are not aligned for this enhancement to occur at or near $T^{(pk.)}$ itself, explaining why none of these metastable levels show a substantial deviation of their fractional abundance in figure 5.19. The *inter*-term transitions involve a parity change in this case, so $E2$ order contributions are not possible, and hence why no modification by proton impact is observed. All of these observations equally apply to the complementary de-excitation Q^{cd}'s in figure 5.20 with the one exception that the two groupings of *intra* and *inter*-term transitions have swapped in magnitude; the *inter*-term de-excitation Q^{cd}'s are of a higher magnitude than their *intra*-term counterparts, an asymmetry because of statistical balance and Boltzmann statistics that are used to convert between excitation and de-excitation rates.

The tightly packed stages between F-like Ar^{9+} and Be-like Ar^{14+} are where the greatest variations of the fractional abundance with IIE are observed in figure 5.19. The Q^{cd}'s for N-like Ar^{11+} and Be-like Ar^{14+} are shown as representative examples in figure 5.21. Those associated with the excitation transitions of Ar^{11+} are in figure 5.21(a), where some rates show a noticeable enhancement of between 15% and 30% due to proton impact at $T^{(pk.)}$. The transitions that are most affected are those connecting levels 2, 3, 4, and 5 in all permutations. They belong to the ^{2}D term (levels 2 and 3) and ^{2}P term (levels 4 and 5) that are situated above the ground ^{4}S in this order. Unlike the two cases in figure 5.20, it is the *inter*-term transitions, $2 \rightarrow \{4, 5\}$ and $3 \rightarrow \{4, 5\}$, that show the greatest enhancement compared to the *intra*-term transitions, $2 \rightarrow 3$ and $4 \rightarrow 5$. The A-values for these *inter*-term transitions are greater than the *intra*-term ones, and this effect more than compensates for the fact that the energy differences for

the *inter*-term transitions are relatively larger, an effect that typically suppresses IIE collisions—see figure 4.18. The maximum energy difference for one of these *inter*-term transitions ($2 \rightarrow 5$) is 4% of $kT^{(\mathrm{pk.})}$, so they are within the appropriate region for influence by IIE. $E2$ IIE transitions involving the ground level, $^4\mathrm{S}_{3/2}$, do exist, but their values are suppressed because the dominant components of the state eigenvectors have different spins for these transitions: selection rules do not apply to spin in *ic*, but spin-changing transitions are still likely to be suppressed, and their influence on the Q^{cd} values is negligible. Overall, the behaviour of the metastable-resolved fractional abundances for Ar^{11+} seen in figure 5.19 is consistent with the Q^{cd} behaviour. The enhancement by proton impact of the Q^{cd}'s from levels 2 and 3 (^{2}D term) to levels 3 and 4 (^{2}P term) causes a transfer of population between these groups, which in turn leads to the fractional abundances of levels 2 and 3 being suppressed (ratio lower than 1) and those of levels 4 and 5 being enhanced (ratio greater than 1) as observed in figure 5.19. The fractional abundance of the ground level (solid line) is also slightly enhanced because level 5 has a fairly large A-value to ground, so the extra population shifted from the ^{2}D term levels to level 5 will also indirectly feed the ground level.

For Be-like Ar^{14+}, figure 5.21(c) gives the Q^{cd}'s associated with excitation, and the group of larger magnitude coefficients correspond to transitions within the ^{3}P metastable term (levels 2, 3, and 4). $E2$ transitions with the ground level, $^1\mathrm{S}_0$, are not possible because of the change in parity, and also transition $2 \rightarrow 3$ cannot have an $E2$ transition because $J = 0 \rightarrow 1$ is forbidden. Therefore, only transitions $2 \rightarrow 4$ and $3 \rightarrow 4$ exhibit any enhancement by proton impact, each by about 40% at $T^{(\mathrm{pk.})}$. This is a much smaller percentage than if the comparison was with the corresponding unaltered EIE rate coefficient for these transitions, as seen in table 5.5 where the proton-impact excitation rate coefficients are about a factor of five larger that the EIE ones near $T^{(\mathrm{pk.})}$. The Q^{cd} accounts for the total flux between the levels according to the population model, so it will differ from the value of the pure EIE collisional rate. The variation of the metastable-resolved fractional abundances for Ar^{14+} in figure 5.19 are explained by these Q^{cd} results and the influence of IIE therein. The enhancement by IIE of some Q^{cd} values for transitions within the ^{3}P term will lead to a quicker redistribution of population amongst these levels and then a suppressive effect because of the

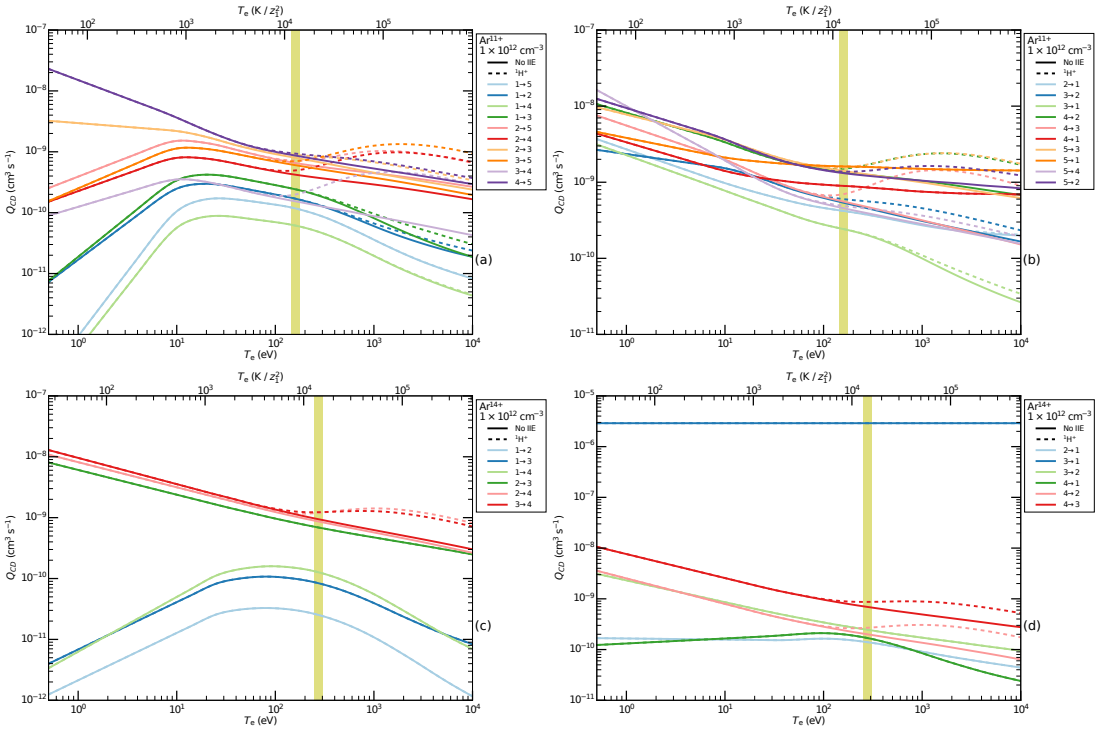

Figure 5.21: Q^{cd} coefficients for Ar^{11+}, (a) and (b), and Ar^{14+}, (c) and (d), with proton-impact excitation supplemented (dashed lines) and without (solid lines). The left column contains the Q^{cd}'s corresponding to excitation, while the right column contains those for de-excitation. $T^{(\mathrm{pk.})} \pm 5\%$ for the ionisation stage is indicated by the yellow vertical bar.

$^3\mathrm{P}_1$ (level 3) $\rightarrow$ $^1\mathrm{S}_0$ spontaneous emission that provides additional pathways to the ground. Hence, the lower abundances for these levels (dashed lines) in figure 5.19 with IIE. The variation of about 10–15% observed here is consistent with the variation in figure 5.17, which used a more rudimentary implementation.

As shown, proton-impact excitation alters the level-resolved fractional abundances, but for fusion plasmas in particular, protons are not the only ions present. Little attention has been given to non-proton projectiles in population modelling, as revealed by the review in section 5.3.1. One example is bare helium-4 nuclei ($^4\mathrm{He}^{2+}$), henceforth alpha particles, which is a primary fuel ion in certain tokamak scenarios. Figure 5.22 presents ratios of the level-resolved fractional abundances including alpha-impact over those including proton impact; in both cases, the ions make up 100% of the positive ion density. The difference near $T^{(\mathrm{pk.})}$ for each metastable level is within about 5%, a fairly minor correction.

For S-like Ar^{2+} only transitions within the ^{5}D term—figure 5.23(b)—are affected by any form of IIE, whether protons or alphas. In general, IIE tends to

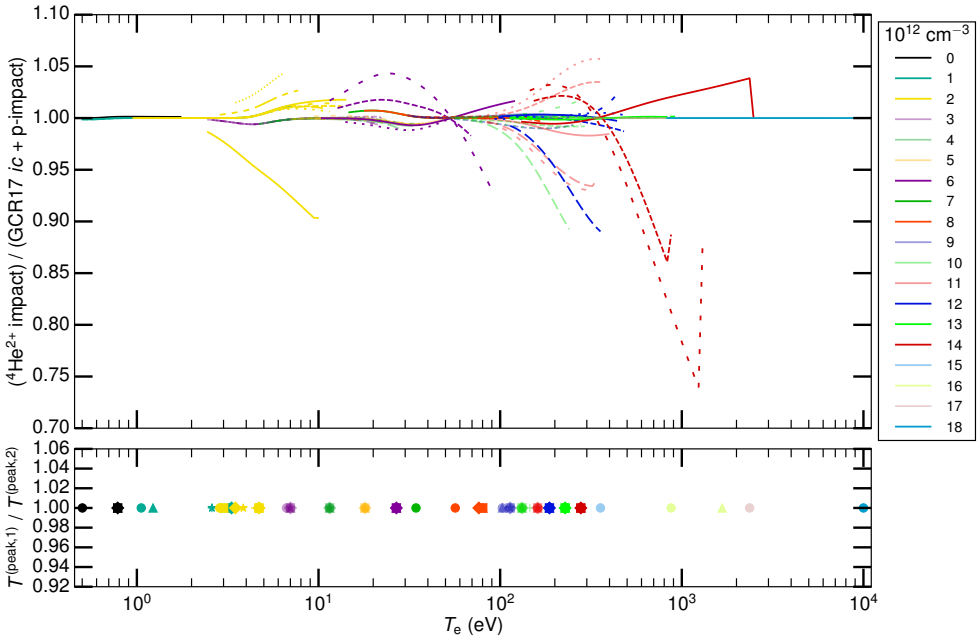

Figure 5.22: Ratios of *ic*-resolved fractional abundances that include 100% alpha-impact (^{4}He^{2+} impact) to those that include 100% proton impact (p-impact) for argon. The legend provides the ionisation stage that corresponds to each line colour, and the different line styles denote the separate metastable levels within each stage. The bottom pane provides the analogous ratio of the temperature at peak abundance, $T^{(\mathrm{pk.})}$, for each *ic* metastable.

affect the same group of transitions, regardless of the projectile involved, meaning new transitions will not be brought into play simply if new projectiles are considered. However near $T^{(\mathrm{pk.})}$, these ^{5}D *intra*-term Q^{cd}'s exhibit a discernible difference for the various ion projectile cases considered. The Q^{cd}'s supplemented with alpha IIE rate coefficients have larger values in this temperature regime than those with proton impact, both of which are larger than the unaltered "No IIE" case. The "mix 1" projectile case results in Q^{cd} values that are slightly larger than the proton projectile case. This ordering is consistent with the projectile parameter variation studies in section 4.4.1.2, which showed that above a certain temperature or energy, increases in m_p and z_p will cause an increase in the relevant IIE collision quantity. $T^{(\mathrm{pk.})}$ for Ar^{2+} is above the rate coefficient intersection point seen in the m_p and z_p scaling plots for this set of transitions—figures 4.14(d) and 4.15(d). Where $T^{(\mathrm{pk.})}$ lies in relation to this "intersection point" is what determines the order of variation of the Q^{cd}'s and, in turn, the fractional abundances.

For proton impact, the increase of the Q^{cd} values caused a number of the ^{5}D levels to be enhanced at the expense of *one* other level relative to the "no IIE" case in figure 5.19. Larger values of the Q^{cd}'s due to alpha-impact amplifies this redistributive effect, meaning those metastable levels that were larger under proton impact will be further so and vice versa: compare figure 5.19 for protons and figure 5.22 for alphas. Likewise, the level that had its fractional abundance reduced by proton impact is even more suppressed by alpha impact in figure 5.22.

A different type of behaviour is observed for the fractional abundances of N-like Ar^{11+}. Inspecting figure 5.23(c) and (d), one sees at $T^{(\mathrm{pk.})}$ that the Q^{cd} values with alpha-impact supplementation are *less* than those with proton impact. The excitation by alphas makes a negligible modification to the EIE driven Q^{cd}'s (solid lines). This dissimilarity between Ar^{11+} and Ar^{2+} is due to the criss-crossing behaviour of the z_p and m_p scaling of IIE collision quantities. The Ar^{2+} IIE transitions had a $T^{(\mathrm{pk.})}$ that lay above the "intersection" point of figures 4.15 and 4.14, whereas the transitions for Ar^{11+} are such that $T^{(\mathrm{pk.})}$ lies below the "intersection" point where increases in m_p or z_p cause the rate coefficient to decrease. Therefore, the changes to the fractional abundances due to alpha-impact are depressed, almost back to the point of the purely EIE-driven Q^{cd}, rather than amplified as in the proton case. This shows that using an accurate projectile mix is important in ionisation balance modelling—one cannot get away with using proton-impact as representative of IIE in the population model.

Finally, Be-like Ar^{14+} and the similar, by atomic structure, Mg-like Ar^{6+} show an interesting criss-cross behaviour for the fractional abundance ratios in figure 5.22. Figure 5.23(e) and (f) show that $T^{(\mathrm{pk.})}$ for Ar^{14+} lies close to the point at which the Q^{cd}'s from different projectile cases are crossing over. Below this intersection point, the Q^{cd}'s supplemented with alpha impact are lower than those supplemented with proton impact, and vice versa above the intersection point. The switch in behaviour is a direct result of the same criss-crossing seen for the scaling of the IIE rates with z_p and m_p and was already discussed for the previous two cases. This mixed, criss-cross behaviour in the Q^{cd}'s propagates to the ratio of the fractional abundances as well.

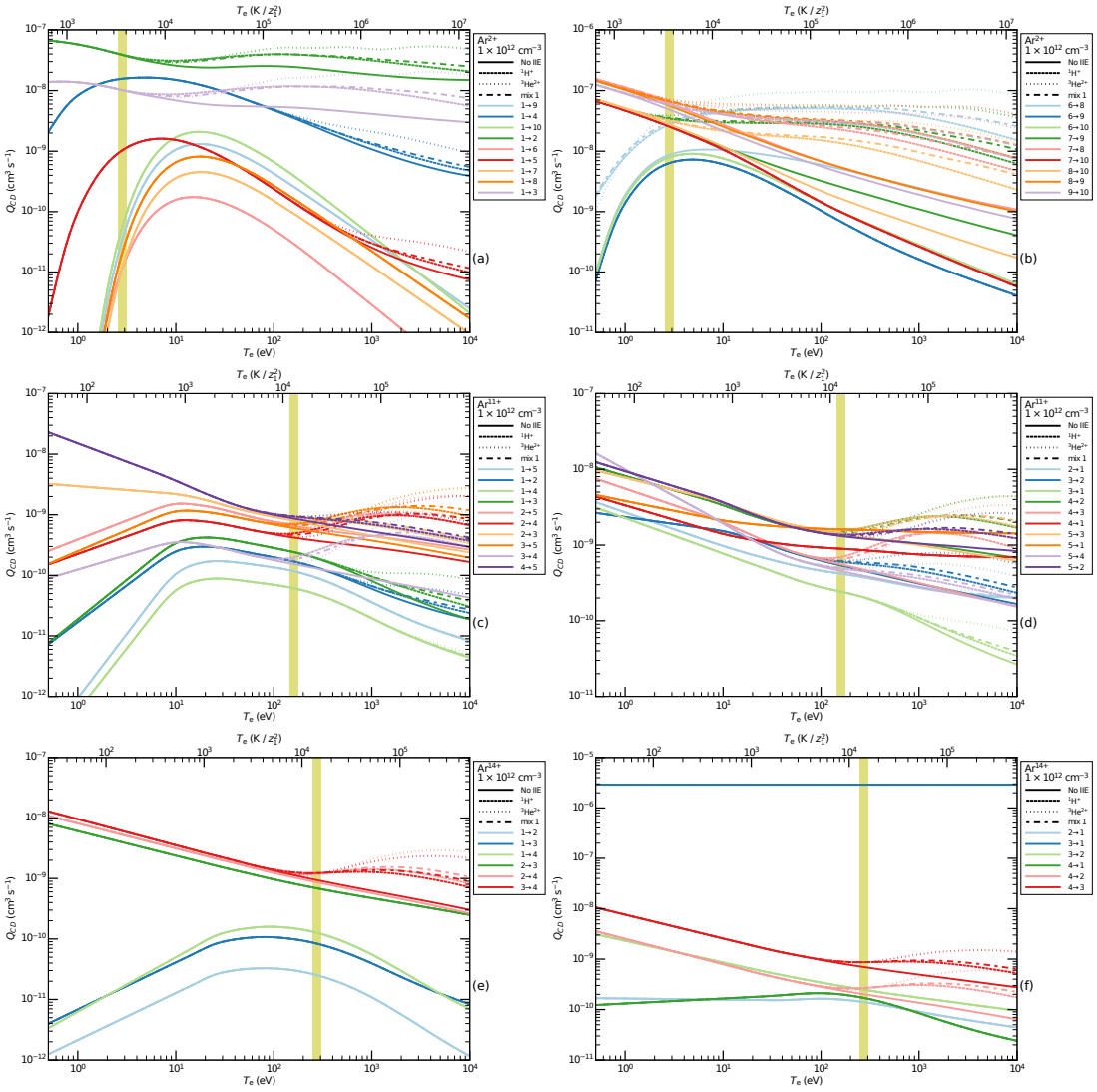

Figure 5.23: Q^{cd} coefficients for Ar^{2+} (a and b), Ar^{11+}, (c and d), and Ar^{14} (e and f) with different mixes of ion projectiles supplemented, distinguished by line styles in the legends. "mix 1" is 98.8% D^{1+}, 1.1% $^{9}Be^{4+}$, and 0.1% $^{12}C^{6+}$. The left column contains the Q^{cd}'s corresponding to excitation, while the right column contains those for de-excitation, except (b) which has the excitation Q^{cd}'s for the ^{5}D term of Ar^{2+}. $T^{(pk.)} \pm 5\%$ for the ionisation stage is indicated by the yellow vertical bar.

5.3.2 Determining Genuine Metastable Levels

Given that there are more levels in *ic* resolution than terms in *LS*, determining which of these low-lying levels are the "true" *ic* metastables is important. By applying the global threshold procedure to the *ic*-resolved metastable fractional abundances across the temperature domain, as in section 5.2.2, a more realistic set of metastables can be determined. Results are presented in column four

of table 5.7, and as with the *LS*-metastables, a more sophisticated approach does not alter this set. Additionally, the predicted *LS* metastables in table 5.4 can be extended to *LSJ* resolution by using the simple vector model of angular momenta addition. The simple ADAS list (column 2) again labels too many levels as metastable. However, there is a remarkable agreement between the *LS* and *ic*-resolved models in terms of the predicted metastable levels. A tentative conclusion is that if an *LS*-term is metastable, according to a GCR model built upon bundled *ic adf04* file, then in all likelihood, the *ic* levels of this term will also be metastable.

For Mg-like Ar^{6+} and Be-like Ar^{14+}, both having a ^1S ground term and a ^3P metastable term sitting immediately above, there is a difference between the *LS* and *ic* classification of metastables. The *ic*-model omits $^3P_1$ as a metastable level, and from the analysis of the previous section, it is known that this level typically has a fairly strong *A*-value to the ground under *ic* conditions, even though this transition is forbidden under *LS* selection rules. The values are 7.13×10^5 s^{-1} and 2.90×10^6 s^{-1} for Mg-like and Be-like respectively, and this comparatively strong radiative pathway depletes the $^3P_1$ level such that it does not exhibit metastability in either case. Figures 5.16 and 5.17 further support this assessment for Be-like Ar^{14+}. The *LS* model does not report the ^3P term as a metastable for Be-like because of spin breakdown in the bundled *LS* data, meaning there is an *A*-value for $^3P \rightarrow {}^1S$ that would not be present under pure *LS* conditions, and in the case of Be-like, this *A*-value is sufficiently large that the metastability of the ^3P term is lost.

Section 5.3.1 showed that many of the metastable populations in the argon isonuclear sequence are sensitive to the inclusion of IIE, and applying the same global cutoff procedure to *ic*-resolved metastable fractional abundances with IIE included produced only one difference compared to the result without IIE. The $^3P_0$ level of Be-like Ar^{14+} is no longer metastable when IIE is included—marked with a † in table 5.7. Therefore, IIE does not significantly alter the metastability for argon ions, but whether this is a general conclusion remains to be seen. Results from more medium and heavy-weight species are needed to determine this.

To summarise, if a *LS* term is metastable according to GCR modelling with bundled *adf04* data, then at least one of its levels will also be metastable at

Table 5.7: *Ic*-level metastables for argon from three sources. The column titled "ADAS" contains the *ic*-level metastables according to the simple, standard ADAS list currently in place. The column titled "*LS* Global Cut" contains the *ic*-level metastables according to the global threshold procedure applied to the *LS*-GCR model fractional abundances, as described in section 5.2.2. The levels are obtained by taking all possible levels produced by the simple vector model of momenta addition with the *LS* terms. The column titled "*ic* Global Cut" contains the *ic*-level metastables according to the global threshold procedure applied to the *ic*-GCR model fractional abundances. Both models were executed at $N_e = 10^{12}$ cm^{-3}. The level marked with a † is *not* present if proton-impact excitation is included in the *ic*-GCR model. A simplified, non-superscript notation for the dominant LSJ component of the *ic* levels has been employed for succinctness: $[2S+1][L]([J]) \equiv {}^{(2S+1)}L_J$.

Ion	**ADAS**	***LS* Global Cut**	***ic* Global Cut**
0	1S(0) 3P(0,1,2)	1S(0)	1S(0)
+1	2P($\frac{1}{2}$, $\frac{3}{2}$) 4D($\frac{1}{2}$, $\frac{3}{2}$, $\frac{5}{2}$, $\frac{7}{2}$)	2P($\frac{1}{2}$, $\frac{3}{2}$)	2P($\frac{3}{2}$, $\frac{1}{2}$)
+2	3P(0,1,2) 1D(2) 1S(0) 5D(0,1,2,3,4)	3P(0,1,2) 1D(2) 1S(0)	3P(2,1,0) 1D(2) 1S(0)
+3	4S($\frac{3}{2}$) 2D($\frac{3}{2}$, $\frac{5}{2}$) 2P($\frac{1}{2}$, $\frac{3}{2}$)	4S($\frac{3}{2}$) 2D($\frac{3}{2}$, $\frac{5}{2}$) 2P($\frac{1}{2}$, $\frac{3}{2}$)	4S($\frac{3}{2}$) 2D($\frac{3}{2}$, $\frac{5}{2}$) 2P($\frac{1}{2}$, $\frac{3}{2}$)
+4	3P(0,1,2) 1D(2) 1S(0) 5S(2)	3P(0,1,2) 1D(2) 1S(0)	3P(0,1,2) 1D(2) 1S(0)
+5	2P($\frac{1}{2}$, $\frac{3}{2}$) 4P($\frac{1}{2}$, $\frac{3}{2}$, $\frac{5}{2}$)	2P($\frac{1}{2}$, $\frac{3}{2}$)	2P($\frac{1}{2}$, $\frac{3}{2}$)
+6	1S(0) 3P(0,1,2)	1S(0) 3P(0,1,2)	1S(0) 3P(0,2)
+7	2S($\frac{1}{2}$)	2S($\frac{1}{2}$)	2S($\frac{1}{2}$)
+8	1S(0) 3P(0,1,2)	1S(0)	1S(0)
+9	2P($\frac{1}{2}$, $\frac{3}{2}$) 4P($\frac{1}{2}$, $\frac{3}{2}$, $\frac{5}{2}$)	2P($\frac{1}{2}$, $\frac{3}{2}$)	2P($\frac{3}{2}$, $\frac{1}{2}$)
+10	3P(0,1,2) 1D(2) 1S(0) 5S(2)	3P(0,1,2) 1D(2)	3P(0,1,2) 1D(2)
+11	4S($\frac{3}{2}$) 2D($\frac{3}{2}$, $\frac{5}{2}$) 2P($\frac{1}{2}$, $\frac{3}{2}$)	4S($\frac{3}{2}$) 2D($\frac{3}{2}$, $\frac{5}{2}$) 2P($\frac{1}{2}$, $\frac{3}{2}$)	4S($\frac{3}{2}$) 2D($\frac{3}{2}$, $\frac{5}{2}$) 2P($\frac{1}{2}$, $\frac{3}{2}$)
+12	3P(0,1,2) 1D(2) 1S(0) 5S(2)	3P(0,1,2) 1D(2)	3P(0,1,2) 1D(2)
+13	2P($\frac{1}{2}$, $\frac{3}{2}$) 4P($\frac{1}{2}$, $\frac{3}{2}$, $\frac{5}{2}$)	2P($\frac{1}{2}$, $\frac{3}{2}$)	2P($\frac{1}{2}$, $\frac{3}{2}$)
+14	1S(0) 3P(0,1,2)	1S(0)	1S(0) 3P(0†,2)
+15	2S($\frac{1}{2}$)	2S($\frac{1}{2}$)	2S($\frac{1}{2}$)
+16	1S(0) 3S(1)	1S(0)	1S(0)
+17	2S($\frac{1}{2}$)	2S($\frac{1}{2}$)	2S($\frac{1}{2}$)

ic resolution, with the tendency towards all levels of a metastable term being themselves metastable. Metastable levels that do not belong to a metastable term are rare but can occur around shell or subshell boundaries (e.g. Be-like Ar^{14+} in table 5.7). Both of these conclusions are consistent with those from section 5.2.2 and 2.3.1.1, which also treated the consistency of metastability at different resolutions. Moreover, the results here have confirmed the *ca* to *ic* comparison of metastability by extension.

5.3.3 Influence of Resolution Upon Fractional Abundances

Many transport codes in fusion operate on the unresolved, i.e. stage-to-stage, description of impurities. Figure 5.24 compares the unresolved fractional abundances generated from the *LS* and *ic*-resolved models. At the two densities presented, there are discernable differences between the results of these two models, particularly for the near-neutral and third period ionisation stages. The peak regions agree fairly well, and the largest discrepancies, of an order of magnitude, tend to occur near the tails of the fractional abundance curves. So, the underlying resolution of the population model does affect the final *unresolved* results. This point was not so clear from the literature comparisons in section 5.2.3.1. Yet the effects of density and resolution are necessarily intertwined: shifting between the two densities in figures 5.24(a) and (b), one observes that the differences between the two resolutions also change. In fact, the discrepancy between the *LS*-resolved model and the *ic*-resolved model appears to be greater at the coronal-regime density of 10^4 cm^{-3} than at the higher, CR-regime density of 10^{12} cm^{-3}. From figure 5.15, it is clear that the largest discrepancies between *LS* and *ic*-resolved metastable populations occurred in the coronal regime, because increasing the density moves the conditions closer to the LTE regime and thus statistical balance of the populations where there is no difference in the predictions of *ic* or *LS*-resolved models. Furthermore, the inclusion of IIE in the *ic*-GCR model has no influence upon the unresolved fractional abundances, a consequence of the observation in section 5.3.1.2 that modifying the Q^{cd}'s will redistribute the metastable populations *within* a stage but not *between* stages.

An alternate comparison is to form *LS* abundances by summing the *ic*-resolved metastable fractional abundances according to the *LS* terms that they belong to:

$$f_{LS}^{(z)} = \sum_{L'S'J' \in L \oplus S} f_{L'S'J'}^{(z)} \,, \tag{5.15}$$

where $\oplus$ is used here to represent the vector-model addition of total spin and angular momenta, producing a set of *LSJ* levels. The ratios of the *LS*-resolved metastable fractional abundances are presented in figure 5.25. The differing resolution of the two models has a notable effect upon the metastable fractional abundances. The peak regions usually agree to within 10%, but outside of this,

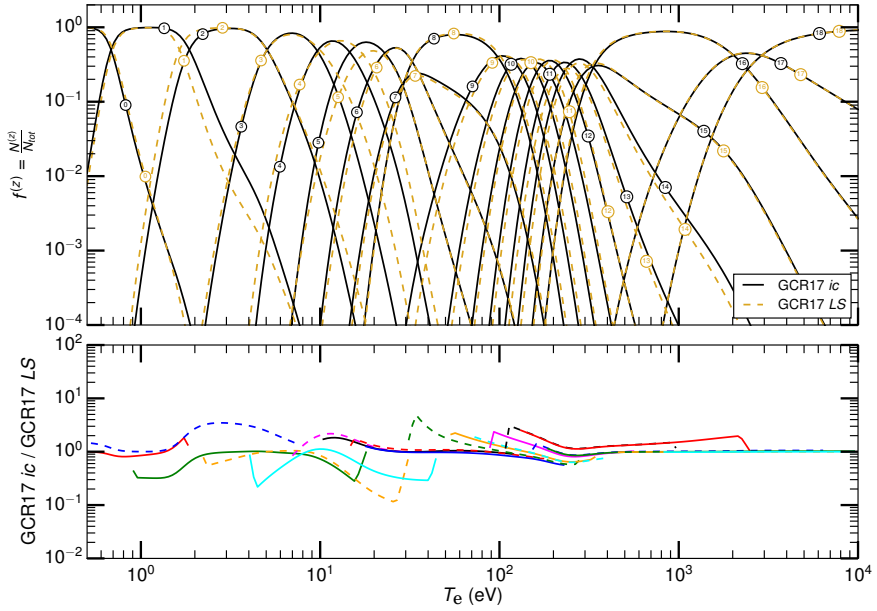

(a)

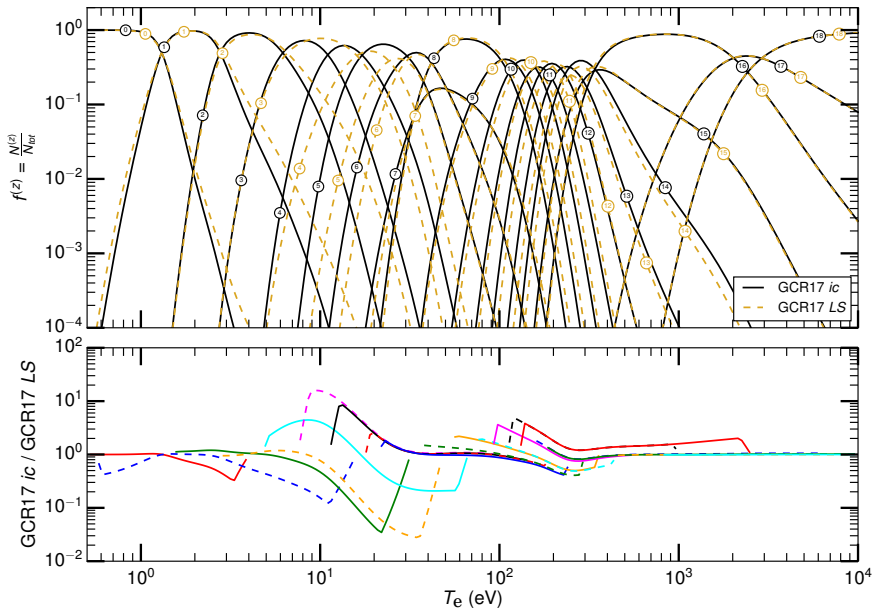

(b)

Figure 5.24: Comparison of the unresolved fractional abundances for argon from the *LS* (GCR17 *LS*) and *ic*-GCR (GCR17 *ic*) models. The two plots contain results for different electron densities: (a) $N_e = 10^{12}$ cm^{-3} and (b) $N_e = 10^{4}$ cm^{-3}.

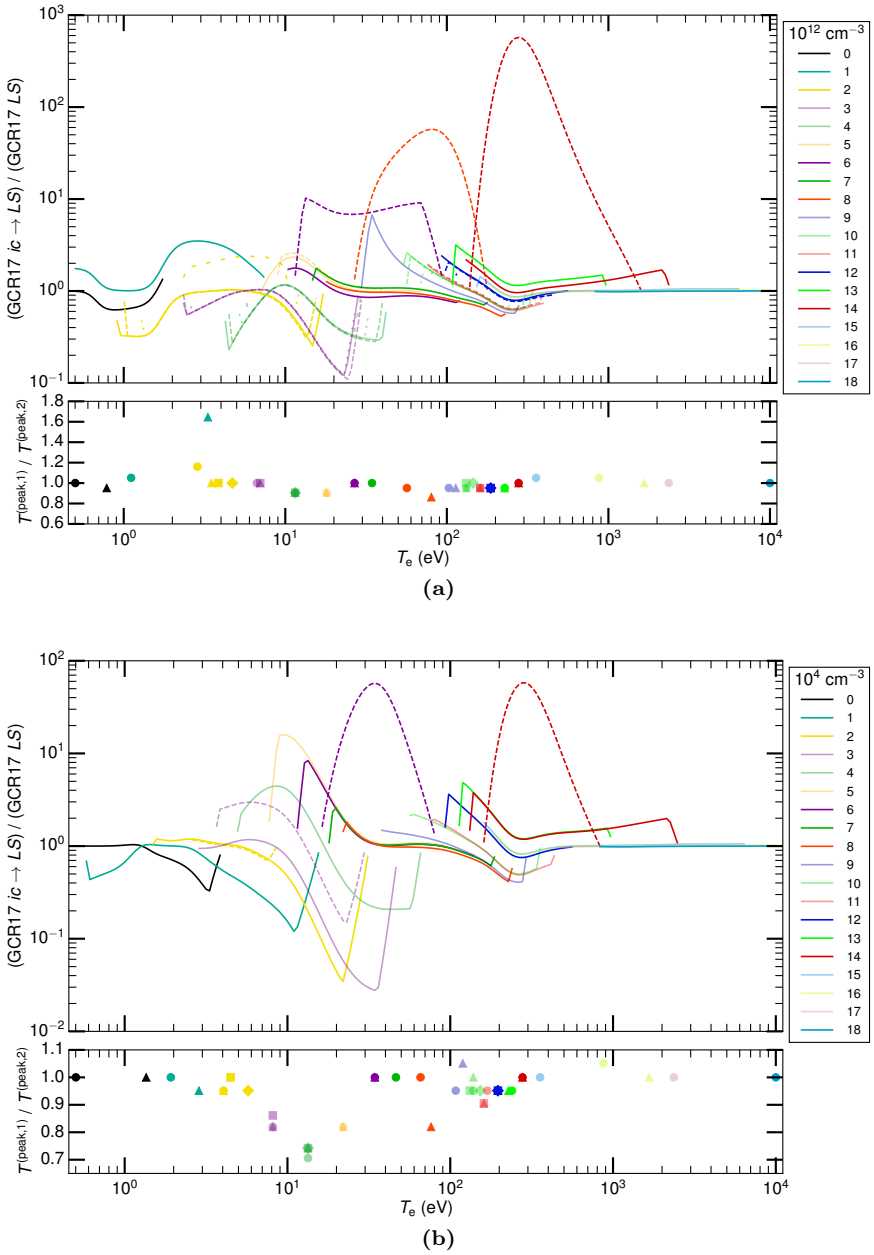

Figure 5.25: Ratios of the *LS*-resolved metastable fractional abundances for argon from the *LS* (GCR17 *LS*) and *ic*-GCR (GCR17 *ic*) models. The two plots contain results for different electron densities: (a) $N_e = 10^{12}$ cm^{-3} and (b) $N_e = 10^4$ cm^{-3}.

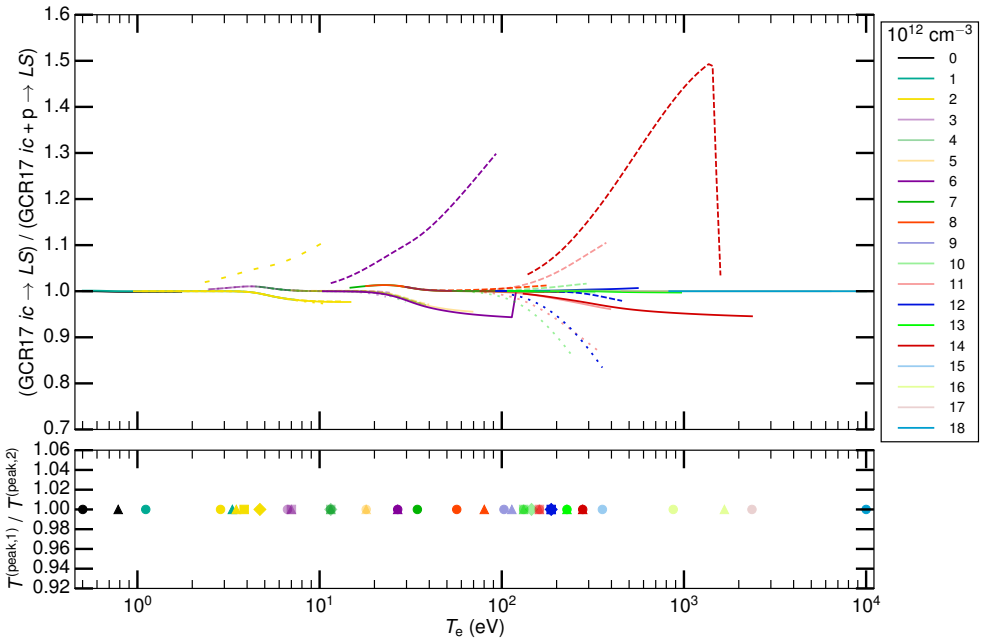

Figure 5.26: Ratios of *LS*-resolved fractional abundances for argon from the *ic*-GCR model, with (GCR17 ic+p $\rightarrow$ *LS*) and without (GCR17 $ic \rightarrow$ *LS*) proton impact. The legend provides the ionisation stage that corresponds to each line colour, and the different line styles denote the separate metastable levels within each stage. The bottom pane provides the analogous ratio of the temperature at peak abundance, $T^{(\mathrm{pk.})}$, for each *LS* metastable.

variation between 10% and an order of magnitude is possible. Although the underlying data for the *LS* model is bundled from *ic* calculations, the results here reveal that the remaining differences between the *ic* and *LS* model should not be underestimated. Assessing the effects of density, it appears that metastable fractional abundances differ more at the higher, CR-regime density (figure 5.25(b)) than they do at the coronal-regime density (figure 5.25(b)), contradicting the conclusion made about the unresolved results above. However, the largest deviations at $N_\mathrm{e} = 10^{12}$ cm^{-3} occur for metastables that are not the dominant ones within a stage. So, the deviations depicted at $N_\mathrm{e} = 10^{4}$ cm^{-3} are actually larger for the metastables that matter most, agreeing with the previous conclusions about how resolution effects depend on density. Unlike the unresolved case, however, the inclusion of IIE in the *ic*-GCR model does influence the *LS*-resolved metastable fractional abundances, but figure 5.26 shows that this constitutes a minor correction relative to the effect of resolution.

Finally, the unresolved fractional abundances from the *ic*-GCR model are com-

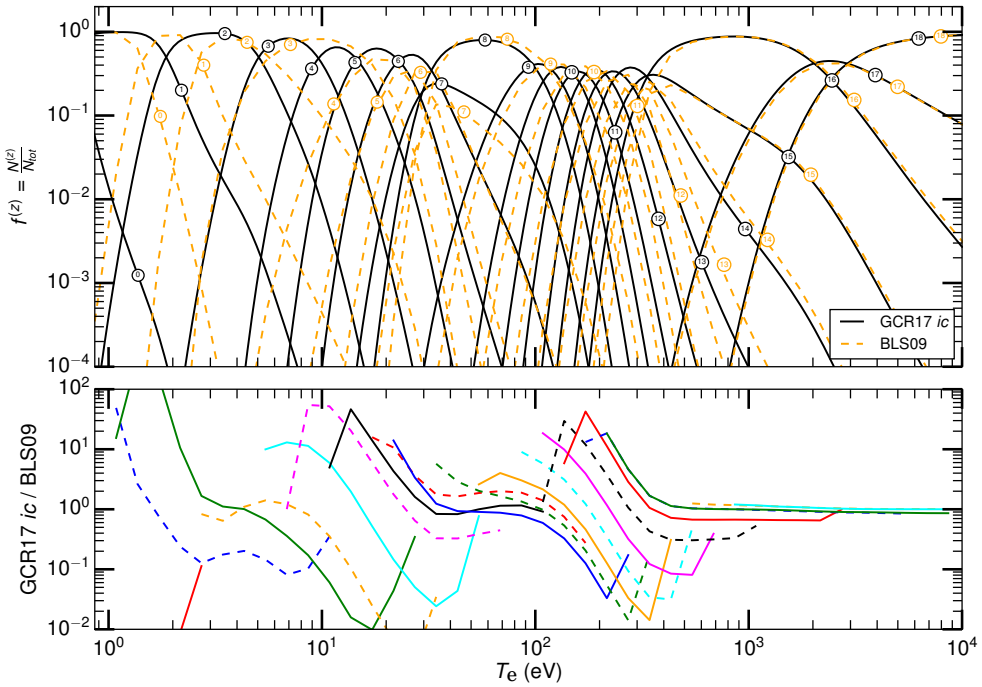

Figure 5.27: Comparison of unresolved fractional abundances: present work using *unresolved* coefficients derived from *ic*-resolved model (GCR17 *ic*) versus Bryans et al. 2009 (BLS09) [189]. The GCR17 *ic* model was calculated at an electron density of $N_e = 10^{12}$ cm^{-3}.

pared to the zero-density, CIE-model abundances of BLS09 [189] in figure 5.27. This exhibits essentially the same features seen previously in figure 5.7(a) when analysing the *LS*-GCR model. Differences are largest for the near neutrals and gradually decrease until convergence is achieved for highly-ionised states, but in this case, the discrepancies are slightly larger than in the *LS* case. Moving to low density removes most of the disagreement of the near neutrals, but the same differences linger for the middle ionisation stages due to the discrepancy in the definitions of the α^{cd} and zero-density, total recombination rate coefficient.

5.4 Radiated Power of Argon

A high-quality cooling curve for argon is one of the primary objectives for the *ic*-resolved GCR model that has been described hitherto. The radiated power coefficients are also a pivotal point of validation for any atomic population model. Section 5.4.1 compares the power coefficients of this work with those available in the literature. The effect of resolution upon the power coefficients produced by

the GCR models is investigated in section 5.4.2. Lastly, the present results, built upon high-quality atomic data, offer the best means with which to assess the new baseline datasets from Chapter 2, which were explicitly designed to optimise the radiated power. Section 5.4.3 performs this assessment.

5.4.1 Power Coefficients in the Literature

The total radiated power function, used to calculate total radiated power loss from a plasma, is defined by

$$P_{\mathrm{tot}} = \sum_{z=0}^{Z_0} \sum_{\sigma=1}^{M_z} \left[\mathcal{P}_{\mathrm{LT},\sigma}^{(z)\ (z)} + \mathcal{P}_{\mathrm{RB},\sigma}^{(z)} + (N_{\mathrm{H}}/N_{\mathrm{e}})\, \mathcal{P}_{\mathrm{RC},\sigma}^{(z)} \right] \left(N_{\sigma}^{(z)}/N_{\mathrm{tot}} \right), \tag{5.16}$$

where $\mathcal{P}_{\mathrm{LT},\sigma}^{(z)\ (z)}$ is the total radiated line power coefficient already defined in equation 2.37, $\mathcal{P}_{\mathrm{RB},\sigma}^{(z)}$ is the recombination-bremsstrahlung-cascade power coefficient, $\mathcal{P}_{\mathrm{RC},\sigma}^{(z)}$ is the charge exchange power coefficient, and the SI units of P_{tot} are the same as all the power coefficients, W cm^3. P_{tot} is sometimes called the cooling curve. The charge exchange power coefficient is not considered in this study because it depends on the neutral hydrogen density (from NBI heating) and is negligible on a global scale. The free-free (bremsstrahlung) contribution to $\mathcal{P}_{\mathrm{RB},\sigma}^{(z)}$ is fairly uniform across the literature because it is the simplest part of the problem. There is more variation seen in the free-bound (DR and RR) contribution, but part of this is already determined by the rates selected to establish the ionisation balance in the previous section: zero-density DR rates are typically used to calculate the emission from stabilisation. The remainder of the problem is bound up with the following remarks about line emission.

It is the $\mathcal{PLT}$ that is typically the dominant contribution in equation 5.16 because line emission from levels in the low-lying set is the strongest photon emission. Therefore, the model of the low-lying atomic levels becomes the key differentiator between estimates of the cooling curve. As was discussed in section 5.1.3.1, this portion of the atomic model is shaped by the data for A-values, energy levels, and collision strengths. The resolution of these quantities determines the resolution of the final model. How these quantities are then combined defines the approach of the model: i.e. are CR effects considered or is CIE being

assumed? How is the cascade portion of the recombination power coefficient handled? A variety of sources of the total radiated power function will be assessed on these points. They are split into two categories: highly-resolved models that consider atoms in *ic*, *LS*, or *ca* resolution with varying levels of CR effects, and lower-resolution models like AIMs.

A direct comparison of P_{tot} from different sources is complicated by the conflation of the power coefficients with the fractional abundances in its definition (5.16). Consequently, it is difficult to determine whether discrepancies of P_{tot} are caused primarily by differences in the fractional abundances or power coefficients. If a separate ionisation balance is provided, then some of this ambiguity can be removed, but ultimately it is a comparison of the power coefficients themselves, $\mathcal{PLT}$ and $\mathcal{P}^{(z)}_{\text{RB},\sigma}$, that offers the clearest interpretation. Unfortunately, these quantities are rarely given in the literature.

Highly-resolved Models FCMG98 [187] calculates various measures of power emission for argon in addition to its CIE fractional abundances given in section 5.2.3.1. For line emission power loss, it uses a CR model for each ion built upon J-resolved atomic data from HULLAC, a DW code that is comparable to the new elevated baseline with AUTOS. It is the only work that employs any form of CR model in the literature, although it is limited in comparison to the GCR model of the present work. The FCMG98 model only includes collisional excitation and radiative decay between levels. So its metastable model is confined to *excitation* from each metastable within the isolated ion system. Indirect contributions from highly-excited states are not considered. Also, the influence of ionisation or recombination processes upon either the excited or metastable states in this model is omitted. Estimates of the DR and RR contribution to the radiated power are calculated using expressions from the AIM of [190] but with improved rates and energies. P_{tot} and separate $\mathcal{PLT}$ values are given for each ion.

A more recent work by Schure et al. [201] presents $\mathcal{P}_{\text{tot}}$ values for a number of solar relevant elements including argon, calculated using the SPEX code [202]. This code uses the CIE fractional abundances from AR85 [179] but with recombination data updated to [178], and although details are not given, it is assumed

the power coefficients are produced from a coronal model of each ionisation stage. This is a zero-density model that should begin to show substantial deviations from our GCR model at electron densities probed in the present work. Energy levels and oscillator strengths are taken from the literature or COWAN otherwise, and collision strengths are mostly sourced from the Zhang and Sampson group or HULLAC. This fundamental atomic data is estimated to be of moderate quality, below that of the present work. The line emission is specifically tuned to the X-ray spectral region for the purposes of solar astrophysics. No details were found on how the recombination or bremsstrahlung power coefficients were estimated.

Finally, Gnat and Ferland [203] present summed power coefficients ($\mathcal{P}^{(z)}_{\mathrm{LT},\sigma} + \mathcal{P}^{(z)}_{\mathrm{RB},\sigma}$) produced by the CLOUDY code (v10.00) for each ion of argon amongst other elements of astrophysical relevance. A CIE model is used for calculating both the fractional abundances and line emission power coefficients, but their approach of embedding data as part of the overall code package presents difficulties when comparing models. It is omitted in the comparisons to follow.

Average Ion Models The AIM approach of P77 [190, 191] is a popular source of cooling curves for a number of fusion-relevant elements including argon. Its foundation was described in the previous section 5.2.3.1, and once the populations of the average ion, $\bar{P}_n$, reach a steady state solution, they are used to determine all of the quantities required for the various radiated power loss expressions. Line emission, RR, DR cascade, and bremsstrahlung power loss are all estimated through hydrogenic forms. This is evidently a coarse result, but an important baseline with which to benchmark.

The FLYCHK code offers a more nuanced and advanced AIM result for radiated power loss. The ry states populations for each ionisation stage, $P^{(z)}_n$, are solved in the same manner as for the fractional abundances: a global steady state condition is imposed, and no self-consistent radiation field is assumed. These populations can then be substituted into expressions very similar to those in P77 to yield the radiated power coefficients, $\mathcal{P}^{(z)}_{\mathrm{LT},\sigma}$ and $\mathcal{P}^{(z)}_{\mathrm{RB},\sigma}$. $\mathcal{P}_{\mathrm{tot}}$ can also be provided by combining these coefficients with the fractional abundances according to equation 5.16.

Comparisons Figure 5.28 displays a comparison of $\mathcal{P}_{\text{tot}}$ curves from a variety of literature sources against the present, *ic*-resolved GCR result (GCR17 *ic*), which we consider to be the best quality to date. A density of 10^{12} cm^{-3} has been used for any non-zero-density model. FCMG98 is closest to the GCR17 *ic* cooling curve. The worst agreement is at lowest temperature, reaching a factor of 5, while over the rest of the temperature domain, the relative difference is within 50%. FCMG98 also provides $\mathcal{PLT}$ values used in forming $\mathcal{P}_{\text{tot}}$, and a sample of these are compared to in figure 5.29. For the ions shown, there is some variation between the FCMG98 and GCR17 *ic* $\mathcal{PLT}$s, but nothing close to the 50% on average observed for $\mathcal{P}_{\text{tot}}$. The $\mathcal{PLT}$ only includes contributions to the radiated power from collisional excitation of the relevant metastable, and this is separate from the more elaborate GCR effects that get bundled into the fractional abundances. Therefore, the ionisation balance is the primary source of the difference in $\mathcal{P}_{\text{tot}}$, and figure 5.9 confirms that the significant differences of the unresolved fractional abundances observed at $N_{\text{e}} = 10^{12}$ cm^{-3} are reflected in the cooling curve. FCMG98 supports what has long been known in ADAS: it is possible to construct a CR model that produces fairly accurate $\mathcal{PLT}$s by using moderate quality atomic data. However, one should should not underestimate the importance of the ionisation balance in forming the final $\mathcal{P}_{\text{tot}}$ values.

The P77 data shows a slightly worse level of agreement for $\mathcal{P}_{\text{tot}}$ in figure 5.28, but this is impressive given the rudimentary nature of the AIM model. However, this result does not go below 30 eV, because AIMs cannot describe the structure of the contributing ions. Due to the nature of this AIM model, $\mathcal{P}_{\text{tot}}$ is not separable into its $\mathcal{PLT}$ and fractional abundance components, so a more precise attribution of the differences with GCR17 *ic* cannot be made. The more sophisticated AIM result from FLYCHK achieves a similar degree of agreement with GCR17 *ic* in the temperature domain that P77 is present, but it becomes notably worse for lower temperatures, nearing an order of magnitude discrepancy. Note that because of the severe disagreement with the fractional abundances produced by FLYCHK in figure 5.10, it was decided that the ionisation balance from GCR17 *ic* should replace that of FLYCHK itself in forming $\mathcal{P}_{\text{tot}}$. Therefore, the differences in $\mathcal{P}_{\text{tot}}$ are entirely attributable to differences in the $\mathcal{PLT}$ and $\mathcal{P}_{\text{RB}}$ coefficients. It does not appear that increased sophistication of the FLYCHK AIM garners much

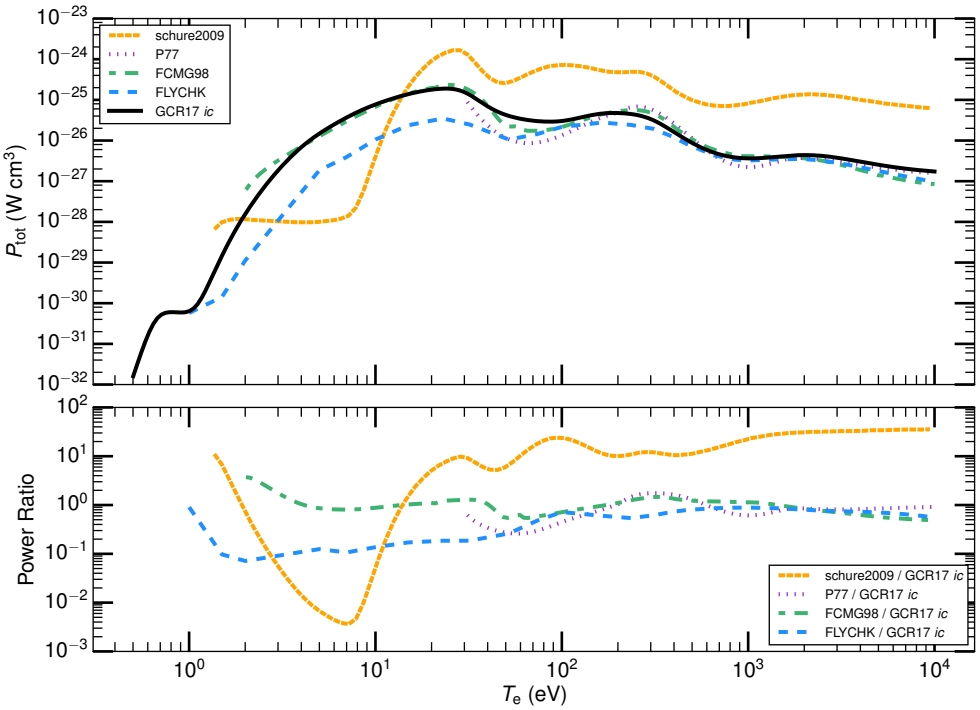

Figure 5.28: Literature comparison of the total radiated power function ($\mathcal{P}_{\text{tot}}$) for argon. The sources are described in the text: schure2009 [201], P77 [190], FCMG98 [187], and FLYCHK [192]. GCR17 *ic* is the result from the current *ic*-resolved GCR model without any IIE. The FLYCHK cooling curve uses the fractional abundances from GCR17 *ic*, and the other sources use their own. The bottom pane displays the ratio of the literature sources with GCR17 *ic*.

improvement over that of P77.

Finally, the result of Schure et al. [201] differs markedly from the others. This is somewhat surprising given the ostensible similarities it shares with FCMG98. The unsuitability of the CIE model at this density has been established, but this cannot alone account for the level of disagreement seen, so there must be another explanation. Unfortunately, their fundamental atomic data are not available for comparison.

5.4.2 Resolution Effects

In section 5.3.3, it was shown that resolution can have a important effect upon the ionisation balance produced by the GCR model. Figure 5.30 shows that some variation is present between the unresolved and resolved versions of the *LS* and *ic*-GCR models of $\mathcal{P}_{\text{tot}}$: as much as 80% variation is seen at very low

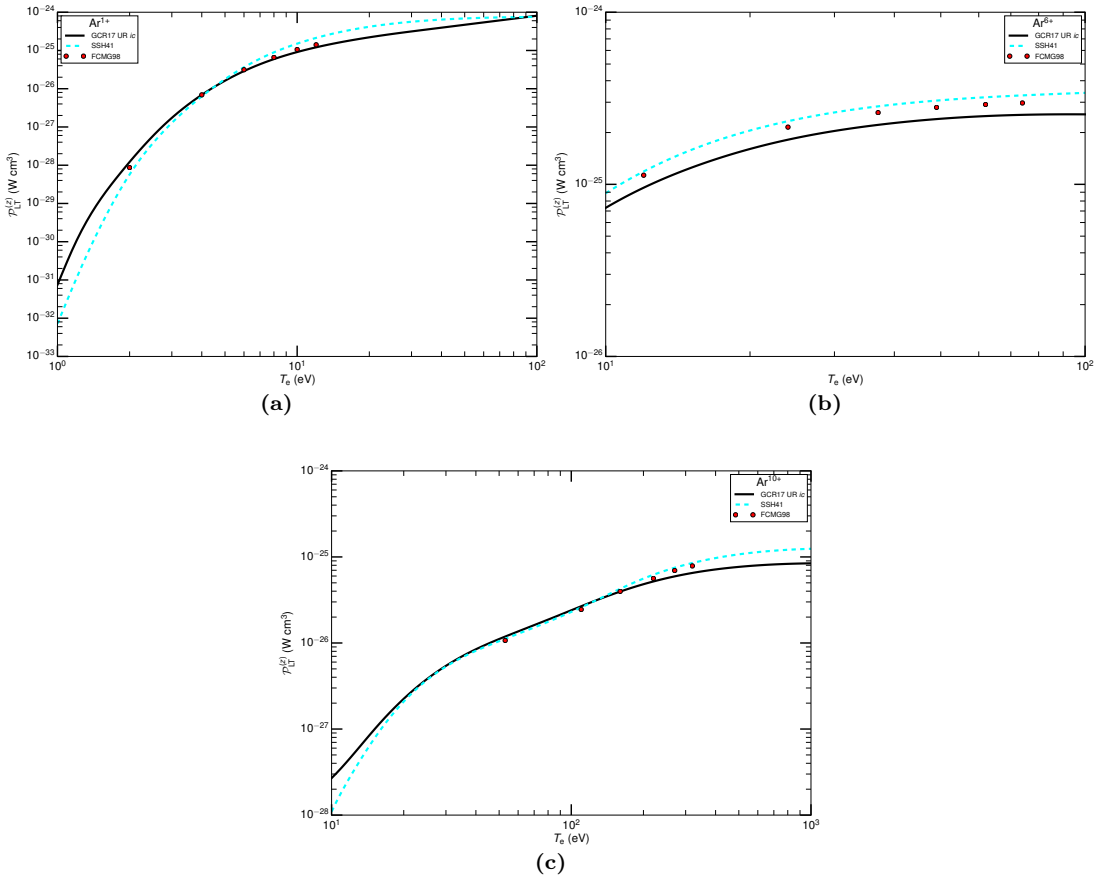

Figure 5.29: Comparison of $\mathcal{PLT}$ coefficients for (a) Ar^{1+}, (b) Ar^{6+}, and (c) Ar^{10+}. GCR17 UR *ic* is the unresolved result from the current *ic*-GCR model. SSH41 is the new COWAN PWB baseline used in the configuration selection work of section 2.3.1. FCMG98 [187] is described in the text.

temperatures and another peak of 30% near 70 eV. However, the majority of the temperature domain exhibits disagreement of under 20%, so a comparable magnitude of changes seen in the ionisation balances are not translated here. $\mathcal{P}_{\text{tot}}$ is not a terribly sensitive diagnostic. Since it is formed by the sum over all ionisation stages and their metastables (equation 5.16), effects that operate on a per ion or per metastable basis tend to get washed out. A similar damping was observed between the fractional abundances and $\mathcal{P}_{\text{tot}}$ for the FCMG98 result in the previous section, where the variation of the fractional abundances relative to GCR17 *ic* were much larger than the variation observed for $\mathcal{P}_{\text{tot}}$.

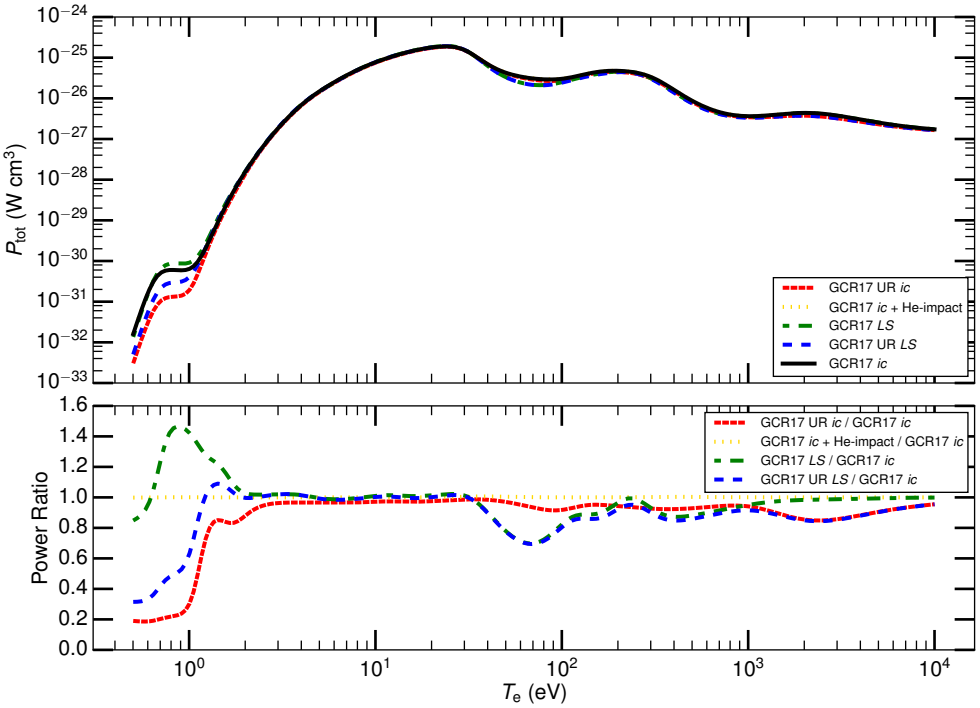

Figure 5.30: The total radiated power function for argon at all resolutions of the current GCR model (GCR17). UR stands for unresolved, and "+ He-impact" indicates that alpha-impact excitation has been added to the *ic*-resolved model. The ratios relative to the GCR17 *ic* result are displayed in the bottom pane. $N_{\text{e}} = 10^{12}$ cm^{-3} has been used in the model.

Moreover, variability in the $\mathcal{PLT}$s due to resolution will have an influence on $\mathcal{P}_{\text{tot}}$, but figure 5.31 displays a high amount of agreement between the unresolved $\mathcal{PLT}$s from the *LS* and *ic*-GCR models, at least at $T^{(\text{pk.})}$. There are two exceptions. Ar^0 possess a large discrepancy between the $\mathcal{PLT}$ from different resolutions, and this contributes to the divergence of the $\mathcal{P}_{\text{tot}}$ curves at low temperature in figure 5.30. Second, Ne-like Ar^{8+} also exhibits a substantial deviation

of its $\mathcal{PLT}$s, and this accounts for a great deal of the variation of $\mathcal{P}_{\text{tot}}$ near 100 eV, which is approximately equal to $T^{(\text{pk.})}$ for this ion. That these notable discrepancies occur at shell boundaries mirrors the similar result found when comparing *ic* to *ca* $\mathcal{PLT}$s in section 2.3.1 with the configuration selection work. Therefore, it can be concluded that resolution—*ca*, *LS*, *ic*—affects $\mathcal{PLT}$s the most at or near shell boundaries.

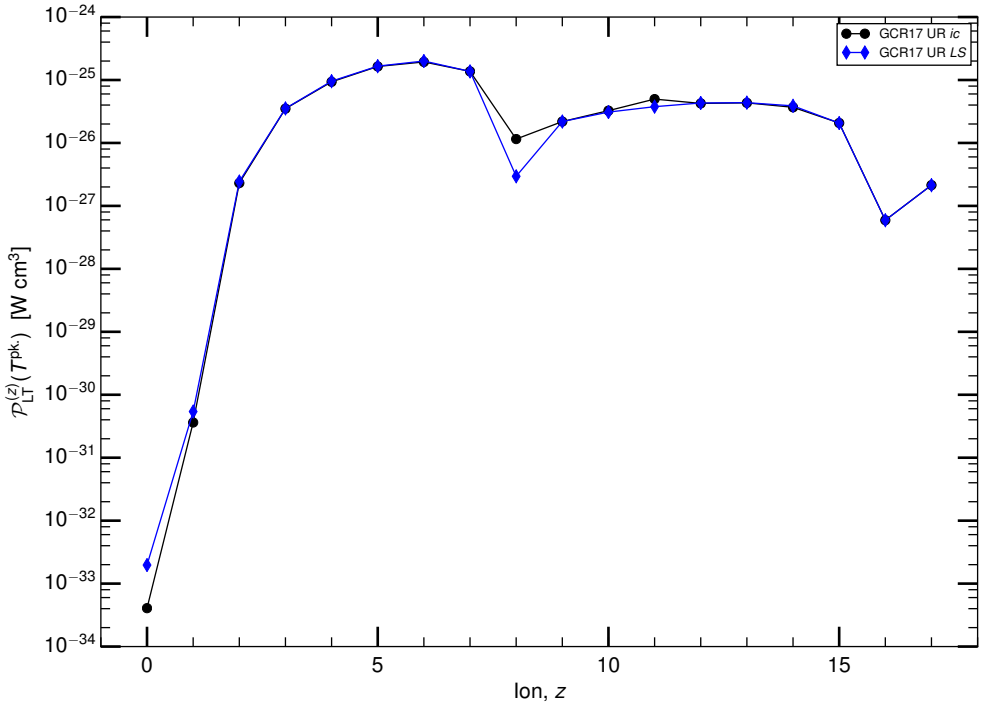

Figure 5.31: $\mathcal{PLT}$ coefficients from the *LS* and *ic*-resolved GCR models at $T^{(\text{pk.})}$across the argon isonuclear sequence. UR stands for unresolved. The temperatures at peak abundance have been taken from the GCR17 UR *ic* result. $N_{\text{e}} = 10^{12}$ cm^{-3} has been used in the model.

An unexpected result from figure 5.30 is that the inclusion of IIE in the *ic*-GCR model does not cause a perceptible change in $\mathcal{P}_{\text{tot}}$—"GCR17 *ic* + He-impact". Any influence of IIE upon $\mathcal{P}_{\text{tot}}$ will enter through the fractional abundances, but even with the dilution effects discussed above, it is strange that the alterations in figure 5.22 are not propagated to $\mathcal{P}_{\text{tot}}$. This will need to be investigated further to judge its validity.

Considering the fair agreement amongst the results from different resolution models, the GCR17 *ic* result is adopted as representative of the GCR models when comparing with other data.

5.4.3 New Argon Power Coefficients

The radiated power is a good fitness function for optimising the configuration set because it is an observable that provides an unbiased and global view of the atomic system. This is the basis upon which the new baseline data in Chapter 2 was developed. Figure 5.32 compares the $\mathcal{P}_{\text{tot}}$ curves from two new ADAS baseline datasets to the new *ic*-GCR standard, and broadly good agreement is observed. SSH41 is the *ic*-resolved, COWAN PWB calculation using the power-optimised (*cs*) configuration sets described in section 2.3.1 and the associated paper [21]. SSH17 is the *ic*-resolved, AUTOS DW calculations using the power-optimised (*cs*) configuration sets and the λ_{nl} from the novel optimisation strategy. This is the lifted ADAS baseline *adf04* data that are the primary product of Chapter 2. A slight modification has been made in producing SSH17 to include some missing configurations in the ground complex, an issue to be handled once the mass-production procedures for this baseline data have been established. For both SSH41 and SSH17 results, it is only the $\mathcal{PLT}$s that can be generated from their undecorated *adf04* files, so the other GCR coefficients needed for modelling—i.e. those that form the ionisation balance—are taken from the GCR17 *ic* data. The difference in figure 5.32 is therefore purely due to the $\mathcal{PLT}$s. Also, the top up from equation 2.22 has been applied to the $\mathcal{PLT}$s of SSH41 and SSH17. The $\mathcal{PLT}$ comparisons in figure 5.33 are unresolved. Metastable-resolved $\mathcal{PLT}$s from these sources are possible but unnecessary to assess their quality.

The comparison of $\mathcal{PLT}$s in figure 5.33 resembles the comparison based on resolution in figure 5.31. The largest differences are observed for the closed-shell states, Ar-like and Ne-like, along with some of the near neutrals. This leads to the low temperature discrepancies of $\mathcal{P}_{\text{tot}}$, and the slightly elevated discrepancy around 100 eV where Ne-like has its $T^{(\text{pk.})}$. That the differences in the $\mathcal{PLT}$s occur near closed-shells is well established from the work in section 2.3.1 which identified resolution, metastability, and approximations in the collision calculations as factors that tend to influence the $\mathcal{PLT}$ most at these shell boundaries. The SSH17 baseline achieves a better agreement of the $\mathcal{PLT}$s with GCR17 *ic* for the near-neutral stages, corresponding to better agreement of $\mathcal{P}_{\text{tot}}$ at low temperature. Over the remainder of the ions and temperature domains, the difference between SSH17 and SSH41 is modest. The optimisation strategies of SSH41 and

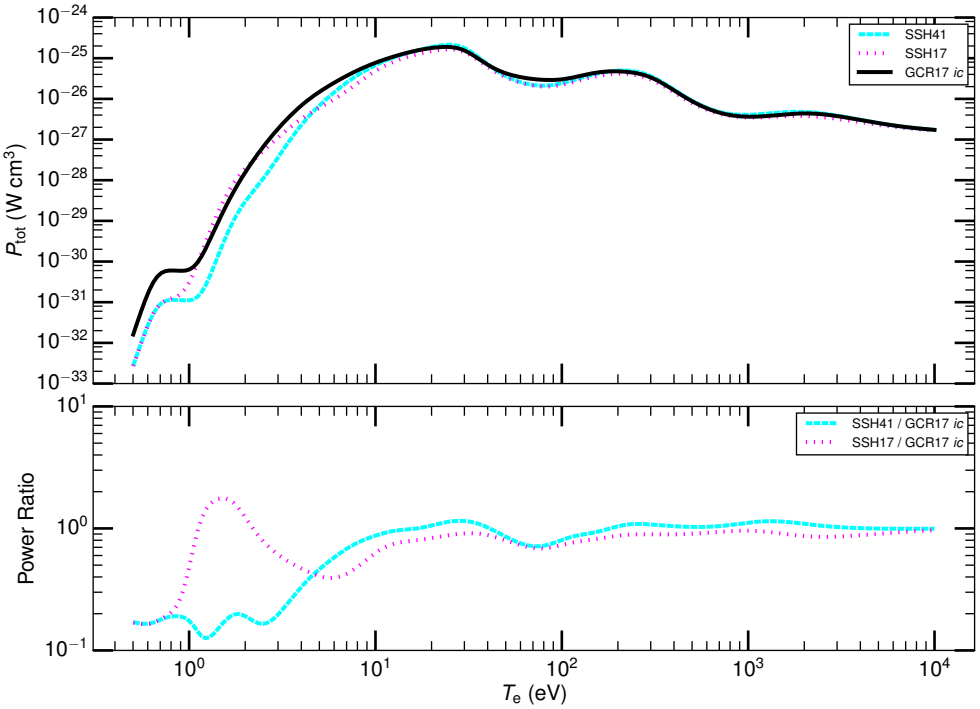

Figure 5.32: Comparison of the argon total radiated power function between the *ic*-GCR model (GCR17 *ic*) and the new ADAS baselines. SSH41 is the new COWAN PWB baseline used in the configuration selection work of section 2.3.1. SSH17 is the new AUTOS DW baseline, which uses the configuration sets optimised on power and the algorithmic strategy for optimising the λ_{nl}. The bottom pane shows the ratio of the $\mathcal{P}_{\rm tot}$ relative to GCR17 *ic*. $N_{\rm e} = 10^{12}$ cm^{-3} has been used in the model.

SSH17 have therefore been validated by comparing to the *ic*-GCR results for argon.

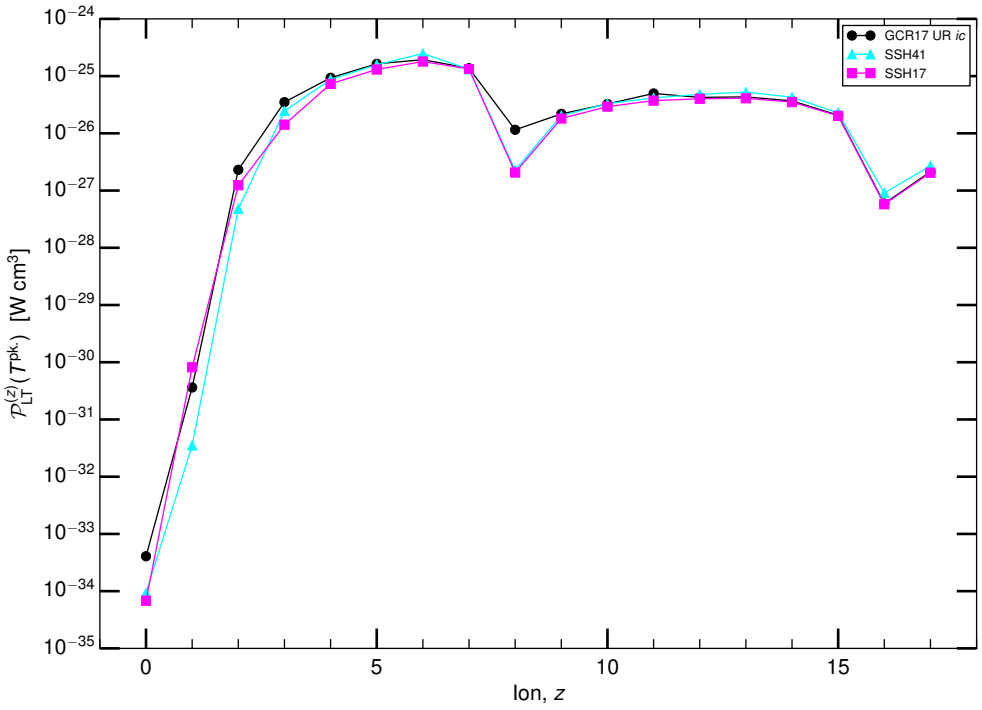

Figure 5.33: $\mathcal{PLT}$ coefficients from the present *ic*-GCR model (GCR17 UR *ic*) and new ADAS baselines at $T^{(\mathrm{pk.})}$across the argon isonuclear sequence. SSH41 is the new COWAN PWB baseline used in the configuration selection work of section 2.3.1. SSH17 is the new AUTOS DW baseline, which uses the configuration sets optimised on power and the algorithmic strategy for optimising the λ_{nl}. UR stands for unresolved. The temperatures at peak abundance have been taken from the GCR17 UR *ic* result. $N_\mathrm{e} = 10^{12}$ cm^{-3} has been used in the model.

Chapter 6

Conclusion

The extension of GCR modelling to medium and heavy species in optically-thin, collisionally-excited plasmas has required progress in a number of areas. Baseline data is pivotal in the modelling of impurity species, and it was discovered that previous baselines are insufficient in the new regimes. Chapter 2 has established the foundations for a new *adf04* baseline using AUTOS with the DW approximation, power-optimised configuration sets, and optimised radial scaling parameters (λ_{nl}) from a novel algorithmic strategy. This constitutes a lift in quality over the antecedent ADAS-EU [20] baseline. With higher Z_0, relativistic effects in atomic structures become prominent and must be treated. AUTOS is fundamentally a non-relativistic code, but it incorporates relativistic corrections through the Breit-Pauli Hamiltonian and κ-averaged, semi-relativistic radial wave functions. Numerous results from the literature, including the previous ADAS baselines, show this to be an accurate and broadly applicable approach, which is further supported by the favorable comparison between AUTOS and DARC for W^{44+} in Chapter 3. In addition, more atomic electrons in heavier species produce complex atomic structures with large degrees of CI, making the task of automated configuration selection a priority. The new baseline uses configuration sets determined by applying electron promotion rules to base metastable configurations and optimising these rules on the $\mathcal{PLT}$ from a *ca*-resolved COWAN PWB calculation (Section 2.3.1). No previous baseline dataset considers the problem of configuration selection except that of Foster [23], but that treatment is flawed since only the ground configuration is used as the base upon with promotion rules are

applied, meaning important metastable configurations are inadvertently omitted. The updated configuration selection procedure proves that configuration sets, including metastables, will not remain constant along isoelectronic sequences, and the list of metastable base configurations can be found in the *adf54* promotion rule files. Those metastables were verified with small atomic population models, but it raises a thematic problem: an ion-specific list of metastables at LS and ic resolution is needed in ADAS. In the end, the improvement garnered by this automatic configuration selection can be judged by looking at the variation in the $\mathcal{PLT}$ caused by moving between the small (cs) and large (cl) set sizes in figure 2.5. The bounding values of truncation error are an order of magnitude difference for tungsten when it has open p-shell configurations and 10% observed for Fe. A potential limitation of this work is that $\mathcal{PLT}$s were calculated using COWAN in ca resolution; however, this was necessary to reduce computation time and because of the reasons below that made AUTOS unsuitable at the time. A top up to the $\mathcal{PLT}$ was another outcome of this work, and comparison with the $\mathcal{PLT}$s from the ic-GCR model—figure 5.33—shows the improvement this garners.

A coincidental discovery during the configuration selection work has been the import of resolution when determining metastable states. The discrepancies between ca and ic populations and metastables were seen most commonly near shell and sub-shell boundaries for many-electron atoms, but it is not believed that any important ic metastables were omitted because of this. Even if this was the case, the flexibility of the automated procedure allows a configuration that contains important ic metastables to be added with relative ease. Spin-changing transitions that proceed through electron exchange along with higher multipole transitions ($> E1$) have proven to be influential in these scenarios: refer to figures 2.6 and 2.17. As such, the necessity to employ the more accurate DW approximation in AUTOS over the PWB approximation in COWAN has been further emphasised because these spin-changing and higher-order transitions can be included.

Another related discovery was that errors in the default structure produced by AUTOS ($\lambda_{nl} = 1$) could propagate to produce errors of 20–30% in the $\mathcal{PLT}$, possibly eliminating any benefit derived from using the DW approximation—figure 2.7. Therefore, a novel algorithmic strategy for optimising the λ_{nl} of AU-

TOS was developed to improve the atomic structure produced, grounded in the physical understanding of orbitals becoming effectively frozen once they constitute part of the core of an atom—Section 2.3.2. The final output was a subclass of the *adf54* file format containing the λ_{nl} for ions on a regular grid within each isoelectronic sequence, facilitating interpolation to obtain the λ_{nl} of any ion desired. Three figures of merit were introduced in Sections 2.4 to evaluate the improvements made, if any, by optimising the λ_{nl} in this manner. All three supported the conclusion that statistically significant improvements by optimisation of the atomic structure were achieved more frequently for the lowly charged ions of an isonuclear sequence, while the default and optimised structures appeared to converge at higher charges—e.g. figure 2.13. It is presently unknown whether these optimised λ_{nl} are strongly coupled to the particular settings used within AUTOS, in particular if these values will only apply when κ-averaged radial wave functions are used.

Although baseline *adf04* and EIE data is important in the context of GCR modelling, it is ultimately the highest-quality EIE collision data that is desired wherever available, and the generation of this data for medium and heavy elements poses unique obstacles. Chapter 3 has used the example of W^{44+} to showcase the difficulties in generating high-quality EIE data using fully-relativistic, partially radiation damped, Dirac R-matrix calculations with the GRASP^0/DARC suite. From the perspective of collision calculations in the literature, the most novel aspect of this work was to incorporate both of the spectroscopically important transition arrays, [$3d^{10}4s^2$–$3d^9 4s^2 4f$] and [$3d^{10}4s^2$–$3d^9 4s4p4d$], which had not been considered before, including in the most recent and similar calculation by Ballance and Griffin [71]. Considering the configurations that open the 3d-subshell required compromises to be made in the CI and CC expansions; configurations $3d^{10}4lnl'$ for $n > 4$ were excluded due to computational restrictions. Comparing to Ballance and Griffin [71], this difference in the CI and CC expansions leads to a systematic difference between the Υ_{ij} datasets which is likely caused by an increase in resonant enhancement of the Ballance and Griffin results, rather than being due to target structure or radiation damping variation.

In the end, evaluation of the differences in fundamental collision data was performed through its application in atomic population modelling. From the

perspective of radiated power loss, it is clear from the $\mathcal{P}^{(z)}_{\mathrm{LT},\sigma}$ and $\mathcal{P}_{L,1,j\to k}$ lines in figure 3.5(a) that the effect of the 3d-subshell transitions was far greater than any effects due to the neglect of the $n = 5$ transitions. Moreover, the non-CC, semi-relativistic calculations (AUTOS DW and COWAN PWB) provide a suitable baseline estimate of the radiated power loss estimates. This supports the conclusions from Chapter 2 that only certain observables require the highest quality data and that the requirements for predicting radiated power loss is adequately served by baseline quality data. Moreover, it seems that these semi-relativistic approaches hold up quite well for this fully-relativistic ion, supporting a broad scope for the new baseline described above. On the other hand, differences in the $\mathcal{F}$-$\mathcal{PEC}$ spectra (figure 3.6) demonstrate that a R-matrix calculation is necessary for detailed spectroscopic applications. The close agreement of our DARC results with those of Ballance and Griffin further supports the conclusion that omitting the $n = 5$ transitions does not have a large effect upon the modelled results. Rather, it is the inclusion of the 3d-subshell transitions, which create a relatively strong spectral feature, that is of greater import. Thus, for heavy species and W^{44+} in particular, the selection of configurations to include in the CI and CC expansions appears to be the most influential and important input to the structure and collision calculation, echoing the premise for why configuration selection was automated in Section 2.3.1 when designing the new ADAS baseline.

The explicit inclusion of IIE collisions in population modelling is an additional consequence of shifting towards medium and heavy species, explained by the rule of thumb specifying that small ΔE_{ij} transitions are most susceptible: $\Delta E_{ij} \approx kT^{(\mathrm{pk.})}/M \approx \chi^{(z)}/M$ for $M \gg 1$ (Section 4.1.1). This imposed the requirement for baseline-quality IIE collision data within ADAS with specific attention given to the $E2$-order transitions between fine-structure metastable levels. Chapter 4 has provided the theoretical and practical basis for a baseline dataset using the SC-1 approach through the new code, `a2iratbt`. It uses symmetrised, first-order perturbative equations with a limiting function, $\phi(x)$, to prevent transition probability overestimates, and at high energies, a cutoff, r_0, is enforced that relates directly to the Born approximation limit, ensuring the collision strength asymptotically approaches ${\Omega_{ij}}^{(\mathrm{inf})}$ (Section 4.3.1). In addition, a new ADAS file format, *adf06*, was required to hold the IIE collision

data (Section 4.3.2). The literature review of Section 4.2 has revealed that the SC-1 method is suitable for producing baseline quality data. There is no discernible error introduced by using a semi-classical versus fully-quantal technique, and use of the long-range quadrupole interaction term is well justified, since the r_0 cutoff prevents the inaccuracies of this term at high energies. However, there is some unresolved uncertainty about the amount of error caused by neglecting the polarisation correction; Heil et al. [114, 126] place the error at about 10% while descendants of Reid and Schwarz [108] claim it can cause variation of 60%. CC effects are minimal for transitions within a doublet term ($< 5\%$) but grow for higher multiplicities, although not outside the acceptable limits of a baseline ($\approx 20\%$).

In addition, extensive parameter variation studies of the IIE collision quantities were performed that confirmed the correct operation of the `a2iratbt` code (Section 4.4.1). The variation of the projectile parameters, z_p and m_p, produced a characteristic "crossing-over" or inflective behaviour in the collision quantities where larger z_p or m_p produce lower values below the energy (temperature) inflection point but then higher values above it—figures 4.14 and 4.15. The target parameters caused the collision quantities to scale as expected, and significantly there was a nearly linear positive correlation with the line strength—figure 4.19. A reoccurring theme of comparisons with the literature was the imperative to match atomic structure inputs when comparing IIE transitions, which revealed that many sources use line strengths or $\langle r^2 \rangle$ values that are underestimated by about 20% on average, leading to a corresponding underestimate of the cross section or other relevant collision quantity. Furthermore, it was shown that if no $\phi(x)$ function is used then the collision strength will be severely overestimated (figure 4.20), while the neglect of r_0 causes the collision strength to incorrectly diverge at high energies (figure 4.21).

Culminating all of these various developments is Chapter 5, which has successfully established a prototype of *ic*-resolved GCR modelling applied to argon, the first in this resolution for any element. The overarching strategy was to build directly upon the foundation of the *LS*-GCR implementation and then split the relevant *LS*-resolved quantities onto the *ic*-resolved manifold using the appropriate statistical weights of the levels or terms involved (Section 5.1.2).

Crucially, a shortcut was made by adding the IIE rate coefficients between fine-structure metastable levels directly to the relevant Q^{cd} coefficients without loss of accuracy—equation 5.8. However, this tactic can only be applied to transitions between metastable levels, so future applications that wish to add IIE rate coefficients to arbitrary levels will require a more integrated approach. Otherwise, the sourcing of data for the *ic*-GCR calculation is similar to that of *LS*-GCR with one exception: a consistent set of both *LS* and *ic*-resolved *adf04* files were required in this instance to facilitate a meaningful comparison between the final outputs of the different resolution models—see Appendix B.

Comparing the *LS* and *ic* models against the *unresolved* results in the literature yielded some important conclusions—Sections 5.2.3 and 5.4.1. The stage-to-stage fractional abundances from both models showed substantial differences at finite densities with the various zero-density models in the literature. Notably, the ionisation balance of Bryans [189] displayed order of magnitude differences for near neutrals, decreasingly gradually to perfect agreement for the highly ionised stages. Most of this is explained by density effects and differences in DR data, but a discrepancy in the defintions of the α^{cd} and total recombination coefficient caused lingering differences for Ne-like Ar^{8+} to Be-like Ar^{14+}. On the other hand, comparisons of $\mathcal{P}_{\mathrm{tot}}$ showed better agreement, generally within 50% for the higher quality CR result of Fournier et al. [187]. The $\mathcal{PLT}$s from this source also compare favourably to within 20%. These comparisons are strong evidence that the present GCR model is valid, particularly the extension to *ic* resolution.

One of the more significant and novel aspects of this work is that it has given the most accurate depiction to date of how IIE rates affect the population models of medium and heavy species. Although there are a number of *ic*-resolved CR models in the literature that include IIE rates [87, 90, 101, 193–199], they only apply to single ion stages and are strictly concerned with determining line ratios. They do prove IIE can have a defining influence upon the interpretation of the models, but this is in a much more limited sense than the objectives of this thesis dictate. Nonetheless, the similarly limited IIE study in Section 5.3.1.1 has produced the valuable notion of a "sweet spot" for IIE influence that loosely defines the bounding parameter space. First, the ion must be one for which it is possible to have a CR regime specific to the metastables; this tends to be

achieved for moderately charged ions, $z \gtrapprox 10$, because they produce an appropriate degree of fine-structure splitting that allows radiative and collisional rates to be comparable. Second, T_e and N_e must actually reside in this CR regime; if ionisation equilibrium is assumed, then T_e will be determined by $T^{(\mathrm{pk.})}$, while N_e will depend on the operational parameters of the relevant plasma environment. Third and last, T_e must lie above the steeply suppressed region of the IIE rate coefficient, something that can again be estimated by the rule of thumb in equation 4.4. Also, the study has found that it is not reasonable to expect the inclusion of IIE rates in an *ic*-resolved model to cause agreement with an *LS*-resolved model at any density other than in the LTE regime, regardless of whether the species is light, medium, or heavy. These conclusions were mirrored in the *ic*-resolved fractional abundances for argon produced by the GCR prototype upon supplementing the Q^cd's with IIE rate coefficients (Section 5.3.1.2). When adding only proton-impact rates, the metastable level fractional abundances that were most influenced belonged to ionisation stages above $z = 10$, although S-like Ar^{2+} saw substantial alteration of its resolved fractional abundances related to fairly anomalous behaviour of the ^{5}D term—figure 5.19. The inclusion of proton-impact could either increase or decrease the fractional abundance of a metastable depending on how the populations are fed and their pathways to the ground. Higher temperatures tended to increase the deviation caused by IIE, agreeing with the general conclusions from Chapter 4 and clearly expressed in the supplemented Q^cd's of figures 5.20 and 5.21. A surprising discovery was that *inter*-multiplet transitions can have Q^cd's substantially altered by IIE and that this translates to the fractional abundances—see N-like Ar^{11+} in figure 5.21. However, *intra*-multiplet transitions are still generally more susceptible to IIE transitions. Varying the ion projectile has produced noticeable differences in the resulting fractional abundances (figure 5.22) with the characteristic "criss-crossing" behaviour of the IIE rate coefficients propagating through in some instances. Three null results are of note: $T^{(\mathrm{pk.})}$, *unresolved* fractional abundances, and $\mathcal{P}_\mathrm{tot}$ were found to be insensitive to IIE.

The resolution of the GCR model also affected the results for argon. Comparing the *unresolved* fractional abundances from the *LS* and *ic* models showed fair agreement of about 50% near the peaks but order of magnitude differences

on the tails. Interestingly, the agreement is worse at low densities, where coronal conditions produce the most discrepancy between the LS and ic pictures. $\mathcal{P}_{\text{tot}}$ also displayed sensitivity to resolution, but to a lesser degree of $< 20\%$ across the majority of the temperature domain. However, the $\mathcal{PLT}$ differed by factors of 3–5 around closed shells because of resolution, causing some limited regions of $\approx 50\%$ difference for $\mathcal{P}_{\text{tot}}$. Ultimately, however, the true impact of the move to ic resolution can only be judged through the use of these results in transport modelling.

Finally, definitive lists of LS-term and ic-level metastables for argon were determined—tables 5.4 and 5.7, respectively. In both cases, the simple ADAS list overestimates the number of metastable states for argon. For LS, the main reasons were the isoelectronic scaling of term energies and that pure LS data differs compared to data bundled from ic calculations. This bundled LS data was found to be more realistic because it reproduced the ic-level metastables with high fidelity, the only exceptions being Mg-like Ar^{6+} and Be-like Ar^{14+}. Overall, these results suggest the imperative of using population modelling to determine metastable sets that can vary isoelectronically.

6.1 Future Work

Thesis work, like any research endeavour, is never really completed but only pushed forward, awaiting further progress. There are a number of areas in this thesis to which the adage readily applies.

The components of a new *adf04* baseline for ADAS, outlined in Chapter 2, are present in the development space of ADAS, but mass production will require a final processing chain to be constructed, linking all of these parts seamlessly together. It was raised above that the λ_{nl} determined in the manner of Section 2.3.2 will inherently depend upon the AUTOS settings used during optimisation; the precise sensitivity of the λ_{nl} to these settings and whether they will yield improvements under all circumstances is yet to be determined. A number of kinks in the isoelectronic λ_{nl} and some strange divergence issues for the 2p value are other areas that merit attention in the future. At the moment, it is posited that the rise in 2p values along an isoelectronic sequence is caused by the structure

becoming increasingly insensitive to the 2p λ_{nl} values because the TFDA potential itself is dominated by the Coulomb term. But this is by no means definitive and requires more substantiating evidence.

An obvious improvement of the W^{44+} EIE work would be to extend the CI/CC expansions of the calculation presented in Chapter 3 to include the $3d^{10}4l5l'$ configurations so as to unequivocally resolve the effect of the additional resonant enhancement upon the lower-lying transitions. Of course, this will require a larger computing facility. However, it turns out that some collaborators at QUB have already made progress towards this goal [204]. A cursory inspection shows good agreement between their new calculations and those presented here, but a full comparison is left to their future publication that is in production [205]. In addition, updating comparisons to use the new AUTOS baseline would be useful to confirm that it maintains fidelity with the high-quality result.

Presently, the `a2iratbt` code only handles $E2$-order transitions, and the most pressing development is to extend it to $E1$ (dipole). This would facilitate the calculation of l-changing transitions that redistribute levels within higher-lying n-shells, something that a fully-integrated bundle-n population code will need to consider. One might also consider borrowing one of the techniques from the literature for estimating the cross section or collision strength of transitions that only proceed through collisional coupling; however, it was concluded in Section 4.2 that the benefit of this is not worthwhile. Rather, the progression towards an SC-CC method should be prioritised if an increase in baseline quality is desired. Concurrently, a definitive ruling on the importance of the polarisation correction should be obtained, which can only be done by implementing it, given the ambiguity in the literature.

The implementation of *ic*-resolved GCR presented here can confidently stand on its own for broad use within ADAS. Even so, it is still a prototype, and as one moves to heavier elements with higher Z_0, some of the assumptions made will become less and less accurate. In particular, the bundle-nS representation of the highly-excited ry states is no longer tenable: spin-system breakdown at high n shells is a well-known phenomenon that occurs even for light elements and is compensated by adding spin-changing autoionisation rates to the ADAS204 calculation in those cases. Rather, the proper treatment of the low-resolution pop-

ulation calculation is a bundle-n or bundle-nl representation built on J-resolved parents: $(\gamma_\nu J_\nu)n$ or $(\gamma_\nu J_\nu)nl$. In many ways, this representation is more straightforward than bundle-nS, but nonetheless it requires an entirely new code because ADAS204 is wholly unsuited to the task. Ironically, this will be achieved by reverting to an ancestor of ADAS204 [206] that uses a bundle-nl model and then rebuilding from there. During the course of this ancestor's development into ADAS204, much of its versatility was lost, particularly the stability of the high nl solution with interpolation in n and l, and safe performance at low *reduced* temperatures. Because of the need to put all GCR coefficients on the same energy and temperature grid in *adf11* files, this low *reduced* temperature limitation caused a number of problems while developing the prototype *ic*-GCR model. Although this will be a new code, the logic of how the highly-excited populations are condensed and then projected onto the low-lying set remains the same, so no new machinery is needed there, and the *ic*-resolved *adf18/a17_p208* files produced for the prototype should work seamlessly. Moreover, this new population code should account for the $E1$ l-changing collisions that redistribute the nl populations once `a2iratbt` has been extended to handle these transitions. A code that will require updating is ADAS211 so that it produces *ic*-resolved radiative recombination rates. The theoretical framework is already present in the ADAS manual [15], but any improvement in accuracy is questioned there.

Finally, there are a few tasks logically set by the work of Chapter 5. First, it must be proven that the method of adding IIE rate coefficients directly to the $Q^{\rm cd}$ coefficient (equation 5.8) is equivalent to supplementing the EIE Υ_{ij}'s in the *adf04* files. Regardless, the capability to directly handle *adf06* files should be added to the highly-resolved population codes (ADAS205 and ADAS208) so that IIE can be arbitrarily included in the population model. Second, the capability to set a separate ion temperature, $T_{\rm i}$, should be added. A number of physical circumstances are known where $T_{\rm i} \neq T_{\rm e}$ because of the slow thermalisation time for heavier positive ion species; this usually results in elevated $T_{\rm i}$, something that would certainly benefit the effect of IIE. Third, an ion-specific list of metastables should be created within ADAS, and the imperative for such information was motivated by the baseline work in Chapter 2 and the move to *ic*-GCR in Chapter 5, which highlighted that not all levels in a metastable LS term will themselves be

metastable.

Appendix A

Definitions for ADAS Codes: Collision Quantities

The following is an update to the definitions used in ADAS for the various collision processes of excitation and ionisation. Crucially, sections have been added to address processes involving *ion* projectiles. A slightly different notation is used here in keeping with other ADAS documentation.

A.1 Electron-impact excitation (EIE)

For the reaction

$$\mathscr{A}_i^{z+}(E_i) + e(\varepsilon_i') \rightarrow \mathscr{A}_j^{z+}(E_j) + e(\varepsilon_j')$$

where $\varepsilon_i' + E_i = \varepsilon_j' + E_j$, $\Delta E_{ij} = E_j - E_i$, E_i is the excitation energy of state i, and ε_i' is the energy of the incident (i) or scattered (j) reduced particle in the COM frame. The COM frame is effectively equivalent to the LAB frame for EIE because $m_\mathrm{e} \ll m_\mathrm{t}$.

The reaction is described by the cross section, $\sigma_{i\rightarrow j}(\varepsilon_i)$, which is only energetically possible if $\varepsilon_i \geq \Delta E_{ij}$.

Define $X = \varepsilon_i / \Delta E_{ij}$ where $X \in [1, \infty]$

The collision strength is dimensionless and symmetrical between initial and final states,

$$\Omega_{ij} = g_i(E_i/I_H)(\sigma_{i\rightarrow j}(\varepsilon_i)/\pi a_0^2) = g_j(E_j/I_H)(\sigma_{j\rightarrow i}(\varepsilon_j)/\pi a_0^2)$$

with g_i and g_j the statistical weights and I_H the Rydberg energy.

To convert (measured/calculated) cross sections (`sigma`) to collision strengths (`omega` $\equiv \Omega_{ij}$) which are tabulated against incident energy,

```
omega = gi * (delta_e * X / 109737.26) * (sigma / 8.7972e-17)
```

where `X` is defined by the user and `sigma` (cm^2) is interpolated for `X * delta_e`.

A *type 1, adf04* file tabulates Ω_{ij} as a function of X.

The Maxwellian distribution function for the *relative* motion of two sets of free particles in thermodynamic equilibrium is:

$$\begin{aligned} f(v_r) &= 4\pi \left(\frac{M}{2\pi kT}\right)^{3/2} v_r^2 \exp(-\frac{mv_r^2}{2kT}) \\ f(\varepsilon_i') &= 2\pi \left(\frac{1}{\pi kT}\right)^{3/2} \varepsilon_i'^{1/2} \exp(-\varepsilon_i'/kT) \end{aligned}$$

where $M = m_p m_t/(m_p + m_t)$ is the reduced mass, T the temperature, and $\int_0^\infty f(v_r)\, dv_r = 1$. Note that $v_r^2 = 2\varepsilon_i'/M$ and $\mathrm{d}v_r = 1/(2M\varepsilon_i')^{1/2}\, \mathrm{d}\varepsilon_i'$. Again, because $M \sim m_\mathrm{e}$ for EIE, these expressions effectively become those for free particles:

$$\begin{aligned} f(v) &= 4\pi \left(\frac{m_\mathrm{e}}{2\pi kT}\right)^{3/2} v^2 \exp\left(-\frac{v^2}{2kT}\right) \\ f(E) &= 2\pi \left(\frac{1}{\pi kT}\right)^{3/2} \varepsilon^{1/2} \exp(-\varepsilon/kT). \end{aligned}$$

The excitation rate is then

$$\begin{aligned} q_{i\to j}(T) &= \langle v_i\, \sigma_{i\to j}(v_i)\rangle \\ &= \int_{\Delta E_{ij}}^{\infty} f(v_i)\, v_i\, \sigma_{i\to j}(v_i)\, \mathrm{d}v_i \\ &= 4\pi \left(\frac{m_\mathrm{e}}{2\pi kT}\right)^{3/2} \int_{v_i(\Delta E_{ij})}^{\infty} v_i^2 v_i \exp(-m_\mathrm{e} v_i^2/2kT)\sigma_{i\to j}(v_i)\, \mathrm{d}v_i \\ &= 4\pi \left(\frac{m_\mathrm{e}}{2\pi kT}\right)^{3/2} \left(\frac{2}{m_\mathrm{e}}\right)^{3/2} \left(\frac{1}{2m_\mathrm{e}}\right)^{1/2} \int_{\Delta E_{ij}}^{\infty} \varepsilon_i \exp(-\varepsilon_i/kT)\sigma_{i\to j}(\varepsilon_i)\, \mathrm{d}\varepsilon_i \\ &= \frac{2\sqrt{2}}{\sqrt{\pi}} \left(\frac{1}{kT}\right)^{3/2} \left(\frac{1}{m_\mathrm{e}}\right)^{1/2} \frac{\pi a_0^2 I_H}{g_i} \int_{\Delta E_{ij}}^{\infty} \Omega_{ij}(\varepsilon_i) \exp(-\varepsilon_i/kT)\, \mathrm{d}\varepsilon_i \end{aligned}$$

where the cross section is replaced by the collision strength.

When the integral is further transformed from ε_i to ε_j ($\varepsilon_i = \varepsilon_j + \Delta E_{ij}$), and noting that $\alpha c = (2I_H/m_\mathrm{e})^{1/2}$, the excitation rate coefficient for electron impact excitation becomes

$$q_{i\to j}(T_e) = 2\sqrt{\pi} a_0^2 \alpha c \left(\frac{I_H}{kT_e}\right)^{1/2} \frac{1}{g_i} \exp(-\Delta E_{ij}/kT_e)\Upsilon_{ij}$$

where Υ_{ij} is the effective collision strength,

$$\Upsilon_{ij} = \int_0^{\infty} \Omega_{ij}(\varepsilon_j)\, \exp(-\varepsilon_j/kT_e)\, d(\varepsilon_j/kT_e).$$

The limits reflect that this integral is defined over electron energies, ε_j, with respect to the final, excited state. However Υ_{ij} is symmetrical between excitation and de-excitation concordant with the collision strength.

A *type 3, adf04* file tabulates Υ_{ij} as a function of T_e .

De-excitation and excitation rates follow:

$$\begin{aligned} q_{j\to i}(T_e) &= 2\sqrt{\pi}a_0^2\alpha c\frac{1}{g_j}\left(\frac{I_H}{kT_e}\right)^{1/2}\Upsilon_{ij} \\ &= \frac{g_i}{g_j}\exp(\Delta E_{ij}/kT_e)\,q_{i\to j}(T_e) \end{aligned}$$

and $2\sqrt{\pi}a_0^2\alpha c = 2.1716\times10^{-8}\mathrm{cm}^3\mathrm{s}^{-1}$.

The offline code `adas7#3/adf04_om2ups.x` can convert a *type 1* to a *type 3 adf04* file. The reverse process is not possible.

A.2 Ion-impact excitation (IIE)

The collision strength is the ratio of the cross section to the squared de Broglie wavelength, and the generalised form is

$$\Omega_{ij}^{ion} = Mg_i(\varepsilon_i/I_H)(\sigma_{i\to j}(\varepsilon_i)/\pi a_0^2) = Mg_j(E_j/I_H)(\sigma_{j\to i}(\varepsilon_j)/\pi a_0^2)$$

where M is the reduced mass of the target-projectile system,

$$M = \frac{m_\mathrm{t}m_\mathrm{p}}{m_\mathrm{t}+m_\mathrm{p}}$$

in atomic units ($m_\mathrm{e}=1$). The energies $(\varepsilon_i,\varepsilon_j)$ are those of the incident and scattered *reduced* projectile. As noted in the previous section, $M\to m_\mathrm{e}\equiv1$ for electron impact, where the target is considered massive compared to the electron projectile. This is not the case where the projectile ion is a proton or a heavier particle, so the reduced mass must be carried through all of the relevant collision expressions.

The threshold parameter $X=\varepsilon_i/\Delta E_{ij}$ is defined the same way as for the electron impact case.

A *type 1, adf06* file tabulates Ω_{ij}^{ion} against X.

The effective collision strength for ion impact is defined identically as the electron impact version, but the *relative* speed Maxwellian distributions and the reduced mass must be tracked throughout:

$$
\begin{aligned}
q_{i\to j}(T) &= \langle v_r\,\sigma_{i\to j}(v_r)\rangle \qquad [a_0^2\alpha c] \\
&= \int\limits_{v_r(\Delta E_{ij})}^{\infty} f(v_r)\,v_r\,\sigma_{i\to j}(v_r)\,\mathrm{d}v_r \\
&= \int\limits_{\Delta E_{ij}}^{\infty} f(\varepsilon_i)\,\left(\frac{2\varepsilon_i}{M}\right)^{1/2}\sigma_{i\to j}(\varepsilon_i)\,\mathrm{d}\varepsilon_i \\
&= 2\pi\left(\frac{1}{\pi kT}\right)^{3/2}\left(\frac{2}{M}\right)^{1/2}\int\limits_{\Delta E_{ij}}^{\infty}\varepsilon_i^{1/2}\exp(-\varepsilon_i/kT)\varepsilon_i^{1/2}\sigma_{i\to j}(\varepsilon_i)\,\mathrm{d}\varepsilon_i \\
&= 2\left(\frac{1}{kT}\right)^{3/2}\left(\frac{2}{\pi M}\right)^{1/2}\int\limits_{\Delta E_{ij}}^{\infty}\varepsilon_i\exp(-\varepsilon_i/kT)\frac{\pi\Omega_{ij}(\varepsilon_i)}{Mg_i\varepsilon_i}\,\mathrm{d}\varepsilon_i \\
&= \frac{2\sqrt{\pi}}{g_i}\left(\frac{2}{kT}\right)^{1/2}\left(\frac{1}{M}\right)^{3/2}\int\limits_{\Delta E_{ij}}^{\infty}\Omega_{ij}\exp(-\varepsilon_i/kT)\,\mathrm{d}(\varepsilon_i/kT)
\end{aligned}
$$

Converting again to ε_j and using Ryd units for energy,

$$
q_{i\to j}^{ion}(T_{ion}) = \frac{2\sqrt{\pi}}{g_i}\left(\frac{I_H}{kT_{ion}}\right)^{1/2}\left(\frac{1}{M}\right)^{3/2}\exp(-\Delta E_{ij}/kT_{ion})\Upsilon_{ij}^{ion} \qquad [a_0^2\alpha c].
$$

Notice the reduced mass factor, $M^{-3/2}$, compared to the analogous expression for electron-impact excitation. A *type 3, adf06* file tabulates Υ_{ij}^{ion} against T_{ion}.

There is no ADAS code to convert between a *type 1* and *type 3 adf06* file. Consider developing `adas7#3/adf06_om2ups.x`

A.3 Electron impact ionization

The reaction

$$
A_\gamma^{z+} + e \to A_p^{(z+1)+} + e + e
$$

where the ion in its initial state, γ, is ionised to a residual state p. The final state may be metastable but often is not specified, being the sum over all possible

final states. This direct ionisation may be augmented by indirect auto-ionisation channels which are manifest as steps in the cross section.

An electron impact ionisation collision strength is defined in the same way as for excitation:

$$\Omega^{ionis}_{\gamma p} = g_\gamma \frac{E}{I_H} \frac{\sigma^{ionis}_{\gamma\to p}}{\pi a_0^2}$$

where E is the energy of the impacting electron and g_γ the statistical weight of the ionising level.

To convert (measured/calculated) cross sections (`sigma`) to collision strengths (`omega_s` $\equiv \Omega^{ionis}$) which are tabulated against incident energy,

```
omega_s = gi * (ip * X / 13.6) * (sigma / 8.7972e-17)
```

where `X` is defined by the user, `ip` is the energy of the level–parent gap (in eV, equivalent to ionisation potential for ground state ionisation) and `sigma` (cm^2) is interpolated for `X * ip`. Any steps, due to auto-ionisation, in the cross section are not scaled separately so the collision strength will retain the energy resolved structure of the cross section.

A *type 1, adf04* file tabulates Ω^{ionis}_{ij} as a function of $X = E/I_{ionis}$.

The ionisation rate coefficient, for a Maxwellian distribution, is:

$$S^{ionis}_{\gamma\to p} = 2\sqrt{\pi}\alpha a_0^2 \frac{1}{g_\gamma} \exp(-I_{ionis}/kT)\, \Upsilon^{ionis}_{\gamma\to p}$$

where $I_{ionis} = I_p(m) - E_i$ with $I_p(m)$ being the ionisation potential of the parent metastable and E_i is the energy relative to ground of the level being ionised. The effective collision strength ($\Upsilon_{\gamma\to p}$) is defined the same way as the excitation case.

The *type 3 adf04* file stores a scaled version of the ionisation rate as a function of temperature. The S-line in the file is defined:

$$S^{scaled}_{\gamma\to p} = \exp(I_{ionis}/kT)\, S_{\gamma\to p}$$

where S is the ionisation rate coefficient ($\mathrm{cm}^3\,\mathrm{s}^{-1}$) and *not* the 'ionisation effective collision strength'.

A.4 Ion impact ionization

The reaction,

$$A_{\gamma}^{z+} + p \rightarrow A_{p}^{(z+1)+} + p + e$$

where the ionising particle projectile, p, can be a proton or a heavier ion.

The ion impact collision strength for ionisation is defined as:

$$\Omega_{\gamma p}^{ion;ionis} = M g_{\gamma}(E/I_H)(\sigma_{\gamma p}(E)/\pi a_0^2)$$

where $M = m_t m_p/(m_t + m_p)$ is the reduced mass of the target-projectile system, in atomic units.

The threshold parameter, $X = E/I_{ionis}$ with $I_{ionis} = I_p(m) - E_i$ with $I_p(m)$ being the ionisation potential of the parent metastable and E_i is the energy relative to ground of the level being ionised.

The *type 1 adf06* file tabulates $\Omega_{\gamma p}^{ion;ionis}$ as a function of the threshold parameter, X.

The ionisation rate is formed in a similar way as the electron impact rate with a mass scaling factor:

$$S_{\gamma\rightarrow p}^{ion;ionis}(T_{ion}) = 2\sqrt{\pi}a_0^2\alpha c\frac{1}{g_{\gamma}}\left(\frac{I_H}{kT}\right)^{1/2}\exp(-I_{ionis}/kT)\left(\frac{1}{M}\right)^{3/2}\Upsilon_{\gamma p}^{ion;ionis}$$

The *type 3 adf06* file tabulates a scaled, mass-free, rate coefficient with ion temperature,

$$S_{\gamma\rightarrow p}^{ion;ionis,scaled} = M^{3/2}\exp(I_{ionis}/kT)\,S_{\gamma\rightarrow p}^{ion;ionis}.$$

A.5 Comments

To calculate ion impact excitation and ionisation rates from the data in the *type 3 adf06* file requires that a mass factor is applied (simple multiplication) when forming the rate from the effective collision strengths. For ionisation this is inconsistent with the definition of the electron impact ionisation S-line in the *adf04* file. However the expectation should be that the way of forming the excitation and ionisation rates from one file, whether *adf04* or *adf06*, should be consistent.

Formally the two formats are consistent since the electron S-line has an implicit mass factor of 1.

Appendix B

Fundamental Data for Argon GCR Modelling

Some of the details related to the fundamental atomic data used in Chapter 5 have been moved here in the interest of maintaining the focus on the results of the GCR modelling rather than the nitty-gritty technicalities. Nonetheless, correctly sourcing and understanding the atomic data is as essential aspect of the modelling process: it underpins the accuracy and validity of the result.

B.1 Preprocessing of *adf04* Data

Before *adf04* data from a literature source can be used with the ADAS GCR codes, they must be preprocessed to ensure a number of criteria are met. Moreover, the provision of ensuring consistency between the LS and ic-resolved files adds to the complexity of the task. A strategy was developed to fulfill these criteria and is outlined in the following steps. The order of the sequence is important, but it should be noted that these steps must be tailored based on the incoming data: some steps may not be needed, or additional ones may have to be added. As much as possible, any anomalies are given in section B.2.

1. Ensure compliance of ic input file (**ICIN**) with *adf04* format in ADAS manual [15]. **ICIN** for each ion is specified in table 5.1. This step usually entails

modifying the configuration string format to standard ADAS notation:

$$n_1 l_1 q_1 \; n_2 l_2 q_2 \; \ldots \; n_i l_i q_i \tag{B.1}$$

where i indexes the shell, n is the single character principal quantum number ($n > 9$ goes alphabetically), l is the orbital angular momentum quantum number in spectroscopic notation (e.g. s, p, d, ...etc.), and q is the single character electron occupancy of the shell. For example, `1s2 2s2 2p6 3s1` is the ground configuration of Na-like.

2. Perform COWAN calculation in *LS* and *ic* resolution with the same configuration as those in **ICIN**.

   - COWAN is executed with the offline ADAS Perl script and the appropriate configurations contained in the *adf34* driver file:

     ```
     $> /home/adas/offline_adas/adas8#1/scripts/run_adas8#1 \
        <adf34> <rcn2_inst> <pp_file>
     ```

   - The resolution of the calculation is controlled in the post-processing file `pp_file`.
   - The *LS adf04* output contains a map between the two resolutions that is used in a subsequent step.
   - Orbital energies needed for the ADAS204 calculation are also produced here and used in a subsequent step.

3. Adjust **ICIN** energy levels to NIST values, producing the intermediate file **NMI**.

   - The NIST energy values are contained in *adf04* stubs in the ADAS database: `/home/adas/adas/adf04/nist#18/ic#ar<z>.dat`
   - First, attempt to use the offline ADAS program `adas7#5.for` to perform a merge of **ICIN** with the NIST energy level *adf04* file. The driver file contains the following:

     ```
     <NIST_adf04_filename>
     <ICIN_adf04_filename>
     ```

```
<merged_output_adf04_filename>
<log_filename>
.true.
.false.
```

- Check the log output to ensure a sensible match has been achieved.
- If not, manually merge the NIST energy values into **ICIN** to produce **NMI**.
- Otherwise, use the merged *adf04* output from `adas7#5.for` as **NMI**.

4. Filter and append orbital energies to produce final *ic* file.
   - Filter **NMI** from previous step using the utility program, `filter04.x`. This utility puts levels in energy order, removes any levels above the ionisation potential (no autoionising levels should be present as they are considered elsewhere), and zeroes any unphysical A-values.
   - Add the orbital energies produced by the COWAN calculation in Step 2.
   - Add comments to the bottom of the file documenting the steps above.
5. Create map from *ic*-resolved **NMI** indices to *LS* bundled indices.
   - Use `adas7#5.for` to match the **NMI** file to the *ic*, COWAN *adf04* file from Step 2. The map between the indices of the two files is contained in the log file output.
   - Take the map between the *ic* and *LS* COWAN files from Step 2.
   - String together the two maps to get a final *LS* bundling map: **NMI** $\mapsto$ *ic* COWAN $\mapsto$ *LS*
6. Perform *LS* bundling of **NMI** file using ADAS IDL program, `bundle_adf04.pro`, and the map generated from step 5.[1]
7. Repeat Step 4 but on the intermediate *LS* produced in Step 6.

[1]There is a small inconsistency in the present work at the bundling step. Some of the *LS* files were generated by bundling the final *ic* file rather than **NMI**. It is not likely this will be a significant effect.

Sequence	Ion	Configurations	Levels	Transitions
H-like	Ar^{17+}	1s–5g	25	300
He-like	Ar^{16+}	$1s^2$, 1s(2s–4f)	31	465
Li-like	Ar^{15+}	$1s^2$(2s–5g), 1s$2s^2$, 1s$2p^2$, 1s2s(2p–4f), 1s2p(3s–4f)	204	19 086
Be-like	Ar^{14+}	$1s^22s^2$, $1s^22s2p$, $1s^22p^2$, $1s^22s$(3s–5g,6s–6d,7s–7d), $1s^22p$(3s–5g,6s–6d,7s–7d)	238	28 203
B-like	Ar^{13+}	$2s^22p$, $2s2p^2$, $2p^3$, $2s^2$(3s–4f), 2s2p(3s-4f), $2p^2$(3s–3d) + $2p^2$(4s–4f), 2s3l3l', 2p3s3l in CI	204	20 710
C-like	Ar^{12+}	$2s^22p^2$, $2s^22p$(3s–4f), $2s2p^3$, $2s2p^2$(3s–3d), $2p^4$	198	19 503
N-like	Ar^{11+}	$2s^22p^3$, $2s^22p^2$(3s–5s), $2s2p^4$, $2s2p^3$3s, $2p^5$	186	17 205
O-like	Ar^{10+}	$2s^22p^4$, $2s^22p^3$(3s–5s), $2s2p^5$, $2s2p^4$3s, $2p^6$	228	25 878
F-like	Ar^{9+}	$2s^22p^5$, $2s2p^6$, $2s^22p^4$(3s–4f), $2s2p^5$(3s–3d)	195	18 915
Ne-like	Ar^{8+}	$2s^22p^6$, $2s^22p^5$(3s–5g, 6s–6d, 7s–7d), $2s2p^6$(3s–5g) + $2s^22p^4$(3s–3d)(3s–5g) in CI	209	21 738
Na-like	Ar^{7+}	$2p^6$(3s–6h), $2p^5$(3s–3p)(3s–3d)	161	9 397
Mg-like	Ar^{6+}	$3s^2$, 3s3p, 3s3d, $3p^2$, 3p3d, $3d^2$, 3s(4s–5g), 3p(4s–5g), 3d(4s–5g)	283	39 903
Al-like	Ar^{5+}	$3s^2$(3p–5s), 3s3p(3d–5s), $3p^3$, $3p^2$3d	155	11 935
Si-like	Ar^{4+}	$3s^23p^2$, $3s^23p$(3d–5s), 3s$3p^3$, 3s$3p^2$3d, $3p^4$, 3s3p$3d^2$	220	24 090
P-like	Ar^{3+}	$3s^23p^3$, $3s^23p^2$(3d–5s), 3s$3p^4$, $3s^23p3d^2$	181	16 290
S-like	Ar^{2+}	$3s^23p^4$, 3s$3p^5$, $3p^6$, $3p^5$3d, $3s^23p^3$(3d–5s)	186	17 205
	LS	$3p^5$, 3s$3p^6$, $3p^4$(3d–5p) + $3p^4$(5d–12g) pseudo	40 + 412 pseudo	780
Cl-like	Ar^{1+}	$3p^5$, 3s$3p^6$, $3p^4$(3d–5p)	147	10 731
Ar-like	Ar^{0+}	$3p^6$, $3p^5nl$, 3s$3p^4nl$; nl = 3d–5p + 5d–14g pseudo	57 + 393 pseudo	1 596

Table B.1: The configuration sets of the Ar *adf04* data used in GCR modelling. The sources of the actual *adf04* files are given in table 5.1.

B.2 Collision Data Sources

Some additional details and synopses of the *adf04* sources for argon in table 5.1 are provided here. These collision data constitute the primary input to the pre-processing steps elaborated in the preceding section B.1. The data sources have been grouped according to methodology and the code used because many of them share the same provenance; thus they share the same limited description provided here with any relevant difference also noted. The configurations used in the CI and CC expansions of the various collision calculations have been consolidated in table B.1.

B.2.1 Parallelized BP RMATRIX I

The *adf04* sources Ludlow et al. (2010) [147] and Munoz Burgos et al. (2009) [151] fall into this category. They cover the ions $Ar^{(17+,12+,11+,10+,5+,4+,3+,2+)}$ corresponding to (H, C, N, O, Al, Si, P, S)-like, respectively. Munoz Burgos et al. (2009) only addresses S-like Ar^{2+}, but it is the progenitor to the extensive isonuclear work in Ludlow et al. (2010). For the structure calculation, AUTOS is used. The BP Hamiltonian with only one-body operators is diagonalized, and the orbital basis set is formed from the TFDA statistical potential (with λ_{nl}) in the

radial wave equation—see section 2.2.1 for more details about AUTOS. In Ludlow et al. (2010), the λ_{nl} are are optimized by hand based on agreement with NIST energy levels for Ar^{17+} through Ar^{5+}, but for the remaining ions, a singular value decomposition code developed in Burgos Munoz et al. (2009) is employed to further tune the λ_{nl} by iterating through matrix operations towards closer agreement of the energies and S_{ij} from NIST. An average percent difference of 1.8% is achieved across these isonuclear ions relative to NIST energy level values.

The scattering calculation is performed with a suite of parallel R-matrix codes derived from the Belfast atomic R-matrix code, RMATRIX I [207], capable of solving the inner-region problem in LS or ic. A non-exchange version, RMATRIX NX, is detailed in [208]. The modifications needed to modernise the codes for massively parallel computers are traced through [80, 81, 209] and the parallel version of the outer-region, asymptotic problem in [210]. The cases presented here conduct the problem in ic resolution by including one-body BP operators in the Hamiltonian, hence the abbreviation to BP R-matrix. These codes can also accommodate the inclusion of pseudo-states in the target, but such measures are only necessary for near-neutral species, so discussion of this subject is deferred to the section addressing neutral and singly-ionised argon: section B.2.3. Refer to table B.1 for the configurations included in the CI and CC expansions of each ion calculation. Some comments specific to the ions treated by these calculations are now made.

H-like Ar XVIII Radiation damping is considered for this highly-charged ion using the optical potential approach [211, 212]. Also, because of the high degree of energy degeneracy amongst hydrogenic levels and terms, the H-like system is only appropriately handled in ry resolution (i.e. bundling by n-shell). This is not a pre-processing step, but rather done after the GCR processing and "decoration" of the input *adf04* file. Bundling is handled by ADAS209 instead of the IDL routine used in the preprocessing because it retains R and S-lines.

B.2.2 RmaX Sequence Work

A number of the *adf04* sources for argon were produced by the UK RmaX/A-PAP Network[2] as part of its work to generate high-quality R-matrix data along entire isoelectronic sequences. Those in this category are He-like Ar^{16+} [148], Li-like Ar^{15+} [149], Be-like Ar^{14+} [49], B-like Ar^{13+} [48], F-like Ar^{9+} [46], Ne-like Ar^{8+} [47], Na-like Ar^{7+} [150], and Mg-like Ar^{6+} [50]. As in the previous category, AUTOS is used at the structure code with one-body BP operators in the Hamiltonian and the TFDA statistical potential including λ_{nl} in the radial equation. The determination of the λ_{nl} is not consistent throughout the publications, and the various techniques are documented for each ion below. Notwithstanding this, a comparison of these λ_{nl} with those from the optimisation work presented in this thesis is given in section 2.3.2.

The codes used to solve the scattering problem have the identical origin to those from the previous section: RMATRIX I [207]. However, the calculation is instead initially performed in LS, and ic-resolved data is generated using the ICFT method [158], described in the Effective Collision Strengths paragraph of section 5.1.3.1. Comment was made therein that ICFT R-matrix calculations produce a remarkably close approximation to the full BP analogue, and it is in this context that the data from this isoelectronic sequence work is preferred over the intersecting cases of BP R-matrix data in the previous section B.2.1. Put simply, there is always a trade-off in collision calculations between the sophistication of the approximation and the size of the CC expansion. Working along an isoelectronic sequence is efficient because the CI and CC expansions only need to be set once for all of the ions calculated. Thus, more time can be allocated to ensuring that these expansions provide the optimal size for the Hamiltonian matrix and encompass the most important configuration mixing effects. In contrast, working along an isoelectronic sequence means that this step must be repeated for each ion, and invariably the consideration of each N-electron problem will be more constrained by the time available to the producer. For all the overlapping cases of argon ions, the ICFT RmaX works have larger CC expansions than the full BP R-matrix calculations of Ludlow et al. (2010) [147], and it is believed that this more than compensates for any loss of accuracy comparing ICFT to BP

[2] `http://amdpp.phys.strath.ac.uk/UK_RmaX`

R-matrix.

The final *adf04* files produced by this series have non-dipole A-values and infinite energy Born limits supplemented from the AUTOS calculation because these are not provided by the R-matrix codes. Again, the configurations included in the CI and CC expansions for these calculations are found in table B.1. Now, some finer details for each ion are made.

He-like Ar XVII The λ_{nl} have been determined by the automatic procedure within AUTOS that minimises the weighted sum of the term energies. It is not clear from the paper, but presumably all terms resulting from the CI are included in the energy functional. Further manual manipulation of the λ_{nl} was not necessary because the initial energy levels agree with those from NIST within 1.8%. Furthermore, the variation between the f_{ij}'s calculated in the length and velocity gauges is also within approximately 10%. Like with the H-like Ar^{17+} ion, the high z of this ion means that radiation damping must be considered, and again the optical potential approach is used. Technically, this ion is not part of the RmaX sequence work, but the methods and codes used are effectively identical, barring some missing parallelization of the codes.

Li-like Ar XVI A number of inner core excited levels, $1s2lnl'$, are included in this calculation, but they lie well above the ionisation potential. As a result, they are filtered out during preprocessing. In addition, both radiation and Auger damping were considered.

Be-like Ar XV The λ_{nl} are determined automatically by AUTOS, but some fairly extreme trends with Z_0 result—refer to section 2.3.2. Nevertheless, agreement with NIST energy levels is within 1.5%. No radiation damping is included after this ion because it is predicted to be negligible.

B-like Ar XIII More attention was devoted to the determination of the λ_{nl} here. First, all terms belonging to the $1s^2 2s^x 2p^y$ $(x + y = 3)$ configurations were included in the weighted energy sum, and the scaling parameters associated with the 1s, 2s, and 2p orbitals were varied and all others fixed. Then, the energies of

the $1s^2 2s3l$ and $1s^2 2s4l$ configurations were separately minimized by varying the $3l$ and $4l$ orbital parameters.

F-like Ar X The λ_{nl} are determined automatically by AUTOS; however, because of the more complex configurations involved, agreement with NIST energies is only within approximately 5%, and so marginally worse than the other cases. Recall that NIST energies are supplemented in the preprocessing steps, so the propagation of this error is mitigated in the GCR modelling.

Ne-like Ar IX Similar to B-like, a manual, two part optimisation of the λ_{nl} was performed. First, the energy of the ground level $2s^2 2p^6\ {}^1S_0$ was minimized by varying the λ_{nl} of the 2s and 2p orbitals. Next, the energy functional for the 14 terms of the $2s^2 2p^5 3l$ configurations was minimized by varying the $3l$ orbital scaling parameters. All other λ_{nl} were set to one.

Na-like Ar VIII The λ_{nl} were determined automatically by minimising the weighted sum of all LS terms included in the CI. Agreement with NIST energies is within 1%. The *adf04* in the ADAS database includes inner core excitations, but the published work does not refer to this. Once again, however, these inner electron excited states lie well above the ionisation potential, so they are filtered out during the preprocessing steps of section B.1.

Mg-like Ar VII The λ_{nl} were determined automatically by minimising the weighted sum of all LS terms included in the CI. Agreement with NIST energy levels is within 1.5%.

B.2.3 RMPS

The accurate calculation of neutral and singly-ionised ions is notoriously difficult for many reasons that have been addressed in this thesis: approximations made in both structure and collision calculations tend to collapse or become inappropriate in this regime. In particular, the physical phenomenon of bound states coupling to the continuum is more pronounced with the smaller ionisation potentials of neutral and singly-ionised species. One approach to dealing with this effect is

to introduce pseudo-states into the structure and collision calculation. Pseudo-states are an effective way of compactly representing high-lying Rydberg states and into the continuum. If this is combined with the R-matrix method, then the R-matrix with pseudo-states (RMPS) approach results, and the sources for neutral argon [213] and Cl-like Ar^1+ [214] both use it. Once again, the computer code that implements this methodology [215] has a very similar heritage with those from the previous two sections: a parallelized version of RMATRIX I [80, 81, 207, 209]. An important step is orthogonalizing the (N+1)-electron continuum orbitals relative to the pseudo-orbitals of the target. Furthermore, AUTOS handles the structure problem in both of these sources, and further details are provided in the separate sections below.

Cl-like Ar II For the structure calculation, AUTOS is again used with one-body BP operators in the Hamiltonian, but in the radial equation an nl-dependent Hartree potential is evaluated with Slater-Type Orbitals (STOs), which are subsequently orthogonalised. Non-orthogonal, Laguerre pseudo-orbitals were generated for subshells 5p–12g. Table B.1 gives the number of resulting "true" states and pseudo-states. Critically, both the structure and collision calculation are performed in LS coupling, meaning this is the only argon ion for which there is no high-quality data directly available in ic resolution.

Accordingly, some additional steps were required for the preprocessing of the *adf04* file from this source [214]. The strategy adopted here was to "unbundle" the LS data using the program ADAS210 to produce an ic-resolved file. This program requires an ic template file onto whic the LS source file is unbundled, and an *adf04* from the improved baseline dataset described in Chapter 2 was used for this purpose. It is yet another example of how universal baseline data can be useful. As a reminder, the improved baseline *adf04* dataset is generated using AUTOS with the DW approximation for the scattering problem, optimised λ_{nl} to improve the structure, and power-optimised configuration sets. The strict requirements of ADAS210 meant that the ic template file had to be truncated quite severely both in terms of levels and temperatures, and a number of the A-values in the output ic file were set to zero because of LS selection rules. To cope with these limitations, the ic output of ADAS210 was used to supplement the original, improved baseline

adf04 from which the template file was derived. This was achieved with the ADAS IDL routine, `merge_adf04.pro`, and the resulting file had all of the missing A-values recovered and any truncated levels and transitions restored. Therefore, the *adf04* for Ar^{1+} must be interpreted a mix of the baseline and R-matrix with pseudo-states (RMPS) data, and so not of the same quality as the other sources for argon.

With a suitable *ic*-resolved file produced, the complete procedure outlined in the preceding section B.1 can be performed like for all other cases. Because of the importance of neutral and singly ionised species from the perspective of emission in laboratory plasmas, experimental radiative data for these stages is more readily available, and the identification of persistent or dominant lines possible. Hence, A-values from the NIST "Handbook of Basic Atomic Spectroscopic Data" [154] were added manually to the **NMI** file in between Steps 3 and 4.

Ar-like Ar I The complete details of the structure and collision calculation are provided in reference [213], which bases itself on the *LS* RMPS calculation in [216]. For the structure, AUTOS is used with one-body BP operators in the Hamiltonian, and the spectroscopic radial orbitals are calculated using the TFDA potential with scaling parameters. Non-orthogonal, Laguerre pseudo-orbitals were generated for subshells 5d–14g, and these were subsequently orthogonalized amongst themselves and the spectroscopic orbitals. This resulted in a total of 749 states for the target. Favourable comparisons with measured results are achieved: energy levels have an average relative difference of 0.26% and A-values have 12.16% relative to the NIST reference values. Regardless of this fact, subsequent spectra modelling revealed that shifting the energy levels and A-values to the NIST values is necessary, and this has been done in the final *adf04* file. The collision calculation uses the RMPS theory with the code cited above in *ic*. Because of the computational expense of this method, the number of target states included in the CC expansion had to be truncated below the ionisation potential. This resulted in the number of states listed in table B.1.

Appendix C

GCR Theory

The purpose of this appendix is to establish some of the notation and equations pertinent to the theory of GCR modelling used in this thesis. It is intended for the convenience of the familiar reader, not as a complete description of GCR theory. For example, it avoids any serious discussion of time scales, taking as a given that metastable states will dominate the populations of a stage and so must be tracked separately. Rather, the reader is referred to references [15, 16, 60, 217].

Consider an ion, X^{z+}, with metastable populations indexed by the Greek letter ρ, N_ρ^{z+}, and ordinary excited populations indexed by the Roman letter i, N_i^{z+}. The adjacent stage $z+1$ is the *recombining* or *parent* ion with metastables $N_\nu^{(z+1)+}$, while the present stage z is the *ionising* or *daughter* ion. This terminology can be extended to any two adjacent ionisation stages, such as $z-1$ which would be the ionising ion relative to the recombining z ion. The statistical balance equations for the ordinary levels below the continuum, $1 \leq i, j \leq \infty$, with

all processes relevant to optically thin, low-density, thermal plasmas, are

$$\begin{aligned}\frac{\mathrm{d}N_i^{z+}}{\mathrm{d}t} = &\sum_\nu N_\mathrm{e} N_\nu^{(z+1)+} \left(\alpha_i^\mathrm{rr} + \alpha_i^\mathrm{dr} + N_\mathrm{e}\alpha_i^\text{3-b} + \left(\frac{N_\mathrm{H}}{N_\mathrm{e}}\right)\alpha_i^\mathrm{cx}\right) \\ &+ N_j \left[\sum_{j>i} \left(N_\mathrm{e} q_{j\to i}^\mathrm{e} + N_\mathrm{p} q_{j\to i}^\mathrm{p} + A_{j\to i}\right) + \sum_{j<i} \left(N_\mathrm{e} q_{j\to i}^\mathrm{e} + N_\mathrm{p} q_{j\to i}^\mathrm{p}\right)\right] \\ &- N_i \left[\sum_{j>i} \left(N_\mathrm{e} q_{i\to j}^\mathrm{e} + N_\mathrm{p} q_{i\to j}^\mathrm{p}\right) + \sum_{j<i} \left(N_\mathrm{e} q_{i\to j}^\mathrm{e} + N_\mathrm{p} q_{i\to j}^\mathrm{p} + A_{i\to j}\right)\right. \\ &\left. + \sum_\nu \left(N_\mathrm{e} s_{i\to\nu} + A_{i\to\nu}^\mathrm{aut}\right)\right].\end{aligned} \tag{C.1}$$

The recombination rate coefficients, α_i, are distinguished by their superscripts: "rr" is for radiative recombination, "dr" for dielectronic recombination, "3-b" for three-body recombination, and "cx" for charge exchange. In this thesis, the contribution from charge exchange is ignored. The collisional-excitation rate coefficient, $q_{i\to j}$, is included for electron (e) and ion (p) projectiles. Ion projectiles are typically indicated by "i" in other sections of this thesis, but "p" has been used here to avoid confusion with the ordinary level index i. For simplicity, the sum over possible ion projectiles has also been omitted. N_H is the density of hydrogen atoms in the neutral beam, which is ignored going forward. $s_{i\to\nu}$ is the electron-impact ionisation rate coefficient, and $A_{i\to\nu}^\mathrm{aut}$ is the autoionisation rate coefficient.

Evidently, manipulating equation C.1 is tedious, especially since a second set needs to be tracked corresponding to the metastables. Therefore, a matrix representation has been developed with the following *collisional-radiative* matrix elements,

$$C_{ij} = A_{j\to i} + N_\mathrm{e} q_{j\to i}^\mathrm{e} + N_\mathrm{p} q_{j\to i}^\mathrm{p} \tag{C.2}$$

$$-C_{ii} = \sum_{j\neq i} C_{ji} + \sum_\nu s_{i\to\nu} \tag{C.3}$$

$$r_{i\nu} = \alpha_{\nu\to i}^\mathrm{rr} + \alpha_{\nu\to i}^\mathrm{dr} + \alpha_{\nu\to i}^\text{3-b} \tag{C.4}$$

$$S_{\nu i} = N_\mathrm{e} s_{i\to\nu} + A_{i\to\nu}^\mathrm{aut}, \tag{C.5}$$

where C_{ii} is the total loss rate from the level i. Thus, the population equations

of z and its adjacent ionisation stages become

$$\frac{\mathrm{d}}{\mathrm{d}t}\begin{bmatrix} N_\mu^{(z-1)+} \\ N_\rho^{z+} \\ N_i^{z+} \\ N_\nu^{(z+1)+} \end{bmatrix} = \begin{bmatrix} \mathcal{C}_{\mu\mu\prime} & N_\mathrm{e}\mathcal{R}_{\mu\sigma} & 0 & 0 \\ N_\mathrm{e}\mathcal{S}_{\rho\mu\prime} & C_{\rho\sigma} & C_{\rho j} & N_\mathrm{e} r_{\rho\nu\prime} \\ 0 & C_{i\sigma} & C_{ij} & N_\mathrm{e} r_{i\nu\prime} \\ 0 & N_\mathrm{e} S_{\nu\sigma} & N_\mathrm{e} S_{\nu j} & \mathcal{C}_{\nu\nu\prime} \end{bmatrix} \begin{bmatrix} N_{\mu\prime}^{(z-1)+} \\ N_\sigma^{z+} \\ N_j^{z+} \\ N_{\nu\prime}^{(z+1)+} \end{bmatrix} \tag{C.6}$$

Repeated indices imply summation, so $C_{ij}N_j^{z+}$ is its own sub-matrix. Some of the elements are intentionally typeset in different font—e.g. $\mathcal{C}_{\mu\mu\prime}$ is calligraphic versus C_{ij} which is the default math font. The calligraphic font is used to indicate that the influence of the ordinary populations has been *condensed* upon the metastables of the relevant stage. This essential process of *condensation* is now explained.

An assumption of *quasi-static equilibrium* is made which means the ordinary populations are treated as being in instantaneous statistical equilibrium with the relevant metastables of their stage, in turn implying $\mathrm{d}N_i^{z+}/\mathrm{d}t = 0$ in equation C.6. Therefore,

$$\begin{bmatrix} N_{\mu\prime}^{(z-1)+} \\ N_\sigma^{z+} \\ N_j^{z+} \\ N_{\nu\prime}^{(z+1)+} \end{bmatrix} = \begin{bmatrix} 1 & 0 & 0 \\ 0 & 1 & 0 \\ 0 & -C_{ji}^{-1}C_{i\rho} & -N_\mathrm{e}C_{ji}^{-1}r_{i\nu} \\ 0 & 0 & 1 \end{bmatrix} \begin{bmatrix} N_\mu^{(z-1)+} \\ N_\rho^{z+} \\ N_\nu^{(z+1)+} \end{bmatrix}, \tag{C.7}$$

and then

$$\frac{\mathrm{d}}{\mathrm{d}t}\begin{bmatrix} N_\mu^{(z-1)+} \\ N_\rho^{z+} \\ N_\nu^{(z+1)+} \end{bmatrix} = \begin{bmatrix} \mathcal{C}_{\mu\mu\prime} & N_\mathrm{e}\mathcal{R}_{\mu\sigma} & 0 \\ N_\mathrm{e}\mathcal{S}_{\rho\mu\prime} & \mathcal{C}_{\rho\sigma} & N_\mathrm{e}\mathcal{R}_{\rho\nu\prime} \\ 0 & N_\mathrm{e}\mathcal{S}_{\nu\sigma} & \mathcal{C}_{\nu\nu\prime} \end{bmatrix} \begin{bmatrix} N_{\mu\prime}^{(z-1)+} \\ N_\sigma^{z+} \\ N_{\nu\prime}^{(z+1)+} \end{bmatrix}. \tag{C.8}$$

Moreover, the *effective* GCR coefficients can be defined from equation C.8:

$$Q^\mathrm{cd}_{\sigma\to\rho} \equiv \mathcal{C}_{\rho\sigma}/N_\mathrm{e} = \left(C_{\rho\sigma} - C_{\rho j}C_{ji}^{-1}C_{i\sigma}\right)/N_\mathrm{e} \tag{C.9}$$

$$\alpha^\mathrm{cd}_{\nu\prime\to\rho} \equiv \mathcal{R}_{\rho\nu\prime} = r_{\rho\nu\prime} - C_{\rho j}C_{ji}^{-1}r_{i\nu\prime} \tag{C.10}$$

$$S^\mathrm{cd}_{\sigma\to\nu} \equiv \mathcal{S}_{\nu\sigma} = S_{\nu\sigma} - S_{\nu j}C_{ji}^{-1}C_{i\sigma}\,, \tag{C.11}$$

named the effective metastable cross-coupling coefficient, the effective recombination coefficient, and the effective ionisation coefficient, respectively. The superscript "cd" denotes "collisional-dielectronic", which is a historic synonym for "collisional-radiative". This abbreviation is used for ADAS naming conventions of the corresponding *adf11* data: e.g. ACD for α^{cd}. Formally, there is also an addition to the $\mathcal{C}_{\nu\nu\prime}$ element of equation C.8, called the parent metastable cross-coupling coefficient:

$$X^{\mathrm{cd}}_{\nu\prime\to\nu} = -(S_{\nu j} C^{-1}_{ji} r_{i\nu\prime})\,. \tag{C.12}$$

The topic of *projection* is raised in the text. It refers to the procedure of condensing the bundle-n calculation, removing the direct couplings between n states in the low-level set, and then expanding the indirect coupling matrix onto the more highly resolved, low-level manifold. This results in terms added to the CR matrix elements in equations C.2–C.5, but does not change the formalism of the low level population model.

Acronyms and Abbreviations

ADAS Atomic Data Analysis Structure.

AIM Average Ion Model.

ASDEX-U Axially Symmetric Divertor Experiment Upgrade.

AUTOS AUTOSTRUCTURE.

BP Breit-Pauli.

ca configuration average.

CC close-coupling.

CCC convergent close-coupling.

CI configuration interaction.

CIE coronal ionisation equilibrium.

COM centre-of-mass.

COWAN ADAS801, descendant of the Cowan Code.

CR collisional-radiative.

CSD charge state distribution.

CX charge exchange.

DARC Dirac Atomic R-matrix Codes.

DEMO DEMOnstration Power Station.

DI direct ionisation.

DR dielectronic recombination.

DW distorted wave.

EA excitation autoionisation.

EBIT electron-beam ion trap.

ECIP Exchange Classical Impact Parameter.

EIE electron-impact excitation.

FAC Flexible Atomic Code.

GCR generalised collisional-radiative.

GRASP^0 General-purpose Relativistic Atomic Structure Package.

HF Hartree-Fock.

HULLAC Hebrew University Lawerence Livermore Atomic Code.

ic intermediate coupling.

ICFT intermediate coupling frame transformation.

IIE ion-impact excitation.

ITER International Thermonuclear Experimental Reactor.

JET Joint European Torus.

LS Russell-Saunders coupling of total angular momentum, L, and total spin, S.

LTE local thermodynamic equilibrium.

MCDF multiconfigurational Dirac-Fock.

MCF magnetic confinement fusion.

MCHF multiconfigurational Hartree-Fock.

NIST National Institute of Standards and Technology.

PFC plasma-facing component.

PWB plane-wave Born.

Q-CC quantal, close-coupled.

RMPS R-matrix with pseudo-states.

RR radiative recombination.

ry Rydberg n-shell.

SC-1 semi-classical, first-order perturbative.

SC-CC semi-classical, close-coupled.

SCF self-consistent field.

STO Slater-Type Orbital.

TDCC time-dependent, close-coupling.

TFDA Thomas-Fermi-Dirac-Amaldi.

Symbols

$\alpha^{\mathbf{cd}}_{\nu l \to \rho}$ Effective recombination coefficient.

$A_{j \to i}$ Einstien A coefficient, also commonly referred to as the A-value, transition probability, or spontaneous emission rate (s^{-1}).

ΔE_{ij} Atomic transition energy from level j to i (Ryd).

$\frac{\mathbf{d}f_{E2}}{\mathbf{d}\Omega}(\theta, \xi)$ Differential excitation cross section function of multipole order $E2$.

$f_{E2}(\xi)$ excitation cross section function, $f_{E2}(\xi) = \int \mathrm{d}f_{E2}/\mathrm{d}\Omega$.

f_{ij} Oscillator strength (dimensionless).

$\mathcal{F}$-$\mathcal{PEC}$ Feature photon emissivity coefficient (photons cm^3 s^{-1}).

I_H Ionisation potential of Hydrogen (Ryd).

$\chi^{(z)}$ Ionisation potential (eV or Ryd).

λ_{nl} radial scaling parameters.

M Reduced mass of the scattering system (au).

m_p Projectile mass (au).

m_t Target mass (au).

ω_i Statistical weight of lower atomic level, i; equal to $2J_i + 1$.

ω_j Statistical weight of upper atomic level, j; equal to $2J_j + 1$.

Ω_{ij} Collision strength (dimensionless).

$\mathcal{PEC}$ Photon emissivity coefficient (photons cm^3 s^{-1}).

$\mathcal{P}^{(z)}_{\mathbf{LT},\sigma}$ Total radiated line power coefficient (W cm^3).

$\mathcal{P}^{(z)}_{\mathbf{RB},\sigma}$ Recombination-bremsstrahlung-cascade radiated power coefficient.

$\mathcal{P}_{\mathbf{tot}}$ total radiated power function.

$Q^{\mathbf{cd}}_{\sigma\to\rho}$ Effective metastable cross-coupling coefficient.

$q_{i\to j}$ Excitation rate coefficient (cm^3 s^{-1}).

r_0 Effective target radius cutoff (a_0).

$S^{\mathbf{cd}}_{\sigma\to\nu}$ Effective ionisation coefficient.

S_{ij} Atomic line strength (au).

Υ_{ij} Maxwell-averaged effective collision strength (dimensionless).

$V_{\mathbf{TFDA}}$ the TFDA atomic potential.

ξ Dimensionless adiabaticity parameter.

z Effective ion charge = Z_0 − (# of electrons).

Z_0 Nuclear charge = atomic number.

z_p Projectile charge number.

z_t Target charge number.

Bibliography

[1] Bolt H, Barabash V, Krauss W, Linke J, Neu R et al. 2004 *J. Nucl. Mater.* **329-333** 66–73

[2] Federici G, Skinner C, and Brooks J 2001 *Nucl. Fusion* **1967**

[3] Pitts R A, Carpentier S, Escourbiac F, Hirai T, Komarov V et al. 2013 *J. Nucl. Mater.* **438** S48–S56

[4] Aymar R 2001 *Summary of the ITER Final Design Report Technical report* ITER URL `http://scholar.google.com/scholar?hl=en&btnG=Search&q=intitle:Summary+of+the+ITER+Final+Design+Report#3`

[5] Aymar R 2002 *Plasma Phys. Control. Fusion* **44** 519–565

[6] Matthews G 2013 *J. Nucl. Mater.* **438** S2–S10

[7] Brezinsek S 2015 *J. Nucl. Mater.* **463** 11–21

[8] Neu R, Asmussen K, Krieger K, Thoma A, Bosch H S et al. 1996 *Plasma Phys. Control. Fusion* **38(12A)** A165

[9] Neu R, Kallenbach A, Balden M, Bobkov V, Coenen J et al. 2013 *J Nucl Mater* **438** S34–S41

[10] Kallenbach A, Neu R, Dux R, Fahrbach H U, Fuchs J C et al. 2005 *Plasma Phys. Control. Fusion* **47(12B)** B207

[11] ITER Physics Expert Group on Divertors, ITER Physics Expert Group on Divertor Modelling and Database, and ITER Physics Basis Editors 1999 *Nucl. Fusion* **39(12)** 2391–2469

[12] Kallenbach A, Balden M, Dux R, Eich T, Giroud C et al. 2011 *J. Nucl. Mater.* **415(1, Supplement)** S19–S26

[13] Kallenbach A, Bernert M, Dux R, Casali L, Eich T et al. 2013 *Plasma Phys. Control. Fusion* **55(12)** 124041

[14] Federici G, Kemp R, Ward D, Bachmann C, Franke T et al. 2014 *Fusion Eng. Des.* **89(7)** 882–889

[15] Summers H 2004 "ADAS User Manual, v2.6" URL `http://www.adas.ac.uk/manual.php`

[16] Summers H P, Dickson W J, O'Mullane M G, Badnell N R, Whiteford a D et al. 2006 *Plasma Phys Control Fusion* **48(2)** 263–293

[17] Hummer D G, Berrington K A, Eissner W, Pradhan A K, Saraph H E et al. 1993 *Astron. Astrophys.* **279** 298–309

[18] Seaton M J 1987 *J. Phys. B At. Mol. Phys.* **20(23)** 6363

[19] Berrington K A, Burke P G, Butler K, Seaton M J, Storey P J et al. 1987 *J. Phys. B At. Mol. Phys.* **20(23)** 6379

[20] The ADAS Project 2013 "ADAS-EU: About ADAS-EU" URL `http://www.adas-fusion.eu/`

[21] Henderson S S, Bluteau M, Foster A, Giunta A, O'Mullane M G et al. 2017 *Plasma Phys. Control. Fusion* **59(5)** 055010

[22] Whiteford A 2004 *On the Spectral Emission of Impurity Species for Diagnostic Application to Magnetically Confined Fusion Plasmas* PhD University of Strathclyde Glasgow URL `http://www.adas.ac.uk/theses/whiteford_thesis.pdf`

[23] Foster A 2008 *On the Behaviour and Radiating Properties of Heavy Elements in Fusion Plasmas* PhD University of Strathclyde Glasgow URL `http://www.adas.ac.uk/theses/foster_thesis.pdf`

[24] Summers H, Foster A, Loch S, O'Mullane M, and Whiteford A 2010 *PUBL3: Heavy Species in Fusion Plasma Modelling and Spectral Analysis Technical Report ADAS-EU R(10)PU03* ADAS URL `http://www.adas-fusion.eu/reports/publ_3.pdf`

[25] Badnell N R 2011 *Comput Phys Commun* **182(7)** 1528–1535

[26] Eissner W and Nussbaumer H 1969 *J. Phys. B At. Mol. Phys.* **2(10)** 1028

[27] Eissner W, Jones M, and Nussbaumer H 1974 *Comput. Phys. Commun.* **8(4)** 270–306

[28] Badnell N R 1997 *J Phys B Mol Opt Phys* **30(1)** 1–11

[29] Badnell N R 2014 "AUTOSTRUCTURE" URL `http://amdpp.phys.strath.ac.uk/autos/`

[30] Cowan R D 1967 *Phys. Rev.* **163(1)** 54–61

[31] Cowan R D 1981 *The Theory of Atomic Structure and Spectra* University of California Press

[32] Gombás P 1956 in "Atoms II / Atome II," Number 7 / 36 in Encyclopedia of Physics / Handbuch der Physik Springer Berlin Heidelberg 109–231 URL `http://link.springer.com/chapter/10.1007/978-3-642-85687-7_2`

[33] Mott N F M and Massey H S W 1965 *The Theory of Atomic Collisions* Oxford University Press, London 3rd edition

[34] Seaton M J 1953 *Philos. Trans. R. Soc. Lond. Math. Phys. Eng. Sci.* **245(901)** 469–499

[35] Burke P G 2011 *R-Matrix Theory of Atomic Collisions* Springer

[36] Kohn W 1948 *Phys. Rev.* **74(12)** 1763–1772

[37] Jones M 1975 *Philos. Trans. R. Soc. Lond. Math. Phys. Eng. Sci.* **277(1273)** 587–622

[38] Lux H, Kemp R, Ward D J, and Sertoli M 2015 *Fusion Eng. Des.* **101** 42–51

[39] Pitts R A, Kukushkin A, Loarte A, Martin A, Merola M et al. 2009 *Phys. Scr.* **2009(T138)** 014001

[40] Pitts R A, Carpentier S, Escourbiac F, Hirai T, Komarov V et al. 2011 *J. Nucl. Mater.* **415(1)** S957–S964

[41] Pütterich T, Neu R, Dux R, Whiteford A D, O'Mullane M G et al. 2008 *Plasma Phys. Control. Fusion* **50(8)** 085016

[42] Pütterich T, Neu R, Dux R, Whiteford A D, O'Mullane M G et al. 2010 *Nucl. Fusion* **50(2)** 025012

[43] Bluteau M M, Mullane M G O, and Badnell N R 2015 *J. Phys. B At. Mol. Opt. Phys.* **48(19)** 195701

[44] Pütterich T, Neu R, Dux R, Whiteford A D, O'Mullane M G et al. 2010 *Nucl. Fusion* **50(2)** 025012

[45] Kasen D, Badnell N R, and Barnes J 2013 *Astrophys. J.* **774(1)** 25

[46] Witthoeft M C, Whiteford A D, and Badnell N R 2007 *J. Phys. B At. Mol. Opt. Phys.* **40(15)** 2969

[47] Liang G Y and Badnell N R 2010 *Astron. Astrophys.* **518** A64

[48] Liang G Y, Badnell N R, and Zhao G 2012 *Astron. Astrophys.* **547** A87

[49] Fernández-Menchero L, Zanna G D, and Badnell N R 2014 *Astron. Astrophys.* **566** A104

[50] Fernández-Menchero L, Zanna G D, and Badnell N R 2014 *Astron. Astrophys.* **572** A115

[51] Palmeri P, Quinet P, Wyart J F, and Émile Biémont 2000 *Phys. Scr.* **61(3)** 323

[52] Grant I P 1974 *J. Phys. B At. Mol. Phys.* **7(12)** 1458

[53] Grant I 2007 *Relativistic Quantum Theory of Atoms and Molecules: Theory and Computation* Springer

[54] Starace A F 1971 *Phys. Rev. A* **3(4)** 1242–1245

[55] Starace A F 1973 *Phys. Rev. A* **8(2)** 1141–1142

[56] Grant I P and Starace A F 1975 *J. Phys. B At. Mol. Phys.* **8(12)** 1999

[57] Kobe D H 1979 *Phys. Rev. A* **19(1)** 205

[58] Hata J and Grant I P 1981 *J. Phys. B At. Mol. Phys.* **14(13)** 2111

[59] Kramida A, Ralchenko Y, Reader J, and NIST ASD Team 2015 "NIST Atomic Spectra Database (Ver. 5.3), [Online]" URL `https://www.nist.gov/pml/atomic-spectra-database`

[60] Giunta A 2011 *Spectral Analysis of the Solar Atmosphere at the Chromosphere-Corona Boundary* PhD University of Strathclyde Glasgow URL `http://www.adas.ac.uk/theses/giunta_thesis.pdf`

[61] Zanna G D and Badnell N R 2014 *Astron. Astrophys.* **570** A56

[62] Pütterich T, Neu R, Dux R, Whiteford A D, O'Mullane M G et al. 2008 *Plasma Phys. Control. Fusion* **50(8)** 085016

[63] Shumack A E 2014 in "20th Top. Conf. High-Temperature Plasma Diagnostics," Atlanta

[64] Kramida A and Shirai T 2009 *At. Data Nucl. Data Tables* **95(3)** 305–474

[65] Kramida A 2011 *Can. J. Phys.* **89(5)** 551–570

[66] Clementson J, Beiersdorfer P, Brown G V, and Gu M F 2010 *Phys Scr* **81(015301)** 1–8

[67] Neill P, Harris C, Safronova A S, Hamasha S, Hansen S et al. 2004 *Can J Phys* **82(11)** 931–942

[68] Fournier K 1998 *Data Nucl Data Tables* **68(1)** 1–48

[69] Spencer S, Hibbert A, and Ramsbottom C A 2014 *J. Phys. B At. Mol. Opt. Phys.* **47(24)** 245001

[70] Robicheaux F, Gorczyca T W, Pindzola M S, and Badnell N R 1995 *Phys. Rev. A* **52(2)** 1319–1333

[71] Ballance C P and Griffin D C 2007 *J Phys B Mol Opt Phys* **40(2)** 247–258

[72] Das T, Sharma L, and Srivastava R 2012 *Phys Scr* **86(3)** 035301

[73] Grant I, McKenzie B, Norrington P, Mayers D, and Pyper N 1980 *Comput Phys Commun* **21(2)** 207–231

[74] McKenzie B, Grant I, and Norrington P 1980 *Comput Phys Commun* **21(2)** 233–246

[75] Dyall K, Grant I, Johnson C, Parpia F, and Plummer E 1989 *Comput Phys Commun* **55(3)** 425–456

[76] Norrington P 2009 "GRASP0 and DARC Repository" URL `http://web.am.qub.ac.uk/DARC/`

[77] Badnell N R, Foster A, Griffin D C, Kilbane D, O'Mullane M et al. 2011 *J. Phys. B At. Mol. Opt. Phys.* **44(13)** 135201

[78] Bauche J and Bauche-Arnoult C 1987 *J Phys B Mol Phys* **20** 1443–1450

[79] Mitnik D M, Griffin D C, and Badnell N R 2001 *J. Phys. B At. Mol. Opt. Phys.* **34(22)** 4455–4473

[80] Mitnik D M, Griffin D C, Ballance C P, and Badnell N R 2003 *J. Phys. B At. Mol. Opt. Phys.* **36(4)** 717–730

[81] Ballance C P and Griffin D C 2004 *J Phys B Mol Opt Phys* **37(14)** 2943–2957

[82] Ballance C P and Griffin D C 2006 *J Phys B Mol Opt Phys* **39(17)** 3617–3628

[83] Seaton M 1983 *Rep. Prog Phys* **167**

[84] Burgess A and Tully J A 1992 *Astron. Astrophys.* **254** 436

[85] Safronova U I and Safronova A S 2010 *J Phys B Mol Opt Phys* **43(7)** 074026

[86] Ballance C P 2014 "Private Communication"

[87] Dufton P L and Kingston A E 1982 in D B a B Bederson (ed.) "Advances in Atomic and Molecular Physics," volume 17 Academic Press 355–418 URL `http://www.sciencedirect.com/science/article/pii/S006521990860072X`

[88] Alder K and Winther A 1966 in "Coulomb Excitation; a Collection of Reprints.", Academic Press, New York 1–9

[89] Seaton M J 1962 *Proc. Phys. Soc.* **79(6)** 1105

[90] Seaton M J 1964 *Mon. Not. R. Astron. Soc.* **127** 191

[91] Alder K, Bohr A, Huus T, Mottelson B, and Winther A 1956 *Rev. Mod. Phys.* **28(4)** 432–542

[92] Burgess A and Tully J A 2005 *J Phys B Mol Opt Phys* **38(15)** 2629–2644

[93] Bely O and Faucher P 1970 *Astron Astrophys*

[94] van Regemorter H 1960 *Mon. Not. R. Astron. Soc.* **121** 213

[95] Landman D A 1973 *Sol. Phys.* **30(2)** 371–380

[96] Masnou-Seeuws F 1974 *Astronomy and Astrophysics* **32** 229

[97] Sahal-Brechot S 1974 *Astron. Astrophys.* **32** 147

[98] Kastner S O 1977 *Astron. Astrophys.* **54** 255–261

[99] Kastner S O and Bhatia A K 1979 *Astron. Astrophys.* **71** 211–213

[100] Bhatia A K and Mason H E 1980 *Astron. Astrophys.* **83** 380–382

[101] Bhatia A K, Feldman U, and Doschek G A 1980 *J. Appl. Phys.* **51(3)** 1464–1480

[102] Reid R H G 1989 in D B a B Bederson (ed.) "Advances in Atomic and Molecular Physics," volume 25 Academic Press 251–266 URL `http://www.sciencedirect.com/science/article/pii/S0065219908600895`

[103] Walling R S and Weisheit J C 1988 *Phys. Rep.* **162(1)** 1–43

[104] Winther A and De Boer J 1966 in A Winther and K Alder (eds.) "Coulomb Excitation; a Collection of Reprints.", Academic Press, New York originial work published 1965-11-18

[105] Bahcall J N and Wolf R A 1968 *Astrophys. J.* **152** 701

[106] Masnou-Seeuws F and McCarroll R 1972 *Astron. Astrophys.* **17** 441

[107] Landman D A 1975 *Astron. Astrophys.* **43** 285–290

[108] Reid R H G and Schwarz J H 1969 236 URL `http://adsabs.harvard.edu/abs/1969peac.conf..236R`

[109] Doyle J G, Kingston A E, and Reid R H 1980 *Astron. Astrophys.* **90** 97–101

[110] Doyle J G 1987 *At. Data Nucl. Data Tables* **37(3)** 441–453

[111] Keenan F P and Reid R H G 1987 *J. Phys. B At. Mol. Phys.* **20(22)** L753

[112] Keenan F P and Reid R H G 1989 *Phys. Scr.* **39(3)** 314

[113] Faucher P and Landman D A 1977 *Astron. Astrophys.* **54** 159–161

[114] Heil T G, Kirby K, and Dalgarno A 1983 *Phys. Rev. A* **27(6)** 2826–2830

[115] Keenan F P and Reid R H G 1989 *J. Phys. B At. Mol. Opt. Phys.* **22(11)** L295

[116] Foster V, Keenan F P, and Reid R 1994 *Phys. Rev. A* **49(4)** 3092–3095

[117] Foster V J, Keenan F P, and Reid R H G 1994 *At. Data Nucl. Data Tables* **58(2)** 227–244

[118] Foster V J, Keenan F P, and Reid R H G 1997 *At. Data Nucl. Data Tables* **67(1)** 99–177

[119] Ryans R S I, Foster-Woods V J, Copeland F, Keenan F P, Matthews A et al. 1998 *At. Data Nucl. Data Tables* **70(2)** 179–229

[120] Ryans R S I, Foster-Woods V J, Keenan F P, and Reid R H G 1999 *At. Data Nucl. Data Tables* **73(1)** 1–42

[121] Landman D A 1973 *Sol. Phys.* **31(1)** 81–89

[122] Landman D A 1978 *Astrophys. J.* **220** 366–369

[123] Landman D A and Brown T 1979 *Astrophys. J.* **232** 636–648

[124] Landman D A 1980 *Astrophys. J.* **240** 709–717

[125] Faucher P 1975 *J. Phys. B: At. Mol. Phys.* **8(11)** 1886

[126] Heil T G, Green S, and Dalgarno A 1982 *Phys. Rev. A* **26(6)** 3293–3298

[127] Kramida A, Ralchenko Y, Reader J, and NIST ASD Team 2018 "NIST Atomic Spectra Database (Ver. 5.5.2), [Online]" URL `https://www.nist.gov/pml/atomic-spectra-database`

[128] Clementi E and Roetti C 1974 *At. Data Nucl. Data Tables* **14(3)** 177–478

[129] Huang K N 1986 *At. Data Nucl. Data Tables* **34(1)** 1–77

[130] Moehs D P and Church D A 1999 *Astrophys. J. Lett.* **516(2)** L111

[131] Aggarwal K M and Keenan F P 2014 *Mon. Not. R. Astron. Soc.* **445(2)** 2015–2027

[132] Born M and Fock V 1928 *Z. Physik* **51(3-4)** 165–180

[133] Griffiths D J 2005 *Introduction to Quantum Mechanics* Pearson, Prentice Hall, Upper Saddle River, NJ 2nd ed. edition

[134] Guzmán F, Badnell N R, Williams R J R, Hoof V, M P A et al. 2017 *Mon. Not. R. Astron. Soc.* **464(1)** 312–320

[135] Guzmán F, Badnell N R, Williams R J R, van Hoof P a M, Chatzikos M et al. 2016 *Mon. Not. R. Astron. Soc.* **459(4)** 3498–3504

[136] Pengelly R M and Seaton M J 1964 *Mon. Not. R. Astron. Soc.* **127(2)** 165–175

[137] Mattioli M, Fournier K B, Carraro L, Coffey I, Giroud C et al. 2001 *J. Phys. B At. Mol. Opt. Phys.* **34(2)** 127

[138] Puiatti M E, Mattioli M, Telesca G, Valisa M, Coffey I et al. 2002 *Plasma Phys. Control. Fusion* **44(9)** 1863

[139] Rapp J, Monier-Garbet P, Matthews G F, Sartori R, Andrew P et al. 2004 *Nucl. Fusion* **44(2)** 312

[140] Fludra A, Griffin D, Caldwell M, Eccleston P, Cornaby J et al. 2013 in "Solar Physics and Space Weather Instrumentation V," volume 8862 International Society for Optics and Photonics 88620F doi:10.1117/12.2027581

[141] Giunta A 2017 "Atomic Data for Solar Orbiter/SPICE: Solar Spectrum and Ground Calibration" ADAS Workshop Presentation

[142] Summers H P and Hooper M B 1983 *Plasma Phys.* **25(12)** 1311

[143] Burgess A and Chidichimo M C 1983 *Mon. Not. R. Astron. Soc.* **203(4)** 1269–1280

[144] Burgess A and Summers H P 1976 *Mon. Not. R. Astr. Soc.* **174** 345–391

[145] Badnell N R, O'Mullane M G, Summers H P, Altun Z, Bautista M A et al. 2003 *Astron. Astrophys.* **406(3)** 1151–1165

[146] Saloman E B 2010 *J. Phys. Chem. Ref. Data* **39(3)** 033101

[147] Ludlow J A, Ballance C P, Loch S D, and Pindzola M S 2010 *J. Phys. B At. Mol. Opt. Phys.* **43(7)** 074029

[148] Whiteford A D, Badnell N R, Ballance C P, O'Mullane M G, Summers H P et al. 2001 *J. Phys. B At. Mol. Opt. Phys.* **34(15)** 3179

[149] Liang G Y and Badnell N R 2011 *Astron. Astrophys.* **528** A69

[150] Liang G Y, Whiteford A D, and Badnell N R 2009 *Astron. Astrophys.* **500(3)** 1263–1269

[151] Munoz Burgos J M, Loch S D, Ballance C P, and Boivin R F 2009 *Astron. Astrophys.* **500(3)** 1253–1261

[152] Griffin D C, Ballance C P, Loch S D, and Pindzola M S 2007 *J. Phys. B At. Mol. Opt. Phys.* **40(23)** 4537

[153] Arnold N I, Loch S, Ballance C, and Thomas E 2015 BP12.084 URL `http://adsabs.harvard.edu/abs/2015APS..DPPB12084A`

[154] Sansonetti J, Martin W, and Quantum Measurement Division, PML 2017 "NIST Handbook of Basic Atomic Spectroscopic Data" URL `https://www.nist.gov/pml/handbook-basic-atomic-spectroscopic-data`

[155] Dolder K T and Peart B 1976 *Rep. Prog. Phys.* **39(8)** 693

[156] Taylor P O, Gregory D, Dunn G H, Phaneuf R A, and Crandall D H 1977 *Phys. Rev. Lett.* **39(20)** 1256–1259

[157] Boland B C, Jahoda F C, Jones T J L, and McWhirter R W P 1970 *J. Phys. B At. Mol. Phys.* **3(8)** 1134

[158] Griffin D C, Badnell N R, and Pindzola M S 1998 *J. Phys. B At. Mol. Opt. Phys.* **31(16)** 3713

[159] Dere K P 2007 *Astron. Astrophys.* **466(2)** 771–792

[160] Gu M F 2008 *Can. J. Phys.* **86(5)** 675–689

[161] Badnell N R, O'Mullane M G, Summers H P, Altun Z, Bautista M A et al. 2003 *Astron. Astrophys.* **406(3)** 1151–1165

[162] Preval S P, Badnell N R, and O'Mullane M G 2016 *Phys. Rev. A* **93(4)** 042703

[163] Badnell N R 2006 *Astron. Astrophys.* **447(1)** 389–395

[164] Bautista M A and Badnell N R 2007 *Astron. Astrophys.* **466(2)** 755–762

[165] Colgan J, Pindzola M S, and Badnell N R 2004 *Astron. Astrophys.* **417(3)** 1183–1188

[166] Colgan J, Pindzola M S, Whiteford A D, and Badnell N R 2003 *Astron. Astrophys.* **412(2)** 597–601

[167] Altun Z, Yumak A, Badnell N R, Colgan J, and Pindzola M S 2004 *Astron. Astrophys.* **420(2)** 775–781

[168] Zatsarinny O, Gorczyca T W, Korista K T, Badnell N R, and Savin D W 2004 *Astron. Astrophys.* **417(3)** 1173–1181

[169] Mitnik D M and Badnell N R 2004 *Astron. Astrophys.* **425(3)** 1153–1159

[170] Zatsarinny O, Gorczyca T W, Korista K T, Badnell N R, and Savin D W 2003 *Astron. Astrophys.* **412(2)** 587–595

[171] Zatsarinny O, Gorczyca T W, Fu J, Korista K T, Badnell N R et al. 2006 *Astron. Astrophys.* **447(1)** 379–387

[172] Zatsarinny O, Gorczyca T W, Korista K, Badnell N R, and Savin D W 2004 *Astron. Astrophys.* **426(2)** 699–705

[173] Altun Z, Yumak A, Badnell N R, Loch S D, and Pindzola M S 2006 *Astron. Astrophys.* **447(3)** 1165–1174

[174] Altun Z, Yumak A, Yavuz I, Badnell N R, Loch S D et al. 2007 *Astron. Astrophys.* **474(3)** 1051–1059

[175] Abdel-Naby S A, Nikolić D, Gorczyca T W, Korista K T, and Badnell N R 2012 *Astron. Astrophys.* **537** A40

[176] Kaur J, Gorczyca T W, and Badnell N R 2017 *Astron. Astrophys.* Forthcoming article

[177] Arnold I, Thomas E, Loch S D, Abdel-Naby S, and Ballance C P 2015 *J. Phys. B At. Mol. Opt. Phys.* **48(17)** 175005

[178] Mazzotta P, Mazzitelli G, Colafrancesco S, and Vittorio N 1998 *Astron. Astrophys. Suppl. Ser.* **133(3)** 403–409

[179] Arnaud M and Rothenflug R 1985 *Astron. Astrophys. Suppl. Ser.* **60** 425–457

[180] Shull J M and van Steenberg M 1982 *Astrophys. J. Suppl. Ser.* **48** 95–107

[181] Jacobs V L, Davis J, Kepple P C, and Blaha M 1977 *Astrophys. J.* **211** 605–616

[182] Burgess A 1965 *Astrophys. J.* **141** 1588–1590

[183] Younger S M 1981 *J. Quant. Spectrosc. Radiat. Transf.* **26(4)** 329–337

[184] Lotz W 1968 *Z. Physik* **216(3)** 241–247

[185] Sutherland R S and Dopita M A 1993 *Astrophys. J. Suppl. Ser.* **88** 253

[186] Loch S D, Abdel-Naby S A, Ballance C P, and Pindzola M S 2007 *Phys. Rev. A* **76(2)** 022706

[187] Fournier K B, Cohen M, May M J, and Goldstein W H 1998 *At. Data Nucl. Data Tables* **70(2)** 231–254

[188] Cohen M, Fournier K B, and Goldstein W H 1998 *Phys. Rev. A* **57(4)** 2651–2671

[189] Bryans P, Landi E, and Savin D W 2009 *Astrophys. J.* **691(2)** 1540

[190] Post D E, Jensen R V, Tarter C B, Grasberger W H, and Lokke W A 1977 *At. Data Nucl. Data Tables* **20(5)** 397–439

[191] Jensen R V, Post D E, Grasberger W H, Tarter C B, and Lokke W A 1977 *Nucl. Fusion* **17(6)** 1187

[192] Chung H K, Chen M H, Morgan W L, Ralchenko Y, and Lee R W 2005 *High Energy Density Phys.* **1(1)** 3–12

[193] Flower D R and Pineau des Forets G 1973 *Astron. Astrophys.* **24** 181

[194] Dufton P L, Berrington K A, Burke P G, and Kingston A E 1978 *Astron. Astrophys.* **62** 111–120

[195] Doschek G A and Feldman U 1976 *J. Appl. Phys.* **47(7)** 3083–3087

[196] Feldman U, Doschek G A, Cheng C C, and Bhatia A K 1980 *J. Appl. Phys.* **51(1)** 190–201

[197] Shevelko V P, Skobelev I Y, and Vinogradov A V 1977 *Phys. Scr.* **16(3-4)** 123

[198] Sato K, Mimura M, Otsuka M, Watari T, Ono M et al. 1986 *Phys. Rev. Lett.* **56(2)** 151–154

[199] Sakaue H A, Yamamoto N, Morita S, Nakamura N, Chen C et al. 2011 *J. Appl. Phys.* **109(7)** 073304

[200] Abramov V A, Gontis V G, and Lisitsa V S 1984 *Sov J Plasma Phys Engl Transl U. S.* **10:2**

[201] Schure K M, Kosenko D, Kaastra J S, Keppens R, and Vink J 2009 *Astron. Astrophys.* **508(2)** 751–757

[202] Bautista M A, Kallman T R, and Pradhan A K 2000 *Atomic Data Needs for X-Ray Astronomy Conference Proceedings NASA/CP-2000-209968, Rept-2000-04370-0, NAS 1.55:209968* NASA Goddard Space Flight Center Greenbelt, MD United States URL `https://ntrs.nasa.gov/search.jsp?R=20000109969`

[203] Gnat O and Ferland G J 2012 *Astrophys. J. Suppl. Ser.* **199(1)** 20

[204] Turkington M 2017 *Heavy Species R-Matrix Calculations in Support of Fusion Diagnostics* PhD Queen's University Belfast Belfast

[205] Turkington M 2018 "Private Communication"

[206] Summers H P 1977 *Mon. Not. R. Astron. Soc.* **178(2)** 101–122

[207] Berrington K A, Eissner W B, and Norrington P H 1995 *Comput. Phys. Commun.* **92(2)** 290–420

[208] Burke V M, Burke P G, and Scott N S 1992 *Comput. Phys. Commun.* **69(1)** 76–98

[209] Mitnik D M, Pindzola M S, Griffin D C, and Badnell N R 1999 *J. Phys. B At. Mol. Opt. Phys.* **32(17)** L479

[210] Gorczyca T W, Pindzola M S, Shieh F S, and McCreary C L 1995 *Comput. Phys. Commun.* **88(2)** 211–216

[211] Robicheaux F, Gorczyca T W, Pindzola M, and Badnell N R 1995 *Phys Rev A* **52(2)** 1319–1333

[212] Gorczyca T W and Badnell N R 1996 *J. Phys. B At. Mol. Opt. Phys.* **29(7)** L283–L290

[213] Arnold N I 2017 *An Investigation into the Role of Metastable States on Excited Populations of Weakly Ionized Argon Plasmas, with Applications for Optical Diagnostics.* PhD Auburn University Auburn, US URL `https://etd.auburn.edu/handle/10415/5798`

[214] Griffin D C, Ballance C P, Loch S D, and Pindzola M S 2007 *J. Phys. B* **48(23)** 4537–4550

[215] Gorczyca T W and Badnell N R 1997 *J. Phys. B At. Mol. Opt. Phys.* **30(17)** 3897

[216] Ballance C P and Griffin D C 2008 *J. Phys. B: At. Mol. Opt. Phys.* **41(6)** 065201

[217] Brooks D H 1997 *On the Radiating and Dynamic Properties of the Solar Upper Atmosphere* PhD University of Strathclyde URL `http://phys.strath.ac.uk/adas/theses/brooks_thesis1.pdf`